N° d'ordre : 189

École Centrale de Lille

THÈSE

présentée en vue
d'obtenir le grade de

Docteur

en

Mécanique

par

Christophe Cuvier

DOCTORAT DELIVRÉ PAR L'ÉCOLE CENTRALE DE LILLE

Titre de la Thèse :

Contrôle actif du décollement d'une couche limite turbulente en gradient de pression adverse

Active control of a separated turbulent boundary layer in adverse pressure gradient

Soutenue le 12 septembre 2012 devant le jury d'examen :

Président du jury,	M. Gérard Bois, Professeur, Arts et Métiers ParisTech, Lille.
Rapporteur,	M. Jean-Paul Bonnet, Directeur de Recherche CNRS, Institut PPRIME, Poitiers.
Rapporteur,	M. Azeddine Kourta, Professeur, Laboratoire PRISME, Orléans.
Examinateur,	M. Bertrand Aupoix, Directeur de Recherche HDR, ONERA, Toulouse.
Directeur de thèse,	M. Michel Stanislas, Professeur, École Centrale de Lille.
Examinateur,	M. Jean-Marc Foucaut, Maître de conférences, École Centrale de Lille.
Invité,	M. Jean-Claude Courty, Ingénieur, Dassault-Aviation, Saint-Cloud.
Invitée,	Mlle. Caroline Braud, Chargé de recherche CNRS, LML, Lille.

Thèse préparée au Laboratoire de Mécanique de Lille

Ecole Doctorale SPI 072 (Lille I, Lille III, Artois, ULCO, UVHC, EC Lille)
PRES Université Lille Nord-de-France

Remerciements

Je tiens tout d'abord à remercier chaleureusement MM. Jean-Paul Bonnet, Azeddine Kourta, Gérard Bois, Bertrand Aupoix et Jean-Claude Courty pour avoir accepté d'être membres du jury. Je tiens à remercier plus particulièrement MM. Jean-Paul Bonnet et Azeddine Kourta pour le temps qu'ils ont consacré à rapporter ce travail.

Ma reconnaissance va aussi à M. Michel Stanislas, mon directeur de thèse, pour m'avoir guidé tout au long de ce travail et pour m'avoir fait profiter de ses connaissances en turbulence. Ses remarques, toujours pertinentes, ont grandement contribué à l'avancement de ce travail.

Ma gratitude va aussi à M. Jean-Marc Foucaut, mon co-encadrant, pour le temps qu'il m'a consacré pour mener à bien les mesures au fil chaud et par PIV ainsi que pour la résolution des divers problèmes rencontrés. Je le remercie aussi pour ses explications claires et toujours données dans la bonne humeur.

Je remercie aussi Mlle Caroline Braud, ma co-encadrante, pour les discussions sur la partie "contrôle d'écoulements" du travail et pour m'avoir épaulé sur le dimensionnement du circuit d'air comprimé alimentant les jets.

Ma reconnaissance va également à M. Sébastien Coudert pour le temps passé en ma compagnie dans la soufflerie pour le réglage de la nappe laser. Sans lui, il m'aurait aussi été très difficile d'implémenter les logiciels en C++ utilisés pour le traitement PIV.

Je remercie aussi tous les membres de l'équipe ER2 du labo qui m'ont accueilli à bras ouverts et qui ont largement contribué à me donner de bonnes conditions de travail. Bien entendu, je n'oublie pas les personnes de l'ENSAM de Lille qui m'ont à leur tour chaleureusement accueilli pour la quatrième année.

Ma reconnaissance va aussi à toutes les personnes du laboratoire de fabrication de Centrale pour la multitude de pièces qu'ils ont réalisées pendant ces quatre ans.

Je remercie aussi tout particulièrement ma femme Delphine pour m'avoir toujours supporté même dans les moments de doute.

Finalement, ma reconnaissance va aussi à mes parents pour m'avoir permis de poursuivre mes études dans de très bonnes conditions.

Résumé

Le contrôle d'écoulement permet d'éliminer le phénomène de décollement de couches limites, très néfaste pour les performances des machines interagissant avec un fluide (avions, voitures, turbomachines ...). Ces travaux s'intéressent plus particulièrement au contrôle actif d'écoulement au moyen de jets continus. Une maquette permettant de manipuler l'équilibre de la couche limite a été conçue et installée dans la soufflerie du Laboratoire de Mécanique de Lille. La première partie du travail a consisté en la caractérisation de l'écoulement autour du modèle à l'aide de visualisations par fils de laine et par enduit gras, de mesures de répartition de pression, de mesures par anémométrie à fils chauds et par PIV. Ceci a permis de définir la configuration du modèle la plus appropriée pour les études de contrôle mais aussi de connaître précisément les caractéristiques de l'écoulement sélectionné. La configuration retenue correspond à un écoulement en gradient de pression adverse suivi d'une séparation sur le volet, un peu comme sur l'extrados d'une aile d'avion. L'utilisation de sondes de frottement associées à des visualisations aux fils de laine ont permis d'étudier et d'optimiser des actionneurs passifs, puis des actionneurs à jets continus. Certaines des configurations actives optimales ont ensuite été caractérisées plus en détail par une mesure par PIV englobant toute la zone de séparation. Il apparaît que les jets continus ne suppriment pas complètement les mécanismes de la séparation mais réduisent leur intensité et les concentrent plus ou moins près de la paroi.

Abstract

Flow control allows to suppress boundary layers separation, which largely deteriorates the performances of machineries which interact with fluid (aircraft, cars, turbomachineries, etc.). This study concentrates more particularly on active flow control with continuous jets. A ramp model which allows to manipulate the boundary layer equilibrium was realized and set in Laboratoire de Mécanique de Lille wind tunnel. The first part of the work was to characterize the flow over the model with wool-tufts and oil-film visualisations, pressure distribution, hot-wire anemometry and PIV measurements. The aim was to define a ramp configuration for the flow control study and to know precisely the characteristics of the retained flow. The selected configuration corresponds to an adverse pressure gradient flow followed by a separation on the flap, which mimics the flow on the suction side of a wing. With friction probes coupled with wool-tufts visualisations, passive actuators and active continuous jets were studied and optimised. Finally, some of the optimum active configurations found were characterized in more details with PIV measurements over the entire separated region. It appears that continuous jets do not suppress the separation mechanisms, but only reduce their intensity and squeeze them more or less against the wall.

Contents

List of Figures

List of Tables

Nomenclature

Reference frame

O	Origin, fixed at the ramp apex and at the middle of the wind tunnel;
X	Streamwise coordinate, attached to the lower wall of the wind tunnel;
Y	Wall-normal coordinate of the wind tunnel;
Z	Spanwise coordinate of the wind tunnel;
s	Curvilinear abscissa of the ramp, origin at O;
x_1, x	Wall-parallel coordinate of the local Frenet reference frame at s;
y_1, y	Wall-normal coordinate of the local Frenet reference frame at s;
z_1, z	Spanwise coordinate of the local Frenet reference frame at s;
t	Time;

Flow

P	Pressure;
T	Temperature;
ρ	Mass density;
μ	Dynamic viscosity;
ν	Kinematic viscosity;
f	Frequency;
u_1, u_2, u_3	Streamwise, wall-normal, spanwise instantaneous velocity component in (x, y, z) reference frame;
u, v, w	Streamwise, wall-normal, spanwise instantaneous velocity component in (x, y, z) reference frame;
U_1, U_2, U_3	Streamwise, wall-normal, spanwise mean velocity component in (x, y, z) reference frame;
U, V, W	Streamwise, wall-normal, spanwise mean velocity component in (x, y, z) reference frame;
u'_1, u'_2, u'_3	Streamwise, wall-normal, spanwise fluctuating velocity component in (x, y, z) reference frame;
u', v', w'	Streamwise, wall-normal, spanwise fluctuating velocity component in (x, y, z) reference frame;
U_{wt}, V_{wt}, W_{wt}	Streamwise, wall-normal, spanwise mean velocity component in (X, Y, Z) reference frame;

Boundary Layer

δ	Boundary layer thickness;
δ^*	Displacement thickness;
θ	Momentum thickness;
H	Shape factor;
τ, τ_w	Wall shear stress;
u_τ	Friction velocity;
$u_{\tau_{Lud-Till}}$	Ludwieg and Tillmann's friction velocity;
C_f	Friction coefficient;
U_e	Local free-stream velocity;
U_∞	Free-stream velocity upstream the ramp;
U_{ZS}	Zagorala and Smits reference velocity, $\frac{U_e \delta^*}{\delta}$;
Re_θ	Momentum Reynolds number;
C_p	Pressure coefficient;
κ	Von Kàrm'an constant;
C	Log-law constant;
C_2	Modified log-law constant;
$(.)^+$	Wall units (u_τ,ν);
$(.)^*$	External units (U_e,δ);
$\overline{(.)}$	Mean;
X, X_T	Distance from the tripping device;
lm	Mixing length;
Λ	Castillo and George's similarity parameter;
$\beta_{Clauser}$	Pressure gradient Clauser's parameter;
χ	Backflow coefficient;
$-\rho\overline{u_i' u_j'}$	Reynolds stresses ;
Q_1	Event with $u' > 0$ and $v' > 0$;
Q_2	Event with $u' < 0$ and $v' > 0$;
Q_3	Event with $u' < 0$ and $v' < 0$;
Q_4	Event with $u' > 0$ and $v' < 0$;
R	Wall Radius of curvature ;
Λ	Integral time scale;
$S()$	Skewness;
$F()$	Flatness;

Ramp

α	Angle of the flat plate relative to wind tunnel floor;
β	Angle of the flap relative to wind tunnel floor;
H_{step}	Wall-normal coordinate Y of the flap corner;

Particle Image Velocimetry

$f_\#$	Lens aperture;
M	Magnification;
λ	Laser wave length;
px	Pixel;
$2D2C$	Two dimensions, two components;
$2D3C$	Two dimensions, three components;
$3D3C$	Three dimensions, three components;
σ_u	PIV random error on u;
σ_v	PIV random error on v;

Passive actuators

h	Device height;
l	Device length;
β_{pd}	Device angle relative to the flow direction;
λ	Co-rotating devices transverse spacing or counter-rotating actuators pair transverse spacing;
L	Spacing between two devices of a counter-rotating pair;
ΔX_{vg}	Distance between the devices trailing edge and the separation line;

Active actuators

Φ	Jet diameter;
β	Device pitch angle, corresponding to the angle between the jet axis and the wall;
α	Device skew angle, corresponding to the azimuthal angle between the free-stream velocity and the projection of the jets axis on the wall (i.e. in the wall normal direction);
U_j	Mean jet exit velocity;
λ	Co-rotating jets transverse spacing or counter-rotating jets pair transverse spacing;
L	Spacing between two jets of a counter-rotating pair;
ΔX_{vg}	Distance between the jet exit center and the separation line;
VR	Velocity ratio, $VR = \frac{U_j}{U_e}$;
f	Pulsed frequency;
DC	Duty cycle;
Q_m	Mass flow rate;
Q_v	Flow rate;
C_μ	Momentum coefficient;

Abbreviations

TBL	Turbulent Boundary Layer;
ZPG	Zero Pressure Gradient;
FPG	Favourable Pressure Gradient;
APG	Adverse Pressure Gradient;
FP	Flat Plate;
2D	Two dimensional;
3D	Three dimensional;
LSS	Low Speed Streak;
HSS	High Speed Streak;
PIV	Particle Image Velocimetry;
LMR	Low Momentum Region;
ID	Incipient Detachment;
ITD	Intermittent Transitory Detachment;
TD	Transitory Detachment;
D	Detachment;
VG	Vortex Generator;
HW	Hot-Wire;
Pi	Friction Probe number i;
co-up	Co-rotating upstream blowing configuration;
counter-up	Counter-rotating upstream blowing configuration;
counter-down	Counter-rotating downstream blowing configuration;

Others

σ	Standard deviation;
s	Estimation of the standard deviation;
T_{aq}	Hot-wire acquisition time;
N_{sample}	Number of uncorrelated hot-wire samples;
R_{uu}	Correlation coefficient of u' by u';
R_{vv}	Correlation coefficient of v' by v';

General introduction

Since the wheel was invented, men have never stop to invent vehicles and to improve their performances. At the beginning, aerodynamic was not important as the velocities reached were really moderate (for example the first car which in 1885 was able to run a hundred kilometers : the "Tricycle Teo" reached only 15 km/h) and vehicles were only terrestrial ones. Rapidly, with the progress of technology, aerodynamic has become an important and unavoidable task for the conception of all transport vehicles. In 1909, Gustave Eiffel created the first wind tunnel which is still today a common tool used for aerodynamics researches. Nowadays, vehicles are so complex that it is quite difficult to improve them even slightly. However, two principal ways of research persist. The first one being to reduce the fuel consumption and second one to improve their safety. Reducing fuel consumption is an important challenge due to the decrease and the possible disappearance of world oil reserve. Moreover, preserving the environment with less greenhouse gas emissions is also important so that life can still be present on earth in the future. Improving vehicles safety has always been important but it can conduct to an increase of weight and so of fuel consumption. The two main routes of improvement for vehicles performances are tightly linked which complexifies the task.

For all bodies in motion in a fluid, boundary layers develop along the walls. These boundary layers generally encounter at a moment or another an adverse pressure gradient region or a sudden discontinuity in curvature which can lead to flow detachment. Flow separation has drastic consequences on vehicles and turbomachineries performances. It increases the drag and so the fuel consumption, can cause loss of control of an aircraft, can create undesirable noise and structure vibrations, etc.. In a way of improving the performances and safeness of all the machineries that interact with fluids (aircraft, turbomachineries, cars, etc.), preventing and/or controlling turbulent boundary layer separation seems to be a crucial point that has to be solved.

Since the beginning of the 1990s, the experiments concerning flow separation control have increased exponentially (Lin et al. (1990, 1991), Lin (1999), Selby et al. (1992), McManus et al. (1994), Godard and Stanislas (2006a,b), etc.). The principal aim of these numerous studies was to optimise actuators allowing to reach flow reattachment. The first vortex generators tested were passive ones, but they were rapidly replaced by active jets as they can be turned off when unnecessary to avoid additional drag. However, for both types of actuators, the flow where they were embedded was found to influence the optimum parameters. Besides, too few studies exist concerning the controlled flow organisation, probably due to the small scales of the considered flows which are difficult to resolve.

The present work proposes to investigate active control strategies of a separated turbulent boundary layer subjected to adverse pressure gradient. Tanks to the large scale provided by the LML wind-tunnel, particular attention will be given to the flow characteristics with and without control. This work follows the ones previously realised by Godard and Stanislas (2006a) and Godard and Stanislas (2006b) on a flow with adverse pressure gradient but without separation. The present study will try to gain insight into the flow reorganisation performed by active control.

This work was partly integrated in the AVERT EC project (Contract No AST5-CT-2006-030914) which has financed the ramp model and the compressed air circuit. The main results of the AVERT contract report (Cuvier et al. (2010)) were presented in 2011 at the TSFP7 conference in Ottawa, Canada. The two submitted papers (Cuvier et al. (2011a) and Cuvier et al. (2011b)) are given in Appendix H.

Chapter 1

Literature review

1 Introduction

When a fluid passes over a solid surface, very near to it, due to the viscosity of the fluid, there is a small region where the velocity of the fluid is smaller than the velocity far away from the surface as the velocity is zero at the surface. This low speed region is known as "boundary layer". Prandtl (1904) was the first one to introduce this concept of boundary layer where the viscosity play an important role.

Blasius (1908) has given the description of the profile of a laminar, two-dimensional flat plate boundary layer, however, when the surface where the boundary layer develops is long enough, or if the external velocity high enough, a critical Reynolds number is reached where the boundary layer transitions to a turbulent state. Turbulent boundary layers are more complex and are not today completely understood.

As in all fluid mechanic applications, turbulent boundary layers are encountered and play an important role in the performances, since Prandtl, many researchers have spent their life to study boundary layers, trying to explain the mechanisms involved in near wall turbulence. The next sections will try to summarized the present understanding of turbulent boundary layers (TBL).

2 The turbulent boundary layer

2.1 The turbulent boundary layer without pressure gradient

2.1.1 Generality

As the turbulent boundary layer is very complex, the major part of the studies is based on two-dimensions TBL without pressure gradient to simplify the problem. Obtaining a strictly zero pressure gradient (ZPG) boundary layer is nearly impossible, and many studies are under slightly favourable pressure gradient (FPG), small enough for its effects to be neglected. The main set-up is the boundary layer that develop along a flat plate. This flat plate (FP) boundary layer gives a two-dimensional canonical BL.

The equations that governed the evolution of a incompressible boundary layer are the Navier-Stokes equations for an incompressible flow (1.1), where u_i is the

instantaneous velocity in the x_i direction of the (x, y, z) = $(x_i)_{i=1,2,3}$ reference frame. The Reynolds decomposition ($u_i = U_i + u_i'$, where U_i is the mean value of $u_i = u_i(t)$, i.e. $U_i = \overline{u_i}$, and u_i' is the fluctuating part of u_i) is commonly introduced in the Navier-Stokes equations to obtain the Reynolds average equations (1.2) :

$$\begin{cases} \dfrac{\partial u_i}{\partial x_i} & = 0 \\ \rho(\dfrac{\partial u_i}{\partial t} + u_j \dfrac{\partial u_i}{\partial x_j}) & = -\dfrac{\partial p}{\partial x_i} + \mu \dfrac{\partial^2 u_i}{\partial {x_j}^2} \end{cases} \tag{1.1}$$

$$\begin{cases} \dfrac{\partial U_i}{\partial x_i} & = 0 \\ \rho(\dfrac{\partial U_i}{\partial t} + U_j \dfrac{\partial U_i}{\partial x_j}) & = -\dfrac{\partial P}{\partial x_i} + \mu \dfrac{\partial^2 U_i}{\partial {x_j}^2} - \rho \dfrac{\partial \overline{u_i' u_j'}}{\partial x_j} \end{cases} \tag{1.2}$$

The description of a stationary 2D flat plate boundary layer is given in Figure 1.1. When this kind of boundary layer becomes turbulent and fully develop (i.e. at the position X, where the Reynolds number ($R_e = \frac{XU_\infty}{\nu}$) reached a value greater than about 5.10^5), the characteristic length scale along y, the wall normal axis, is much smaller than the characteristic length scale along x, the streamwise direction (i.e. $\delta << X$, with δ the boundary layer thickness (see Figure 1.1), defined by the distance y from the wall where the velocity reaches 99% of the free-stream velocity U_∞). By adding to this hypothesis, the 2D and stationary nature of the flow, equation (1.2) can be reduced to (1.3) (with $u = u_1$, $v = u_2$, $x = x_1$ and $y = x_2$), by taking into account the order of magnitude of each terms in equation (1.2).

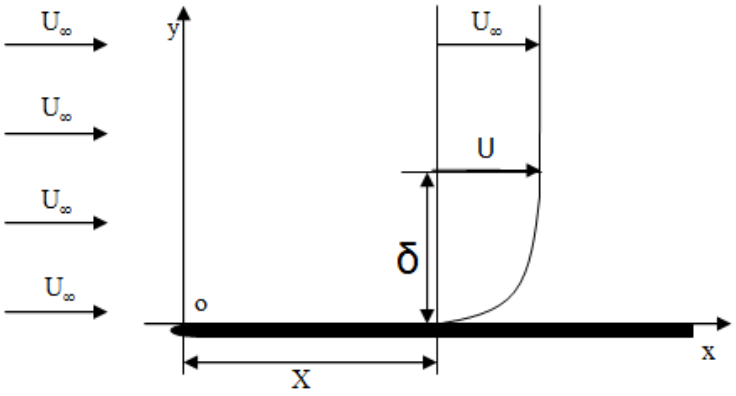

Figure 1.1: Scheme for a two-dimensions flat plate boundary layer.

$$\begin{cases} \dfrac{\partial U}{\partial x} + \dfrac{\partial V}{\partial y} & = 0 \\ \rho(U\dfrac{\partial U}{\partial x} + V\dfrac{\partial U}{\partial y}) & = -\dfrac{\partial P}{\partial x} + \mu\dfrac{\partial^2 U}{\partial y^2} - \rho\dfrac{\partial \overline{u'v'}}{\partial y} \\ \dfrac{\partial P}{\partial y} + \rho\dfrac{\partial \overline{v'^2}}{\partial y} & = 0 \end{cases} \tag{1.3}$$

The ZPG equation is obtained by putting $\frac{\partial P}{\partial x} = 0$ in (1.3). As in all turbulence problems, equation (1.3) cannot be solved due to the unknown Reynolds stress term $-\rho\frac{\partial \overline{u'v'}}{\partial y}$. The boundary layer is then usually divided into two regions : an inner region near the wall, and an outer region above. This two regions will be described in the following sections.

2.1.2 The inner region

2.1.2.1 Basic equations

This near wall region is defined by a characteristic length scale (L_y) along y largely smaller than the typical characteristic length scale along y of the whole boundary layer (i.e. $L_y << \delta$). A value of $L_y = 0.1\delta$ is now well accepted (George (2006),George (2007), Zagorala and Smits (1998b), etc.). The convective terms on the left-hand side of the momentum equation of ZPG turbulent boundary layer (1.3) are then negligible compared to the viscous term. The equation reduces to equation (1.4). By integrating it, and taking into account the wall boundary condition, equation (1.5) is obtained for the inner part, with $u_\tau = \sqrt{\frac{\tau_{y=0}}{\rho}}$. By looking at equation (1.5), the mean velocity U can be only a function of y, u_τ, ρ and μ (equation (1.6)). Based on similarity, equation (1.6) leads to equation (1.7) for the whole inner region, with $U^+ = \dfrac{U}{u_\tau}$ and $y^+ = \frac{yu_\tau}{\nu}$. This means that in the inner region, u_τ should be the velocity scale, $\frac{\nu}{u_\tau}$ the length scale, and $\frac{\nu}{u_\tau^2}$ the time scale.

$$\mu\frac{\partial^2 U}{\partial y^2} - \rho\frac{\partial \overline{u'v'}}{\partial y} = \frac{\partial}{\partial y}(\mu\frac{\partial U}{\partial y} - \rho\overline{u'v'}) = \frac{\partial \tau}{\partial y} = 0 \tag{1.4}$$

$$\tau = \mu\frac{\partial U}{\partial y} - \rho\overline{u'v'} = \tau_{y=0} = \rho u_\tau^2 \tag{1.5}$$

$$U = f(y, u_\tau, \rho, \mu) \tag{1.6}$$

$$U^+ = f(y^+) \tag{1.7}$$

Very near the wall, $\rho\overline{u'v'}$ becomes negligible compare to the viscous terms. This region is call "viscous sublayer", and its extent commonly accepted is between 3 to 5 wall units (i.e. $y^+ \leq 3 - 5$). Equation (1.5) leads then in this region to a linear relation between U^+ and y^+ : $U^+ = y^+$. Nickels (2004) gave a slightly modified law with a Taylor expansion near $y^+ = 0$. Very near the wall, the viscous

sublayer law and Nickels (2004)'s law superimpose, but the law defined by Nickels (2004) leads to an other definition for the size of this viscous sublayer. For him, the viscous sublayer size is about 12 wall units, which corresponds to the position of the peak of turbulent kinetic energy production. With his new definition for the size of the viscous sublayer, he build a new empirical model for the entire profile of the boundary layer, with and without pressure gradient, that will not be discuss here, but shows that the mean velocity profile remains an open question, especially in the region above the viscous sublayer as will be see below.

Above the viscous sublayer, there is a region where the turbulent shear stress $\rho\overline{u'v'}$ becomes predominant compared to the viscous term. Equation (1.8) is then obtained. Prandtl (1926, 1932) and Von-Kármán (1930) modelled the turbulent shear stress by an eddies viscosity argument, and, by integration, they obtained a log-law for the mean profile. The eddies argument leads to equation (1.9). Prandtl (1926, 1932) modelled the eddies viscosity μ_t by $\rho l_m^2 \frac{\partial U}{\partial y}$, where l_m is the mixing length. This model is commonly called "mixing length theory". l_m was also specified as $l_m = \kappa y$, where κ is the Von Kármán constant. Equations (1.8) and (1.9) and the mixing length theory, leads to equation (1.10) that can be integrated to give the standard log-law equation (1.11).

$$-\rho\overline{u'v'} = \rho u_\tau^2 \tag{1.8}$$

$$-\rho\overline{u'v'} = \mu_t \frac{\partial U}{\partial y} \tag{1.9}$$

$$\kappa^2 y^2 \left(\frac{\partial U}{\partial y}\right)^2 = u_\tau^2 \tag{1.10}$$

$$U^+ = \frac{1}{\kappa} \ln y^+ + C \tag{1.11}$$

This part of the inner region where the turbulent shear stress becomes predominant compared to the viscous stress is usually called "log-layer". Its extent is commonly between $y^+ \geq 30$ - 50 and $y \leq 0.1\delta$. Presently, this law is put in question. George and Castillo (1997), George (2006, 2007) propose a power-law. They give two arguments for that. First, there is no reliable theory for the log-law, and secondly, it seems that there is two different velocity scales for the inner (u_τ) and outer region (U_e, with U_e the local free-stream velocity) that leads to an impossibility of a log-law (George (2006)). Moreover, according to George (2006), in the region $30 \leq y^+ \leq 300$, the viscous effects seem to remain non negligible even if they can be neglected in the inner equation. This region is called "meso layer", and seems to break the argument that leads to the log-law in that region. The universality of this log-law is also contested as values for κ vary between 0.38 and 0.45 (0.38 corresponds to the value claimed by Österlund (2000) for ZPG boundary layers at high Reynolds numbers, and 0.45 corresponds to the value observed in super-pipe flows by Zagorala and Smits (1998a). The most common value used for ZPG boundary layers is $\kappa = 0.41$), and values for C vary between 4 and 10 (George (2007)), with the most common value of $C = 5.0$. According to George (2007), the

main reason of the strong persistence of the log-law is that many researchers used the Clauser's chart method (Clauser (1956)) to determine u_τ by fitting the log-law on the mean streamwise velocity profile, and by doing that, their profiles exhibit an imposed log-law region, even if this log region does not exist.

Buschmann and Gad-El-Hak (2003) have shown however that these two laws (log-law and power-law) do not contradict as they do not represent the same region of the boundary layers. They found that the log-law begin after $y^+ = 30$, then this log-law is followed by a power-law.

Between the viscous sublayer region and the log region (i.e. $3-5 \leq y^+ \leq 30-50$) there is a transitional region called "buffer layer". For this region, there is no available explicit form of the solution of equation (1.7) for the mean velocity profile. Only, the semi-explicit form of equation (1.7) for the whole inner region of a ZPG boundary layer given by Van-Driest (1956) (equation (1.12)) is available for this region. Equation (1.12) expresses the law of the wall (i.e. linear function in the viscous sublayer plus log-law above) in only one function.

$$\begin{cases} U^+ = \displaystyle\int_0^{y^+} \frac{2dy^+}{1+\sqrt{1+4.a(y^+)}} \\ \\ a(y^+) = [\kappa y^+(1-exp(-\frac{y^+}{c^+})]^2 \\ \\ c^+ = 26 \end{cases} \tag{1.12}$$

2.1.2.2 The structural organisation

The inner region is characterized by a strong turbulent activity. Although the turbulence seems to be a random process, it has been showed that the inner turbulence is well organised with coherent structures (Kline et al. (1967), Kim et al. (1971), Stanislas et al. (2008), etc.). The coherent structures are more dense in the viscous sublayer and in the buffer layer, and are responsible of the major part of production of turbulent kinetic energy in these regions (Robinson (1991)). The "streaky" structures (defined by region of low or high momentum fluid compared to the local mean velocity) were first evidenced by Kline et al. (1967) and Kim et al. (1971) using hydrogen bubble visualisations. They are mostly under $y^+ \leq 30$ and are elongated in the steamwise direction (Blackwelder and Kovasznay (1972), Lagraa et al. (2004), Lin (2006), etc.).

The streaky structures are classified into two categories, the low speed streaks (LSS) and high speed streaks (HSS). Recently, detail characteristics of these HSS and LSS structures where obtained by Lin (2006). He applied pattern recognition techniques to velocity fields parallel to the wall obtained by Particle Image Velocimetry (PIV) at different y^+. He found that the width of LSS is around 31^+ for y^+ under 30, and increases with y^+ for $y^+ \geq 30$. The width of HSS was found slightly larger with a width between 42^+ and 47^+. The spacing between two streaks in the spanwise direction z was found to be between 114^+ and 135^+ and increases with y^+. The length of the streaks in the streamwise direction was estimated between 500^+ and 2000^+ by Carlier and Stanislas (2005). This length is difficult to obtain as it

requires very long PIV fields along the streamwise direction. However, Zhou and Lu (1997), using the hydrodynamic stability theory with a resonant triad (three waves considered with the wave number of one being the sum of the wave numbers of the two others : spatial resonance), found a streamwise length for the streaks of 800^+, coherent with the estimation of Carlier and Stanislas (2005).

Around this streaky structures near the wall, ejections and sweeps are observed (Robinson (1991), Lin (2006), etc.). Ejection corresponds to an outward motion of low streamwise momentum fluid and sweep corresponds to an inward motion of high streamwise momentum fluid. In the quadrant-splitting scheme introduced by Wallace et al. (1972), sweeps are associated with Q_4 events ($u' > 0$ and $v' < 0$) and ejections to Q_2 events ($u' < 0$ and $v' > 0$)(Robinson (1991)). These structures were also characterized in detail by Lin (2006). He found that the sweeps are located very near the wall. Their width was found between 20^+ and 30^+, their length about 90^+, and the transverse spacing between two sweeps between 118^+ and 128^+. Concerning the ejections, he found that there is a concentration peak of ejections at $y^+ = 22$. Their width was found between 18^+ and 24^+, their length about 92^+ near the wall and 107^+ away from the wall with a peak value of 117^+ for $22 \leq y^+ \leq 33$, and the transverse spacing between two ejections was found to be the same as for the sweeps.

Streamwise elongated vortices were also observed in the inner region by many researchers (Robinson (1991), Zhou et al. (1996), Adrian et al. (2000), Lin (2006), etc.). Lin (2006) found a concentration peak of streamwise vortices at $y^+ = 22$. He found also that a positive streamwise vortex ($\omega_x > 0$, where ω_x is the vorticity around x-axis) is very often associated with a negative streamwise vortex with a spanwise separation between 39^+ and 55^+. Their length was found by Lin (2006) to be around 96^+ and their width around 16^+. Schoppa and Hussain (2000) have shown a strong relation between streamwise vortices and streaks. Indeed, they have shown that a streak can generate a streamwise vortex and they have also shown that streamwise vortices generate low momentum regions. Finally, they concluded that, maybe, through an instability, the streaks generate streamwise vortices to survive.

Hairpin vortices or horseshoes vortices were also observed by Robinson (1991), Adrian et al. (2000), Stanislas et al. (2008), etc.. The legs of an hairpin structure are seen as two counter-rotating streamwise vortices connected by a head corresponding to a spanwise rotating vortex. The most probable hairpin structure was found to be an asymmetric one-legged hairpin vortex (Robinson (1991), Stanislas et al. (2008)). Adrian et al. (2000) have shown that hairpin vortices are organized in packets which induce low speed regions aligned in the streamwise direction. They proposed an organisational model for boundary layer given in Figure 1.2, that is now well accepted.

2.1.3 The outer region

2.1.3.1 Basic equations

The outer region is above $y = 0.1\delta$ (George (2006)), with δ the boundary layer thickness, which is well accepted as characteristic length scale (George (2006, 2007)). A deficit law is commonly used to describe the mean velocity profile which takes the

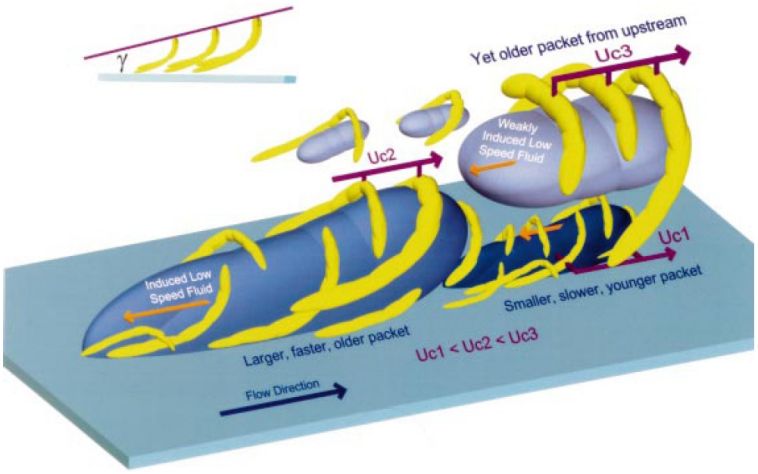

Figure 1.2: Conceptual organisational model of the boundary layer proposed by Adrian et al. (2000).

form of equation (1.13), where U_{ref} is the characteristic velocity scale. "A deficit form is used to remove the influences of what happens near the wall in the viscous layer" (George (2006)).

$$\frac{U_e - U}{U_{ref}} = f(\frac{y}{\delta}) \tag{1.13}$$

Since Von-Kármán (1930), the velocity scale characteristic of the outer part is the friction velocity ($U_{ref} = u_\tau$). The function f in equation (1.13) was then specified by Millikan (1938) with an overlap argument of the inner law (equation (1.7)) and the outer law (equation (1.13)). This argument supposes that there is a region, defined by $y^+ \to \infty$ and $y^* = \frac{y}{\delta} \to 0$, where the two laws apply. This region exists only if the Reynolds number $\delta^+ = \frac{\delta u_\tau}{\nu} \to \infty$ (i.e. the inner length scale $\frac{\nu}{u_\tau}$ has to be big and the outer length scale δ also). If the inner law is written: $U^+ = f_1(y^+)$ and the outer law: $U_e^+ - U^+ = f_2(y^*)$, with $y^* = \frac{y}{\delta}$, in the overlap region, the continuity of the velocity gradient leads to equation (1.14).

$$-y^* \frac{df_2(y^*)}{dy^*} = y^+ \frac{df_1(y^+)}{dy^+} \tag{1.14}$$

Integrating equation (1.14) leads to the log-law (equation (1.11)) for f_1 in the inner region, and to equation (1.15) for f_2, with B a constant. The continuity of the velocity in the overlap region leads to equation (1.16), which gives a relation between B, C, U_e, u_τ and δ. By supposing the existence of a log-law, Coles (1956) extended the validity of the law of the wall (equation (1.5)) up to $y^* = 1$, by adding a wake function to the log-law. The general form of Coles law is given in equation (1.17), where Π is the wake parameter and ω the wake function, normalised by $\omega(1) = 2$. The compatibility of Coles law (1.17) and the outer deficit law (1.15) gives $\Pi = \frac{B.\kappa}{2}$. From the tabulated values of $\omega(y^*)$ given by Coles (1956), the best suited wake function is given in equation (1.18). The Π parameter is very sensitive to external conditions (Gad-El-Hak and Bandyopadhyay (1994)). Coles (1956) give a

value around 0.55 for constant pressure gradient boundary layers and Carlier (2001), Carlier and Stanislas (2005) found it constant and about 0.4 for $Re_\theta > 11500$.

$$U_e^+ - U^+ = -\frac{1}{\kappa}\ln y^* + B \tag{1.15}$$

$$U_e^+ = \frac{1}{\kappa}\ln \delta^+ + B + C \tag{1.16}$$

$$U^+ = \frac{1}{\kappa}\ln y^+ + C + \frac{\Pi}{\kappa}\omega(y^*) \tag{1.17}$$

$$\omega(y^*) = 2.\sin^2(\frac{\pi}{2}y^*) \tag{1.18}$$

Nowadays, the use of u_τ as velocity scale for the outer region is more and more controversial (George and Castillo (1997), George (2006), Zagorala and Smits (1998a,b), etc.). George and Castillo (1997), through a new asymptotic invariant principle, arrived to the conclusion that U_e, the local free-stream velocity, is the appropriated outer length scale for the mean streamwise velocity at infinite Reynolds number. Townsend (1956) arrived to the same conclusion, but maybe this was forgotten until George and Castillo (1997). According to George and Castillo (1997), the appropriated outer defect form is then given by equation (1.13), with $U_{ref} = U_e$. They show that this defect form gives better scaling than the standard outer defect form, but the result is not perfect. Zagorala and Smits (1998a,b) proposed an other outer velocity scale : $U_{ZS} = \frac{U_e\delta^*}{\delta}$, with δ^* the displacement thickness. This outer scaling was found to give better results than the one of George and Castillo (1997) (Maciel et al. (2006)). Castillo and Walker (2002), Maciel et al. (2006), George (2006) explain that the Zagorala Smits scaling gives a Reynolds number correction to the scaling proposed by George and Castillo (1997). To date, no better scaling was found, even if, the Zagorala Smits scaling was found to fail in some circumstances (Maciel et al. (2006)). So the appropriated description of the outer mean velocity profile remains an open question.

2.1.3.2 The structural organisation

The outer part of a boundary layer is less subject to turbulence kinetic energy production, so one could supposes that no structure are present in this region. However two major kind of structures are observed. The first one is an hairpin like structure (Adrian et al. (2000), Lee and Sung (2009)). The hairpin structures in the outer region was first observed by Brown and Thomas (1977) using two-points cross-correlation from hot-wire measurements in the boundary layer. They called the observed structure "horseshoe" vortex, however the shape is similar to the hairpin vortex. They found that the length of these horseshoe structures can reach 2δ in length, and they have an oblique angle of 18° relative to the wall.

The outer hairpin structures look like the ones in the inner region but with a much bigger size. From a PIV (Particle Image Velocimetry) analysis of a ZPG boundary layer, Adrian et al. (2000) characterized carefully these structures. They found that the hairpin vortices are organized in packets of more than 10. Moreover, they found also that the hairpin vortices of a packet evolved in the boundary layer

with the same convection speed (between $0.8U$ and $0.9U$, where U is the mean streamwise velocity at the considered position y in the outer region). According to Adrian et al. (2000), the size of the hairpin packet in the outer region is in the order of the boundary layer thickness δ. The packet length was found between 0.8δ and 2.3δ, with an average length at 1.3δ, and the height between 0.2δ and 0.4δ. The hairpin packets were found also to grow upward in the streamwise direction at a mean angle of 12°.

Adrian et al. (2000) have shown also that the hairpin packets induce regions of low momentum fluid. These "super streaky structures" were also observed and characterised by Lee and Sung (2009). Lee and Sung (2009) found that, at the bottom of the outer part (i.e. at $\frac{y}{\delta} \simeq 0.2$), these low momentum regions (LMRs) can reach a length of more than 4δ and a width of about 0.4δ. The mean length of LMRs in this region was found to be between 0.7δ and 0.8δ, and the width was found to be between 0.2δ and 0.3δ. In the middle of the outer region, the LMR events were found more difficult to evidence, because the larger hairpin packets in this region induce weaker and less pronounced low speed momentum regions (Adrian et al. (2000)).

The complete organisation of the whole boundary layer is then described by the conceptual organisation model proposed by Adrian et al. (2000) (Figure 1.2). This model exhibits small packets of hairpin vortices of small size in the inner region linked with the low speed streaks, and larger packets of hairpin vortices of larger size in the outer region associated with large low speed momentum regions.

2.2 The turbulent boundary layer with pressure gradient

2.2.1 Introduction

In almost all real applications (aircraft, turbo-machinery, etc.), the boundary layer is subjected to pressure gradients. The next two subsections will describe the main differences induced by a pressure gradient in the turbulent boundary layer (i.e. the term $\frac{\partial P}{\partial x}$ is now non zero in equations (1.3) and (1.4)). For boundary layers with pressure gradient, the inner region is governed by equation (1.19). Integrating equation (1.19) with the wall condition leads to equation (1.20). The viscous sublayer equation (1.21) is obtained by integrating equation (1.20) after neglected the turbulent shear stress near the wall. It shows that the effect of the pressure gradient on the mean profile begins very close to the wall as the term $\frac{1}{2}\frac{\partial P}{\partial x}^{+} y^{+^2}$ (with $\frac{\partial P}{\partial x}^{+}$ defined by equation (1.22)) is quadratic in y^+. Above the sublayer, it is compulsory to take into account the pressure gradient in the description of the mean profile. As the effects of $\frac{\partial P}{\partial x} > 0$ and $\frac{\partial P}{\partial x} < 0$ are opposite (Zhou and Lu (1997)), the two will be discussed separately.

$$\frac{\partial P}{\partial x} = \mu \frac{\partial^2 U}{\partial y^2} - \rho \frac{\partial \overline{u'v'}}{\partial y} = \frac{\partial}{\partial y}(\mu \frac{\partial U}{\partial y} - \rho \overline{u'v'}) = \frac{\partial \tau}{\partial y} \tag{1.19}$$

$$\tau = \mu \frac{\partial U}{\partial y} - \rho \overline{u'v'} = \frac{\partial P}{\partial x} y + \rho u_\tau^2 \tag{1.20}$$

$$U^+ = \frac{1}{2}\frac{\partial P^+}{\partial x}\, y^{+^2} + y^+ \tag{1.21}$$

$$\frac{\partial P^+}{\partial x} = \frac{\nu}{\rho u_\tau^3}\frac{\partial P}{\partial x} \tag{1.22}$$

2.2.2 Effects of favourable pressure gradient

2.2.2.1 Generality

Favourable Pressure Gradient (FPG) is defined by $\frac{\partial P}{\partial x} < 0$. It is encountered when the free-stream flow accelerates. This is the case for example on the pressure side of a wing or at the beginning of the suction side, where the shape of the wing imposes a converging shape of the streamlines. The favourable pressure gradient inhibits the genesis of coherent structures (Fernholz and Warnack (1998), Zhou and Lu (1997), Dixit and Ramesh (2008), etc.), that inhibits the production of turbulent kinetic energy. When the FPG is strong enough, turbulence can become inactive and the streamwise mean velocity profile looks like a laminar one. In this case, it is said that the strong FPG has led to relaminarization.

2.2.2.2 Mean Profile

Strong departures from the standard log-law (equation (1.11)), described in Section 2.1.2.1 are observed in FPG (Spalart (1986), Fernholz and Warnack (1998), Dixit and Ramesh (2008, 2009), Nickels (2004), etc.). The possible universality of the log-law in ZPG boundary layer is then broken in strong FPG. To compensate the departure from the standard log-law, some authors have suggested that the Von Kármán constant κ and the constant C of the standard log-law are in reality function of the dimensionless pressure gradient parameter $\frac{\partial P}{\partial x}^+$ defined by (1.22). Nickels (2004) proposed equation (1.23) for the variation of κ with $\frac{\partial P}{\partial x}^+$, for $\frac{\partial P}{\partial x}^+$ between -0.02 and 0.06, and where y_c^+ is the sublayer size in wall units and $\kappa_0 = 0.39$. y_c^+ is obtained by solving equation (1.24), where R_c is the sublayer critical Reynolds number which is equal to 12.

$$\frac{1}{\kappa} = \frac{1}{\kappa_0}\sqrt{1 + \frac{\partial P^+}{\partial x}\, y_c^+} \tag{1.23}$$

$$\frac{\partial P^+}{\partial x}\, y_c^{+^3} + y_c^{+^2} - R_c = 0 \tag{1.24}$$

Dixit and Ramesh (2009), for equilibrium boundary layer in pressure gradient (i.e. where the production of turbulent kinetic energy is balanced by the dissipation as defined by Townsend (1961)) gave the variation of κ (equation (1.25)) and C (equation (1.26)) of the log-law equation (1.11) with $\frac{\partial P}{\partial x}^+$ for $\frac{\partial P}{\partial x}^+$ between -0.03 and 0.04. Their results are in good agreement with the Nickels equation (1.23) only in the FPG part.

$$\frac{1}{\kappa} = 2.452 + 19.534\frac{\partial P^+}{\partial x} + 113.08\left(\frac{\partial P^+}{\partial x}\right)^2 \tag{1.25}$$

$$C = 5.3048 - 185.82\frac{\partial P^+}{\partial x} + 1033.2\left(\frac{\partial P^+}{\partial x}\right)^2 + 25172\left(\frac{\partial P^+}{\partial x}\right)^3 \tag{1.26}$$

In strong FPG (i.e. when $|\frac{\partial P^+}{\partial x}|$ is greater than 0.005), the mean velocity profile is strongly affected and determining the friction velocity u_τ with a Clauser's chart method is controversial. However, Fernholz and Warnack (1998) have shown that, in small FPG, and when the boundary layer is near equilibrium as defined by Townsend (1961), a standard log-law is observed with $\kappa = 0.4$ and $C = 5.1$.

As far as the outer part is concerned, there is no accepted equation for FPG boundary layers. Castillo and George (2001), based on similarity analysis propose that, for FPG boundary layers in equilibrium (i.e. $\Lambda = -1.92$, with Λ defined by (1.27)) and at infinite Reynolds numbers, the outer profile should be self similar in the outer deficit form given by equation (1.13), still with the outer velocity scale $U_{ref} = U_e$. However, for finite Reynolds numbers, the Zagorala scaling ($U_{ref} = U_{ZS} = \frac{U_e\delta^*}{\delta}$) was found more adapted (Maciel et al. (2006)).

$$\Lambda = \frac{\delta}{\rho U_e^2 \frac{d\delta}{dx}} \frac{dP}{dx} \tag{1.27}$$

2.2.2.3 Structural Organisation

As the FPG decreases the boundary layer thickness δ and increases the friction velocity u_τ (that leads to a decrease of the shape factor $H = \frac{\delta^*}{\theta}$, with θ the momentum thickness), only few studies exist on the characterisation of the turbulence structures of FPG boundary layers, as it is more difficult to resolved the structures in a more confined region. However, Zhou and Lu (1997) have noticed that the FPG leads to elongate the streaks in the streamwise direction, but there was no effect on the spacing between streaks in the spanwise direction. They found that the length of the streaks is about 950^+ in FPG ($\beta_{clauser} = \frac{\delta^*}{\rho u_\tau^2}\frac{\partial P}{\partial x} = -0.34$) compared to 800^+ in ZPG, and the spanwise spacing between two streaks is about 100^+, which corresponds to the value in ZPG.

2.2.3 Effects of adverse pressure gradient

2.2.3.1 Generality

Adverse Pressure Gradient (APG) is defined by $\frac{\partial P}{\partial x} > 0$. It is encountered when the free-stream decelerates. This is the case for example on the suction side of a wing, where the shape of the profile forces the streamlines to diverge, just after the converging part, near the leading edge. It has been observed that, contrary to FPG, the Adverse Pressure Gradient tends to enhance the production of turbulence (Krogstad and Skåre (1995)).

2.2.3.2 Mean profile

Controversies exist on the description of the mean profile of a boundary layer in APG, as a strong departure from the standard log-law (1.11) is observed, even for small APG (i.e. $0 < \frac{\partial P^+}{\partial x} < 0.005$). Moreover, the "controversial log region" have

been found to shrink (Webster et al. (1996), Bernard et al. (2003), Aubertine and Eaton (2005), Angele and Muhammad-Klingmann (2006), Dixit and Ramesh (2009), etc.), as the wake region increases with the strength of the APG. It seems that the upper part of the inner region cannot be described by a standard log-law, or even, by a none universal one. However, the combined studies of Bernard et al. (2003) and Pailhas et al. (2009) on APG boundary layers, have shown that the estimations of u_τ, with a Clauser's chart method in the small region where a log-law seems to exist, are in good agreement with the direct measurement with a oil droplet interferometric method. Maybe a smaller log-law region could exit.

As for FPG, Dixit and Ramesh (2009) proposed that the constants κ and C of the log-law are pressure gradient dependent. The explicit form of the variation of κ and C with the pressure gradient are given in equations (1.25) and (1.26). With these new expressions and with the Clauser's chart method they succeed to reduce the uncertainty on the determination of the friction velocity to $\pm 3\%$ compared to the $\pm 10 - 15\%$ uncertainty given by the classical Clauser's chart method.

Skote (2001), Skote and Henningson (2002), with a similarity analysis of the total shear stress τ in the inner and outer regions, and with a similar overlap argument as Millikan (1938), proposed equation (1.28) for the log region in APG, with $\kappa = 0.41$, the Von Kármán constant and C the same constant as in the log-law. Equation (1.28) was also obtained by Afzal (1996) and it is similar to the equation obtained by Townsend (1961) from a mixing length argument. When the pressure gradient is zero, equation (1.28) leads to equation (1.11), the standard log-law equation. Skote (2001), Skote and Henningson (2002) found that equation (1.28) gives a better description of the profiles than the log-law, but with C set to 1.5.

$$U^+ = \frac{1}{\kappa}(\ln y^+ - 2\ln\frac{\sqrt{1+\frac{\partial P^+}{\partial x}y^+}+1}{2} + 2(\sqrt{1+\frac{\partial P^+}{\partial x}y^+}-1)) + C \qquad (1.28)$$

Bernard et al. (2003), based on the mixing length theory ($l_m = \kappa y$) to model the Reynolds shear stress $\rho\overline{u'v'}$, integrated equation (1.20) and obtained equation (1.29), very similar to the Skote's equation (1.28). Bernard et al. (2003) took $\kappa = 0.41$ and found also that equation (1.29) gives a better agreement with the profiles than the log-law in APG, but they found that C was not a constant and was pressure gradient dependent.

$$U^+ = \frac{2}{\kappa}[\sqrt{1+\frac{\partial P^+}{\partial x}y^+} - arcth\left(\frac{1}{\sqrt{1+\frac{\partial P^+}{\partial x}y^+}}\right)] + C \qquad (1.29)$$

To explain the pressure gradient dependences of the constant C found by Bernard et al. (2003), equation (1.29) can be rewritten as equation (1.30), with C_2, a constant that can be different from C. As at the beginning of the inner fully turbulent region ($y^+ \simeq 30$) a log-law is observed (Webster et al. (1996), Bernard et al. (2003), Aubertine and Eaton (2005), Angele and Muhammad-Klingmann (2006), Dixit and Ramesh (2009), etc.), equation (1.30) should be identified to equation (1.11) of the log-law in this region. In this near wall region, the term $\frac{\partial P^+}{\partial x}y^+$ can be considered

largely smaller than 1, so equation (1.30) admit equation (1.31) as asymptote. By identifying this asymptote to the standard log-law (1.11), an expression of C_2 with the pressure gradient and the constant C of the standard log-law is found (equation (1.32)). This explain the observation of Bernard et al. (2003) concerning the dependence of C with the pressure gradient. Finally the Skote and Bernard's equations (equations (1.28) and (1.29)) are linked, as by adding the expression of C_2 of equation (1.32) in the constant C of the Bernard's equation (1.29), leads to the Skote's equation (1.28).

$$U^+ = \frac{1}{\kappa}(2\sqrt{1+(\frac{\partial P}{\partial x})^+ y^+} + \ln(\sqrt{1+(\frac{\partial P}{\partial x})^+ y^+} - 1) - \ln(\sqrt{1+(\frac{\partial P}{\partial x})^+ y^+} + 1)) + C_2 \tag{1.30}$$

$$U^+ = \frac{1}{\kappa}\ln y^+ + \frac{1}{\kappa}(2 - 2\ln(2) + \ln\frac{\partial P^+}{\partial x}) + C_2 \tag{1.31}$$

$$C_2 = \frac{1}{\kappa}(-2 + 2\ln(2) - \ln\frac{\partial P^+}{\partial x}) + C \tag{1.32}$$

Townsend (1961, 1976), also proposed a law for APG boundary layers in equilibrium. In the inner part of BL (i.e. for $30 \lesssim \hat{y} \lesssim 300$), his complex formula can be approached by a power law (equation (1.33)) for large pressure gradient (Skote (2001), Skote and Henningson (2002)), with C_t a constant. By taking the asymptote of equation (1.30) when $\frac{\partial P}{\partial x}^+$ is large (i.e. the term $\frac{\partial P}{\partial x}^+ y^+$ is large compared to 1), the Townsend's equation (1.33) is found. At the limit, the two descriptions are equivalent, so the power-law claimed by some researchers as George (2006, 2007), etc., could be a solution in APG. However, to date, none of the above theories have given a good description of the inner mean streamwise velocity profile (Skote (2001), Skote and Henningson (2002), Bernard et al. (2003), etc.). This remains an open question.

$$\begin{cases} u_p^3 = (\frac{\partial P}{\partial x})^+ . u_\tau^3 \\ \hat{u} = \frac{u}{u_p} \\ \hat{y} = \frac{y.u_p}{\nu} \\ \hat{u} = \frac{2}{\kappa}\sqrt{\hat{y}} + C_t \end{cases} \tag{1.33}$$

For the outer profile it is the same. From their similarity analysis, Castillo and George (2001) found that, for APG boundary layers in equilibrium (i.e. $\Lambda = -0.22$, see equation (1.27) for the definition of Λ) and at infinite Reynolds number, the outer profile should be similar in the outer deficit form defined by equation (1.13), with the outer velocity scale $U_{ref} = U_e$. However, for finite Reynolds numbers, the outer deficit Zagorala scaling ($U_{ref} = U_{ZS} = \frac{U_e \delta^*}{\delta}$) was found more appropriate by Maciel et al. (2006) and Indinger et al. (2006).

2.2.3.3 Structural Organisation

The structural organisation of an APG boundary layer is very different from a ZPG one (Krogstad and Skåre (1995), Skote and Henningson (2002), Aubertine and Eaton (2005), Lee and Sung (2009), etc.). It may come from Krogstad and Skåre (1995) and Krogstad and Kaspersen (2002) observations as they found that the turbulent kinetic energy diffusion is reversed in APG (in other words, the diffusion of turbulent kinetic energy is toward the wall in APG). A second peak of turbulent kinetic energy appears in APG in the outer region near $\frac{y}{\delta} = 0.5$, due to the appearance also of a second peak near $\frac{y}{\delta} = 0.5$ for all the turbulent Reynolds shear stresses (Webster et al. (1996), Wu and Squires (1998), Aubertine and Eaton (2005), etc.).

In the near wall region (below $y^+ = 50$), the streaks are observed but with a lower intensity (Lee and Sung (2009)). According to Lee and Sung (2009), with two-points cross-correlation method, the spanwise width of streaks seems to remain unchanged, however their length is shortened and the spanwise spacing between streaks is increased. Lee and Sung (2009) found a length of LSS of about 700^+ for $\beta_{Clauser} = 1.68$ compared to about 1000^+ in ZPG. They found also that the length of HSS is about 520^+ for $\beta_{Clauser} = 1.68$ compared to about 600^+ in ZPG. Finally, concerning the spanwise streaks spacing, they found $\lambda_z^+ = 400$ for $\beta_{Clauser} = 1.68$ as opposed to 100^+ observed in ZPG. This increase in streaks spacing was also observed by Skote and Henningson (2002) (λ_z^+ reached 130 when the shape factor H reached 1.6 due to the pressure gradient).

In the near wall region of APG boundary layer, as for the ZPG boundary layer, quasi-streamwise vortices exist. Lee and Sung (2009) found that these vortices are more present in the APG case, however the quasi-streamwise vortices present an angle to the streamwise direction slightly larger than in ZPG. The radius of these structures was found about 25 wall units, unchanged by the pressure gradient.

Krogstad and Skåre (1995), Nagano et al. (1998), Krogstad and Kaspersen (2002), Aubertine and Eaton (2005), Lee and Sung (2009), etc., have noticed that, in this near wall region, the frequency of appearance of quadrant events, defined by Wallace et al. (1972), are increased in APG compared to ZPG. The Q_4 events, corresponding to a sweep structure, appears much more often in APG than in ZPG and are stronger. The Q_2 events, corresponding to an ejection structure, appears less often in APG than the Q_4 events, however, the sum of the appearance of Q_4 events and Q_2 event in APG is larger than in ZPG. The increase of Q_4 events in APG could explain why the turbulent kinetic energy diffusion is reversed compared to ZPG (i.e. toward the wall). Krogstad and Skåre (1995), Nagano et al. (1998), Krogstad and Kaspersen (2002), Aubertine and Eaton (2005) have also noticed that the increase of Q_4 events in APG is accompanied by the appearance of Q_1 events that are not present in ZPG. Q_1 events eject high momentum fluid near the wall and are closely related to Q_4 events in APG. Q_1 events seem then created in APG to balance the increase of Q_4 events (Krogstad and Skåre (1995)).

In the outer region of APG boundary layers, Lee and Sung (2009) have also observed "streaky structures" defined by low momentum regions (LMRs) as in ZPG. These LMR structures were also found to be associated with hairpin packets. The conceptual organisational model (Figure 1.2) proposed by Adrian et al. (2000) for ZPG boundary layer seems to remain valid in APG. Lee and Sung (2009) found these

LMRs more intense and regular in APG than in ZPG. They supposed that these LMRs structures in the outer region, re-enforced in APG, are related to the peaks of Reynolds stresses observed in the outer region of APG flow around $\frac{y}{\delta} = 0.5$. In APG, Song and Eaton (2004) found that the streamwise length of these structures can reach more than 2δ. Lee and Sung (2009) found that the mean streamwise length of LMR structures in the outer region of APG ($\beta_{Clauser} = 1.68$) is nearly constant of about 0.7δ, slightly under the value in ZPG ($0.7 - 0.8\delta$). The mean LMRs width was found to be 0.25δ in APG, that is about the same value as in ZPG. In the log region, LMRs were also observed, and the length in APG, as in ZPG, was found to increase with y, the wall normal position. However, the length of LMRs in APG was found to remain smaller than the length in ZPG. The LMRs width in the log region was found to follow the same trend as the LMRs length, but the width of LMRs in APG was found greater than in ZPG.

2.3 The turbulent boundary layer and surface curvature

2.3.1 Introduction

In many aerodynamic applications, the flow is subjected to both pressure gradient and wall curvature effects. It was shown very early that the wall curvature effects are not negligible, even for very small one (Meroney and Bradshaw (1975), Patel and Sotiropoulos (1997), Tulapurkara et al. (2001), etc.). The curvature introduces an "extra rate of strain" ($\frac{\partial V}{\partial y} \neq 0$) with the streamline curvature that can not be neglected in the equations (Baskaran et al. (1987)). The curvature is quantified by the parameter $\frac{\delta}{R}$ (or sometimes by $R^+ = \frac{Ru_\tau}{\nu}$), with R the algebraic radius of curvature along the y-axis (i.e. wall-normal axis). Patel and Sotiropoulos (1997) classified the curvature strength in three categories : $\frac{\delta}{|R|} < 0.01$ corresponds to small curvatures, $0.01 < \frac{\delta}{|R|} < 0.1$ corresponds to mild curvatures and $\frac{\delta}{|R|} > 0.1$ corresponds to strong curvatures.

The curvature effects are not linear. For a small curvatures, strong effects are noticed on the turbulent intensity but for mild curvatures, the effects are just slightly higher than for small curvatures (Patel and Sotiropoulos (1997)). As for APG and FPG, the effects of convex curvature ($R > 0$) are opposite to the effects of concave curvature ($R < 0$) (Patel and Sotiropoulos (1997), Meroney and Bradshaw (1975), Tulapurkara et al. (2001), etc.). Baskaran et al. (1987) have noticed that, when there is a change in curvature, a "new internal layer" can be triggered when the parameter Δk^+ is greater than $3.7\ 10^{-5}$, with $\Delta k^+ = (\frac{1}{R_2} - \frac{1}{R_1}) * \frac{\nu}{u_{\tau_1}}$ (with R_2 the downstream radius of curvature, R_1 the upstream radius of curvature and u_{τ_1} the friction velocity upstream of the curvature change). This "new internal layer" is defined by Baskaran et al. (1987) as a new layer, which develops near the wall, which is not affected by the external conditions. This new layer dictates the turbulence behaviour near the wall and the friction velocity. The external layer is then a free layer with its turbulence decaying. The internal layer is evidenced by a "knee point" in the external region of the turbulent intensity profile (Baskaran et al. (1987), Webster et al. (1996), Wu and Squires (1998), etc.).

2.3.2 Effects of convex curvature

Convex curvature tends to attenuate turbulence in the near wall region (i.e. $\frac{y}{\delta} < 0.5$) and to separate the inner and outer layers (Patel and Sotiropoulos (1997)). The response of a boundary layer to a sudden convex curvature is found very fast in the inner region, especially on u_τ. Patel and Sotiropoulos (1997) have also noticed that convex curvature increases the shape factor, and decreases the friction velocity. It has then similar effects as an APG. The mean inner velocity profile shows strong departure from the standard log-law (equation (1.11)) with increasing convex curvature. It tends to be above the standard log law (Patel and Sotiropoulos (1997)), and the log region extent seems to shrink. However, Meroney and Bradshaw (1975) have shown that the modified log-law equation (1.34) given by Bradshaw (1973) works prettily well, with $\beta = 7$ the correction constant of Bradshaw, R the radius of curvature and κ and C the constants of the standard log law (1.11).

$$U^+(1 - \frac{5}{3}\beta\frac{y}{R}) = \frac{1}{\kappa}ln(y^+) + \frac{C}{R} \tag{1.34}$$

2.3.3 Effects of concave curvature

The effects of concave curvature is opposite to that of convex curvature (Patel and Sotiropoulos (1997)). It increases turbulence near the wall by increasing mixing (Meroney and Bradshaw (1975)). The response of a boundary layer to a sudden concave curvature was shown to be slower than a convex one. Patel and Sotiropoulos (1997) also noticed that concave curvatures induce a decrease of the shape factor and an increase of the friction velocity. It has thus similar effects as a FPG. The mean inner velocity profile shows strong departure from the standard log-law (equation (1.11)) with increasing the concave curvature. It tends to be below the standard log-law (Patel and Sotiropoulos (1997)), and the log region seems to shrink as for convex curvature. However, Meroney and Bradshaw (1975) have also shown that the modified log-law equation (1.34) of Bradshaw, with $\beta = 7$, works sometimes for concave curvatures. When the parameter $Re_\theta\sqrt{\frac{\theta}{R}}$ is above 0.6, stable streamwise counter-rotating vortices, called "Taylor-Görtler vortices" appear, even in turbulent flow (Tani (1962), Patel (1969), etc.). Their existence may explain the increase of turbulence and boundary layer thickness for concave curvatures.

2.4 Boundary layers separation

2.4.1 Introduction

When a flow along a surface decelerates too strongly, streamlines may detach from the surface. This is called separation. A reverse flow bubble is then created. Separation can be created by a strong APG on a smooth surface or by a strong discontinuity of curvature. When separation is caused by a curvature discontinuity, it is called "imposed separation". Flow separation has drastic consequences on real applications. For example, they can cause a loss of control of an aircraft and they lead to a drop in efficiency of a turbomachinery.

2.4.2 Separation detection

Simpson (1989) gave a good review concerning 2D separation caused by strong APG. He defined several steps in the separation process based on the backflow coefficient χ, which is defined as the ratio of the time where the flow is reversed (i.e. opposite to streamwise direction), over the total time. Incipient Detachment (ID) is defined by $\chi \simeq 1\%$. ID characterises flow with rare backflow occurrences. Intermittent Transitory Detachment (ITD) is defined by $\chi \simeq 20\%$, Transitory Detachment (TD) by $\chi \simeq 50\%$ and Detachment (D) by the mean wall shear stress equal 0 ($\overline{\tau_w} = 0$).

Two criteria for separation point detection are given by Simpson (1989). The mean separation point corresponds to either D or TD events, the first one being mostly used. In most experiments, the two criteria give the same positions. D and TD are equivalent only if the probability density function of the streamwise velocity is symmetric at the separation point. In the same way, the mean reattachment point can also be defined with D or TD events. For flow where strong APG leads to separation, positions of the instantaneous separation and reattachment points fluctuate around the mean separation point and the mean reattachment point respectively (Simpson (1989)), so the flow can be affected largely upstream of the mean separation point. However, for an "imposed separation", the separation point is fixed and only the instantaneous reattachment point position fluctuate around the mean one. By analogy, the border of the mean separation bubble can be defined either by $\chi = 50\%$ or $U = 0$, with U the mean streamwise velocity. The mean separation bubble is then defined either by $\chi \geq 50\%$ or $U \leq 0$. Experimentally, there are simple methods to detect and evident separation, such as wool tufts, oil-film and dye or smoke filaments visualisations, etc. (Simpson (1989)).

Separation criterion based on the shape factor H have also been developed. For Dengel and Fernholz (1990), the beginning of the separation is characterized by a shape factor above 2.85 ± 0.1. However, Mellor and Gibson (1966) suggested a limit value of 2.35 and Bradshaw (1967) suggested a limit value of 2.5 ± 0.1, so this kind of criterion seems to be not reliable. High values of the shape factor are then weak BL's characteristic, but the separation point can not be locate reliably with the shape factor (Angele (2003)).

2.4.3 Mean backflow profile

For mild APG, low curvature and upstream ID events, the law of the wall seems to remain valid as long as the peak of the Reynolds shear stress $-\rho\overline{u'v'}$ remains below $1.5\tau_w$ (Simpson (1989, 1996)). The estimation of u_τ by a Clauser's chart method and the estimation of the friction coefficient C_f with the law of Ludwieg and Tillmann (1949) (equation (1.35)) remain then valid as long as the shape factor H is below 2. When appreciable backflow occurs (i.e. near ITD event), Standborn and Kline (1961) found that a not universal power-law seems to describe the mean velocity profile and leads to relation (1.36). Simpson (1989) found that the relation (1.36) characterizes ITD events.

Between ID and ITD events, when the Reynolds shear stress $-\rho\overline{u'v'}$ is above $1.5\tau_w$, Perry and Schofield (1973) proposed a defect law (equation (1.37)) to model the mean profile, with U_s determined by fitting equation (1.37), $\eta = \frac{y}{\Delta}$, $\Delta = \frac{\delta^*}{C_s}\frac{U_e}{U_s}$

and C_s a universal constant estimated at about 0.35. U_s is linked with the Reynolds shear stress by (1.38), where L corresponds to the distance from the wall in the y direction of the peak of Reynolds shear stress $-\rho\overline{u'v'}$.

$$C_f = \frac{u_\tau^2}{\frac{1}{2}U_e^2} = 0.246 \times 10^{-0.678H} \times Re_\theta^{-0.268} \tag{1.35}$$

$$\frac{H-1}{H} = \left(2 - \frac{\delta^*}{\delta}\right)^{-1} \tag{1.36}$$

$$\frac{U_e - U}{U_s} = 1 - 0.4\sqrt{\eta} - 0.6\sin\frac{\pi}{2}\eta \tag{1.37}$$

$$\frac{U_s}{\sqrt{-\rho\overline{u'v'}_{max}}} = 8\sqrt{\frac{\Delta}{L}} \tag{1.38}$$

Simpson (1983) tried to model the mean velocity profile in a separation bubble defined by $\chi \geq 50\%$. He shows that the mean separation bubble can be divided into 3 regions : a viscous sublayer region near the wall, an overlap region between the viscous sublayer and the outer region, and an outer backflow region dominated by large-scale motions. Simpson (1983) shows that the overlap region follows a semi-logarithmic law defined by equation (1.39) for $\frac{N}{\delta} < 0.06$, with δ the boundary layer thickness upstream the separation, U_N the minimum negative value of the streamwise velocity profile, N the position y from the wall where U_N is obtained, and A a constant estimated by Simpson (1983) as 0.3. Equation (1.39) is valid in the middle region of the backflow for $0.02 < \frac{y}{N} < 1$, but failed for $\frac{y}{N} > 1$ as the outer backflow region is influenced strongly by the large-scale structures in the outer region.

$$\frac{U}{|U_N|} = A(\frac{y}{N} - ln\frac{y}{N} - 1) - 1 \tag{1.39}$$

In the near wall region ($\frac{y}{N} < 0.02$), Simpson (1983) proposed equation (1.40) to describe the mean backflow profile, with C a constant and $P_1 = \frac{N^2}{\rho\nu|U_N|}\frac{\partial P}{\partial x}$. For P_1 under 125, Simpson and Shivaprasad (1983) found that the parameter $\frac{|U_N|}{U_e}$ is varying linearly with $\frac{1}{H}$, with H the shape factor, and takes the value 0.15 for $H = 10$.

$$\frac{U}{|U_N|} = -C\frac{y}{N} + \frac{P_1}{2}\left(\frac{y}{N}\right)^2 \tag{1.40}$$

2.4.4 Turbulent organisation in the separation region

When the flow is approaching separation due to strong APG, the structural organisation have been shown to be seriously modified (Skote (2001), Skote and Henningson (2002), Marquillie et al. (2008), etc.). The streaks tend to be killed by the separation or seriously reduced (Skote and Henningson (2002), Marquillie et al. (2008)). The streaks become transversally thinner when approaching separation, however, this spanwise width in wall units increases which leads to their disappearance. Near

separation, the vortices generated are found to be stronger than the coherent structures observed in ZPG boundary layers (Marquillie et al. (2008)). The separation can thus be seen as an instability that leads to generation of strong coherent structures. The streaks are found to reappear around 1000^+ after the mean reattachment point (Marquillie et al. (2008)) for a separation length of about 4000^+ (u_τ was taken at the inlet).

The turbulent kinetic energy production in the mean separation bubble is nearly zero (Simpson (1989)). Turbulence in this bubble is then provided by the shear layer by turbulent diffusion. The peaks in the wall-normal shear stress and Reynolds shear stress near the middle of the boundary layer (i.e. at $\frac{y}{\delta} \simeq 0.5$) are then responsible of the maintain of the turbulence in the separation. Chehroudi and Simpson (1985) with space-time correlations have shown that, structures of the size of δ in width and height, directed toward the wall, provide the flow in the separation. These structures bring high values of the wall-normal velocity fluctuation component (v') in the separation bubble. Because of continuity requirements, near the wall, these v' fluctuations should defect in streamwise (u') and spanwise (w') velocity fluctuations. Thus, they contribute to increase the streamwise shear stress ($\overline{u'^2}$) and spanwise shear stress ($\overline{w'^2}$). Nagabushana et al. (1988) have shown that the most energetic frequencies in the separation bubble due to these structures are in the range $10 \leq \frac{U_e}{\delta f} \leq 50$, where f designs the frequency.

3 Flow separation control

3.1 Introduction

As flow separation can produce drastic effects, such as drop in lift, increase of drag, even a loss of control for an aircraft, a drop in efficiency of a turbo-machinery and it can create undesirable noise, etc., controlling separation appears to be an important challenge. The first experiment concerning flow separation control was done by Taylor (1947). This experiment was based on vane-type passive vortex generators (VGs), with their height h of the size of the boundary layer thickness δ, to eliminate the separation in a diffuser. Several flow control techniques exist but the review here will be limited to few examples. Most of the time, actuators generate a streamwise vortex structures which can entrain high-momentum fluid towards the wall. This energizes the boundary layer by increasing the mixing near the wall or by reorganising the mean flow. The boundary layer becomes then less prompt to separate. These VGs can be separated into two kinds : passive and active. The passive VGs take energy from the fluid far away from the wall and redistribute it in the near wall region without energy supply. On the contrary, active VGs need energy supply to achieve a similar goal (Gad-El-Hak (2000)).

3.2 Flow separation control through passive techniques

3.2.1 Generality

Passive VGs were the first one used to control flows as they are simple to set-up. The vane-type VGs are the most popular (Lin et al. (1991), Lin (1999, 2002), Angele and Muhammad-Klingmann (2005), Godard and Stanislas (2006a), etc.). The review will then be more focused on these VGs. They consist of a row of small plates or airfoils, mounted normal to the surface with an angle β_{pd} to the flow, which produce an array of streamwise vortices. The first experiments were based on VGs with a height h comparable to the boundary layer thickness δ (Taylor (1947), Lin (2002), etc.). Rapidly, due to the high residual drag introduced, they where replaced by submerged VGs ($h < \delta$) (Lin (1999, 2002), etc.). When the boundary layer profile is full enough near the wall, these submerged VGs were found as efficient as the bigger ones (Lin (1999, 2002), Godard and Stanislas (2006a), etc.).

3.2.2 Optimum Vane-type configuration

3.2.2.1 Description of the VGs

The vane-type VGs can be arranged in co or counter-rotating set-up. The parameters used are illustrated in Figure 1.3. h is the devices height, β_{pd} is the devices angle relatively to the flow direction, λ is the spacing between two devices in co-rotating arrangement and the spacing between two pairs of devices in counter-rotating arrangement, L is the distance between two devices of a pair in counter-rotating arrangement and ΔX_{vg} is the distance between the VGs trailing edge and the separation line.

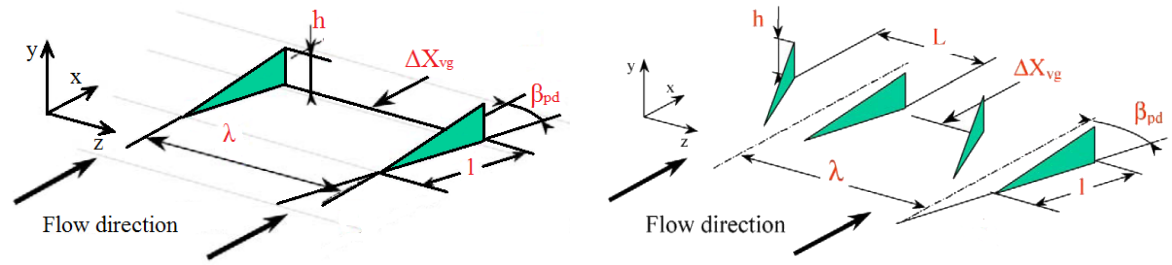

Figure 1.3: a) Co-rotating, b) Counter-rotating passive parameters definition.

Different shapes have been tested. The mostly used shapes are rectangular (Angele and Muhammad-Klingmann (2005), Angele and Grewe (2007), etc.), trapezoidal (Lin (1999), etc.) and triangular (Lin (1999, 2002), Godard and Stanislas (2006a), etc.). Two different organisations of the flow are created just after the devices (Figure 1.4): a down-wash region, where high momentum fluid is brought toward the wall by the vortices and where the local boundary layer thickness is reduced, and an up-wash region, where low momentum fluid is brought away from the wall by the vortices and where the local boundary layer thickness is increased (Godard and Stanislas (2006a)).

Many studies were done on these type of submerged VGs to try to find an optimum configuration (Lin (1999), Betterton et al. (2000), Lin (2002), Angele (2003),

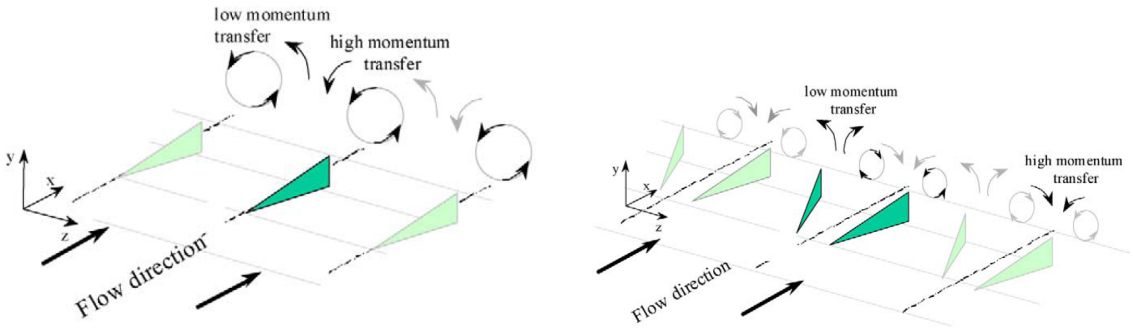

a) b)

Figure 1.4: a) Co-rotating, b) Counter-rotating passive vane-type flow organization.

Angele and Muhammad-Klingmann (2005), Godard and Stanislas (2006a), Angele and Grewe (2007), etc.). However, it was found that the optimum configuration depends on the flow in which VGs are embedded. For example, APG promotes interactions between the vortices that leads to a drop in control efficiency (Betterton et al. (2000), Lin (2002), etc.).

3.2.2.2 Effects of distance between the mean separation line and the VGs position ($\frac{\Delta X_{vg}}{h}$)

Lin (1999) has estimated the life time of the vortices to be around $100h$ for an APG flow caused by an imposed separation, but he found that, to suppress separation, the devices should be close enough to the separation line, with a maximum distance ΔX_{vg} of about $5-10h$ and $30h$ as an extreme limit (Lin (2002)). On the contrary, for VGs of the size of the boundary layer, Angele and Muhammad-Klingmann (2005) and Angele and Grewe (2007) found, for an APG flow with separation, that the optimum distance is in the range $17 < \frac{\Delta X_{vg}}{h} < 52$, and Lögdberg et al. (2010), on a the same set-up as Angele and Muhammad-Klingmann (2005), found that they are still efficient until $\frac{\Delta X_{vg}}{h} = 118$. The physics of submerged VGs seems to be different from that of VGs of the order of δ. Maybe the dynamics of the vortices is different as, for VGs of the size of the boundary layer, Angele and Muhammad-Klingmann (2005) and Angele and Grewe (2007) found that, $17h$ behind the VGs, the streamwise vortices become equidistant in the spanwise direction and give the maximum control efficiency after. Maybe for small VGs, they become equidistant faster and disappear after a shorter distance due to higher turbulence intensity near the wall.

3.2.2.3 Effects of the height of the VGs ($\frac{h}{\delta}$)

For the efficiency of submerged VGs, Lin (2002) gave a criterion on the devices height h : h should be at least 300 wall units. Godard and Stanislas (2006a) found however, for an APG flow without separation, an optimum value of 0.28 for $\frac{h}{\delta}$, which corresponds to value of more than 1000 wall units. The optimum value given by Godard and Stanislas (2006a) corresponds to a good compromise between the control efficiency (i.e. the gain in friction) and the induced drag (linked with the

devices height). The value of 300^+ given by Lin (2002) is then only a minimum to obtain visible control effects. If the induced drag of the VGs is not taken into account, increasing the device height h increases the vortex strength and then the length on which the device is efficient (Godard and Stanislas (2006a), Angele and Muhammad-Klingmann (2005), Angele and Grewe (2007), etc.).

3.2.2.4 Effects of the angle of the VGs to the mean flow (β_{pd})

The optimum angle between the VGs and the mean flow β_{pd} was found to be 18° by Godard and Stanislas (2006a) for triangular vanes, but values in the range from 17 to 25° where also found to give good results. Increasing β_{pd} increases the vortex strength, but after an angle of approximately 28°, a vortex breakdown appears that leads to a drop in control efficiency (Tilmann et al. (2000), Godard and Stanislas (2006a)).

3.2.2.5 Effects of the spacing parameter ($\frac{\lambda}{h}$)

The spacing between VGs (λ) was found to be also an important parameter as interactions between induced vortices could improve the control efficiency (Lin (2002), Godard and Stanislas (2006a), etc.). Godard and Stanislas (2006a) found $\frac{\lambda}{h} = 6$ as an optimum value for triangular vanes which is in agreement with the value given by Lin (1999) ($\frac{\lambda}{h} = 5$). For trapezoidal vanes, Lin (1999) found however a higher optimum value of $\frac{\lambda}{h} = 12.5$. Values in the range $4 \leq \frac{\lambda}{h} \leq 10$ are then effective (Godard and Stanislas (2006a), Lin (1999, 2002), Angele and Muhammad-Klingmann (2005), Angele and Grewe (2007), etc.), depending on the shape of devices.

3.2.2.6 Effects of the device length ($\frac{l}{h}$)

The length of the devices l drives the strength of the produced vortices (Smith (1994)). Godard and Stanislas (2006a) found 2 as an optimum value of $\frac{l}{h}$ for triangular vanes, but values in the range 1 to 3 also give good results. For trapezoidal vanes, Lin (1999) found an optimum of $\frac{l}{h} = 7$, so here again, the optimum value depends on the devices shape.

3.2.2.7 Effects of the counter-rotating device spacing ($\frac{L}{h}$)

For counter-rotating vanes, the parameter $\frac{L}{h}$ plays an important role as it tunes the distances between the generated counter-rotating vortices (Angele and Muhammad-Klingmann (2005), Angele and Grewe (2007), etc.). For triangular vanes, Godard and Stanislas (2006a) and Lin (1999) found an optimum values in the range 2 to 3, with a best at 2.5 for Godard and Stanislas (2006a). Angele and Muhammad-Klingmann (2005) and Angele and Grewe (2007) found the same range for the optimum value of $\frac{L}{h}$ of rectangular vanes. However, Lin (1999) found an optimum value slightly higher of about 8 for trapezoidal vanes. Here again, the optimum value seems to be dependent of the device shape.

3.2.2.8 Comparison between co and counter-rotating configurations

Finally, Godard and Stanislas (2006a) found that, for their 2D bump configuration, the optimum counter-rotating arrangement of triangular vanes gives best results

with a factor of two compared to the optimum co-rotating configuration. However, for a 3D separation on a backward-facing ramp (i.e. a separation dominated by the two corner vortices), Lin (2002) has noticed that the co-rotating configurations give better results. The problem of finding the optimum configuration is then highly complex as it depends on the flow considered. However, the research in the past two decades has given quite narrow ranges for the optimum parameters of passive vane type vortex generators.

3.2.3 Other passive vortex generators

Many other passive vortex generators have also been tested with more or less success. A complete review will not be given here as it would be very long. Lin (1999) has studied a huge number of passive VGs for flow separation control on a ramp. The main devices tested which gave good results, were vane-type VGs, wishbones (Figure 1.5 a)), Wheeler's doublets (Figure 1.5 b)), spanwise cylinders and large longitudinal grooves. The height h of all these VGs were 0.2δ except for the Wheeler's doublets for which h was 0.1δ. The diameter for the transverse cylinders was also 0.2δ. Lin (1999) found that the vane-type submerged VGs were giving the best results and were as effective as vane-type VGs with a height of 0.8δ. The wishbone VGs were nearly as efficient as the submerged vane-type VGs but with more induced drag. The Wheeler's doublet VGs and the spanwise cylinders gave similar results, but slightly worst, than the wishbone VGs. The longitudinal grooves were also giving good control results but slightly under the others.

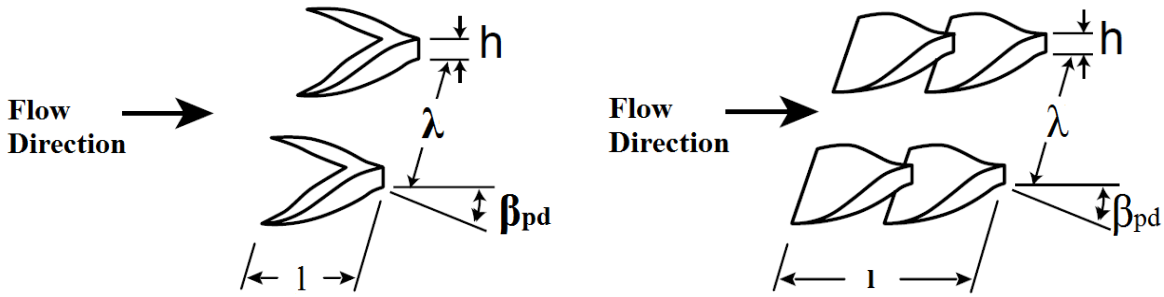

a) b)

Figure 1.5: a) Wishbone device pattern, b) Wheeler's doublets pattern.

Except for the spanwise cylinders, Lin (1999) concluded that the most effective group of devices is the one that generates streamwise vortices. This conclusion was reinforced by Lin (2002), as for devices that generate spanwise vortices, more actuators are needed per unit of span, which induces more additional drag. From Lin (1999, 2002), the submerged vane-type devices appears to be the most efficient as they give good results in reducing the separation and induce less drag than the others. Moreover, their height can be tuned such as they generate just strong enough vortices to suppress the separation without persisting vortices. This can explain why that type of passive vortex generators are mostly used. However, it should be noted that Lin (2002) point out that the Wheeler's doublets are more effective when using

vane-type submerged VGs of the size of 0.1δ because of the extend of their chord (double row).

3.3 Flow separation control through active techniques

3.3.1 Introduction

In many applications where flow control can be applied, there are conditions where the control is unneeded or leads to a worst result. This is the case on the wings of an aircraft for example. During the landing and take-off phases, flow control can improve the aircraft performances, as the wings are working at hight angle of attack, which can lead to massive flow separation on the suction-side of the wings. However, during cruise condition, no separation risk exist, and flow control in this case has been shown to lead to a decrease in performances (Tilmann (2001), etc.). Then, if passive vortex generators are used on an aircraft, they will deteriorate the performances during cruise conditions, and especially, they will increase drag. Solutions have been proposed to eliminate this problem by putting the passive devices on the removable flap for example, so that vortex generators can be stored into the wing with the flap when not necessary, especially, during cruise conditions (Lin (2002), etc.). However, this leads to a high constraint on the size of the devices, as the size has to be smaller than the gap between the wing and the flap.

To overcomes this problem, active devices have been developed as they can be turn off when unneeded. Moreover, reactive control can be achieved through active VGs which leads to a better robustness of the control and a better efficiency by reducing the energy consumption for example. Round jets are the most popular active VGs as there are easy to set-up (Selby et al. (1992), McManus et al. (1994), Tilmann et al. (2000), Godard and Stanislas (2006b), etc.). As continuous jets VGs need a lot of energy to create the vortices, pulsed-jets VGs have been developed to reduce the need in energy in view of integration in real applications (Tilmann et al. (2000), Tilmann (2001), etc.). Steady jets and pulsed jets VGs have been firstly used in open-loop (i.e. without feedback from the flow) as it is simpler to do (Selby et al. (1992), Tilmann et al. (2000), Godard and Stanislas (2006b), etc.). Then closed-loop control has been carried out, especially with pulsed jets (Magill et al. (2001), Becker et al. (2007), Shaqarin (2011), etc.). Steady jets and pulsed jets VGs in open loop will be described in the next sections.

3.3.2 Steady jets

3.3.2.1 Description

Figure 1.6 used by Godard and Stanislas (2006b) gives the description of the parameters used to describe jets configurations. β is the pitch angle which corresponds to the angle between the jet axis and the wall. α is the skew angle which corresponds to the azimuthal angle between the free-stream velocity and the projection of the jets axis on the wall (i.e. in the wall normal direction). Φ is the jet diameter, U_j is the mean jet exit velocity, λ is the spacing between two jets in co-rotating arrangement and the spacing between two pairs of jets in counter-rotating arrangement, L is the distance between two jets of a pair in counter-rotating arrangement and ΔX_{vg} is

the distance between the jet exits and the mean separation line. Commonly, the jet exit velocity (U_j) is compared to the free-stream velocity (U_e) which results in a parameter call VR, the jet velocity ratio, defined by $VR = \frac{U_j}{U_e}$ (Tilmann et al. (2000), Tilmann (2001), Godard and Stanislas (2006b), etc.).

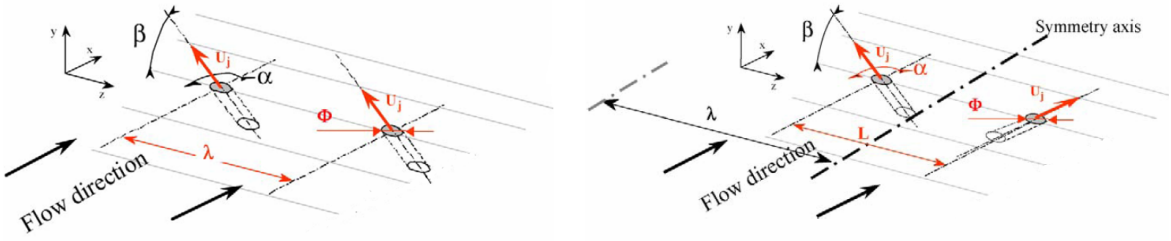

a) b)

Figure 1.6: a) Co-rotating , b) Counter-rotating jets parameters definition.

Compton and Johnston (1992) studied the flow of a single steady jet VG in a TBL cross-flow. They confirmed that vortices produced by the jet are qualitatively similar as those produced by small passive vortex generators, but tend to decay faster. For jets with $\beta = 90°$ (i.e. normal to the wall) and VR strong enough (typically $VR \gtrsim 1$), a shears layer appears around its perimeter which generate vorticity. The top of the jet is blocked by the cross-flow and it is deforming into a kidney shape (Milanovic and Zaman (2004), Gopalan et al. (2004), etc.). The induced vorticity and the lateral velocities induced at the top of the jet develop into a counter-rotating vortex pair on each side of the jet (Compton and Johnston (1992), Zaman and Foss (1997), Milanovic and Zaman (2004), Gopalan et al. (2004), etc.). This vortex pair was found to have similar effects as passive devices by creating an upwash region where the boundary layer is thickening and a downwash region where the boundary layer thickness is reduced (Khan and Johnston (2000)). The vortex pair generated by a wall normal jet is highly modified by changing jets parameters, such as β, α, Φ and VR (Compton and Johnston (1992), Khan (1999), Khan and Johnston (2000), Milanovic and Zaman (2004), etc.). When more than one jet is used, interactions between vortices occur and the effects of the other jets parameters (such as λ, L and ΔX_{vg}) are not negligible (Selby et al. (1992), Godard and Stanislas (2006b), etc.). The effects of these parameters are described in the next section.

3.3.2.2 Effects of jets parameters

3.3.2.2.1 Effects of pitch angle β

The pitch angle was found to tune the jet penetration into the cross-flow, so the position of the induced vortices (Milanovic and Zaman (2004), Khan (1999), Khan and Johnston (2000), etc.). By increasing β from 0 to 90°, the jet penetration into the cross-flow is increased which increases the strength of the main induced vortex. However, the center of this vortex moves away from the wall, which can lead to a drop in control efficiency (Milanovic and Zaman (2004), Khan (1999), Khan and Johnston (2000), etc.). Selby et al. (1992) did a parametric study of flow separation

control on a backward-facing ramp with separation through active steady jets. They found that the best results are obtained for $15° \leq \beta \leq 25°$, and $\beta = 90°$ was giving negligible effects on the separation. However, $\beta = 45°$ was also giving positive effects. They concluded that values of β in the range 15° to 45° are appropriated for flow control applications. This range was confirmed by the studies of Khan (1999) and Khan and Johnston (2000), where an optimum value of 30° was found. However, $\beta = 45°$ is the mostly used value in flow control studies (Tilmann et al. (2000), Tilmann (2001), Godard and Stanislas (2006b), etc.).

3.3.2.2.2 Effects of skew angle α

The skew angle α was found to remove the symmetry of the counter-rotating vortex pair generated by a wall normal jet. The vortex with positive vorticity along x-axis ($\omega_x > 0$) is reinforced and become dominant (Compton and Johnston (1992), Milanovic and Zaman (2004), etc.). The dominant vortex becomes weaker by increasing α, which is accompanied with a drop in the peak of vorticity along the x-axis (Milanovic and Zaman (2004)). Milanovic and Zaman (2004) found also that the dominant vortex is moving laterally in the jet direction by increasing α. Khan (1999), Khan and Johnston (2000) found that increasing α gives a larger region of high turbulence which improves the mixing so which may improve the control efficiency.

Compton and Johnston (1992), for flat plate boundary layer, found that maximum vorticity is observed on the dominant vortex for skew angle between 45° and 90°. Khan (1999), Khan and Johnston (2000), also for flat plate boundary layer, confirmed this range as they found that a stronger dominant vortex is obtained for $\alpha = 60°$ and $\beta = 30°$. Selby et al. (1992) observed the same optimum skew angle range as Compton and Johnston (1992) on flow separation control. They found also that the optimum skew angle value depends on the pitch angle value β. For $\beta = 15°$, the optimum α was found to be 60°, and for $\beta = 45°$, the optimum α was found to be 90°. However, Godard and Stanislas (2006b), for an APG boundary layer on a bump, found that this parameter is not very sensitive in the range $45° \leq \alpha \leq 90°$, so values of α in this range seem to be appropriate for flow control.

3.3.2.2.3 Effects of the jet velocity ratio VR

The jet velocity ratio VR is a key parameter for flow separation control purposes. It plays an important role in the power consumption of the VGs and it was found to govern the strength of the induced vortex (Tilmann et al. (2000), Selby et al. (1992), Khan (1999), etc.). Except in the study of Milanovic and Zaman (2004) on flat plate boundary layer, who found an optimum VR value for the vortex strength in the range 2 to 2.8, all the others studies show that increasing VR increases the strength of the vortex but leads to a vortex further away from the wall (Tilmann et al. (2000), Khan (1999), etc.). As a stronger vortex improves the control efficiency and a vortex further away from the wall leads to a drop in control efficiency, an optimum VR should exist. However, Selby et al. (1992), on flow separation control, found that the control efficiency continuously increases with increasing VR up to the maximum VR value tested ($VR_{max} = 6.8$). Godard and Stanislas (2006b) confirmed this result up to $VR = 6.2$. However, Godard and Stanislas (2006b) have noticed that after

$VR = 3.1$, the gain in control efficiency increases less rapidly. Lögdberg (2008) obtained almost the same conclusion as Godard and Stanislas (2006b). Lögdberg (2008) found that $VR = 1$ was a minimum to obtain control effects and was sufficient to eliminate the mean backflow. He found also that after $VR = 2$, the gain in control efficiency is still increasing but at a lower rate. After $VR = 5$, he noticed a drop in control efficiency.

The lower rate increase of control efficiency noticed by Godard and Stanislas (2006b) above $VR = 3.1$ and Lögdberg (2008) above $VR = 2$, could be linked to the optimum VR value for the vortex strength observed by Milanovic and Zaman (2004), as the beginning of the change in control gain slope corresponds to VR values in the optimum Milanovic's range. In conclusion, high values of VR can be necessary for flow separation control and an optimum value should exist but seems to depend on the flow considered. Value around 2.5 to 3 are typical in flow control applications (Tilmann et al. (2000), Tilmann (2001), Selby et al. (1992), Lögdberg (2008), etc.).

3.3.2.2.4 Effects of the jet hole diameter Φ

The hole diameter is an important parameter as for a given VR, it fixes the flow rate so the energy to introduce. Smaller holes which give similar control efficiency are then better. Selby et al. (1992) found that the smallest diameter that they have tested ($\frac{\Phi}{\delta} = 0.024$) was the best one, as with the same flow rate, higher value of VR was reached with the smallest diameter, leading to a better control efficiency. Godard and Stanislas (2006b) arrived to the same conclusion as at constant VR, the configurations with $\frac{\Phi}{\delta} = 0.024$ gave about the same results as configurations with $\frac{\Phi}{\delta} = 0.036$ but with 1.5 times less flow rate. As very small holes are very restrictive, value of $\frac{\Phi}{\delta}$ around 0.024 seems then a good compromised for boundary layer thickness δ greater than 20 mm. For small δ (below 20 mm), the optimum holes diameter should be 0.5 mm or 1 mm, which corresponds to the smallest realistic and feasible holes diameter.

3.3.2.2.5 Effects of the spacing parameter λ

This parameter tunes the distances between the induced vortices, so it can promote or kill the interactions between vortices (Godard and Stanislas (2006b)). If it is too small, strong interactions between vortices will exist and this can leads to an ejection of the vortices from the wall and a drop in control efficiency. On the contrary, a too large value of λ leads to isolated vortices and no control between two vortices. An optimum value should exist. Godard and Stanislas (2006b) found 6 as an optimum for $\frac{\lambda}{\Phi}$ in co-rotating arrangement, and suggested a value around 32 for counter-rotating. Selby et al. (1992), found also that $\frac{\lambda}{\Phi} = 6.25$ gives good control results for co-rotating configurations.

3.3.2.2.6 Effects of the counter-rotating spacing parameter L

The counter-rotating spacing parameter L as similar effects as λ. It tunes the spacing between the counter-rotating vortex pair (Godard and Stanislas (2006b)). Godard and Stanislas (2006b) found an optimum range of $\frac{L}{\Phi}$ between 12.5 and 16, with a best at 15.

3.3.2.2.7 Effects of the distance from the mean separation line ΔX_{vg}

As for the passive devices, the induced vortices have a certain life time, then increasing ΔX_{vg} will reduce the control efficiency (Lin et al. (1990), Selby et al. (1992), etc.). Selby et al. (1992) found an optimum value of $\frac{\Delta X_{vg}}{\delta}$ between 3 and 10, but with largely perceptible effect at $\frac{\Delta X_{vg}}{\delta} = 40$. Lin et al. (1990) have also noticed that steady jets vortex generators are still efficient until $\frac{\Delta X_{vg}}{\delta} = 40$.

3.3.2.2.8 Comparison between co and counter-rotating arrangement

As the co-rotating arrangement is easier to set-up than the counter-rotating one due to less constraints (the two tubes of a pair have to be crossed in counter-rotating arrangement (Godard and Stanislas (2006b))), it is interesting to know which one gives the best results. According to Godard and Stanislas (2006b), the counter-rotating configurations seem to give better results with less flow rate. Lögdberg (2008)'s study tends to confirm Godard and Stanislas (2006b)'s conclusion as the optimum counter-rotating configuration proposed by Godard and Stanislas (2006b) has suppressed Lögdberg (2008)'s separation at a very low VR ($VR = 1$). Only the study of Selby et al. (1992) seems to contradict Godard and Stanislas (2006b)'s conclusion, but the counter rotating configuration that they used, was fairly different from the Godard and Stanislas (2006b)'s optimum configuration. Counter-rotating configurations seem to be better, but depending on the constraints of the application, co-rotating configurations can also be used as they give also good control results (Selby et al. (1992), Tilmann (2001), Godard and Stanislas (2006b), etc.).

3.3.3 Pulsed-jets

3.3.3.1 Description

As the flow rate needed for continuous jets is often large and leads to a huge energy consumption, pulsed-jets have been imagined to replace continuous jets as they need less energy (Tilmann et al. (2000), McManus et al. (1994), etc.). The principle of pulsed-jets is to generate intermittent vortices that could merged to form a streamwise vortex similar to the vortex generated by the equivalent steady jet. As the pulsed-jet is not continuously open, less mass flow rate is needed, so less energy is needed.

Two new parameters are involved : the pulsed frequency f and the duty cycle DC. The duty cycle DC corresponds to the ratio of the time where the jets is on during one period, over the time of a period. Generally, pulsed-jets studies are based on the optimum continuous jets configuration, and the only parameters which are varied are the jet exit velocity VR, the duty cycle DC and the pulsed frequency f (Tilmann et al. (2000), Kostas et al. (2007, 2009), Shaqarin (2011), etc.).

3.3.3.2 Conception and realisation

To activate the jet, commercial solenoid valves can be used as in the studies of Kostas et al. (2007, 2009), Shaqarin (2011) (FESTO valves, type MH2). This type of valves are however limited to a maximum frequency of about $100Hz$ at $DC = 50\%$ (Kostas et al. (2007, 2009)). This low frequency could be very limiting for real applications,

as for example, Tilmann (2001) found that, for a wing at high angle of attack at Mach about 0.7, better control on the drag is obtained for $f > 200Hz$.

An other solution was then used by Tilmann (2001). He developed a specific actuator for his study. It consists of a rotating hollow shaft connected at its end to compressed air supply. This shaft had 8 holes on its perimeter at the position of each jet. When the shaft position corresponds to a position where a shaft hole is in front of a jet hole, the jet is open. By rotating the shaft, the jets are then open-close 8 times per turn. This device is very compact and was successfully integrated by Tilmann (2001) in a DERA M2303 airfoil and he showed that performances can be improved in high lift conditions with pulsed-jets VGs. He found also that pulsed-jets VGs can give comparable results to continuous jets but with less drag and less mass flow rate.

3.3.3.3 Effects of the pulsed-jets parameters

Kostas et al. (2007, 2009) have done a parametric study of pulsed-jets VGs on a bump with APG but without separation. The control efficiency was then quantified by the gain in friction downstream the VGs, as was done by Godard and Stanislas (2006a,b). When opening the valve, they found a jet exit overshoot compared to the same steady jet (with same pressure supply), that rapidly goes down to a value closed to the steady jet. This overshoot leads to higher VR values at the beginning that leads to better control efficiency as was seen in section 3.3.2, but with the same needed pressure supply.

When jets are pulsed, Kostas et al. (2007, 2009) also found, as for steady jets, that the gain in friction continuously increases with increasing VR. They found that the gain in friction continuously increases with increasing the duty cycle DC. The gain in friction was also found to continuously increase with the total mass flow rate. However, they found about no influence of the pulsed frequency in the investigated range 2 to $40Hz$. Maybe the maximum tested frequency was to small to evident frequency effect as Tilmann (2001) found better results when increasing the pulsed frequency f.

Finally, Kostas et al. (2007, 2009) found that pulsed counter-rotating jets gave best results than the co-rotating ones and it was also found that the flow react more rapidly with the counter-rotating configuration. They finally proposed a control strategy for optimising pulsed-jets : first, the optimum steady jets configuration has to be found, then on this configuration, pulsed-jets has to be tested to find an optimum pulsed frequency. Finally the duty cycle has to be optimized or used as input parameter for closed-loop control.

3.3.4 Synthetic jets

Synthetic jets have also been developed for flow control purposes. They differ from the pulsed-jets by a suction phase that follows the discharge phase. No compressed air is then needed. They are generated by imposing oscillations to a membrane in a cavity under the jet hole (Milanovic and Zaman (2005)). The oscillations of the membrane creates an oscillating pressure in the cavity, that creates the discharge phase when the pressure in the cavity is higher than the outside pressure, and a

suction phase when the pressure in the cavity is lower than the outside pressure. These devices have a zero net mass flow rate, but as the cross-flow does not react in the same way to the suction phase and the discharge phase, a net momentum flux is created that leads to flow control effects (Milanovic and Zaman (2005)). Milanovic and Zaman (2005) found that synthetic jets can give similar vortices and similar jet penetration in the cross-flow as continuous jets, so employing synthetic jets should be possible for real flow separation control applications. Other synthetic actuators exist, such as plasma jets, etc., but will not be described here as it is not the aim of this paragraph.

3.3.5 Closed loop active control

As was seen in the previous sections, optimising the devices is an important issue for flow control applications as no benefice is done if more energy is injected for the control than the save by control. When an optimal steady or pulsed-jets configuration is found, the next step is then to introduce closed-loop control (or reactive control) to inject just the needed energy into the flow to achieve the desired effect. Closed-loop control minimises then the energy consumption, but can also prevent a reappearance of separation due to variations of the flow conditions (Shaqarin (2011)).

To achieve closed-loop control, a feedback sensor has to be set in the separation region to give, in real time, the control efficiency, so that one control parameter can be readjusted. In closed-loop flow control studies, most of the time, the feedback sensor used is an unsteady pressure sensor placed in the separation region. However, Simpson (1996) has shown that wall friction fluctuations are more sensitive to detect the separation than wall pressure fluctuations. Recently, Shaqarin (2011), Shaqarin et al. (2011) used a friction probe sensor as feedback sensor and succeed to reattached the thick boundary layer, which is also the aim of the present study. The actuators configurations used was based on the optimum co-rotating configuration found in the present study. The input variable parameter was the duty cycle DC, and the pulsed frequency and VR were fixed. The work of Shaqarin (2011) opens interesting possibilities for applying closed-loop control to real configurations.

4 Conclusion and objectives of the present work

Significant progress have been done toward the understanding of a ZPG turbulent boundary layer. However, strong controversies are still remaining on the mean profile of ZPG boundary layer, and none of the theories proposed has proven to be fully adequate. It is the same concerning the turbulent intensity and higher moments. When considering a perturbed turbulent boundary layer, such as with APG, FPG, curvature, etc., there is stronger divergence between the theories, and the flow separation process seems not fully understood. Before going to flow control, it appears that more studies are needed to obtain a better understanding of the behaviour of a perturbed turbulent boundary layer. It would then be possible to determined the modifications of the flow that control has to bring to achieve the desired results. This can lead to a universally optimum flow control.

However, understanding the physics of a perturbed turbulent boundary layer is a difficult task as many researchers all over the world have not succeeded since about seven decades. Parametric studies of flow separation control for finding optimum configurations can then be a way to answer the question, but to achieve this goal, careful comparisons of the controlled and uncontrolled flow has to be done to evident the differences.

The aim of the present work follows this idea. It presents a parametric study of passive and active flow separation control. This is accompanied with details characterisation of the considered APG turbulent boundary layer flow with separation, and this with and without control. Detailed characteristics of these flows are obtained thanks to the large scales of the LML turbulent boundary layers wind tunnel (Carlier (2001), Carlier and Stanislas (2005)) where the specific model used was set.

This thesis is organised in six main parts. In the first one (i.e. Chapter 2), the experimental set-up is presented. In the second one (i.e. Chapter 3), the characteristics of the flow over the ramp model are given. The third (i.e. Chapter 4) and fourth (i.e. Chapter 5) parts present the results concerning the parametric passive control study and the parametric active control study respectively. The fifth part (Chapter 6) presents the flow physics of some active control configurations. Finally, the last part (i.e. Chapter 7) is a general conclusion and gives also some perspectives.

Chapter 2

Experimental set-ups

1 Introduction

All the studies presented in the present chapter were performed in the "Laboratoire de Mechanique de Lille" (LML). The aim of this chapter will be to describe the facility, the tools and the metrology that were used for this study. First, the LML wind tunnel and the ramp model will be presented. Then the actuators used for flow control will be described. Finally, the metrology used (such as flow visualisation, pressure measurements, hot-wire anemometry, hot-film friction probe and Particle Image Velocimetry (PIV)) will be presented.

2 The LML wind tunnel facility

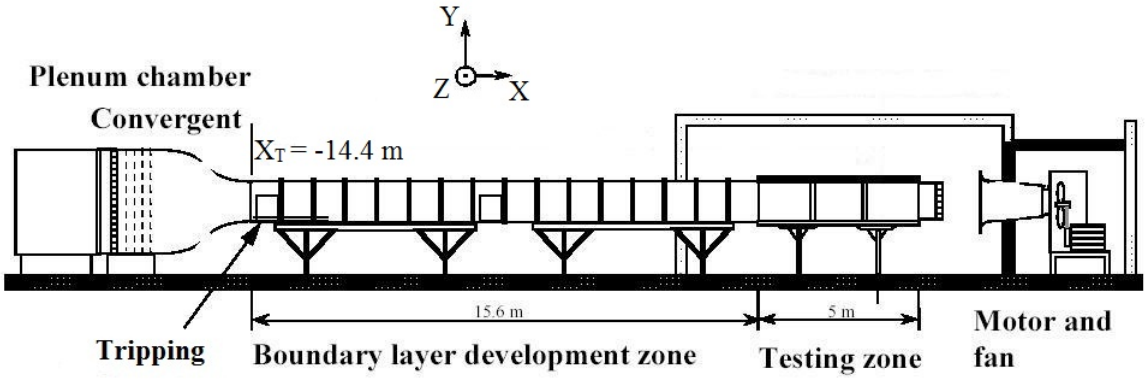

Figure 2.1: Front view of the turbulent boundary layers wind tunnel.

Figure 2.1 is a front view of the turbulent boundary layers (TBL) wind tunnel used. It is about 20 m long. The last 5 m are transparent on all sides for optical access purpose, and the test section is $1 \times 2\ m^2$. The free-stream velocity is ranging from 1 to 10 m/s. The wind tunnel can be used in closed loop with temperature regulation or opened to the outside to allow the use of smoke. In the present study, it was used in the closed loop configuration. The free-stream velocity is regulated at $\pm 0.5\%$ and the temperature at $\pm 0.2\ ^\circ C$. The origin O of the wind tunnel coordinate

system that will be used in all this work (see Figure 2.2) is placed at midspan on the lower wall, at the beginning of the converging part of the ramp described in the next paragraph. The X-axis is along the streamwise direction, the Y-axis is normal to the wall and this reference frame is direct. The boundary layer under study develops on the lower wall. It is tripped at the entrance of the wind tunnel by a grid laid on the floor at $X_T = -14.4$ m. The boundary layer thickness reaches about 30 cm at $X = 5.2$ m (or 19.6 m from the trip, see Carlier (2001) and Carlier and Stanislas (2005)).

3 The AVERT ramp model

The ramp is divided into four parts (see Figure 2.2). The first part is a smooth converging part with a contraction ratio of 0.75 and a length of 1330 mm. The equation is a third order polynomial (X and Y in mm) : $Y = -\frac{500}{1200^3}.X^3 + \frac{750}{1200^2}.X^2$ for $0 \leq X \leq 1200$ mm, and Y = 250 mm for $1200 \leq X \leq 1330$ mm. It is used for two purposes. The first one is to be able to generate an adverse pressure gradient. The second one, is to be able to apply a suction through a porous slot, placed near the inflexion point, in order to vary the incoming boundary layer thickness.

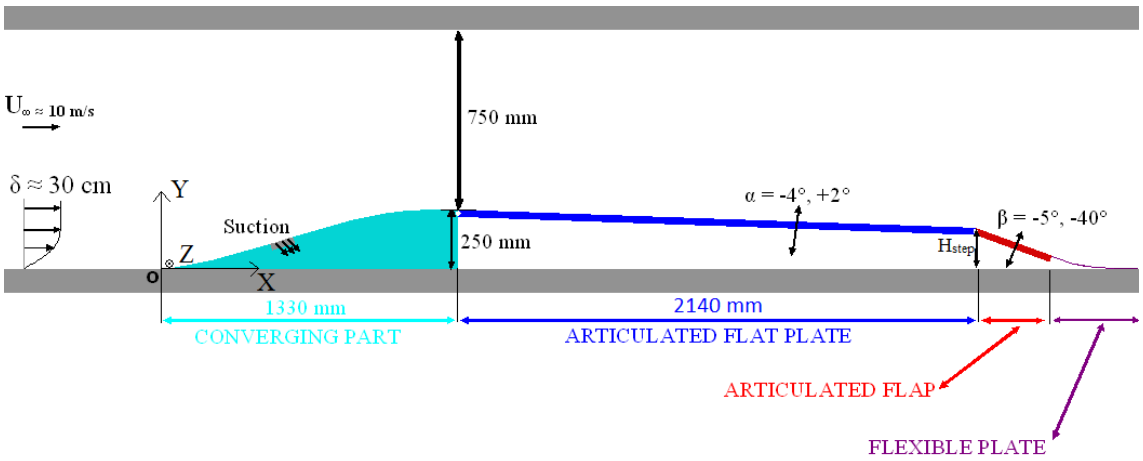

Figure 2.2: Schematic view of the AVERT ramp model.

The second part is an articulated flat plate of 2140 mm in length, used to tune the pressure gradient. It can rotate from $\alpha = 2°$ to $\alpha = -4°$ around its leading edge. For $\alpha = 0°$ the flat plate is parallel to the streamwise direction. α is counted positive if it corresponds to a positive rotation around the Z-axis. For positive values of α the boundary layer is under favourable pressure gradient. For negative values of α, adverse pressure gradients are encountered. This flat plate is made of four interchangeable parts (two of 0.7 m and two of 0.35 m). One of them is composed of six inserts ($625 \times 135\ mm^2$) in which different equipments can be installed (actuators, sensors, glass for optical access, etc.).

The third part is again an articulated flat plate of 34 cm (called "flap" latter in the text). It can rotate from $\beta = -5°$ to $\beta = -40°$ around its leading edge.

For $\beta = 0°$ the flap is parallel to the streamwise direction. β is counted positive if it corresponds to a positive rotation around the Z-axis. The aim of this part is to fix the separation when it exists. By decreasing β, the adverse pressure gradient is increased. Therefore, it can modify the extend of an existing separation or initiate one. This flap is made of three inserts (625×240 mm^2) for equipment purpose (actuators, sensors, glass for optical access, etc.).

Finally, the fourth part is a flexible plate used to enable a smooth connection between the end of the flap and the floor of the wind tunnel.

In order to represent the velocity results along the ramp and in the separation region, a curvilinear abscissa s will be used on the model with the origin at the beginning of the ramp and a local Frenet (x, y, z) reference frame with the origin at s, the x-axis tangent to the wall, the y-axis normal and the z-axis spanwise.

4 Actuators for flow control

4.1 Passive actuators

The passive actuators used were thin plate vortex generators as suggested by Lin et al. (1991). They were manufactured with aluminium plate 0.5 mm in thickness. The shape was triangular (see Figure 1.3). Three sizes were manufactured and tested ($h = 15, 30, 60$ mm). The parameter $\frac{l}{h}$ and the angle β_{pd} were fixed to respectively 2 and 18°, that correspond to the optimum parameters found by Godard and Stanislas (2006a). At the base of the actuator, there is a 90° and 10 mm long fold to glue the actuator to the surface with double sided tape. The orientation of this fold was opposite to the side of the actuator that faces the flow in order to put it in the wake to minimize the perturbation.

4.2 Active actuators

4.2.1 Actuators description

For the active flow control, it was decided to test 2 diameters of jets (6 and 12 mm) in co and counter-rotating arrangement. Figure 1.6 gives the definition of the parameters used to defined the co and counter-rotating configurations. Five configurations of three inserts were designed and manufactured for the active control experiments. The chosen configurations are two co-rotating (one for 6 mm and one for 12 mm diameter), and three counter-rotating (one for 6 mm and two for 12 mm diameter).

The angle β was chosen at 35° and α was chosen at 55° or 125°, 55° corresponds to downstream blowing, and 125° corresponds to upstream blowing. As the drills were realized at the center of the inserts, the configurations $\alpha = 55°$ and $\alpha = 125°$ are obtained with the same inserts, just by turning around the assembly on the ramp. The chosen angles correspond to the optimum angles found by Godard and Stanislas (2006b).

Also from the study of Godard and Stanislas (2006b), the $\frac{L}{\Phi}$ parameter for the counter-rotating configurations was taken as 15, except for one of the counter-

rotating configurations with $\Phi = 12$ mm, where it was 12.3. For co-rotating jets, the optimum $\frac{\lambda}{\Phi}$ found by Godard is 6. This was out of reach due to technical constraints. For $\Phi = 12$ mm, the minimum value tested was $\frac{\lambda}{\Phi} = 6.8$, and for $\Phi = 6$ mm, the minimum value was $\frac{\lambda}{\Phi} = 13.6$. For the counter-rotating configurations, Godard suggested $\frac{\lambda}{\Phi}$ around 32. Due to technical constraints, this value was not accessible and $\frac{\lambda}{\Phi}$ was set at 27.3.

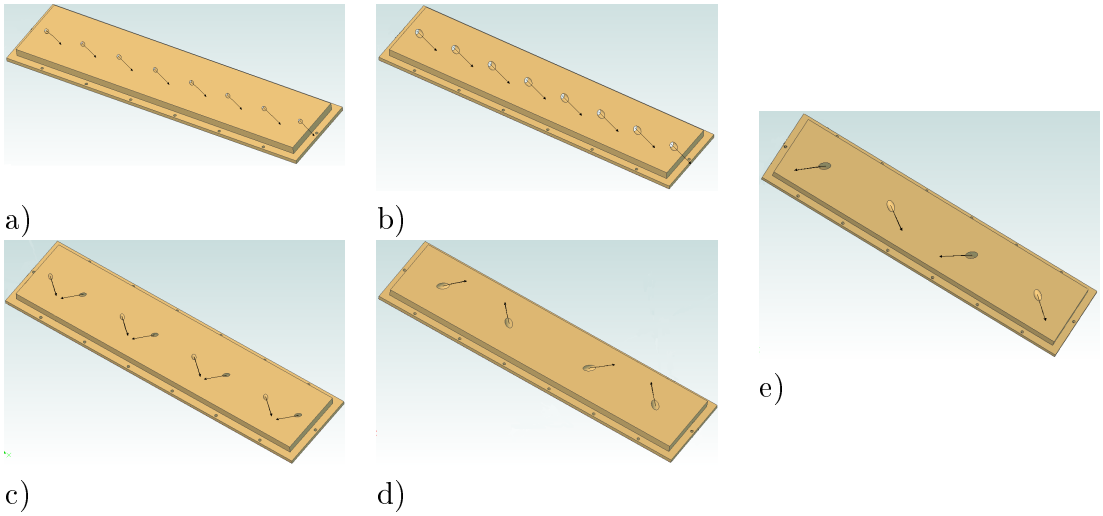

Figure 2.3: Insert for a) co-rotating $\Phi = 6$ mm, b) co-rotating $\Phi = 12$ mm, c) counter-rotating $\Phi = 6$ mm, d) counter-rotating $\Phi = 12$ mm and $\frac{L}{\Phi} = 15$, e) counter-rotating $\Phi = 12$ mm and $\frac{L}{\Phi} = 12.3$.

Figure 2.3 gives the CAO design for the 5 insert configurations. The drills were 8 mm for the 6 mm jets, and 14 mm for the 12 mm jets. A polyamide tube of same diameter was inserted in these drills and cut adjusted to the surface.

The 12 mm actuator tubes were connected to a tank with 12 mm tubes of 2.4 m long using quick connectors. The total length of tube from the tank to the surface was about 2.5 m, which represents around 210 internal diameters. The pipe flow at the jets outlet can thus be supposed fully developed. The 6 mm actuator tubes were connected to an enlargement of 12 mm. These enlargements were connected to the tank with tubes of 12 mm diameter and 2.4 m long. As the length of the 6 mm tubes is 50 internal diameters (30 cm), the pipe flow at the jets exit is again supposed fully developed. The tubes connections are illustrated in Figure 2.4.

4.2.2 Compressed air supply and quantification circuit

The compressed air is provided by a 75 kW compressor which delivers 880 m^3/h at 7.5 bars relative to the atmospheric pressure in a 2 m^3 tank. Before this tank, the compressed air is filtered and dried by a dryer of 5 kW so that it is free of water and particles. The compressor regulates the gauge pressure in the tank between 6.5 and 7.5 bars. The 2 inches outlet of the tank is connected to the regulation and quantification circuit (Figure 2.5). This circuit is composed first by a pressure regulator of 1.5 inches (Figure 2.6). It can regulate the gauge pressure between 0.5 bars and its inlet pressure with a maximum flow rate of 960 m^3/h.

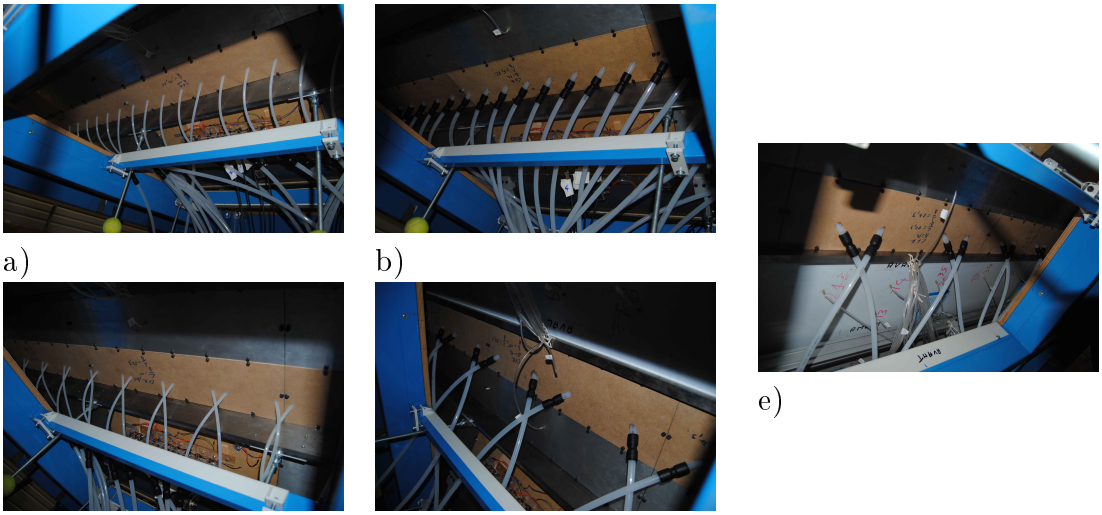

Figure 2.4: Tubes connections for a) co-rotating $\Phi = 6$ mm, b) co-rotating $\Phi = 12$ mm, c) counter-rotating $\Phi = 6$ mm, d) counter-rotating $\Phi = 12$ mm and $\frac{L}{\Phi} = 15$, e) counter-rotating $\Phi = 12$ mm and $\frac{L}{\Phi} = 12.3$.

Figure 2.5: Compressed air regulation and quantification circuit.

Then there is a 2 inches progressive valve that serves to tune the guage pressure between 0 and 7.5 bars (Figure 2.6). After that pressure regulator system, the compressed air supply circuit is divided into two circuits : one of 2 inches for large flow rates, and one of 0.5 inch for small flow rates. The two circuits begin by a valve so that the appropriate circuit can be selected. On the 2 inches circuit, after 60 DN of straight pipe, there is a vortex meter VTX 2 of DN50 from Bopp & Reuther which measures air flow rate between 15 and 560 m^3/h at less than 1.5% (even for air at 1 bar absolute) (Figure 2.7). On the 0.5 inch circuit, after 300 DN of straight pipe, there is a vortex meter VTX 2 of DN15 from Bopp & Reuther which measures air flow rate between 2 and 25 m^3/h at less than 1.5% (even for air at 1 bar absolute) (Figure 2.7).

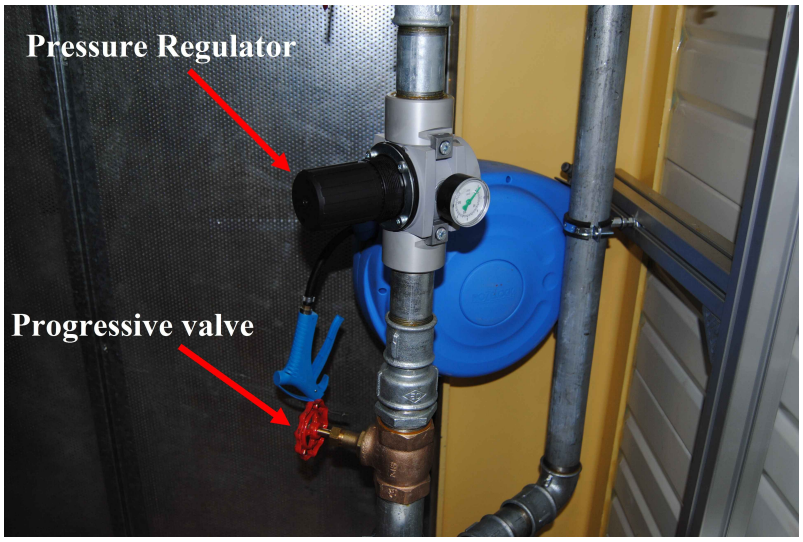

Figure 2.6: Compressed air circuit : zoom on the pressure regulation part.

After each vortex meter, there is stitching of 0.5 inch to measure the pressure in the pipe with an absolute manometer (0 to 10 bars) having an uncertainty of ±0.1% of the full scale (Figure 2.7).

After the reconnection of the two circuits, there is a temperature sensor (-50 to 400°C) with an uncertainty less than ±0.2% of the reading value. With the pressure (P) and the temperature (T), the air density can be calculated with $\rho = \frac{P}{rT}$ (r = 287 kJ/kg/K) at ±1%. With the density ρ and the flow rate Q_v, the mass flow rate can be calculated as : $Q_m = \rho Q_v$ at less than ±2%.

Finally, the circuit is connected to a 90 l tank through a 2 inches tube (Figure 2.8). The tank inlet tube is 3 inches in diameter, and goes 60 cm inside the tank. The maximum velocity in the tank was 1.5 m/s for the maximum flow rate needed for the present experiments (i.e. 400 m^3/h). The corresponding residence time in the tank was 0.8 s. On the cover of the tank, 49 drills ($G3/8$) have been realized to supply compressed air to the actuators. A set of 12 mm diameter and 2.4 m long polyamid tube was connected to these 49 outputs with $G3/8$ quick connectors. The other end of the tubes was connected to the actuators with quick connectors.

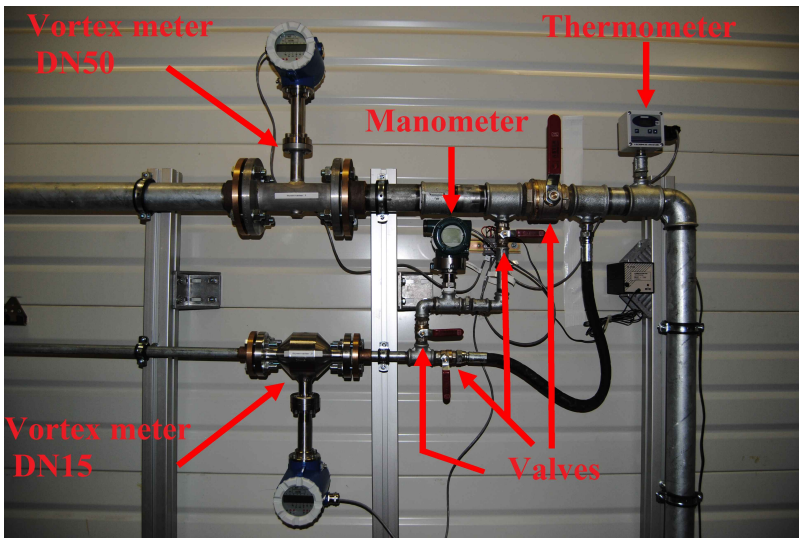

Figure 2.7: Compressed air circuit : zoom on the mass flow rate measurement part.

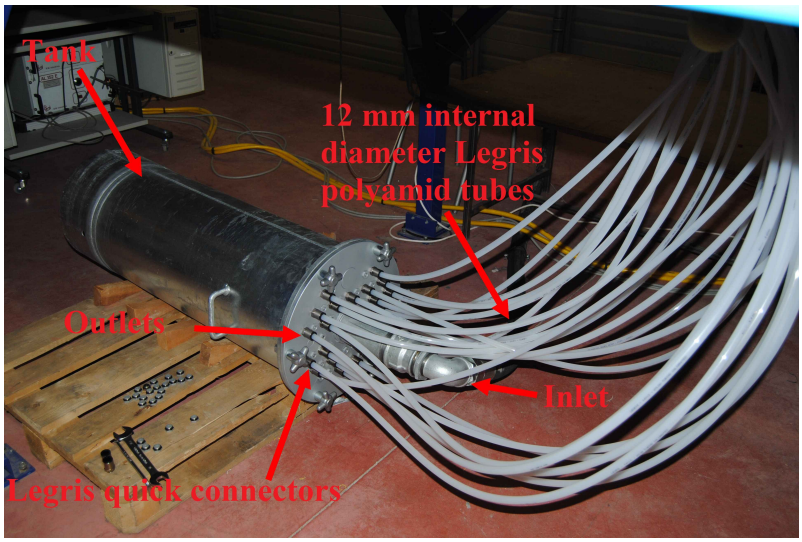

Figure 2.8: Compressed air circuit : the tank.

5 Metrology

5.1 Standard metrology

5.1.1 Flow visualisations

Basic flow visualisations were carried-out to check quickly the behaviour of the flow over the ramp. Wool tufts visualisations were used to check the transverse homogeneity of the flow, that no separation appears on the flat plate and to evidence the separation when it exists on the flap. The length of the green cotton wool tufts used were 4 cm. The tufts were stuck on the ramp wall with electrical insulation tape. Six transverse lines (s = 1360 mm, s = 2100 mm, s = 2450 mm, s = 2800 mm, s = 3150 mm and s = 3500 mm) of wool tufts, spaced by 4 cm in the transverse direction, were placed on the flat plate. Also, a dense distribution of wool tufts was set on the flap for a visual check of the separation (every 4 cm in the transverse direction and every 2 cm in the streamwise direction, in staggered rows). As interactions were found between wool tufts when separation exist on the flap, to obtain a better flow separation visualisation, one row over two of wool tufts on the flap was removed and two tufts over four were also removed in the transverse direction.

To characterize more precisely the separation on the flap for the configuration that was used for flow separation control ($\alpha = -2°$ and $\beta = -22°$), oil film visualisations were carried out on the flap. The mixture used was composed of paraffin oil, oleic acid and titanium dioxide based on the study of Gardarin (2009). With the angle of $-22°$, it was difficult to find a mixture that compensates the gravity effects and shows only the flow effects. Various compositions with different percentages of the three products were tested. The titanium dioxide serves for the contrast. The paraffin oil is the most viscous liquid of the two, so it was impossible to apply a thin film of a mixture composed of paraffin oil and 9% of titanium dioxide. The tests with only oleic acid and titanium dioxide have shown nothing due to the predominance of gravity effects as when adding oleic acid, the mixture becomes less and less viscous. Adding oleic acid also ensure a good mixing of the titanium dioxide into the mixture. The optimum mixture that was found and used was composed of 82% of paraffin oil, 9% of oleic acid and 9% of titanium dioxide. All the flap and a little bit upstream of it was painted as quick as possible with this mixture with a paintbrush to obtain an uniform thin film. Then the wind tunnel was switched on as quick as possible to limit the gravity effects on the film. It was found that 3h of blowing was needed to obtain a good oil visualisation.

5.1.2 Pressure distribution

5.1.2.1 Localisation and description of the pressure taps

The ramp was originally equipped with 26 pressure taps (14 pressure taps in the streamwise direction and 12 in spanwise direction) to allow ramp pressure distribution measurements. However, there was no tap at the beginning of the study on the flap and at the end of the flat plate. After the first campaign of pressure measurements, it was shown that pressure measurements in the separated region will be

interesting, so it was decided to add 12 taps (call taps number 15 to 26), 9 on the flap and 3 on the flat plate just before the flap articulation. The final distribution of pressure taps is shown in Figure 2.9 and the coordinates s and z are given in Table 2.1, with s the curvilinear abscissa.

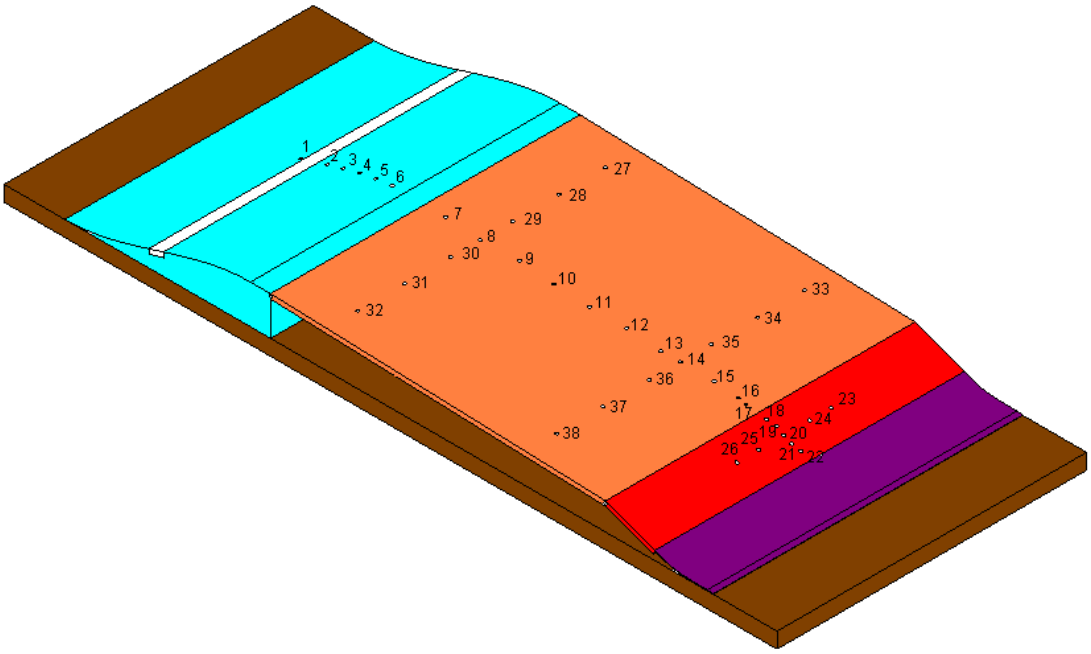

Figure 2.9: Localisation of the pressure taps on the ramp.

Each pressure tap is composed of an insert, 4 mm in diameter and 30 mm in length, inserted in the ramp wall. It was then stuck and adjusted to the ramp surface. On the lower side, there is a hole of 3 mm in diameter and 28 mm length. On the upper side the hole is 0.5 mm in diameter. The quality of these 0.5 mm holes was checked with care using binocular microscope.

Pressure taps number 1 to 22 are distributed streamwise at midspan and give the streamwise pressure distribution. The other taps give three spanwise measurements to check the transverse homogeneity.

5.1.2.2 Pressure and pressure gradient distributions measurements

Pressure measurements were realised using a manual scanivalve and a Furness micro-manometer (reference FC014, range: 0 to 10 mmH_2O, accuracy : $\pm 0.5\%$ of the measured value in the range 0.01 to 10 mmH_2O).

The streamwise pressure taps drilled on the ramp give access to the streamwise pressure distribution (pressure taps number 1 to 22 : see Figure 2.9). The pressure taps number 23 to 38 were used to check the homogeneity of the mean flow in the transverse direction at three streamwise positions : $s = 1727$ mm, $s = 3010$ mm and $s = 3656.5$ mm (with s the curvilinear coordinate of the ramp). The pressure coefficient $C_p = \frac{P-P_6}{\frac{1}{2}\rho U_\infty^2}$ can thus be calculated with P_6 the reference pressure corresponding to tap number 6, ρ the air density and U_∞ the free stream velocity upstream of the

Table 2.1: Coordinates s and z of pressure taps. (s is the curvilinear abscissa)

tap number	1	2	3	4	5	6	7	8
s(mm)	539	689	800	944	1045	1146	1495	1727
z(mm)	0	-10	10	-5	5	0	0	10
tap number	9	10	11	12	13	14	15	16
s(mm)	1960	2192	2426	2660	2893	3010	3219	3384
z(mm)	-10	0	5	-5	7.5	0	-10	0
tap number	17	18	19	20	21	22	23	24
s(mm)	3443	3544	3599.25	3656.5	3713.75	3769	3656.5	3656.5
z(mm)	10	5	-5	0	5	-5	-305	-163.5
tap number	25	26	27	28	29	30	31	32
s(mm)	3656.5	3656.5	1727	1727	1727	1727	1727	1727
z(mm)	163.5	305	-800	-500	-200	200	500	800
tap number	33	34	35	36	37	38		
s(mm)	3010	3010	3010	3010	3010	3010		
z(mm)	-800	-500	-200	200	500	800		

ramp. The pressure gradient was computed between two measurement points (at $i+1/2$ where i and $i+1$ are two successive measurement points) as follow (equation (2.1)):

$$\left(\frac{dP}{ds}\right)_{i+1/2} = \frac{P_{i+1} - P_i}{\Delta s} \tag{2.1}$$

with P_i the pressure at point i.

To achieve a better accuracy on the pressure gradient, taps number 1 to 5, number 8 and 19 to 22 were read with P_6 as reference (P_6 is the smallest pressure). Taps number 7 and 9 to 18 were read with P_8 as reference. The pressure taps numbers 23 to 26 were read with P_{20} as reference. The taps number 27 to 32 were read with P_8 as reference and taps numbers 33 to 38 with P_{14} as reference.

All the pressure measurements were smaller than the atmospheric pressure. The flow accelerates in the converging part $0 \leq s \leq 1360$ mm which induces a decrease of the pressure coefficient until the suction peak at $s = 1146$ mm (pressure tap number 6 (see Figure 2.10)). Then a pressure recovery occurs on the flat plate which is modified by α. At the flap articulation, a new suction peak occurs which can be seen at $s = 3443$ mm corresponding to pressure tap 17. Then a pressure recovery is observed on the flap which can be tuned by β.

5.1.2.3 Pressure and pressure gradient distributions accuracy

5.1.2.3.1 Introduction

To validate conclusions, the first thing to look at in measurements is the accuracy. To achieve the best possible accuracy, the time constant of the Furness was set at its maximum value and two minutes were waited at minimum to be sure that the

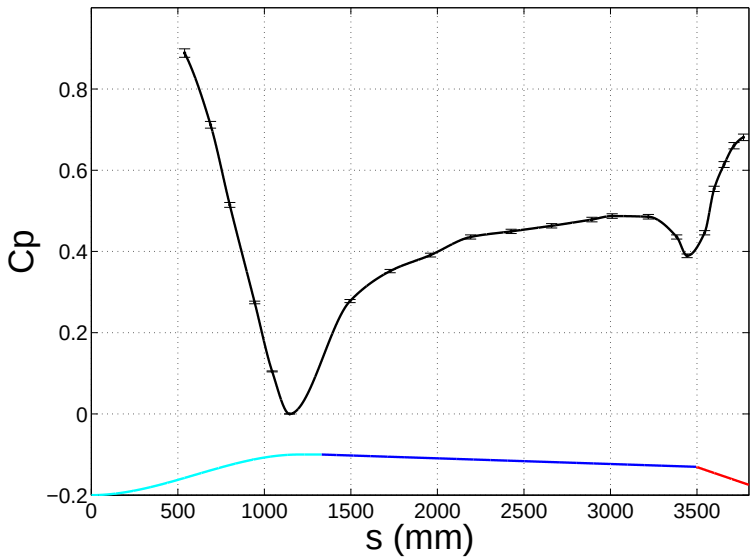

Figure 2.10: Pressure coefficient distribution along the ramp for $U_\infty = 10\ m/s$, $\alpha = -2°$ and $\beta = -22°$.

measurement was stabilized. For the points on the flap, due to stronger pressure fluctuations in the separated area, five minutes were waited to reach stabilization.

5.1.2.3.2 Accuracy given by the quadratic mean estimation

The first approach used to estimate the uncertainty was the quadratic mean estimation. As $C_p = \frac{P-P_6}{\frac{1}{2}\rho U_\infty^2}$, and $\rho = \frac{P_a}{rT}$, with P_a the atmospheric pressure, r the constant of ideal gas, $r = 287\ J/kg/K$ and T the temperature, the error on C_p is given by equation (2.2) :

$$(\Delta C_p)^2 = \left(\Delta(P-P_6)\frac{\partial C_p}{\partial(P-P_6)}\right)^2 + \left(\Delta P_a \frac{\partial C_p}{\partial P_a}\right)^2 + \left(\Delta T \frac{\partial C_p}{\partial T}\right)^2 + \left(\Delta U_\infty \frac{\partial C_p}{\partial U_\infty}\right)^2 + \left(\Delta r \frac{\partial C_p}{\partial r}\right)^2 \tag{2.2}$$

This expression can be rearranged as equation (2.3) :

$$\frac{\Delta C_p}{C_p} = \sqrt{\left(\frac{\Delta(P-P_6)}{P-P_6}\right)^2 + \left(\frac{\Delta P_a}{P_a}\right)^2 + \left(\frac{\Delta T}{T}\right)^2 + \left(2\frac{\Delta U_\infty}{U_\infty}\right)^2 + \left(\frac{\Delta r}{r}\right)^2} \tag{2.3}$$

The estimation of $\Delta(P - P_{reference})$ is given by the Furness uncertainty which should be $\pm 0.5\%$ of the value $P - P_{reference}$. As $P - P_{reference}$ is read on the Furness scale, the accuracy is slightly lower. The real Furness uncertainty is estimated at $\pm 0.6\%$ of the measuring value. So, for a point number i which is directly read with $P_{reference} = P_6$, the uncertainty $\frac{\Delta(P_i - P_6)}{P_i - P_6}$ is $\pm 0.6\%$, and for a point number i which is read with $P_{reference} = P_j$, $j = 8$ or 20, the uncertainty $\Delta(P_i - P_6)$ is

$\frac{0.6}{100}(|P_i - P_j| + |P_j - P_6|)$. Finally, for a point which is read with $P_{reference} = P_{14}$, the uncertainty $\Delta(P_i - P_6)$ is $\frac{0.6}{100}(|P_i - P_{14}| + |P_{14} - P_8| + |P_8 - P_6|)$.

The other uncertainties are $\Delta P_a = \pm 100$ Pa, $\Delta T = \pm 0.2°C$ and $\Delta U_\infty = \pm 0.5\%$ of U_∞. The uncertainty on r was neglected.

After computing it in all cases investigated, the uncertainty was found almost independent of α and β, because C_{p_i} keeps the same order whatever α and β. It was also found independent of the free-stream velocity because the pressure coefficient distribution was found independent of it too. This uncertainty is varying between $\pm 1.1\%$ and $\pm 1.4\%$ with a mean at $\pm 1.2\%$. So the accuracy on the pressure coefficient is $\pm 1.2\%$.

To estimate the uncertainty on the pressure gradient, the same method can be used. As $\left(\frac{dC_p}{ds}\right)_{i+1/2} = \frac{C_{p_{i+1}} - C_{p_i}}{\Delta s} = \frac{P_{i+1} - P_i}{\frac{1}{2}\rho U_\infty^2 \Delta s}$, the error on $\frac{dC_p}{ds}$ is given by equation (2.4) :

$$\left(\frac{\Delta \frac{dC_p}{ds}}{\frac{dC_p}{ds}}\right)^2 = \left(\frac{\Delta(P_{i+1} - P_i)}{P_{i+1} - P_i}\right)^2 + \left(\frac{\Delta(s_{i+1} - s_i)}{s_{i+1} - s_i}\right)^2 + \left(\frac{\Delta P_a}{P_a}\right)^2 + \left(\frac{\Delta T}{T}\right)^2 + \left(2\frac{\Delta U_\infty}{U_\infty}\right)^2 + \left(\frac{\Delta r}{r}\right)^2 \tag{2.4}$$

In most cases, the estimation of $\Delta(P_{i+1} - P_i)$ is given by two sources : first by the Furness uncertainty on $P_{i+1} - P_{ref}$ ($\pm 0.6\%$ of this value) and secondly by the Furness uncertainty on $P_i - P_{ref}$ ($\pm 0.6\%$ of this value). If $P_{i+1} - P_i$ is directly read on the Furness, $\Delta(P_{i+1} - P_i)$ is estimated as $\frac{0.6}{100}(P_{i+1} - P_i)$. If P_{i+1} and P_i are read with the same reference P_{ref}, the uncertainty $\Delta(P_{i+1} - P_i)$ is estimated with a quadratic mean of the two errors as $\frac{0.6}{100}\sqrt{(P_{i+1} - P_{ref})^2 + (P_i - P_{ref})^2}$. Finally, if P_{i+1} and P_i are read with different references ($P_{ref_j} = P_8$ or P_6), the uncertainty $\Delta(P_{i+1} - P_i)$ is estimated with a quadratic mean of the three errors as $\frac{0.6}{100}\sqrt{(P_{i+1} - P_{ref_{i+1}})^2 + (P_i - P_{ref_i})^2 + (P_8 - P_6)^2}$.

The estimation of $\Delta(s_{i+1} - s_i)$ is ± 4 mm ($\Delta s_i = \pm 2$mm) for $i = 1$ to 14 and ± 0.4 mm ($\Delta s_i = \pm 0.2$mm) for $i = 15$ to 21.

After computing it in all cases investigated, this uncertainty was found dependent on α and β because these two angles tune the pressure gradient. This uncertainty can be important when $\frac{dC_p}{ds}$ is small. On average, for $U_\infty = 10\ m/s$, it is of the order of $\pm 6.5\%$. For $U_\infty = 7\ m/s$, it is about $\pm 7\%$. Finally, for $U_\infty = 5\ m/s$, it is about $\pm 7.5\%$. These average estimations are representative of the real uncertainties, except when $\frac{dC_p}{ds}$ is very small where the uncertainty can reached 30%.

5.1.2.3.3 Accuracy given by the standard deviation method

An other way to estimate the uncertainty is to repeat the same measurement several times, in the same day and on different days. This has been done on the configuration $\alpha = -2°$ and $\beta = -20°$. The pressure distribution in this configuration was acquired seven times. Two acquisitions were performed on the 6^{th} of July 2009, two on July 23^{nd}, two on July 24^{th} and one on August 31^{th}. The results obtained for the pressure

coefficient distribution and for the pressure gradient distribution are given in Figure 2.11. As can be seen, all curves collapse quite well for both streamwise pressure coefficient and pressure gradient distribution. The curves are inside the error bars obtained by the mean quadratic method described in section 5.1.2.3.2. This shows that the mean quadratic method estimates quit well the uncertainty.

Based on these seven measurements, the uncertainty can be estimate by an other method based on the estimation of the standard deviation at each point (Dixon and Massey (1957)). The mean on seven measurements for a pressure tap i is estimated by $\overline{x_i} = \frac{1}{N}\sum_{j=1}^{N} x_{i_j}$ ($N = 7$ here) and σ_i by $s_i.c$ supposing that the repartition of the measurements follows a normal law, with $s_i^2 = \frac{1}{N-1}.\sum_{j=1}^{N}(x_{i_j} - \overline{x_i})^2$ and $c = 1 + \frac{1}{4(N-1)}$. The uncertainty is given for $\overline{x_i}$ by $\pm 1.96 \times \sqrt{\frac{s_i^2}{N}}$ (the number 1.96 is given for a confidence index of 95%) and for x_{i_j}, by $\pm 2.\sigma_i$ with a confidence index of 95%. The uncertainty on x_{i_j} correspond to the same uncertainty evaluated in section 5.1.2.3.2 by the mean quadratic method.

This standard deviation method gives an error on $\overline{C_{p_i}}$ between ± 0.2 and $\pm 1.25\%$, with a mean for the 22 pressure taps of $\pm 0.5\%$ and with a confidence index of 95%. Concerning $\overline{\frac{dC_{p_i}}{ds}}$, the error obtained is between from ± 0.7 and $\pm 17\%$ with a mean for the 22 pressure taps of $\pm 2.2\%$ and a confidence index of 95%. For $C_{p_{i_j}}$ this standard deviation method gives an uncertainty from ± 0.7 to $\pm 4\%$ with a mean of $\pm 1.3\%$ and a confidence index of 95%. Finally, on $\frac{dC_{p_{i_j}}}{ds}$ the uncertainty is from ± 2 to $\pm 42\%$ with a mean of $\pm 6\%$ and a confidence index of 95%. On the configuration $\alpha = -2°$ and $\beta = -22°$, the acquisition was done 3 times, and with the standard deviation method, the results obtained are close.

As a conclusion, the repeatability of the measurements is quite good, and the accuracy, given by the standard deviation method, is $\pm 1.3\%$ on C_p and $\pm 6\%$ on $\frac{dCp}{ds}$, with a confidence index of 95%. The uncertainties given by the mean quadratic method in section 5.1.2.3.2 are then very close to the uncertainties given by the standard deviation method, so these two methods can be indifferently used to estimate the uncertainty on the pressure distribution and on the pressure gradient distribution. On all the pressure curves that will be presented, the error bars are given by the mean quadratic method which needs only one acquisition.

5.1.3 Single hot-wire

5.1.3.1 Principle

A single hot-wire allows to access locally the instantaneous streamwise velocity of the flow. Hot-wire anemometry was initiated by King (1904) based on his study of the flow around a cylinder. The principle of hot-wire anemometry is based on the heat exchanges between the flow and a thin electrical conducting wire kept at high temperature by the application of a current through it. The modification of the flow around the wire changes the heat equilibrium which changes the temperature of the wire. As the resistance of the wire is a function of its temperature, a change in flow conditions changes the resistance of the wire. To keep constant the temperature of the wire, it is set in a Wheatstone's bridge, which is equilibrated with a control loop. The current needed to equilibrate the Wheatstone's bridge is then a function of the

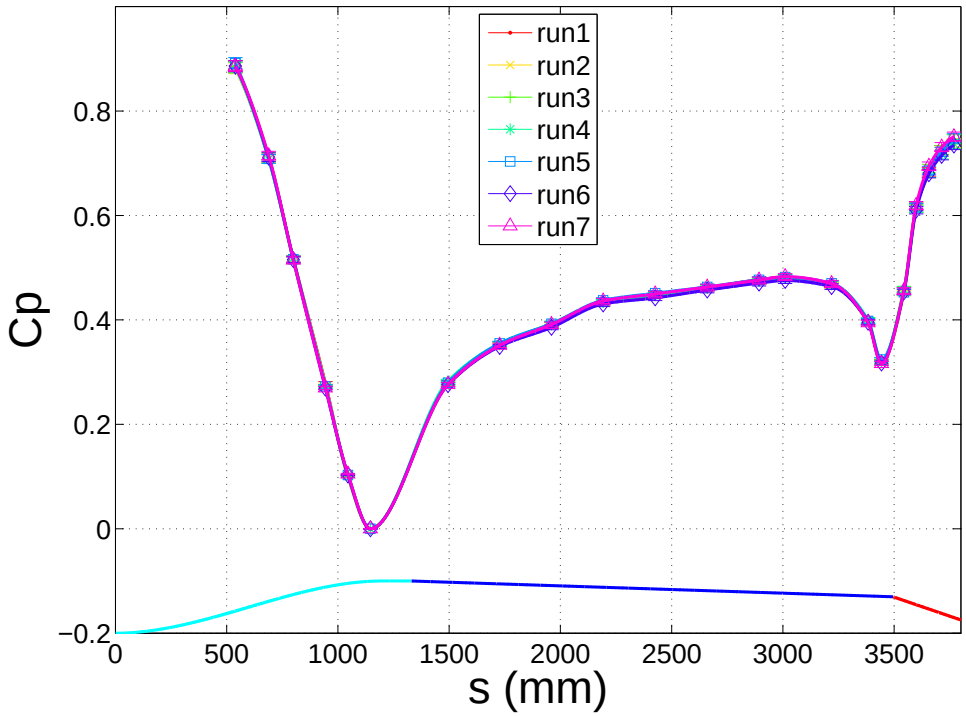

a)

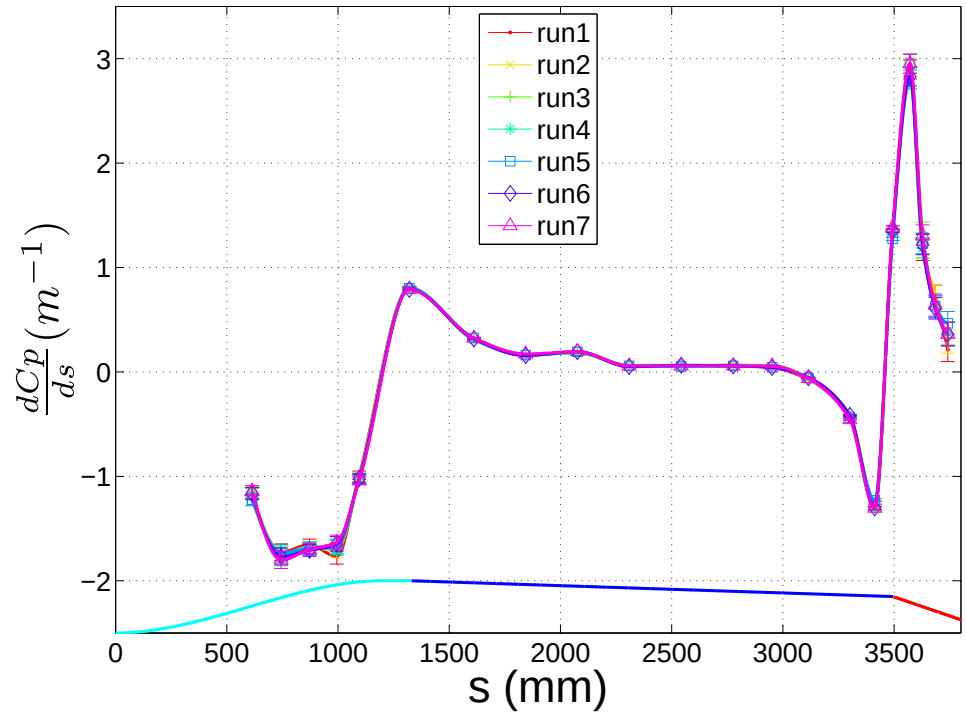

b)

Figure 2.11: a) Streamwise pressure coefficient distribution b) streamwise pressure gradient distribution, $\alpha = -2°$ and $\beta = -20°$ and $U_\infty = 10$ m/s, for different acquisitions.

local velocity. With a calibration procedure, this current can then be converted into velocity. Generally, a King's law ($E^2 = E_0^2 + bU^n$, with E the output voltage of the bridge, and U the velocity) is used to convert the current signal into the velocity. By similarity analysis, the value of n obtained is 0.5 so the calibration has to give a value for n near this value. When the temperature of the wire is kept constant, the anemometer is called "constant temperature anemometer", but other types of anemometer exist such as "constant current" or "constant voltage".

The frequency response of a hot-wire anemometer is usually high (about 50 kHz for a wire diameter of 2.5 μm), so high frequency velocity variations are accessible with this technique. If the maximum frequencies in the flow are smaller than the frequency response of the wire, the heat exchanges can be considered as quasi-steady. Usually the length of the wire is much larger than its diameter, so that the heat conductions to the prongs can be neglected. Also, the wire temperature is usually below 300°C, so that, heat radiation is also negligible. In most applications, free convection is also negligible, so that the principle of a hot-wire anemometer is mainly based on the equilibrium between the heat dissipated by Joule's effect in the wire and the forced heat convection at the surface of the wire.

As very small diameter of hot-wire is used in turbulence applications (as for example, to measure accurately the turbulence intensity peak of a turbulent boundary layer near the wall. Klewicki and Falco (1990) have shown that the wire length l has to be under 8 wall units, and as the diameter of the wire should respect $d \ll l$, this leads to a wire diameter of a few micrometers), only wires in platinum or in tungsten or a mix of the two are used, as these materials present a high enough tensile strength to sustain the flow constraints. Moreover, these materials have a high resistance temperature coefficient leading to good sensitivity and accurate measurements.

5.1.3.2 Measurements description and methodology

5.1.3.2.1 Measurements description

To characterize the boundary layer for the configuration $\alpha = -2°$ and $\beta = -22°$, which was used for control study, hot-wire profiles were measured at 5 streamwise stations. Figure 2.12 gives the positions on the ramp. The anemometer used was a constant temperature AN 1003 manufactured by AAlabSystems with a tungsten platinum boundary layer type hot-wire with a diameter of 2.5 μm and a length of 0.5 mm. The probe was moved normal to the surface with a displacement system having an accuracy of $\pm 1 \mu m$ for displacements below $\pm 1000 \mu m$ and $\pm 10 \mu m$ for displacements above $\pm 1000 \mu m$. The hot-wire signal was amplified and offset to use the full range of the 16 bits data acquisition board. A detailed description of the acquisition chain can be found in Carlier (2001).

For each measurement stations, to ensure the results, several profiles were measured until reaching three superimposed profiles at less than 2%. Each profile is composed of 49 points distributed logarithmically along the wall normal. The first point was about 0.2 mm from the wall and was measured with a cathetometer (accuracy ± 0.05 mm). By measuring the distance from the wall of the first measurement point, vibrations was observed at the selected stations. They were then quantified

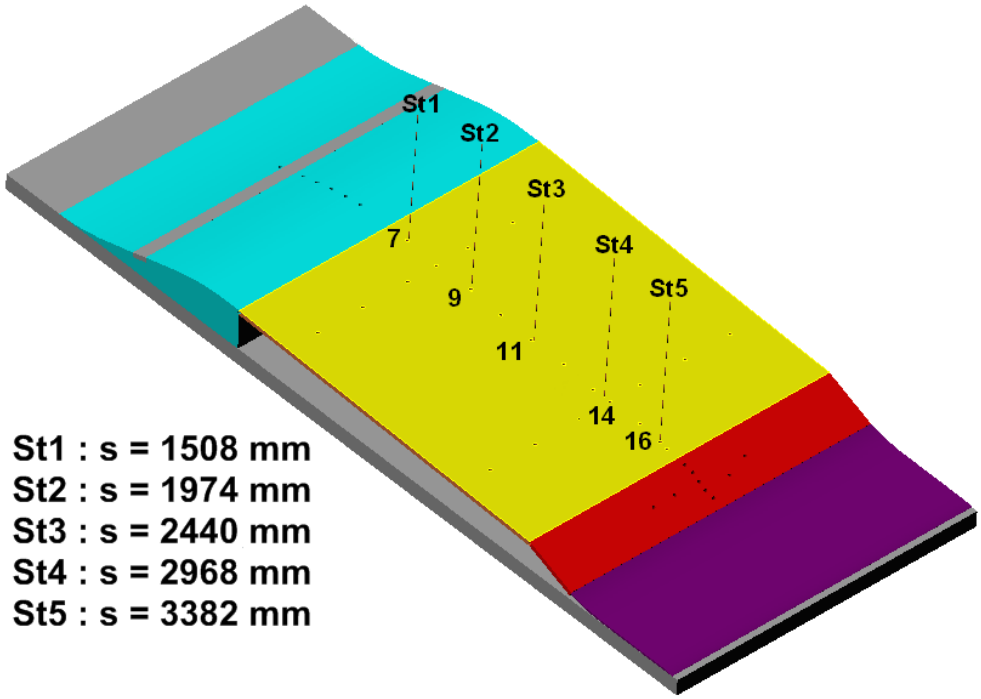

Figure 2.12: Positions of the hot-wire profiles, $\alpha = -2°$ and $\beta = -22°$.

by an acceleration sensor stuck on the wall. The displacement was obtained by integrating two times the output of the acceleration sensor. 10 s were acquired for each station at 11 kHz and with a cut-off frequency at 5 kHz to allow to compute spectrum and statistics.

All measurements were done with $U_\infty = 10$ m/s and the flow temperature was keep constant at $\pm 0.15°C$. At station 4, an additional profile was obtained at $U_\infty = 5$ m/s.

5.1.3.2.2 Selection of the cut-off and acquisition frequencies

Based on the study of Carlier (2001), the cut-off frequency of the anti-aliasing filter (slope -160 dB per decade) was chosen at 5 kHz, and the acquisition frequency at 11 kHz (corresponding to the maximum of the acquisition system) to respect Shannon's theorem. The cut-off frequency has normally to be greater than the maximum frequency of turbulence given by the Kolmogorov time scale : $F_k = \frac{1}{\sqrt{\frac{\nu}{\epsilon}}}$, with ν the kinematic viscosity and ϵ the kinetic energy dissipation rate. ϵ is given by : $\epsilon = \frac{u^3}{l}$, with u a velocity scale of turbulence and l a length scale of the largest structures in the flow. u is estimated as 10% of U_e, the external velocity, and l as 100 wall units. Unfortunately, the Kolmogorov frequency is 6 kHz in the present study, so in the spectrum, the dissipation is slightly biased by the cut-off frequency. However, the cut-off frequency is not so far from the Kolmogorov frequency, so the turbulence intensity is not affected.

5.1.3.2.3 Acquisition times

The acquisition time was chosen to be 100 s in ten packets of 10 s for the first 30

points (corresponding to $y^+ \lesssim 350$), 200 s in twenty packets of 10 s for the following 14 points (corresponding to $350 \lesssim y^+ \lesssim 4500$) and 400 s in forty packets of 10 s for the last 5 points. These acquisition times have been chosen based on the previous study of Carlier (2001). Indeed, he found that the acquisition time needed to reach convergence at less than 5% on the four order moment is given by $T_{aq} = 3000\frac{\delta}{U_e}$ for a point in the inner layer ($y^+ \lesssim 350$). This time corresponds to 3000 time scales of the larger structures estimated by $\frac{\delta}{U_e}$. He found also that the acquisition time has to be doubled for a point between 350 and 4500 wall units. Finally, he found that the acquisition time has to be doubled again for a point with $y^+ \gtrsim 4500$. The acquisition times chosen here fulfil the convergence criterion of Carlier with a safety factor of 2. For $U_\infty = 5$ m/s, all acquisition times were doubled as $\frac{\delta}{U_e}$ is doubled.

5.1.3.2.4 Calibration procedure

The calibration of the hot-wire was done in situ. The probe was placed at mid height of the wind-tunnel. A pitot tube was set at the same place separated by 20 cm in span. Ten velocity points were acquired with the pitot tube connected to a Furness FC014. A King's law ($E^2 = E_0^2 + bU^n$, with E the output voltage of the wire, and U the velocity) was least square fitted to these measurements. For the calibration, the cut-off frequency was fixed to 50 Hz, and the acquisition frequency to 200 Hz. 15 + n packets of 10 s were taken for the point n ($n = 1$ correspond to 10 m/s, 2 to 9 m/s ...etc.) to be sure that the mean is converged. The standard deviation e of E was also acquired for each points. For each profile, one calibration was performed before and one after the measurement to be sure that no change of the hot-wire properties has appeared during the measurement.

5.1.3.3 Accuracy

5.1.3.3.1 Mean velocity

The uncertainty on hot-wire anemometry is more complex to estimate than that on pressure measurements. Indeed, four sources of uncertainty were identified. The first one is due to the least square fit, the second one is due to the uncertainty on the velocity given by the Furness, the third one is due to a thermal drift of the anemometer and the last one is due to a lack of convergence. The first two give the total calibration uncertainty.

The first uncertainty can be estimated by the method developed by Neuilly and Cetama (1998). Details to compute this uncertainty is given in Appendix A. Table 2.2 gives the calibration fit uncertainty for each calibration point for the worst calibration obtained during the measurement campaign. This uncertainty is quite small except for the last two points, but these values are for the worst case. For the best case, this uncertainty is under $\pm 0.15\%$ for all the calibration points. This small uncertainty shows that the King's law it well adapted for hot-wire calibration which is well recognized.

The uncertainty of the Furness is given by the standard deviation method (Dixon and Massey (1957)) like in Section 5.1.2.3.3. For each calibration and acquisition, one value was taken, so many measurements are available for each calibration velocity. The uncertainty is given by $\pm(1.96\sigma)$, with $\sigma = s.c$, $c = 1 + \frac{1}{4(N-1)}$ and

Table 2.2: Calibration uncertainty due to King's law fit for the different velocities used for calibration

$U_\infty(m/s)$	10	9	8	7	6	5	4	3	2	1.5
$\frac{\Delta U}{U}(\%)$	0.4	0.4	0.4	0.4	0.4	0.4	0.4	0.4	0.7	1.2

$s^2 = \frac{1}{N-1}.\sum_{i=1}^{N}(x_i - \overline{x})^2$ (N is the number of measurements for the considered point) and $\overline{x} = \frac{1}{N}\sum_{i=1}^{N} x_i$ (the number 1.96 is given for a confidence of 95%). The results for this uncertainty is given in Table 2.3.

Table 2.3: Calibration uncertainty due to the Furness

$U_\infty(m/s)$	10	9	8	7	6	5	4	3	2	1.5
$\frac{\Delta U}{U}(\%)$	0.6	0.6	0.6	0.6	0.6	0.6	0.6	0.6	0.8	1.5

Concerning the temperature drift, for all the profiles that were carried out, the maximum differences observed between the free stream velocities measured just before and just after the profile is less than 3%. This uncertainty is larger than the uncertainty due to calibration (less than 1%). Many tests were carried out to explain this drift. The result obtained is that this drift comes from the change of temperature in the room. Indeed, a smaller difference is observed when the room temperature stays constant. For all the acquisitions, the room temperature was kept as constant as possible. As the room temperature changes very slowly, and the acquisition takes about four hours, this drift affects only the last 12 points. So this does not affect the inner part of the mean velocity profile, but it affects the accuracy on δ.

Concerning the lack of convergence, it can be estimated by $\pm 1.96\sqrt{\frac{s^2}{N_{sample}}}\frac{1}{\overline{U}}$ with the standard deviation method, where $s^2 = \frac{1}{N_{aq}-1}.\sum_{i=1}^{N_{aq}}(x_i - \overline{U})^2 = \overline{u'^2}$, N_{aq} is the number of points acquired and N_{sample} is the number of uncorrelated acquisitions (Dixon and Massey (1957), Klewicki and Falco (1990)). Two successive acquisitions are not correlated if the time between the two is greater than the integral time scale that can be estimated by $\Lambda = \frac{\delta}{U_e}$. As $N_{sample} = \frac{T_{aq}}{\Lambda}$, this error is given in Table 2.4.

Table 2.4: Statistical Convergence uncertainty for the different velocities used for calibration

$U_\infty(m/s)$	10	9	8	7	6	5	4	3	2	1.5
$\frac{\Delta U}{U}(\%)$	0.1	0.2	0.3	0.3	0.4	0.5	0.7	0.8	0.8	0.8

To obtained the total uncertainty, the quadratic method is used. The uncertainty is given by $\sqrt{error_1^2 + error_2^2 + error_4^2}$. The thermal drift is not taken into account because it affects only the last points. The result is given in Table 2.5.

In conclusion, for $U_\infty = 10$ m/s, the uncertainty of hot-wire measurements is less than 1% on the mean profiles. The accuracy near the wall is lower at about

Table 2.5: Total uncertainty for the different velocities used for calibration

.

$U_\infty(m/s)$	10	9	8	7	6	5	4	3	2	1.5
$\frac{\Delta U}{U}(\%)$	0.7	0.7	0.8	0.8	0.8	0.9	1.0	1.1	1.3	2.1

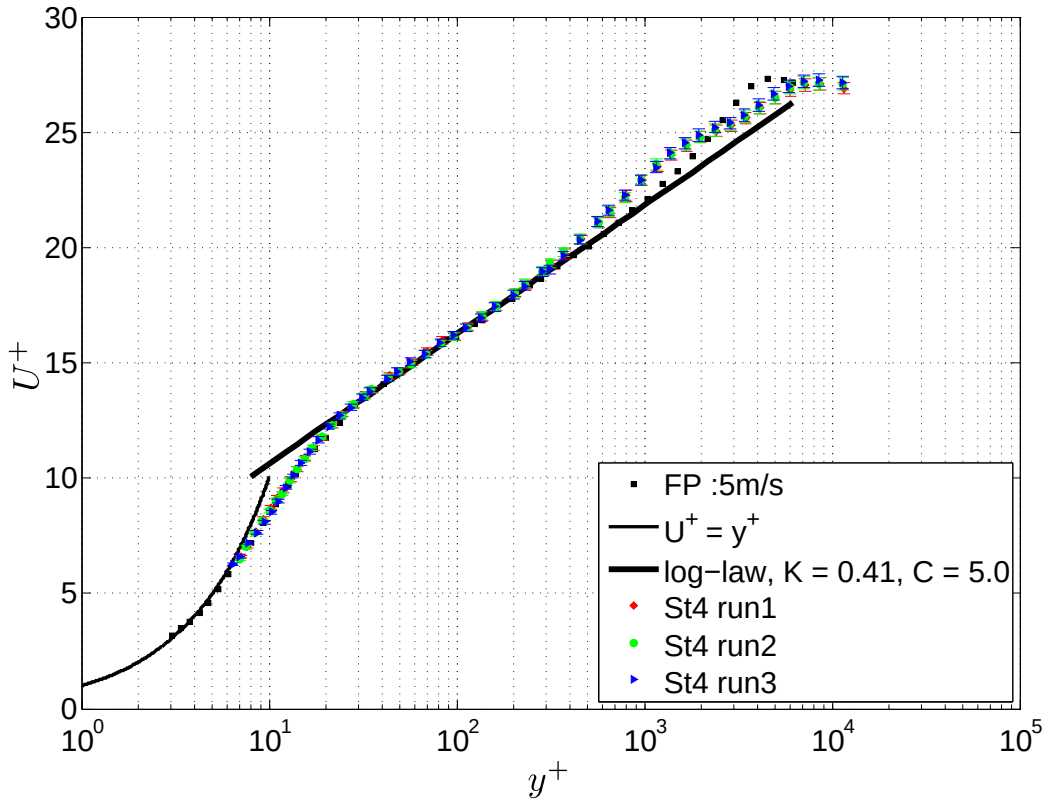

Figure 2.13: Superimposed mean streamwise velocity profiles for three different hot-wire measurements of station 4 , $\alpha = -2°$, $\beta = -22°$ and $U_\infty = 10$ m/s, and compared to the flat plate (FP) profile at 5 m/s. The error bars are fixed to 1%.

1.3% due mostly to calibration errors because the velocity is around 4 m/s in this area, but it concerns only the five first points. The uncertainty can reach 3% for the last 12 points in the worst case, principally due to thermal drift. This evaluated uncertainty is in agreement with the superposition of the three profiles acquired for each position (see Figure 2.13). For $U_\infty = 5$ m/s the accuracy is around 2% near the wall and less than 1% away from the wall.

5.1.3.3.2 Turbulence intensity

Concerning the turbulent intensity profiles, the uncertainty can be estimated by the standard deviation method. The statistical convergence uncertainty of $\overline{u'^2}$ is given by $\Delta\overline{u'^2} = \pm 1.96\sqrt{\frac{2}{N_{sample}-1}} * \overline{u'^2}$ (Dixon and Massey (1957), Klewicki and Falco (1990)) with a confidence index of 95%. As $\frac{\Delta\sqrt{\overline{u'^2}}}{\sqrt{\overline{u'^2}}} = \frac{1}{2}\frac{\Delta\overline{u'^2}}{\overline{u'^2}}$ (as $\overline{u'^2} = \left(\sqrt{\overline{u'^2}}\right)^2$, then $\Delta\overline{u'^2} = 2\Delta\sqrt{\overline{u'^2}} * \sqrt{\overline{u'^2}}$, so $\frac{\Delta\sqrt{\overline{u'^2}}}{\sqrt{\overline{u'^2}}} = \frac{1}{2}\frac{\Delta\overline{u'^2}}{\overline{u'^2}}$), the statistical convergence uncertainty on $\sqrt{\overline{u'^2}}$ is then given by : $\frac{\Delta\sqrt{\overline{u'^2}}}{\sqrt{\overline{u'^2}}} = \pm 1.96\sqrt{\frac{1}{2(N_{sample}-1)}}$. As in Section 5.1.3.3.1, N_{sample} is the number of uncorrelated samples and is given by : $N_{sample} = \frac{T_{aq}}{\Lambda}$ with $\Lambda = \frac{\delta}{U_e}$. The convergence uncertainty on $\frac{\Delta\sqrt{\overline{u'^2}}}{\sqrt{\overline{u'^2}}}$ was found constant and equal to 1.8% for a point with 100 s of acquisition time and lower for the other points. As $u' = U - \overline{U}$, the error on the mean value $\overline{U}$ has to be added to the convergence error on $\frac{\Delta\sqrt{\overline{u'^2}}}{\sqrt{\overline{u'^2}}}$ to obtain the total error on the turbulence intensity. The total uncertainty on $\frac{\Delta\sqrt{\overline{u'^2}}}{\sqrt{\overline{u'^2}}}$ is then ±2.8% with a confidence index of 95%. This uncertainty is slightly larger near the wall to about 3.1%. Figure 2.14 shows the superposition of three measurements of $\sqrt{\overline{u'^2}}$ at station 4. The estimated uncertainty is coherent with the superposition of the curves.

5.1.3.3.3 Third and the fourth order moments

As for the turbulence intensity, two sources of uncertainty exist for these quantities : the convergence error and the error on $\overline{U}$. For the fourth order moment, the convergence uncertainty is given by $\frac{1.96}{\sqrt{\frac{3N_{sample}}{8}}}$ (Dixon and Massey (1957), Klewicki and Falco (1990)). This error is 4.2% for a point with 100 s of acquisition time and lower for the other points. The total uncertainty on the fourth order moment is then about 5.2%. Concerning the third order moment, as for a Gaussian distribution this moment is zero, the uncertainty cannot be estimated. If it is not zero but close to Gaussian, the convergence uncertainty can be estimated by $\sqrt{\frac{\frac{15}{S^2}-1}{N_{sample}}}$, where S is the skewness (George (2010)). Here, in a significant part of the BL, S is of order 0.8. The convergence uncertainty on the third order moment is then 6.2% for a point with 100 s of acquisition time and lower for the other points. This uncertainty is in agreement with the study of Klewicki and Falco (1990). The total uncertainty on the third order moment is then about 7.2%. Figure 2.15 shows the superposition

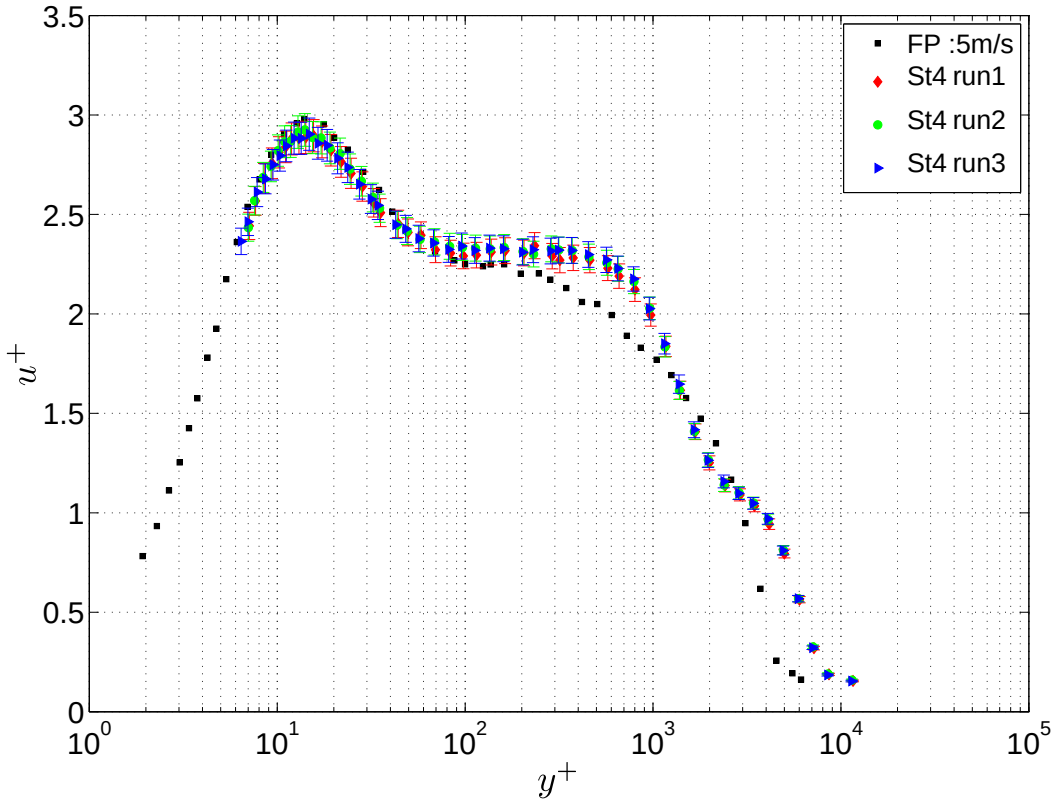

Figure 2.14: Superimposed turbulent intensity profiles for three different hot-wire measurements at station 4 , $\alpha = -2°$, $\beta = -22°$ and $U_\infty = 10$ m/s, and compared to the FP profile at 5 m/s. The error bars are fixed at 2.8%.

of three runs for the third and fourth order moments at station 4. The estimated uncertainty is coherent with the superposition of the curves.

5.1.4 Hot-film friction probes

5.1.4.1 Principle

The principle of hot-film friction probes is based on heat exchanges between the flow and the hot-film which is kept at constant temperature. It is very similar to hot-wire, which was described in Section 5.1.3.1. The sensitive element of the probe is stuck on the wall such as the sensor measures the velocity of the flow, at a position y from the wall, in the viscous sublayer region where $u^+ = y^+$ (See Chapter 1). As the position y and the dynamic viscosity μ are fixed, the relation $u^+ = y^+$ can be rewritten $u = \frac{y}{\mu}\tau_w = k\tau_w$, where k is a constant. Then, from the measure of the velocity, the wall friction can be deduced. Friction probes are calibrated using a King's type law ($E^2 = E_0^2 + b.\tau_w^n$, with E the output voltage of the bridge) as for hot-wire probes. In almost all the experiments, the sensor element of a friction probe is deposited on a substrate that create a small forward facing step (on the order of 10 wall units) that disturbs the measurement. The relation between the velocity and the friction is then not simply $u^+ = y^+$ but $u^+ = f(y^+)$. This imply

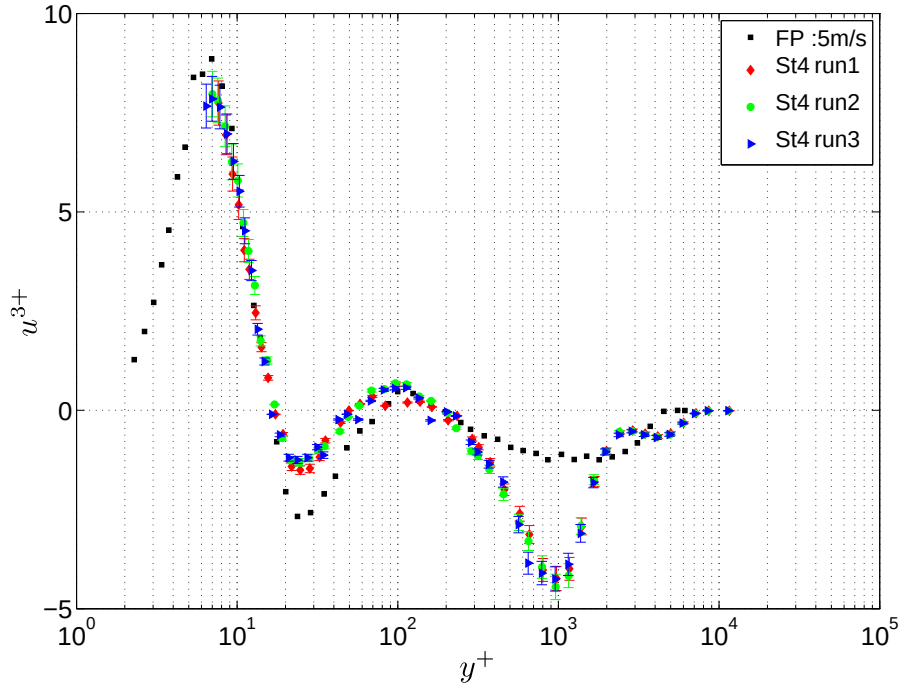

a)

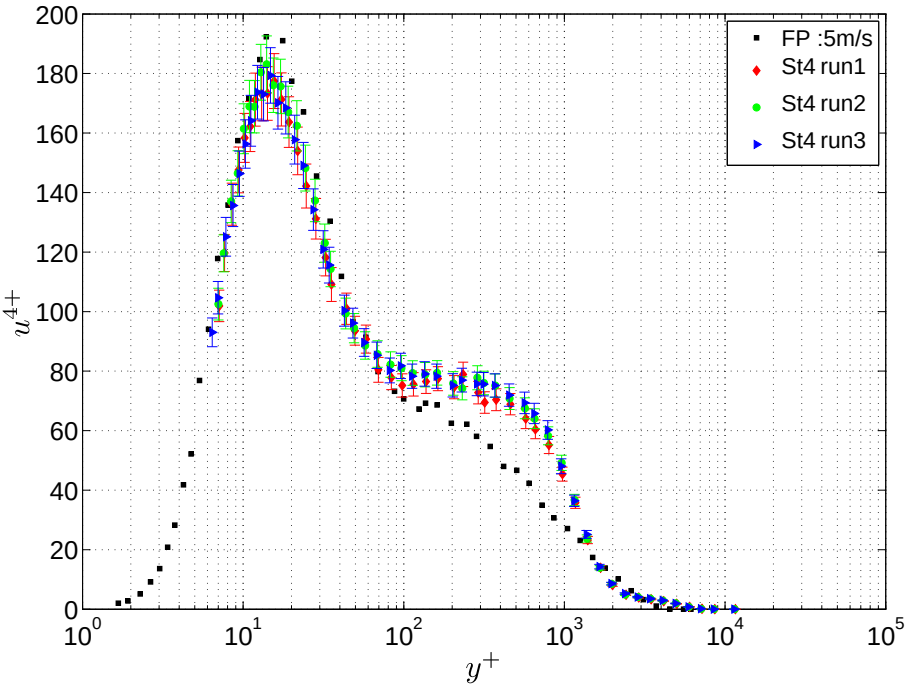

b)

Figure 2.15: a)Third order moment, b) Fourth order moment, for three measurements at station 4, $\alpha = -2°$, $\beta = -22°$ and $U_\infty = 10$ m/s, and compared to the FP profile at 5 m/s. The error bars are 7.2% for the third order moment, and 5.2% for the fourth order moment

that the coefficient n of the King's law is not near 0.5 as for hot-wire. It was found near $\frac{1}{3}$ by Godard and Stanislas (2006a).

5.1.4.2 Description of the friction probes used

The friction probes that were used are Senflex SF9902 hot-film probe. The sensor part is 1.5 mm long and 0.1 mm wide. It is deposited on a polyamyde substrate with a thickness less than 0.2 mm. These friction probes were glued directly on the surface with 60 μm double-sided tape. As was introduced by Godard and Stanislas (2006a), a hole of 2 mm in diameter and 1 mm in depth was drilled under the sensor to minimize heat losses to the substrate. The probes were connected to a 4 channels AN 1003 anemometer manufactured by AAlab Systems (the same as for hot-wire measurements). The acquisition frequency was 11 kHz and the cut-off frequency 5 kHz. Fifteen packets of 10 s were acquired for each measurement to achieve good convergence on the mean value, standard deviation, PDF and spectrum.

Four friction probes were used which corresponds to the number of available channels of the anemometer. They were placed on the flap. The coordinates of the probes are given in Table 2.6 and Figure 2.16 gives a picture of the localisation of the probes on the ramp together with a wool tufts visualisation of the separation. The name of the probes given in Table 2.6 (P1, P2, P3, P4) will be kept in all this work.

Table 2.6: Coordinates of the friction probes.

probe	s (mm)	z (mm)
P1	3555	164
P2	3555	-205
P3	3759	0
P4	3759	-286

5.1.4.3 "Pseudo" calibration

An in-situ calibration of the hot-film friction probes was not possible. A "pseudo" calibration based on the calibrations done by Godard and Stanislas (2006a), Godard et al. (2006), Godard and Stanislas (2006b) for the same type of probes was developed. The King's law is : $E^2 = E_0^2 + b.\tau^n$, were E is the output voltage of the bridge, and τ the wall friction. The parameters to be estimated are E_0, b and n. The pseudo calibration consists in estimating the coefficient of the King's law with $E_{0_{wts}}$, which corresponds to the output voltage of the bridge when the wind tunnel is stopped and at the temperature of calibration ($T_{calibration}$). For all calibrations done by Godard, the value $\left(\frac{E_0}{E_{0_{wts}}}\right)^2$ and $\frac{b}{E_{0_{wts}}^2}$ were computed. It was appearing that these two values were almost constants and equal respectively to 0.91 and 0.52. The constant value of $\left(\frac{E_0}{E_{0_{wts}}}\right)^2$ whatever $T_{calibration}$ can be explained by the fact that the natural convection is constant whatever $T_{calibration}$ is ($\Delta T = T_{probe} - T_{calibration}$ is almost constant because $T_{probe} >> T_{calibration}$). So by measuring only $E_{0_{wts}}$, the estimated values of E_0 and b were obtained. For n, it was easier because Godard found it constant and equal to $\frac{1}{3}$.

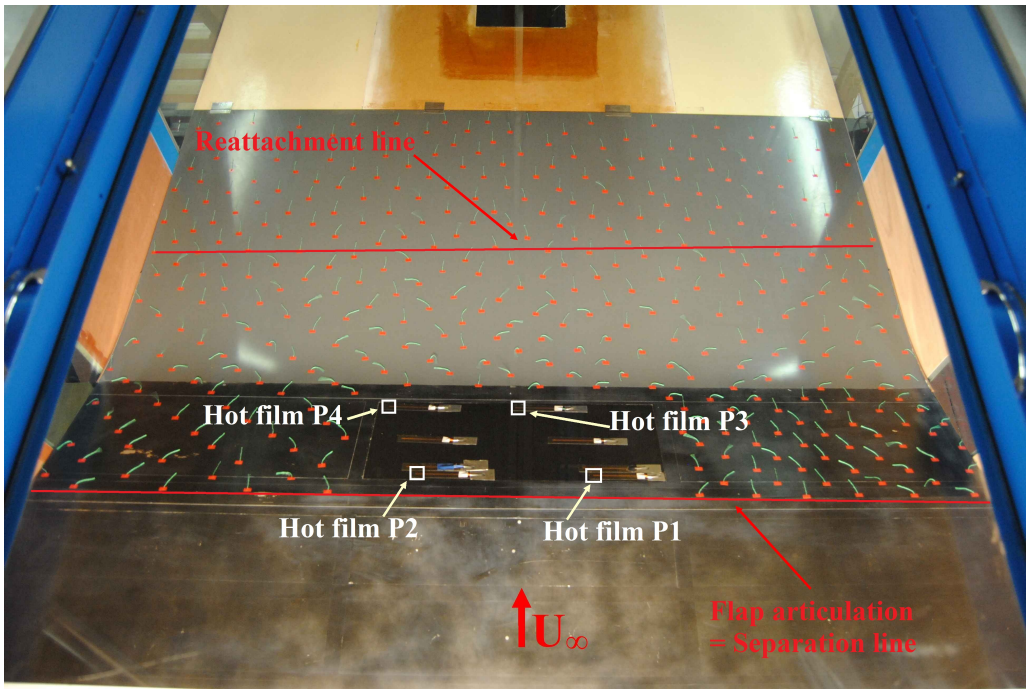

Figure 2.16: Visualisation of the friction probes positions ($\alpha = -2°$, $\beta = -22°$ and $U_\infty = 10$ m/s).

5.1.4.4 Accuracy

A lot of configurations were acquired without control at different temperatures and on different days, to check the repeatability of this "pseudo" calibration method. The accuracy was then estimated of about $\pm 10\%$. This accuracy is not so good because of the room temperature which was varying significantly on one day. Indeed, two reference values without control acquired with 2 h delay can have a difference of $\pm 5\%$.

5.2 Particle Image Velocimetry (PIV)

5.2.1 Principle

The PIV method allows to measure the velocity of a fluid in a plane (or recently in a volume with the development of the Tomo-PIV (Elsinga et al. (2006), Atkinson (2011), etc.). It is an indirect method as the velocity of the flow is deduced from the velocity of small particles (called "tracer") that follow the fluid. The principle of the 2D2C PIV set-up (i.e. two components of the fluid velocity in a plane) is illustrated in Figure 2.17. First, the flow is seeded with small particles (typically 1-2 μm in diameter) that have negligible lag. A laser sheet (typically 1 mm in thickness) is then generated from a double pulsed laser (typically Nd-YAG) through an optical system (usually generated from one spherical lens and one cylindrical lens) to illuminate the measurement plane at t and $t + \Delta t$. Finally, a PIV camera set normal to the measurement plane records images of the particles positions in the measurement plane at t and $t + \Delta t$.

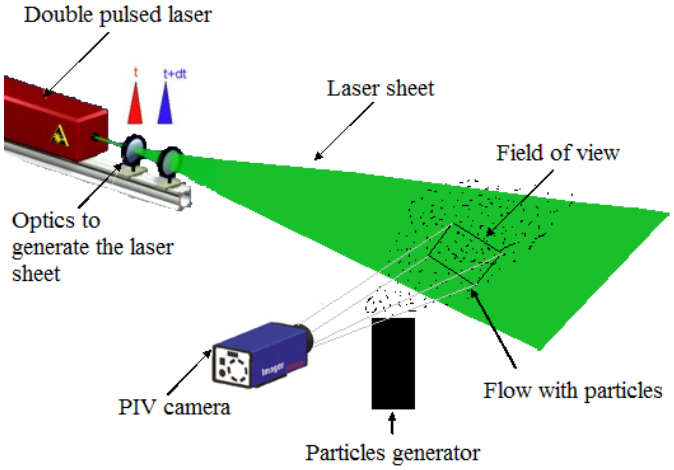

Figure 2.17: Scheme for a 2D2C PIV measurement.

These images are then cut into small interrogation windows, small enough to have a particles displacement between t and $t + \Delta t$ almost uniform. The most probable particles displacement in pixels d_i is then obtained by cross-correlation. The magnification M can be obtained by calibration, so the displacement d_o in the real space (i.e in meters) can be deduced in each interrogation windows. As the time between two images (Δt) is known, the velocity in each interrogation windows is finally obtained by $V = d_o/\Delta t$. The final result corresponds to a map of in-plane velocity components in the measurement plane. The interrogation windows size is chosen as small as possible, with a significant number of particle images inside, to obtain a good signal to noise ratio. A windows overlap of 50% allows to fulfil the Nyquist criteria and gives the spatial resolution. However the number of vectors can be increased by increasing the overlap. Adrian (1991), Keane and Adrian (1992), Raffel et al. (1998), Foucaut et al. (2003), etc. have studied the PIV uncertainty and have shown that window shifting, multi-pass and Gaussian sub-pixel fit improve the PIV accuracy.

Several sources of uncertainty are present in the 2D2C PIV set-ups (Adrian (1991), Keane and Adrian (1992), Raffel et al. (1998), Foucaut et al. (2003), etc.). The main sources are : the out of plane motion of particles, the non-uniform displacement of the particles in the interrogation windows, the non-uniform particles concentration and the particles displacement too large compared to the interrogation window size. To minimize the effects of the out of plane velocity component, a stereo PIV cameras system can be used. In this case, the particles displacement is viewed from two different directions and the three velocity components can be reconstructed. This PIV set-up is called "2D3C" PIV or "Stereo" PIV. If more than 2 cameras are used, the full three components of the velocity in a volume can be obtained. This method is called "Tomo-PIV" or "3D3C" PIV. If high-speed PIV cameras are used for the different PIV set-ups described just above, the evolution of the velocity with time is accessible and the method is called "Time Resolved PIV".

To obtain good PIV measurements, one should follow the recommendations given

by Keane and Adrian (1992) and Foucaut et al. (2003) : the particles image diameter has to be around 2 pixels, the particles concentration has to be about 0.04 particles per pixel, the maximum difference in particles displacement in the interrogation windows has to be less than half the particles image diameter and the out of plane displacement has to be less than 20% of the laser sheet thickness.

5.2.2 Description of the set-up used

A streamwise 2D2C PIV set-up at mid-span of the ramp and on all the ramp flap was used in the present study (see Figure 2.18). To obtain a very large field that contains all the separation region and a part of the flow upstream and downstream of the separation, four synchronized 2D2C PIV set-ups were used. Between two PIV set-ups, there was a common region in order to obtain a large continuous field from the four PIV set-ups. Four 12 bits Hamamatsu C9300 cameras of 2048 x 2048 px^2 and with a pixel size of 7.4 x 7.4 μm^2 were used. Nikon lenses of focal length f = 50 mm were placed on the cameras at 1.08 m from the measurement plane. The magnification M obtained was about 0.049. The aperture was set at $f_{\#} = 5.6$, which allows particle image diameters slightly larger than one pixel (the formula given by Goodman (1968) (equation (2.5)), with λ the laser wave length, gives a particles image diameter of 1.03 px. By analysing the PIV images, a value about 1.3 px is obtained), which increases the uncertainty as it is below the optimum value. The Hiris software was used to acquire simultaneously the images of the four cameras. The size of the total field was about 28.7 cm in height above the wall and the curvilinear length was about 94 cm (with about 17.5 cm upstream the separation).

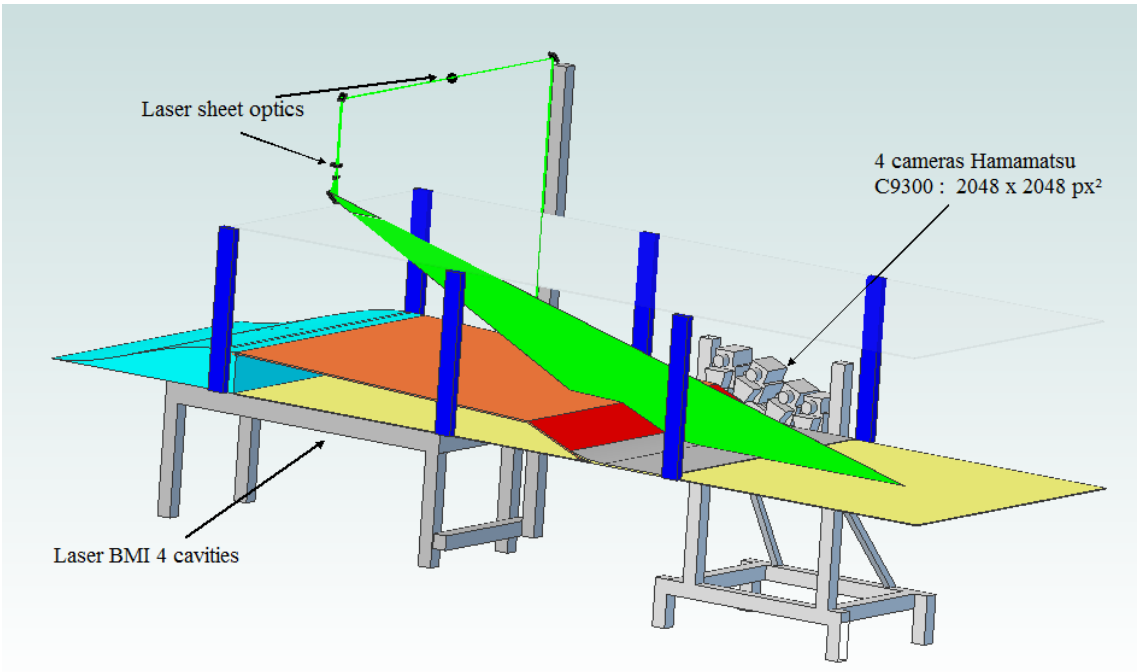

Figure 2.18: Scheme for the 2D2C PIV set-up used.

$$D_i = 2.44(1 + M)f_{\#}\lambda \tag{2.5}$$

The LML BMI Nd:YAG laser was used for this experiment. As the light sheet was entering into the wind tunnel through a top wall window with an angle around 68°, to obtain enough light in the very big field, the BMI laser was set in amplifying mode (2 cavities as oscillators and 2 as amplifiers) in order to obtain about 425 mJ per pulse. A telescope at the laser output was used with a converging lens of 800 mm focal length and with a diverging lens of -600 mm focal length, placed 200 mm downstream the converging one, to obtain a parallel laser beam of 5 mm in diameter. Then, a spherical lens of 4 m focal length was used to set the beam-waist in the middle of the PIV field, and two cylindrical lenses of -40 mm focal length were used to realize the light sheet. The light sheet obtained was 0.8 mm thick in the four PIV fields and about 60 cm wide in the middle of the field.

To minimized the laser reflection on the wall, the last flat plate insert and the insert of the flap were replaced by glass windows. However the wall reflections were still too strong on the metal parts, so a 2 cm wide special rhodamine paint developed by ONERA (Office National de Recherches en Aérospatiales) was applied on the ramp all along the light sheet position. The rhodamine paint was not directly applied on the ramp surface, so that it was possible to renew it easily (this paint was found to resist only about 5 h of laser impacts). A 2 cm wide and 0.18 mm thick black electrical insulation tape was set before on the ramp surface and the rhodamine paint was applied on its surface. Five layers of rhodamine were applied to obtain a uniform layer. The total thickness of the tape and the rhodamine paint was about 0.25 mm, which corresponds to about 8 wall units before the separation.

The role of the rhodamine paint was to absorb the 532 nm wave length of the laser, and remit it at larger wave lengths (i.e. into the orange part). The rhodamine that was selected by ONERA was the 6G one as its wave length absorption peak is at 526 nm, very near the wave length of Nd:YAG lasers, and its emission peak is at 555 nm. 50 mm diameter bandpass filters, centred at the laser wave length (i.e. 532 nm), and with a bandwidth of ±5 nm and a transmission coefficient greater than 85% from Edmund Optics (ref NT65-216) were set on the 50 mm Nikon lenses, to filter the rhodamine emission. It was found that these filters, combined with the rhodamine paint, were reducing the wall reflection by two and a half $f_{\#}$ step, (without the filters and rhodamine paint but with the black electrical insulation tape, the cameras were not too much saturated at $f_{\#} = 11$, and the same level of saturation was obtained with rhodamine and filters between $f_{\#} = 4$ and $f_{\#} = 5.6$).

For the aperture that was retained for the experiments ($f_{\#} = 5.6$), the particles signal was coded into the first 8 bits of the cameras, and the wall reflection was just saturating the cameras in some small isolated areas. This was found sufficient to obtain acceptable PIV results. As in the separation region, the spanwise velocity component is not negligible and leads to a high out of plane motion, and as the thickness of the light sheet was only 0.8 mm, the time between the two laser pulses was set at $\Delta t = 80\mu$s, so that the out of plane motion was limited, as recommended by Foucaut et al. (2003).

The estimation of the out of plane motion was done from the study of Webster et al. (1996), as for a boundary layer in strong APG, they found a peak value of $\frac{\overline{w'^2}}{U_e^2}$

of 0.0055 which leads to $\sqrt{\overline{w'^2}}_{max} \simeq 0.074U_e$. This maximum value was then taken as an order of magnitude for the spanwise velocity component in the separation region. As 95% of the values of the spanwise velocity component are in the range $\pm 2\sqrt{\overline{w'^2}}_{max}$, the maximum out of plane motion for $\Delta t = 80\mu$s is then equal to $\pm 20\%$ ($U_e \simeq 13m/s$) of the laser sheet thickness, that is two times greater than the recommended value given by Foucaut et al. (2003). However, this estimation corresponds to an upper limit. Moreover, it was not possible to reduce more the Δt as it was found to give displacements of the order of 0.3 pixels in the separation region, so close to the order of magnitude of the PIV accuracy (Foucaut et al. (2003)). The free-stream displacements were then in the order of 6 to 7 pixels.

The calibration needed to obtain the magnification for each camera and the merging regions, was obtained by placing a wall normal plate with crosses which was crossing all the field. The obtained images of this target by the four cameras were then processed with a home made software, which was merging the four camera target pictures into one picture (see Figure 2.19) and was also giving the magnification of each camera together with the coordinates in this picture of the four extreme points of the fields of view of each camera. This full target picture and these output parameters will then be used by the meshing programme.

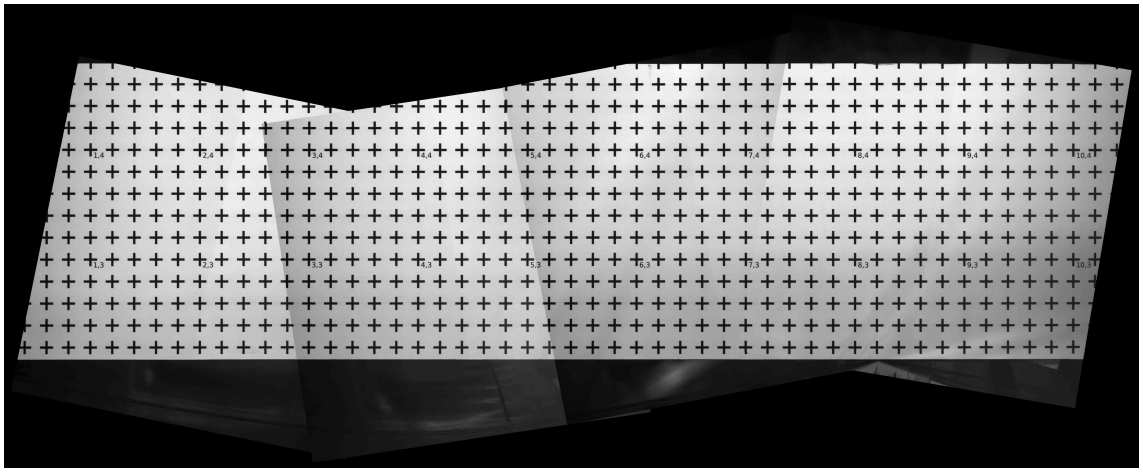

Figure 2.19: Picture of the calibration target reconstructed from the four camera images.

5.2.3 Meshing and PIV analysis

5.2.3.1 Meshing Procedure

A $C++$ home made software was developed to build the PIV analysis mesh. First, the user constructs graphically, in the full calibration target image, a "wall path" which fits the laser reflection on the surface, with lines and Bezier curves. The software constraints automatically the tangents direction of the Bezier curves so that the obtained "wall path" has a continuous derivative. A scheme of the meshing procedure is given in Figure 2.20. When this "wall path" is defined, the software computes a "meshing path" which is used to build the mesh.

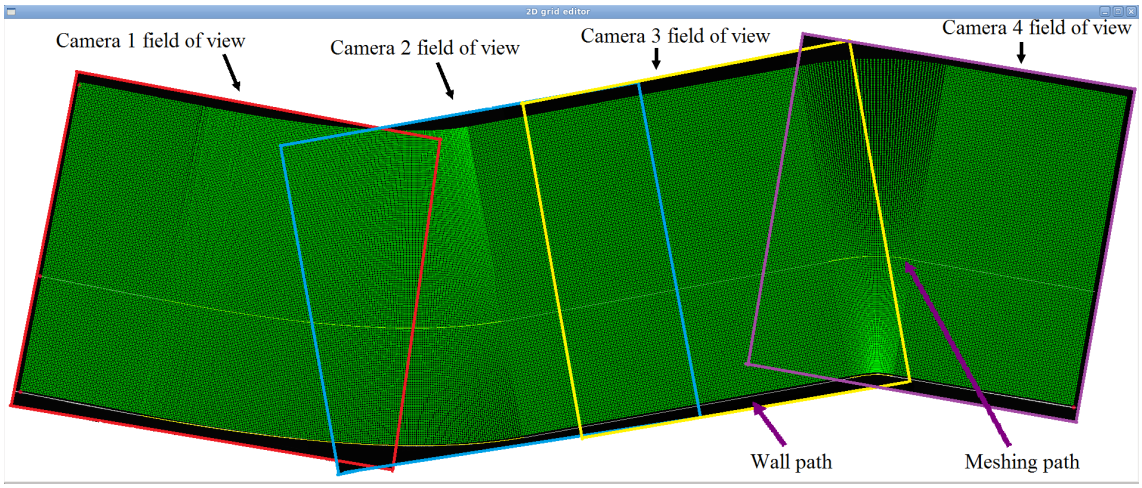

Figure 2.20: Scheme of the meshing procedure.

The "meshing path" is obtained by translating of a constant value dy the "wall path" curves in the local normal direction. A mesh is then computed along the "meshing path" with a constant spacing and along each normal direction of this path with eventually an other constant mesh size. Each "vertical" mesh line (i.e. for a fixed mesh point on the "meshing path") obtained is then normal to the wall. This procedure causes mesh refinement at the wall for convex curvatures and at the top of the mesh for concave curvatures.

The distance from the wall of the first mesh point can be adjusted in order to limit the influence of the laser reflection on the wall in the interrogation window. The dy translation value can also be adjusted to optimize the mesh size at the top of the mesh of concave curvature regions and near the wall of convex curvature regions. When the mesh is computed, the programme extracts the part of the grid that belongs to each camera and the number of common wall normal mesh lines that exist between two cameras in each merging region. The programme also writes the complete grid and extracts the angle of each wall normal lines in the cameras pictures.

The meshes size used were 10×10 pixels^2. The distance from the wall of the first mesh point was 16 pixels to prevent laser reflection to be inside the interrogation windows. This grid was then designed to used 32 x 32 px^2 interrogation windows. The equivalent overlapping is then about 70%. However, on the top grid of concave surface and at the bottom grid of a convex one, the overlapping obtained is bigger (with a maximum of 90%). This leads to oversampled PIV regions. However, these regions have been kept to avoid undersampled regions at the bottom grid of concave surface and at the top grid of convex surface (the minimum overlap obtained was 35%). The final grid obtained has then 642 points along the wall and 188 points along the wall-normal direction. This leads to a mean grid spacing of 1.5 mm $\times$ 1.5 mm. This corresponds to about 45 wall units, with u_τ taken upstream of the separation (i.e. at station 5 of hot-wire ($u_\tau = 0.465m/s$)). The first measurement point is at 2.4 mm from the wall which corresponds to about 72 wall units.

5.2.3.2 PIV analysis

The MatPIV.1.6.1 toolbox for Matlab software, written by J. K. Sveen from mathematical department of Oslo University, was modified and used to perform the 2D2C PIV processing of the acquired images on the specific grid. The toolbox was firstly adapted to run on the free software Octave. Then modifications were done to make the software compatible with the grid. Four passes were used, a first one with 64 x 64 px^2 interrogation window and three with 32 x 32 px^2. The first pass was done on one point over two in each direction of the grid and the result was linearly interpolated for the second pass. Between each pass, a local filter was applied to remove spurious vectors which were deviating from the median of their nine neighbours by 3 times the standard deviation of them.

The removed vectors were then replaced by the second correlation peak and the local filter was applied again. Then, the same method was applied using the third correlation peak for the new spurious vectors. After the third peak replacing, all the remaining spurious vectors were linearly interpolated with their neighbours. For the final pass, a 1D Gaussian fit based on three points for the three main correlation peaks was done to obtain displacement accuracy under 1 px.

The obtained velocity vectors for the four cameras and on each grid point were then projected on the local reference frame so that, the final u-velocity component obtained is the velocity parallel to the wall and the v-velocity component is the velocity normal to the wall. In the merging regions, the velocity was taken as the mean value of the two different estimations given by two cameras. However, these two estimations were kept to compute the PIV uncertainty (see next Section).

After the final pass, a filter was applied on the PIV fields to remove area of spurious vectors. This filter was eliminating vectors which were above a maximum velocity value (i.e. $1.5U_\infty$), and vectors which were below a minimum one (i.e. $-0.5U_\infty$). If the PIV fields were showing more than 160 spurious vectors (i.e. more than 0.15% of the total number of vectors), it was found that these vectors were organized in large area which were impossible to eliminate by neighbours interpolation. These fields were then eliminated. The computation was run on the new LML supercomputer with 80 processors in parallel. To analyse the 5000 fields, 50 hours of computation on each processor were necessary.

5.2.4 Accuracy

5.2.4.1 PIV accuracy determination

The accuracy estimation of PIV is a complex topic. However, Kostas et al. (2005) and Herpin et al. (2008) proposed to estimate the accuracy with the merging regions of the PIV field. The PIV uncertainty can then be obtained from the same velocity measured by two independent PIV systems. In the merging region, the random PIV uncertainty, with a 95% confidence index, is estimated by $\sigma_u = \pm(u_{syst1} - u_{syst2})_{RMS}$ for the u component (i.e. parallel to the wall) and by $\sigma_v = \pm(v_{syst1} - v_{syst2})_{RMS}$ for the v component (i.e. normal to the wall), where RMS refer to the root mean square value. Concerning the mean velocity components, as the random error goes to zero by definition when taking enough samples, only the bias error affects their accuracy. The PIV uncertainty on the mean streamwise velocity U is then estimated

by $\Delta U = \pm(\overline{u_{syst1} - u_{syst2}})$, and on the wall-normal velocity component by $\Delta V = \pm(\overline{v_{syst1} - v_{syst2}})$.

The PIV random uncertainty gives a bias error for the Reynolds stresses. The uncertainty on $\overline{u'^2}$ is then given by $\Delta\overline{u'^2} = \pm((u_{syst1} - u_{syst2})_{RMS})^2$, and on $\overline{v'^2}$ by $\Delta\overline{v'^2} = \pm((v_{syst1} - v_{syst2})_{RMS})^2$. As seen in Section 5.1.3.3.2, the relative uncertainty on the turbulent intensity $\sqrt{\overline{u'^2}}$ is given by $\frac{\Delta\sqrt{\overline{u'^2}}}{\sqrt{\overline{u'^2}}} = \frac{1}{2}\frac{\Delta\overline{u'^2}}{\overline{u'^2}}$ and on the wall normal turbulent intensity $\sqrt{\overline{v'^2}}$ by $\frac{\Delta\sqrt{\overline{v'^2}}}{\sqrt{\overline{v'^2}}} = \frac{1}{2}\frac{\Delta\overline{v'^2}}{\overline{v'^2}}$. The uncertainty on $\overline{u'v'}$ is usually larger because both errors on u and v affect this value. The uncertainty can however be estimated by a quadratic mean of the uncertainties on $\sqrt{\overline{u'^2}}$ and on $\sqrt{\overline{v'^2}}$

For each PIV measurements, the number of fields recorded was 5000. This leads to a convergence uncertainty of less than $\pm 0.8\%$ on the mean streamwise velocity and on the mean wall normal velocity components. These uncertainties were estimated respectively by $\frac{\Delta U}{U} = 1.96\sqrt{\frac{1}{5000}}\frac{\sqrt{\overline{u'^2}}}{U}$ and by $\frac{\Delta V}{V} = 1.96\sqrt{\frac{1}{5000}}\frac{\sqrt{\overline{v'^2}}}{V}$ (Dixon and Massey (1957), Klewicki and Falco (1990)) (As the acquisition frequency is 3 Hz, which corresponds to about 20 integral scales (estimated by $\Lambda = \frac{\delta}{U_e}$) between two records, the 5000 PIV fields are uncorrelated in time. The maximum values of the terms $\frac{\sqrt{\overline{u'^2}}}{U}$ and $\frac{\sqrt{\overline{v'^2}}}{V}$ were estimated at 0.3). The convergence uncertainties on $\overline{u'^2}$ and on $\overline{v'^2}$ are also $\pm 4\%$ (estimated by $\pm 1.96\sqrt{\frac{2}{5000}}$ (Dixon and Massey (1957), Klewicki and Falco (1990))).

The convergence uncertainties could be reduced by increasing the number of records. However, doubling the number of fields leads to a data supplement of 312.5 Go to process and decreases only the convergence uncertainty by 0.2%. 5000 fields is then a good compromise between the convergence ($\pm 0.8\%$ on the mean velocity) and the size of the database (less than 1.3 To for the four PIV tests).

5.2.4.2 PIV accuracy results

The different PIV uncertainties have been computed for the uncontrolled flow and the three active control cases selected in each merging region. Only the main results are given in Table 2.7 (co-up means upstream blowing co-rotating case, counter-up counter-rotating upstream blowing case and counter-down counter-rotating downstream blowing case). For detailed results, see Appendix B. For the random error columns, the first value corresponds to the region near $X = 3.5$ m (i.e. near the flap articulation) and the second one to $X = 3.95$ m (i.e. downstream part of the flap). Figure 2.21 shows the result of the uncertainty obtained for the mean streamwise velocity U and gives the positions of the merging regions on the flap (the separation border is also represented but it will be described only in Chapter 3).

The uncertainty on the mean flow is increased by each control test, which is due to more out of plane motion introduces by the streamwise vortices generated. Near the wall, for the counter-rotating tests, this uncertainty is slightly reduced compared to the uncontrolled flow due to much higher velocities observed in this region for these two tests. Globally, the uncertainty remains quite good, however, it must be kept in mind that in the region where the mean velocity is small, the uncertainty relative to the local value can be very high as small velocity is difficult

Table 2.7: Table of the PIV uncertainty result for the different test cases.

Set-up	region	$\frac{\Delta U}{U_\infty}$ or $\frac{\Delta V}{U_\infty}$ (%)	$\frac{\Delta u}{U_\infty}$ or $\frac{\Delta v}{U_\infty}$ (%)	random error (% of U_∞)	random error (px)
Uncontrolled	Outer flow	1	0.8	2 - 4	0.11 - 0.23
	Near wall	4	3	5	0.28
co-up	Outer flow	1.5	2	2.5 - 9	0.13 - 0.51
	Near wall	4	4	15	0.85
counter-up	Outer flow	1.5	2	2.5 - 8	0.13 - 0.45
	Near wall	3.5	4	15	0.85
counter-down	Outer flow	1.5	2	2.5 - 4.5	0.13 - 0.25
	Near wall	3.5	4	15	0.85

to measure accurately. Here, this is the case in the very near wall region and near the separation border where the relative uncertainty on U can reach $\pm 15\%$. For the V component, as it is smaller than U, the uncertainty relative to the local value is higher than for U (about 5 times more). On the top of the field (Figure 2.21), slightly higher uncertainty is observed probably due to a possible worse laser sheets superposition in this region or to optical distortions that where not corrected (in the image mapping process, the projection errors near the image borders can reach 3 px, which was supposed small enough to be neglected for a 2D2C PIV analysis). The same phenomenon was observed for the three control tests.

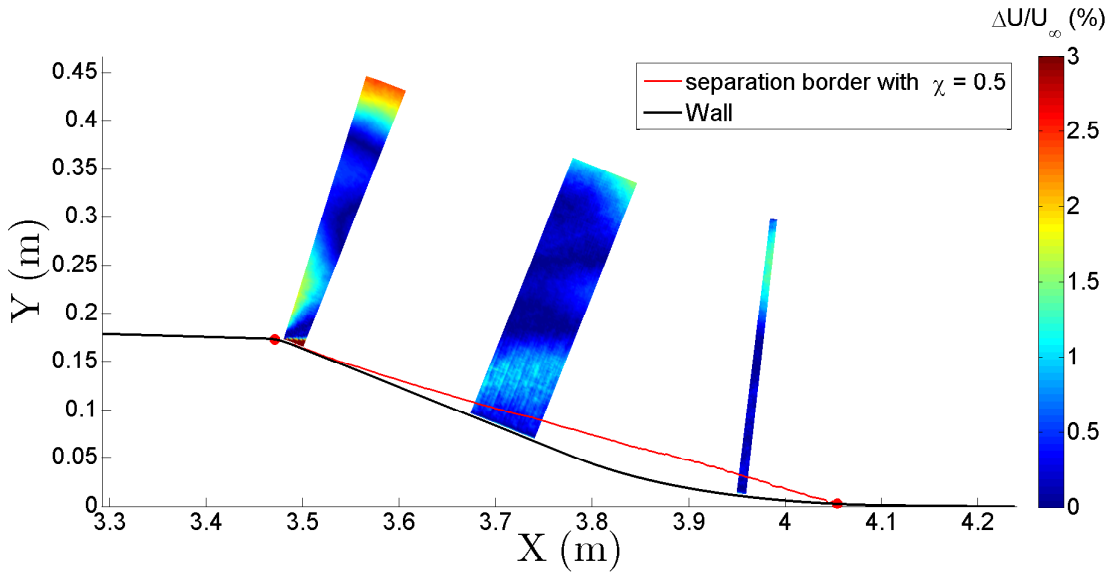

Figure 2.21: PIV uncertainty on the mean streamwise velocity component (U) without control.

The uncertainty for the turbulence intensity components is almost doubled in

each control case due to higher uncertainty on the mean velocity. Nevertheless, it remains quite small. However, as for the V component, the uncertainty relative to the local value can reach about $\pm 5\%$ on the flap for the uncontrolled flow as the turbulence intensity is only several percent of U_∞.

Concerning the random error, for each case, it increases with X. At minimum, it is 0.11 px, which is larger than the one obtained by Foucaut et al. (2003). This is not surprising as the set-up used is not optimum (the particle images are too small; the out of plane motion and the mean velocity gradient non negligible; etc.). For each case, near the wall, this uncertainty is higher due to a stronger mean velocity gradient, and especially for the control tests which significantly increase the near wall velocity. Predictably, for the control tests, the uncertainty is higher than for the uncontrolled flow due to higher out of plane motion caused by the streamwise vortices. For the counter-down test, it is lower on the flap compared to the two other control cases due to weaker vortices for this case (its VR is lower : 2.5 compared to 3.5 for the others) which induce less out of plane motion.

6 Conclusion

In this chapter, the tools used for this work were presented in detail. Attention was focussed on the accuracy of the different measurement techniques used, to be sure of the quality of the results that will be presented in the next chapters. The uncertainty on the pressure coefficient is $\pm 1.2\%$ and on the pressure gradient $\pm 6.5\%$. For the hot-wire profiles, the uncertainty is below $\pm 1\%$ for the mean velocity, $\pm 2.8\%$ for the turbulent intensity, $\pm 7.2\%$ for the third order moment and $\pm 5.2\%$ for the fourth order moment. For the friction measurements, the uncertainty was estimated at $\pm 10\%$.

Finally, for the PIV measurement without flow control, the uncertainty on the mean velocities is about $\pm 1\%$ of U_∞ and higher near the wall ($\pm 4\%$ of U_∞). For the turbulence intensity components, the uncertainty is about $\pm 0.8\%$ of U_∞ in the external region and $\pm 3\%$ of U_∞ near the wall. Due to more out of plane motion, for each control case tested, the uncertainties increase in the external region compared to the uncontrolled flow but are almost the same in the near wall region. In the external region of the control cases, the uncertainty on the mean velocities is about $\pm 1.5\%$ of U_∞ and for the turbulence intensity components about $\pm 2\%$ of U_∞. It is however important to note that these uncertainties are given in percentage of a constant, and then for small quantity, the uncertainty relative to its local value can be high. For example, this is the case for the mean streamwise velocity in the near wall region and near the separation border, where the uncertainty relative to the local value can reach $\pm 15\%$.

Chapter 3

Ramp flow characterisation

1 Introduction

This chapter presents the flow characterisation of the ramp model. In this chapter, α is the ramp flat plate angle and β the flap angle (see Figure 2.2 and Chapter 2 for the definition of these angles). Several configurations of the ramp were investigated by varying α ($-2° \leq \alpha \leq 0°$) and β ($-22° \leq \beta \leq -6°$). The aim was to check the pressure gradient on the flat plate, the transverse homogeneity and the nature (separated or not) and influence of the flow over the flap. Also, different Reynolds numbers were investigated. Then, on the configuration which was finally retained for the flow control studies ($\alpha = -2°$ and $\beta = -22°$, corresponding to an adverse pressure gradient on the flat plate and a separation on the flap), five single hot-wire profiles were measured on the flat plate at midspan, to characterize in more details the BL development. Finally, on the same ramp set-up, a 2D2C streamwise PIV measurement at midspan on all the flap was performed to characterize the flow separation.

2 Wool tufts visualisations

Wool tufts visualisations were first carried out to check qualitatively the behaviour of the flow over the ramp. Figure 3.1 shows such a visualisation for $\alpha = 0°$ and $\beta = -13.8°$. On the flat plate, all the tufts are attached to the surface and parallel to the streamwise direction. This was the case for all the configurations investigated, except after $s = 3150$ mm where, when decreasing β, end effects appear near the side walls and grow near the flap to reach about 10 cm at the flap articulation when $\beta = -22°$. In conclusion, for $-2° \leq \alpha \leq 0°$ and $-22° \leq \beta \leq -6°$, no separation appears on the flat plate and the mean flow remains parallel to the streamwise direction on more than 90% of the span despite end wall effects which develop close to the flap articulation and which increase with decreasing β.

On the flap, two distinct behaviours were observed. For $\alpha = -2°$ and $\beta \geq -19°$, the wool tufts remain attached to the surface and parallel to the streamwise direction with end effects near the side walls that can reach 25 cm at $\beta = -19°$. When $\alpha = -2°$ and $\beta \leq -19°$, there is a separation on the flap. The end effects near the

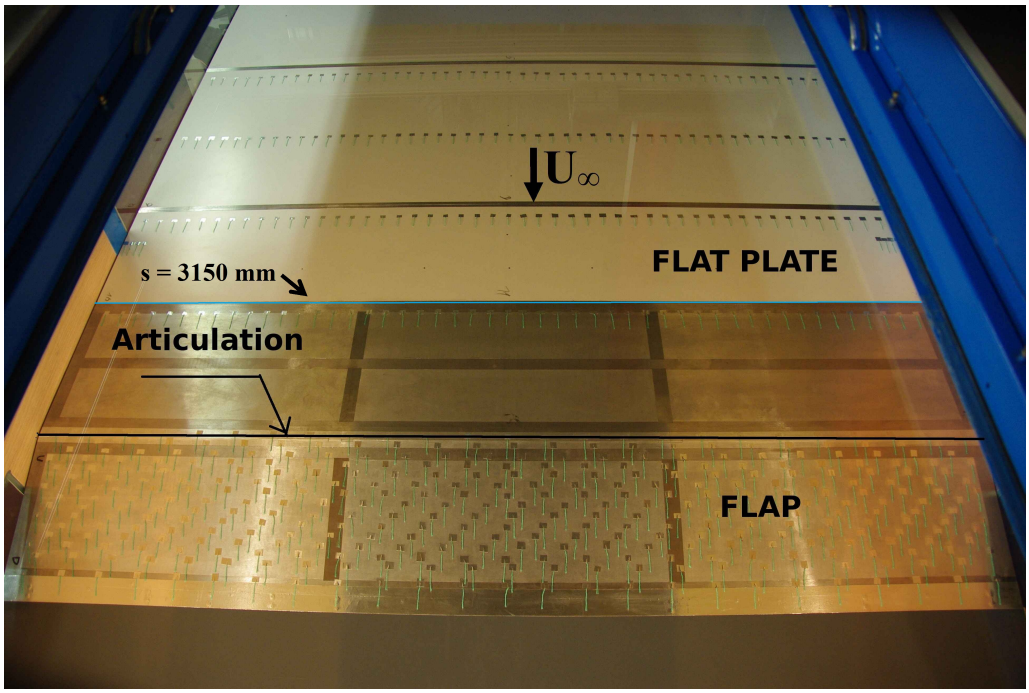

Figure 3.1: Wool tufts attached on the flat plate for U_∞ =10 m/s, $\alpha = 0°$ and $\beta = -13.8°$.

side walls reach in maximum 30 cm at $\beta = -22°$. In the central part, the behaviour seem to be homogeneous. In conclusion, when no separation is present on the flap, the flow remains 2D at least on 75% of the span. When there is a separation, the flow remains more or less 2D at least on 70% of the span. On the ramp set-up with $\alpha = -2°$ and $\beta = -22°$, the separation length was estimated at $L_{sep} = 80$ cm.

3 Oil film visualisation of the separation

On the configuration $\alpha = -2°$ and $\beta = -22°$, oil film visualisation was then carried out to obtain a better charaterization of the separation than with wool tufts. Figure 3.2 shows the oil film on the flap before turning the wind tunnel on. It was tried to keep the film thickness as uniform as possible as was discussed in Chapter 2. Figure 3.3 gives the result of the oil film visualisation. Figure 3.3 a) gives the global result. All the oil on the flat plate has been carried away to the flap articulation, showing that the separation is on the flap and not at the end of the flat plate. A clear white line is formed just after the flap articulation which locates the separation line exactly at the flap articulation ($s = 3500$ mm) for more than 85% of the span. End effects can be seen on this separation line and reach about 15 cm from each wall.

Figure 3.3 b) and c) show the end effects near the side walls. This may be the trace of a corner vortex created by the adverse pressure gradient on the flap. The two sides are not strictly identical but show the same tendency. The differences can be attributed to the thickness of the oil film. Indeed, the side $0 > z > -1000$ mm has been painted first, and during the time taken to paint the other side, the thickness of the film may have decreased due to gravity effects. The main result

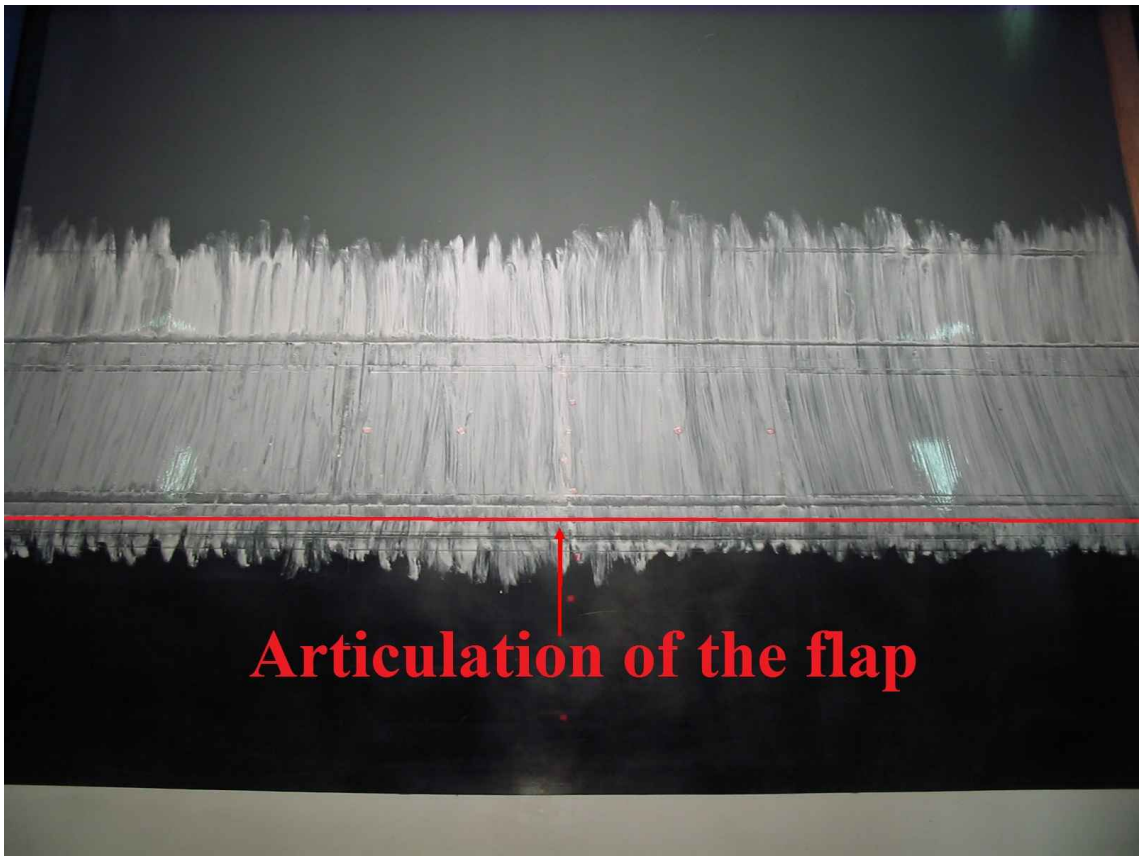

Figure 3.2: Oil film on the flap before turning on the wind tunnel, $\alpha = -2°$ and $\beta = -22°$.

given by these two pictures is that the corner vortices reach a width of about 30 cm at the end of the flap. The same conclusion as with the wool tufts is then obtained : the separation on the flap remains more or less 2D on 70% (i.e. 1400 mm) of the flap span.

4 Wall pressure distribution

4.1 Description of the database acquired

A large number of pressure measurements with different α and β were acquired to see the influence of these parameters on the pressure distribution. In most cases, the pressure taps number 15 to 26 were not acquired because they were added after the first test campaign (see Chapter 2). Taps number 23 to 38 were not acquired each time because of the acquisition time needed. They were used only to check the spanwise homogeneity. They were acquired only for some representative configurations. Examples will be given in Section 4.2 and in Figure 3.5.

Two campaigns of pressure measurements were realized (see Tables 3.1 and 3.2). In campaign 1, measurements were carried out with a reference velocity measured at a different position from campaign 2. The pitot tube used for the wind tunnel

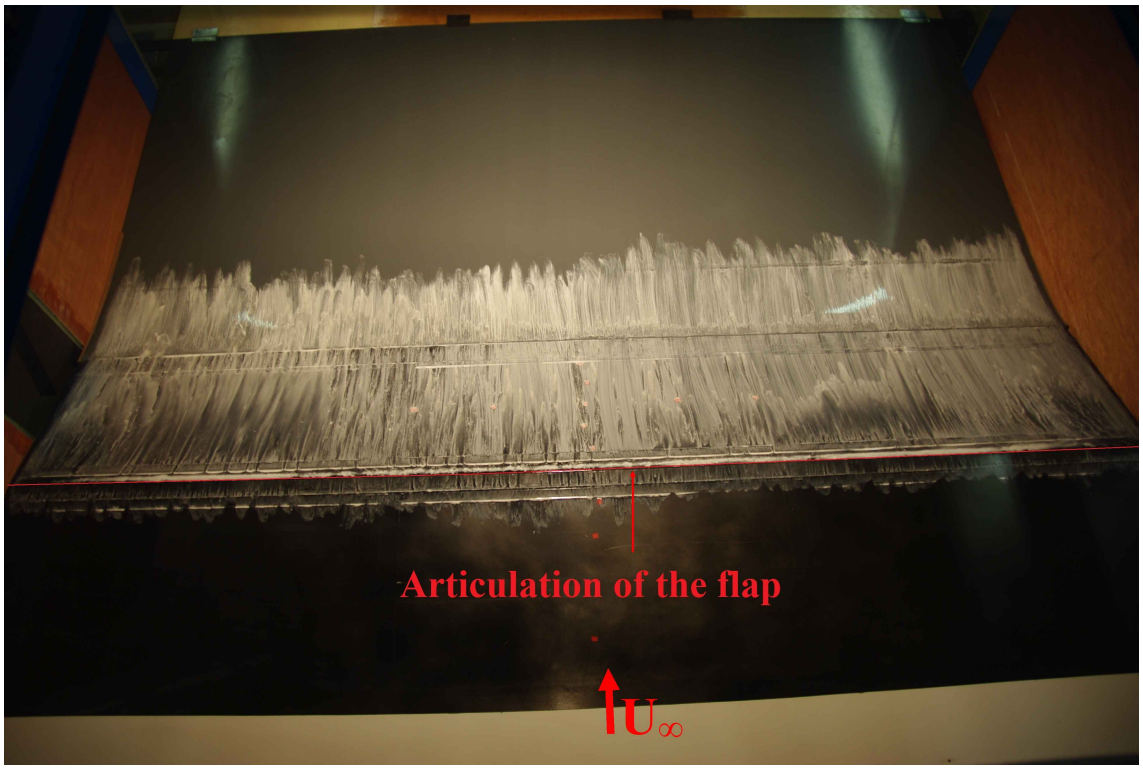

a)

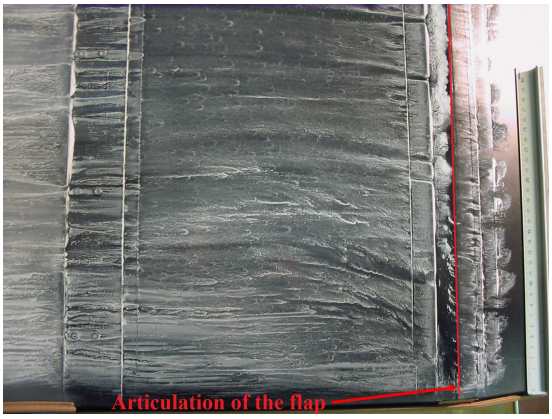

b)

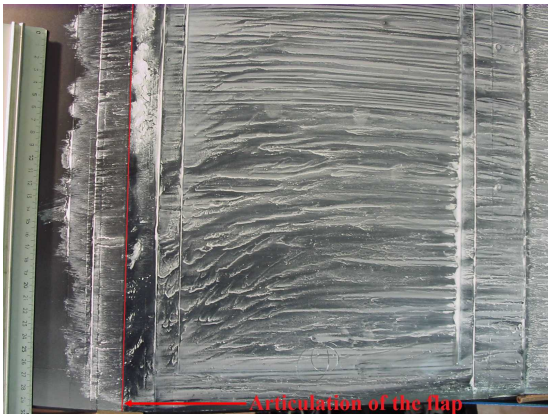

c)

Figure 3.3: a) Oil film result on the center of the flap b) Oil film result near $z = -1000$ mm on the flap c) Oil film result near $z = +1000$ mm on the flap. $\alpha = -2°$, $\beta = -22°$ and $U_\infty = 10$ m/s.

speed regulation in campaign 1 was placed at $X = 5.2$ m in the reference frame defined in Section 2 in Chapter 2, and at $X = -1.03$ m for campaign 2. The change of reference velocity U_∞ was checked and has no influence on the results as shown by Figure 3.4, where the common results of the two test campaigns are superimposed. In this Figure, the β angle is not the same for a given angle α, but as will be shown in Section 4.4, the β angle has no influence on the flat plate until

tap number 14 ($s = 3010$ mm). The curves are quite well superimposed, showing the repeatability (three months between campaign 1 and 2). Tables 3.1 and 3.2 give all the configurations that have been tested in campaigns 1 and 2 respectively.

Table 3.1: List of the configurations tested in campaign 1

α (°)	0.0	-0.1	-0.2	-0.3	-0.4	-0.5	-0.6	-0.7
β (°)	-13.8	-13.3	-12.7	-12.1	-11.6	-11.1	-10.6	-10.2
U_∞	10.7	10.7	10.7	10.7	10.7	10.7	10.7	10.7
number of acquisitions	9	3	3	1	1	1	2	1
α (°)	-0.8	-0.9	-1.0	-1.2	-1.5	-2.0	-2.0	-2.0
β (°)	-9.7	-9.2	-8.7	-7.8	-6.5	-12.0	-14.0	-18.0
U_∞	10.7	10.7	10.7	10.7	10.7	10.7	10.7	10.7
number of acquisitions	1	1	2	1	1	5	3	2
α (°)	-2.0	-2.0	-2.0					
β (°)	-19.0	-20.0	-22.0					
U_∞	10.7	10.7	10.7					
number of acquisitions	2	10	3					

Table 3.2: List of the configurations tested in campaign 2

α (°)	-2.0	-2.0	-2.0	-2.0	-2.0	-2.0	-2.0	-2.0
β (°)	-12.0	-15.0	-17.0	-18.0	-19.0	-20.0	-21	-21.5
U_∞	10	10	10	10	10	10	10	10
number of acquisitions	1	1	1	1	1	7	1	1
α (°)	-2.0	-2.0	-2.0	-2.0	0.0	-0.7		
β (°)	-22.0	-22.0	-20.0	-20.0	-12.0	-12.0		
U_∞	10	5	5	7	10	10		
number of acquisitions	3	1	3	3	1	1		

4.2 Transverse homogeneity

The transverse pressure distribution qualifies more quantitatively the two dimensionality of the flow than wool tufts visualisations. Figure 3.5 gives the spanwise pressure coefficient distribution at two streamwise positions : $s = 1727$ mm and $s = 3010$ mm corresponding to pressure taps number 8 and 14 (see Figure 2.9). The pressure distribution is almost constant at the two stations and it was the same for all the configurations (with different α and β) that have been tested. The small variations that can be observed are in the error bars.

In Figure 3.5 a), a small difference close to the uncertainty appears at $z = 0$ mm. This is attributed to the change in reference pressure for the reading (tap number 8 serves as reference for these measurements). In conclusion, on the flap plate, the transverse pressure distribution confirms that the flow is two dimensional in the investigated area $-800 \leq z \leq 800$ mm.

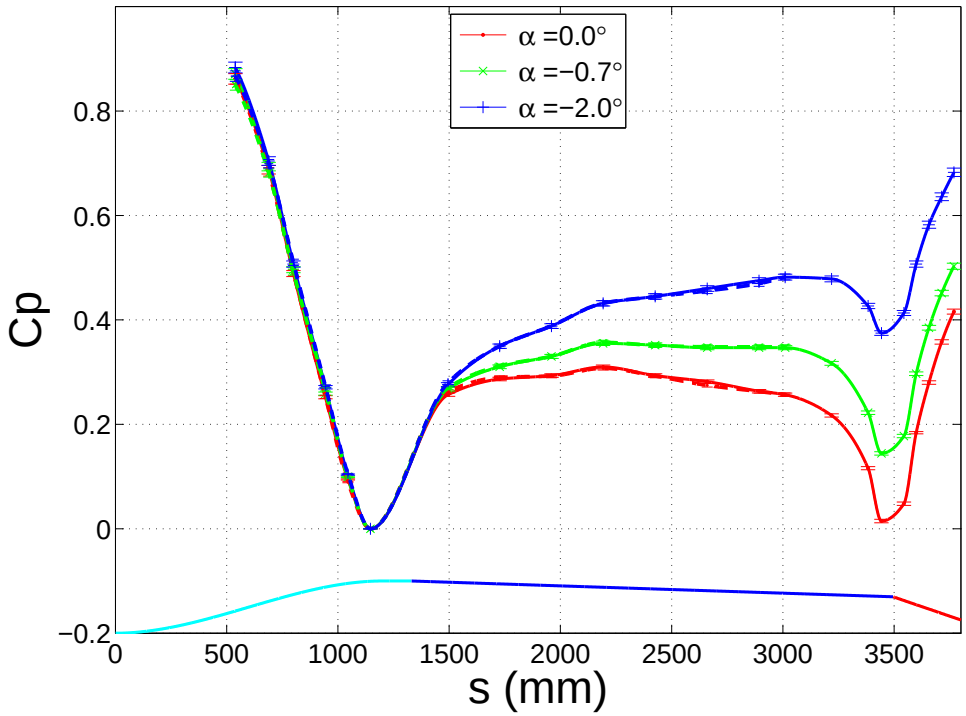

a)

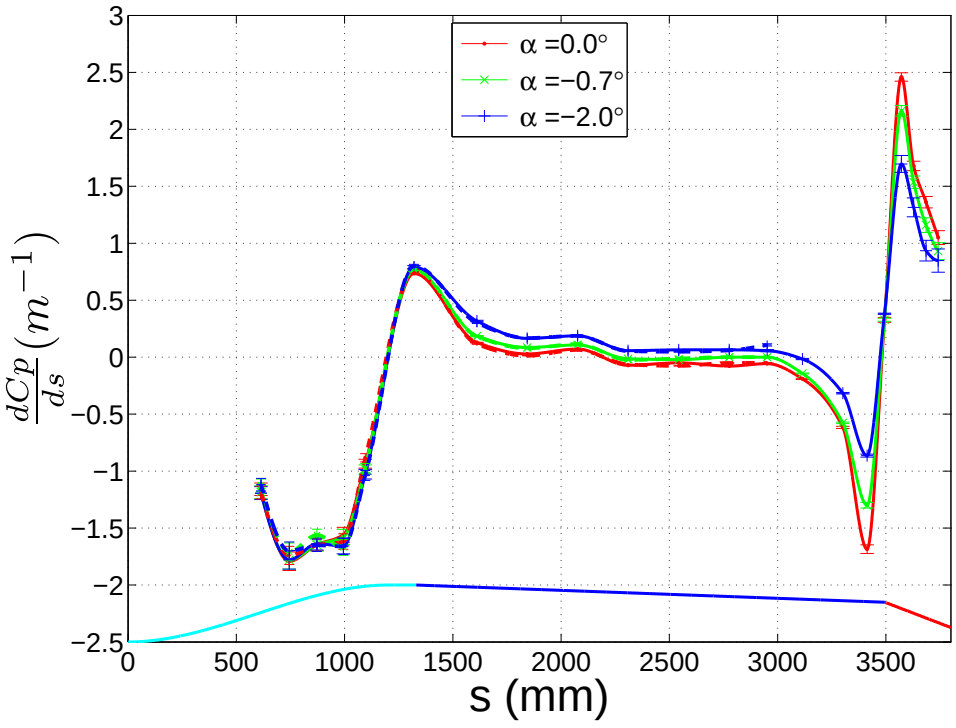

b)

Figure 3.4: a) Streamwise pressure coefficient distribution, b) streamwise pressure gradient distribution, for different α and β, with $U_\infty = 10$ m/s. Dashed lines correspond to campaign 1 and solid lines to campaign 2.

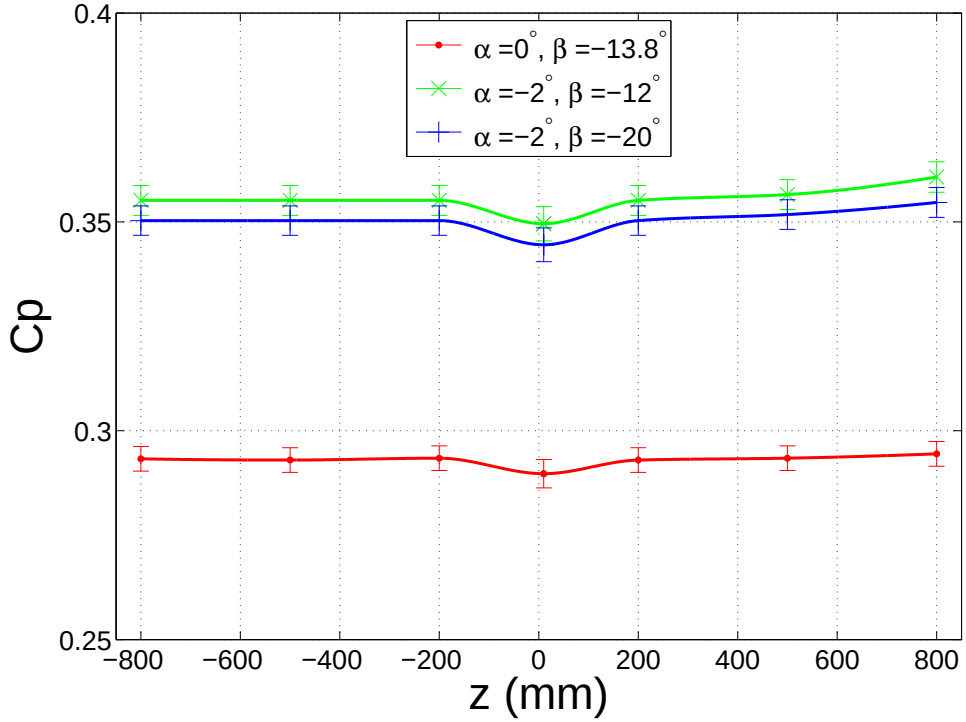

a)

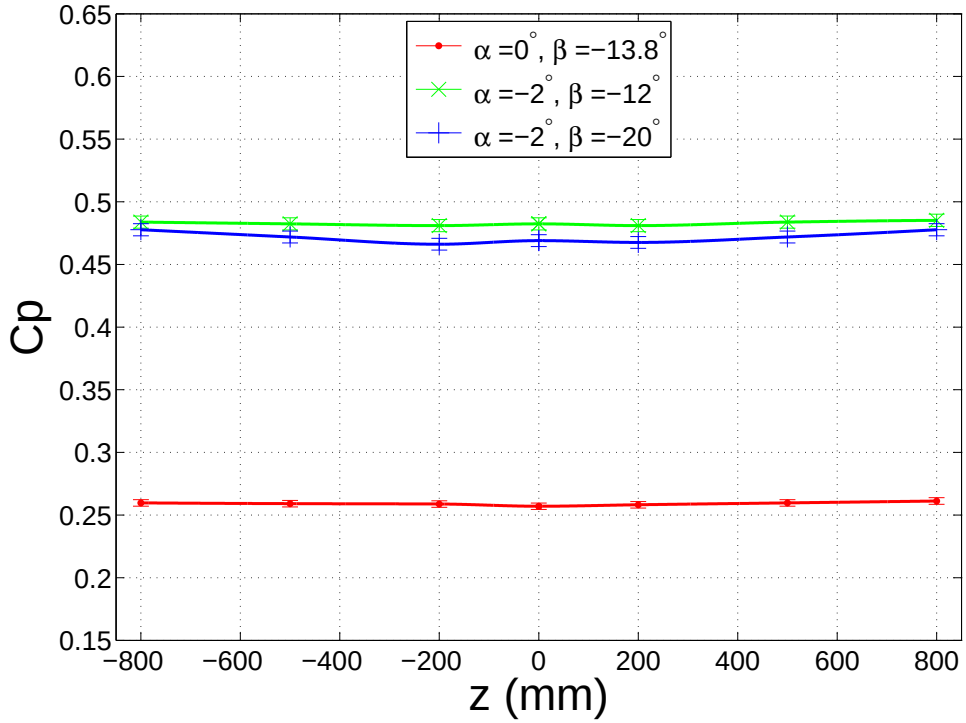

b)

Figure 3.5: Spanwise pressure coefficient distribution a) at $s = 1727$ mm and b) at $s = 3010$ mm, for different α and β, with $U_\infty = 10$ m/s.

On the flap, no significant pressure variations was observed in the transverse direction for $-305 \leq z \leq 305$ mm. This confirms the results of oil film visualisation (Section 3).

4.3 Influence of α on the flat plate pressure distribution

The pressure distribution over the flat plate (which starts at $s = 1360$ mm) can be significantly tuned by a variation of α from 0° to −2° (see Figure 3.6 a)). Three evolutions of the pressure gradient are observed. The first one from a suction peak at $s = 1146$ mm (or tap number 6 (see Figure 2.9)) to $s = 2192$ mm (or tap number 10), where the boundary layer seems not in an equilibrium state (see Figure 3.6 b)). Then, the second one where the pressure gradient is stabilized. For $\alpha = -0.7°$, in this stabilized pressure gradient area, the value is near zero (the average of $\frac{dC_p}{ds}$ between pressure taps number 10 to 14 is about $-0.009\ m^{-1}$, compared to $0.061\ m^{-1}$ in the case $\alpha = -2°$ and $\beta = -12°$, and between taps 12 to 14, the pressure gradient is smaller and is equal to zero within the available accuracy). Table 3.3 gives the four values of $\frac{dC_p}{ds}$ available between pressure taps 10 to 14 in the configurations $\alpha = 0°$, $\alpha = -0.7°$ and $\alpha = -2°$, with $\beta = -12°$ and $U_\infty = 10$ m/s. In conclusion, a favourable pressure gradient is reached for $\alpha > -0.7°$ and an adverse pressure gradient for $\alpha < -0.7°$. A zero pressure gradient is reached for $\alpha = -0.7°$ on a distance of about 25 cm before the upstream influence of the flap. Finally, the pressure distribution over the flat plate ends with a suction peak at pressure tap number 17, due to the change in curvature at the flap articulation.

Table 3.3: Values of $\frac{dC_p}{ds}$ between taps 10 to 14, for different α, with $\beta = -12°$ and $U_\infty = 10$ m/s.

α (°)	s (mm)	$\frac{dC_p}{ds}$ (m^{-1})
0	2309	-0.071
	2543	-0.050
	2776.5	-0.078
	2951.5	-0.057

α (°)	s (mm)	$\frac{dC_p}{ds}$ (m^{-1})
-0.7	2309	-0.014
	2543	-0.021
	2776.5	0
	2951.5	0

α (°)	s (mm)	$\frac{dC_p}{ds}$ (m^{-1})
-2	2309	0.057
	2543	0.064
	2776.5	0.065
	2951.5	0.057

4.4 Influence of the flap angle β

To analyse separately the influence of both α and β, it is important to check, by tuning β, that the modification of the flap pressure gradient is decoupled from the pressure gradient on the flat plate (tuned by α). Nine values of β were tested for a fixed $\alpha = -2°$. The separation, observed with wool tufts visualisations on the flap, occurs for angles smaller than $\beta = -19°$ as was seen in Section 2. For all the tested β, no significant modifications of the pressure coefficient distribution is found on the flat plate until tap 14 at $s = 3010$ mm, which is 490 mm from the articulation (see Figure 3.7).

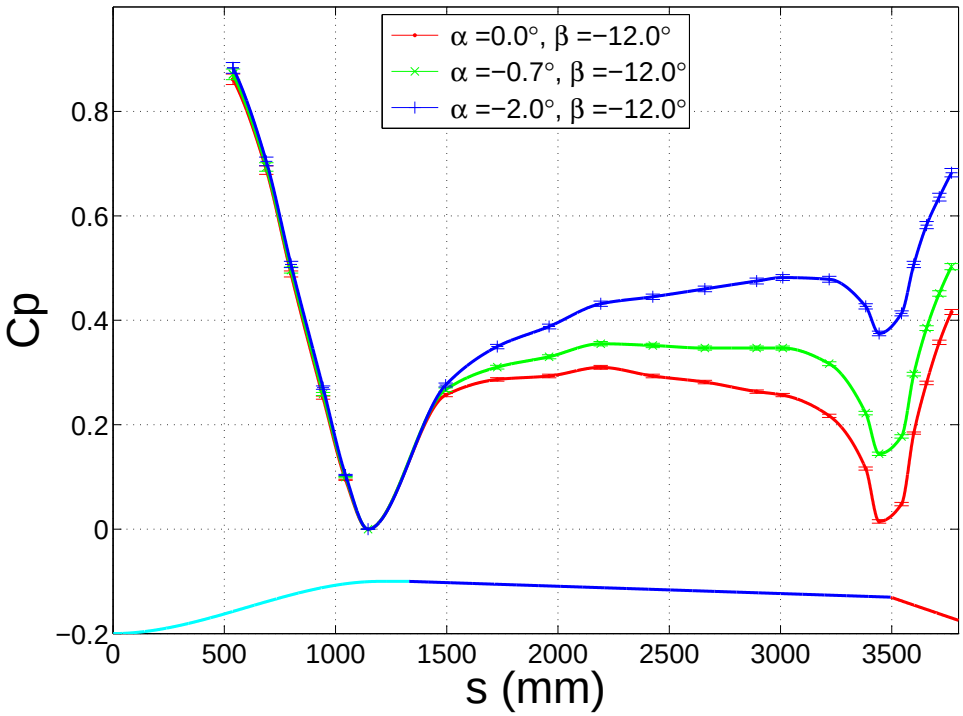

a)

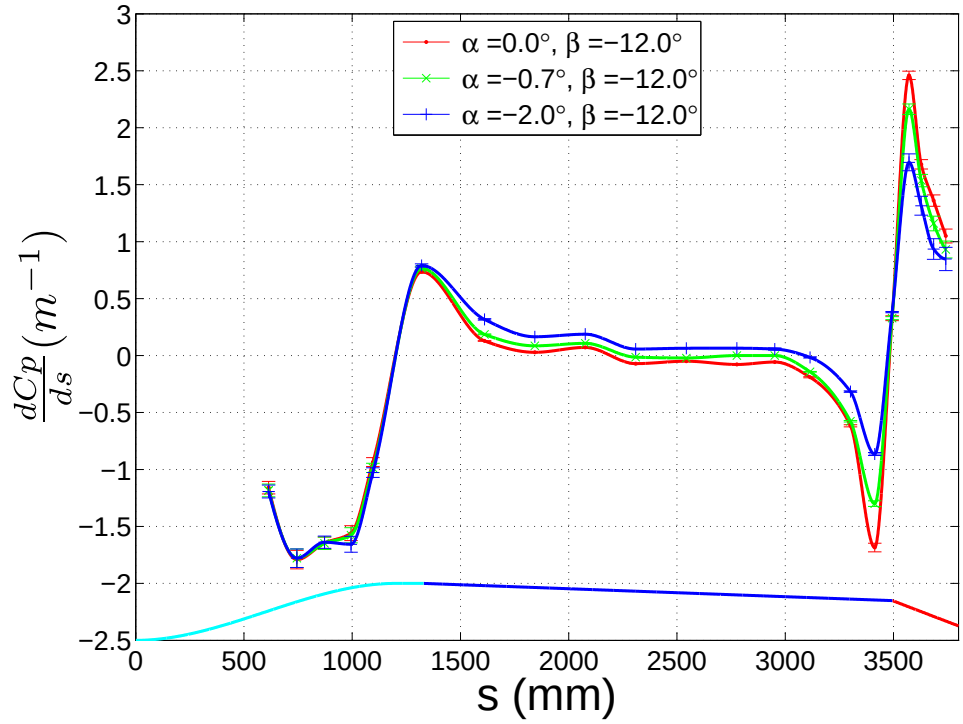

b)

Figure 3.6: a) Streamwise pressure coefficient, b) streamwise pressure gradient, for different α, with $\beta = -12°$ and $U_\infty = 10$ m/s.

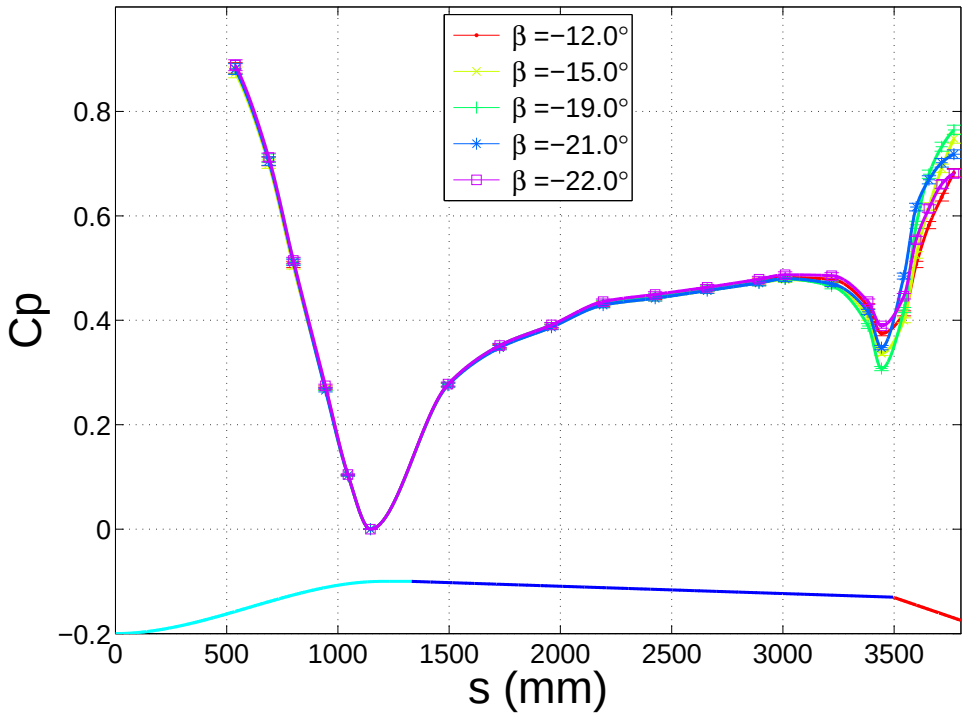

a)

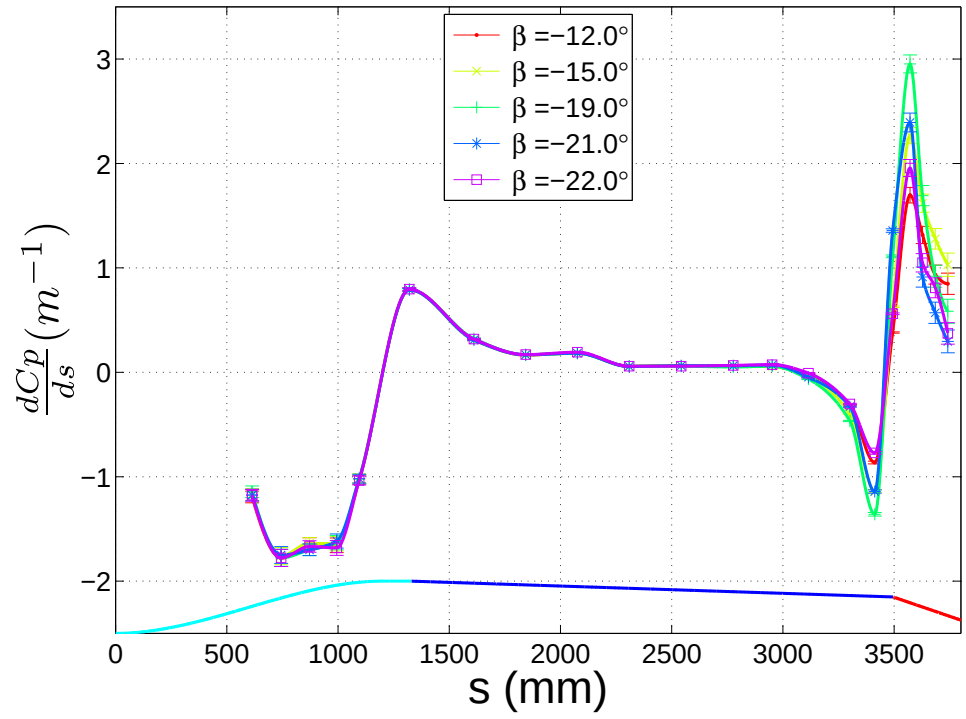

b)

Figure 3.7: a) Streamwise pressure coefficient, b) streamwise pressure gradient, for different β, with $\alpha = -2°$ and $U_\infty = 10$ m/s.

On the contrary, the angle β has a significant effect on the suction peak just before the flap articulation (see Figure 3.7). The same behaviour is observed for both pressure and pressure gradient distributions, but more marked for the pressure gradient. When decreasing β from -12 to $-19°$, the suction peak level increases and it decreases when decreasing β from -19 to $-22°$. This behaviour is the witness that separation appears for β below $-19°$, which is consistent with wool tufts visualisations. The level of the suction peak upstream of the flap articulation could be used to detect separation, but unfortunately, the differences are small and too near the uncertainty. Table 3.4 gives the value of C_p and $\frac{dC_p}{ds}$ at the suction peak ($s = 3443$ mm) upstream of the flap articulation for different angles β with $\alpha = -2°$ and $U_\infty = 10$ m/s.

Table 3.4: Values of C_p and $\frac{dC_p}{ds}$ at the suction peak at $s = 3443$ mm, for different β, with $\alpha = -2°$ and $U_\infty = 10$ m/s.

$\beta(°)$	-12	-15	-17	-18	-19	-20	-21	-21.5	-22
C_p	0.375	0.337	0.310	0.307	0.308	0.320	0.347	0.362	0.389
$\frac{dC_p}{ds}(m^{-1})$	-0.86	-1.14	-1.34	-1.32	-1.36	-1.25	-1.14	-0.98	-0.77

4.5 Influence of the Reynolds number on the pressure distribution

The influence of the Reynolds number (based on U_∞ and a length of 1 m) was investigated for an adverse pressure gradient on the flat plate ($\alpha = -2°$) and a flow separation on the flap ($\beta = -20°$) (see Figure 3.8). Three values of R_e were obtained by varying U_∞. Except for small variations in the converging and flap parts, the overlap of the three curves is fairly good which indicates that there is no significant influence of the Reynolds number on this model configuration (in the limit of the Reynolds number range tested $321000 \leq Re \leq 641000$).

4.6 Conclusion

For the flow control study, it was decided to retain a ramp configuration which mimics a real application, such as a suction side of a wing or a car roof. Based on the wall pressure distribution tests and on the wool-tufts and oil film visualisations shown in the previous sections, the ramp set-up finally retained was the one with $\alpha = -2°$ and $\beta = -22°$. This configuration is similar to the one used by Lin (1999) and Selby et al. (1992), however it differs slightly by an adverse pressure gradient on the flat plate which is nearer to real applications. The flap angle here is also lower than the one of these authors so that the separation is not three dimensional but strong enough to be evidenced by wool-tufts visualisations.

The ramp step height (i.e. the distance to the wind-tunnel floor of the flap articulation in the Y direction, see Figure 2.2) is $H_{step} = 17.5$ cm. The separation length obtained by wool tufts, normalised by the step height is then $\frac{L_{sep}}{H_{step}} \simeq 4.6$.

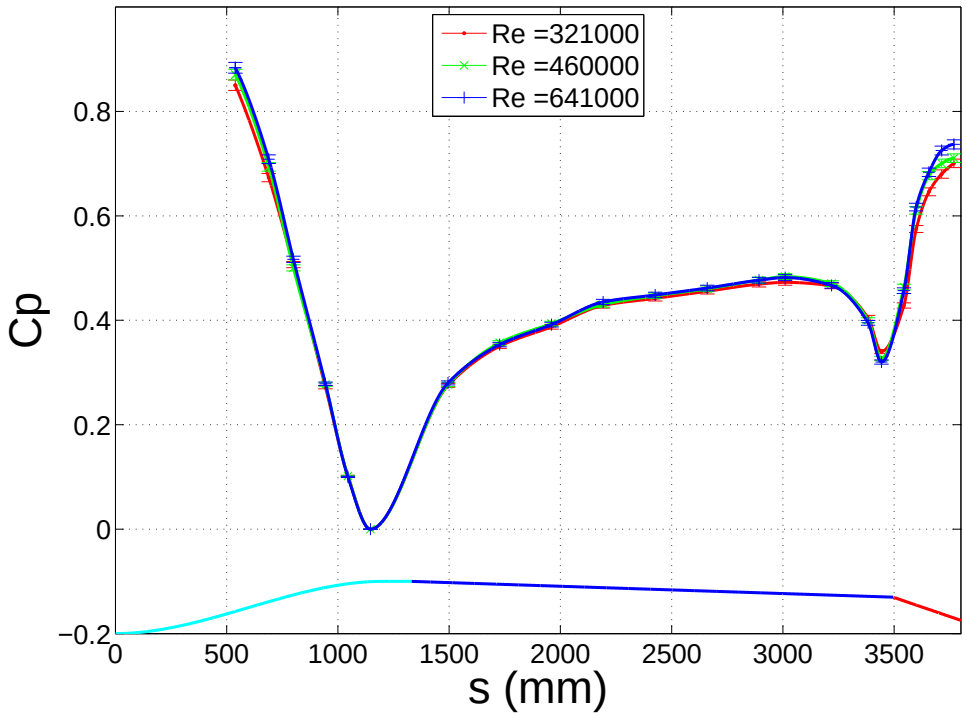

a)

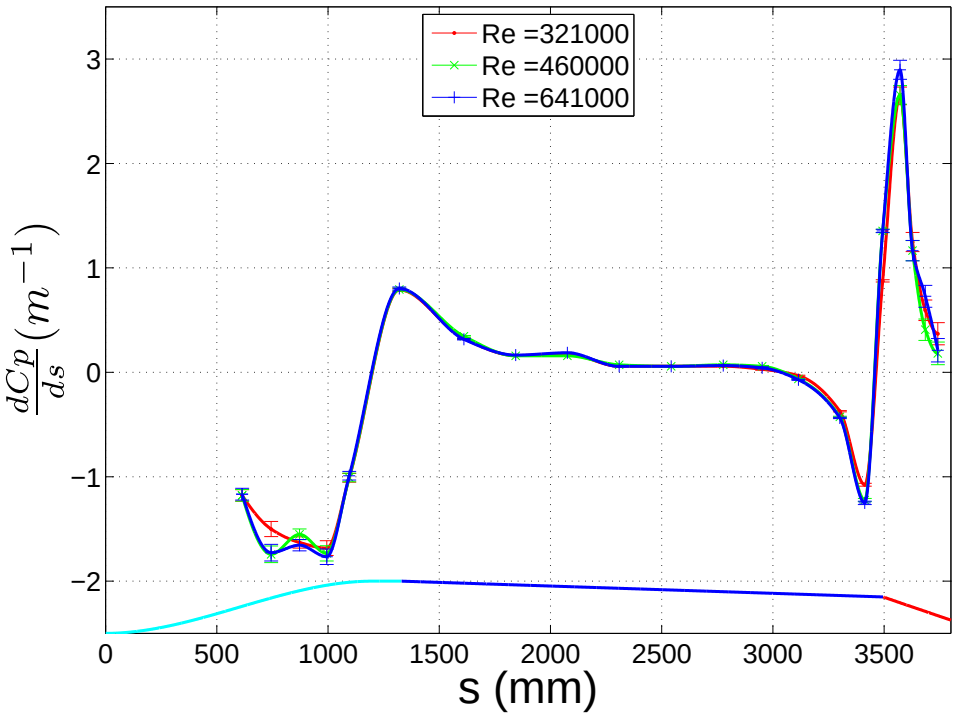

b)

Figure 3.8: a) Streamwise pressure coefficient, b) streamwise pressure gradient, for different U_∞ (5, 7 and 10 m/s), with $\alpha = -2°$ and $\beta = -20°$.

This value is larger than the one of Lin (1999) and Selby et al. (1992) ($\frac{L_{sep}}{H_{step}} \simeq 1.3$) although, as will be seen in the next section, the Reynolds number of the upstream boundary layer is in the same order here as the one of these authors ($Re_\theta \simeq 9000$). This difference can be explained by a possible over estimation of the separation length by wool-tufts or by a larger momentum thickness compared to the one of Lin (1999) and Selby et al. (1992) ($\theta = 3.3$ mm) which was noticed by Simpson (1989) to increase $\frac{L_{sep}}{H_{step}}$ for a backward facing step.

5 Single hot-wire measurements

5.1 Description of the measurements

Five single hot-wire profiles were carried out at different streamwise positions along the flat plate in the configuration $\alpha = -2°$ and $\beta = -22°$. The aim was to characterize the APG boundary layer development. Figure 2.12 given in Chapter 2 shows the location along the ramp of the five profiles. The hot-wire accuracy was also described in Chapter 2 Section 5.1.3.3. As measurements were repeated three times at each station, the uncertainty on the boundary layer parameters can be determined.

5.2 Determination of the friction velocity u_τ

As was discussed in Chapter 1, the wall friction velocity, for a zero pressure gradient turbulent boundary layer, can be computed from the mean streamwise velocity profile by fitting the log-law equation (equation (1.11)) on the mean velocity profile in the area $30 < y^+ < 500$ with $\kappa = 0.41$ (Clauser (1956)). The value of C has then to be about 5.0 to be confident about the result. However, as was also discussed in Chapter 1, this Clauser's chart method is risky in pressure gradient boundary layers as the log-law region shrinks. For that reason, in adverse pressure gradient, the log-law was replaced by a "modified log-law" (equation (1.30)) to determined u_τ, as this law was found to give better results in APG boundary layers (Skote (2001), Skote and Henningson (2002), Bernard et al. (2003), etc. (see Chapter 1)). In FPG however, the standard log-law (equation (1.11)) was used instead of the modified log-law as a better fit is obtained.

The position of the first point, measured with a cathetometer, was $y_0 \simeq 0.2 \pm 0.05$ mm. The value y_0 was thus adjusted in the uncertainty interval to optimised the fit. As a value of C of the log-law was needed for the fit, it was set at 5.0. The value C2 of the modified log-law was then given by equation (1.32).

Figure 3.9 illustrates the result of the fit of the modified log-law for stations 1 to 4 (APG), and the result of the fit of the standard log-law for station 5 (FPG). In this figure, the LML boundary layer flat plate (FP) profile at $U_\infty = 5$ m/s (corresponding to the same Reynolds number based on the momentum thickness θ (Re_θ)) is also plotted for comparisons. For APG boundary layers (stations 1 to 4), the curvature of the modified log-law is in the right direction, and it was found possible to fit this law on a larger part of the mean velocity profile than for the log-law ($30 < y^+ \lesssim 150 - 300$ for the modified log-law and $30 < y^+ \lesssim 80 - 100$ for the log-law). However the result of the fit is not totally perfect. The estimation of

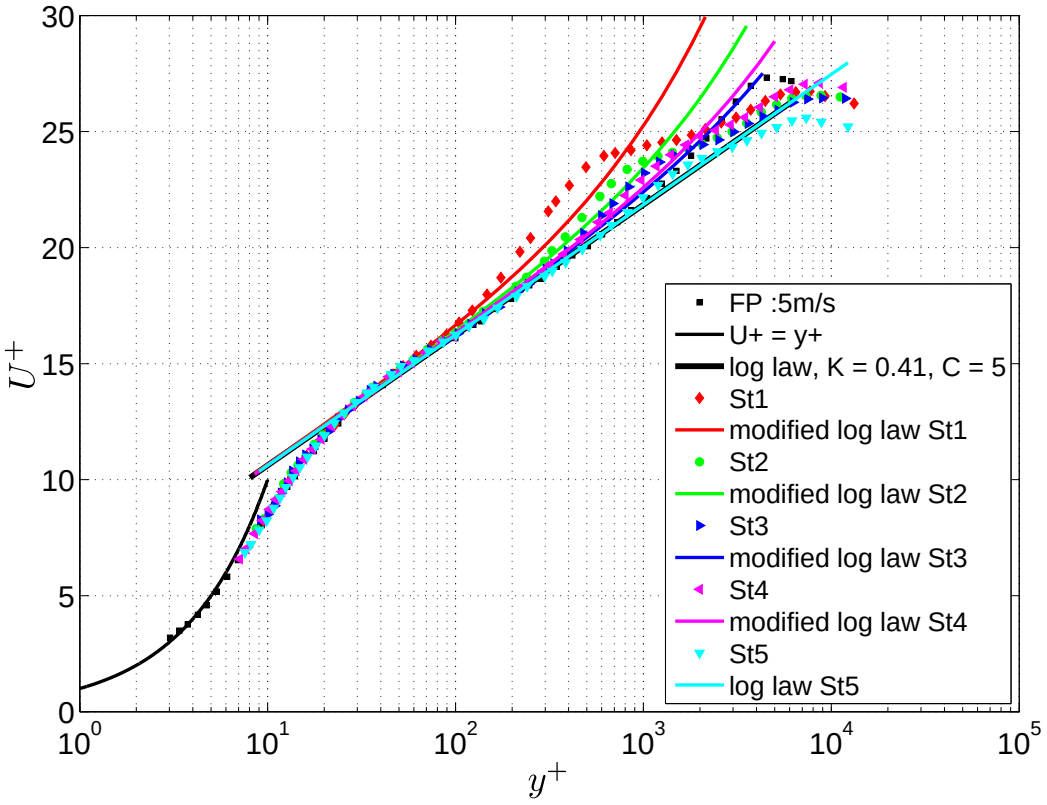

Figure 3.9: Mean streamwise velocity profiles for the five stations compared to a FP case at the same Re_θ, $\alpha = -2°$, $\beta = -22°$ and $U_\infty = 10$ m/s.

the uncertainty on u_τ is then $\pm 5\%$. Indeed, less than 3% differences was observed on the 3 independent values of u_τ obtained with the three coherent profiles realized at each station, and a difference of less than 1% is observed by adding or removing 2 points for the fit.

5.3 Boundary layer characteristics

Figure 3.10 shows the mean streamwise velocity profile evolution at the five stations. From these measurements, the boundary layer characteristics can be determined and are given in Table 3.5. δ is defined by the position y from the wall, where the streamwise velocity U reaches 99% of the external velocity U_e. The displacement thickness and the momentum thickness are obtained by integrating the profile with a trapeze method. The shape factor is $H = \frac{\delta^*}{\theta}$. The Reynolds number based on θ is computed with U_e as reference velocity : $Re_\theta = \frac{U_e \theta}{\nu}$. The Clauser parameter is $\beta_{Clauser} = \frac{\partial P}{\partial s} \frac{\delta^*}{\rho u_\tau^2}$. The pressure gradient in wall units is given by equation (1.22). Finally, the friction velocity u_τ is obtained as described in Section 5.2. For comparison, $u_{\tau_{Lud-Till}}$ is obtained from the equation (1.35) given by Ludwieg and Tillmann (1949).

The uncertainty on δ is about $\pm 10\%$ which is quit big, but this value is always difficult to estimate. Concerning δ^*, θ, Re_θ and u_τ, the accuracy is around $\pm 5\%$.

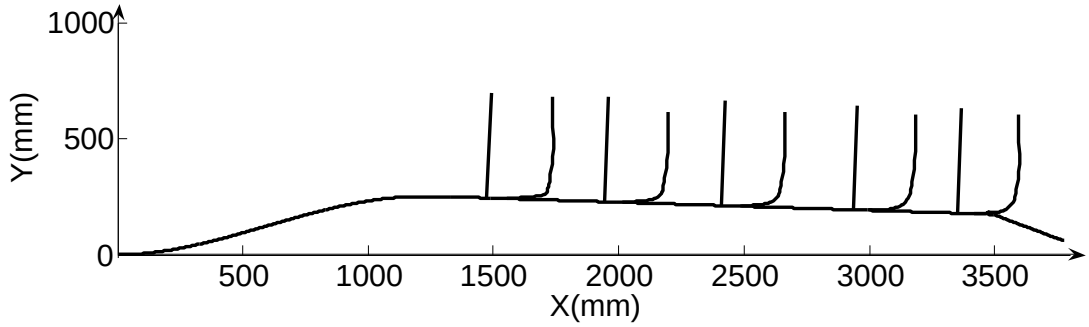

Figure 3.10: Evolution of the mean streamwise velocity profiles for the five stations, $\alpha = -2°$, $\beta = -22°$ and $U_\infty = 10$ m/s.

Table 3.5: Boundary layer characteristics at $U_\infty = 10$ m/s (and between brackets at $U_\infty = 5$ m/s for station 4).

St	s (mm)	δ (cm)	δ^* (mm)	θ (mm)	Re_θ	H
St1	1508	17.4	14.4	12.2	10100	1.18
St2	1974	19.6	16.5	13.7	10600	1.21
St3	2440	20.3	17.9	14.7	11700	1.22
St4	2968	21.2	20.3	16.5	12600	1.23
		(22.3)	(24.1)	(19.1)	(7500)	(1.27)
St5	3382	19.0	16.4	13.5	10100	1.21

St	s (mm)	U_e (m/s)	u_τ (m/s)	$u_{\tau_{Lud-Till}}$ (m/s)	$(\frac{\partial P}{\partial s})^+$ ($\times 10^3$)	$\beta_{Clauser}$
St1	1508	12.9	0.482	0.525	3.28	1.44
St2	1974	12.6	0.459	0.481	1.47	0.70
St3	2440	12.5	0.462	0.476	0.46	0.24
St4	2968	12.4	0.435	0.448	0.67	0.38
		(6.2)	(0.230)	(0.239)	(1.14)	(0.60)
St5	3382	12.3	0.465	0.471	-5.54	-2.56

The uncertainty on the shape factor H is small about ±2%, probably because the uncertainties on δ^* and θ are linked (both are obtained by integration of the mean profile). The uncertainty on $(\frac{\partial P}{\partial s})^+$ is around ±15% due to the large uncertainty on the pressure gradient. The uncertainty on the Clauser parameter is around ±20%. Finally the uncertainty on U_e is ±0.6% as was seen in Section 5.1.3.3.1 in Chapter 2. These uncertainty have been estimated by the standard deviation method based on the three measurement points for each parameter as was done for the pressure gradient and for the hot-wire measurements (Dixon and Massey (1957)).

The agreement between the friction velocity u_τ determined with the modified Clauser's chart method and with equation (1.35) from Ludwieg and Tillmann (1949) is quite good (less than 5% for the last four stations and 9% for the first station). This validate the estimation of u_τ with the modified Clauser's chart method. The higher difference observed between the two estimations of u_τ at the first station can be attributed to the downstream influence of the converging part.

The small value of the shape factor H at station 1 can be explained by the strong favourable pressure gradient that the flow encountered in the converging part, which reduces the shape factor of the incoming turbulent boundary layer. Then, H increases from station 1 to station 4 due to the mild adverse pressure gradient encountered. Finally, between station 4 and 5 it decreases slightly again due to the change of sign of the pressure gradient caused by the change in slope of the wall at the flap articulation. The boundary layer thickness δ, the displacement thickness δ^*, the momentum thickness θ and the momentum Reynolds number Re_θ follow the same trend as the shape factor H as there are also strongly linked to the pressure gradient as was discussed in Chapter 1.

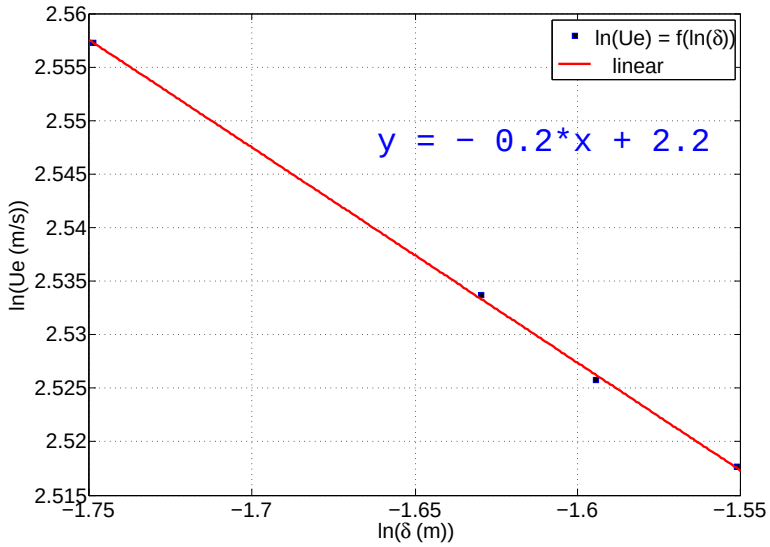

Figure 3.11: $\ln(U_e)$ versus $\ln(\delta)$ for the first four stations, $\alpha = -2°$, $\beta = -22°$ and $U_\infty = 10$ m/s.

Between stations 3 and 4, the Clauser pressure gradient parameter $\beta_{Clauser}$ is about constant, so in this region the boundary layer is in equilibrium state as de-

fined by Clauser (1954). This result is coherent with the pressure gradient distributions (see Section 4.3 and Figure 3.6). However, as was discussed in Chapter 1, Castillo and George (2001) defined the boundary layer equilibrium state differently. For them, the boundary layer is in equilibrium state if the free-stream velocity is proportional to the boundary layer thickness at power $-\Lambda = constant$, with Λ given by equation (1.27). The equilibrium definition of Castillo and George (2001) was checked for the first four stations which are in adverse pressure gradient. Figure 3.11 gives a plot of $\ln(U_e)$ versus $\ln(\delta)$. The evolution is linear, so, in this area, the boundary layer is in the equilibrium state defined by Castillo and George (2001), with $\Lambda = 0.2$, which is close to the value of 0.22 observed by these authors for adverse pressure gradient. The two definitions of boundary layers equilibrium state are then different, however, when the boundary layer is in the equilibrium state as defined by Clauser (1954), it is also in the sense of Castillo and George (2001). This second definition appears more general.

5.4 Mean streamwise velocity profiles

Figure 3.12 shows the five mean velocity profiles obtained along the ramp plotted in wall units and Figure 3.13 in external units. In wall units, all the profiles collapse for $8 \leq y^+ \leq 200$ (see Figure 3.12). This is coherent with the TBL theory as the near wall velocity scale is u_τ and the length scale is $\frac{\nu}{u_\tau}$ (see Chapter 1). These profiles, are compared in Figure 3.12 with the log-law with $\kappa = 0.41$ and $C = 5$. The log region extension increases with s, the curvilinear abscissa. This is coherent because the adverse pressure gradient decreases with s, and changes its sign at the last station.

The profiles begin at $y^+ = 9$ for stations 1 to 3, and at $y^+ = 7.5$ for stations 4 and 5, which corresponds to $y \simeq 0.2$ mm. For the three first stations, the probe was not approached nearer to the wall as non negligible vibrations were observed and measured by an acceleration sensor stuck on the wall. The amplitude of these vibrations (estimated as 2σ with σ the standard deviation) is given in Table 3.6. It is less than two wall units and the frequency is small (under 20 Hz), so the flow is not affected. These vibrations are due to the vibration of the wind tunnel.

Table 3.6: Amplitude of the vibrations at the positions of hot-wire measurements at $U_\infty = 10$ m/s.

St	s (mm)	A (mm)	A (+)
St1	1508	0.018	0.6
St2	1974	0.060	1.8
St3	2440	0.063	1.9
St4	2968	0.051	1.5
St5	3382	0.015	0.5

Using external units (Figure 3.13), higher velocities are observed between $\frac{y}{\delta} =$

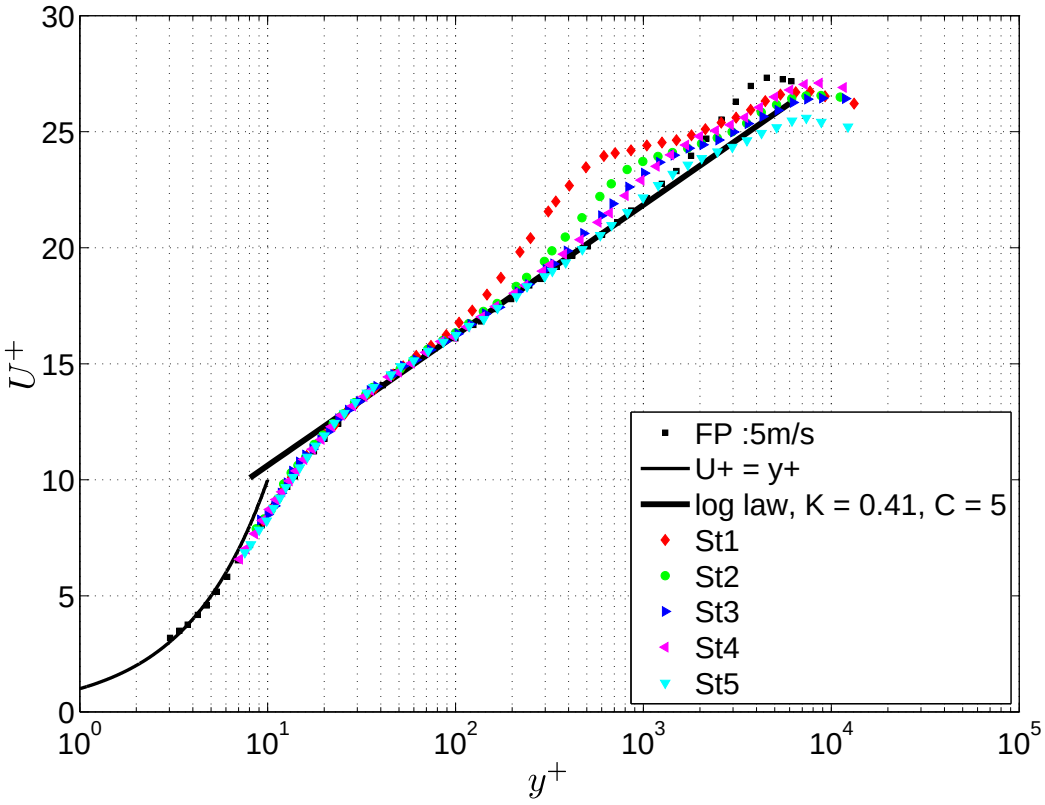

Figure 3.12: Mean streamwise velocity profiles at the five stations in wall units, $\alpha = -2°$, $\beta = -22°$ and $U_\infty = 10$ m/s.

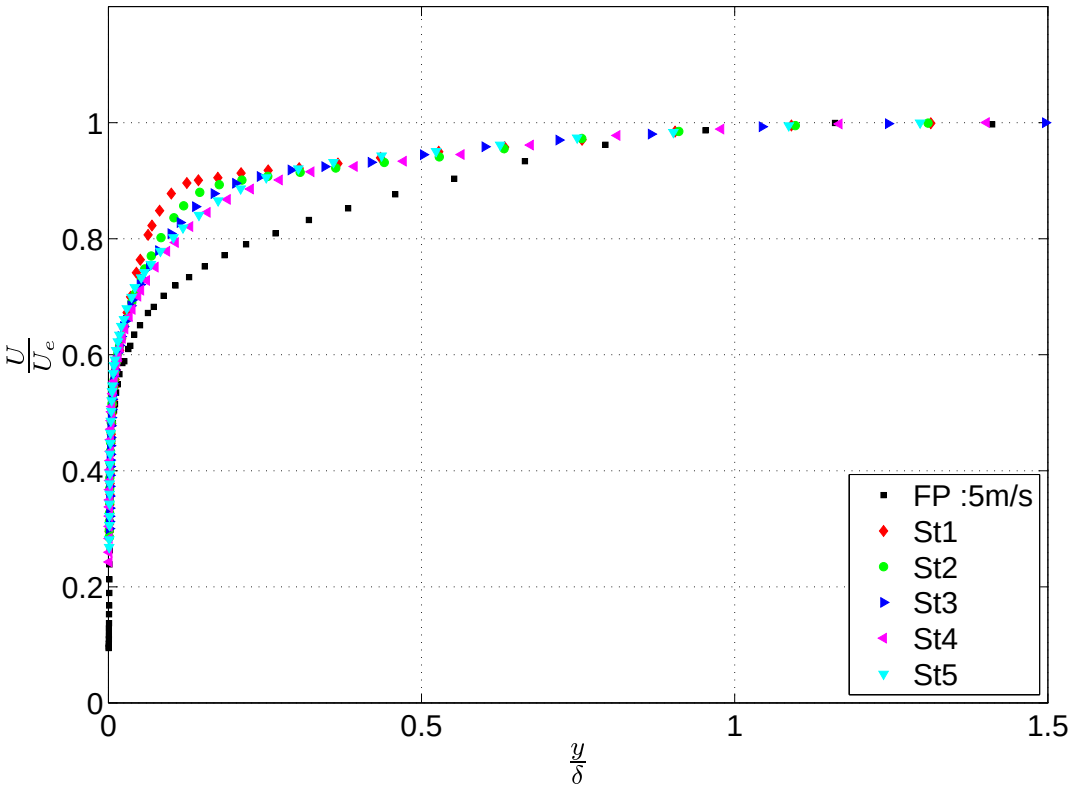

Figure 3.13: Mean streamwise velocity profiles at the five stations in external units, $\alpha = -2°$, $\beta = -22°$ and $U_\infty = 10$ m/s.

0.05 and 0.75 compared to the FP. This difference is attributed to the acceleration of the flow in the converging part. It decreases from station 1 to station 4, and then increases again due to the change of sign of the pressure gradient between stations 4 and 5.

5.5 Turbulence intensity profiles

Figure 3.14 shows the evolution of the turbulence intensity profile ($u^+ = \frac{\sqrt{\overline{u'^2}}}{u_\tau}$) along the ramp in wall units. The y^+ axis is logarithmic to show in the same plot the near wall region and the region away from the wall.

Except for station 5 and FP, all the profiles collapse for $8 \leq y^+ \leq 40$. A first peak of turbulence is observed for all the profiles at $y^+ \simeq 14$ which is characteristic of near wall turbulence. This peak has a value of 2.9 for stations 1 to 4, slightly under the value of the FP case. This difference on the peak level can be attributed to the length of the hot-wire used here ($l^+ \simeq 15$), compared to the recommended value given by Klewicki and Falco (1990) ($l^+ \leq 8$), which lead to under estimate this near wall peak level (for the FP, l^+ was 6). The value of this turbulence peak is smaller at station 5 because the pressure gradient is favourable at this station and tends to attenuate turbulence.

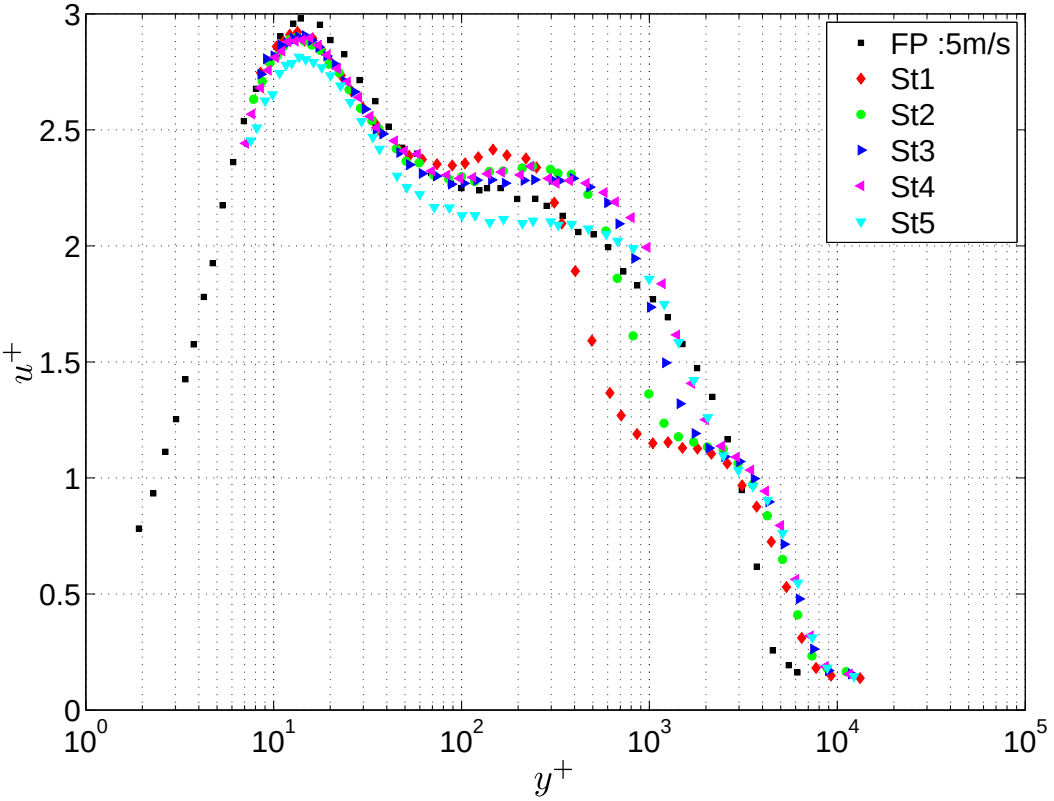

Figure 3.14: Turbulence intensity profiles in wall units, $\alpha = -2°$, $\beta = -22°$ and $U_\infty = 10$ m/s.

A second peak is observed at the first four stations, around $y^+ \simeq 150$ at station 1, and is moving away from the wall with s, to reach $y^+ \simeq 350$ at station 4. This peak is replaced by a plateau at station 5 and for the FP case. This second peak is accompanied with a knee point at $y^+ \simeq 2000$ for the first four stations. The second peak and the knee point were also observed by Webster et al. (1996), Wu and Squires (1998), Baskaran et al. (1987), etc.. The knee point is attributed by Webster et al. (1996) to a proof that a new internal layer near the wall, as defined by Baskaran et al. (1987), has been triggered in the converging part by the change in curvature. The second peak on the profiles is then attributed to a remnant of the near wall peak of the upstream internal layer.

Here, this interpretation is questionable as the knee point position stays nearly at the same position with s. It should be more related to the external turbulence intensity of the incoming boundary layer that has been seriously attenuated by the favourable pressure gradient encountered in the converging part. The second peak in the turbulence intensity profiles may thus be interpreted as an instability triggered by the change of sign of the pressure gradient near pressure tap 6 (i.e. at the end of the converging part (see Figure 2.9)). The first turbulence peak is not attenuated in the converging part by the favourable pressure gradient encountered. This first peak is then only governed by the shear due to the wall and it explains why it scales with wall units. In Webster et al. (1996)'s study, the same explanations on the turbulence intensity profiles seems to apply as the first turbulence peak that they found, scales with wall units at the beginning of the APG region. However, contrary to the present study, they have found that the second peak becomes predominant in the APG region which leads to the disappearance of the first peak near the wall. These differences can be explained by the difference in the strength of their pressure gradient, as compared to the present study, their pressure gradient $\frac{\partial P}{\partial x}^+$ is ten time larger.

5.6 Third order moment and skewness profiles

Figure 3.15 a) shows the third order moment profiles ($u^{3+} = \frac{\overline{u'^3}}{u_\tau^3}$) at the five stations compared to the FP case. The profiles superimpose with the FP case below $y^+ \leq 14$. A first peak seems to appear around $y^+ \simeq 7$ but no data is available below $y^+ = 7$ and the uncertainty is higher due to the proximity of the wall. The third order moment is zero at $y^+ \simeq 14$ and shows a first minimum at $y^+ \simeq 25$ like in the FP case. After $y^+ \simeq 14$, the third order moment profiles differ from the FP case. A second minimum appears around $y^+ \simeq 300$ at station 1, which moves away from the wall with s to reach $y^+ \simeq 1000$ at station 5. The first minimum may corresponds to the near wall peak of the turbulence intensity, and the second to the instability triggered by the change of sign of the pressure gradient near pressure tap 6 as was seen in Section 5.5.

Figure 3.15 b) shows the skewness profiles ($S(u) = \frac{\overline{u'^3}}{\overline{u'^2}^{\frac{3}{2}}}$) at the five stations in wall units compared to the FP case. All profiles superimpose with the FP case below $y^+ \simeq 200$. The skewness decreases with y^+ to reach zero at $y^+ \simeq 14$. After it stays constant near zero in the logarithmic region and decreases in the wake region. Contrary to the FP case, it shows a local minimum at $y^+ \simeq 500$ for station 1,

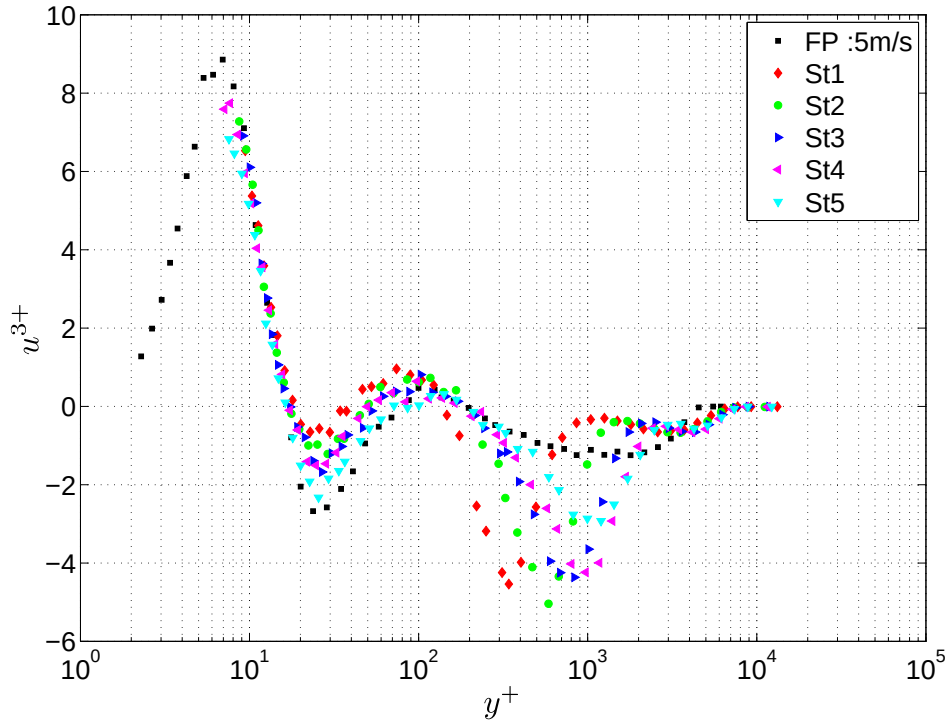

a)

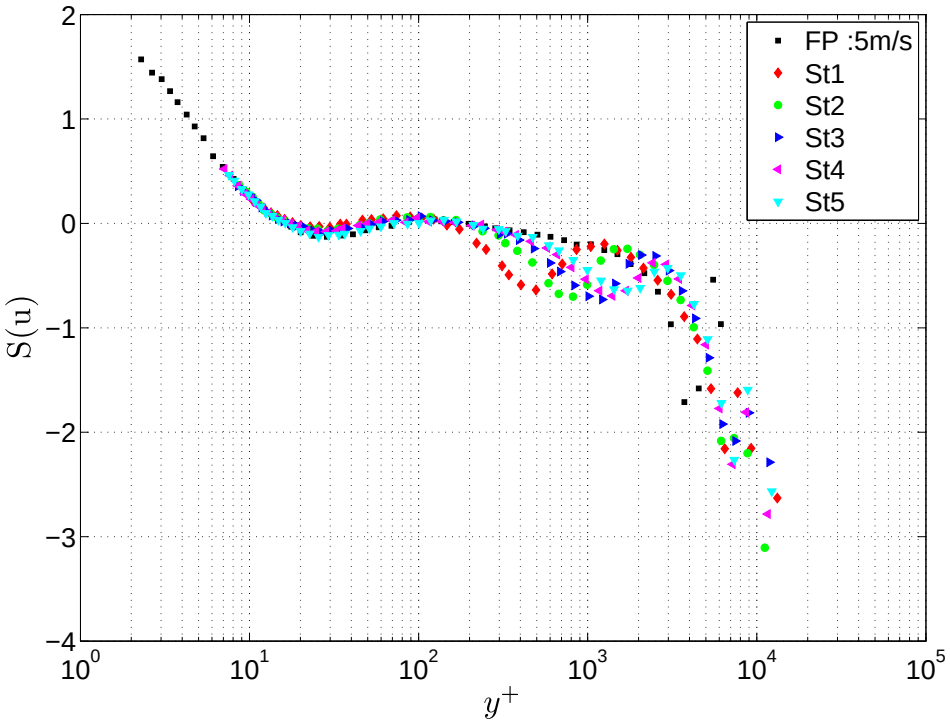

b)

Figure 3.15: a) Third order moment profiles for the five stations in wall units, b) skewness profiles for the five stations in wall units, $\alpha = -2°$, $\beta = -22°$ and $U_\infty = 10$ m/s.

which moves away from the wall to $y^+ \simeq 1700$ at station 5. After this minimum, all the profiles superimpose with the FP case. The positive values of the skewness under $y^+ \simeq 14$ are the result of wall intermittency (low and high speed streaks, ejections and sweeps). The negative values of the skewness in the wake region are the result of external intermittency (low momentum regions and hairpin structures). The minimum of skewness near $y^+ \simeq 500$ to 1700 is clearly related again to the instability triggered near pressure tap 6.

5.7 Fourth order moment and flatness profiles

Figure 3.16 a) shows the fourth order moment profiles ($u^{4+} = \frac{\overline{u'^4}}{u_\tau^4}$) at the five stations in wall units compared to the FP case. The behaviour is comparable to the turbulence intensity profiles. A first peak appears at $y^+ \simeq 14$ that corresponds to near wall turbulence. As for the turbulence intensity, this peak has a constant value for the first four stations, slightly under the value of the FP case. At station 5 the value is lower. A second peak appears around $y^+ \simeq 150$ at station 1, which moves away from the wall with s to reach $y^+ \simeq 400$ at station 4. This peak disappears at station 5. This second peak is similar to the peak and plateau observed on the turbulence intensity. It is then related to the instability triggered near pressure tap 6.

Figure 3.16 b) shows the flatness profiles ($F(u) = \frac{\overline{u'^4}}{\overline{u'^2}^2}$) at the five stations in wall units compared to the FP case. All the profiles superimpose for $y^+ \leq 300$. The flatness decreases from the wall with y^+, to reach a minimum at $y^+ \simeq 14$. Then it slightly increases to reach a value around 2.6 - 2.7 in the logarithmic region. After, the flatness profiles for the five stations differ from the FP case. Indeed, a peak appears around $y^+ \simeq 500$ for station 1, which moves away from the wall with s to reach $y^+ \simeq 2000$ at station 5. This peak is clearly related again to the instability triggered near pressure tap 6. After this second peak, the flatness increases strongly at all five stations, due to intermittency, and superimpose with the FP case.

6 Streamwise 2D2C PIV measurement of the separation

6.1 Introduction

On the same ramp configuration as for hot-wire measurements, a streamwise 2D2C PIV measurement at mid-span all over the separation region was performed to obtain statistics about the separated part of the flow, such as the mean separation and reattachment point positions, the separation length and the separation height. The second aim of this measurement was to obtain mean velocity profiles upstream, in and downstream of the separation. The experimental set-up used was described in Chapter 2. The free-stream velocity was fixed at $U_\infty = 10$ m/s.

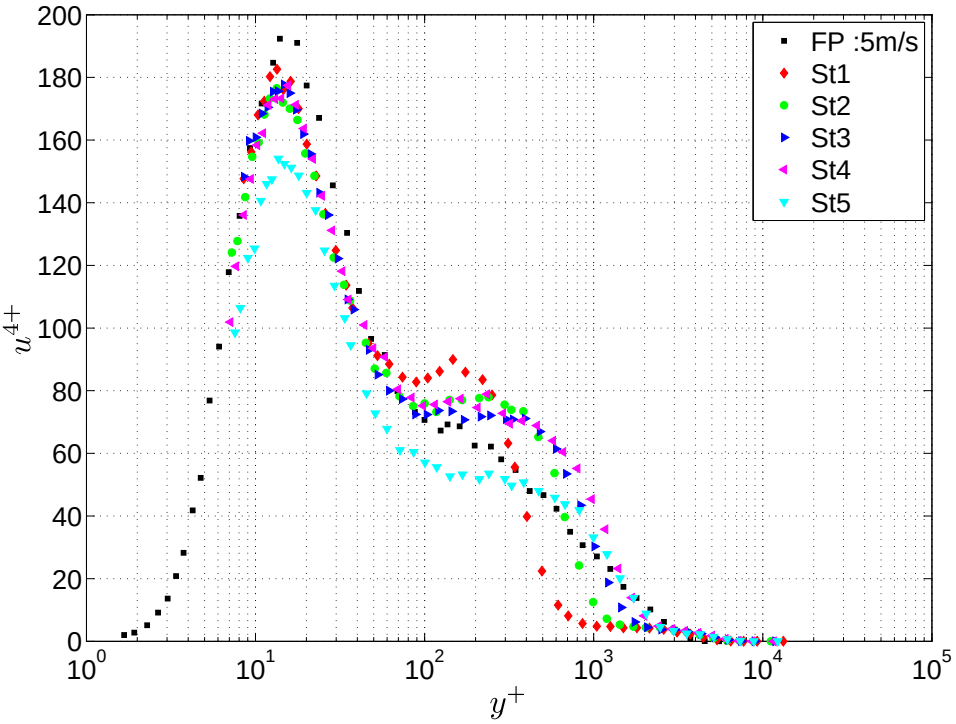

a)

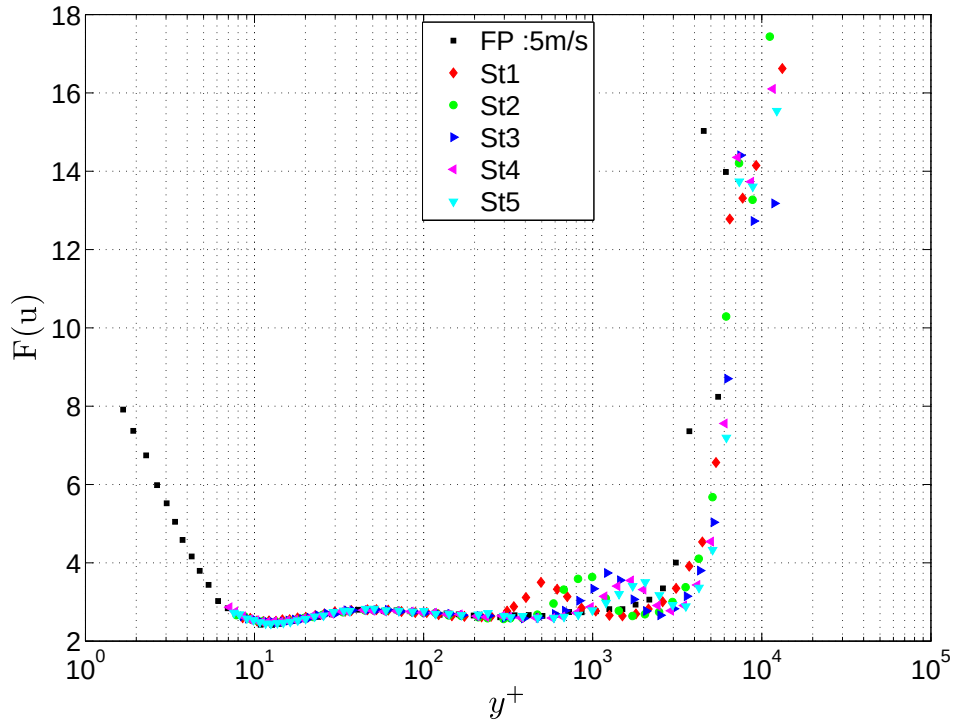

b)

Figure 3.16: a) Fourth order moment profiles for the five stations in wall units, b) flatness profiles for the five stations in wall units, $\alpha = -2°$, $\beta = -22°$ and $U_\infty = 10$ m/s.

6.2 Validation of the PIV measurements

6.2.1 Mean velocity at hot-wire station 5

Figure 3.17 shows the mean streamwise velocity profile in wall units at $s = 3382$ mm, corresponding to station 5 of hot-wire measurements. As for the corresponding hot-wire profile, u_τ was determined by fitting a standard log-law, with $\kappa = 0.41$ and $C = 5.0$. The hot-wire profile at station 5 and the FP one at 5 m/s are also added for comparison. The agreement is fairly good, except for the first 2 points near the wall where differences less than 9% are observed (an error bar of 9% is represented for these points). This is attributed to the PIV uncertainty in the near wall region which can reach ±15% (see Chapter 2). Small differences can also be evidenced in the wake region above $y^+ = 2000$, which remain in the PIV uncertainty of ±1%. A higher difference appears for the last hot-wire point, maybe due to the cumulation of the errors of the hot-wire (which can reach ±3% for this point as seen in Section 5.1.3.3.1 in Chapter 2) and of the PIV (±1%).

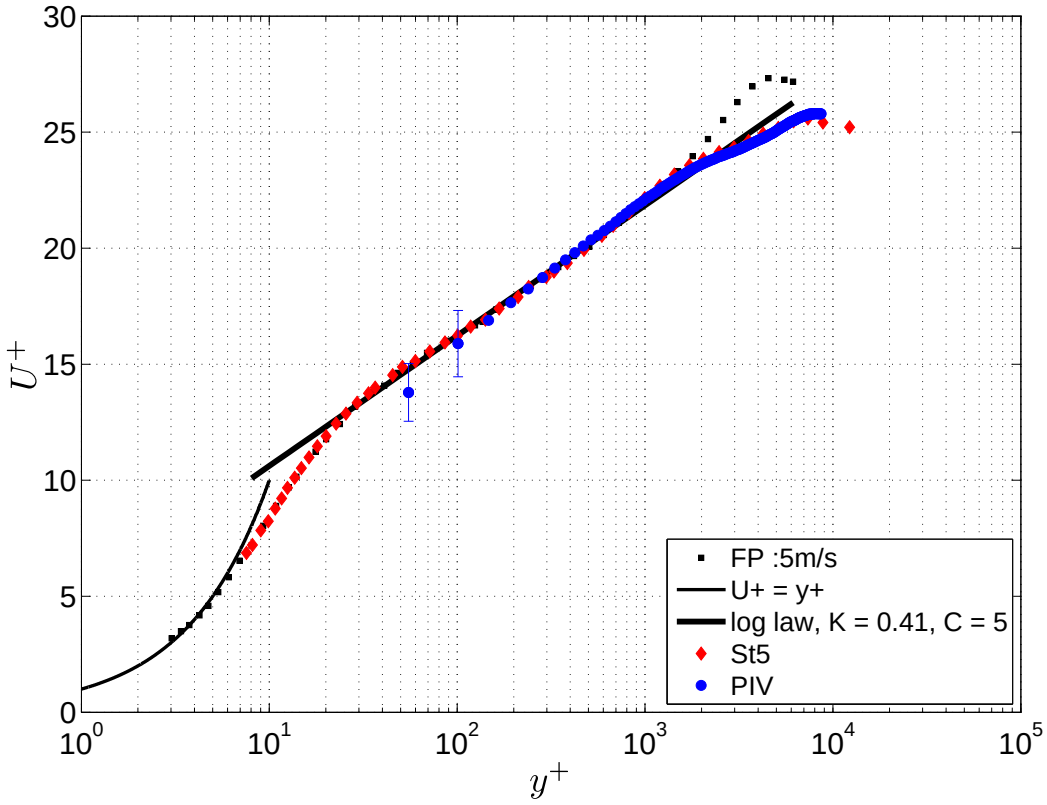

Figure 3.17: Mean streamwise velocity PIV profile in wall units at station 5 of hot-wire measurements compared to the hot-wire and FP profiles.

The u_τ obtained by the fit is 0.48 m/s, which results in less than 3.5% difference compared to the value obtained from hot-wire measurements ($u_{\tau_0} = 0.465$ m/s). This remains in the uncertainty interval on u_τ obtained by a Clauser's chart method. The boundary layer thickness obtained is 21.1 cm, which is also higher than the value

obtained from hot-wire ($\delta_0 = 19$ cm), but remains also in the uncertainty interval ($\pm 10\%$). The displacement thickness obtained is $\delta^* = 18.5$ mm and the momentum thickness is $\theta = 14.8$ mm, which results in about 10% difference compared to the hot-wire values. This is higher than the estimated uncertainties on these two values. Maybe the uncertainties on the hot-wire values were slightly underestimated or the repeatability of the experiment is not perfect as the ramp was dismounted and mounted again between the hot-wire and PIV tests. The shape factor is $H = 1.25$, which is coherent with the value obtained from hot-wire (less than 3.5% difference).

Figure 3.18 shows the mean wall-normal velocity profile in wall units at hot-wire station 5. This velocity remains quite small as the flow tends to follow the wall. Near the wall, positive values are observed which is coherent with the wall blockage. The negative part of the profile is probably upstream influence of the converging part of the ramp. This wall-normal velocity is minimum near $y+ = 700$ and reaches very small value at the end of the profile which indicates a flow nearly parallel to the surface.

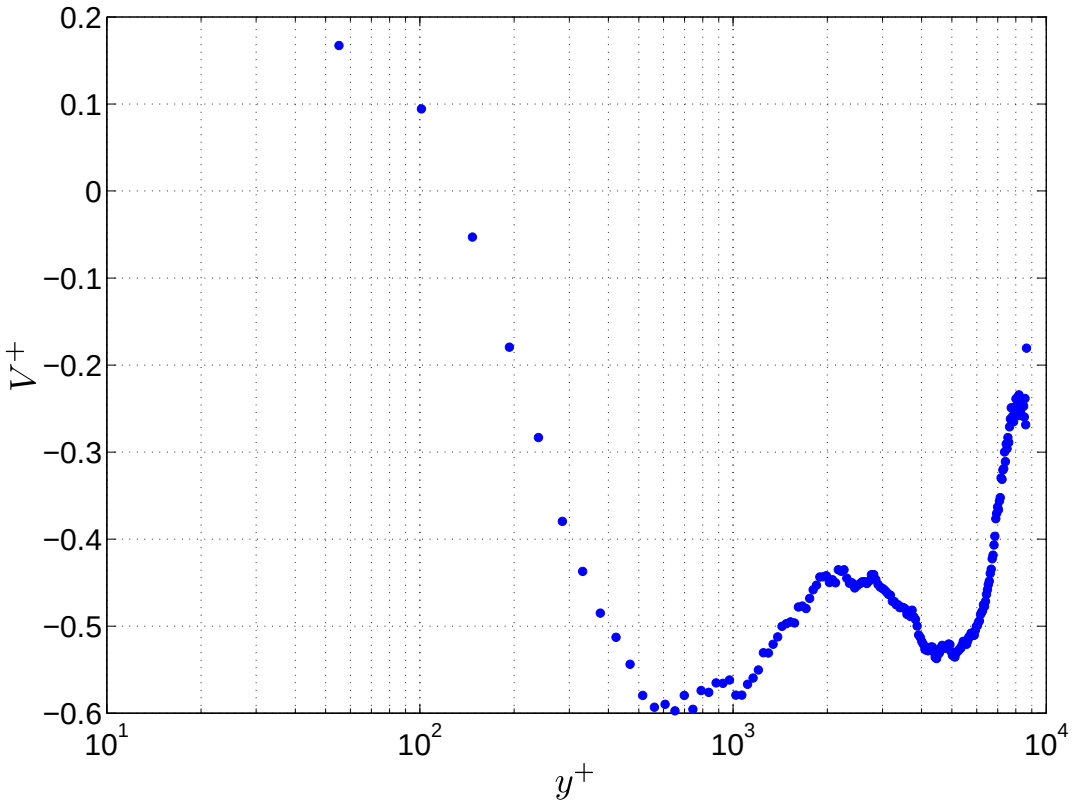

Figure 3.18: Mean wall normal velocity PIV profile in wall units at station 5 of hot-wire measurements.

6.2.2 Turbulence intensity at hot-wire station 5

Figure 3.19 shows the streamwise turbulence intensity ($u = \sqrt{\overline{u'^2}}$), the wall normal turbulence intensity ($v = \sqrt{\overline{v'^2}}$) and the Reynolds shear stress profiles ($-uv = -\overline{u'v'}$)

in wall units at hot-wire station 5. For comparison, the corresponding hot-wire and FP data at 5 m/s are also plotted. For the streamwise component, the agreement with the hot-wire is poor, but coherent with the PIV uncertainty determined in Chapter 2 (about $\pm 10\%$ of the local value and about $\pm 30\%$ near the top of the field and in the very near wall region). An error bar of $\pm 25\%$ is represented for the first two points. The knee point near $y^+ \simeq 4000$ is however captured.

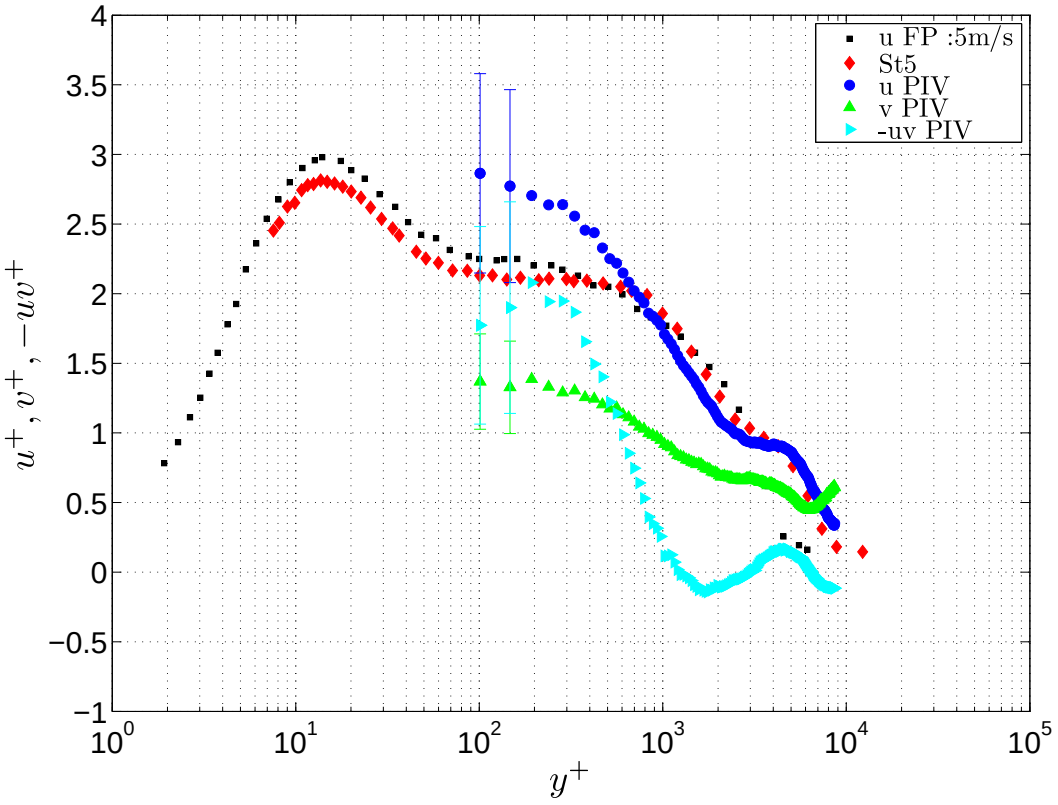

Figure 3.19: Turbulence intensities and Reynolds shear stress PIV profiles in wall units at hot-wire station 5 compared to hot-wire measurements and FP.

Concerning the wall normal component, there is a plateau between $y^+ = 100$ and 400. Its value is about 1.4 wall units. Fernholz and Finley (1996) have concatenated several experimental data from different authors for this quantities and have noticed also a kind of plateau in this region. Its value was found between 0.9 and 1.2 which suggests an overestimation on $\sqrt{\overline{v'^2}}$ here, especially in the near wall region. However, the differences seem to stay in the uncertainty interval (less than $\pm 15\%$ in the middle field region and less than $\pm 35\%$ near the wall and in the top field. The error bar represented for the first two points is set at $\pm 25\%$).

The Reynolds shear stress seems also to exhibit a kind of plateau between $y^+ = 100$ and 400 with a value close to 2 wall units. This seems largely over-estimated as Fernholz and Finley (1996) have noticed a value between 0.8 and 1 wall units in this region. This is attributed to a larger uncertainty on this quantity (for the first two points, the error bar is set at $\pm 40\%$). After $y^+ = 1000$, this component

oscillates which is unrealistic. It can be concluded that in this oscillating region, the Reynolds shear stress can not be measured as its value is below the uncertainty of the measurements.

6.3 Mean velocity above the flap

6.3.1 Mean velocity field in wind tunnel reference frame

Figure 3.20 shows the vectors plot of the mean velocity field in the separated region above the flap (for clarity, only 1 vector every 7 in each direction is represented). Figures 3.21 and 3.22 give respectively the U_{wt} and V_{wt} components in the wind tunnel floor reference frame. In the outer part, upstream the flap articulation (at $X = 3.47$ m), the flow is almost parallel to the surface. At the articulation, negative V_{wt} appear due to the sudden change in wall direction. At the end of the field of view, where the ramp surface reaches the wind tunnel floor, these negative velocities decrease but persist. Concerning the streamwise component U_{wt}, it decreases slightly with the streamwise position X due to the section enlargement.

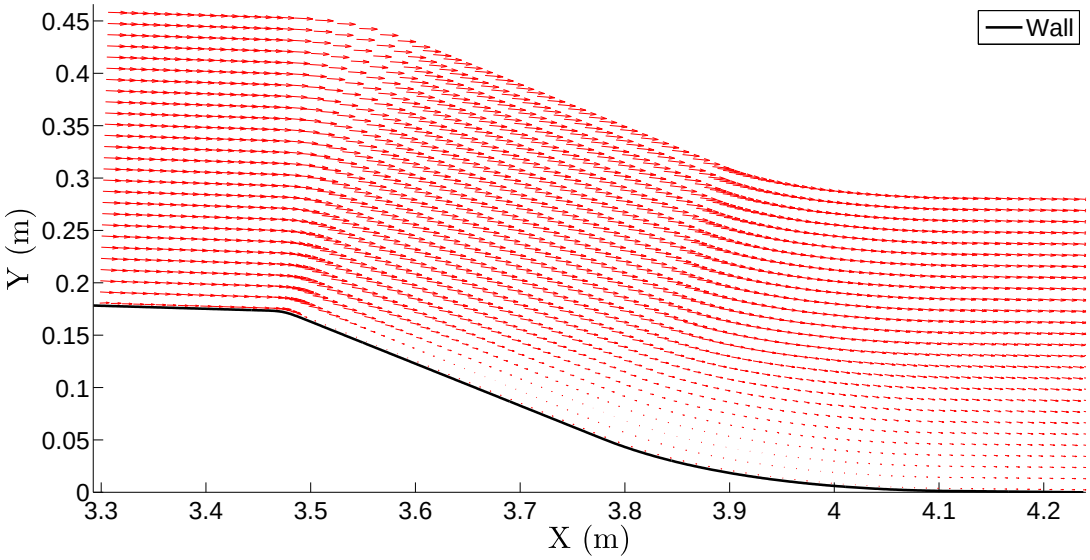

Figure 3.20: Vectors representation of the mean PIV velocity field on the flap.

Near the wall, before the articulation (at $X = 3.47$ m), when approaching it, higher velocities are observed. This is coherent with the decrease of the boundary layer thickness (δ) observed with hot-wire anemometry in this region. This decrease of δ is due to the strong favourable pressure gradient just upstream of the flap articulation as seen in Section 3.5. On the flap, a small region of negative streamwise velocities is exhibited which corresponds to the separation. The shear layer is clearly visible and extends rapidly in the wall-normal direction with the streamwise position X. At the end of the field of view, the size of this shear layer is of the order of the flap height (H_{step}).

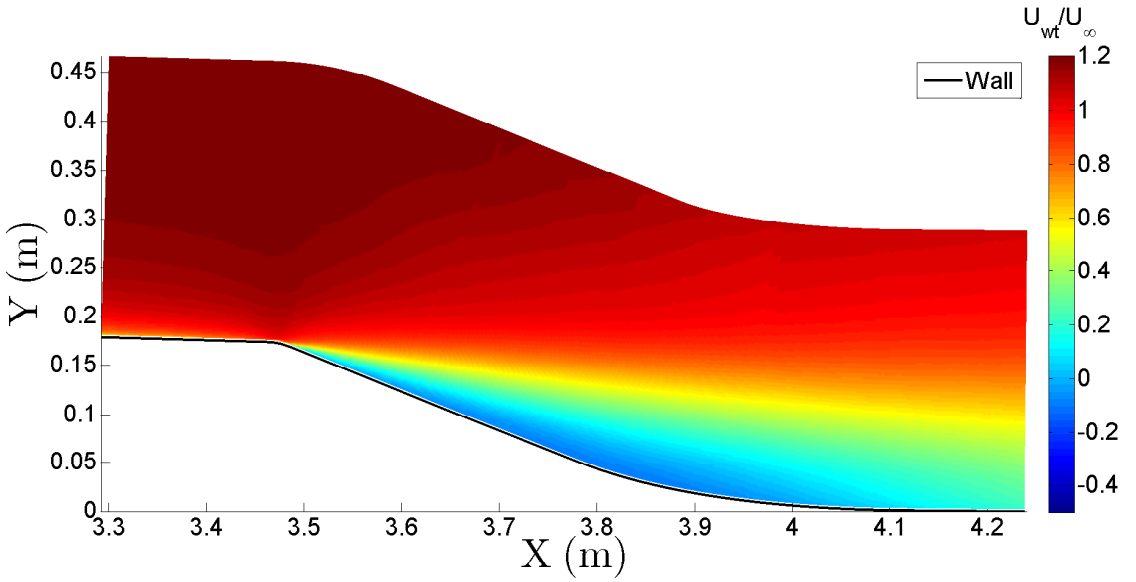

Figure 3.21: Mean streamwise PIV velocity field on the flap in the wind tunnel reference frame.

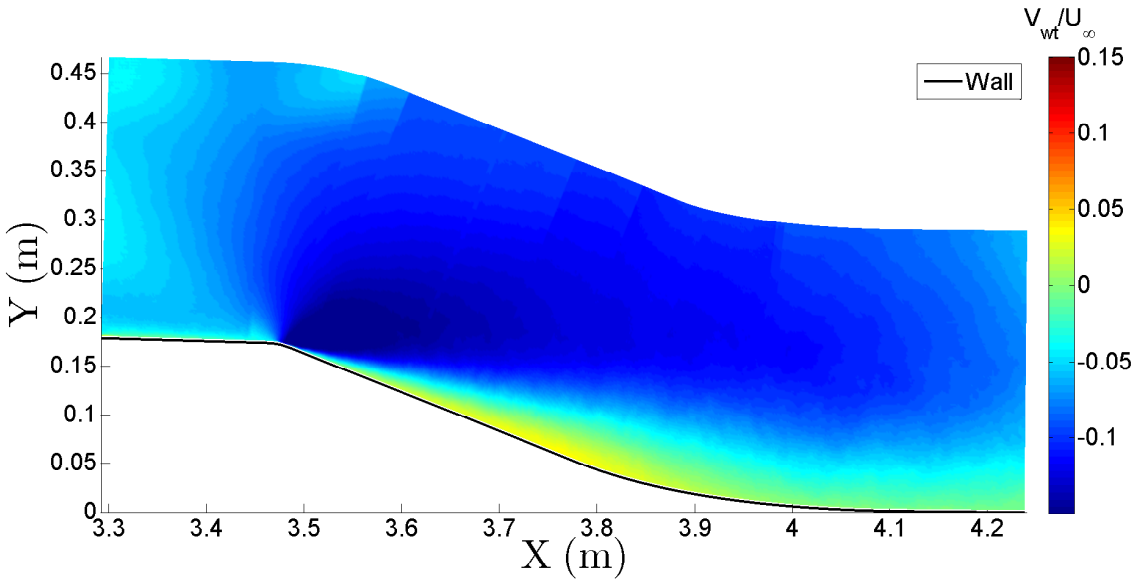

Figure 3.22: Mean wall normal PIV velocity field on the flap in the wind tunnel reference frame.

Looking now at V_{wt} near the wall, a region of strong negatives values is observed just above and after the articulation. This region extends slightly upstream of the wall corner in the outer part. In the separated region, positive values are observed close to the wall, corresponding to the backflow inside the separated bubble. In the shear layer, V_{wt} is nearly zero. This is also true in the rear part of the field of view in the near wall region (indicating that here, the flow is parallel to the wind tunnel wall).

6.3.2 Detection of the separation line

In order to obtain a better assessment of the near wall flow behaviour, the velocities will now be represented in the local reference frame attached to the wall. U will be now on the velocity parallel to the wall and V the velocity normal to it. This change in reference frame allows to detect the separation line. It was determined here using the two criteria defined by Simpson (1989) : $U = 0$ and $\chi = 50\%$ (with χ the backflow coefficient seen in Chapter 1). The result of these two criteria is given in Figure 3.23 which shows the mean streamwise velocity field (U) normalized by the reference velocity $U_\infty = 10\ m/s$).

For the first criterion, for each grid line normal to the wall, the point $U = 0$ was detected by scanning the line from the top of the field down to the wall, to find the first point where U is negative. Then $U = 0$ was obtained by linear interpolation between this point and the previous one. The separation point position (represented on the left of Figure 3.23 by a dot of the same color as the separation border) was defined as the first position from the left of Figure 3.23 where the separation border was different from the wall. Similarly, the reattachment point position was defined as the first position from the right of Figure 3.23 where the separation border was different from the wall.

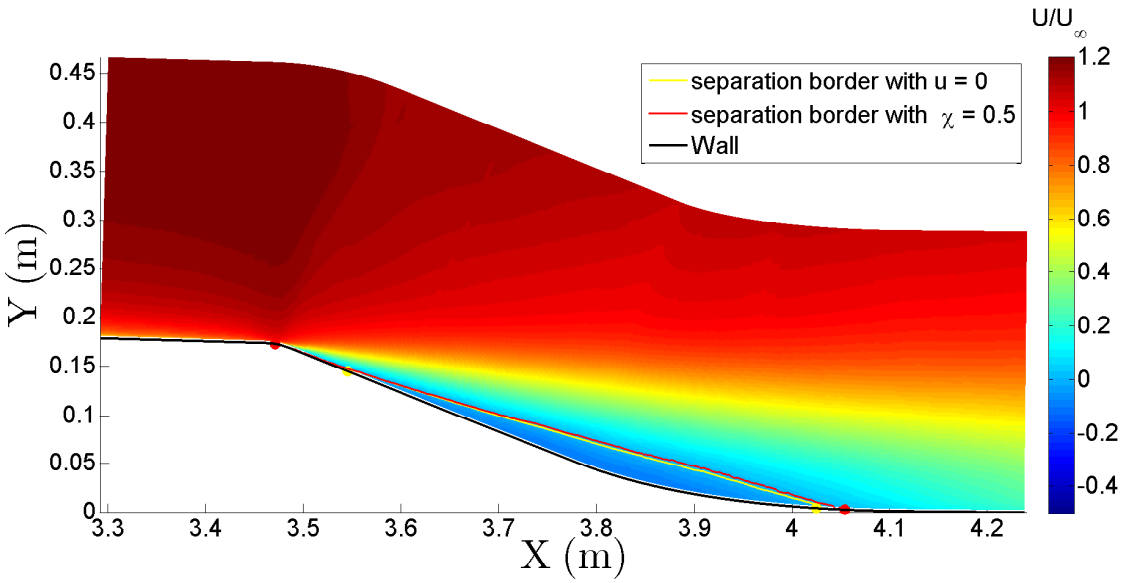

Figure 3.23: Mean streamwise PIV velocity field (U) on the flap.

For the second criterion ($\chi = 50\%$), the algorithm to detect the point $\chi = 50\%$ on each wall normal grid line was similar to the one for $U = 0$. However, according to Dengel and Fernholz (1990) and Lögdberg et al. (2010), when the first two points near the wall of a grid line have a coefficient χ lower than 50% but higher than 30%, a linear regression was performed, on all the points near the wall having a χ greater than 30%, to determine the backflow coefficient at the wall (χ_w). This gives a better resolution on the separation border and on the separation and reattachment points position than with the first separation criteria. The separation and reattachment points position correspond then respectively to the first point on the left and the first point on the right of Figure 3.23 where χ_w is greater than or equal to 50%.

6.3.3 Mean velocity fields

Figure 3.23 shows the mean streamwise velocity distribution normalized by $U_\infty = 10\ m/s$, in the local reference frame. Apart from a shear layer slightly closer to the wall in the recirculation region, this velocity distribution is very similar to the one in the wind tunnel reference frame given in Figure 3.21.

In Figure 3.23, the two criteria used to detect the separation border give fairly similar results. However, the criterion $U = 0$ gives a separation border slightly closer to the wall. The maximum difference in wall-normal direction is 4.6 mm corresponding to 3 times the PIV mesh size in this direction or to 2.6% of the step height H_{step}. This difference is due to the asymmetry of the probability density function (PDF) of u' in the shear layer.

Not surprising, the separation point is found more upstream by $\chi = 50\%$ than by $U = 0$. The same for the reattachment point which is more downstream. With $\chi = 50\%$, the separation point is located at $s = 3502$ mm compared to $s = 3500$ mm for the flap articulation (this corresponds to a distance of three PIV grid points along the wall in this region). This position of the separation point is in close agreement with the visualisation results of Sections 2 and 3. The characteristics of the separation given by $\chi = 50\%$ can thus be considered as the best estimation. The shape factor at the separation point is 1.3, which is largely below the classical value given by Dengel and Fernholz (1990) (about 2.85, see Chapter 1) and close to the ZPG value. For an imposed separation, as it is the case here, the shape factor is not a separation indicator.

The reattachment point position is at $X = 4.02$ m for $U = 0$ criterion. For $\chi = 50\%$, it is at $X = 4.05$ m. This leads to an attached flow development region downstream of the separation of about 18.5 cm (or about one δ_0, with δ_0 the boundary layer thickness obtained at hot-wire station 5) in the PIV field of view. The beginning of the boundary layer recovery can be characterized in this region.

With $U = 0$, the separation length was found to be 50 cm and the maximum height 2.7 cm. With $\chi = 50\%$, the separation length is about 61 cm and the maximum height close to 3 cm. These last values are retained hereafter. These separation lengths are smaller than the value obtained by wool-tufts visualisations (80 cm, see Section 2). The difference can however be attributed to the difficulty of detecting precisely the mean reattachment point with wool-tufts as the instantaneous reattachment point fluctuate.

As the separation height is small compared to the upstream boundary layer thickness δ_0 at hot-wire station 5 ($\frac{H_{sep}}{\delta_0} = 0.16$), if the field of view was large enough, it would be possible to define a local boundary layer thickness in the separation region with the standard definition (i.e. the distance from the wall where 99% of the free-stream velocity is reached). Here, on the flap, the streamwise velocity is still slightly increasing at the upper border of the field. Then, δ can be estimated only in the upstream part of the field of view. Nevertheless, to have an indication, the displacement and momentum thicknesses were computed as they should not be influenced too much by this field limitation. The maximum height of the separation compared to the local displacement thickness is then $\frac{H_{sep_{max}}}{\delta^*} = 0.30$ and to the momentum thickness $\frac{H_{sep_{max}}}{\theta} = 1.14$. The height of the separation is then small compared to the step height ($\frac{H_{sep}}{H_{step}} = 0.17$) but comparable to the integral thicknesses.

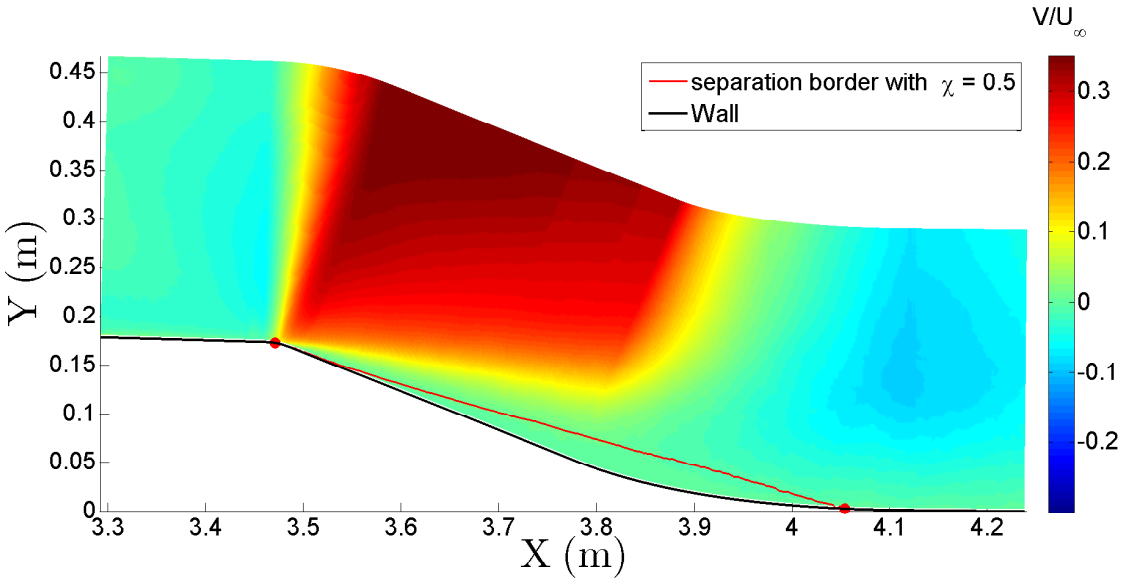

Figure 3.24: Mean wall-normal velocity field (V) on the flap at mid-span of the ramp.

Figure 3.24 shows the mean wall-normal velocity distribution (V) normalized by $U_\infty = 10\ m/s$, in the local reference frame. Upstream of the flap articulation, this velocity component is small which confirms that the flow follows the wall. When approaching the turning point, in agreement with the observations done on the streamwise velocity, positive velocities are observed as the flow cannot follow the sudden change in wall direction. In the separation region, the small wall-normal velocities region close to the wall increases in size with the streamwise position X. This means that rapidly, near the wall, the flow direction adapts itself to the wall surface and forces progressively the region above it to take the same direction. After $X = 4$ m, in agreement with Figure 3.22, small negative wall-normal velocities persist which means that the flow needs a distance longer than the field of view to eliminate the perturbation introduced at the flap articulation and to re-adapt itself to the wind tunnel floor.

6.3.4 Mean velocity profiles

In order to look in more details at the separation, Figure 3.25 shows six mean streamwise velocity profiles in the separation region and in the recovery region. The velocity is scaled by $U_\infty = 10$ m/s and the wall-normal coordinate by the step height $H_{step} = 17.5$ cm (see Figure 2.2 for the definition of H_{step}). The selected profiles correspond to $s = 3502$ mm the separation point, $s = 3624$ mm the first quarter of the detached region, $s = 3793$ mm the middle of the separation bubble, $s = 3949$ mm the three-quarters of the separation, $s = 4113$ mm the reattachment point and $s = 4297$ mm the end of the field of view.

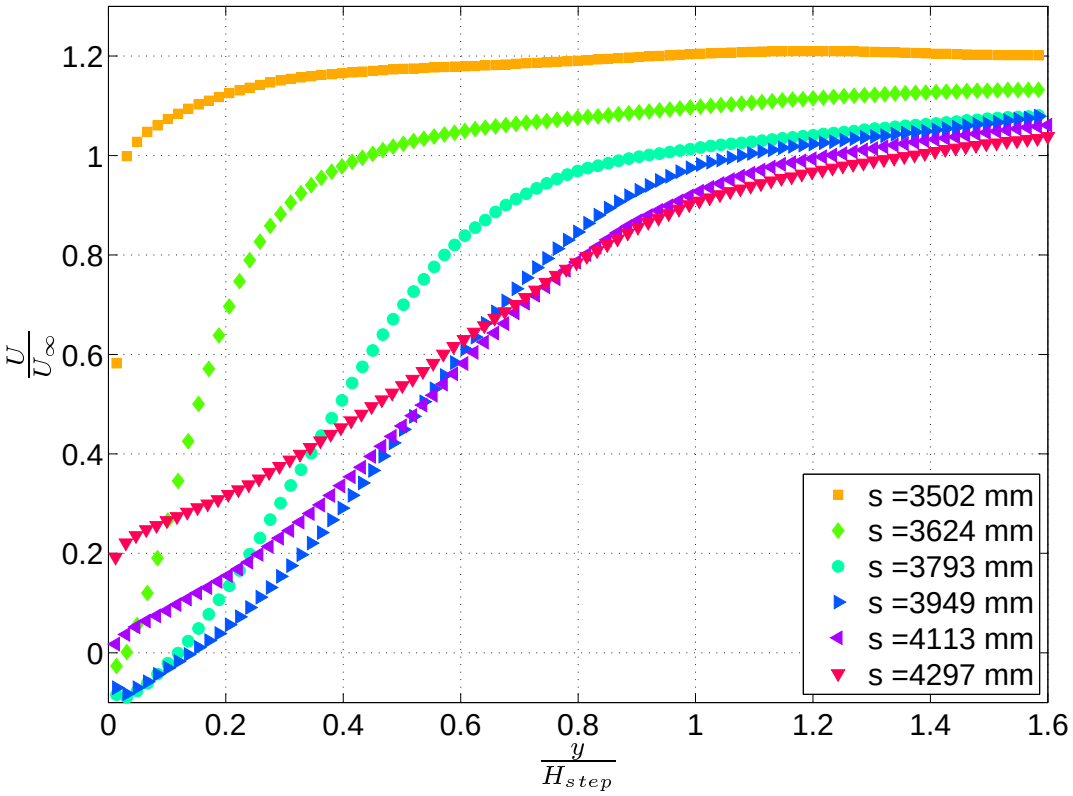

Figure 3.25: Six mean streamwise velocity profiles on the flap.

The separation is visible on the profiles at $s = 3624$, 3793 and 3949 mm with a negative velocities region near the wall. This region develops in the wall-normal direction with s to reach $\frac{y}{H_{step}} \simeq 0.14$ at $s = 3949$ mm. In the separation region, after $s = 3793$, a negative peak of $-0.085U_\infty$ appears very close to the wall at $\frac{y}{H_{step}} \simeq 0.03$. As the criterion $\chi = 50\%$ is used here, the profile at the reattachment point ($s = 4113$ mm) does not show a $\frac{\partial U}{\partial y} = 0$ at the wall. This point is found more upstream at $s = 4082$ mm.

After $s = 3502$ mm, all the profiles show an important velocity deficit region below $\frac{y}{H_{step}} = 1$ due to the shear layer. This deficit increases in the detached flow region with s due to the development of the separation. The profiles at the reattachment point ($s = 4113$ mm) and at the end of the field of view ($s = 4297$

mm) begin to fill again near the wall which creates an inflexion point on the profiles near $\frac{y}{H_{step}} = 0.2$. Not surprising, in the external region, the velocity continuously decreases with s due to the section enlargement.

6.4 Turbulence intensity

6.4.1 Turbulence intensity fields

Following the presentation of the mean velocity fields in the previous section, the turbulence quantities will be given here in the local reference frame to better assess the near wall behaviour. As this representation is not conventional to Navier-Stokes solvers, a global reference frame representation is given in Appendix D.

6.4.1.1 Streamwise turbulence intensity

Figure 3.26 shows the streamwise turbulence intensity distribution $u = \sqrt{\overline{u'^2}}$ on the flap normalized by $U_\infty = 10\ m/s$. Very high turbulent levels are observed originating at the separation point. This region develops downstream above the separation bubble border and is generated by the shear due to separation. This peak of turbulence intensity in the external region is commonly observed in adverse pressure gradient and separated flows (Simpson (1989), Webster et al. (1996), Wu and Squires (1998), etc.). The level of the peak is more than 2 times the level of the near wall region peak upstream of the separation. The level of $u = \sqrt{\overline{u'^2}}$ in the separation bubble is largely below the peak level, which is coherent with the observations of Simpson (1989) who shows that there is little turbulence production in the separated region.

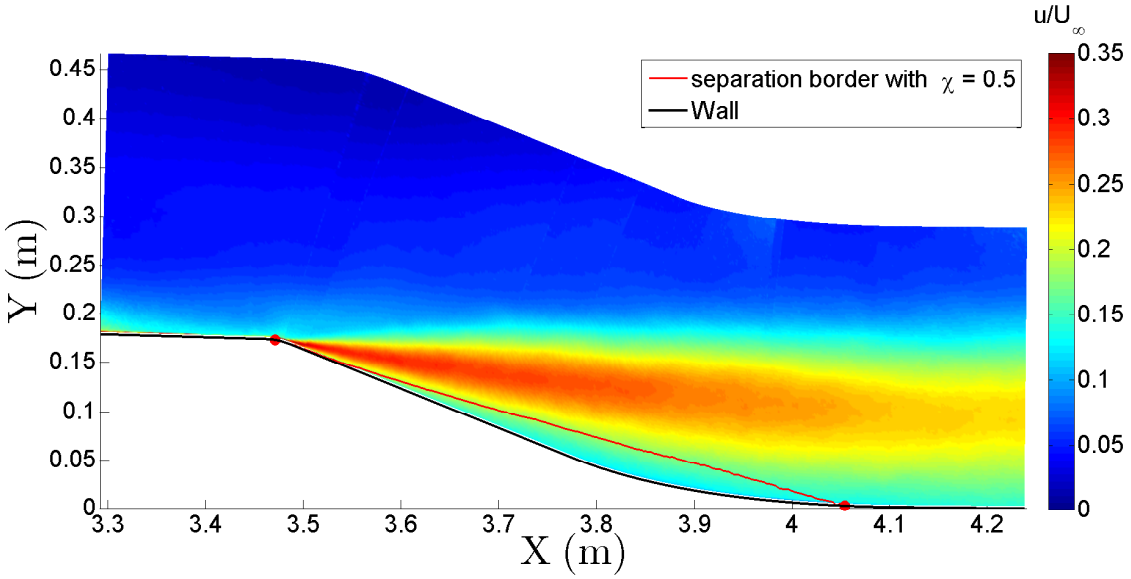

Figure 3.26: Turbulence intensity field ($u = \sqrt{\overline{u'^2}}$) on the flap at mid-span of the ramp.

When looking at the instantaneous u-fluctuations, large coherent structures characterized by strong values of u' (both positive and negative which can be above 25% of the maximum velocity) are observed in the region of high turbulence intensity. These structures can reach more than $3\delta_0$ in length and $0.5\delta_0$ in width, with δ_0 the upstream boundary layer thickness at $s = 3382$ mm (or $X = 3353$ mm). Their origin is at the flap articulation where the separation starts. An instantaneous snapshot of u' is given in Figure 3.27 as an example (u' is normalized by $U_\infty = 10\ m/s$).

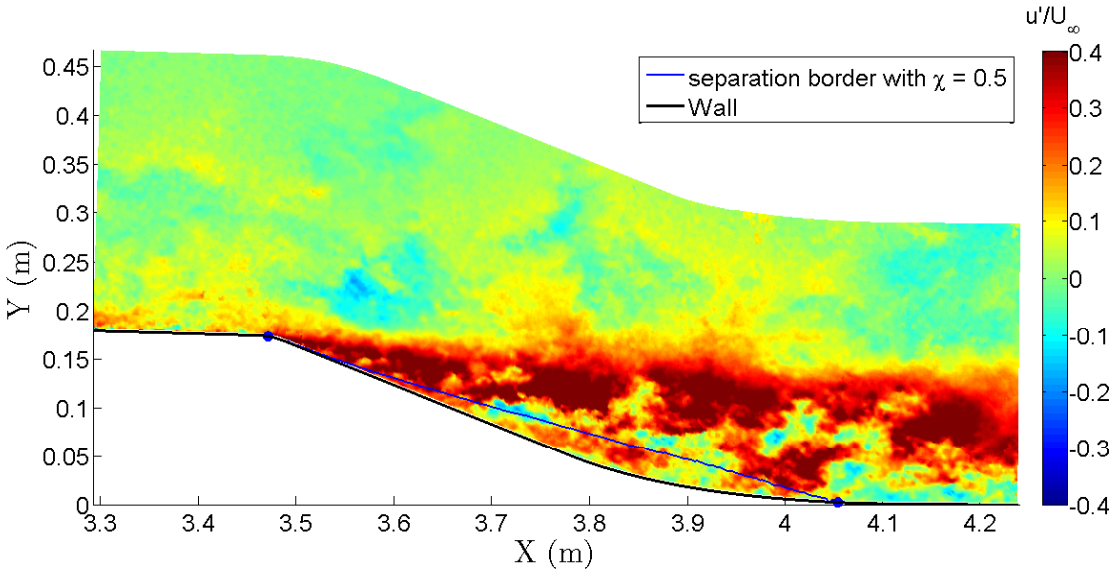

Figure 3.27: Instantaneous streamwise fluctuation field (u') on the flap at mid-span of the ramp.

Figure 3.28 shows the correlation coefficient R_{uu} (equation (3.1)) on the flap for a fixed point near the middle of the separation ($X \simeq 3.74$ m and $Y \simeq 0.09$ m). A large region of positive correlation ($R_{uu} > 0.2$) is observed. This region begins at the flap articulation and extends beyond the end of the PIV fields. It is coherent with the structures characterized by strong values of u' which can be observed in Figure 3.27.

$$R_{uu} = \frac{\overline{u'(X_0, Y_0).u'(X_0 + \Delta X, Y_0 + \Delta Y)}}{\sqrt{\overline{u'^2(X_0, Y_0)}}.\sqrt{\overline{u'^2(X_0 + \Delta X, Y_0 + \Delta Y)}}} \tag{3.1}$$

Figures 3.29 and 3.30 show respectively the distribution of $-\overline{u'v'}\frac{\partial U}{\partial y}$ and $-\overline{u'^2}\frac{\partial U}{\partial x}$ normalized by U_∞^3/H_{step}. These terms correspond to the accessible production terms of half the streamwise Reynolds stress ($\frac{1}{2}\overline{u'^2}$) (due to the more or less 2D nature of the flow under study, the other production terms can be neglected. See Appendix C equation (C.1) for the detailed Reynolds stresses transport equations). These quantities are also present in the production terms of the turbulent kinetic energy equation (see equation (C.4)).

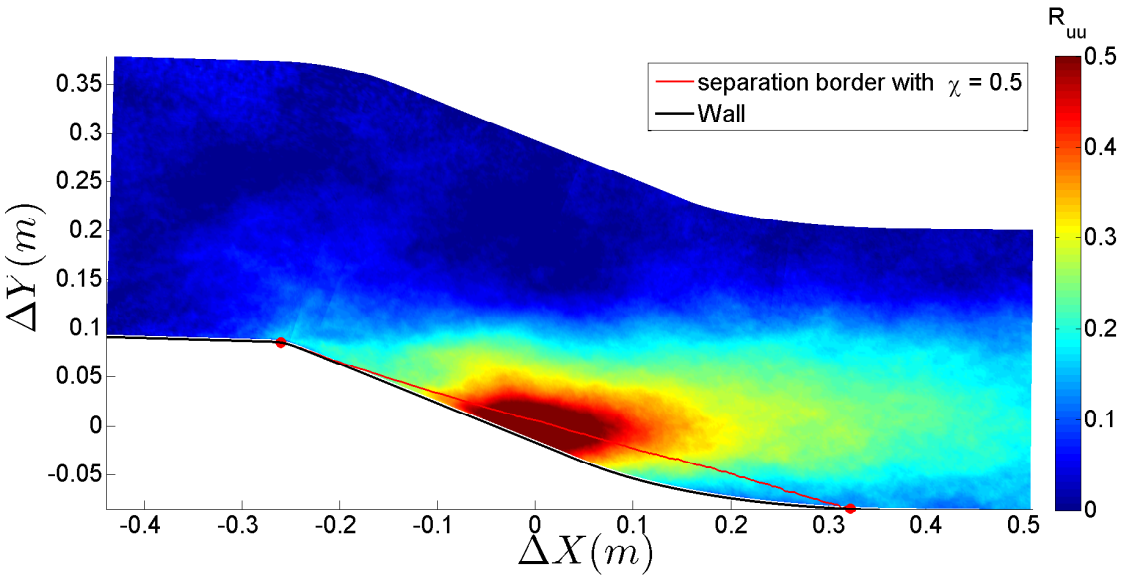

Figure 3.28: Correlation coefficient R_{uu} on the flap at mid-span of the ramp for a fixed point near the middle of the separation.

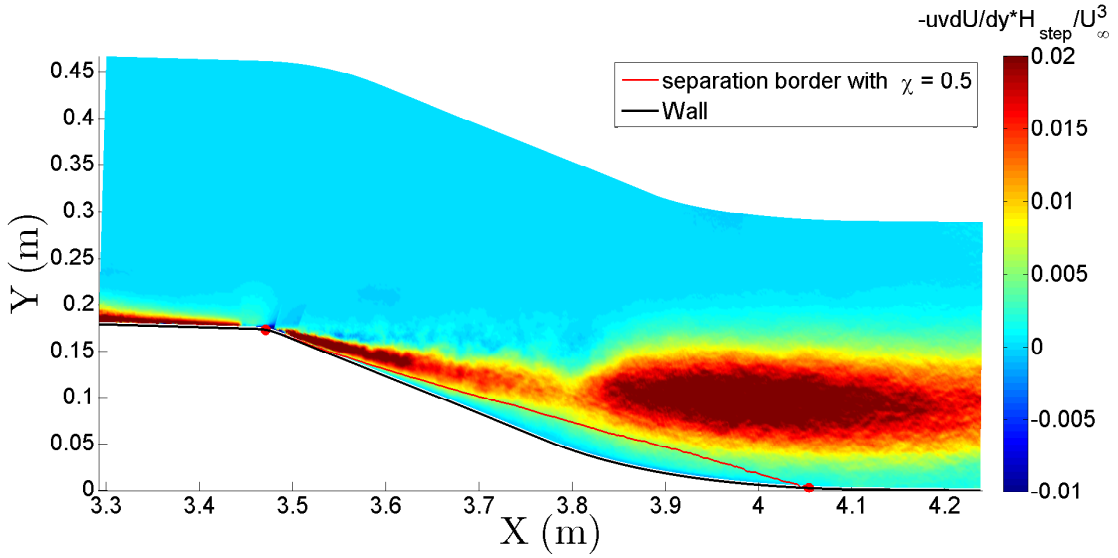

Figure 3.29: Production term $-\overline{u'v'}\frac{\partial U}{\partial y}$ of $\frac{1}{2}\overline{u'^2}$ on the flap at mid-span of the ramp.

Concerning $-\overline{u'v'}\frac{\partial U}{\partial y}$ (Figure 3.29), upstream the flap, very close to the wall, high production levels are observed which correspond to the classical near wall turbulence production peak. However, the extends in wall-normal direction is largely higher than usual probably due to PIV uncertainty in the near wall region (the peak is usually at $y^+ \simeq 10$ (DeGraaff and Eaton (2000)), and the first measurement point here is at $y^+ \simeq 70$). In this region, the term $-\overline{u'^2}\frac{\partial U}{\partial x}$ (Figure 3.30) is negligible compared to the production term in Figure 3.29, which agrees with the standard approximations of 2D boundary layers.

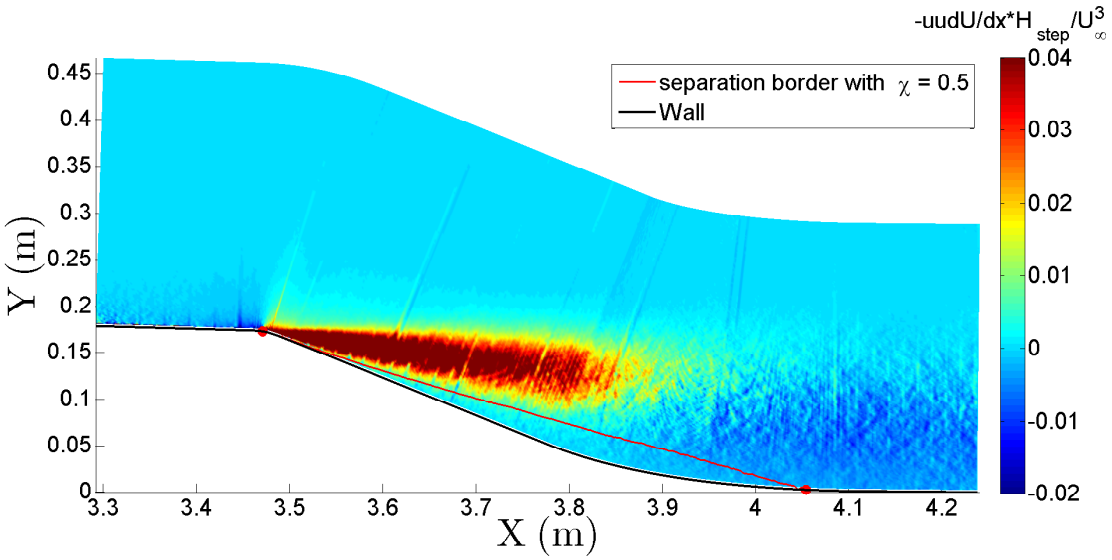

Figure 3.30: Production term $-\overline{u'^2}\frac{\partial U}{\partial x}$ of $\frac{1}{2}\overline{u'^2}$ on the flap at mid-span of the ramp.

On the flap, in agreement with Simpson (1989), there is a strong streamwise Reynolds stress production region located above the separation border. However, it is dispatched into two distinct regions above the bubble : one in the first half of the separation and an other which starts near the middle of the separation and extends beyond the end of the PIV fields. The first region is characterized by high values of both production terms. However, these peak regions are not at the same wall-normal distance. For $-\overline{u'v'}\frac{\partial U}{\partial y}$ it is less intense and closer to the wall. As a good superposition is observed in this region between the production term $(-\overline{u'^2}\frac{\partial U}{\partial x})$ and $\sqrt{\overline{u'^2}}$ (Figure 3.26), it can be concluded that, along the first part of the flap, the streamwise turbulent intensity production is principally governed by $-\overline{u'^2}\frac{\partial U}{\partial x}$, which is itself cause by the strong deceleration generated by the sudden change in slope of the wall.

The downstream part of the separation is dominated by $-\overline{u'v'}\frac{\partial U}{\partial y}$ as for a 2D ZPG boundary layer. It can be due to the flapping motion of the large scale structures observed on instantaneous fields, which creates high levels of $\overline{u'v'}$. This region is probably linked to the change in wall direction near $X = 3.8$ m. Nevertheless, the second production region is highly linked to the separation as downstream of it, the production intensity decreases. In the downstream part of the flap, $-\overline{u'^2}\frac{\partial U}{\partial x}$ becomes

slightly negative due to the flow acceleration, as for a favourable pressure gradient boundary layer.

6.4.1.2 Wall-normal turbulence intensity

Figure 3.31 shows the wall-normal turbulence intensity distribution $v = \sqrt{\overline{v'^2}}$ on the flap normalized by $U_\infty = 10\ m/s$. As for the streamwise component, high levels are observed in the external region above the separation bubble border. The origin is also at the separation point but the maximum is much more downstream than for the streamwise component and the peak is also wider in wall normal direction. Probably linked to the change in wall direction, after $X = 3.8$ m, the high level region is more intense and wider. The results are coherent with those of Chehroudi and Simpson (1985) and Simpson (1989) who find structures of size δ_0 which entrain high values of v' in the separation region.

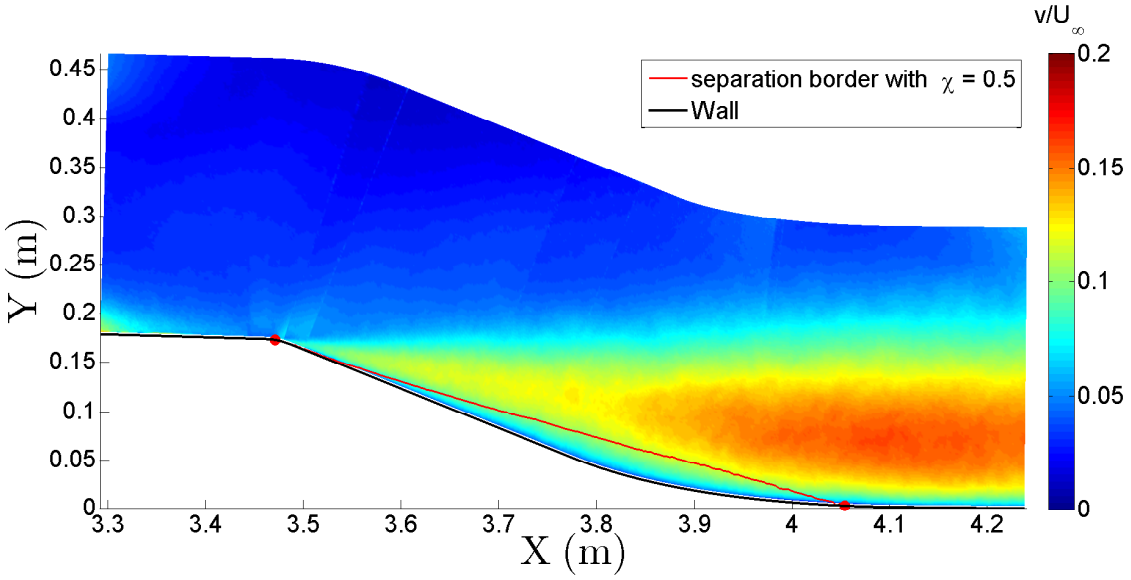

Figure 3.31: Wall normal turbulence intensity field ($v = \sqrt{\overline{v'^2}}$) on the flap at mid-span of the ramp.

Figure 3.32 shows the correlation coefficient R_{vv} (definition similar to equation (3.1)) on the flap for a fixed point near the middle of the separation (the same as for R_{uu}). A region of positive correlations ($R_{vv} > 0.1$) is exhibited, which is much smaller in the streamwise direction than for R_{uu} but extends comparatively far in wall normal direction. It size is about $0.5\delta_0$ which is two times less than the size of the structures observed by Chehroudi and Simpson (1985) and Simpson (1989). Far from the fixed point, a lack of convergence is observed due to the small number of samples used.

The accessible production terms for the wall-normal Reynolds stress $\frac{1}{2}\overline{v'^2}$ are $-\overline{u'v'}\frac{\partial V}{\partial x}$ and $-\overline{v'^2}\frac{\partial V}{\partial y}$. The first one was found negligible compared to the production terms of the streamwise component (more than 40 times lower). The second one is

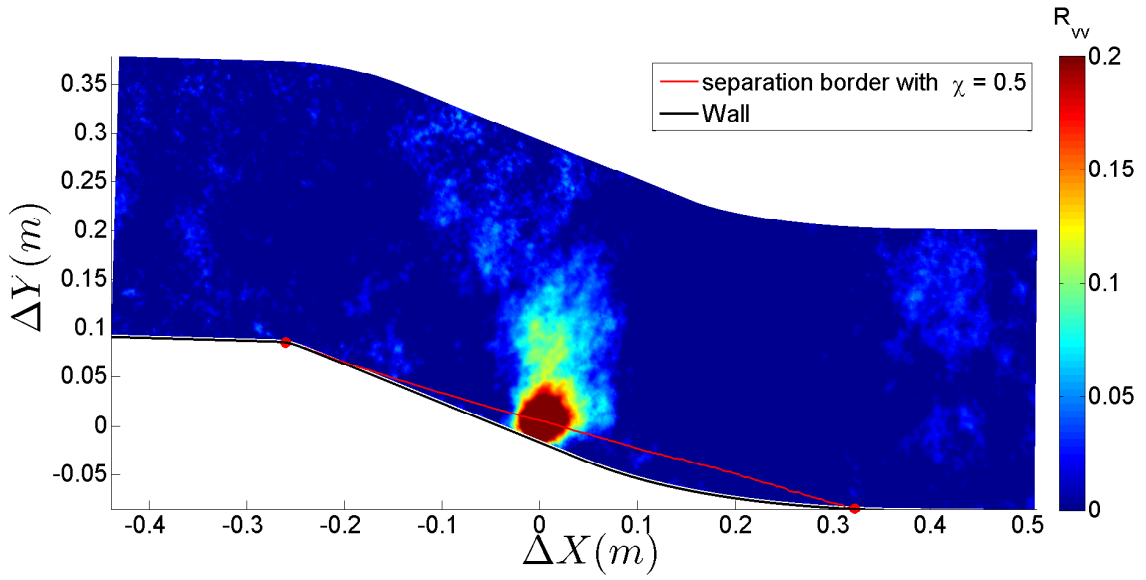

Figure 3.32: Correlation coefficient R_{vv} on the flap at mid-span of the ramp for a fixed point near the middle of the separation.

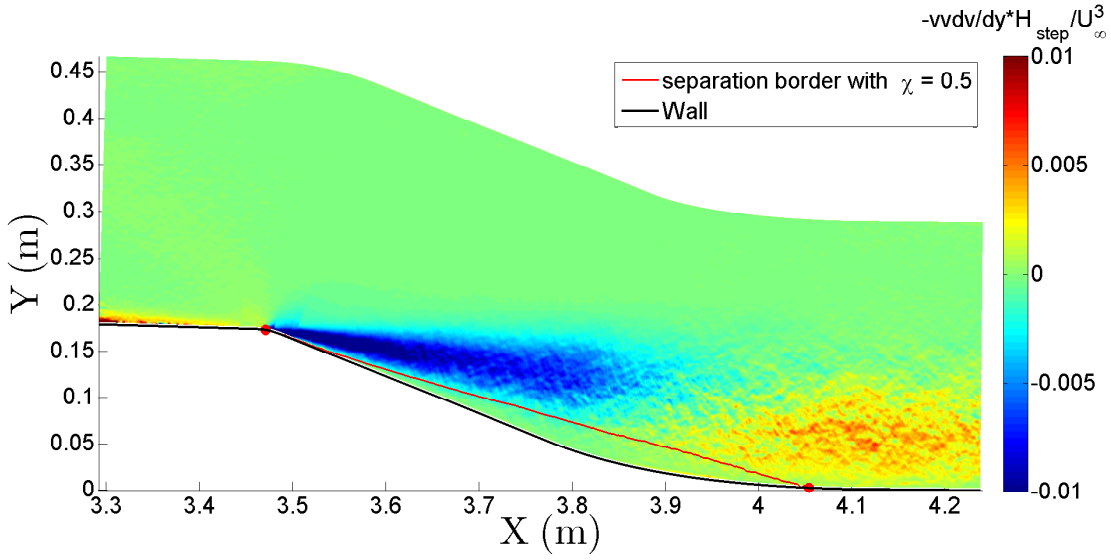

Figure 3.33: Production term $-\overline{v'^2}\frac{\partial V}{\partial y}$ of $\frac{1}{2}\overline{v'^2}$ on the flap at mid-span of the ramp.

given in Figure 3.33. It is about 10 times lower but similar to the opposite of $-\overline{u'^2}\frac{\partial U}{\partial x}$ as expected from the 2D continuity equation and from the fact that $\overline{v'^2}$ is about 10 times lower than $\overline{u'^2}$ in this region. Globally, negative or negligible production is found for $\overline{v'^2}$ compared to $\overline{u'^2}$ in the whole field. But, looking at Figure 3.31, the level of this Reynolds stress increases with X. The redistribution term is the only one able to contribute to this increase. This is confirmed by a significant return toward isotropy in the rear part of the field by comparing $\sqrt{\overline{u'^2}}$ and $\sqrt{\overline{v'^2}}$ in Figures 3.26 and 3.31. It should be noted that the peaks of these two stresses are not at the same wall-normal distance in this region.

As the production for the wall-normal component is negligible compared to the one of $\overline{u'^2}$, the turbulent kinetic energy production is then principally given by the production of the streamwise component.

6.4.1.3 Reynolds shear stress

Figure 3.34 shows the Reynolds shear stress distribution normalized by U_∞^2. The strong similarity between distributions of v and $-uv$ should be noted and also the fact that for both quantities, the peak develops in the rear part of the separation and downstream of it. This is coherent with Chehroudi and Simpson (1985) and Simpson (1989) as the structures of size δ_0 that they observed bring also with them high values of $-uv$ in the separation region.

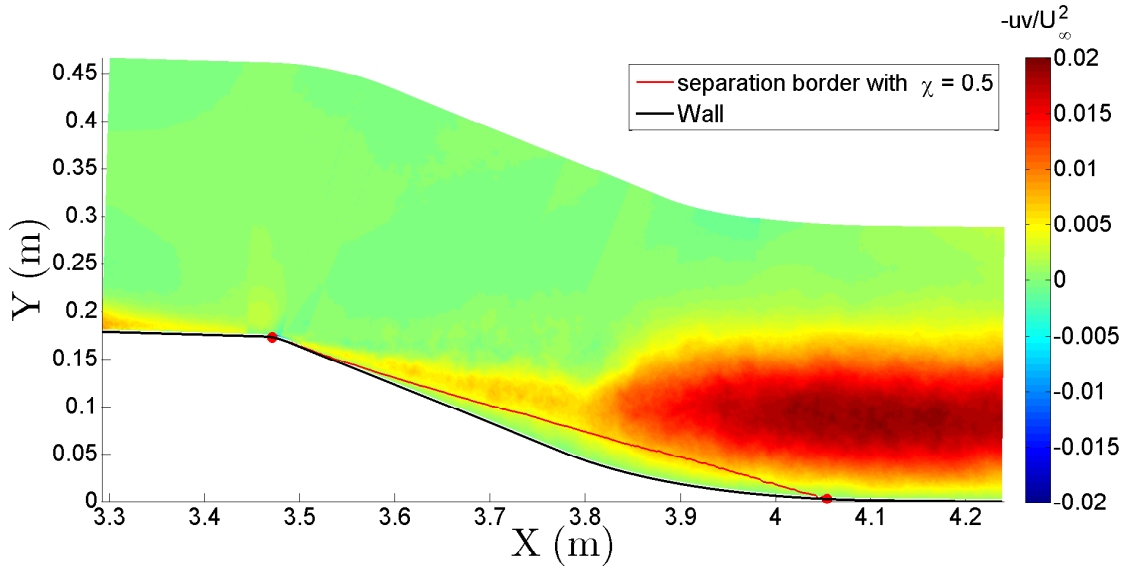

Figure 3.34: Reynolds shear stress field ($uv = \overline{u'v'}$) on the flap at mid-span of the ramp.

Concerning the four production terms of the Reynolds shear stress accessible with the PIV set-up used, it was found that $\overline{v'^2}\frac{\partial U}{\partial y}$ largely dominates the three others. This term is then given in Figure 3.35 normalised by U_∞^3/H_{step}. The strong similarity between distributions of v and $-uv$ can then be explained by this term with produces Reynolds shear stress from the wall-normal Reynolds stress. This

process is also found for boundary layers and it is also observed here upstream the of flap articulation.

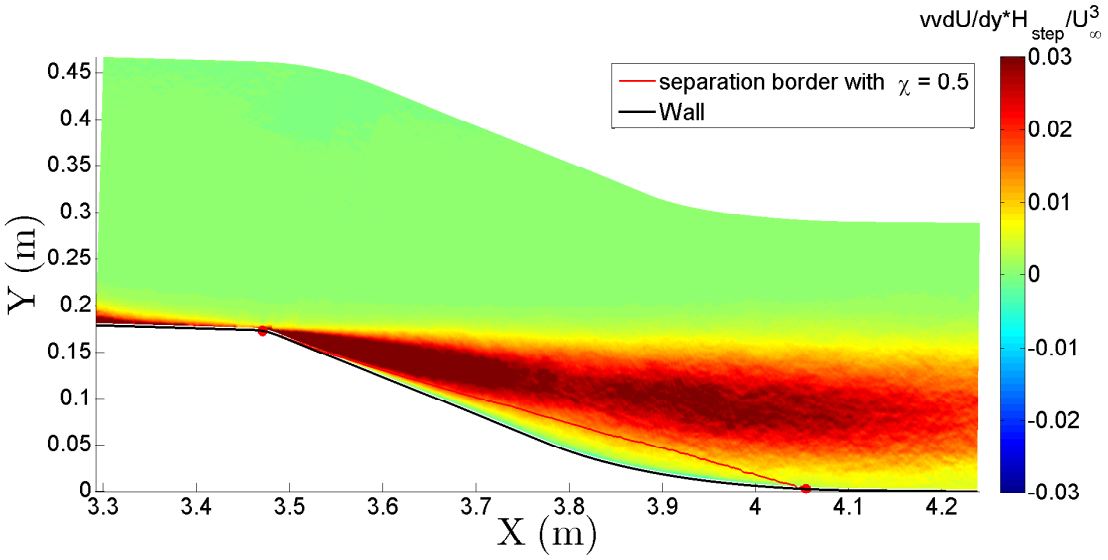

Figure 3.35: Production term $\overline{v'^2}\frac{\partial U}{\partial y}$ of $-\overline{u'v'}$ on the flap at mid-span of the ramp.

6.4.2 Turbulence intensity profiles

6.4.2.1 Streamwise turbulence intensity profiles

Figure 3.36 shows six streamwise turbulence intensity profiles at the same positions as the mean streamwise profiles shown in Section 6.3.4. The profiles are scaled with the same velocity (U_∞) and length (H_{step}) scales. An external turbulence peak is clearly evidenced after the separation point. In the separation region, it moves away from the wall with s. At one quarter of the separation region (i.e. at $s = 3624$ mm) it is at $\frac{y}{H_{step}} \simeq 0.14$. At the reattachment point it is at $\frac{y}{H_{step}} \simeq 0.57$. These values agree with Simpson (1989) who noticed this peak near $\frac{y}{\delta_0} = 0.5$ (here $\frac{H_{step}}{\delta_0} = 1.09$). The peak spreads and decreases with s. After $s = 3949$ mm, the peak motion away from the wall is less marked. At $s = 4297$ mm a second classical near wall peak reappears which indicates a possible boundary layer recovery.

Figure 3.37 shows six profiles of the production term $-\overline{u'v'}\frac{\partial U}{\partial y}$ of $\frac{1}{2}\overline{u'^2}$ at the same positions. After the separation point, a clear production peak appears which moves away from the wall in the first part of the flap (i.e. until $s = 3949$ mm). This production peak is very high at the beginning of the separation then it decreases and spreads around the middle of the bubble, then re-increases and continues to spread until the end of the separation. After the reattachment, it finally decreases.

Figure 3.38 shows the profiles of the second production term $-\overline{u'^2}\frac{\partial U}{\partial x}$ at the same positions. The profiles at $s = 3624$ mm and 3793 mm show a largely stronger peak (4 times) than the corresponding one of $-\overline{u'v'}\frac{\partial U}{\partial y}$ (Figure 3.37). The peak is even about $0.1H_{step}$ further away from the wall. Downstream $s = 3949$ mm, this peak has almost totally disappeared and the near wall region becomes slightly negative.

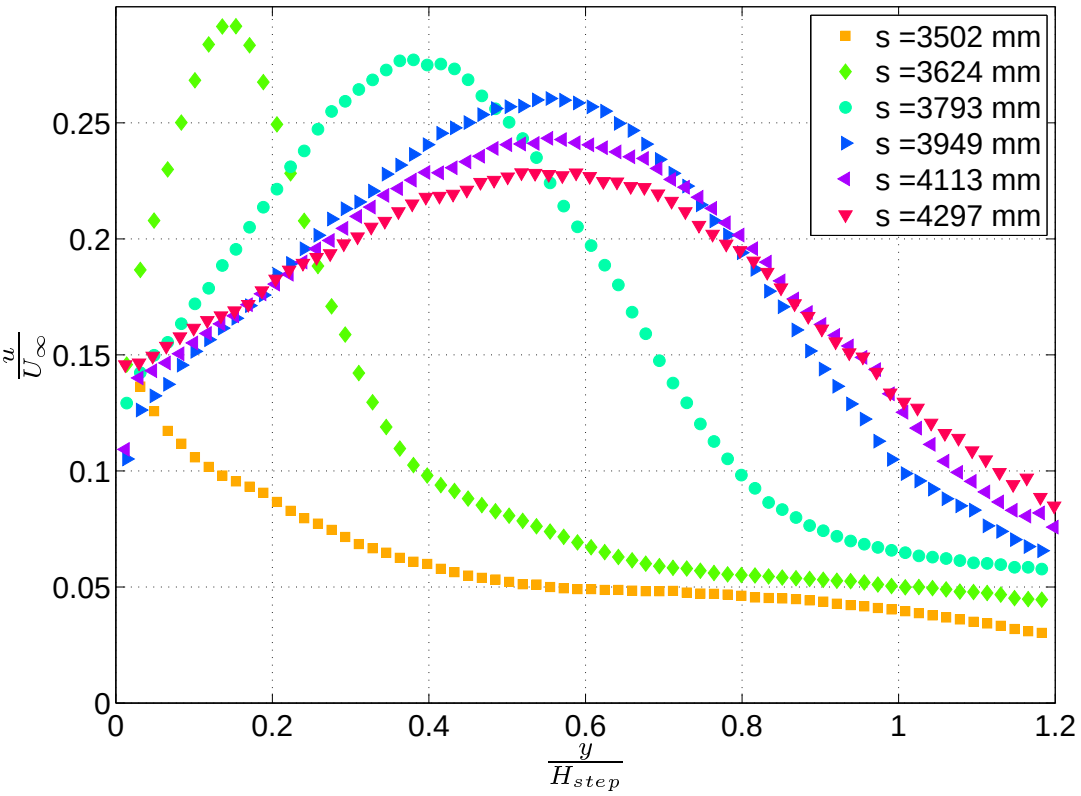

Figure 3.36: Six streamwise turbulence intensity profiles on the flap.

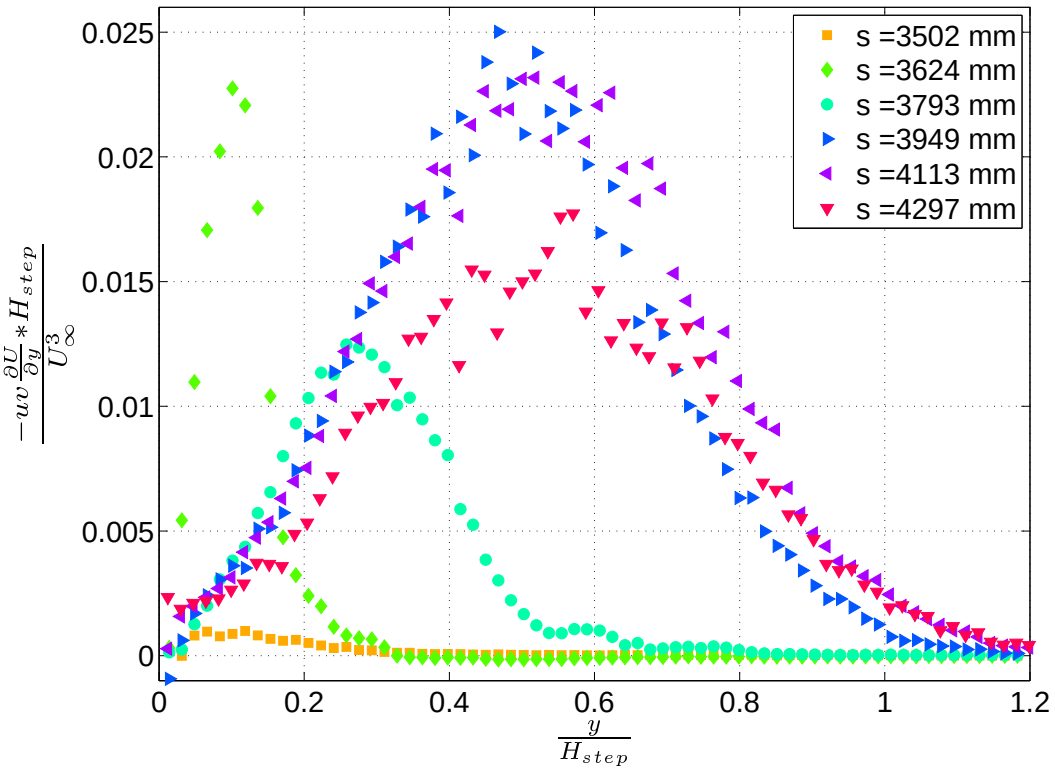

Figure 3.37: Six profiles of the production term $-\overline{u'v'}\frac{\partial U}{\partial y}$ of $\frac{1}{2}\overline{u'^2}$ on the flap.

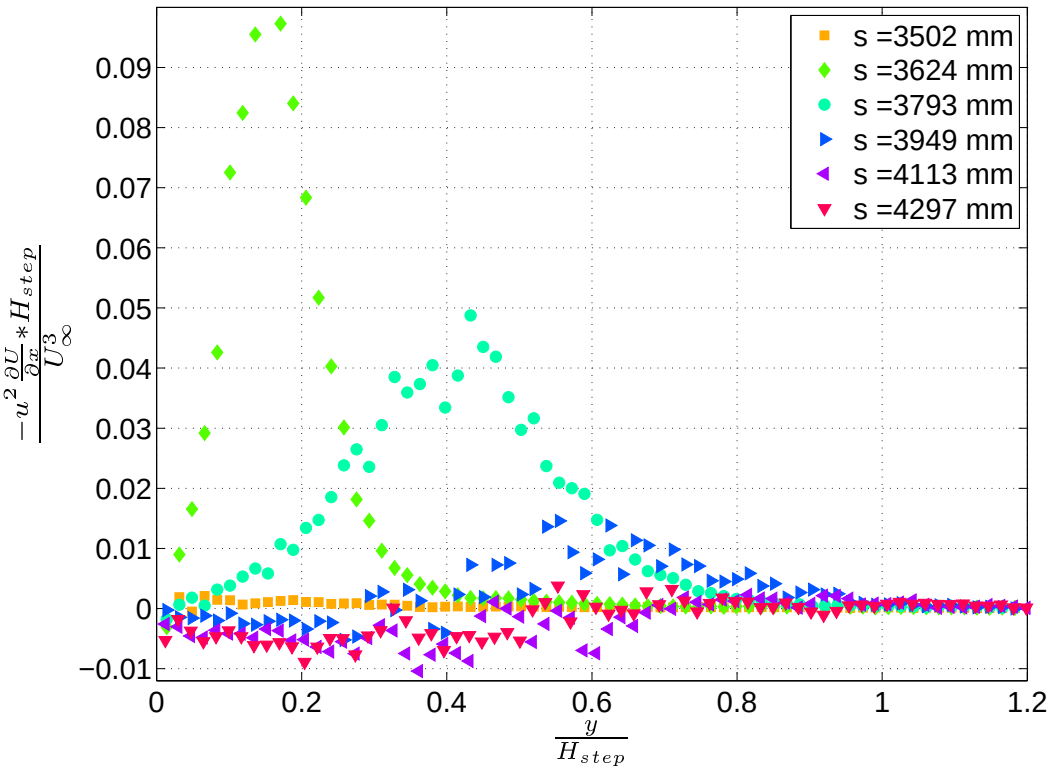

Figure 3.38: Six profiles of the production term $-\overline{u'^2}\frac{\partial U}{\partial x}$ of $\frac{1}{2}\overline{u'^2}$ on the flap.

6.4.2.2 Wall-normal turbulence intensity profiles

Figure 3.39 shows six wall normal turbulence intensity profiles at the same positions as above. An external peak is also evidenced after the separation point which also moves away from the wall with s in the separation region. At $s = 3624$ mm, it is at $\frac{y}{H_{step}} \simeq 0.11$ and at $s = 4113$ mm it is at $\frac{y}{H_{step}} \simeq 0.43$. This peak is then closer to the wall than the one of the streamwise component. Contrary to $\sqrt{\overline{u'^2}}$, the height of this peak increases with s. This suggests a conversion of the streamwise component to the wall-normal one as was evoked in Section 6.4.1. After the reattachment, the profiles almost collapse which indicates an equilibrium between the dissipation on one side and production and redistribution on the other side, this, associated to negligible diffusion. At $s = 4297$ mm, higher values near the wall reappear due to the possible boundary layer recovery.

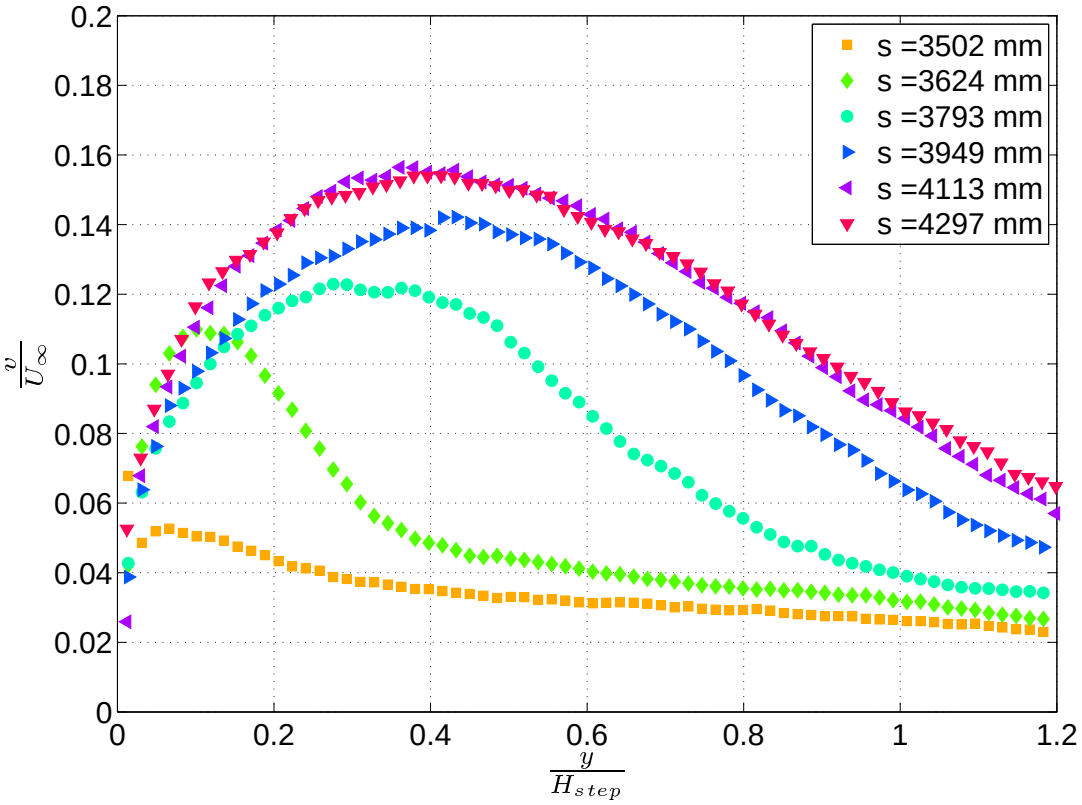

Figure 3.39: Six wall normal turbulence intensity profiles on the flap.

The redistribution of $\overline{u'^2}$ to $\overline{v'^2}$ was hypothesized in Section 6.4.1 due to the small level of direct production. The non zero production term of $\frac{1}{2}\overline{v'^2}$ $(-\overline{v'^2}\frac{\partial V}{\partial y})$ is given in Figure 3.33 for quantification. In the first part of the flap, a non negligible destruction peak is observed. This destruction almost disappears at $s = 3949$ mm and then, a small production peak develops which confirms the return to the standard boundary layer production organisation as suggested for the streamwise component in Section 6.4.1.

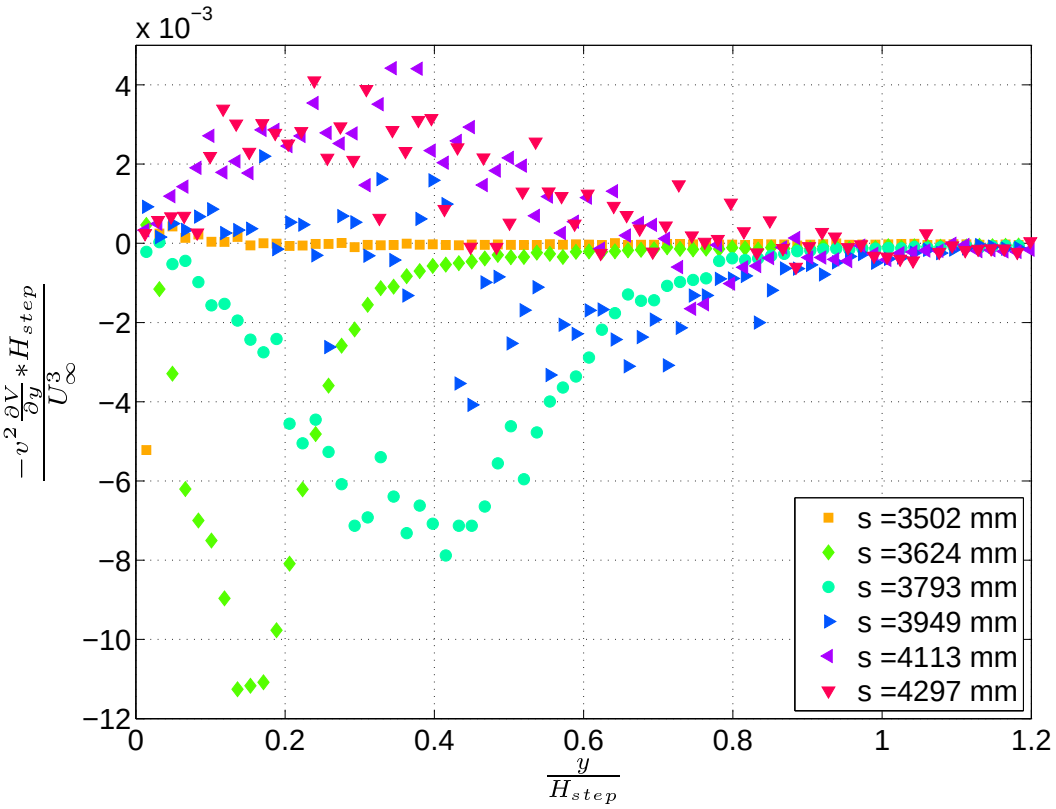

Figure 3.40: Six profiles of the production term $-\overline{v'^2}\frac{\partial V}{\partial y}$ of $\frac{1}{2}\overline{v'^2}$ on the flap.

6.4.2.3 Reynolds shear stress profiles

Figure 3.41 shows six Reynolds shear stress profiles at the same positions. In agreement with the observations done in Section 6.4.1, the behaviour is very similar to the wall-normal component. However, the peak height increases more significantly with s. On the first half of the separation (i.e. $s \leq 3793$ mm), the peak is exactly at the same position as for the wall-normal component. After $s = 3793$ mm, the peak is slightly away from the wall compared to $\sqrt{\overline{v'^2}}$ but remains below the peak on $\sqrt{\overline{u'^2}}$. As for the streamwise component, the profiles at $s = 4113$ mm and at 4297 mm are very similar except a small decrease on the peak height for the last profile.

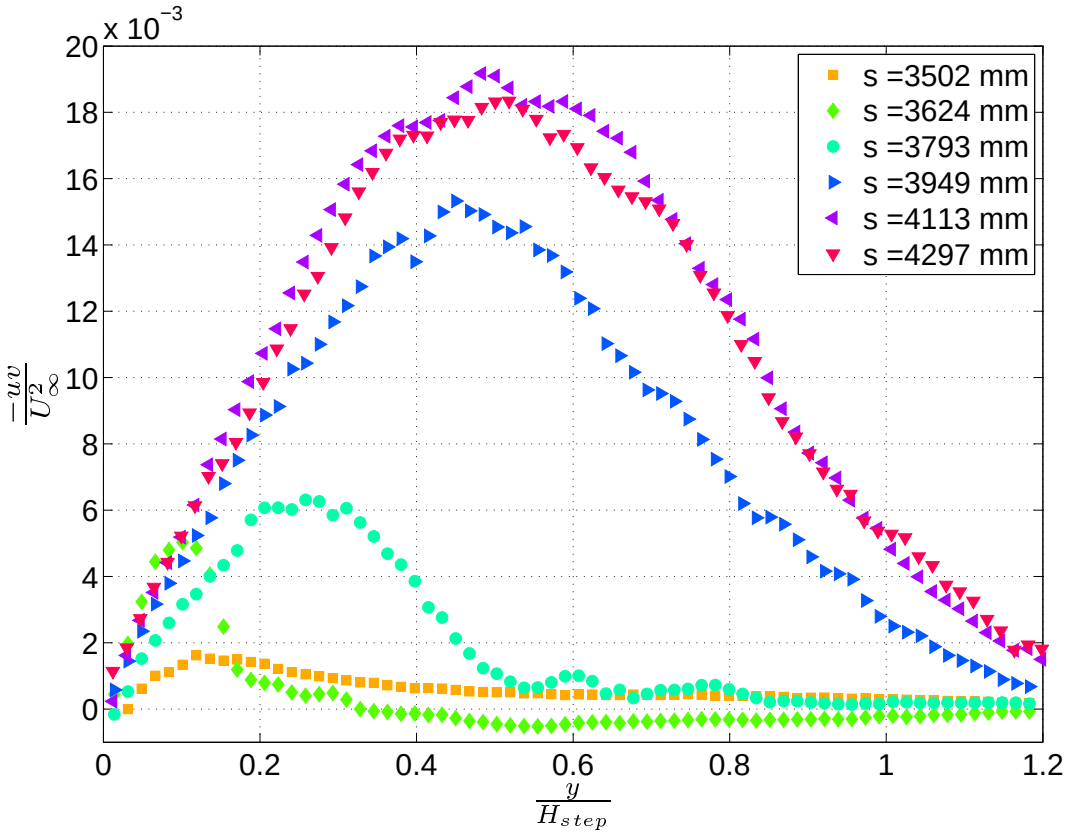

Figure 3.41: Six Reynolds shear stress profiles on the flap.

The strong similarity between the Reynolds shear stress and the wall-normal component was explained in Section 6.4.1 by its production largely dominated by $\overline{v'^2}\frac{\partial U}{\partial y}$. The profiles at the six selected stations of this term are given in Figure 3.42. After the separation point, the profiles show a very strong peak which decreases and spreads out in the first part of the flap. Downstream $s = 3949$ mm, the peak remains at the same position and is nearly self similar. At the last station, the peak has significantly decreased and a near wall peak seems to develop which also agrees with a standard boundary layer production mechanism.

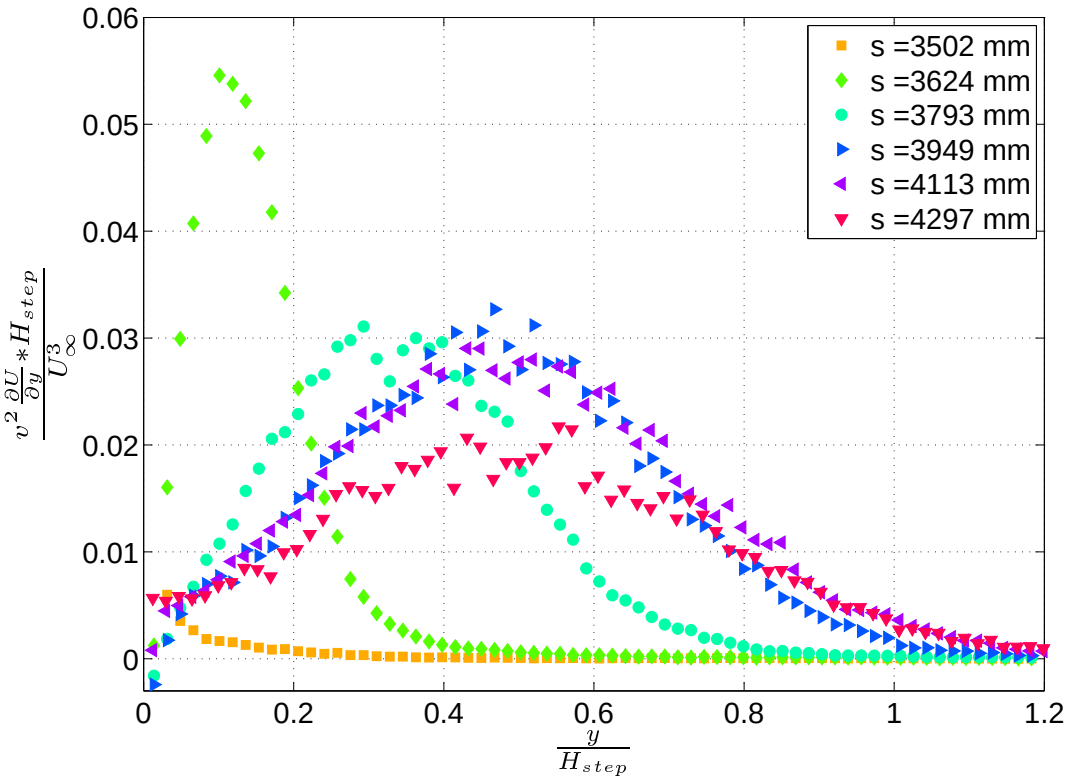

Figure 3.42: Six profiles of the main production term $\overline{v'^2}\frac{\partial U}{\partial y}$ of the Reynolds shear stress on the flap.

6.5 Reattachment region

Figure 3.43 shows two mean streamwise velocity profiles after the reattachment point (located at $s = 4113$ mm) in wall units. The log-law and the FP case profile at 5 m/s are added for comparisons. The friction velocity was determined using the standard Clauser's chart method. A log-law reappears 14 cm (or about 80% of the step height H_{step} or 23% of the separation length L_{sep}) downstream of the reattachment point (i.e. at $s = 4250$mm). The boundary layer recovery seems then very fast. This is in agreement with the study of DeGraaff (1999). At the end of the field (i.e. at $s = 4297$ mm), clearly a log-law region exist and the wake region is reduced compared to $s = 4250$ mm.

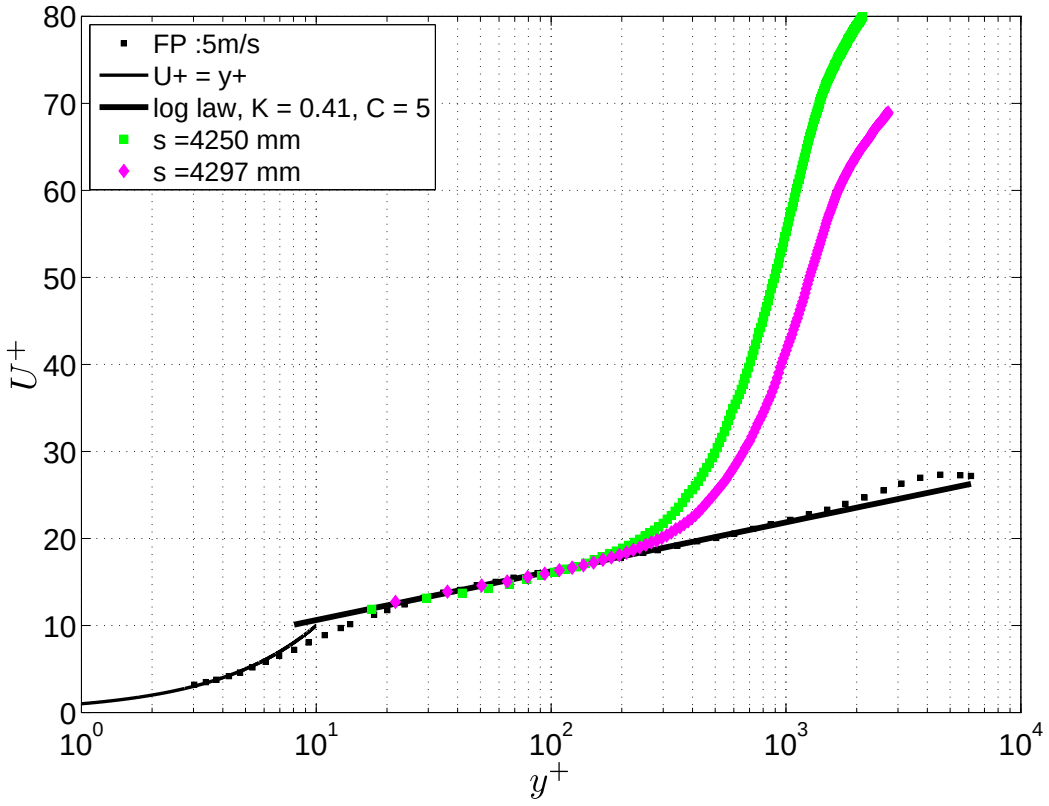

Figure 3.43: Mean streamwise velocity profiles after the reattachment point in wall-unit and compared to the log-law and FP case at 5 m/s.

The friction velocity obtained after the reattachment is more than three times smaller than upstream of the flap at hot-wire station 5. However, it increases rapidly (+13% from $s = 4250$ mm to $s = 4297$ mm). At the end of the field ($s = 4297$ mm), $u_\tau = 0.15$ m/s, $\delta = 27.6$ cm, $\delta^* = 9$ cm, $\theta = 4.2$ cm and $H = 2.2$. The Reynolds number based on θ is then higher than 26000. The high value of H shows however that the boundary layer remains highly perturbed even if a recovery of the log-law is observed. The Reynolds stresses are much higher than for an equilibrium boundary layer (a factor around 3 is observed). The boundary layer recovery seems then fast for the mean velocity but slower for the Reynolds stresses.

7 Conclusion

The flow around the AVERT ramp model has been characterized in view of studying flow control strategies. This ramp, made of three parts (a contraction, a flat plate and a flap), allows manipulating the turbulent boundary layer equilibrium on the flat plate by varying α, and the separation on the flap by varying β.

Zero, favourable and adverse pressure gradients can be obtained on the flat plate at respectively $\alpha = -0.7°$, $\alpha > -0.7°$ and $\alpha < -0.7°$. A separation occurs on the flap for β smaller than $-19°$ and $\alpha = -2°$. The flap adverse pressure gradient tuned by β has no significant effects on the flat plate pressure distribution fixed by α, except for the suction peak just before the flap articulation. The amplitude of this suction peak is characteristic of the separation. Finally, the Reynolds number was found to have little impact on the overall pressure distribution on the ramp.

The configuration $\alpha = -2°$, $\beta = -22°$ and $U_\infty = 10$ m/s, which was selected for flow separation control, has been characterized more precisely with single hot-wire anemometry and PIV. This configuration corresponds to a mild adverse pressure gradient on the flat plate and a separation on the flap. The boundary layer thickness on this ramp configuration was found around 20 cm and the Reynolds number based on the momentum thickness θ about 11000, which is of the same order as for the LML FP case at $U_\infty = 5$ m/s. This boundary layer was found to develop with a mild adverse pressure gradient on the flat plate with a Clauser pressure parameter ($\beta_{Clauser}$) between 0.2 and 1.4 (and about 0.4 in the constant APG region).

The separation on the flap of the selected ramp configuration was studied in more details with a 2D2C PIV set-up. The mean profile at hot-wire station 5 gives a good collapse with the one obtained with hot-wire, which shows the good quality of the PIV data. However, due to larger uncertainty, the agreement on the streamwise turbulence intensity at this station is not so good. The length L_{sep} of the separation is about 61 cm (or $\frac{L_{sep}}{H_{step}} = 3.5$, with H_{step} the ramp step height) and the maximum height H_{sep} about 3 cm (or $\frac{H_{sep}}{H_{step}} = 0.17$). The separation point was detected very near to the flap articulation, which confirms the results obtained with wool-tufts and oil-film visualisations. In agreement with Simpson (1989), an intense turbulence intensity region (streamwise, wall-normal and Reynolds shear stress) is evidenced above the separation region for $0.1 \leq \frac{y}{H_{step}} \leq 0.6$.

The production of streamwise Reynolds stress in the separated region is the main production source of turbulent kinetic energy. This production on the flap was found strong but dispatched into two parts, one near the beginning of the separation and an other which starts at the middle of the bubble (i.e. at $X = 3.8$ m) where there is a change in wall direction. The first region is due to the deceleration and is dominated by the term $-\overline{u'^2}\frac{\partial U}{\partial x}$. The second region, in the downstream part of the flap, is dominated by $-\overline{u'v'}\frac{\partial U}{\partial y}$ as for a 2D ZPG boundary layer. This region is probably due to the wall-normal flapping motion of the large scale structures characterized by high u' fluctuations, which induces high levels of v' so high levels of $-\overline{u'v'}$. The production of $\overline{v'^2}$ was found negative in the first half of the separation region and negligible in the rest of the field. As the $\overline{v'^2}$ increases with X, a redistribution from $\overline{u'^2}$ to $\overline{v'^2}$ was supposed to explain the observations. Concerning the Reynolds shear stress, its production was found governed by $\overline{v'^2}\frac{\partial U}{\partial y}$, and this explains the strong

similarity observed between the wall-normal turbulence intensity and the Reynolds shear stress distributions. Finally, on the rear part of the flap, the turbulence production organisation was found similar to that of a 2D ZPG boundary layer, but more away from the wall.

The boundary layer recovery downstream the separation was found very fast for the mean velocity profile and slower concerning the Reynolds stresses ones. At the end of the PIV field a log-law region is observed, however the boundary layer remains quite destabilised with a shape factor of 2.2. The quantitative results obtained about the separation will be used in Chapter 6 to study the effects of active flow control.

Chapter 4

Passive flow control

1 Introduction

This chapter presents the results of a parametric passive control study using thin triangular vane-type vortex generators (VGs). All the control tests were realized at $U_\infty = 10$ m/s on the ramp configuration with $\alpha = -2°$ and $\beta = -22°$ (which corresponds to an adverse pressure gradient on the flat plate and a flow separation on the flap (see Chapter 3)). The VGs used were described in Chapter 2. Passive control strategies were tested before the active ones to be sure that the flow separation can be suppressed. The aim was also to build tools to quantify the control efficiency. Firstly, these tools will be described, then the results of the parametric study will be presented.

2 Control efficiency quantification

The control efficiency was characterized using wool tufts visualisations coupled with four friction probes placed on the flap (see Chapter 2). The wool tufts visualisations were used to give a qualitative information about the control efficiency (such as an estimation of the delay of the separation or an estimation of the remaining separation length, etc.), and the hot-film probes to give a more quantitative information.

However, hot-film friction probes are not sensitive to the flow direction, so they give the absolute value of the wall friction $|\tau|$. The criterion to detect the separation with friction probes is then not as easy as $\tau < 0$: the flow is separated and $\tau > 0$: the flow is attached. Building a criterion only on $|\tau|$ is difficult and risky. Indeed, as the velocity in the reverse flow is usually smaller than the external velocity, the friction, in absolute value, can be smaller when the flow is separated than when it is attached, so an increase of $|\tau|$ can be interpreted as a reattachment. This is not guaranteed because, if the control increases the separation bubble size, it may lead to an increase of friction due to a strengthening of the reverse flow. As well, a decrease of the friction can be also a positive effect of control as if the control gives a flow near separation at the probe position, the friction obtained will be small and could be even smaller than the friction of the separated flow. So, it was impossible to build a criterion only on $|\tau|$ to detect separation. Others parameters given by the

friction probes were then analysed to try to find quantitative information about the control efficiency.

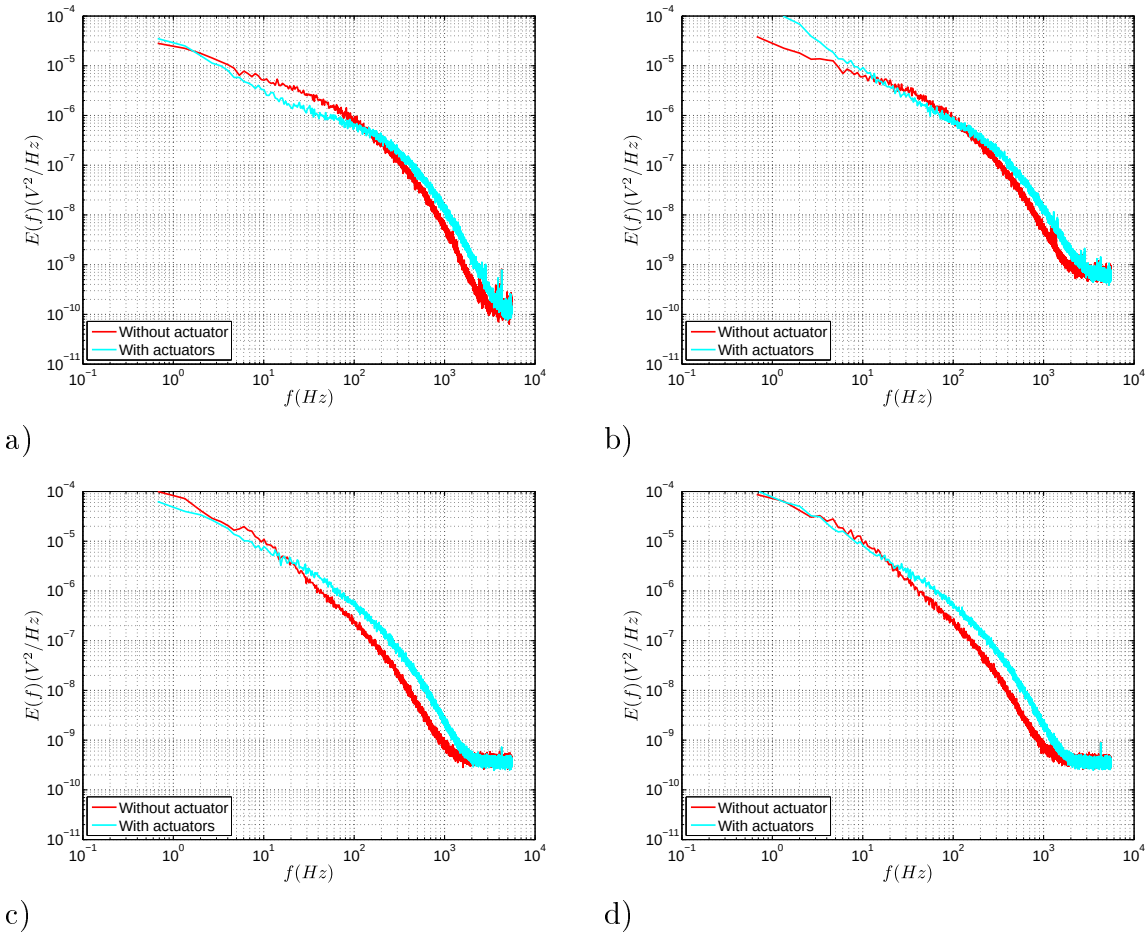

Figure 4.1: Spectrum of the friction probes output voltage, with and without control. a) probe number 1, b) number 2, c) number 3, d) number 4.

The first idea was to look at the changes in the power spectrum of the output voltage of the hot-film probes introduced by the control. Figure 4.1 shows the spectrum of the output signal of the friction probes for a passive case of control where the separation was totally suppressed on the wool tufts (i.e. passive counter-rotating configuration, $h = 15$ mm, $\frac{\lambda}{h} = 6$, $\frac{L}{h} = 2.5$), compared with the uncontrolled case. Unfortunately, it appears that there is no typical band of frequencies of the separation. Only common effects of the reattachment on the four probes is a small increase in the spectrum at high frequencies (from 100 Hz for probes 1 and 2, and 20 Hz for probes 3 and 4). At low frequencies, it seems that the control decreased the spectrum, may be because the vortex generators introduce low frequencies in the flow, but for probe number 2 it is not the case. Building a criterion on the spectrum to detect separation was thus difficult and was eliminated.

Looking at the probability density function (PDF) of the output voltage of the probes, it was found possible to build a criterion to detect and quantify the separation. This criterion was build with the variations of $|\tau|$ and the variations of the

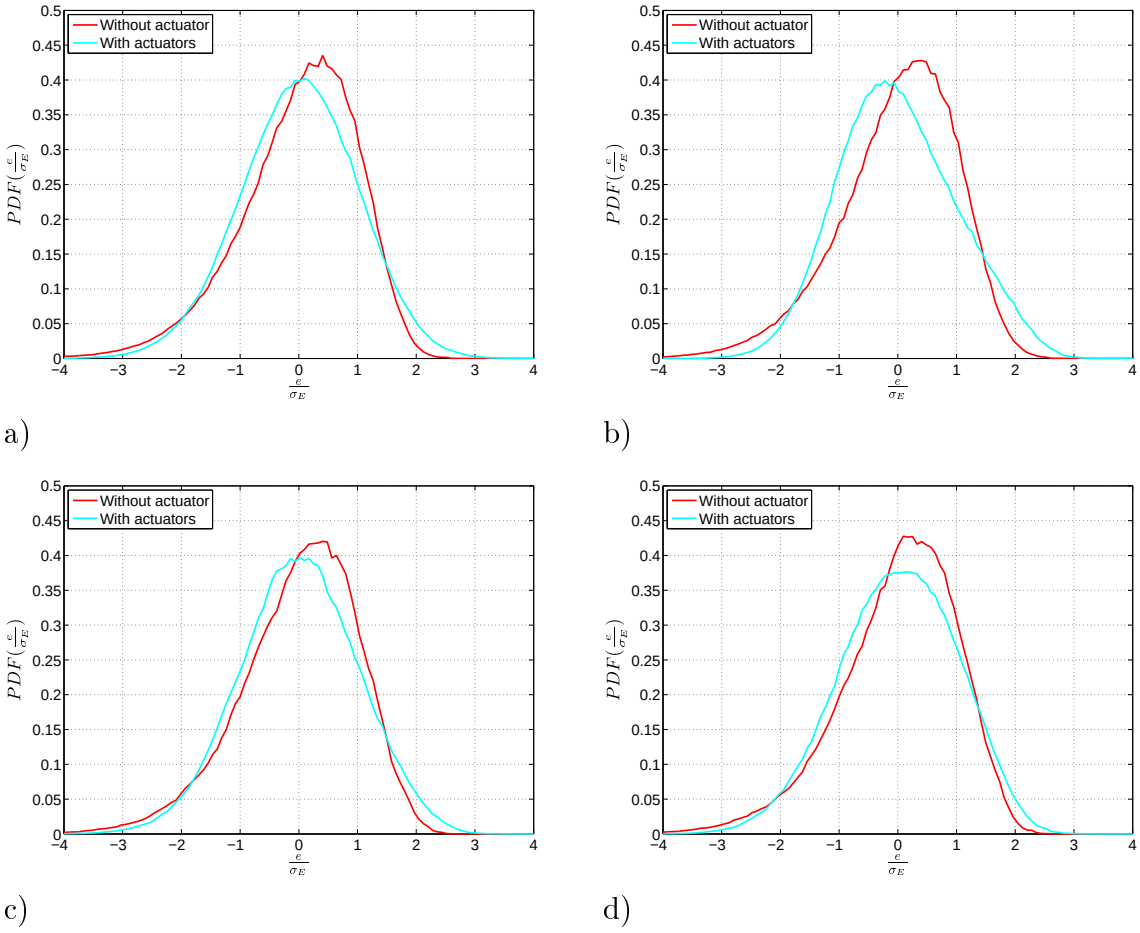

Figure 4.2: PDF of the friction probes output voltage, with and without control. a) probe number 1, b) number 2, c) number 3, d) number 4..

skewness and flatness of the output voltage of the friction probes. For the flow without control, the PDF of the output voltage of a probe was not Gaussian which leads to a skewness between -0.8 and -0.7, and a flatness between 3.7 and 4. When the flow was completely attached (which was verified with wool tufts visualisations), the PDF of the output voltage tended to be Gaussian. The skewness was then between -0.2 and 0 and the flatness between 2.9 and 3.1. Figure 4.2 illustrates the change in PDFs for a passive control case where the separation was totally suppressed on wool tufts (i.e. passive counter-rotating configuration, $h = 15$ mm, $\frac{\lambda}{h} = 6$, $\frac{L}{h} = 2.5$).

So, the final criterion to detect separation at the friction probe position was a skewness of the output voltage of a probe around -0.7 and a flatness around 4. When the skewness was larger than -0.4 and the flatness smaller than 3.4, the separation was found totally suppressed. As in all control cases investigated, an increase in skewness was giving a decrease in flatness and vice versa, the criterion was reduced only to the variations of $|\tau|$ and the variations of the skewness.

A decrease of the separation at a probe position corresponds then to an increase of $|\tau|$ accompanied principally by an increase of skewness. A strengthening of the separation which corresponds to a reduction of the intermittency of the separation (i.e. fully separated flow forced by the control), is characterized by an increase in skewness. A delay of the separation is finally evidenced when no indication of separation (i.e. a skewness greater than -0.4) is present at the probes at $s = 3555$ mm and when a small reduction of $|\tau|$ accompanied by a decrease in skewness is present at the probes at $s = 3759$ mm.

3 Passive control results

3.1 Co-rotating configurations

3.1.1 Tests description

Figure 1.3 a) shows the arrangement of passive vortex generators (VGs) in co-rotating configurations. Based on the study of Godard and Stanislas (2006a), the optimum value of $\frac{\lambda}{h}$ is 6, so it was decided to test only some values around this optimum one. The values of $\frac{\lambda}{h}$ tested were 3, 6, 12 and 24 at control stations 1 ($s = 3383$ mm) and 2 ($s = 3219$ mm). At stations 3 ($s = 2968$ mm) and 4 ($s = 2440$ mm) only $\frac{\lambda}{h} = 6$ was tested. The four control stations correspond to four distances (ΔX_{vg}) from the VGs position to the separation line ($s = 3500$ mm) (see Figure 1.3). The control stations 4, 3 and 1 correspond respectively to the stations number 3, 4 and 5 of hot-wire measurements (Figure 2.12). For the control station 2, the boundary layer was not characterized. At this station, the external velocity, measured with a pitot tube, is 12.35 m/s for $U_\infty = 10$ m/s. As the boundary layer thickness varied slowly on the flat plate of the ramp (see Table 3.5), a linear estimation for δ at this station 2 was done between the hot-wire stations 4 and 5. With this method, the estimation of δ for station 2 is 20.2 cm. As the variations of δ at the four control stations are small (less tan 10%), h was kept constant to keep constant the parameter $\frac{h}{\delta}$ at these four stations.

To be sure of the friction variation measured, for each height h tested at station

i, one reference without actuator was taken first, then the case with the smallest $\frac{\lambda}{h}$ was installed and tested. Then actuators were removed progressively to increase $\frac{\lambda}{h}$. Finally, all actuators were removed and a final reference was taken. If these two references were the same within $\pm 5\%$, the test was validated.

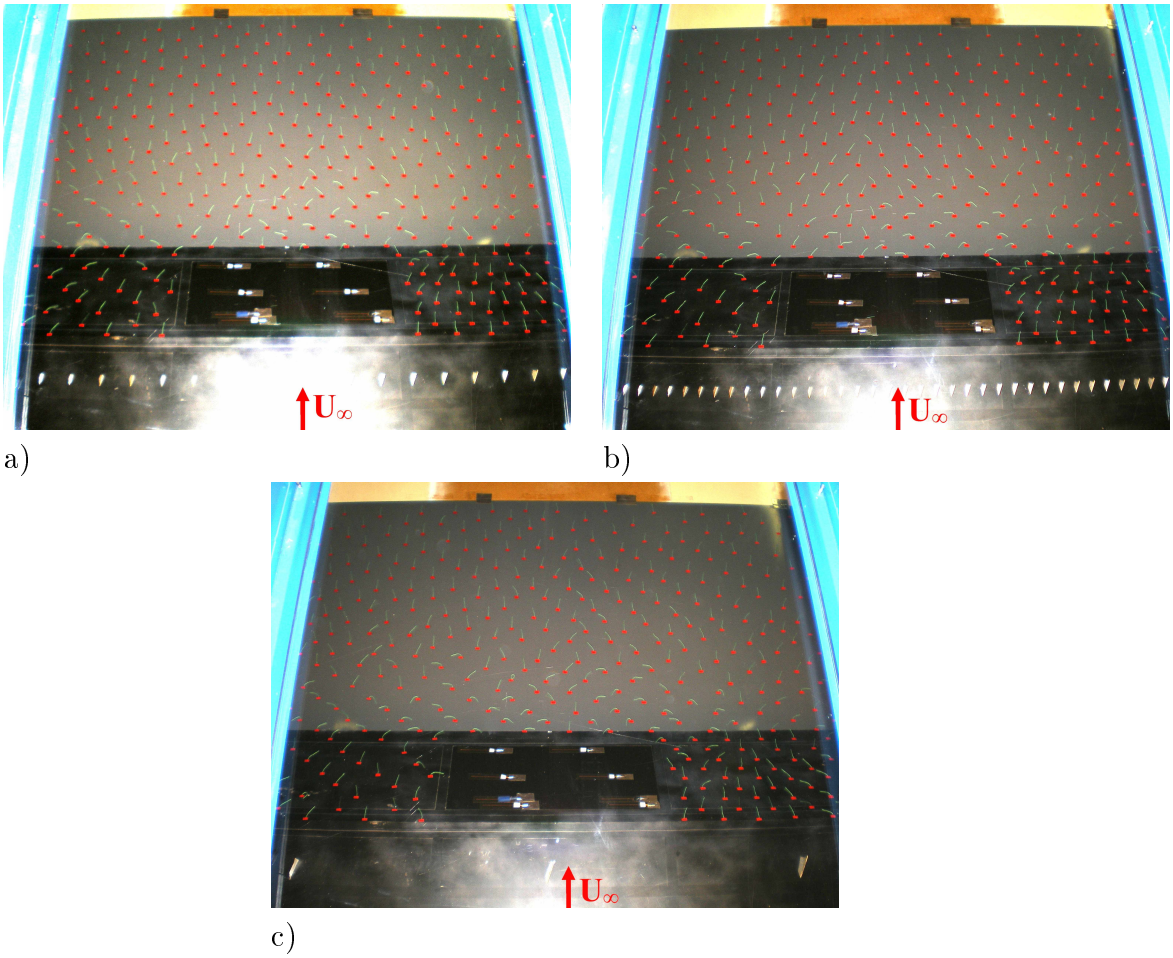

a) b)

c)

Figure 4.3: Wool tufts visualisation for a) PA (case 2), b) VPA (case 1), c) S (case 8).

3.1.2 Results

3.1.2.1 General results

Table 4.1 presents all the passive co-rotating cases investigated and the main conclusions obtained with wool tufts and friction probes. The legend for the state column (illustrated by Figure 4.3) is :
- PA = Partially Attached : a small separation is evidenced by the wool tufts.
- VPA = Very Partially Attached : a very small reduction of the separation is evidenced by the wool tufts.
- S = Separated : no reduction of the separation is evidenced by the wool tufts.

The last two columns of Table 4.1 contain the best quantitative control results obtained with friction probes at station $s = 3555$ mm (penultimate column) and

Table 4.1: List of the co-rotating configurations tested

Case	s (mm)	h (mm)	$\frac{\lambda}{h}$	state	$\frac{\Delta(\lvert\tau\rvert-\lvert\tau_0\rvert)}{\lvert\tau_0\rvert}(\%)$ $s = 3555mm$	$\frac{\Delta(\lvert\tau\rvert-\lvert\tau_0\rvert)}{\lvert\tau_0\rvert}(\%)$ $s = 3759mm$
1	3383	15	3	VPA	11	-20
2	3383	15	6	PA	28	-15
3	3383	15	12	PA	29	-12
4	3383	15	24	S	5	-4
5	3383	30	3	PA	38	-9
6	3383	30	6	PA	55	-10
7	3383	30	12	VPA	1	21
8	3383	30	24	S	0	21
9	3383	60	3	VPA	48	-1
10	3383	60	6	VPA	4	-4
11	3383	60	12	VPA	1	19
12	3219	15	3	PA	13	-19
13	3219	15	6	PA	18	-2
14	3219	15	12	VPA	19	-7
15	3219	15	24	S	2	4
16	3219	30	3	PA	22	-2
17	3219	30	6	PA	41	-5
18	3219	30	12	VPA	6	19
19	3219	30	24	S	-1	19
20	3219	60	3	PA	39	-10
21	3219	60	6	PA	4	2
22	3219	60	12	VPA	0	11
23	2968	15	6	VPA	9	-6
24	2968	30	6	PA	36	-3
25	2968	60	6	S	5	22
26	2440	15	6	S	1	-12
27	2440	30	6	VPA	15	-7
28	2440	60	6	S	5	19

station $s = 3759$ mm (last column). As can be seen, none of the passive co-rotating configurations tested could suppress the separation. In most cases, a delay of separation was observed together with a reduction of the separated bubble size.

3.1.2.2 Effects of $\frac{\lambda}{h}$

Figures 4.4 to 4.9 present for different cases with different values of $\frac{\lambda}{h}$, the gain in friction and the skewness obtained with the four friction probes versus the spanwise direction z. At the bottom of these figures (and for the rest of this chapter), the spanwise positions of the friction probes used are represented. Probes P1 and P2 are the nearest to the separation line and P3 and P4 are the farthest from the separation line (see Chapter 2 and Table 2.6). A schematic top view of the VGs is also represented in the bottom part of the figures, corresponding to the smallest $\frac{\lambda}{h}$ of the cases presented in the figure.

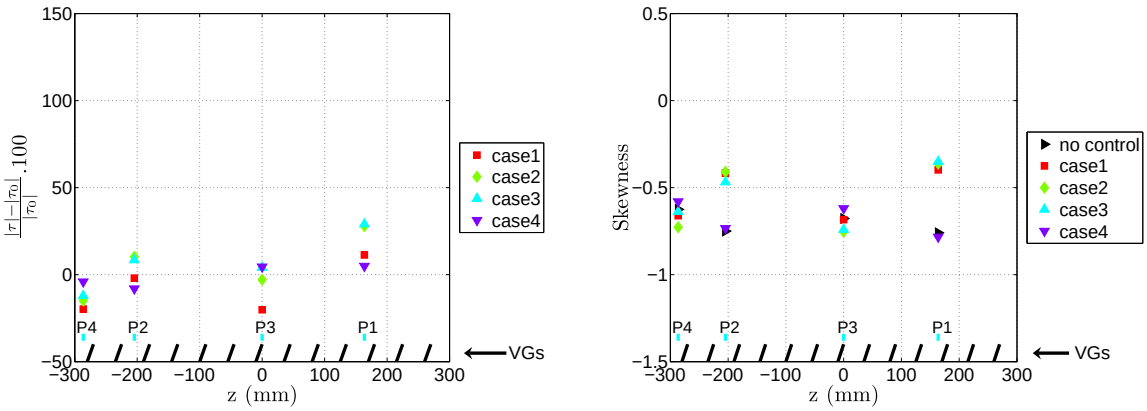

a) b)

h (mm)	β_{pd}	$\frac{l}{h}$	$\frac{\Delta X_{vg}}{h}$	$\frac{\lambda}{h}$:	case 1	case 2	case 3	case 4
15	18°	2	7.8		3	6	12	24

Figure 4.4: a) Gain in friction and b) Skewness for cases 1, 2, 3 and 4 (i.e. for four different values of $\frac{\lambda}{h}$ and the other parameters kept constant).

To obtain the configuration with $\frac{\lambda}{h} = 6$ from the configuration with $\frac{\lambda}{h} = 3$, one actuator over two was removed, keeping the actuator at $z = 0$. The same method was used to obtain the configuration with $\frac{\lambda}{h} = 12$ from the configuration with $\frac{\lambda}{h} = 6$ and etc.. Cases 1 to 4 (Figure 4.4), correspond to $h = 15$ mm at station 1 and all parameters are constant except $\frac{\lambda}{h}$. Cases 2 ($\frac{\lambda}{h} = 6$) and 3 ($\frac{\lambda}{h} = 12$) are almost identical and give the best results. Indeed, they give an increase in friction for probes P1 and P2 accompanied with an increase in skewness, and a decrease in friction for probes P3 and P4 with no variation in skewness, which means that the separation has been delayed and reduced. For cases 12 to 15 (Figure 4.5), which correspond to the same VGs configurations but at station 2, the same conclusions can be drawn. For $h = 15$ mm, it seems that the optimum parameter for $\frac{\lambda}{h}$ is between 6 and 12.

Cases 5 to 8, corresponding to $h = 30$ mm at station 1 with all parameters constant except $\frac{\lambda}{h}$ are given in Figure 4.6. Case 6 ($\frac{\lambda}{h} = 6$) gives the best results.

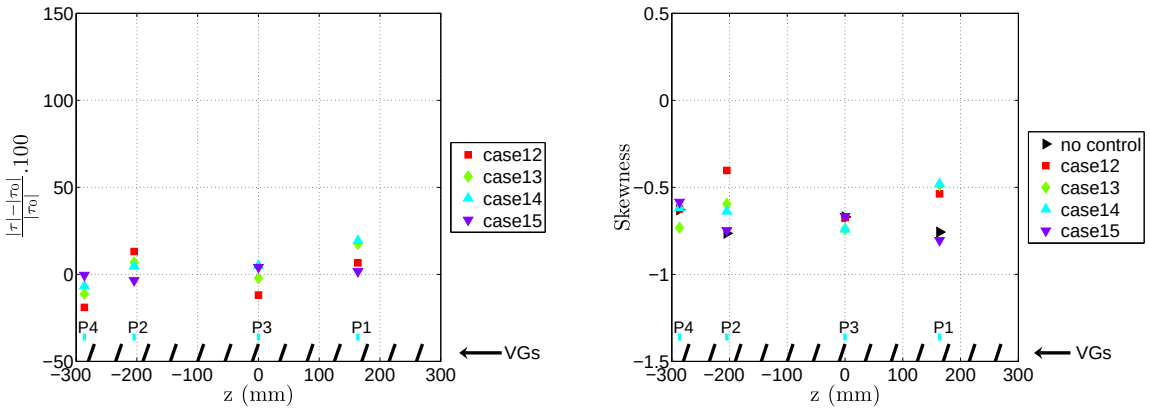

a) b)

h (mm)	β_{pd}	$\frac{l}{h}$	$\frac{\Delta X_{vg}}{h}$	$\frac{\lambda}{h}$:	case 12	case 13	case 14	case 15
15	18°	2	18.7		3	6	12	24

Figure 4.5: a) Gain in friction and b) Skewness for cases 12, 13, 14 and 15 (i.e. for four different values of $\frac{\lambda}{h}$ and the other parameters kept constant).

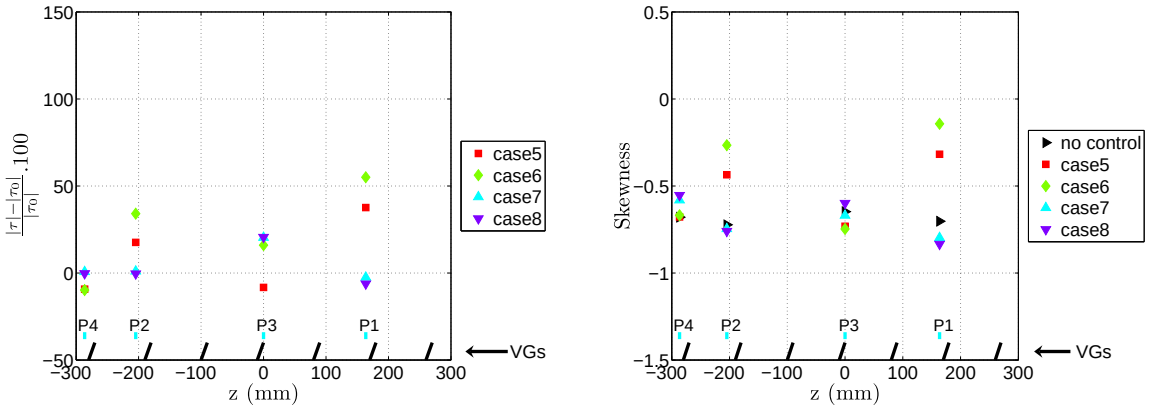

a) b)

h (mm)	β_{pd}	$\frac{l}{h}$	$\frac{\Delta X_{vg}}{h}$	$\frac{\lambda}{h}$:	case 5	case 6	case 7	case 8
30	18°	2	3.9		3	6	12	24

Figure 4.6: a) Gain in friction and b) Skewness for cases 5, 6, 7 and 8 (i.e. for four different values of $\frac{\lambda}{h}$ and the other parameters kept constant).

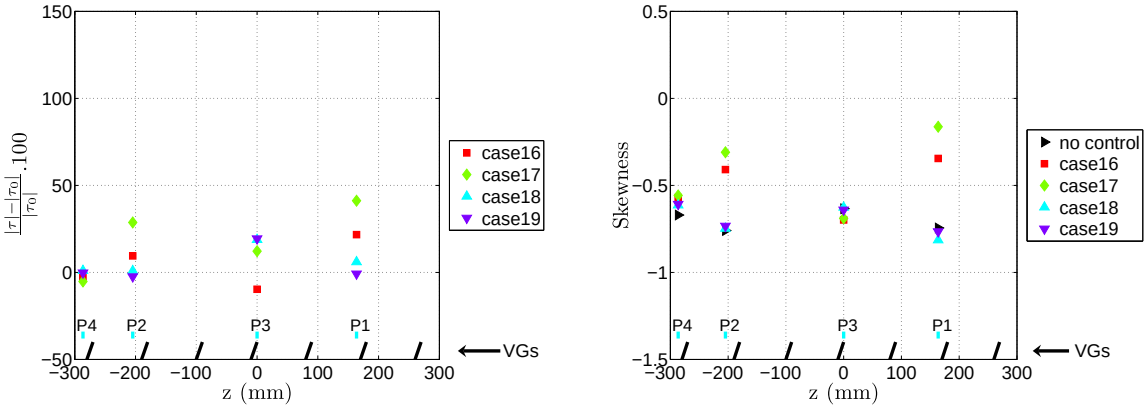

h (mm)	β_{pd}	$\frac{l}{h}$	$\frac{\Delta X_{vg}}{h}$	$\frac{\lambda}{h}$:	case 16	case 17	case 18	case 19
30	18°	2	9.4		3	6	12	24

Figure 4.7: a) Gain in friction and b) Skewness for cases 16, 17, 18 and 19 (i.e. for four different values of $\frac{\lambda}{h}$ and the other parameters kept constant).

Here again, the separation has been delayed and reduced. Cases 16 to 19 correspond to the same VGs configurations but at station 2 (Figure 4.7). Here, cases 17 and 18 are identical and give the best results. For $h = 30$ mm, it seems that the optimum $\frac{\lambda}{h}$ is around 6 at the station 1, but between 6 and 12 as for $h = 15$ mm at the station 2.

Cases 9 to 11, corresponding to $h = 60$ mm at station 1 with all parameters constant except $\frac{\lambda}{h}$, are given in Figure 4.8. The best results are obtained for case 9 ($\frac{\lambda}{h} = 3$). Cases 20 to 22 correspond to the same VGs configurations but at station 2 (Figure 4.9). The same results are obtained. For $h = 60$ mm, it seems that the optimum $\frac{\lambda}{h}$ is between 3 and 6, but nearer to 3.

In conclusion concerning the optimum value of $\frac{\lambda}{h}$, the conclusion differs slightly from Godard and Stanislas (2006a). Two different behaviours are observed. When the parameter $\frac{\Delta X_{vg}}{h}$ is over 8, the optimum $\frac{\lambda}{h}$ is between 6 and 12. When the parameter $\frac{\Delta X_{vg}}{h}$ is above 8, the optimum $\frac{\lambda}{h}$ is between 3 and 6 and nearer to 3 when $\frac{\Delta X_{vg}}{h}$ decreased. The optimum $\frac{\lambda}{h}$ is 6 only if the control station corresponds to $\frac{\Delta X_{vg}}{h} = 8$.

3.1.2.3 Effects of $\frac{\Delta X_{vg}}{h}$

Figure 4.10 shows the gain in friction and the skewness at the four control stations (corresponding to four values of $\frac{\Delta X_{vg}}{h}$) for $h = 15$ mm and $\frac{\lambda}{h} = 6$. The best results are obtained at the station 1, corresponding to $\frac{\Delta X_{vg}}{h} = 7.8$. Figure 4.11 shows the results of the four friction probes for $h = 30$ mm and $\frac{\lambda}{h} = 6$ at the four control stations. Stations 1 and 2 give almost the same results. After station 2, the control efficiency decreases. For $h = 30$ mm, station 1 corresponds to $\frac{\Delta X_{vg}}{h} = 3.9$ and 2 to $\frac{\Delta X_{vg}}{h} = 9.4$. Finally, Figure 4.12 shows the results of similar cases with $h = 60$

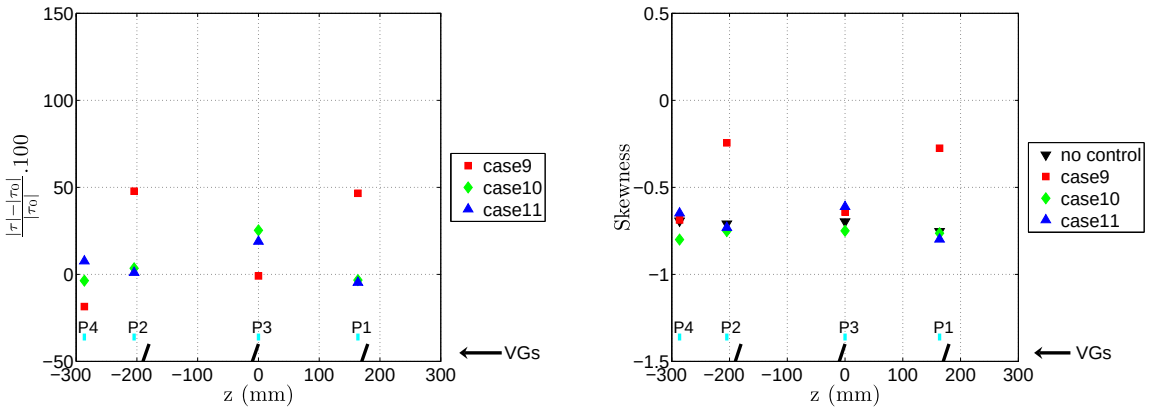

a) b)

h (mm)	β_{pd}	$\frac{l}{h}$	$\frac{\Delta X_{vg}}{h}$	$\frac{\lambda}{h}$:	case 9	case 10	case 11
60	18°	2	2		3	6	12

Figure 4.8: a) Gain in friction and b) Skewness for cases 9, 10 and 11 (i.e. for three different values of $\frac{\lambda}{h}$ and the other parameters kept constant).

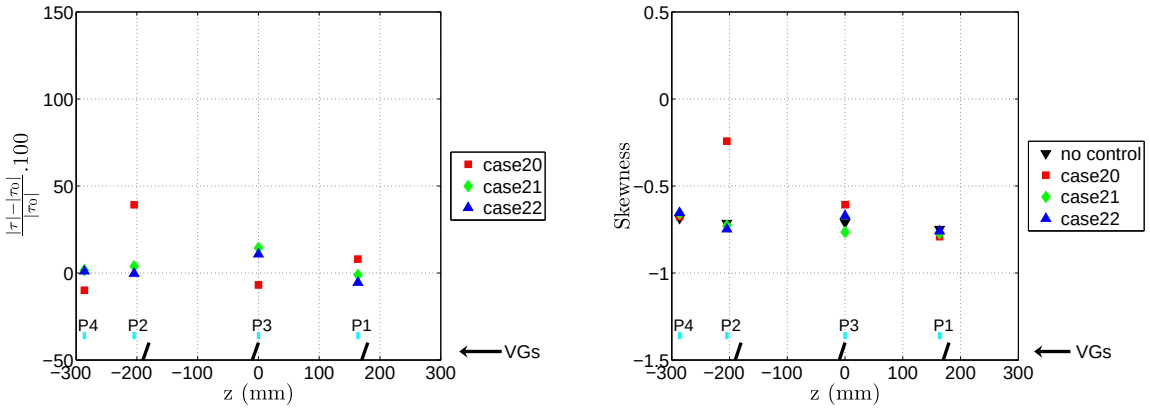

a) b)

h (mm)	β_{pd}	$\frac{l}{h}$	$\frac{\Delta X_{vg}}{h}$	$\frac{\lambda}{h}$:	case 20	case 21	case 22
60	18°	2	4.7		3	6	12

Figure 4.9: a) Gain in friction and b) Skewness for cases 20, 21 and 22 (i.e. for three different values of $\frac{\lambda}{h}$ and the other parameters kept constant).

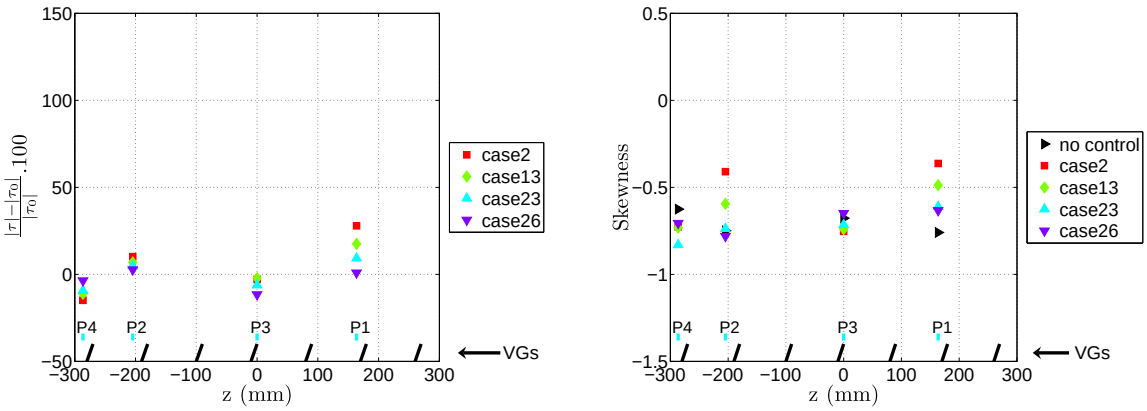

a) b)

h (mm)	β_{pd}	$\frac{l}{h}$	$\frac{\lambda}{h}$	$\frac{\Delta X_{vg}}{h}$:	case 2	case 13	case 23	case 26
15	18°	2	6		7.8	18.7	35.5	70.7

Figure 4.10: a) Gain in friction and b) Skewness for cases 2, 13, 23 and 26 (i.e. for four different values of $\frac{\Delta X_{vg}}{h}$ and the other parameters kept constant).

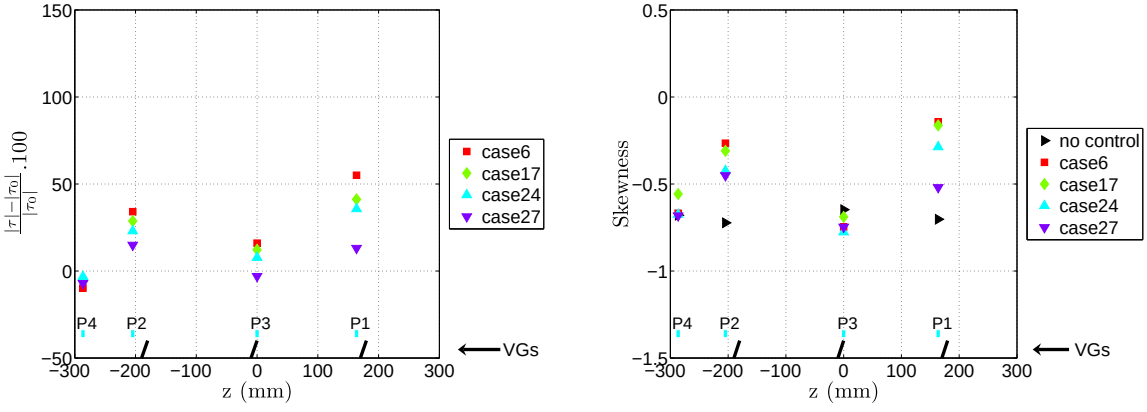

a) b)

h (mm)	β_{pd}	$\frac{l}{h}$	$\frac{\lambda}{h}$	$\frac{\Delta X_{vg}}{h}$:	case 6	case 17	case 24	case 27
30	18°	2	6		3.9	9.4	17.8	35.3

Figure 4.11: a) Gain in friction and b) Skewness for cases 6, 17, 24 and 27 (i.e. for four different values of $\frac{\Delta X_{vg}}{h}$ and the other parameters kept constant).

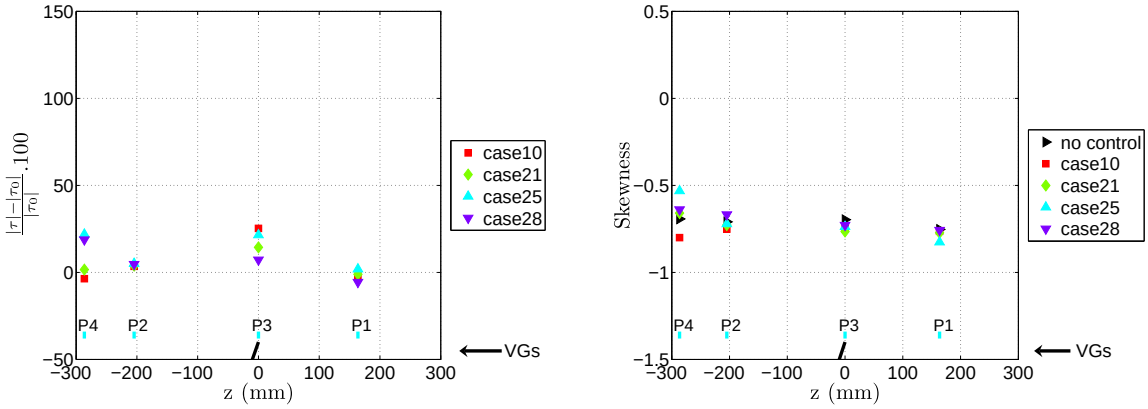

a) b)

h (mm)	β_{pd}	$\frac{l}{h}$	$\frac{\lambda}{h}$	$\frac{\Delta X_{vg}}{h}$:	case 10	case 21	case 25	case 28
60	18°	2	6		2	4.7	8.9	17.7

Figure 4.12: a) Gain in friction and b) Skewness for cases 10, 21, 25 and 28 (i.e. for four different values of $\frac{\Delta X_{vg}}{h}$ and the other parameters kept constant).

mm and $\frac{\lambda}{h} = 6$. The best results are obtained at the station 3, corresponding to $\frac{\Delta X_{vg}}{h} = 8.9$.

As a conclusion, the best parameter found for $\frac{\Delta X_{vg}}{h}$ is between 4 and 10 and seem to be near 8. This value is in agreement with Lin (1999). After $\frac{\Delta X_{vg}}{h} = 10$, the efficiency decreases rapidly. The optimum for $\frac{\Delta X_{vg}}{h}$ is then largely smaller than the vortices life distance of about $100.h$ (Lin (1999)).

3.1.2.4 Effects of $\frac{h}{\delta}$

Figure 4.13 shows the gain in friction and the skewness for 3 values of $\frac{h}{\delta}$ (0.08, 0.15 and 0.28) with $\frac{\lambda}{h} = 6$ and $\frac{\Delta X_{vg}}{h} \simeq 8 - 9$. It appears that the best value of $\frac{h}{\delta}$ is 0.15 (which corresponds to $h^+ \simeq 900$). This value is in agreement with the value found by Lin (1999).

3.1.3 Conclusion

In this study, it was shown that co-rotating passive VGs can only delay and reduce the separation. The optimum parameters that were found are almost in agreement with the previous studies of Lin (1999) and Godard and Stanislas (2006a). It was found that the optimum value is 8 for $\frac{\Delta X_{vg}}{h}$ and 0.15 for $\frac{h}{\delta}$ (which corresponds to $h^+ \simeq 900$ in the present study). The optimum value of $\frac{\lambda}{h}$ is 6 if $\frac{\Delta X_{vg}}{h}$ is optimum (i.e. $\frac{\Delta X_{vg}}{h} = 8$). If $\frac{\Delta X_{vg}}{h}$ is below its optimum value, $\frac{\lambda}{h}$ should be between 3 and 6. If $\frac{\Delta X_{vg}}{h}$ is above its optimum value, $\frac{\lambda}{h}$ should be between 6 and 12. Unlike Godard and Stanislas (2006a), it was found that the efficiency of co-rotating passive VGs is very small for $\frac{\Delta X_{vg}}{h}$ greater than 18. So even if co-rotating configurations lead to a significant increase in friction for $\frac{\Delta X_{vg}}{h}$ greater than 18 as was found by Godard and

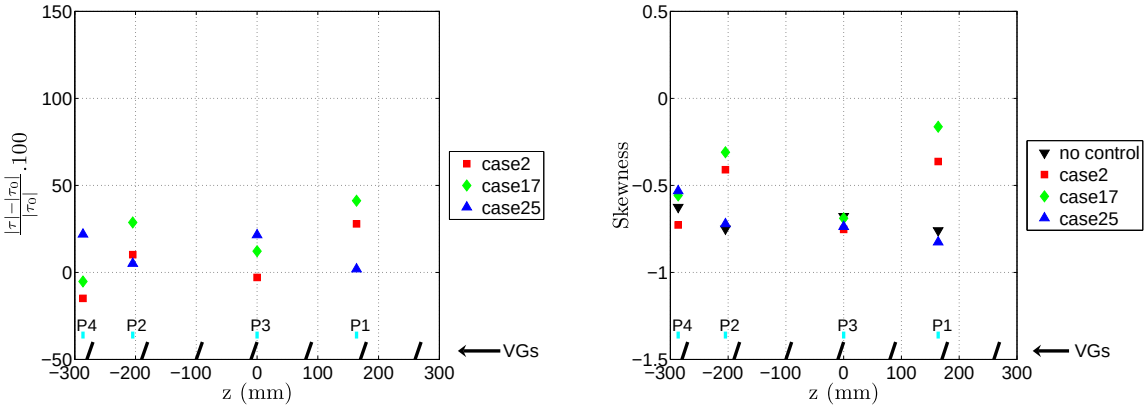

a) b)

β_{pd}	$\frac{l}{h}$	$\frac{\lambda}{h}$	$\frac{\Delta X_{vg}}{h}$	h (mm) :	case 2	case 17	case 25	$\frac{\Delta X_{vg}}{h}$:	case 2	case 17	case 25
18°	2	6	$\simeq 8-9$		15	30	60		7.8	9.4	8.9

Figure 4.13: a) Gain in friction and b) Skewness for cases 2, 17 and 25 (i.e. for three different values of $\frac{h}{\delta}$ (or h) and the other parameters kept constant).

Stanislas (2006a), it doesn't mean that these configurations will succeed to prevent or suppress a flow separation for large values of $\frac{\Delta X_{vg}}{h}$.

3.2 Counter-rotating configurations

3.2.1 Tests description

Figure 1.3 b) shows the arrangement of the passive VGs in counter-rotating configurations. Based on the study of Godard and Stanislas (2006a), the optimum parameter $\frac{\lambda}{h}$ is 6, so it was decided to test only some values around this optimum one. The values of $\frac{\lambda}{h}$ tested were 6, 12 and 24 at the same control stations as for co-rotating VGs (see Section 3.1.1). The parameter $\frac{L}{h}$ was chosen at 2.5, corresponding to the optimum found by Godard. $\frac{L}{h} = 5$ was however tested at station 1 and 2 for $\frac{\lambda}{h} = 12$, $h = 15$ mm and $h = 30$ mm.

To be sure of the friction variation measured, the same methodology as for co-rotating VGs was used (see Section 3.1.1) to validate the experiments.

3.2.2 Results

3.2.2.1 General results

Table 4.2 presents all the passive counter-rotating cases investigated and the main conclusions obtained with wool tufts and friction probes. The legend for the state column (illustrated by Figure 4.14) is :
- FA = Fully Attached : no separation is seen on the wool tufts.
- PA = Partially Attached : a small separation is evidenced by the wool tufts.
- VPA = Very Partially Attached : a very small reduction of the separation is evidenced by the wool tufts.

Table 4.2: List of the counter-rotating configurations tested

Case	s (mm)	h (mm)	$\frac{L}{h}$	$\frac{\lambda}{h}$	state	$\frac{\Delta(\lvert\tau\rvert-\lvert\tau_0\rvert)}{\lvert\tau_0\rvert}(\%)$ $s = 3555mm$	$\frac{\Delta(\lvert\tau\rvert-\lvert\tau_0\rvert)}{\lvert\tau_0\rvert}(\%)$ $s = 3759mm$
29	3383	15	2.5	6	FA	142	71
30	3383	15	2.5	12	PA (BVG)	107	52
31	3383	15	2.5	24	VPA (BVG)	4	50
32	3383	15	5	12	VPA	49	31
33	3383	30	2.5	6	FA	133	84
34	3383	30	2.5	12	PA (BVG)	5	88
35	3383	30	2.5	24	VPA (BVG)	4	87
36	3383	30	5	12	PA	5	41
37	3383	60	2.5	6	PA (BVG)	8	107
38	3383	60	2.5	12	VPA (BVG)	1	115
39	3219	15	2.5	6	FA	88	13
40	3219	15	2.5	12	PA (BVG)	57	24
41	3219	15	2.5	24	PA (BVG)	-2	27
42	3219	15	5	12	PA	38	11
43	3219	30	2.5	6	FA	106	67
44	3219	30	2.5	12	PA (BVG)	1	84
45	3219	30	2.5	24	VPA (BVG)	-1	85
46	3219	30	5	12	PA	4	45
47	3219	60	2.5	6	PA (BVG)	6	81
48	3219	60	2.5	12	VPA (BVG)	0	95
49	2968	15	2.5	6	PA	55	-14
50	2968	30	2.5	6	FA	93	26
51	2968	60	2.5	6	FA	3	84
52	2440	15	2.5	6	VPA	36	-14
53	2440	30	2.5	6	PA	74	-8
54	2440	60	2.5	6	FA	13	60

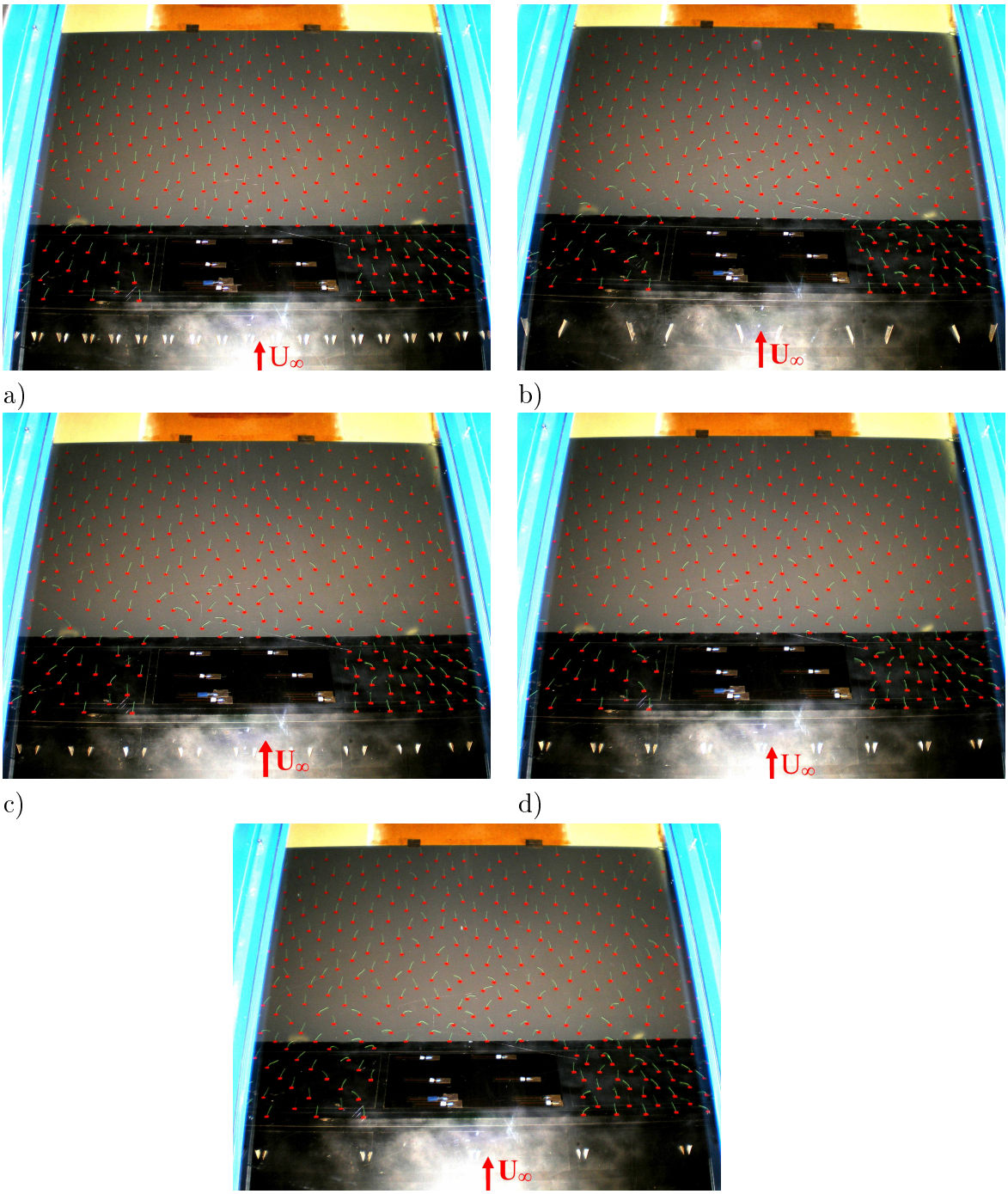

Figure 4.14: Wool tufts visualisation for a) FA (case 29), b) PA (case 36), c) VPA (case 32), d) PA (BVG) (case 30), e) VPA (BVG) (case 31).

- PA (BVG) = Partially Attached Between counter-rotating Vortex Generators : a small separation is evidenced by the wool tufts between two vortex generators. Behind the vortex generators, no separation is seen on the wool tufts.
- VPA (BVG) = Very Partially Attached Between counter-rotating Vortex Generators : a very small reduction of the separation is evidenced by the wool tufts between two vortex generators. Behind the vortex generators, no separation is seen on the wool tufts.

The last two columns of Table 4.2 contained the best quantitative control results obtained with friction probes at station $s = 3555$ mm (penultimate column) and station $s = 3759$ mm (last column). As can be seen, some passive counter-rotating configurations tested have suppressed totally the separation.

3.2.2.2 Effects of $\frac{\lambda}{h}$

Figure 4.15 to 4.20 presents the gain in friction and the skewness for different counter-rotating cases with different values of $\frac{\lambda}{h}$. As for the co-rotating configurations and for all the following figures, the spanwise friction probes position and a schematic top view of the VGs (which corresponds to the smallest $\frac{\lambda}{h}$ of the cases presented in the figure) are given at the bottom of the figures. To obtain the configuration with $\frac{\lambda}{h} = 12$, one pair of actuators over two was removed from the configuration with $\frac{\lambda}{h} = 6$, keeping the pair at the center, and etc. for the configuration with $\frac{\lambda}{h} = 24$.

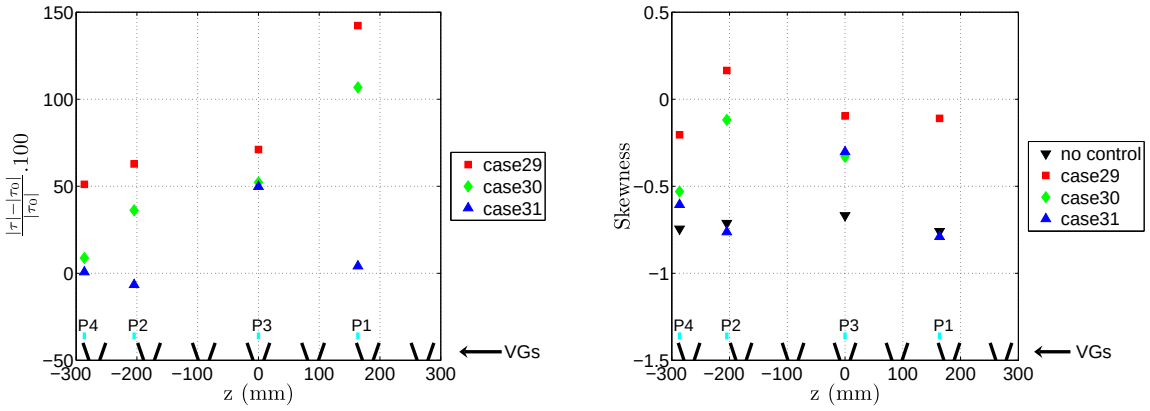

a) b)

h (mm)	β_{pd}	$\frac{l}{h}$	$\frac{L}{h}$	$\frac{\Delta X_{vg}}{h}$	$\frac{\lambda}{h}$:	case 29	case 30	case 31
15	±18°	2	2.5	7.8		6	12	24

Figure 4.15: a) Gain in friction and b) Skewness for cases 29, 30 and 31 (i.e. for three different values of $\frac{\lambda}{h}$ and the other parameters kept constant).

Cases 29 to 31, corresponding to $h = 15$ mm VGs at station 1 with all parameters constant except $\frac{\lambda}{h}$ are given in Figure 4.15. Case 29 ($\frac{\lambda}{h} = 6$) gives the best results. It gives an increase in friction for all the probes, accompanied with an increase in skewness (for the uncontrolled flow the skewness is around -0.7 as seen in Section 2).

This means that the separation is totally suppressed. Cases 39 to 41 correspond to the same VGs configurations but at station 2 (Figure 4.16). The same conclusions can be drawn, however, the control efficiency has decreased. For $h = 15$ mm, it seems that the optimum $\frac{\lambda}{h}$ is 6 as was found by Godard and Stanislas (2006a).

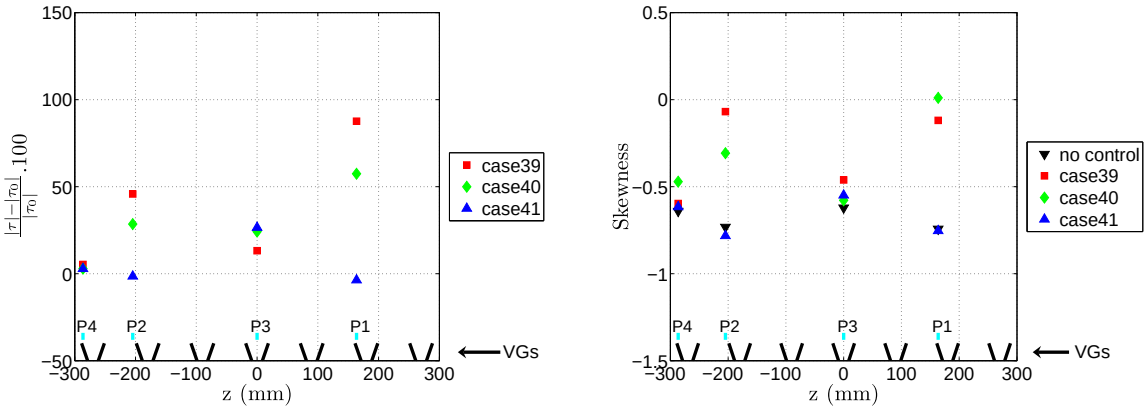

h (mm)	β_{pd}	$\frac{l}{h}$	$\frac{L}{h}$	$\frac{\Delta X_{vg}}{h}$	$\frac{\lambda}{h}$:	case 39	case 40	case 41
15	±18°	2	2.5	18.7		6	12	24

Figure 4.16: a) Gain in friction and b) Skewness for cases 39, 40 and 41 (i.e. for three different values of $\frac{\lambda}{h}$ and the other parameters kept constant).

Cases 33 to 35, correspond to three different value of $\frac{\lambda}{h}$ for $h = 30$ mm at station 1 (Figure 4.17). Case 33 ($\frac{\lambda}{h} = 6$) gives the best results. The separation is also totally suppressed. Cases 43 to 45 correspond to the same VGs configuration but at station 2 (Figure 4.18). The same conclusions can be drawn but as for the $h = 15$ mm actuators, the control efficiency has slightly decreased. For $h = 30$ mm, it seems that the optimum $\frac{\lambda}{h}$ is also 6 as was found by Godard and Stanislas (2006a).

Cases 37 and 38, correspond to three different value of $\frac{\lambda}{h}$ for $h = 60$ mm at station 1 (Figure 4.19). Case 37 ($\frac{\lambda}{h} = 6$) gives the best results. The separation is also totally suppressed. Finally, cases 47 and 48 correspond to the same VGs configurations but at station 2 (Figure 4.20). The same conclusions can be drawn. For $h = 60$ mm, it seems that, as for the two other actuators height tested, the optimum $\frac{\lambda}{h}$ is 6 as was found by Godard and Stanislas (2006a).

The conclusion for $\frac{\lambda}{h}$ is then the same as in Godard and Stanislas (2006a). The optimum seems to be 6 and independent of the value of $\frac{\Delta X_{vg}}{h}$. This value is the same as the optimum value obtained for co-rotating passive VGs at an optimum value of $\frac{\Delta X_{vg}}{h}$.

3.2.2.3 Effects of $\frac{\Delta X_{vg}}{h}$

Figure 4.21 shows the gain in friction and the skewness at the four control stations for $h = 15$ mm and $\frac{\lambda}{h} = 6$. The best results are obtained at station 1, corresponding to $\frac{\Delta X_{vg}}{h} = 7.8$. Figure 4.22 shows the corresponding configurations for $h = 30$ mm

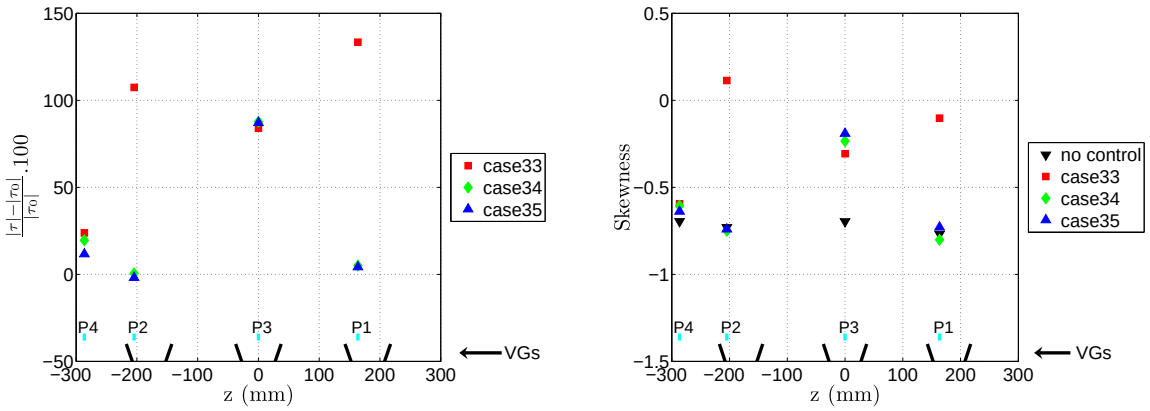

a) b)

h (mm)	β_{pd}	$\frac{l}{h}$	$\frac{L}{h}$	$\frac{\Delta X_{vg}}{h}$	$\frac{\lambda}{h}$:	case 33	case 34	case 35
30	±18°	2	2.5	3.9		6	12	24

Figure 4.17: a) Gain in friction and b) Skewness for cases 33, 34 and 35 (i.e. for three different values of $\frac{\lambda}{h}$ and the other parameters kept constant).

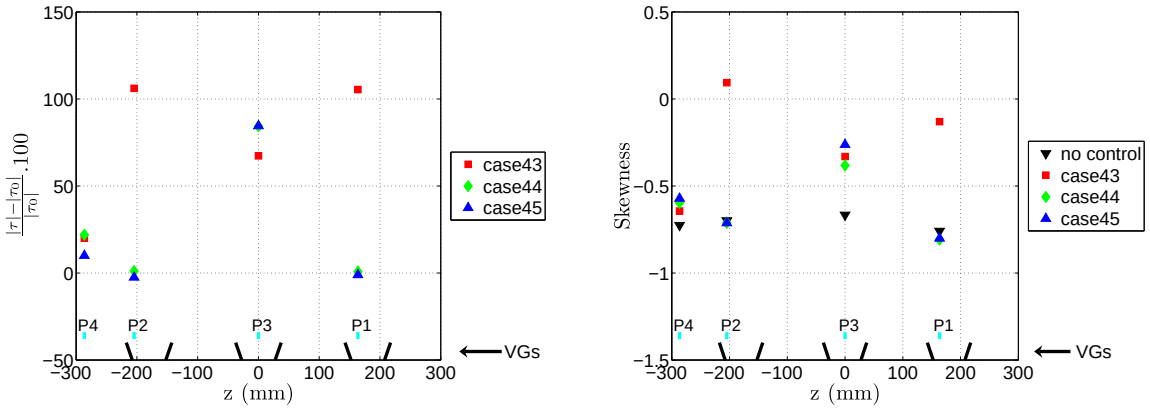

a) b)

h (mm)	β_{pd}	$\frac{l}{h}$	$\frac{L}{h}$	$\frac{\Delta X_{vg}}{h}$	$\frac{\lambda}{h}$:	case 43	case 44	case 45
30	±18°	2	2.5	9.4		6	12	24

Figure 4.18: a) Gain in friction and b) Skewness for cases 43, 44 and 45 (i.e. for three different values of $\frac{\lambda}{h}$ and the other parameters kept constant).

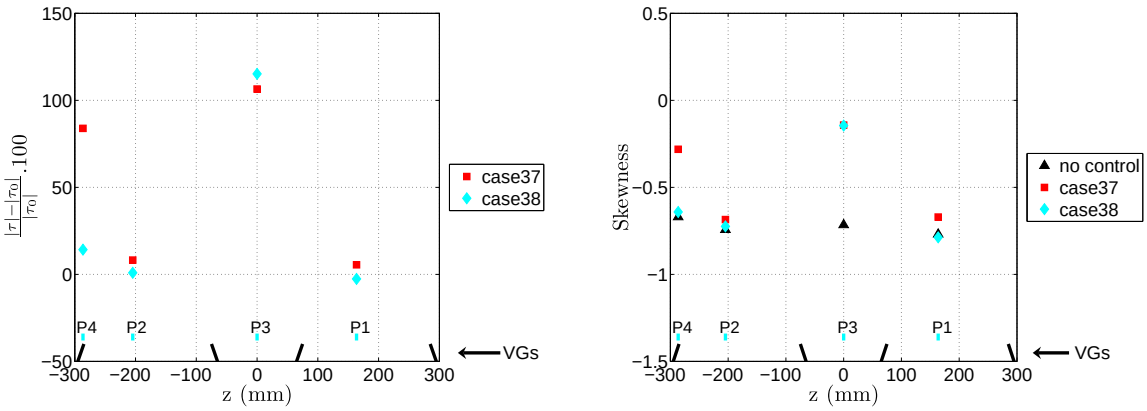

a) b)

h (mm)	β_{pd}	$\frac{l}{h}$	$\frac{L}{h}$	$\frac{\Delta X_{vg}}{h}$	$\frac{\lambda}{h}$:	case 37	case 38
60	±18°	2	2.5	2		6	12

Figure 4.19: a) Gain in friction and b) Skewness for cases 37 and 38 (i.e. for two different values of $\frac{\lambda}{h}$ and the other parameters kept constant).

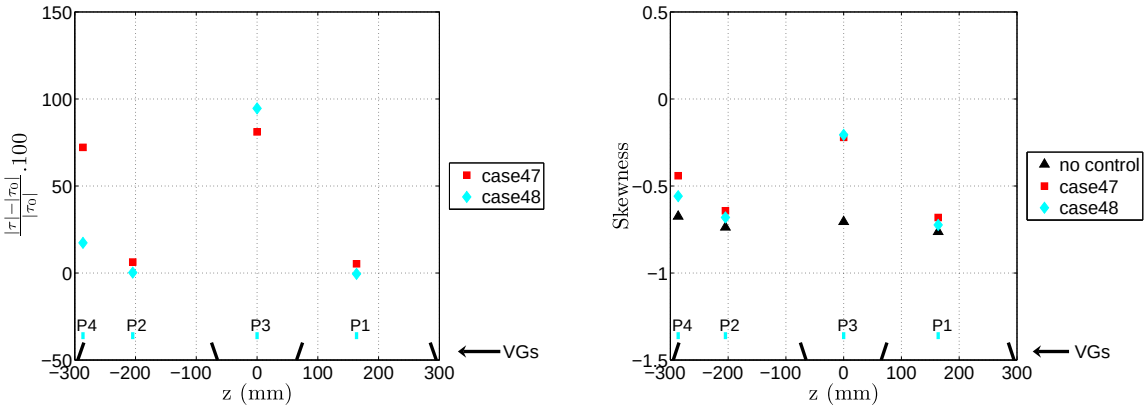

a) b)

h (mm)	β_{pd}	$\frac{l}{h}$	$\frac{L}{h}$	$\frac{\Delta X_{vg}}{h}$	$\frac{\lambda}{h}$:	case 47	case 48
60	±18°	2	2.5	4.7		6	12

Figure 4.20: a) Gain in friction and b) Skewness for cases 47 and 48 (i.e. for two different values of $\frac{\lambda}{h}$ and the other parameters kept constant).

and $\frac{\lambda}{h} = 6$. Station 1 and 2 give almost the same results. After station 2, the control efficiency decreases. For $h = 30$ mm, station 1 corresponds to $\frac{\Delta X_{vg}}{h} = 3.9$ and station 2 to $\frac{\Delta X_{vg}}{h} = 9.4$. Finally, Figure 4.23 shows the same plots for $h = 60$ mm and $\frac{\lambda}{h} = 6$. The best results are obtained at station 3, corresponding to $\frac{\Delta X_{vg}}{h} = 8.9$. However, station 4 seems to be more homogeneous, but the control efficiency begin to decrease compared to station 3.

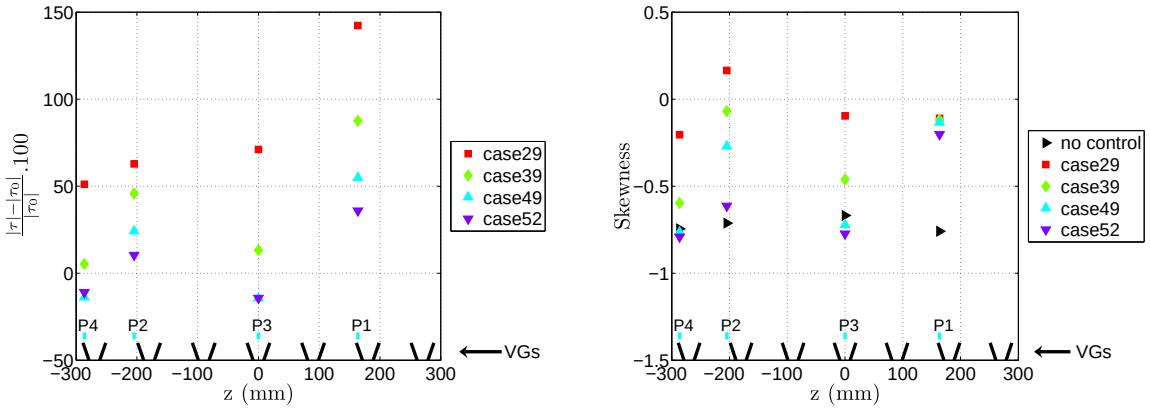

a) b)

h (mm)	β_{pd}	$\frac{l}{h}$	$\frac{L}{h}$	$\frac{\lambda}{h}$	$\frac{\Delta X_{vg}}{h}$:	case 29	case 39	case 49	case 52
15	±18°	2	2.5	6		7.8	18.7	35.5	70.7

Figure 4.21: a) Gain in friction and b) Skewness for cases 29, 39, 49 and 52 (i.e. for four different values of $\frac{\Delta X_{vg}}{h}$ and the other parameters kept constant).

As a conclusion, the best parameter found for $\frac{\Delta X_{vg}}{h}$ is between 4 and 10 and seems to be near 8. This is the same optimum value that was found for co-rotating passive VGs. This value is in agreement with Lin (1999), but not with Betterton et al. (2000) and Angele (2003), Angele and Muhammad-Klingmann (2005), Angele and Grewe (2007). Betterton and Angele have concluded that the passive counter-rotating control is efficient for $17 < \frac{\Delta X_{vg}}{h} < 52$, which is not the case here. For Angele and Muhammad-Klingmann (2005), to suppress a separation, the circulation parameter Γ ($\Gamma = \frac{Z}{\lambda}.h.U_{(y=h)}$, where Z is the span of control, $U_{(y=h)}$ is the streamwise velocity at the distance h from the wall and at the position of the VGs and $\frac{Z}{\lambda}$ is the number of VGs placed on the span of the wind-tunnel) has to be greater than 2.7 m^2/s and the parameter $\frac{\Delta X_{vg}}{h}$ has to be greater than 17 so that the vortices become equidistant. Here Γ is almost constant for the four control stations and larger than 2.7 m^2/s. It is 3.1 m^2/s for $h = 15$ mm, 3.4 m^2/s for $h = 30$ mm and 3.7 m^2/s for $h = 60$ mm. It appears clearly that the conclusions of Angele do not applied here, maybe, because Angele studied VGs of the size of δ which can have different behaviour than submerged VGs as was supposed in Chapter 1. The difference in conclusions for $\frac{\Delta X_{vg}}{h}$ from one study to an other can also be attributed to the differences in the flow under study, as the adverse pressure gradient in the present study is small compared to the studies of Angele (2003), Angele and Muhammad-Klingmann (2005), Angele and Grewe (2007), Betterton et al. (2000).

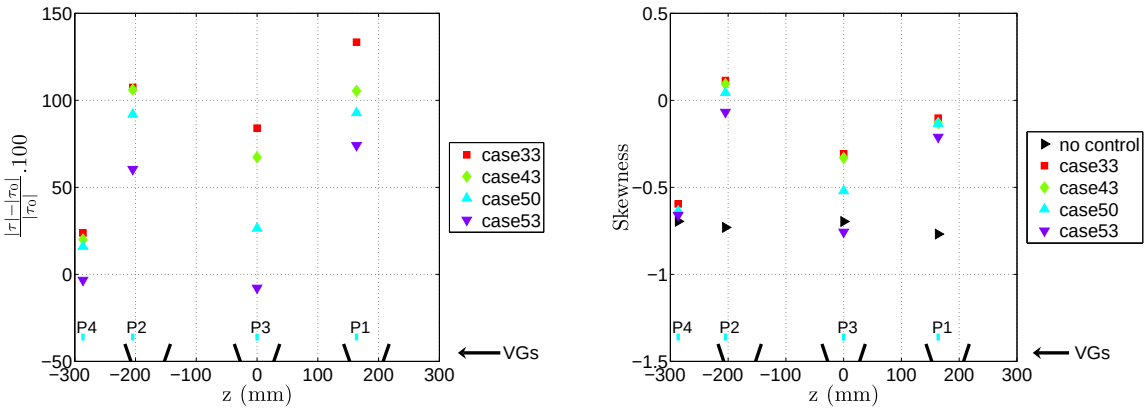

a) b)

h (mm)	β_{pd}	$\frac{l}{h}$	$\frac{L}{h}$	$\frac{\lambda}{h}$	$\frac{\Delta X_{vg}}{h}$:	case 33	case 43	case 50	case 53
30	±18°	2	2.5	6		3.9	9.4	17.8	35.3

Figure 4.22: a) Gain in friction and b) Skewness for cases 33, 43, 50 and 53 (i.e. for four different values of $\frac{\Delta X_{vg}}{h}$ and the other parameters kept constant).

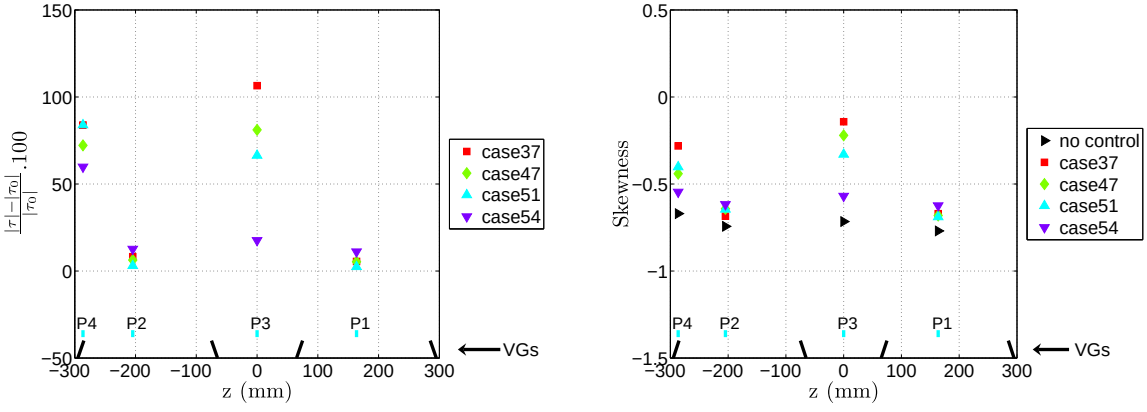

a) b)

h (mm)	β_{pd}	$\frac{l}{h}$	$\frac{L}{h}$	$\frac{\lambda}{h}$	$\frac{\Delta X_{vg}}{h}$:	case 37	case 47	case 51	case 54
60	±18°	2	2.5	6		2	4.7	8.9	17.7

Figure 4.23: a) Gain in friction and b) Skewness for cases 37, 47, 51 and 54 (i.e. for four different values of $\frac{\Delta X_{vg}}{h}$ and the other parameters kept constant).

3.2.2.4 Effects of $\frac{L}{h}$

Figure 4.24 shows the gain in friction and the skewness at stations 1 and 2 for $h = 15$ mm, $\frac{\lambda}{h} = 12$ and $\frac{L}{h} = 2.5$ and 5. At the bottom of the figure, a schematic top view of the VGs is represented which corresponds to $\frac{\lambda}{h} = 12$ and $\frac{L}{h} = 2.5$. The center of the passive counter-rotating VGs pair with $\frac{L}{h} = 5$ were the same as for $\frac{L}{h} = 2.5$. It appears that the best results are obtained for $\frac{L}{h} = 2.5$ (case 30 compared to case 32 and case 40 compared to case 42). Figure 4.25 shows the results at stations 1 and 2 for $h = 30$ mm, $\frac{\lambda}{h} = 12$ and $\frac{L}{h} = 2.5$ and 5. The same conclusions as for $h = 15$ mm are obtained.

So, the optimum parameter for $\frac{L}{h}$ seems to be 2.5 as was found by Godard and Stanislas (2006a).

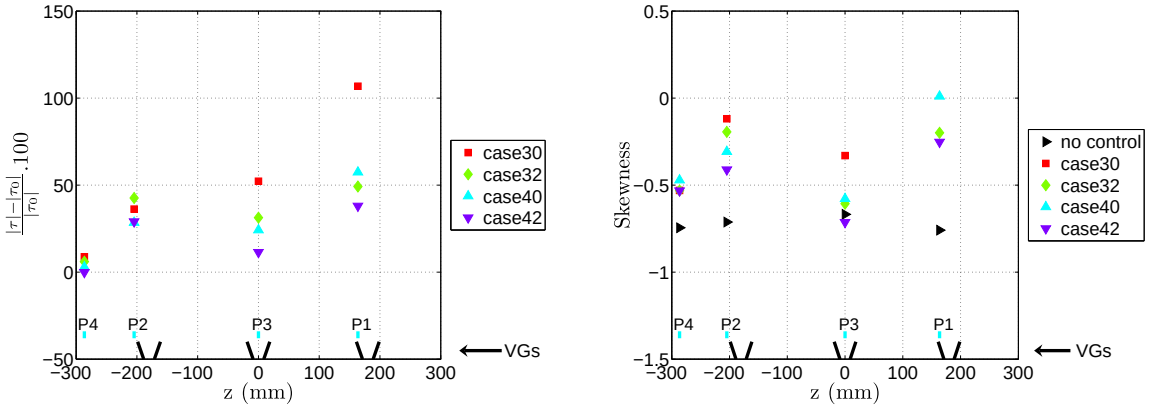

h (mm)	β_{pd}	$\frac{l}{h}$	$\frac{\lambda}{h}$	$\frac{\Delta X_{vg}}{h}$:	case 30 & 32	case 40 & 42	$\frac{L}{h}$:	case 30 & 40	case 32 & 42
15	±18°	2	12		7.8	18.7		2.5	5

Figure 4.24: a) Gain in friction and b) Skewness for cases 30, 32, 40 and 42 (i.e. for two different values of $\frac{L}{h}$ and $\frac{\Delta X_{vg}}{h}$, and the other parameters kept constant).

3.2.2.5 Effects of $\frac{h}{\delta}$

Figure 4.26 shows the gain in friction and the skewness for 3 values of $\frac{h}{\delta}$ (0.08, 0.15 and 0.28) with $\frac{\lambda}{h} = 6$, $\frac{L}{h} = 2.5$ and $\frac{\Delta X_{vg}}{h} \simeq 8-9$. It appears that the best parameter of $\frac{h}{\delta}$ is between 0.08 and 0.15, but nearer to 0.08 (which corresponds to $h^+ \simeq 450$). This value is in agreement with the value found by Lin (1999), but four times lower than the Godard and Stanislas (2006a) one. The optimum $\frac{h}{\delta}$ value found by these authors, which optimizes the gain in friction and the induced drag, differs then to the optimum value that gives the best control effect on a separation.

3.2.3 Conclusion

In this study, it was shown that counter-rotating passive VGs can totally suppress the separation. The optimum parameters that were found are almost in good agreement with the previous studies of Lin (1999) and Godard and Stanislas (2006a). It

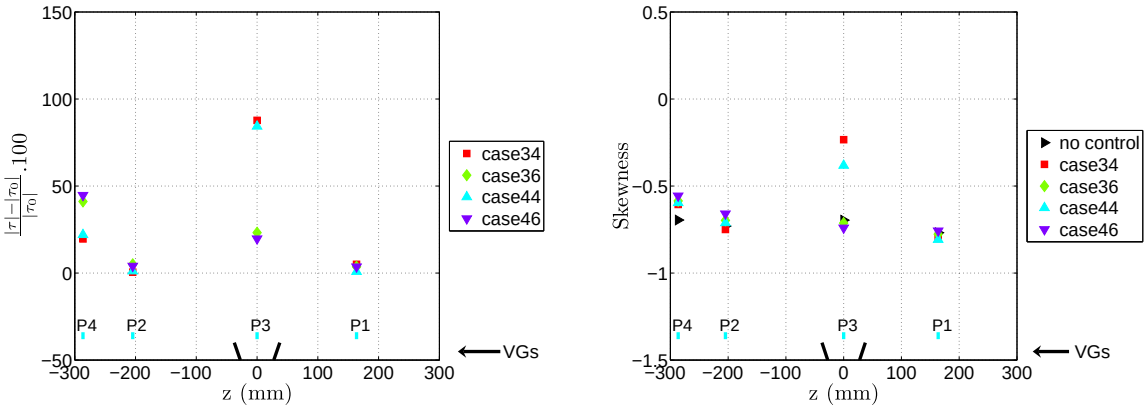

h (mm)	β_{pd}	$\frac{l}{h}$	$\frac{\lambda}{h}$	$\frac{\Delta X_{vg}}{h}$:	case 34 & 36	case 44 & 46	$\frac{L}{h}$:	case 34 & 44	case 36 & 46
30	±18°	2	12		3.9	9.4		2.5	5

Figure 4.25: a) Gain in friction and b) Skewness for cases 34, 36, 44 and 46 (i.e. for two different values of $\frac{L}{h}$ and $\frac{\Delta X_{vg}}{h}$, and the other parameters kept constant).

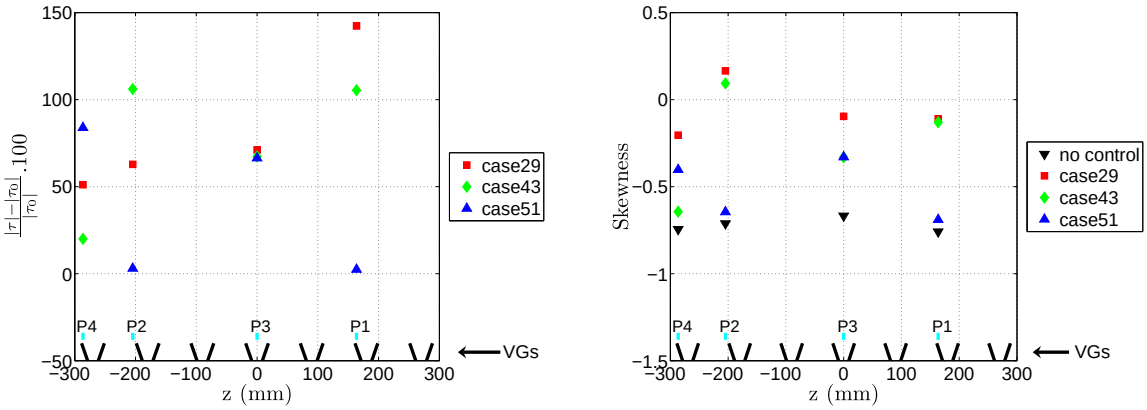

β_{pd}	$\frac{l}{h}$	$\frac{L}{h}$	$\frac{\lambda}{h}$	$\frac{\Delta X_{vg}}{h}$	h (mm) :	case 29	case 43	case 51	$\frac{\Delta X_{vg}}{h}$:	case 29	case 43	case 51
±18°	2	2.5	6	$\simeq 8-9$		15	30	60		7.8	9.4	8.9

Figure 4.26: a) Gain in friction and b) Skewness for cases 29, 43 and 51 (i.e. for three different values of $\frac{h}{\delta}$ (or h) and the other parameters kept constant).

was found that the optimum value of $\frac{\Delta X_{vg}}{h}$ is 8 and that the best $\frac{h}{\delta}$ is between 0.08 and 0.15, but nearer to 0.08 (which corresponds to $h^+ \simeq 450$). It was also found that the optimum value is 6 for $\frac{\lambda}{h}$ and 2.5 for $\frac{L}{h}$. Finally, it was shown that these optimum values seem dependant on the flow under study because some differ slightly from previous studies of Godard and Stanislas (2006a), Betterton et al. (2000), Angele (2003), Angele and Muhammad-Klingmann (2005), Angele and Grewe (2007).

4 Conclusion

Co and counter-rotating triangular vane-type passive actuators have been tested. The first aim of these tests was to be sure that it was possible to suppress the separation with flow control, and secondly they were done to build a criterion to quantify the control effects. It was found that an increase in skewness of the output voltage of a friction probe placed on the flap corresponds to a reduction of the separation, and a skewness greater than -0.4 was found characteristic of reattachment.

Then, a parametric study of these submerged VGs was performed to validate the conclusions of Godard and Stanislas (2006a) as their conclusions were based only on the increase of friction in an adverse pressure gradient flow without separation. It was found that the counter-rotating configurations give the best results and were the only ones that can totally suppress the separation. It is in agreement with previous studies as passive counter-rotating configurations have been found more effective than co-rotating ones (Betterton et al. (2000), Godard and Stanislas (2006a), etc.). The optimum parameters that were found are almost in good agreement with those found by Lin (1999) and Godard and Stanislas (2006a). These optimum parameters are (for both co and counter-rotating arrangement) : $\frac{\Delta X_{vg}}{h} = 8$, $\frac{\lambda}{h} = 6$ and $\frac{h}{\delta} = 0.08-0.15$. For the counter-rotating actuators, the optimum $\frac{L}{h}$ is 2.5. These optimum parameters are summarized in Table 4.3, where the bold parameters correspond to the best of the best.

Table 4.3: Optimum parameters for co and counter-rotating passive configurations tested.

	β	$\frac{h}{\delta}$	$\frac{l}{h}$	$\frac{L}{h}$	$\frac{\lambda}{h}$	$\frac{\Delta X_{vg}}{h}$
co-rotating	18°	0.08 - **0.15**	2	-	6	8
counter-rotating	±18°	**0.08** - 0.15	2	2.5	6	8

Chapter 5

Active flow control

1 Introduction

This chapter presents the results of the parametric study of active control with round jets vortex generators (VGs). As for the passive devices, all the tests were realized at $U_\infty = 10$ m/s on the ramp configuration with $\alpha = -2°$ and $\beta = -22°$ (which corresponds to an adverse pressure gradient on the flat plate and a flow separation on the flap (see Chapter 3)). The VGs that were used are described in Chapter 2. Active control strategies have been tested as they present an important issue for real flow control applications as was discussed in Chapter 1. This chapter presents the results concerning the optimisation of steady co and counter-rotating round jets VGs. The active control efficiency was quantified with the same tools as for the passive devices in Chapter 4 (i.e. with the gain in friction and in skewness on the four friction probes fixed on the flap and with wool tufts visualisations). The velocity ratio VR was measured and tuned by the flow rate regulation and quantification circuit described in Chapter 2. First of all, the jet exits were characterized to be sure that all jets were similar, then the parametric study was performed.

2 Jets characterisation

As the total mass flow rate Q_m was measured by the flow rate regulation and quantification circuit (see Chapter 2) better than $\pm 2\%$, the jets velocity ratio VR was defined with the mean jet velocity V_{mean} (i.e. $VR = \frac{V_{mean}}{U_e}$, where U_e is the free-stream velocity at the position of the actuators). V_{mean} is obtained from Q_m by supposing that the total mass flow rate is dispatched uniformly among the jets. Jets exit characterisation was performed to check this hypothesis.

The 12 mm jets exit temperature was measured with a PT 100 sensor for flow rate between 10 m^3/h and 400 m^3/h, corresponding to the minimum and maximum flow rate used in the active control tests. No significant difference between the jets exit temperature and the compressed air temperature measured just after the vortex meters (see Chapter 2) was observed. In the control tests, the compressed air temperature was then taken as the jets exit temperature. The equality of these two temperatures can be explained by two facts. First, there is no heat exchange

after the vortex meters between the room and the jets compressed air due to the small residence time between the vortex meters and the output (less than 30 s for the minimum flow rate used). Also, the compressed air undergoes a very small expansion (the maximum pressure needed in the control tests was 1.2 bars absolute at the vortex meters).

The pressure at the jets exit is the local pressure in the test section, which is close to the atmospheric one (the differences is less than 6 mm H_20), so V_{mean} is given by : $V_{mean} = \frac{Q_v.P}{N_{jet}.S_{jet}.P_a}$, where Q_v is the volumetric flow rate given by the vortex meter, P_a the atmospheric pressure, P the pressure at the vortex meter, N_{jet} the number of jets and S_{jet} the cross section of one jet (the temperature disappears as the jets exit temperature was found equal to the compressed air temperature at the vortex meter).

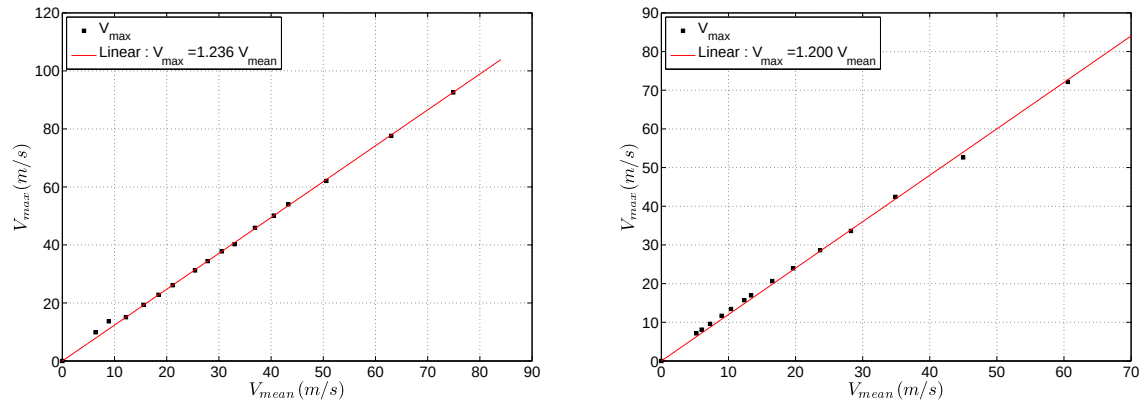

a) b)

Figure 5.1: V_{max} versus V_{mean} for a) the 6 mm, b) the 12 mm jets.

To be sure that there is no difference between the jets, only the maximum jet exit velocity (V_{max}) was measured for each jet and for 3 flow rates (corresponding to VR = 0.5, 3 and 5) with a total pressure probe at one internal diameter from the jet exit and connected to a Furness FC014 (0-1000 mm H_20 with an accuracy of ±0.5% of the measuring value between 1 and 1000 mm H_20). The probe was moved across the jet and the maximum value observed was taken as the maximum exit velocity. For the 12 mm jets, it was found that the maximum relative difference on the maximum exit velocity between jets is less than 10 % whatever VR between 0.5 and 5 and whatever the arrangement of the jets (co or counter-rotating configurations). This variation can be considered as negligible because a part of this variation is due to the large uncertainty on the maximum exit velocity estimated at ±5%. This difference tends to increase with VR, that is logical because it was impossible to obtain the same curvature on all the tubes that supply the jets, so the pressure drop is slightly different from one tube to an other, which gives differences on the flow rate repartition between tubes.

For the 6 mm internal diameter, it was found that the maximum relative difference on the maximum exit velocity between jets is less than ±2% whatever is VR between 0.5 and 5 and whatever the arrangement of the jets (co or counter-rotating configurations). This difference is almost constant with VR.

In conclusion, no significant difference was observed between the jets for all the configurations investigated. The maximum jet exit velocity and the mean jet exit velocity for all the jets depend then only on the mass flow rate measured. Figure 5.1 gives the relation between V_{max} and V_{mean} for the 6 mm and 12 mm internal diameter jets. It appears that for the two diameters, this relation is linear with a director coefficient of 1.236 for the 6 mm and of 1.200 for the 12 mm.

3 Active control results

3.1 Co-rotating configurations

3.1.1 Tests description

Figure 1.6 a) shows the arrangement of active VGs for co-rotating configurations. Based on the study of Godard and Stanislas (2006b), the optimum $\frac{\lambda}{\Phi}$ is 6. It was then decided to test the effects of this parameter for a starting values near 6. The values of $\frac{\lambda}{\Phi}$ tested were 6.8, 13.6, 20.4 and 27.2 for $\Phi = 12$ mm and $\alpha = 125°$. For $\alpha = 55°$ and $\Phi = 12$ mm, only $\frac{\lambda}{\Phi} = 6.8$ and 13.6 were tested. For $\Phi = 6$, only $\frac{\lambda}{\Phi} = 13.6$ and 27.2 were tested. All these configurations were tested at control stations 1 ($s = 3383$ mm) and 2 ($s = 3219$ mm). For each configuration, the velocity ratio VR was varying between 0.5 and 3.5 by steps of 0.5.

To be sure of the wall friction measured, for each configuration (i.e for one Φ, one $\frac{\lambda}{\Phi}$ and one α), one reference with VR = 0 was taken first, then the case with the smallest VR was tested then the second one etc., until reaching VR = 3.5. Then a final reference was taken with VR = 0. If these two references were the same within $\pm 5\%$, the test was validated.

3.1.2 Results

3.1.2.1 General results

Table 5.1 presents all the co-rotating active cases investigated and the main conclusions obtained with wool tufts and friction probes. The legend for the state column (illustrated by Figure 5.2) is :
- FA = Fully Attached : no separation was seen on the wool tufts.
- PA = Partially Attached : a small separation was evidenced by the wool tufts.
- VPA = Very Partially Attached : a very small reduction of the separation was evidenced by the wool tufts.
- S = Separated : no reduction of the separation was seen on the wool tufts.
- FA (JD) = Fully Attached (Jets Direction) : no separation was seen on the wool tufts, but the wool tufts took the direction of the jets.

The last two columns of Table 5.1 contained the best quantitative results obtained with friction probes at station $s = 3555$ mm (penultimate column) and station $s = 3759$ mm (last column). As can be seen, some co-rotating configurations tested can suppress totally the separation.

Table 5.1: List of the co-rotating configurations tested

Case	s (mm)	Φ (mm)	α (°)	$\frac{\lambda}{\Phi}$	VR (best)	state	$\frac{\lvert\tau\rvert-\lvert\tau_0\rvert}{\lvert\tau_0\rvert}(\%)$	
							$s = 3555mm$	$s = 3759mm$
1	3383	12	125	6.8	2.5	FA (JD)	44	-25
2	3383	12	125	13.6	3	FA	94	10
3	3383	12	125	20.4	3.5	PA	102	-17
4	3383	12	125	27.2	3.5	VPA	86	-20
5	3383	12	55	6.8	2.5	FA (JD)	115	11
6	3383	12	55	13.6	1.5	PA	40	-6
7	3383	6	125	13.6	3	FA	101	-18
8	3383	6	125	27.2	3.5	PA	90	-20
9	3383	6	55	13.6	2	PA	80	-17
10	3383	6	55	27.2	2	VPA	45	-10
11	3219	12	125	6.8	3	FA (JD)	32	-26
12	3219	12	125	13.6	3.5	FA	79	44
13	3219	12	125	20.4	3.5	PA	71	-17
14	3219	12	125	27.2	3.5	VPA	71	-10
15	3219	12	55	6.8	2	FA (JD)	86	30
16	3219	12	55	13.6	2	PA	39	-10
17	3219	6	125	13.6	3.5	FA	68	10
18	3219	6	125	27.2	3.5	PA	62	-23
19	3219	6	55	13.6	2	PA	62	-13
20	3219	6	55	27.2	2	S	29	-9

Figure 5.2: Wool tufts visualisation for a) FA (case 17), b) PA (case 6), c) VPA (case 4), d) S (case 20), e) FA (JD) (case 5).

3.1.2.2 Effects of VR

The control effects was found largely depend of the velocity ratio VR (see Section 2 for the definition of VR). For $\alpha = 125°$ (i.e. upstream blowing), 2 distinct behaviours were observed depending on the value of $\frac{\lambda}{\Phi}$. First, for $\frac{\lambda}{\Phi} \geq 13.6$, it was found that increasing the velocity ratio VR increased the efficiency of control (i.e increasing VR gives an increase in skewness). This is illustrated by Figures 5.3, 5.4 and 5.5 which present the gain in friction and skewness obtained for different control cases on the four friction probes and for all the VR tested, versus the spanwise direction z. As for the passive tests, the spanwise position of the friction probes and a schematic view of the jets axis position projected in (oyz) plane are represented in the bottom of the figures (this will be also the case for all the following figures in this chapter). The beginning of the jets axis lines correspond to the spanwise jets position. It was checked rapidly, with only wool tufts visualisations, if it exits a maximum of control efficiency with VR. For value of VR around 8-10, the efficiency of the control seems to increase again. In all the cases investigated with $\frac{\lambda}{\Phi} \geq 13.6$ and $\alpha = 125°$, a total suppression of the separation was reached by increasing VR.

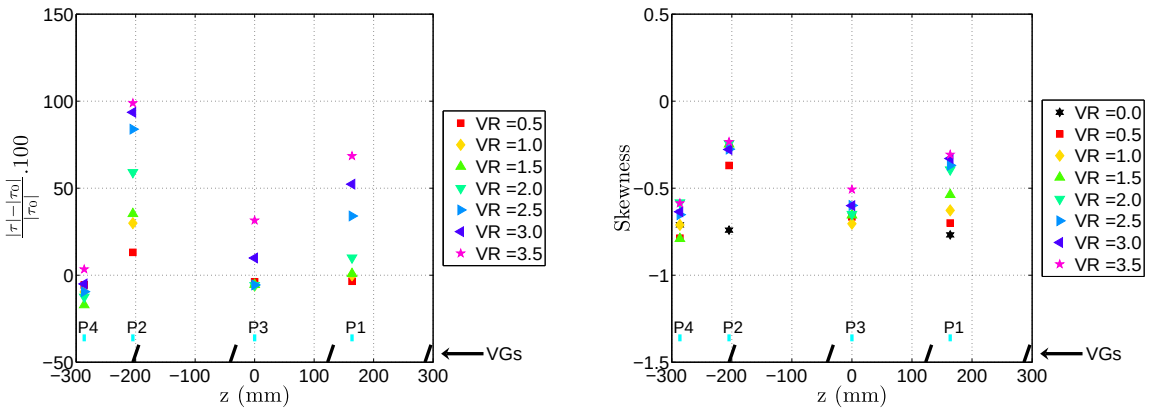

a) b)

case	Φ (mm)	β	α	$\frac{\lambda}{\Phi}$	$\frac{\Delta X_{vg}}{\Phi}$	VR :
2	12	35°	125°	13.6	9.8	0.5 - 3.5

Figure 5.3: a) Gain in friction and b) Skewness for case 2 (i.e. for different values of VR and the other parameters kept constant).

Secondly, for $\frac{\lambda}{\Phi} = 6.8$ and $\alpha = 125°$, it was found that increasing the velocity ratio VR from 0.5 to 2.5 increases the control efficiency, but after $VR = 2.5$, increasing VR decreases the efficiency and for VR greater than 2, the wool tufts take the direction of the jets. This means that the flow has been rearranged but this does not correspond to a good control result. In fact, the reattachment is defined by a total suppression of reverse flow, but here the flow seems to be skewed in the z direction. This result is illustrated in Figures 5.6 and 5.7 where an increase in skewness with VR is observed for VR less than 2.5 and a drop in skewness with VR after 2.5. Figure 5.8 gives the power spectrum for friction probes number P3 and P4 for cases 1 ($\frac{\lambda}{\Phi} = 6.8$) and 2 ($\frac{\lambda}{\Phi} = 13.6$) and VR between 2 and 3.5. As was seen

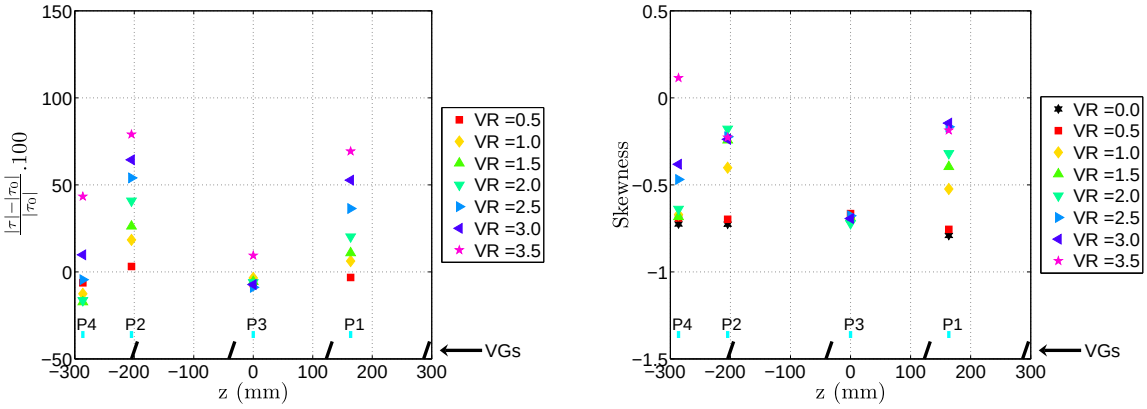

a) b)

case	Φ (mm)	β	α	$\frac{\lambda}{\Phi}$	$\frac{\Delta X_{vg}}{\Phi}$	VR :
12	12	35°	125°	13.6	23.4	0.5 - 3.5

Figure 5.4: a) Gain in friction and b) Skewness for case 12 (i.e. for different values of VR and the other parameters kept constant).

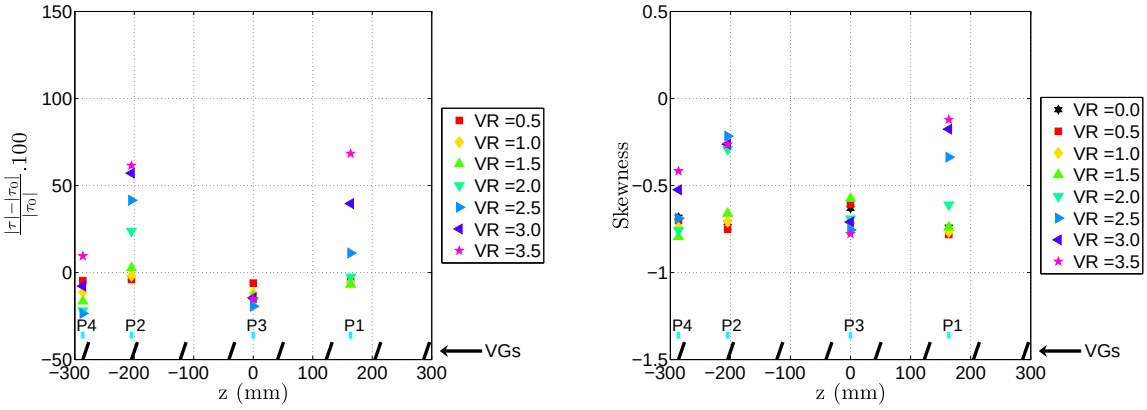

a) b)

case	Φ (mm)	β	α	$\frac{\lambda}{\Phi}$	$\frac{\Delta X_{vg}}{\Phi}$	VR :
17	6	35°	125°	13.6	46.8	0.5 - 3.5

Figure 5.5: a) Gain in friction and b) Skewness for case 17 (i.e. for different values of VR and the other parameters kept constant).

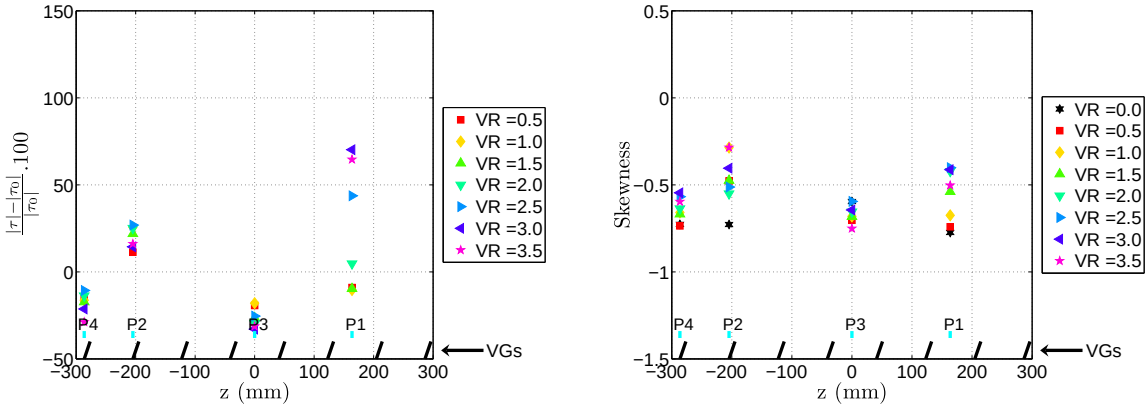

a) b)

case	Φ (mm)	β	α	$\frac{\lambda}{\Phi}$	$\frac{\Delta X_{vg}}{\Phi}$	VR :
1	12	35°	125°	6.8	9.8	0.5 - 3.5

Figure 5.6: a) Gain in friction and b) Skewness for case 1 (i.e. for different values of VR and the other parameters kept constant).

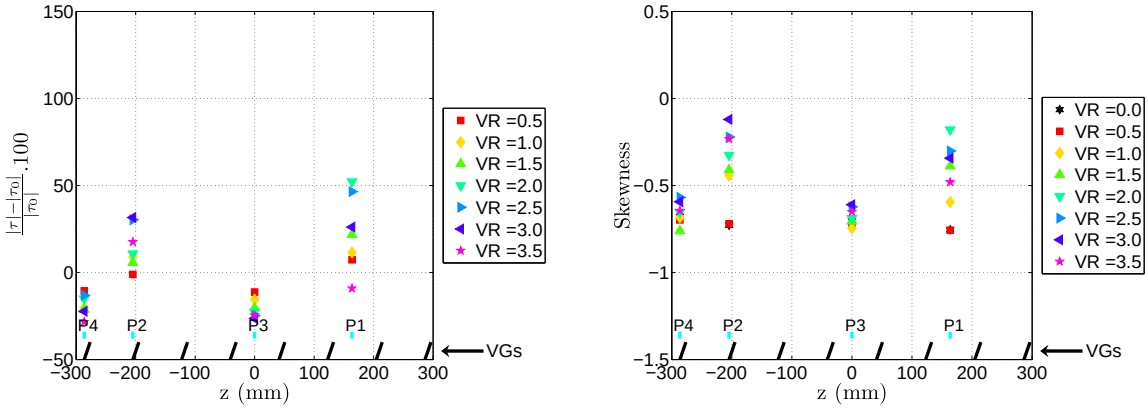

a) b)

case	Φ (mm)	β	α	$\frac{\lambda}{\Phi}$	$\frac{\Delta X_{vg}}{\Phi}$	VR :
11	12	35°	125°	6.8	23.4	0.5 - 3.5

Figure 5.7: a) Gain in friction and b) Skewness for case 11 (i.e. for different values of VR and the other parameters kept constant).

in Section 2 in Chapter 4, the control efficiency is evidenced on the spectrum by an increase of the power spectrum for frequencies greater than 100 Hz. This is not the case for case 1 whereas it is true for case 2. For case 1, the power spectrum decreased with VR for frequencies greater than 100 Hz. This shows that this result cannot be considered as a good control, even for the optimum VR found for the cases with $\frac{\lambda}{\Phi} = 6.8$ and $\alpha = 125°$ (cases 1 and 11).

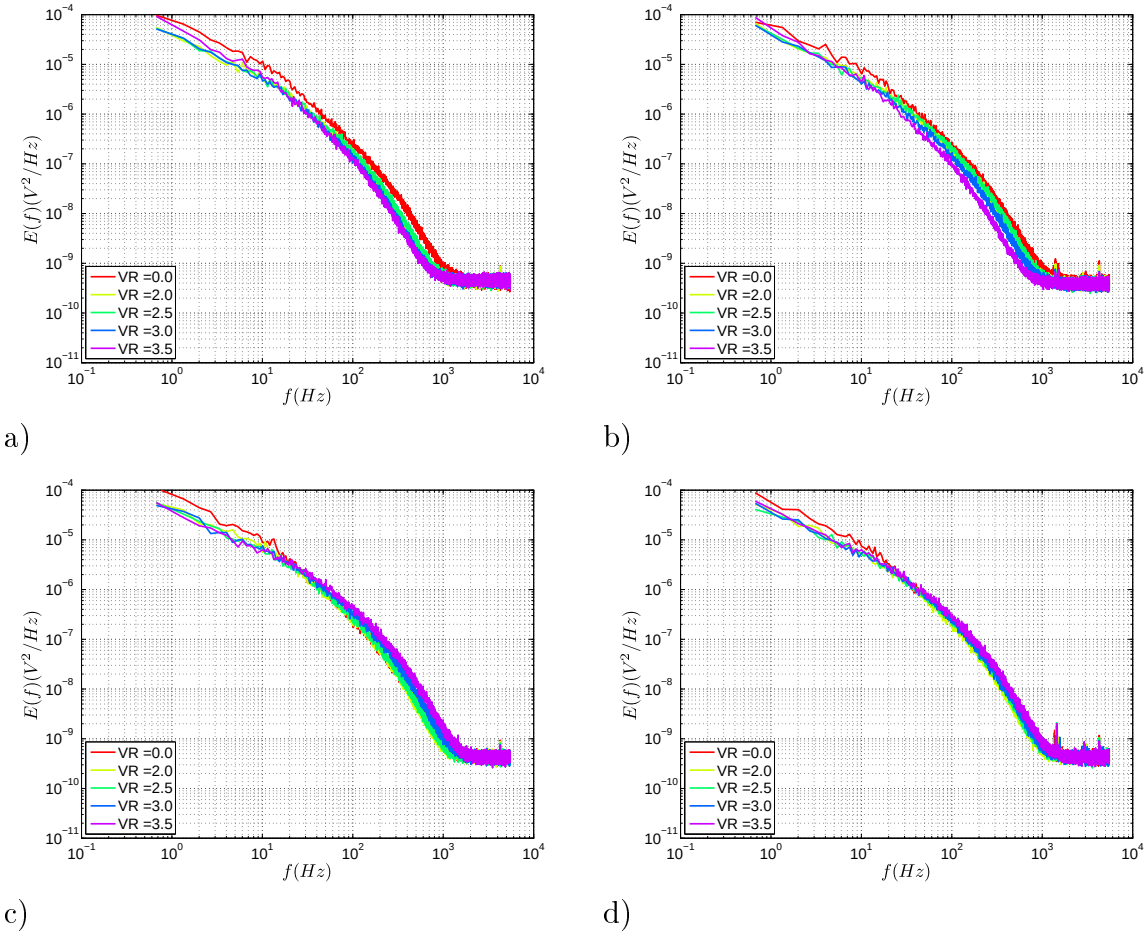

Figure 5.8: Power spectrum of friction probes output voltage for probes a) P3 and case 1 ($\frac{\lambda}{\Phi} = 6.8$), b) P4 and case 1, c) P3 and case 2 ($\frac{\lambda}{\Phi} = 13.6$), d) P4 and case 2, $VR = 2$ to 3.5.

For $\alpha = 55°$ (i.e. downstream blowing), here again, two distinct behaviours were observed depending on the value of $\frac{\lambda}{\Phi}$. For $\frac{\lambda}{\Phi} \geq 13.6$, it was found that increasing VR increases the efficiency of control until 1.5 to 2.5. After, increasing VR decreases the control efficiency. This is illustrated by Figures 5.9, 5.10 and 5.11. As there is an optimum value of VR below 2.5 for $\frac{\lambda}{\Phi} \geq 13.6$ and $\alpha = 55°$, the control was not efficient enough to suppress totally the separation.

For $\frac{\lambda}{\Phi} = 6.8$ and $\alpha = 55°$, it was found that increasing VR from 0.5 to 2.5 increases the control efficiency, but, at $VR = 2.5$, as for upstream blowing, the wool tufts were slightly aligned with the jets direction. After $VR = 2.5$, increasing VR decreases the efficiency and the wool tufts take the direction of the jets (See Figures

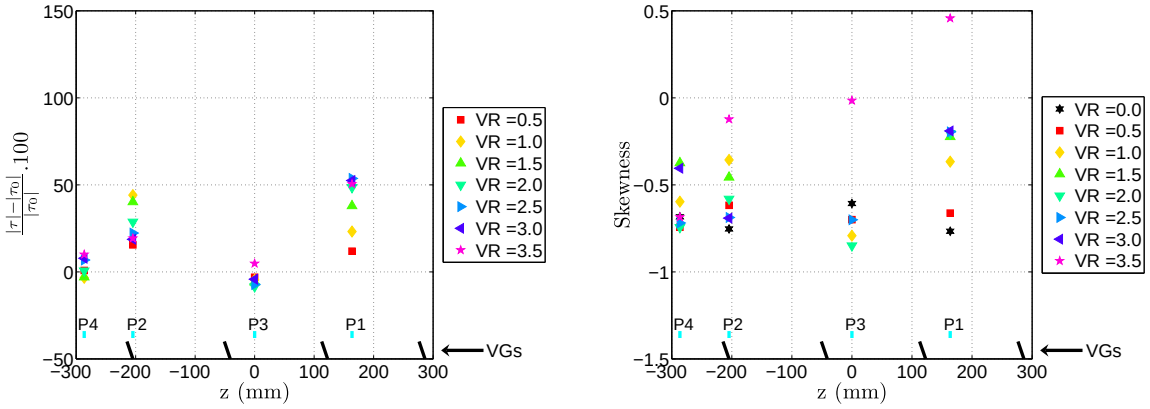

a) b)

case	Φ (mm)	β	α	$\frac{\lambda}{\Phi}$	$\frac{\Delta X_{vg}}{\Phi}$	VR :
6	12	35°	55°	13.6	9.8	0.5 - 3.5

Figure 5.9: a) Gain in friction and b) Skewness for case 6 (i.e. for different values of VR and the other parameters kept constant).

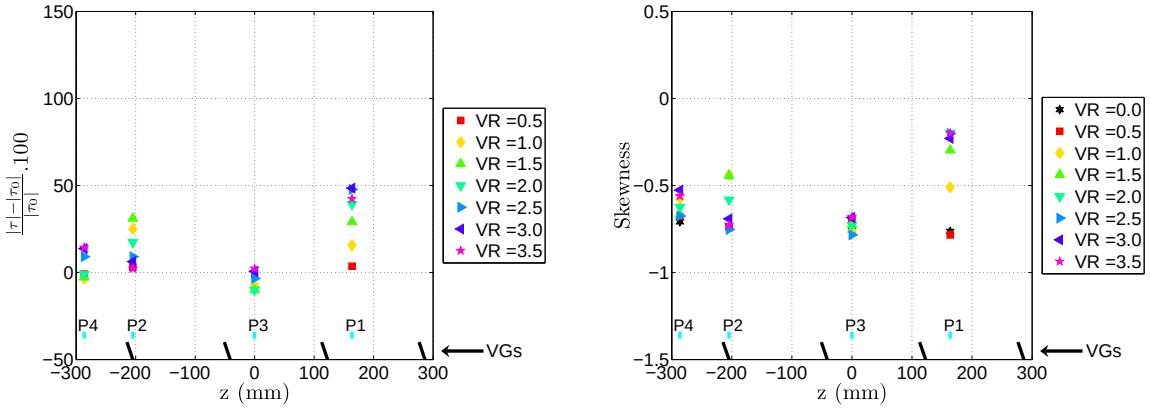

a) b)

case	Φ (mm)	β	α	$\frac{\lambda}{\Phi}$	$\frac{\Delta X_{vg}}{\Phi}$	VR :
16	12	35°	55°	13.6	23.4	0.5 - 3.5

Figure 5.10: a) Gain in friction and b) Skewness for case 16 (i.e. for different values of VR and the other parameters kept constant).

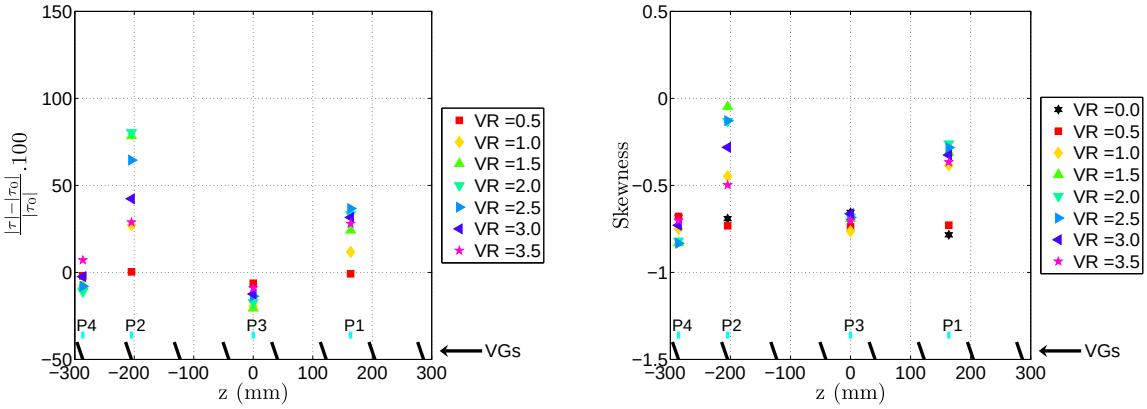

a) b)

case	Φ (mm)	β	α	$\frac{\lambda}{\Phi}$	$\frac{\Delta X_{vg}}{\Phi}$	VR :
9	6	35°	55°	13.6	19.5	0.5 - 3.5

Figure 5.11: a) Gain in friction and b) Skewness for case 9 (i.e. for different values of VR and the other parameters kept constant).

5.12 and 5.13 where an increase in skewness with VR is observed for VR less than 2.5 and a drop for VR larger than 2.5). However, a more coherent flow is obtained here than for upstream blowing, but, this is not a proof that these cases correspond to a good control result. Figure 5.14 gives the power spectrum for probes P3 and P4 for cases 5 and 15 ($\frac{\lambda}{\Phi} = 6.8$) and VR between 2 and 3.5. An increase with VR of the power spectrum for frequencies greater than 100 Hz is observed here, however, the spectrum does not gives a clear information about the control efficiency as seen in Chapter 4. As for $\frac{\lambda}{\Phi} = 6.8$ and $\alpha = 125°$, reattachment is not clearly evidenced, these cases can not be considered as good control configurations.

In conclusion, it was found that the optimum VR parameter depends on α and $\frac{\lambda}{\Phi}$. For $\frac{\lambda}{\Phi} \geq 13.6$ and $\alpha = 55°$ (downstream blowing), it was found that the optimum value of VR is between 1.5 to 2.5. In agreement with Godard and Stanislas (2006b), the minimum value to detect control effect is 1.5, but here the efficiency does not increase continuously with VR for downstream blowing. This is in contradiction with the studies of Godard and Stanislas (2006b), Betterton et al. (2000), Tilmann et al. (2000), McManus et al. (1994) and Selby et al. (1992), but tends to confirm the optimum VR value found by Milanovic and Zaman (2004) for the vortex strength. The divergences about VR effects can also be explained by the fact that in most of the previous studies, α was fixed at a different value of 90° which may lead to a different VR behaviour.

For $\frac{\lambda}{\Phi} \geq 13.6$ and $\alpha = 125°$ (upstream blowing), it was found that the efficiency of control increases continuously with VR even for values of VR greater than 8. It was also found that the control effects begins at VR around 1.5. These results are in good agreement with previous studies (Godard and Stanislas (2006b), Betterton et al. (2000), Tilmann et al. (2000), McManus et al. (1994), Selby et al. (1992), etc.) and confirm that the optimum VR depends strongly on pitch angle α.

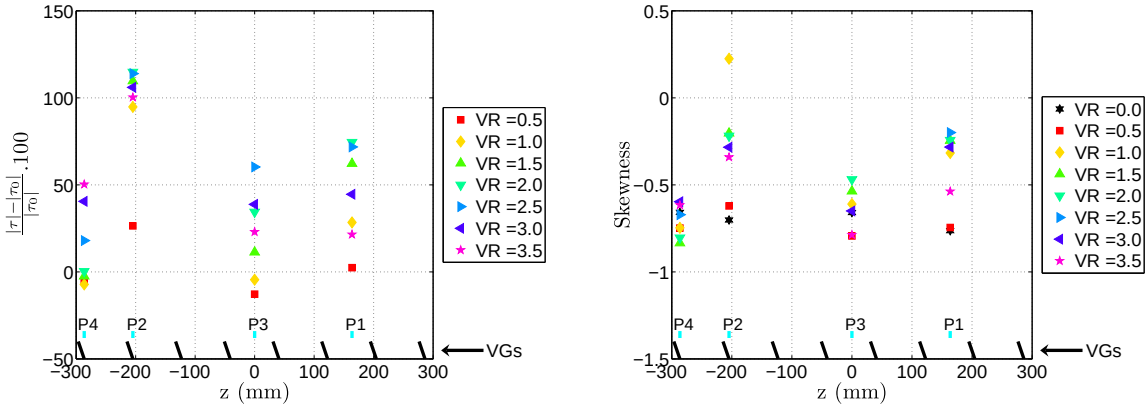

a) b)

case	Φ (mm)	β	α	$\frac{\lambda}{\Phi}$	$\frac{\Delta X_{vg}}{\Phi}$	VR :
5	12	35°	55°	6.8	9.8	0.5 - 3.5

Figure 5.12: a) Gain in friction and b) Skewness for case 5 (i.e. for different values of VR and the other parameters kept constant).

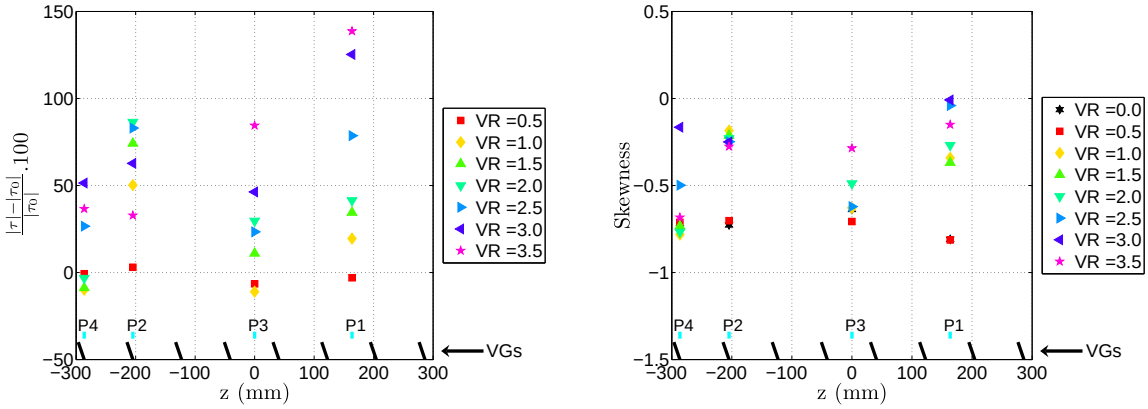

a) b)

case	Φ (mm)	β	α	$\frac{\lambda}{\Phi}$	$\frac{\Delta X_{vg}}{\Phi}$	VR :
15	12	35°	55°	6.8	23.4	0.5 - 3.5

Figure 5.13: a) Gain in friction and b) Skewness for case 15 (i.e. for different values of VR and the other parameters kept constant).

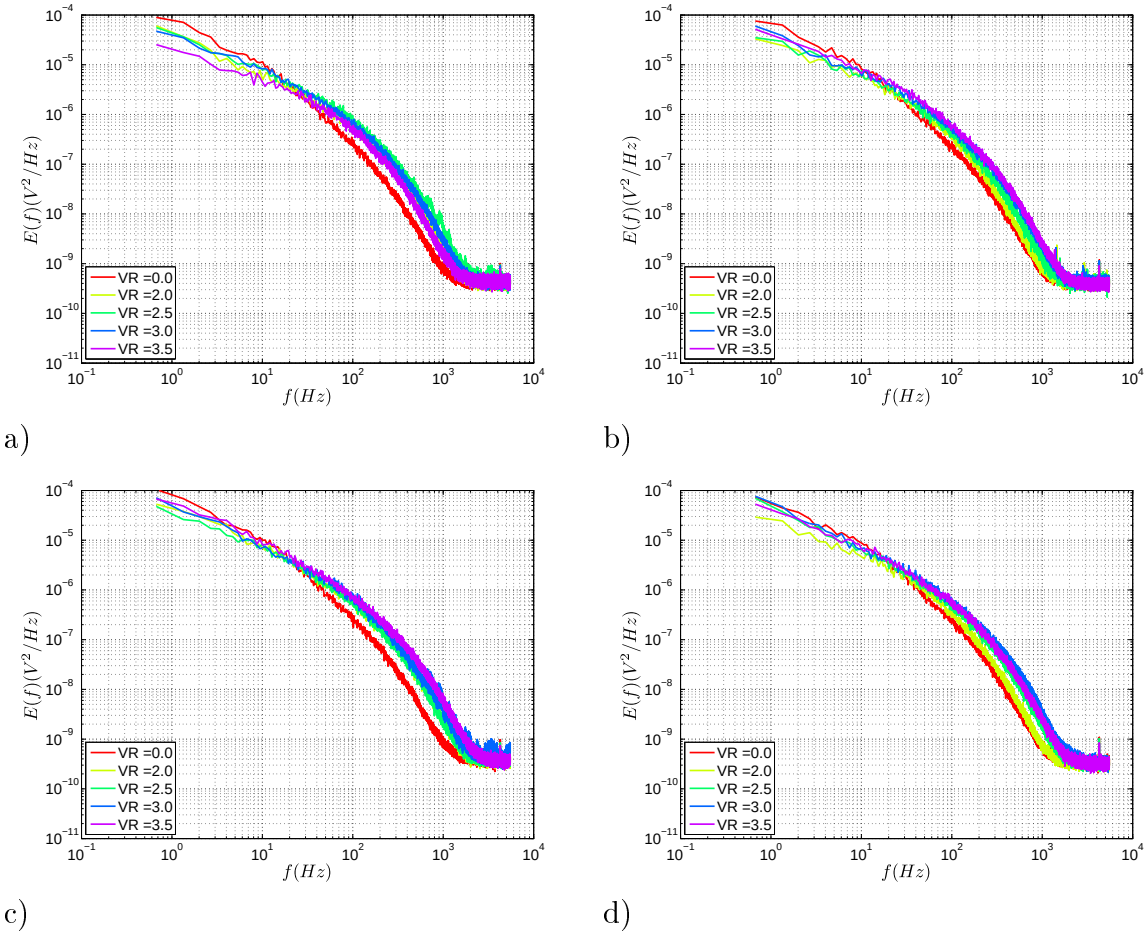

Figure 5.14: Power spectrum of friction probes output voltage for probes a) P3 and case 5 ($\frac{\lambda}{\Phi} = 6.8$), b) P4 and case 5, a) P3 and case 15 ($\frac{\lambda}{\Phi} = 13.6$), b) P4 and case 15, $VR = 2$ to 3.5.

For $\frac{\lambda}{\Phi} = 6.8$, no optimum value of VR was found, and moreover, no control results were obtained with these configurations. By looking to the optimum VR parameter, it was also found that the optimum angle α is 125° (i.e. upstream blowing) because the efficiency of control increases continuously with VR and a total suppression of the separation can be reached whereas only a reduction and a delay of the separation can be reached for $\alpha = 55°$.

3.1.2.3 Effects of $\frac{\lambda}{\Phi}$

As was seen in the Section 3.1.2.2, $\frac{\lambda}{\Phi} = 6.8$ gives no control results. The optimum parameter for $\frac{\lambda}{\Phi}$ is then higher than 6.8. Figure 5.15 gives the gain in friction and skewness for case 2 ($\Phi = 12$ mm and $\frac{\lambda}{\Phi} = 13.6$) and $VR = 2$ and for case 3 ($\Phi = 12$ mm and $\frac{\lambda}{\Phi} = 20.4$) and $VR = 3.5$. These cases correspond to upstream blowing. As can be seen from Figure 5.15, these two results are almost the same. The volume flow rate being almost the same (for case 2 and $VR = 2$, $Q_{v_2} = 110m^3/h$ and for case 3 and $VR = 3.5$, $Q_{v_3} = 123m^3/h$, with Q_v given by $Q_v = N_{jet}.S_{jet}.VR.U_e$), it is impossible to determined which from case 2 or case 3 is the best.

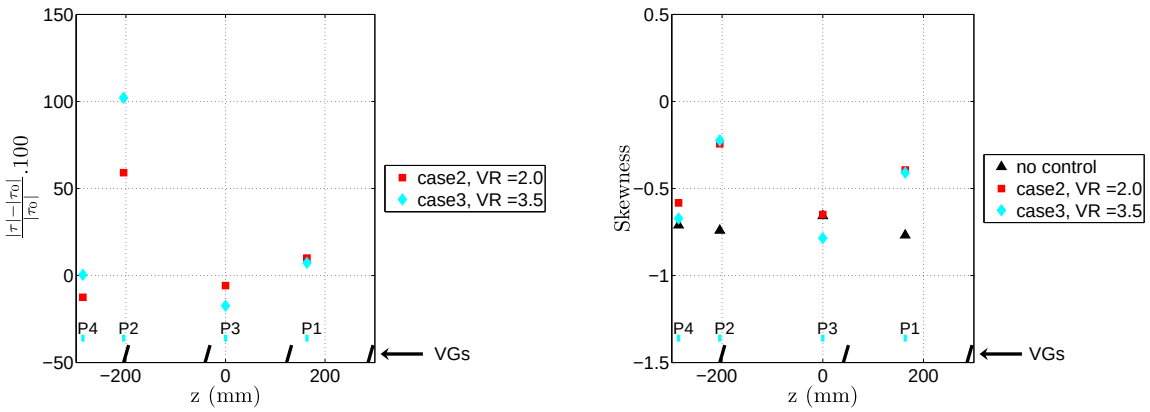

Φ (mm)	β	α	$\frac{\Delta X_{vg}}{\Phi}$	$\frac{\lambda}{\Phi}$:	case 2	case 3	VR :	case 2	case 3
12	35°	125°	9.8		13.6	20.4		2	3.5

Figure 5.15: a) Gain in friction and b) Skewness for case 2, $VR = 2$, and for case 3, $VR = 3.5$ (i.e. for two different values of $\frac{\lambda}{\Phi}$ and VR and the other parameters kept constant).

The momentum coefficient C_μ has then to be computed to conclude between these 2 tests. C_μ is defined by : $C_\mu = \frac{\rho_{jet}.N_{jet}.S_{jet}.U_{jet}^2}{\frac{1}{2}.\rho_e.\Delta z.\delta.U_e^2}$, with ρ_{jet} the density of the jet (here as the pressure of the jet is the same as in the wind tunnel, $\frac{\rho_{jet}}{\rho_e} = \frac{T_e}{T_{jet}}$, where T_e is the temperature in the wind tunnel and T_{jet} the temperature of the jet), U_{jet} the mean jet velocity, Δz the difference in z between the 2 extreme spanwise jets of the case and δ the boundary layer thickness. C_μ can be simplified as : $C_\mu = \frac{T_e.N_{jet}.S_{jet}.VR^2}{\frac{1}{2}.T_{jet}.\Delta z.\delta}$. For case 2 and $VR = 2$, $C_{\mu_2} = 0.031$ and for case 3 and $VR = 3.5$, $C_{\mu_3} = 0.068$. There is a factor of two on the momentum coefficient

between these two cases, so it can be concluded that case 2, with $\frac{\lambda}{\Phi} = 13.6$, gives better results than case 3 with $\frac{\lambda}{\Phi} = 20.4$. For case 4, with $\frac{\lambda}{\Phi} = 27.2$, with the same methodology, it appears that it gives worse results than case 3. For the same corresponding cases at station 2, the same results are obtained, so for $\Phi = 12$ mm, and upstream blowing, it appears that the optimum parameter for $\frac{\lambda}{\Phi}$ is 13.6.

Figure 5.16 gives the gain in friction and skewness for case 7 ($\Phi = 6$ mm and $\frac{\lambda}{\Phi} = 13.6$) and $VR = 2.5$ and for case 8 ($\Phi = 6$ mm and $\frac{\lambda}{\Phi} = 27.2$) with $VR = 3.5$. These cases correspond to upstream blowing. As can be seen in Figure 5.16, these two cases give almost the same results. For case 7 and $VR = 2.5$, $Q_{v_7} = 69m^3/h$ and $C_{\mu_7} = 0.023$, and for case 8 and $VR = 3.5$, $Q_{v_8} = 48m^3/h$ and $C_{\mu_3} = 0.024$. From these results, case 8, with $\frac{\lambda}{\Phi} = 27.2$ and $VR = 3.5$, gives the best results. However, to obtain a complete suppression of the separation for case 8, a velocity ratio of 5.5 is needed, which is unrealistic for aircraft or car applications. For the same corresponding cases at station 2 (cases 17 and 18), the same conclusions are obtained. So for $\Phi = 6$ mm, and upstream blowing, it appears that $\frac{\lambda}{\Phi} = 13.6$ is a good compromise.

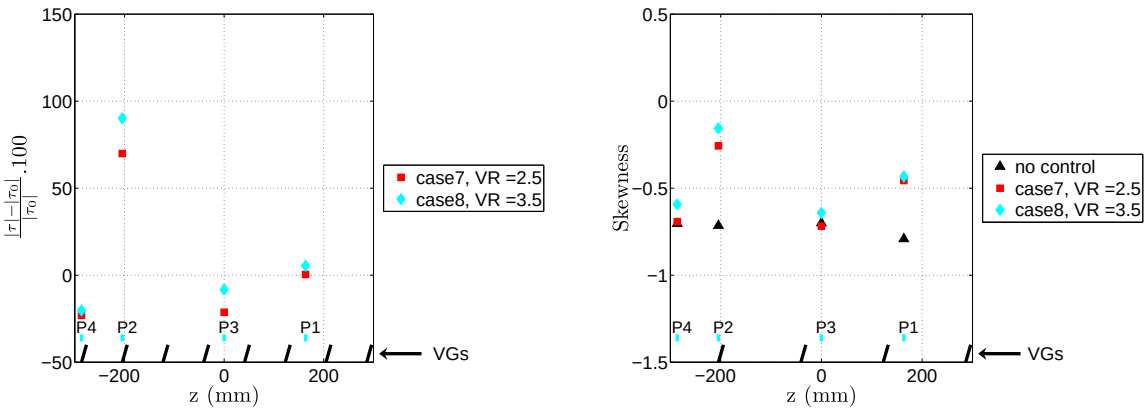

a) b)

Φ (mm)	β	α	$\frac{\Delta X_{vg}}{\Phi}$	$\frac{\lambda}{\Phi}$:	case 7	case 8	VR :	case 7	case 8
6	35°	125°	19.5		13.6	27.2		2.5	3.5

Figure 5.16: a) Gain in friction and b) Skewness for case 7, $VR = 2.5$, and for case 8, $VR = 3.5$ (i.e. for two different values of $\frac{\lambda}{\Phi}$ and VR and the other parameters kept constant).

For downstream blowing, the conclusion is easier because cases with $\frac{\lambda}{\Phi} = 27.2$ and $\Phi = 6$ mm give poor results. Moreover, for $\Phi = 12$ mm, cases with $\frac{\lambda}{\Phi} = 27.2$ were not carried out because cases with $\frac{\lambda}{\Phi} = 13.6$ and $\Phi = 12$ mm give poor results. So in conclusion, as for upstream blowing, for downstream blowing, it appears that the optimum $\frac{\lambda}{\Phi}$ is 13.6.

In conclusion, the optimum parameter that was found for $\frac{\lambda}{\Phi}$ is 13.6. This value is sightly larger than the optimum value found by Godard and Stanislas (2006b) ($\frac{\lambda}{\Phi} = 6$). However, it is in agreement with the results obtained in the AVERT ONERA L1 wind tunnel tests (Dandois et al. (2009)).

3.1.2.4 Effects of $\frac{\Delta X_{vg}}{\delta}$ and $\frac{\Delta X_{vg}}{\Phi}$

In the tests that were carried out, the parameter $\frac{\Delta X_{vg}}{\delta}$ is 0.6 for station 1, and 1.4 for station 2. Figures 5.17, 5.18, 5.19 and 5.20 show the evolution of the control efficiency with $\frac{\Delta X_{vg}}{\delta}$ at optimum VR and $\frac{\lambda}{\Phi}$. In each of these figures, the first case presented is at station 1, and the second case at station 2. As can be seen, the results seem to be independent of $\frac{\Delta X_{vg}}{\delta}$ for $0.6 \leq \frac{\Delta X_{vg}}{\delta} \leq 1.4$. This result is coherent with those of Godard and Stanislas (2006b) and Lin et al. (1990). Godard and Stanislas (2006b) found that co-rotating continuous jets are efficient at $\frac{\Delta X_{vg}}{\delta} = 7.2$ and Lin et al. (1990) at $\frac{\Delta X_{vg}}{\delta} = 40$, so much further upstream of the separation line.

As there is no influence of $\frac{\Delta X_{vg}}{\delta}$ for the 2 diameters tested, there is also no influence of the parameter $\frac{\Delta X_{vg}}{\Phi}$ in the range investigated (i.e. $9.8 \leq \frac{\Delta X_{vg}}{\Phi} \leq 46.8$).

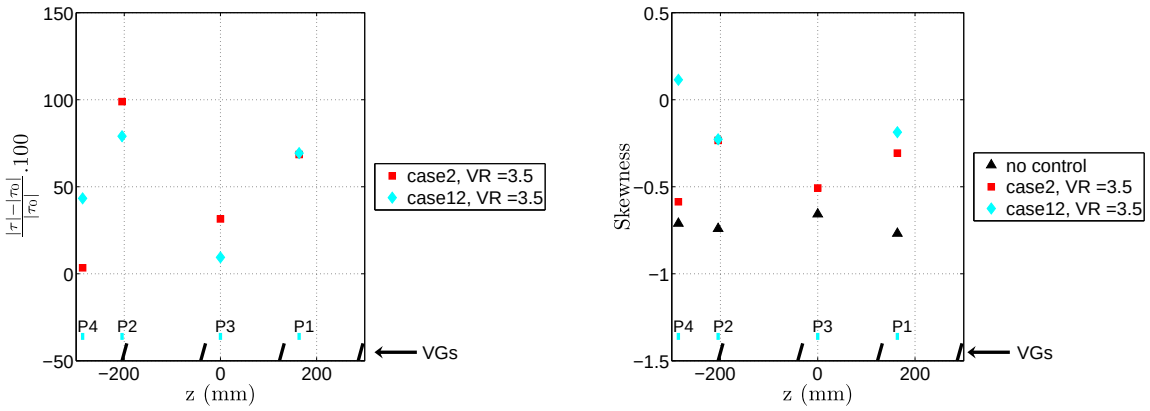

a) b)

Φ (mm)	β	α	$\frac{\lambda}{\Phi}$	VR	$\frac{\Delta X_{vg}}{\Phi}$:	case 2	case 12
12	35°	125°	13.6	3.5		9.8	23.4

Figure 5.17: a) Gain in friction and b) Skewness for cases 2 and 12, $VR = 3.5$ (i.e. for two different values of $\frac{\Delta X_{vg}}{\Phi}$ and the other parameters kept constant).

3.1.2.5 Effects of $\frac{\Phi}{\delta}$

Two values of $\frac{\Phi}{\delta}$ were tested : $\frac{\Phi}{\delta} = 0.03$ and 0.06. These values are near the values tested by Godard and Stanislas (2006b). Figure 5.21 gives the evolution of the friction and the skewness for cases 2 ($\frac{\Phi}{\delta} = 0.06$) and 7 ($\frac{\Phi}{\delta} = 0.03$) at the optimum VR. Case 2 gives slightly better results than case 7. The same results are obtained by comparing cases 12 and 17 corresponding to same VGs configuration but at station 2. So, for upstream blowing, at constant VR, the optimum value of $\frac{\Phi}{\delta}$ is 0.06.

3.1.3 Conclusion on the co-rotating continuous jets

Two diameters of co-rotating continuous jets (6 and 12 mm) were tested in different arrangements. For each arrangement, the velocity ratio VR tested was from 0.5 to

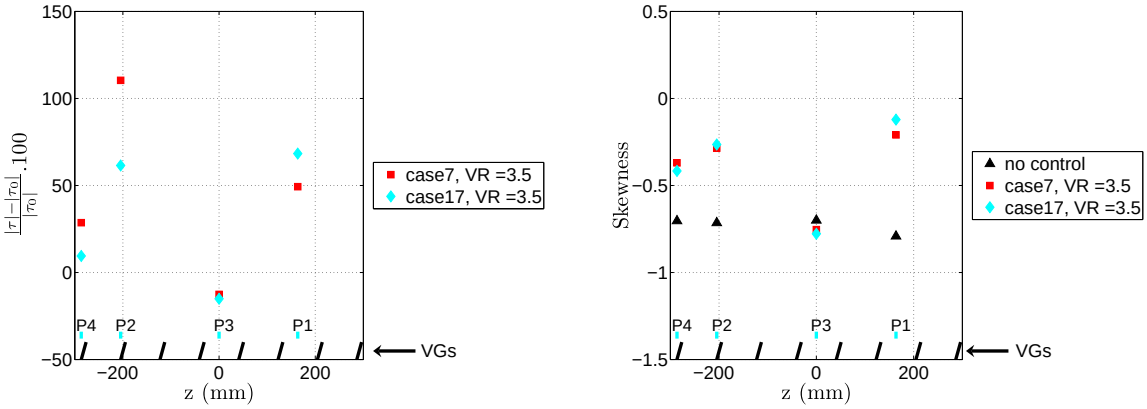

a) b)

Φ (mm)	β	α	$\frac{\lambda}{\Phi}$	VR	$\frac{\Delta X_{vg}}{\Phi}$:	case 7	case 17
6	35°	125°	13.6	3.5		19.5	46.8

Figure 5.18: a) Gain in friction and b) Skewness for cases 7 and 17, $VR = 3.5$ (i.e. for two different values of $\frac{\Delta X_{vg}}{\Phi}$ and the other parameters kept constant).

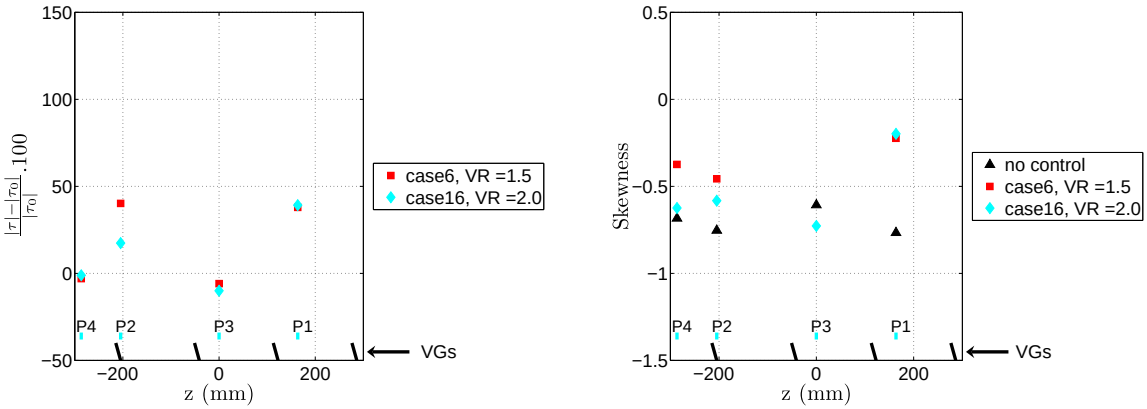

a) b)

Φ (mm)	β	α	$\frac{\lambda}{\Phi}$	VR :	case 6	case 16	$\frac{\Delta X_{vg}}{\Phi}$:	case 6	case 16
12	35°	55°	13.6		1.5	2		9.8	23.4

Figure 5.19: a) Gain in friction and b) Skewness for cases 6 with $VR = 1.5$ and 16 with $VR = 2$ (i.e. for two different values of $\frac{\Delta X_{vg}}{\Phi}$ and VR and the other parameters kept constant).

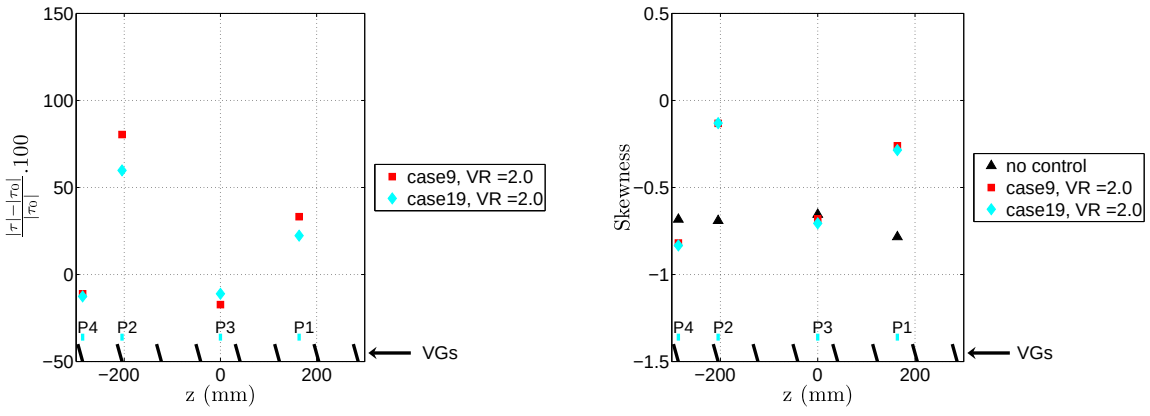

a) b)

Φ (mm)	β	α	$\frac{\lambda}{\Phi}$	VR	$\frac{\Delta X_{vg}}{\Phi}$:	case 9	case 19
6	35°	55°	13.6	2		19.5	46.8

Figure 5.20: a) Gain in friction and b) Skewness for cases 9 and 19, $VR = 2$ (i.e. for two different values of $\frac{\Delta X_{vg}}{\Phi}$ and the other parameters kept constant).

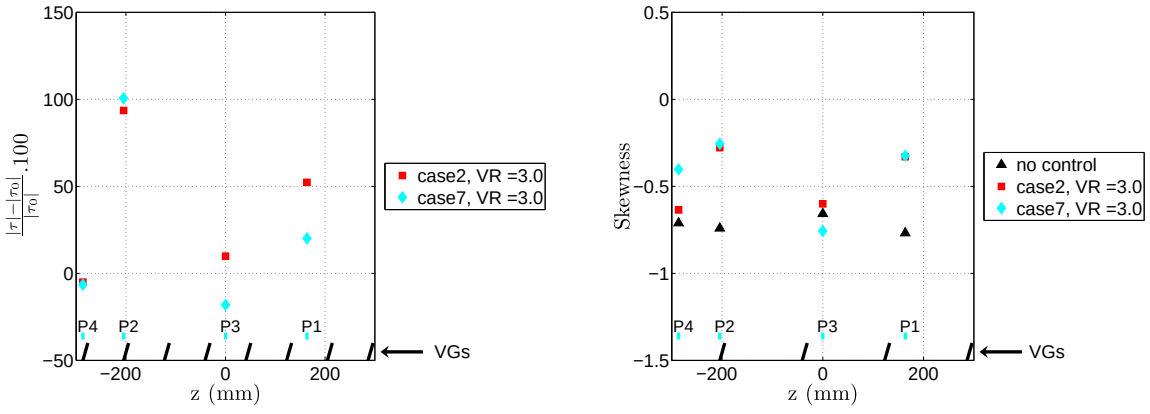

a) b)

β	α	$\frac{\lambda}{\Phi}$	VR	$\frac{\Delta X_{vg}}{\Phi}$:	case 2	case 7	Φ (mm) :	case 2	case 7
35°	125°	13.6	3		9.8	19.5		12	6

Figure 5.21: a) Gain in friction and b) Skewness for cases 2 and 7, $VR = 3$ (i.e. for two different values of $\frac{\Phi}{\delta}$ (or Φ) and the other parameters kept constant ($\frac{\Delta X_{vg}}{\Phi}$ has no influence as seen in the previous section)).

3.5 by steps of 0.5. It was found that the optimum $\frac{\lambda}{\Phi}$ is 13.6. This is slightly bigger than the value of 6 found by Godard and Stanislas (2006b), but coherent with the AVERT ONERA L1 wind tunnel tests (Dandois et al. (2009)).

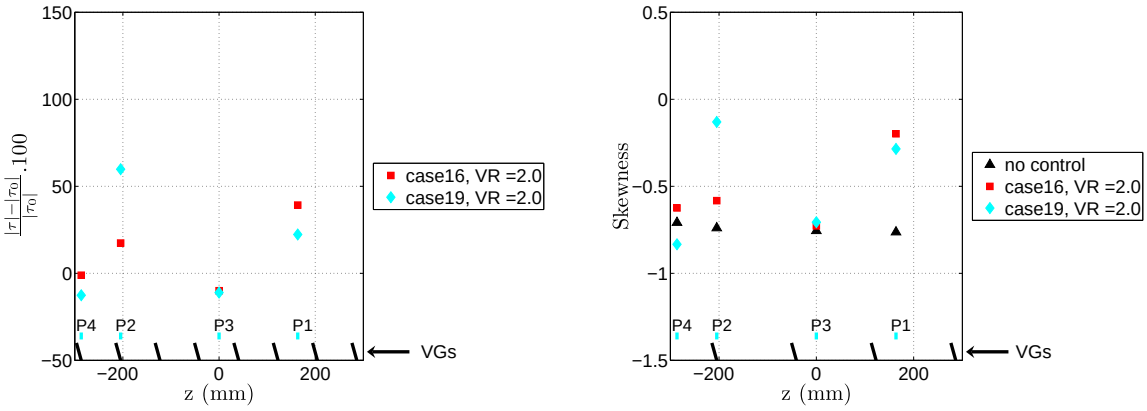

a) b)

β	α	$\frac{\lambda}{\Phi}$	VR	$\frac{\Delta X_{vg}}{\Phi}$:	case 16	case 19	Φ (mm) :	case 16	case 19
35°	55°	13.6	2		23.4	46.8		12	6

Figure 5.22: a) Gain in friction and b) Skewness for cases 16 and 19, $VR = 2$ (i.e. for two different values of $\frac{\Phi}{\delta}$ (or Φ) and the other parameters kept constant ($\frac{\Delta X_{vg}}{\Phi}$ has no influence as seen in the previous section)).

Figure 5.22 gives the evolution of the friction and the skewness for cases 16 and 19 at the optimum VR. Case 16 corresponds to $\frac{\Phi}{\delta} = 0.06$ and 19 to $\frac{\Phi}{\delta} = 0.03$. Case 19 gives slightly better results than case 16. The same results are obtained by comparing the similar cases at station 1 (cases 6 and 9). So, for downstream blowing, at constant VR, the optimum value of $\frac{\Phi}{\delta}$ is 0.03.

In conclusion, at constant VR, it was found that for upstream blowing, the optimum $\frac{\Phi}{\delta}$ parameter is 0.06, and for downstream blowing, it is 0.03. But as the differences given by the variation of $\frac{\Phi}{\delta}$ between 0.03 to 0.06 is small, if the criterion on VR is changed to a criterion on Q_v or C_μ, it appears clearly that for all the cases investigated, the optimum value of $\frac{\Phi}{\delta}$ is then 0.03.

For all the configurations tested, it was found that the minimum VR that gives control effect is 1.5, which is coherent with the previous studies of Godard and Stanislas (2006b), Betterton et al. (2000), Tilmann et al. (2000), McManus et al. (1994), Selby et al. (1992), etc.. For upstream blowing, it was found that increasing VR increases the efficiency of control, whereas, for downstream blowing, there is an optimum VR parameter between 1.5 to 2.5. Upstream blowing is then more robust than downstream blowing as the maximum available efficiency is higher and for upstream blowing, VR can be continuously increased up to $VR = 8$ without perturbing the reattachment whereas for downstream blowing it is limited by 2.5.

It was also found that there is no influence of the parameter $\frac{\Delta X_{vg}}{\delta}$ for $0.6 \leq \frac{\Delta X_{vg}}{\delta} \leq 1.6$, which is again coherent with the studies of Godard and Stanislas (2006b) and Lin et al. (1990). Finally, it was found that at constant VR, the 2 diameters give

almost the same results, but at constant momentum coefficient C_μ or at constant flow rate Q_v, it was found that the smallest diameter tested ($\frac{\Phi}{\delta} = 0.03$) gives the best results.

3.2 Counter-rotating configurations

3.2.1 Tests description

Figure 1.6 b) shows the arrangement of active VGs for counter-rotating configurations. Based on the study of Godard and Stanislas (2006b), the optimum $\frac{L}{\Phi}$ is 15, and the $\frac{\lambda}{\Phi}$ suggested is 32. As seen in Chapter 2, due to technical constraints, in this study, the minimum for $\frac{\lambda}{\Phi}$ parameter tested was 27.3. It was decided to test also the value $\frac{\lambda}{\Phi} = 54.6$. The value of $\frac{L}{\Phi}$ was fixed to 15 for the 2 diameters tested (6 mm and 12 mm), however, one configuration of diameter 12 mm was added with $\frac{L}{\Phi} = 12.3$ and $\frac{\lambda}{\Phi} = 27.3$ to test the $\frac{L}{\Phi}$ effects. All these configurations were tested at stations 1 ($s = 3383$ mm) and 2 ($s = 3219$ mm). For each configurations, the velocity ratios VR was from 0.5 to 3.5 by steps of 0.5.

The validation test procedure was the same as for the co-rotating actuators (see Section 3.1.1).

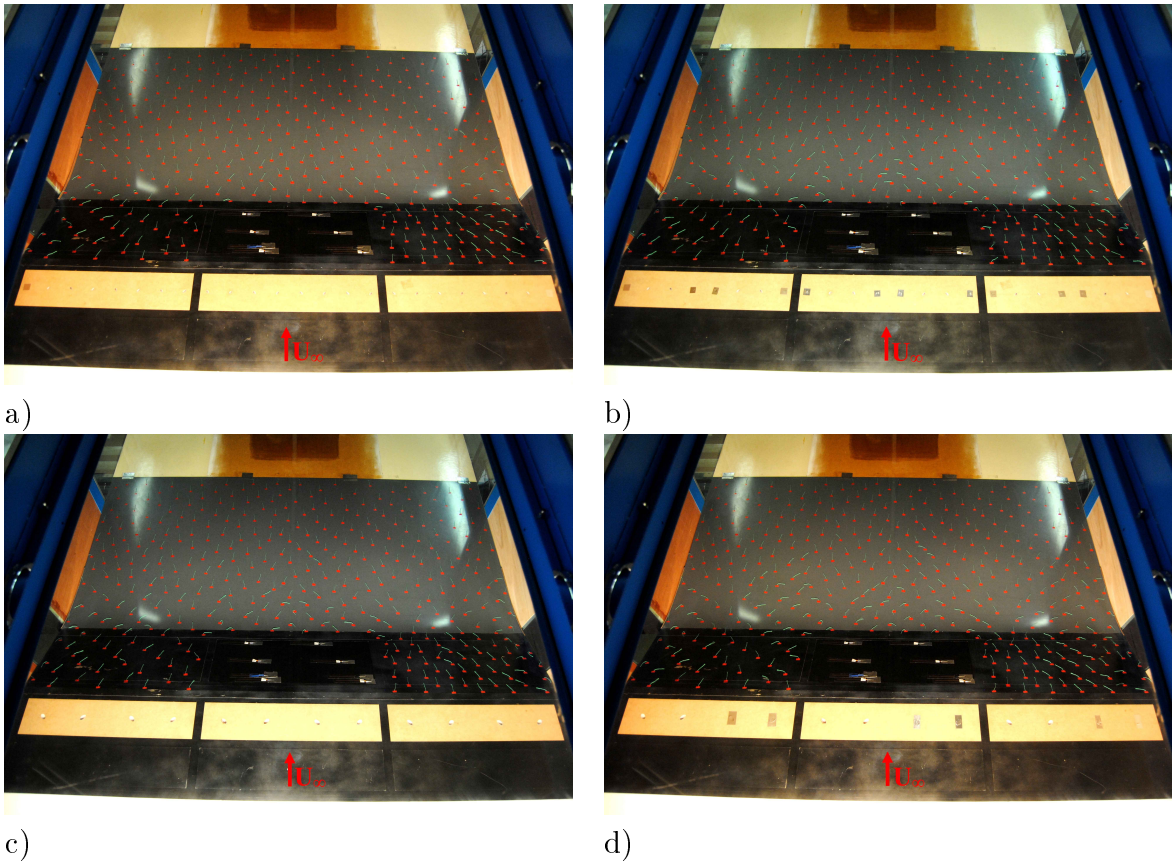

Figure 5.23: Wool tufts visualisation for a) FA (case 25), b) PA (BVG) (case 26), c) PA (case 39), d) S (case 40).

Table 5.2: List of the counter-rotating configurations tested

Case	s (mm)	Φ (mm)	α (°)	$\frac{\lambda}{\Phi}$	$\frac{L}{\Phi}$	VR (best)	state	$\frac{\lvert\tau\rvert-\lvert\tau_0\rvert}{\lvert\tau_0\rvert}(\%)$	
								$s = 3555mm$	$s = 3759mm$
21	3383	12	125	27.3	15	3	FA	45	10
22	3383	12	125	54.6	15	3.5	PA (BVG)	14	12
23	3383	12	55	27.3	15	1.5	FA	21	-17
24	3383	12	55	54.6	15	1.5	PA (BVG)	6	20
25	3383	6	125	27.3	15	3	FA	82	19
26	3383	6	125	54.6	15	3.5	PA (BVG)	90	9
27	3383	6	55	27.3	15	1.5	FA	40	0
28	3383	6	55	54.6	15	1.5	PA (BVG)	26	7
29	3219	12	125	27.3	15	3	FA	35	-24
30	3219	12	125	54.6	15	3.5	PA (BVG)	6	18
31	3219	12	55	27.3	15	1.5	FA	42	-13
32	3219	12	55	54.6	15	2	PA (BVG)	7	18
33	3219	6	125	27.3	15	3	FA	68	2
34	3219	6	125	54.6	15	3.5	PA (BVG)	60	9
35	3219	6	55	27.3	15	2	FA	67	-9
36	3219	6	55	54.6	12.3	2.5	PA (BVG)	37	8
37	3383	12	125	27.3	12.3	3.5	FA	87	20
38	3383	12	125	54.6	12.3	3.5	PA (BVG)	73	-10
39	3383	12	55	27.3	12.3	1.5	PA	42	18
40	3383	12	55	54.6	12.3	1.5	S	37	7
41	3219	12	125	27.3	12.3	3.5	FA	59	-19
42	3219	12	125	54.6	12.3	3.5	PA (BVG)	54	7
43	3219	12	55	27.3	12.3	1.5	FA	49	19
44	3219	12	55	54.6	12.3	2	PA (BVG)	53	7

3.2.2 Results

3.2.2.1 General results

Table 5.2 presents all the active counter-rotating cases investigated and the main conclusions obtained with wool tufts and friction probes. The legend for the state column (illustrated by Figure 5.23) is :
- FA = Fully Attached : no separation was seen on the wool tufts.
- PA = Partially Attached : a small separation was evidenced by the wool tufts.
- S = Separated : no reduction of the separation was seen on the wool tufts.
- PA (BVG) = Partially Attached Between counter-rotating Vortex Generators : a small separation was evidenced by the wool tufts between two vortex generators. Behind the vortex generators, no separation was seen on the wool tufts.

The last two columns of Table 5.2 give the best quantitative control results obtained with friction probes at station $s = 3555$ mm (penultimate column) and station $s = 3759$ mm (last column). It can be noted that most of the counter-rotating configurations tested can suppress totally the separation.

3.2.2.2 Effects of VR

As for the co-rotating configurations, the control effectiveness was found largely dependent on the velocity ratio VR. For $\alpha = 125°$ (i.e. upstream blowing), it was found, in all cases, that increasing VR increases continuously the efficiency of control. This is illustrated by Figures 5.24, 5.25 and 5.26. It was checked rapidly, with only wool tufts visualisations, if it exits a maximum of control efficiency with VR. For value of VR up to 8-10, the efficiency of control seems to increase continuously (no perturbation of the reattachment was evidenced). In all the cases investigated with $\alpha = 125°$, a total suppression of the separation can be reached by increasing VR (however, for cases with $\frac{\lambda}{\Phi} = 54.6$, the VR parameter has to be greater than 6). The minimum VR to obtain control effect is 1.5 as for the co-rotating configurations. These results are in agreement with the previous studies of Godard and Stanislas (2006b), Betterton et al. (2000), Tilmann et al. (2000), McManus et al. (1994), Selby et al. (1992), etc..

For $\alpha = 55°$ (i.e. downstream blowing), it was found, as for the co-rotating ones (Section 3.1.2.2), that the optimum VR is between 1.5 to 2.5. This is illustrated by Figures 5.27, 5.28 and 5.29. As for the co-rotating active VGs, this optimum was not observed by the previous studies of Godard and Stanislas (2006b) and Selby et al. (1992) but it is coherent with the observations of Milanovic and Zaman (2004). In all cases investigated with $\alpha = 55°$, $\frac{\lambda}{\Phi} = 27.3$ and $\frac{L}{\Phi} = 15$, a total suppression of the separation can be reached. As for upstream blowing, the minimum VR to obtain control effect is 1.5.

In conclusion, as for co-rotating active VGs, it appears that there is no optimum value of VR for upstream blowing because the efficiency of control continuously increases with VR. For downstream blowing however, there is an optimum value for VR between 1.5 to 2.5. For both configurations (upstream or downstream blowing), the minimum value of VR to obtain control effect is 1.5. These results are in good agreement with previous studies of Godard and Stanislas (2006b), Betterton et al.

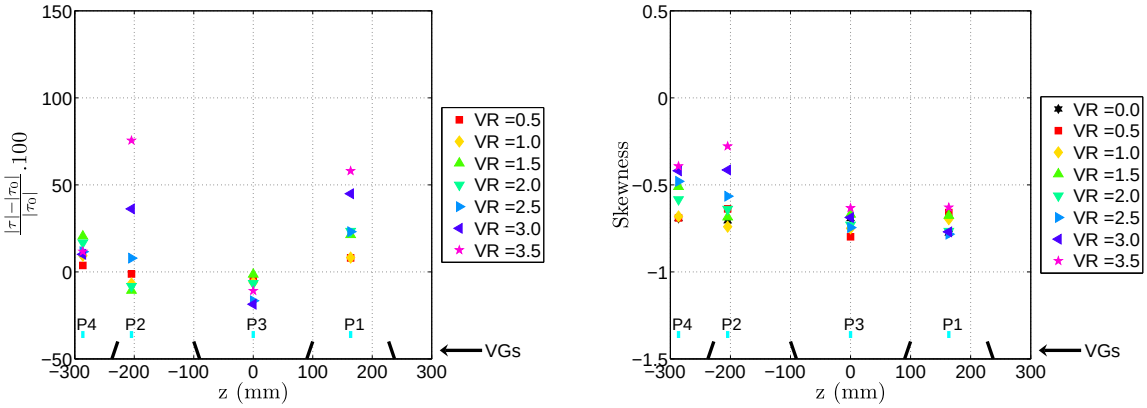

a) b)

case	Φ (mm)	β	α	$\frac{\lambda}{\Phi}$	$\frac{L}{\Phi}$	$\frac{\Delta X_{vg}}{\Phi}$	VR :
21	12	35°	125°	27.3	15	9.8	0.5 - 3.5

Figure 5.24: a) Gain in friction and b) Skewness for case 21 (i.e. for different values of VR and the other parameters kept constant).

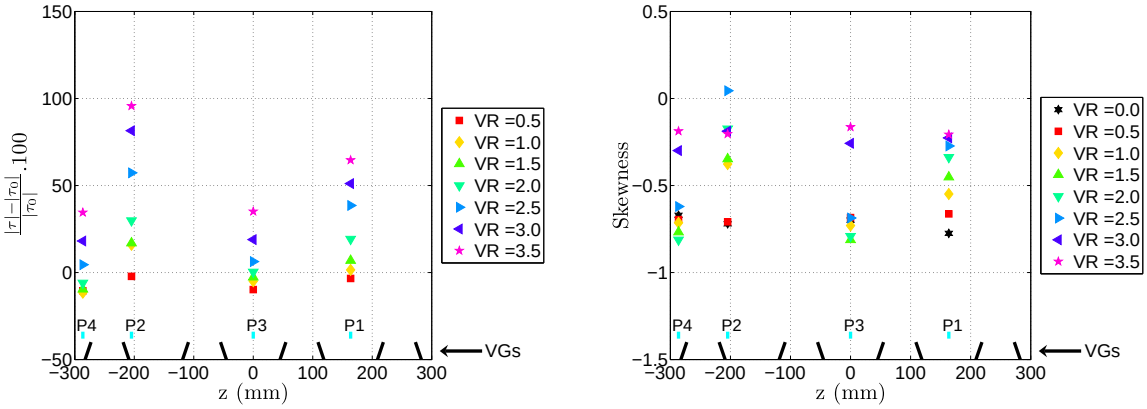

a) b)

case	Φ (mm)	β	α	$\frac{\lambda}{\Phi}$	$\frac{L}{\Phi}$	$\frac{\Delta X_{vg}}{\Phi}$	VR :
25	6	35°	125°	27.3	15	19.5	0.5 - 3.5

Figure 5.25: a) Gain in friction and b) Skewness for case 25 (i.e. for different values of VR and the other parameters kept constant).

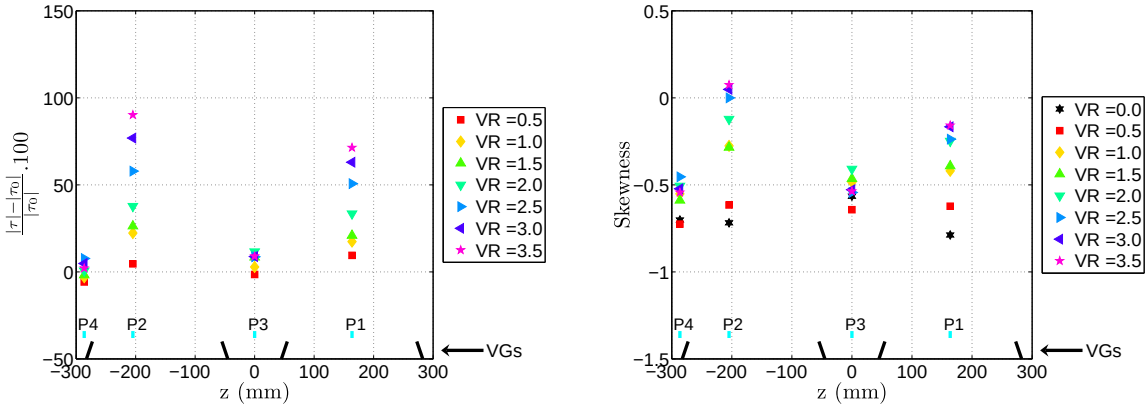

a) b)

case	Φ (mm)	β	α	$\frac{\lambda}{\Phi}$	$\frac{L}{\Phi}$	$\frac{\Delta X_{vg}}{\Phi}$	VR :
26	6	35°	125°	54.6	15	19.5	0.5 - 3.5

Figure 5.26: a) Gain in friction and b) Skewness for case 26 (i.e. for different values of VR and the other parameters kept constant).

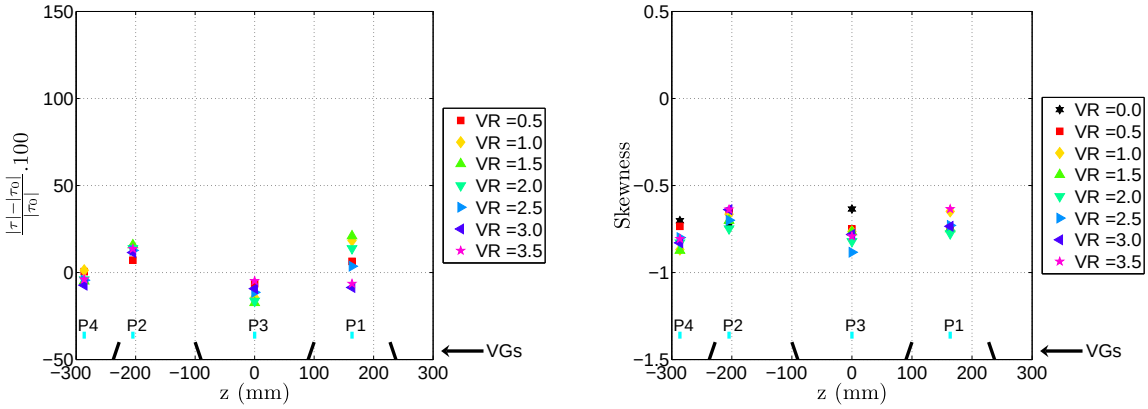

a) b)

case	Φ (mm)	β	α	$\frac{\lambda}{\Phi}$	$\frac{L}{\Phi}$	$\frac{\Delta X_{vg}}{\Phi}$	VR :
23	12	35°	55°	27.3	15	9.8	0.5 - 3.5

Figure 5.27: a) Gain in friction and b) Skewness for case 23 (i.e. for different values of VR and the other parameters kept constant).

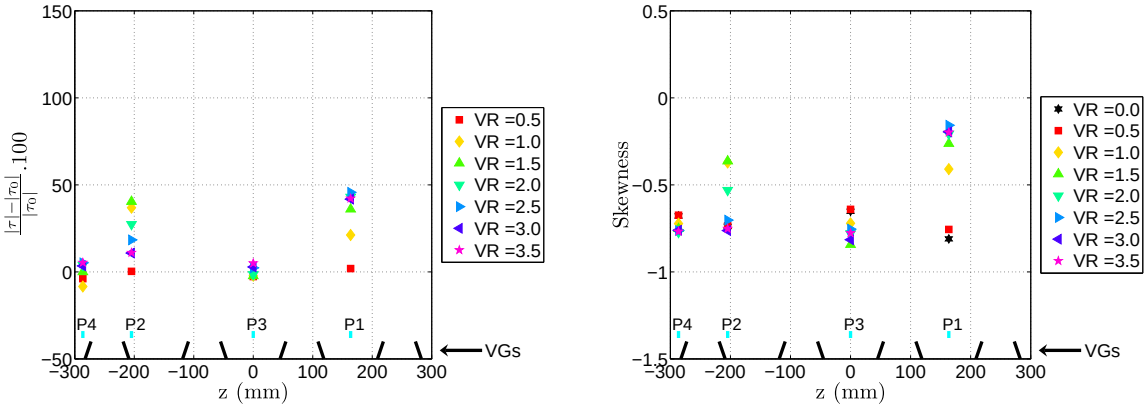

a) b)

case	Φ (mm)	β	α	$\frac{\lambda}{\Phi}$	$\frac{L}{\Phi}$	$\frac{\Delta X_{vg}}{\Phi}$	VR :
27	6	35°	55°	27.3	15	19.5	0.5 - 3.5

Figure 5.28: a) Gain in friction and b) Skewness for case 27 (i.e. for different values of VR and the other parameters kept constant).

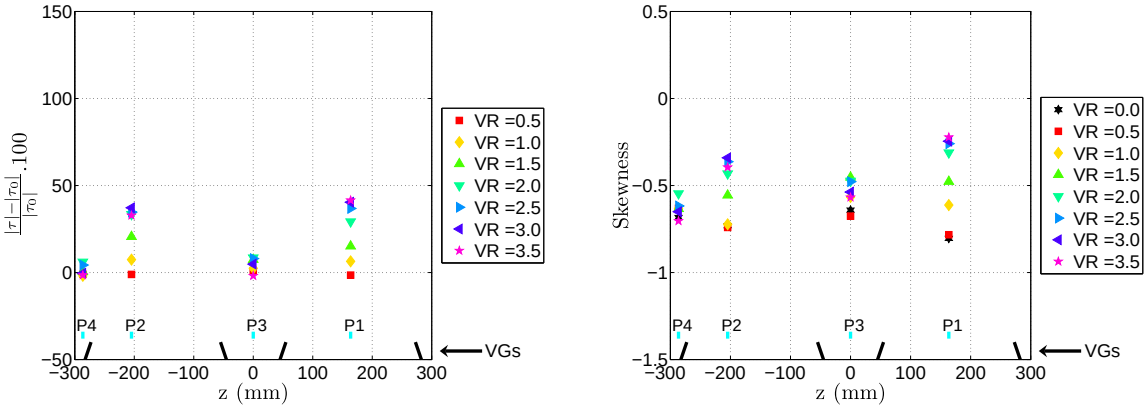

a) b)

case	Φ (mm)	β	α	$\frac{\lambda}{\Phi}$	$\frac{L}{\Phi}$	$\frac{\Delta X_{vg}}{\Phi}$	VR :
36	6	35°	55°	54.6	15	46.8	0.5 - 3.5

Figure 5.29: a) Gain in friction and b) Skewness for case 36 (i.e. for different values of VR and the other parameters kept constant).

(2000), Tilmann et al. (2000), McManus et al. (1994), Selby et al. (1992), Milanovic and Zaman (2004), etc.. Finally, as for the co-rotating configurations in Section 3.1.2.2, blowing upstream is more robust because the maximum available efficiency is higher. However, it was found that downstream blowing can suppress totally the separation at lower VR (so at lower flow rate Q_v or lower momentum coefficient C_μ) compared to the same upstream blowing configuration.

3.2.2.3 Effects of $\frac{\lambda}{\Phi}$

From the state column of Table 5.2, it seems that $\frac{\lambda}{\Phi} = 27.3$ gives better results than $\frac{\lambda}{\Phi} = 54.6$. Indeed, for upstream blowing, for all the cases investigated with $\frac{\lambda}{\Phi} = 27.3$, the separation was totally suppressed at VR around 3 - 3.5 whereas an unrealistic VR around 6 - 7 had to be reached to obtain the same result for configurations with $\frac{\lambda}{\Phi} = 54.6$. As was seen in Section 3.1.2.3, as the momentum coefficient C_μ is proportional to $N_{jet}.VR^2$, C_μ is then multiply by more than 1.5 by changing $\frac{\lambda}{\Phi}$ from 27.3 to 54.6, so more energy is needed for configurations with $\frac{\lambda}{\Phi} = 54.6$. For downstream blowing the conclusion is the same, as all the configurations with $\frac{\lambda}{\Phi} = 54.6$ give worse results than the corresponding configurations with $\frac{\lambda}{\Phi} = 27.3$ (no total suppression of the separation was reached with the configurations with $\frac{\lambda}{\Phi} = 54.6$).

In conclusion, it seems that the optimum parameter of $\frac{\lambda}{\Phi}$ is 27.3 here. This value is in agreement with the proposed value given by Godard and Stanislas (2006b).

3.2.2.4 Effects of $\frac{L}{\Phi}$

Figures 5.30 and 5.31 show the gain in friction and the skewness for two comparative cases, the first one with $\frac{L}{\Phi} = 15$, and the second one with $\frac{L}{\Phi} = 12.3$. The schematic view of the jets axis position projected in (oyz) plane in Figures 5.30 a) and 5.31 a), corresponds to the configurations with $\frac{L}{\Phi} = 15$ (cases 21 and 31), and to the configurations with $\frac{L}{\Phi} = 12.3$ (cases 37 and 43) in Figures 5.30 b) and 5.31 b). Cases with $\frac{L}{\Phi} = 12.3$ give better results.

The same conclusions can be drawn for downstream blowing by comparing cases 29 and 41 (station 2) and cases 23 and 39 (station 1). However, in Table 5.2, it can be seen that case 39 ($\frac{L}{\Phi} = 12.3$) does not suppress totally the separation whereas case 23 does. This result is then not coherent with what can be observed with the friction probes. This can be explained by the fact that, for case 39, the friction probes are nearer to the center of a counter-rotating device. So for $\frac{L}{\Phi} = 12.3$, the results seems to be better behind one counter-rotating VGs pair but worse between two counter-rotating VGs pair. It seems then, that a better configuration can be reached with $\frac{L}{\Phi} = 12.3$, but the value of $\frac{\lambda}{\Phi}$ has to be reduced. However, an optimum configuration for $\frac{L}{\Phi} = 12.3$ will have more jets, so the efficiency of this configuration, based on the momentum coefficient C_μ, will be comparable to the configuration $\frac{\lambda}{\Phi} = 27.3$ and $\frac{L}{\Phi} = 15$. This result indicates also that the parameter $\frac{\lambda}{\Phi}$ has to be smaller than $2\frac{L}{\Phi}$. Godard and Stanislas (2006b) found that the optimum parameter of $\frac{L}{\Phi}$ is between 12.5 to 16, so the results found for $\frac{L}{\Phi}$ is in good agreement with their study.

In conclusion, the value $\frac{L}{\Phi} = 15$ is effective (a total suppression of separation can be obtained), but it does not seems to be optimum. The value $\frac{L}{\Phi} = 12.3$ gives

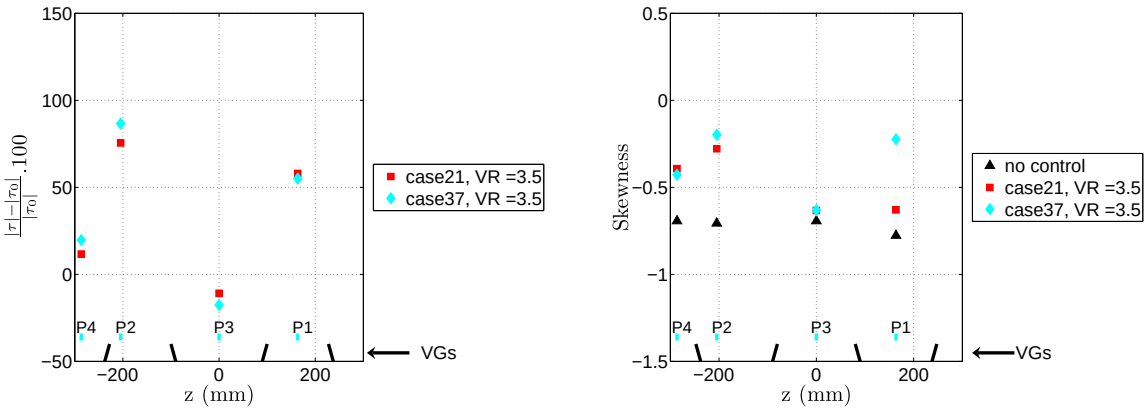

a) b)

Φ (mm)	β	α	$\frac{\lambda}{\Phi}$	$\frac{\Delta X_{vg}}{\Phi}$	VR	$\frac{L}{\Phi}$:	case 21	case 37
12	35°	125°	27.3	9.8	3.5		15	12.3

Figure 5.30: a) Gain in friction and b) Skewness for cases 21 and 37, $VR = 3.5$ (i.e. for two different values of $\frac{L}{\Phi}$ and the other parameters kept constant).

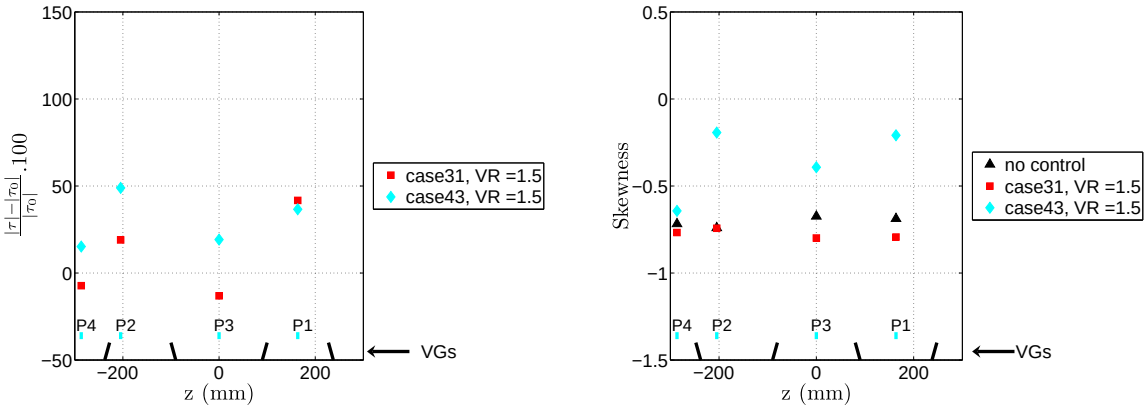

a) b)

Φ (mm)	β	α	$\frac{\lambda}{\Phi}$	$\frac{\Delta X_{vg}}{\Phi}$	VR	$\frac{L}{\Phi}$:	case 31	case 43
12	35°	55°	27.3	23.4	1.5		15	12.3

Figure 5.31: a) Gain in friction and b) Skewness for cases 31 and 43, $VR = 1.5$ (i.e. for two different values of $\frac{L}{\Phi}$ and the other parameters kept constant).

better results, but this configuration uses more jets. Also, $\frac{\lambda}{\Phi}$ has to be smaller than $2\frac{L}{\Phi}$. As the distance between the two nearby jets of neighbouring counter-rotating VGs pair has to be not too small, the best value here, normalized by Φ is 12.3, corresponding to the value used for the configurations with $\frac{L}{\Phi} = 15$. The corresponding $\frac{\lambda}{\Phi}$ parameter is then 27.3.

3.2.2.5 Effects of $\frac{\Delta X_{vg}}{\delta}$ or $\frac{\Delta X_{vg}}{\Phi}$

Figures 5.32, 5.33 and 5.34 show the evolution of the control efficiency with $\frac{\Delta X_{vg}}{\delta}$ at optimum VR and $\frac{\lambda}{\Phi} = 27.3$. In each of these figures, the first case presented is at station 1, and the second at station 2. As can be seen, as for the co-rotating configurations, the results seem to be independent of $\frac{\Delta X_{vg}}{\delta}$ for $0.6 \leq \frac{\Delta X_{vg}}{\delta} \leq 1.4$. This result is in agreement with the studies of Godard and Stanislas (2006b) and Lin et al. (1990) as Godard and Stanislas (2006b) found that counter-rotating continuous jets are efficient for $\frac{\Delta X_{vg}}{\delta} = 7.2$, so much further away from the separation line.

As there is no influence of $\frac{\Delta X_{vg}}{\delta}$ for the 2 diameters tested, there is no influence of the parameter $\frac{\Delta X_{vg}}{\Phi}$ in the range investigated (i.e. $9.8 \leq \frac{\Delta X_{vg}}{\Phi} \leq 46.8$).

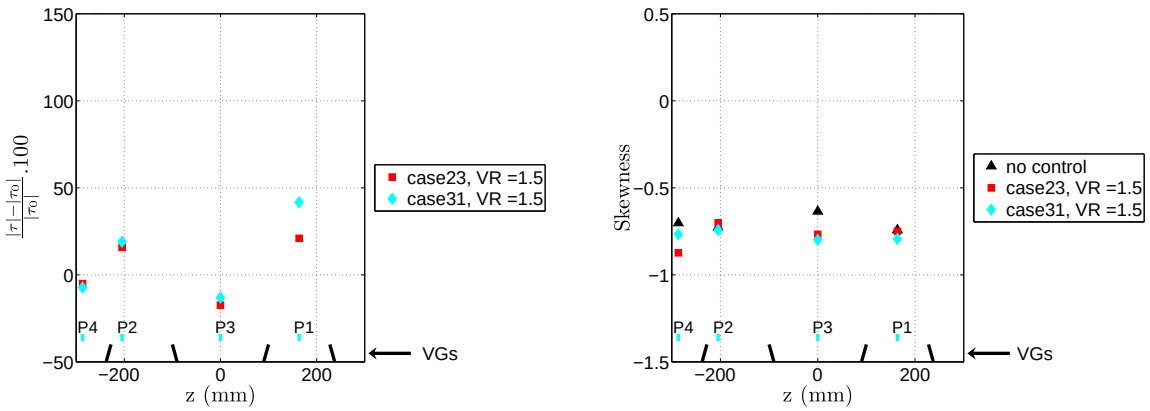

Φ (mm)	β	α	$\frac{\lambda}{\Phi}$	$\frac{L}{\Phi}$	VR	$\frac{\Delta X_{vg}}{\Phi}$:	case 23	case 31
12	35°	55°	27.3	15	1.5		9.8	23.4

Figure 5.32: a) Gain in friction and b) Skewness for cases 23 and 31, $VR = 1.5$ (i.e. for two different values of $\frac{\Delta X_{vg}}{\Phi}$ and the other parameters kept constant).

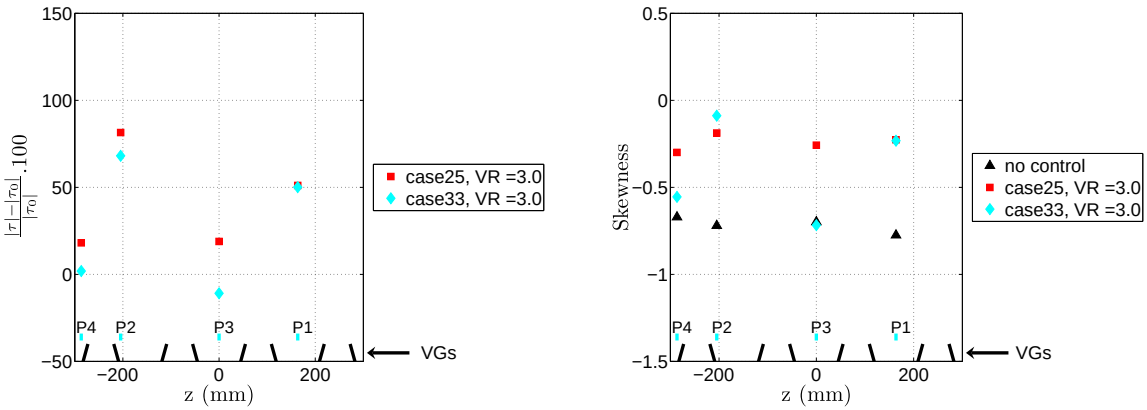

a) b)

Φ (mm)	β	α	$\frac{\lambda}{\Phi}$	$\frac{L}{\Phi}$	VR	$\frac{\Delta X_{vg}}{\Phi}$:	case 25	case 33
6	35°	125°	27.3	15	3		19.5	46.8

Figure 5.33: a) Gain in friction and b) Skewness for cases 25 and 33, $VR = 3$ (i.e. for two different values of $\frac{\Delta X_{vg}}{\Phi}$ and the other parameters kept constant).

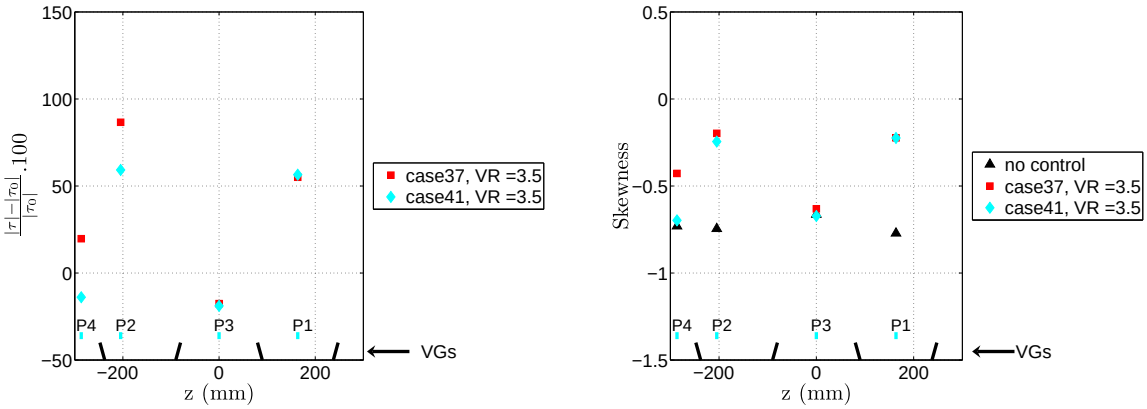

a) b)

Φ (mm)	β	α	$\frac{\lambda}{\Phi}$	$\frac{L}{\Phi}$	VR	$\frac{\Delta X_{vg}}{\Phi}$:	case 37	case 41
12	35°	125°	27.3	12.3	3.5		9.8	23.4

Figure 5.34: a) Gain in friction and b) Skewness for cases 37 and 41, $VR = 3.5$ (i.e. for two different values of $\frac{\Delta X_{vg}}{\Phi}$ and the other parameters kept constant).

3.2.2.6 Effects of $\frac{\Phi}{\delta}$

Two values of $\frac{\Phi}{\delta}$ were tested : $\frac{\Phi}{\delta} = 0.03$ and $\frac{\Phi}{\delta} = 0.06$. These values are near the values tested by Godard and Stanislas (2006b). Figures 5.35, 5.36, 5.37 and 5.38 give the evolution of the control efficiency with $\frac{\Phi}{\delta}$ at the optimum VR. The first case plotted in these figures corresponds to $\frac{\Phi}{\delta} = 0.06$ and the second to $\frac{\Phi}{\delta} = 0.03$. It appears clearly that the cases with $\frac{\Phi}{\delta} = 0.03$ give the best results at constant VR.

It seems that, for counter-rotating devices, the optimum parameter $\frac{\Phi}{\delta}$ found in these experiments is 0.03. On contrary to the co-rotating configurations, this is the case whatever the criterion used (constant VR, constant C_μ or constant Q_v).

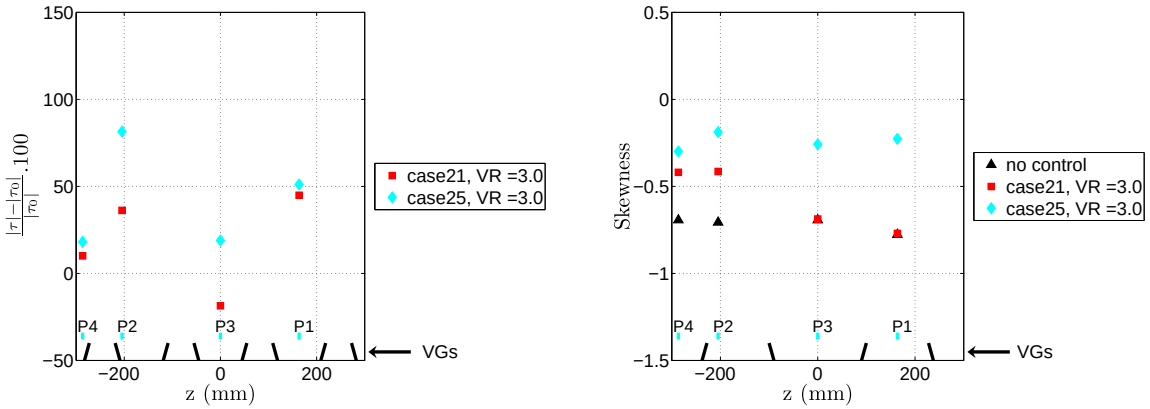

a) b)

β	α	$\frac{\lambda}{\Phi}$	$\frac{L}{\Phi}$	VR	$\frac{\Delta X_{vg}}{\Phi}$:	case 21	case 25	Φ (mm) :	case 21	case 25
35°	125°	27.3	15	3		9.8	19.5		12	6

Figure 5.35: a) Gain in friction and b) Skewness for cases 21 and 25, $VR = 3$ (i.e. for two different values of $\frac{\Phi}{\delta}$ (or Φ) and the other parameters kept constant ($\frac{\Delta X_{vg}}{\Phi}$ has no influence as seen in the previous section)).

3.2.3 Conclusion on the counter-rotating configurations

Two diameters of counter-rotating continuous jets (6 and 12 mm) were tested in different arrangements. For each arrangement, the velocity ratio VR tested was from 0.5 to 3.5 by steps of 0.5. It was found that the optimum $\frac{\lambda}{\Phi}$ has to be below $2\frac{L}{\Phi}$ (the value used for the experiments was 27.3 with $\frac{L}{\Phi} = 15$). This value is slightly smaller than the value of 32 suggested by Godard and Stanislas (2006b). These experiments confirm the interval $[12.5; 16]$ given by Godard and Stanislas (2006b) for the optimum value of $\frac{L}{\Phi}$.

For all the configurations tested, the minimum VR that gives control effect is 1.5, that is coherent with the previous studies of Godard and Stanislas (2006b), Betterton et al. (2000), Tilmann et al. (2000), McManus et al. (1994), Selby et al. (1992), etc.. As for co-rotating configurations, for upstream blowing, it was found that increasing VR increases continuously the control efficiency, whereas, for downstream blowing,

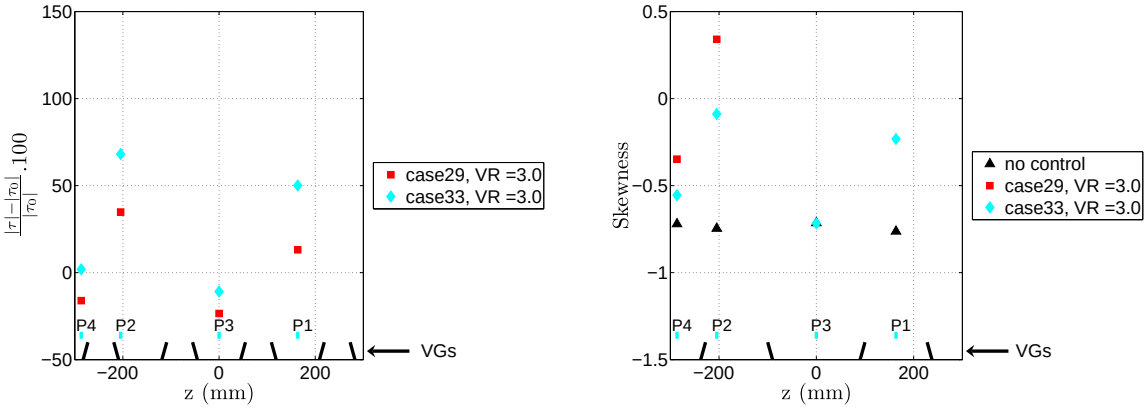

a) b)

β	α	$\frac{\lambda}{\Phi}$	$\frac{L}{\Phi}$	VR	$\frac{\Delta X_{vg}}{\Phi}$:	case 29	case 33	Φ (mm) :	case 29	case 33
35°	125°	27.3	15	3		23.4	46.8		12	6

Figure 5.36: a) Gain in friction and b) Skewness for cases 29 and 33, $VR = 3$ (i.e. for two different values of $\frac{\Phi}{\delta}$ (or Φ) and the other parameters kept constant ($\frac{\Delta X_{vg}}{\Phi}$ has no influence as seen in the previous section)).

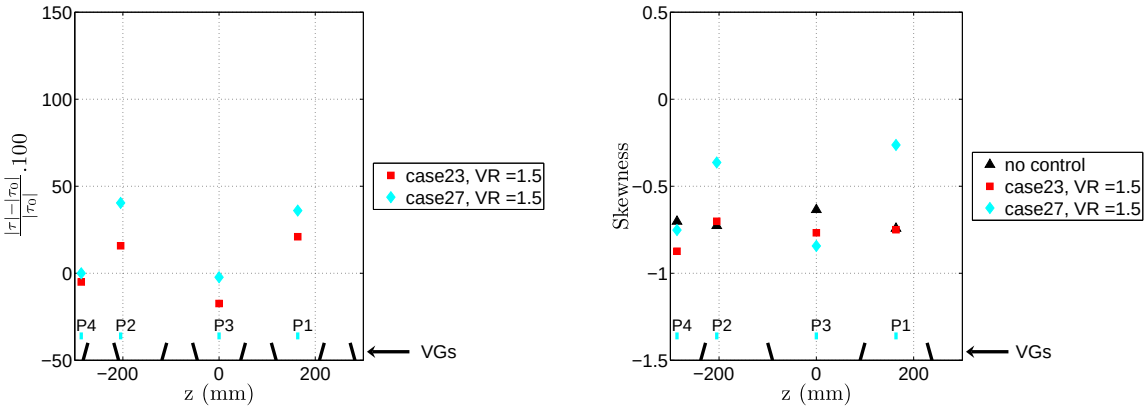

a) b)

β	α	$\frac{\lambda}{\Phi}$	$\frac{L}{\Phi}$	VR	$\frac{\Delta X_{vg}}{\Phi}$:	case 23	case 27	Φ (mm) :	case 23	case 27
35°	55°	27.3	15	1.5		9.8	19.5		12	6

Figure 5.37: a) Gain in friction and b) Skewness for cases 23 and 27, $VR = 1.5$ (i.e. for two different values of $\frac{\Phi}{\delta}$ (or Φ) and the other parameters kept constant ($\frac{\Delta X_{vg}}{\Phi}$ has no influence as seen in the previous section)).

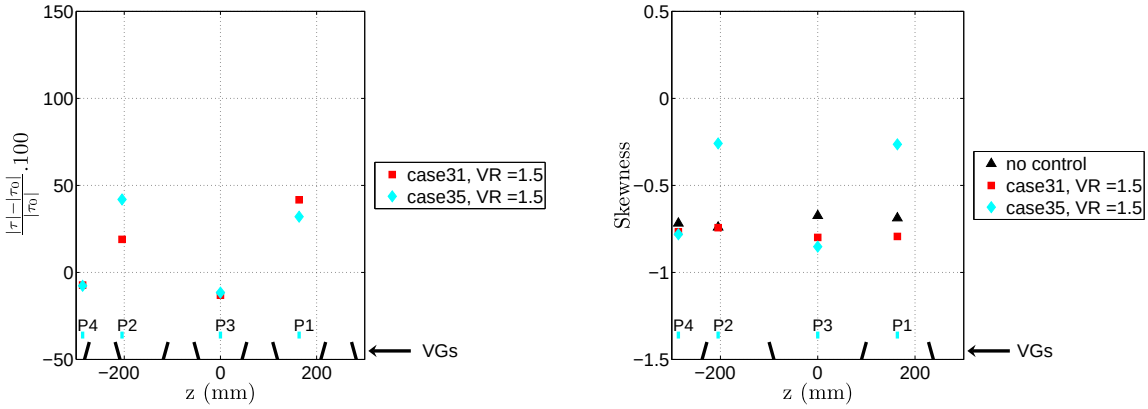

a) b)

β	α	$\frac{\lambda}{\Phi}$	$\frac{L}{\Phi}$	VR	$\frac{\Delta X_{vg}}{\Phi}$:	case 31	case 35	Φ (mm) :	case 31	case 35
35°	55°	27.3	15	1.5		23.4	46.8		12	6

Figure 5.38: a) Gain in friction and b) Skewness for cases 31 and 35, $VR = 1.5$ (i.e. for two different values of $\frac{\Phi}{\delta}$ (or Φ) and the other parameters kept constant ($\frac{\Delta X_{vg}}{\Phi}$ has no influence as seen in the previous section)).

there is an optimum VR between 1.5 and 2.5. Upstream blowing is consequently more robust than downstream blowing because VR can be increased up to $VR = 8$ without perturbing the reattachment. It was also found that there is no influence of the parameter $\frac{\Delta X_{vg}}{\delta}$ for $0.6 \leq \frac{\Delta X_{vg}}{\delta} \leq 1.6$, that is coherent with the study of Godard and Stanislas (2006b). Finally, it was found that the smallest diameter tested ($\frac{\Phi}{\delta} = 0.03$) gives the best results.

3.3 Comparison between co and counter-rotating configurations

As for a fixed diameter of jet tested (6 or 12 mm), the optimum configuration found for co-rotating arrangement has the same number of jets as the optimum configuration for counter-rotating (for $\Phi = 6$ mm, 22 jets for 2 m span, and for $\Phi = 12$ mm, 12 jets), the criterion based on constant VR is equivalent to constant flow rate Q_v and to constant momentum coefficient C_μ.

Figure 5.39 gives the comparative results for co and counter-rotating configurations with $\Phi = 12$ mm, $\alpha = 125°$ and $VR = 3$ at station 1. Here, the co-rotating configuration (case 2) gives better results than the counter-rotating one. The same conclusion is obtained by comparing cases 12 and 29. So for upstream blowing and $\Phi = 12$ mm, it seems that the co-rotating configurations give better results than the counter-rotating ones.

Figure 5.40 gives the comparative results for co and counter-rotating configurations with $\Phi = 12$ mm, $\alpha = 55°$ and $VR = 2$ at station 2. Here, the co-rotating configuration (case 16) gives better results than the counter-rotating one. The same conclusion is obtained by comparing cases 6 and 23. So for downstream blowing, as

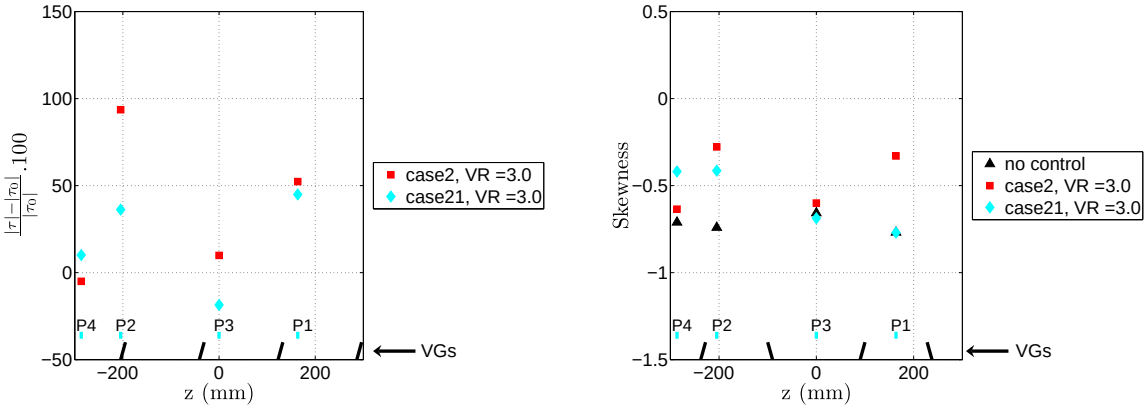

a) b)

Φ (mm)	β	α	$\frac{\Delta X_{vg}}{\Phi}$	VR	$\frac{\lambda}{\Phi}$:	case 2	case 21	$\frac{L}{\Phi}$:	case 2	case 21
12	35°	125°	9.8	3		13.6	27.3		-	15

Figure 5.39: a) Gain in friction and b) Skewness for cases 2 (co-rotating configuration) and 21 (counter-rotating configuration), $VR = 3$ (i.e. for co and counter-rotating VGs configurations with similar parameters).

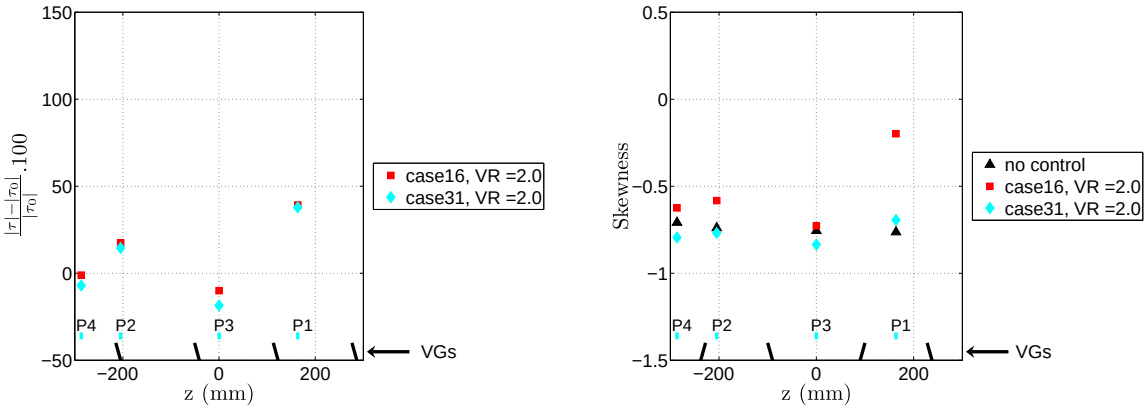

a) b)

Φ (mm)	β	α	$\frac{\Delta X_{vg}}{\Phi}$	VR	$\frac{\lambda}{\Phi}$:	case 16	case 31	$\frac{L}{\Phi}$:	case 16	case 31
12	35°	55°	23.4	2		13.6	27.3		-	15

Figure 5.40: a) Gain in friction and b) Skewness for cases 16 (co-rotating configuration) and 31 (counter-rotating configuration), $VR = 2$ (i.e. for co and counter-rotating VGs configurations with similar parameters).

for upstream blowing, for $\Phi = 12$ mm, it seems that the co-rotating configurations give better results than the counter-rotating ones.

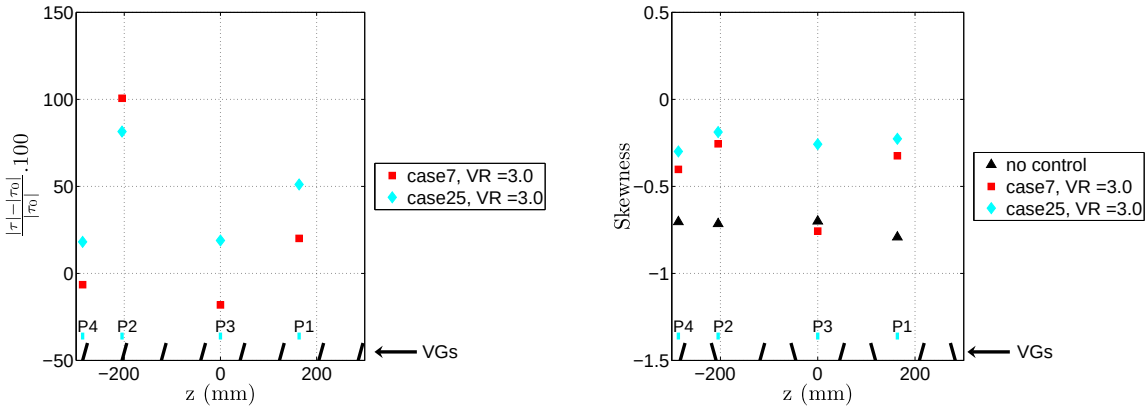

Φ (mm)	β	α	$\frac{\Delta X_{vg}}{\Phi}$	VR	$\frac{\lambda}{\Phi}$:	case 7	case 25	$\frac{L}{\Phi}$:	case 7	case 25
6	35°	125°	19.5	3		13.6	27.3		-	15

Figure 5.41: a) Gain in friction and b) Skewness for cases 7 (co-rotating configuration) and 25 (counter-rotating configuration), $VR = 3$ (i.e. for co and counter-rotating VGs configurations with similar parameters).

Figure 5.41 gives the comparative results for co and counter-rotating configurations with $\Phi = 6$ mm, $\alpha = 125°$ and $VR = 3$ at station 1. Here, the counter-rotating configuration (case 25) gives better results than the co-rotating one. The same conclusion is obtained by comparing cases 17 and 33. So for upstream blowing and $\Phi = 6$ mm, it seems that the counter-rotating configurations give better results than the co-rotating ones.

Figure 5.42 gives the comparative results for co and counter-rotating configurations with $\Phi = 6$ mm, $\alpha = 55°$ and $VR = 2$ at station 2. Again, the counter-rotating configuration (case 35) gives better results than the co-rotating one. The same conclusion is obtained by comparing cases 9 and 27. So for downstream, as for upstream blowing, for $\Phi = 6$ mm, it seems that the counter-rotating configurations give better results than the co-rotating ones.

In conclusion, for the larger diameter tested ($\Phi = 12$ mm or $\frac{\Phi}{\delta} = 0.06$), it appears that the optimum co-rotating configuration found gives better results than the optimum counter-rotating one. On the contrary, for the smaller diameter ($\Phi = 6$ mm or $\frac{\Phi}{\delta} = 0.03$), the optimum counter-rotating configuration is better than the co-rotating one. As the optimum of $\frac{\Phi}{\delta}$ is 0.03, it can be concluded that the optimum counter-rotating configuration gives better results than optimum co-rotating one which is coherent with the previous study of Godard and Stanislas (2006b). However, some co-rotating configurations are efficient enough to suppress totally the separation.

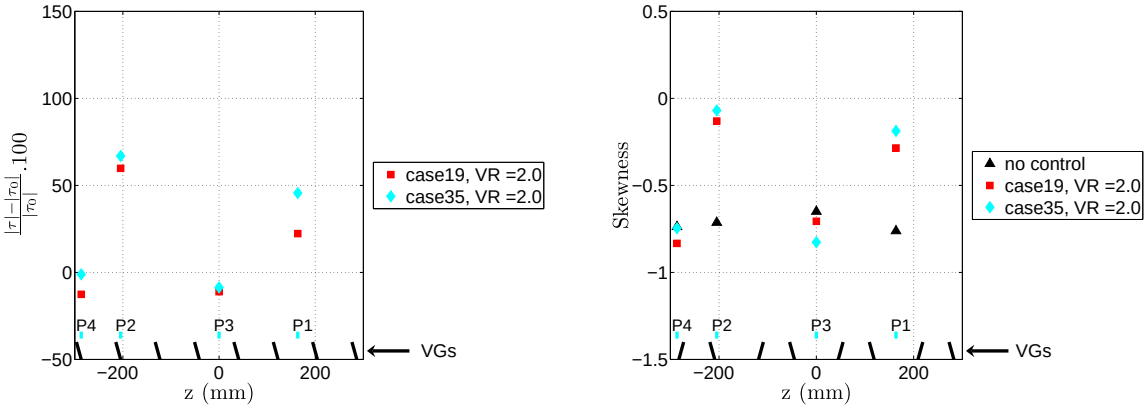

a) b)

Φ (mm)	β	α	$\frac{\Delta X_{vg}}{\Phi}$	VR	$\frac{\lambda}{\Phi}$:	case 19	case 35	$\frac{L}{\Phi}$:	case 19	case 35
6	35°	55°	46.8	2		13.6	27.3		-	15

Figure 5.42: a) Gain in friction and b) Skewness for cases 19 (co-rotating configuration) and 35 (counter-rotating configuration), $VR = 2$ (i.e. for co and counter-rotating VGs configurations with similar parameters).

4 Conclusion on active devices

Co and counter-rotating continuous jets were tested to suppress an existing separation. Upstream and downstream blowing were tested for two jets diameters ($\Phi = 6$ and 12 mm). Some of the tested configurations suppress totally the separation. Some common results were found between co and counter-rotating configurations. First, for upstream blowing, the control effect begins at $VR = 1.5$, and increases continuously with VR. This result agrees with the previous studies of Godard and Stanislas (2006b), Betterton et al. (2000), Tilmann et al. (2000), McManus et al. (1994), Selby et al. (1992), etc.. Secondly, for downstream blowing, the control effect begins at $VR = 1.5$ too, but an optimum VR exists between 1.5 and 2.5. Blowing upstream is then more robust than blowing downstream, because the maximum efficiency is higher and a total suppression of separation can be reached. Thirdly, a value of $\frac{\Phi}{\delta} = 0.03$ is better than $\frac{\Phi}{\delta} = 0.06$, and finally, in agreement with Godard and Stanislas (2006b), there is no influence of the parameter $\frac{\Delta X_{vg}}{\delta}$ for $0.6 \leq \frac{\Delta X_{vg}}{\delta} \leq 1.4$.

For co-rotating configurations, the optimum value of $\frac{\lambda}{\Phi}$ is 13.6, that is twice the optimum value found by Godard and Stanislas (2006b). For counter-rotating configurations, the value $\frac{\lambda}{\Phi}$ has to be smaller than $2\frac{L}{\Phi}$. The value $\frac{\lambda}{\Phi} = 27.3$ that was used in these experiments for $\frac{L}{\Phi} = 15$ is then acceptable. The results also confirm that the optimum value for $\frac{L}{\Phi}$ is between 12 and 16.

This optimization leads, at constant diameter, to the same number of jets for co and counter-rotating configurations. The optimum co-rotating configuration for $\Phi = 12$ mm gives better results than the optimum counter-rotating configuration with the same jets diameter. However, optimum counter-rotating actuators with $\Phi = 6$ mm give better results than the optimum co-rotating configurations with the

same diameter. As the best parameter of $\frac{\Phi}{\delta}$ is 0.03, the best configuration found in this study is the counter-rotating, $\Phi = 6$ mm, $\frac{\lambda}{\Phi} = 27.3$, $\frac{L}{\Phi} = 15$ and $\alpha = 125°$ (upstream blowing), with a VR larger than 3. As diameters smaller than 6 mm were not tested, maybe a better counter-rotating configuration can be obtained with a smaller diameter. The optimum parameters found are summarized in Table 5.3, where the bold parameters correspond to the best of the best.

Table 5.3: Optimum parameters for co and counter-rotating active configurations tested.

	$\frac{\Phi}{\delta}$	β	α	$\frac{\lambda}{\Phi}$	$\frac{L}{\Phi}$	VR
co	0.03	35	55	13.6	-	2
	0.03	35	**125**	13.6	-	3.5
counter	0.03	35	55	27.3	15	2
	0.03	35	**125**	27.3	15	3.5

The co-rotating passive configurations seem to be clearly different from the active ones. Indeed, the best passive co-rotating configuration is obtained for $\frac{\lambda}{\delta} = 0.9$ and the best active co-rotating configuration is obtained for $\frac{\lambda}{\delta} = 0.4$. There is a factor 2 between the two configurations. The active configuration has then 2 times more actuators than the passive one, but it is the only one that can suppress the separation. The difference between the two can be explained by a difference in the physic of the vortex generation.

The counter-rotating passive configurations seem however to behave similarly to the active ones. The best passive counter-rotating configuration is obtained for $\frac{\lambda}{\delta}$ between 0.5 to 0.9, and for $\frac{L}{\delta}$ between 0.20 to 0.38. The best active counter-rotating configuration is obtained for $\frac{\lambda}{\delta} = 0.8$ and for $\frac{L}{\delta}$ between 0.36 to 0.48. The parameters $\frac{\lambda}{\delta}$ and $\frac{L}{\delta}$ are thus very close for the best passive and the best active counter-rotating configurations. This can explain why they give almost the same results.

As a general conclusion, as passive counter-rotating configurations give comparable results as co and counter-rotating active steady jets ones, the flow separation can be control indifferently by passive counter-rotating or by active co or counter-rotating configurations. The major part of the results are in good agreement with Godard and Stanislas (2006a,b), Selby et al. (1992), etc., although some result differ slightly. Consequently, it seems that the optimum parameters, for a given actuators configuration, is dependent on the flow characteristics. More details studies are then needed for a better understanding on the physic of flow control.

Chapter 6

Flow physics of some active control tests

1 introduction

This chapter presents the results concerning the flow physics of some selected active control tests which were done and described in Chapter 5. The ramp configuration is the same as in the two previous chapters ($\alpha = -2°$, $\beta = -22°$ and $U_\infty = 10\ m/s$). The aim of these additional tests was to obtain more quantitative informations about the flow organisation of some efficient active control configurations. These results can then be used to conclude about the optimum configuration, and maybe the control mechanism can be explained from them. Firstly, the streamwise pressure distribution of some selected active configurations will be discussed. Then the flow characteristics of these configurations, obtained by a streamwise 2D2C PIV measurement on the flap, will be presented.

2 Pressure distribution for some active control tests

2.1 Active configurations selection

As seen in Chapter 5, the round jets configurations with the smallest diameter tested ($\frac{\Phi}{\delta} = 0.03$) were giving the best results. The configurations retained for the present tests were those with this jet diameter. As no effect of the distance from the separation line ($\frac{\Delta X_{vg}}{\Phi}$) was observed in the investigated range, and as the suction peak just before the flap articulation was found characteristic of the separation (see Chapter 3), only the configurations with $\frac{\Phi}{\delta} = 0.03$ at control station 2 ($s = 3219$ mm) were retained. At this station, the suction peak measurement was available to see the control effect on it. As the optimum upstream and downstream blowing configurations were having a different velocity ratio VR, both were tested to see the difference between upstream and downstream blowing. Both co and counter-rotating configurations were also tested to try to exhibit difference between them.

The selected configurations were then the co and counter-rotating configurations of Chapter 5, with $\frac{\Phi}{\delta} = 0.03$, $\frac{\Delta X_{vg}}{\Phi} = 46.8$ (i.e. control station 2), and $\alpha = 55°$ (downstream blowing) and $\alpha = 125°$ (upstream blowing). The velocity ratio for

these configurations was selected at the optimum. However, some values of VR different from the optimum were also tested. As the actuators were mounted at control station 2, pressure tap 15 (see Chapter 2) was not available, which can conduct to enlarge the suction peak when representing the pressure distribution with curves.

2.2 Co-rotating configurations

Figure 6.1 shows the pressure and pressure gradient coefficient distribution for the co-rotating configurations. The distribution without control is added for comparison. The upstream blowing configuration with $VR = 1.5$ (i.e. the minimum one to detect control efficiency) has no effect on the pressure and pressure gradient distributions. The only difference is near tap 15, which was not available in the control tests. The minimum VR (1.5) which was giving control effect in Chapter 5 is not evidenced by the pressure distribution. Maybe because it is measured at mid-span, in the middle of two jets which, for this VR, is a critical region with no evident upwash or downwash (Kostas et al. (2007)).

The three other tests in Figure 6.1 give similar results for the pressure distribution. Compared to the uncontrolled flow, the suction peak decreases to reach a value close to 0.28, which can then be considered as characteristic of attached flow (the upstream blowing configuration at $VR = 3.5$ corresponds to a fully attached flow (see Chapter 5)). For the downstream blowing configuration with $VR = 3.5$, this suction peak is slightly more intense, which suggests a better efficiency. This contradicts the results obtained in Chapter 5, were the optimum VR found for this configuration was between 1.5 and 2.5. However, only one spanwise position for the streamwise pressure distribution is available, so no information about the transverse control efficiency is available and then a conclusion is difficult to draw. The drop in efficiency for downstream blowing configurations with increasing VR beyond $VR = 2.5$ could be due to a loss of control transverse homogeneity which cannot be observed by only one streamwise pressure distribution.

Concerning the pressure gradient distribution (Figure 6.1 b)), these three control tests give similar results for the pressure recovery on the flap. However, the favourable pressure gradient peak for the upstream blowing configuration with $VR = 3.5$ is less intense but slightly wider. As a wider suction peak on the suction side of a wing conducts to more lift, the upstream blowing configuration with $VR = 3.5$ seems then the best one which agrees with the results obtained in Chapter 5.

2.3 Counter-rotating configurations

Figure 6.2 shows the pressure and pressure gradient coefficient distributions for the counter-rotating configurations, compared to the case without control. The upstream blowing configuration with $VR = 2$, which was found partially attached in Chapter 5, gives a suction peak value of 0.33 which is close to the value of attached flow (i.e. 0.28 as seen in the previous section). The pressure distribution is close here to the two other configurations which are known to be fully attached. This result seems to contradict those obtained in Chapter 5. However, the pressure

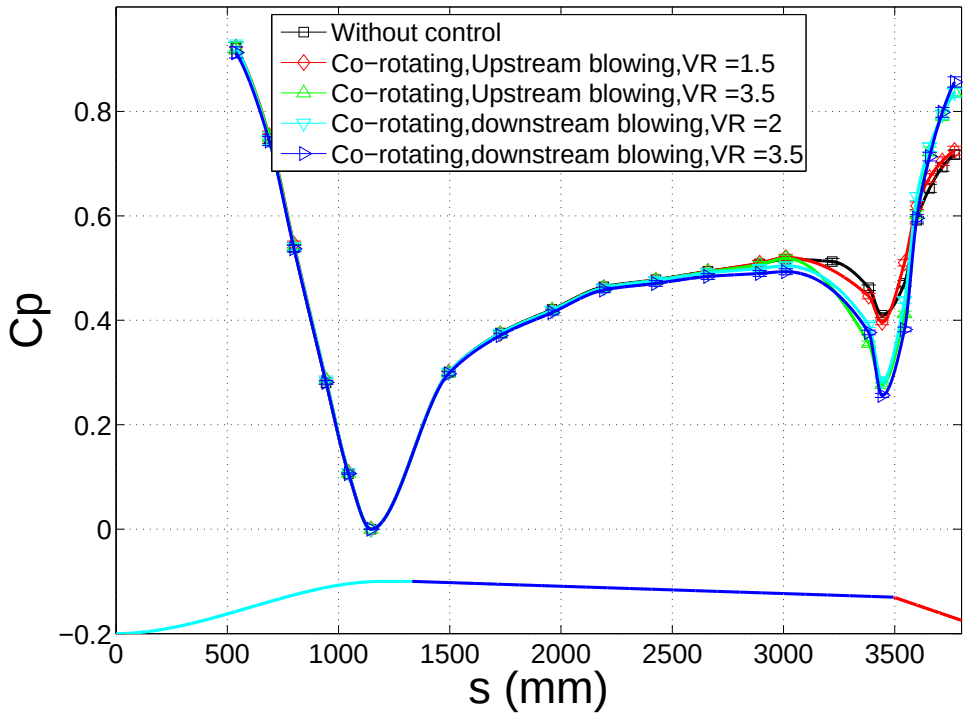

a)

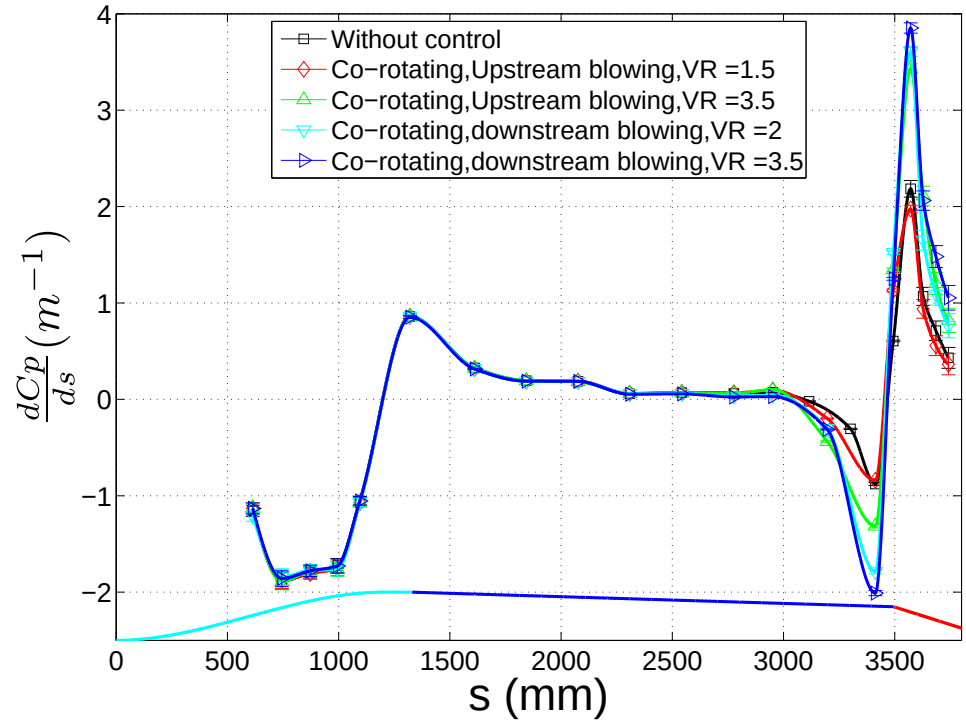

b)

Figure 6.1: a) Streamwise pressure, b) streamwise pressure gradient coefficient, for different co-rotating configurations (i.e. different α and VR) at $s = 3219$ mm.

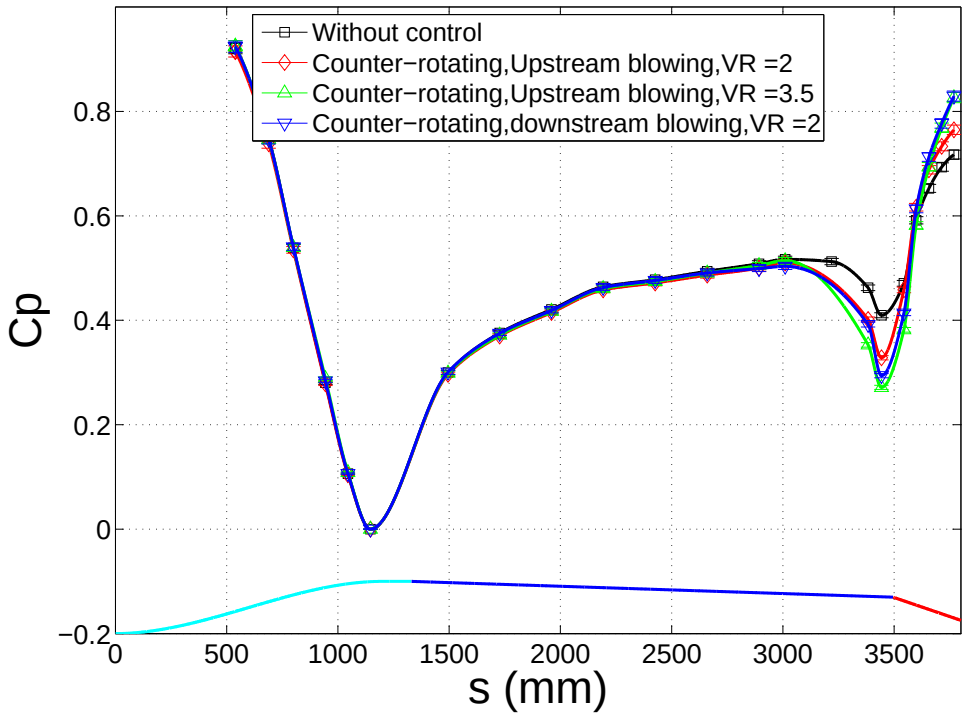

a)

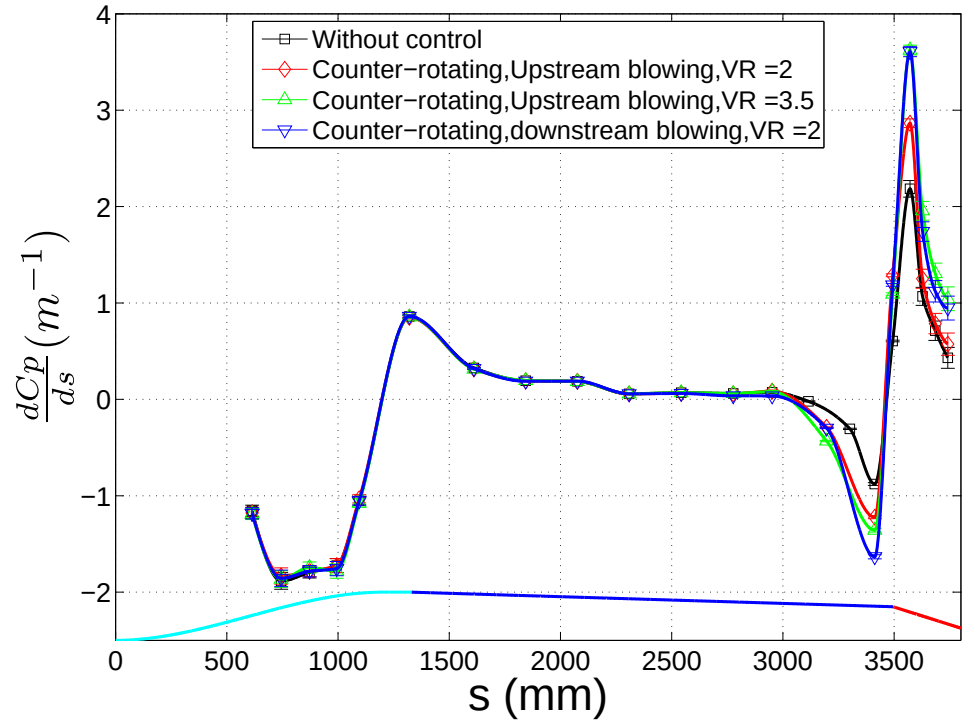

b)

Figure 6.2: a) Streamwise pressure, b) streamwise pressure gradient coefficient, for different counter-rotating configurations (i.e. different α and VR) at $s = 3219$ mm.

distribution is measured in the middle of a pair of counter-rotating VGs, which corresponds to a downwash region (Kostas et al. (2007)) which is less sensitive to partial reattachment.

The upstream blowing configuration at $VR = 3.5$ gives a slightly better suction peak (more intense and wider) than the two others. This is in agreement with Chapter 5 where this configuration was found optimum.

2.4 Comparison between the optimum co and counter-rotating configurations

Figure 6.3 shows the pressure and pressure gradient coefficient distributions for the optimum co and counter-rotating configurations. The distribution without control is added for comparison. All these configurations correspond to a full reattachment, except for co-rotating downstream blowing, which corresponds to a delay and a significant reduction of the separation (i.e. nearly fully attached flow).

The suction peak level is the same for all these configurations (about 0.28). This confirms that this value is characteristic of attached flow. It is remarkable that both pressure and pressure gradient distributions are quite close for the optimum co and counter-rotating upstream blowing configurations. The same is true for the downstream blowing configurations. This seems to contradict the results obtained in Chapter 5, where it was concluded that for this jets diameter, the counter-rotating configurations are more efficient. As was seen before, this disagreement can however be explained by the fact that, only one streamwise pressure distribution is available, so no conclusion can be drawn concerning the spanwise control efficiency.

However, as the suction peak is slightly larger, the upstream blowing configurations appear a bit better than the downstream ones. This is in agreement with Chapter 5 results.

3 Flow organisation of some active control tests

3.1 Active configurations selection

The configurations selected were the same as for the pressure distribution. However, to decrease the quantity of data to post-process, the downstream blowing co-rotating configuration was not carried out. Also, to try to confirm the optimum VR range of downstream blowing, VR was 2.5 for the counter-rotating configuration, which corresponds to the optimum range limit (see Chapter 5). In summary, the tested configurations with PIV measurements correspond to $\frac{\Phi}{\delta} = 0.03$ at station 2 ($s = 3219$ mm or $\frac{\Delta X_{vg}}{\Phi} = 46.8$), $\alpha = 55°$ and $\alpha = 125°$ for counter-rotating ones and $\alpha = 125°$ for the co-rotating one. For the upstream blowing configurations, VR was set at 3.5, and for the downstream blowing one at 2.5.

In the following of this chapter, the reference flow without control will be called "Without control", the co-rotating case "co-up", the counter-rotating upstream blowing case "counter-up" and counter-rotating downstream blowing case "counter-down". Table 6.1 summarizes the parameters of the control tests selected.

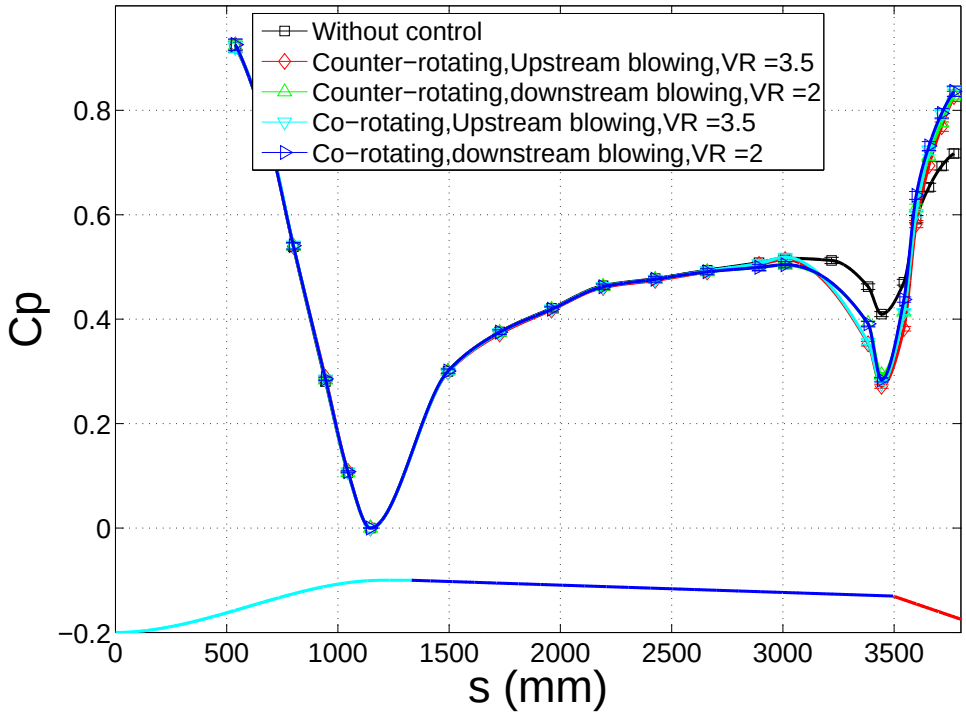

a)

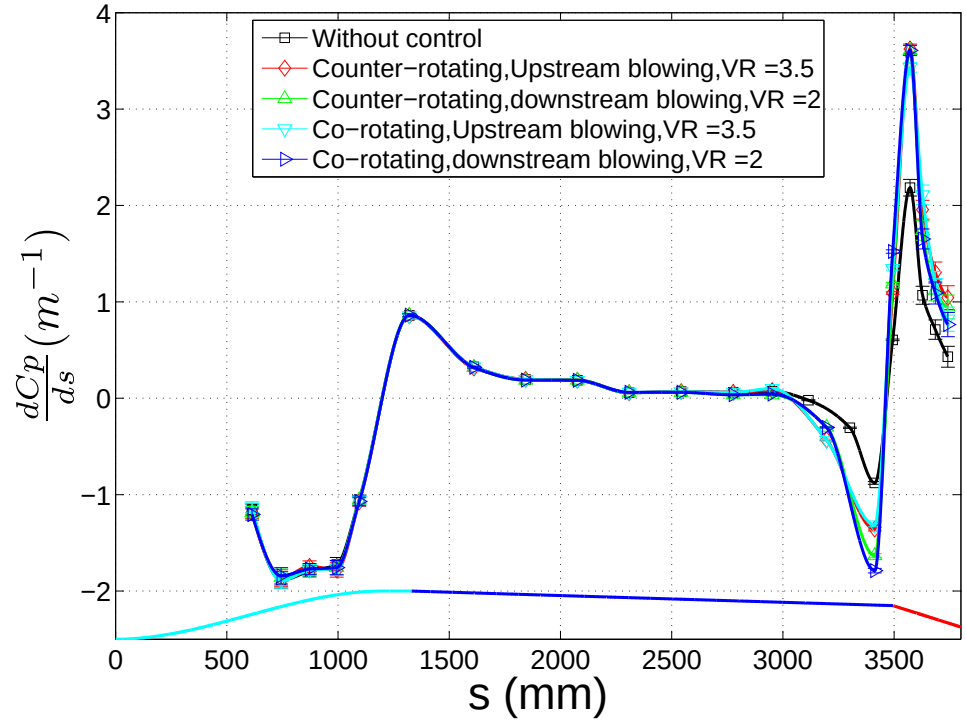

b)

Figure 6.3: a) Streamwise pressure, b) streamwise pressure gradient coefficient, for the optimum co and counter-rotating configurations at $s = 3219$ mm.

Table 6.1: Table of the parameters of the control configurations selected.

Set-up	Φ (mm)	$\frac{\Delta X_{vg}}{\Phi}$	β (°)	α (°)	VR
co-up	6	46.8	35	125	3.5
counter-up	6	46.8	35	125	3.5
counter-down	6	46.8	35	55	2.5

The flow organisation and the separation characteristics of these control cases were obtained with the streamwise 2D2C PIV set-up described in Chapter 2. The PIV fields obtained are then at the same spanwise position as the streamwise pressure distribution given in the previous section. For the co-rotating configuration, it is midway between two jets, and for the counter-rotating configurations, in the middle of a counter-rotating jets pair.

3.2 Mean velocity at hot-wire station 5

Figure 6.4 shows the mean streamwise velocity profile in external units at hot-wire station 5 for the three control cases. The hot-wire and the PIV without control are added for comparison. For all cases, above $\frac{y}{\delta} = 0.3$, the collapse with hot-wire is very good. Below $\frac{y}{\delta} = 0.3$, the co-up case profile shows a significant deficit compared to the uncontrolled one. This is the trace of an upwash region (low momentum near wall fluid ejected). This is in good agreement with the position of the vortex cores found by Kostas et al. (2007) at $VR = 2.3$ for co-rotating continuous jets (indeed, Kostas et al. (2007) and Milanovic and Zaman (2004) found that, when increasing VR, the vortex core moves in the transverse direction according to the jets direction. The upwash region moves then in the same way and reaches the measurement plane at midway between two jets. This is illustrated in Figure 6.5 a)).

The S-shaped profile for the co-up case below $\frac{y}{\delta} = 0.3$ is in agreement with the studies of McManus et al. (1994), Godard and Stanislas (2006b) and Kostas et al. (2007). This S-shape imposed then an inflection point in the profile near $\frac{y}{\delta} \simeq 0.23$. The jet penetration in this measurement plane can be estimated as the size of the deficit region and is then about 0.3δ (or 6 cm). The maximum velocity deficit is about $0.2\,U_e$ at $\frac{y}{\delta} \simeq 0.1$, with U_e the local free-stream velocity, which is quite strong.

For the counter-up case, below $\frac{y}{\delta} = 0.2$, the profile is above the uncontrolled one, which is the result of a downwash region. This agrees with the study of Kostas et al. (2007) (Figure 6.5 b)) as the measurement plane is in the middle of a counter-rotating jets pair. The jet penetration in this measurement plane is estimated at 0.2δ (or 4 cm), which is below the value obtained for co-up. The maximum velocity benefit is about $0.1\,U_e$ at $\frac{y}{\delta} \simeq 0.06$. No S-shape is observed on this profile which agrees with Godard and Stanislas (2006b) who found less evident S-shape for the counter-rotating active configurations at the same spanwise position.

The profile for the counter-down case is very similar to the counter-up one. The downwash region observed agrees again with the study of Kostas et al. (2007). The jet penetration is comparable to the counter-up case (about 0.2δ or 4 cm). The

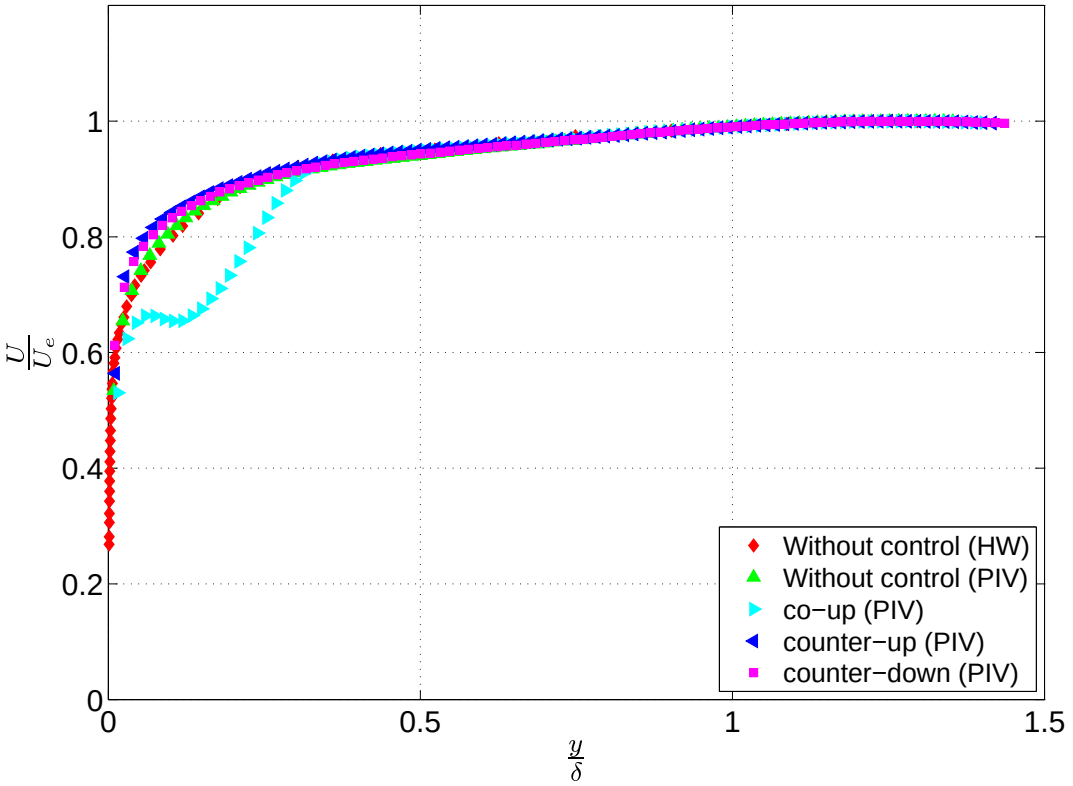

Figure 6.4: Mean streamwise velocity profiles in external units at hot-wire station 5, for the three control cases, compared to the hot-wire and PIV ones without control.

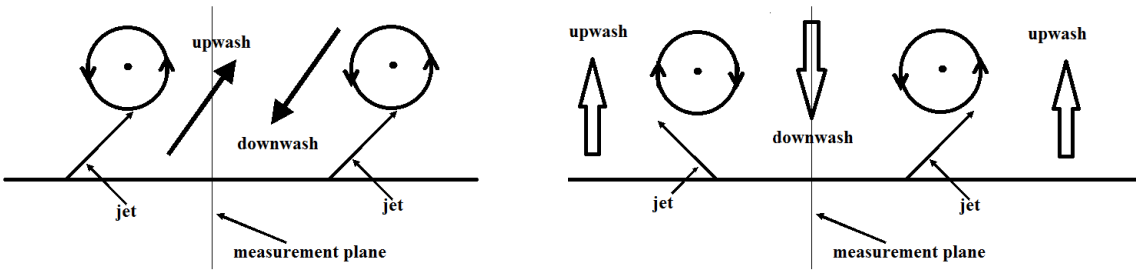

a) b)

Figure 6.5: Induced flow by a) co-rotating jets, b) counter-rotating jets.

Table 6.2: Table of the boundary layer characteristics obtained by PIV at hot-wire station 5 for the different test cases.

Set-up	u_τ (m/s)	δ (cm)	δ^* (mm)	θ (mm)	H
without control	0.48	21.1	18.5	14.8	1.25
co-up		20.4	24.0	17.0	1.41
counter-up		20.2	15.6	12.5	1.24
counter-down		20.0	16.6	13.3	1.25

maximum velocity benefit is about 0.07 U_e at the same position as for the counter-up case. In agreement with Godard and Stanislas (2006b), no S-shape is observed on the profile.

Table 6.2 gives the boundary layer characteristics obtained by PIV at hot-wire station 5 for the different test cases. The friction velocity was not estimated for the control cases as no log-law is evidenced. For all control cases the boundary layer thickness decreases slightly compared to the uncontrolled case. For the counter-rotating cases, the integral thicknesses are decreased and the shape factor is conserved, which is coherent with a downwash region. On contrary, the co-up case leads to a significant increase of both the integral thicknesses and the shape factor. The co-up boundary layer obtained is consequently less resistant to separation, which confirms the critical nature of upwash region.

Figure 6.6 shows the mean wall normal velocity profile in external units at hot-wire station 5 for the three control cases. The PIV profile without control is added for comparison. For the co-up case, below $\frac{y}{\delta} = 0.25$, positive values are observed which confirms the upwash. At $\frac{y}{\delta} = 0.3$ the profile crosses the uncontrolled one and remains close to it in the outer part.

For the counter-up case, the downwash is confirmed by the negative peak near the wall ($\frac{y}{\delta} \simeq 0.2$). The counter-down profile shows a similar trend as the counter-up one. The negative velocities peak is at $\frac{y}{\delta} = 0.17$, slightly nearer to the wall compared to the counter-up. This suggests a lower jets penetration which was not observed on the streamwise velocity. However, this agrees with the lower VR for the counter-down case compared to the two other test cases. In the outer part, the profiles are quite close and in the range of the uncertainty. Nevertheless, the counter-down profile is clearly below the others above $\frac{y}{\delta} = 0.6$, which indicates a flow more directed toward the wall in the whole boundary layer thickness. This may explain why downstream blowing reattaches the flow at lower VR than upstream blowing.

3.3 Turbulence intensity at hot-wire station 5

Figures 6.7, 6.8 and 6.9 show respectively the streamwise turbulent intensity ($u = \sqrt{\overline{u'^2}}$), the wall normal turbulent intensity ($v = \sqrt{\overline{v'^2}}$) and the Reynolds shear stress profiles ($-uv = -\overline{u'v'}$) in external units at hot-wire station 5 for the three control cases. For comparison, the corresponding uncontrolled profiles are also plotted. For

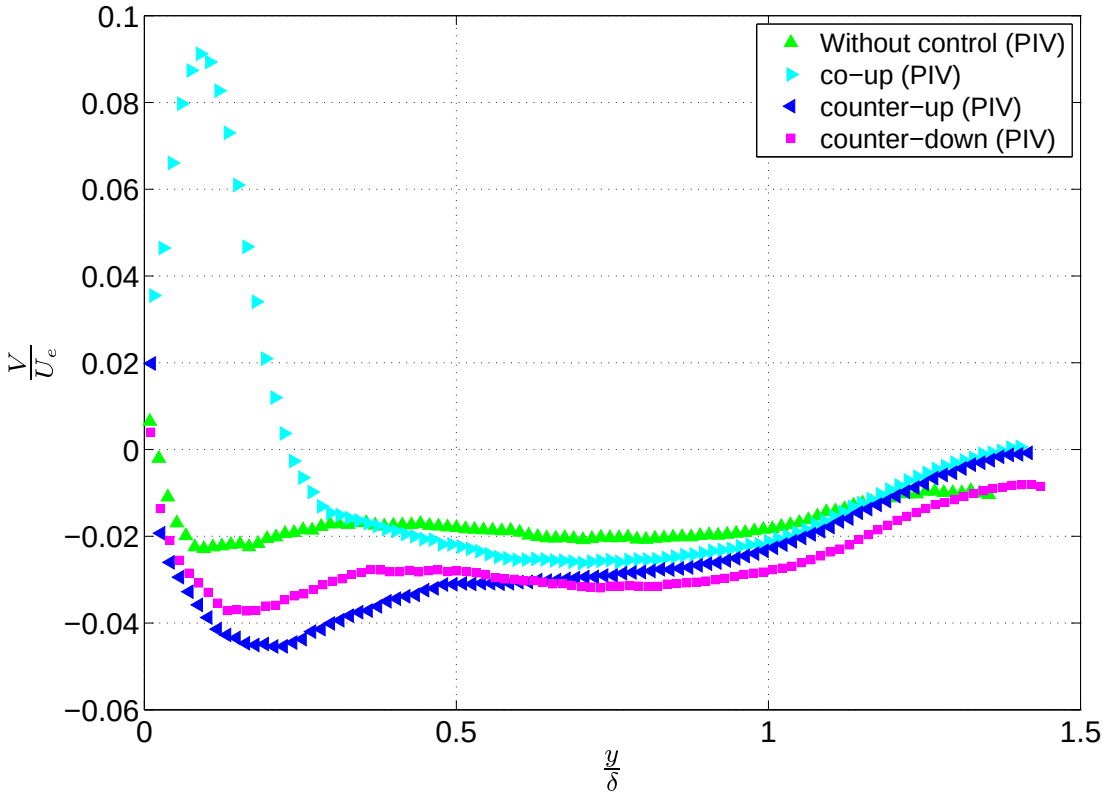

Figure 6.6: Mean wall-normal velocity profiles in external units at hot-wire station 5, for the three control cases, compared to PIV profile without control.

the streamwise turbulence intensity, the hot-wire profile is also added to keep in mind the PIV uncertainty. For the co-up case, a significant peak develops around $\frac{y}{\delta} = 0.2$ for all Reynolds stresses. These peaks confirm the jets penetration as they probably correspond to the unsteady motion of the streamwise structures generated by the actuators under the excitation of the large scale structures of the oncoming boundary layer.

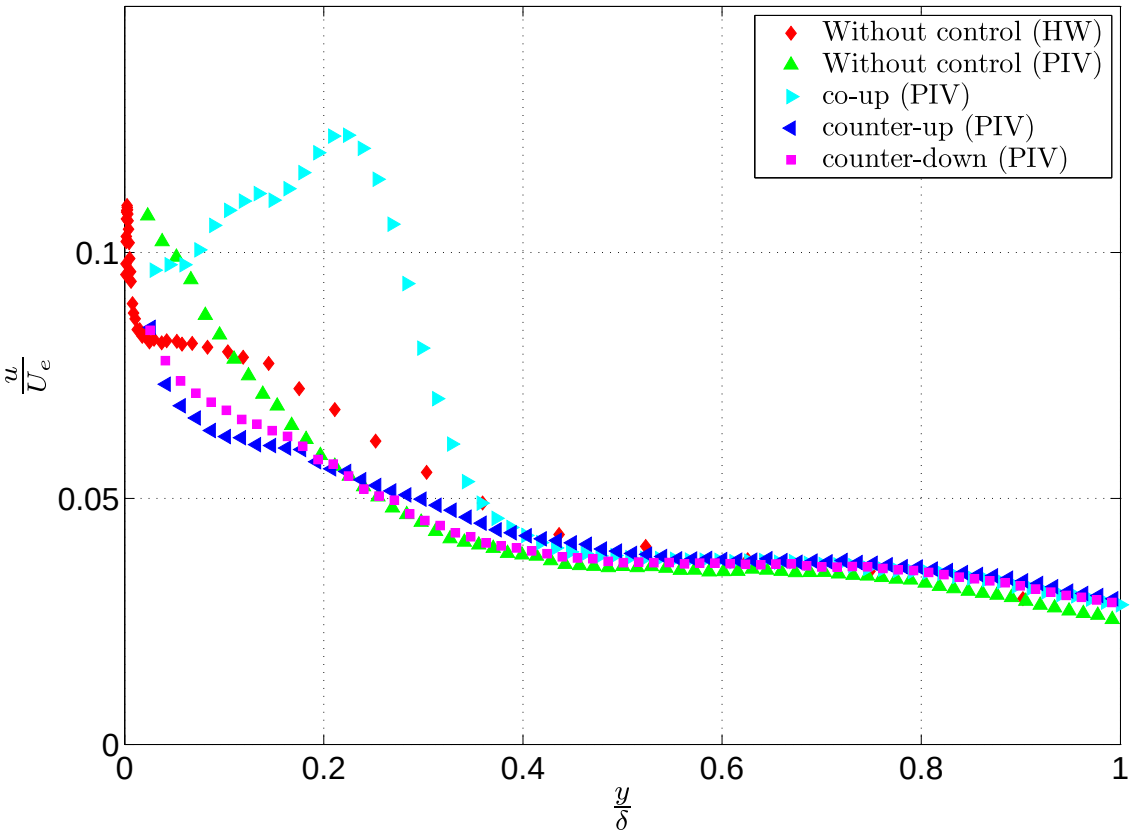

Figure 6.7: Streamwise turbulence intensity profiles in external units at hot-wire station 5, for the three control cases, compared to the hot-wire and PIV ones without control.

The counter-up and counter-down cases profiles are quite similar. Below $\frac{y}{\delta} \simeq 0.2$, the turbulence intensities and the Reynolds shear stress are below the ones of the uncontrolled case. This is attributed to the downwash region, which brings to the wall external flow which has a low turbulence level. Above $\frac{y}{\delta} \simeq 0.2$, the counter-down profiles seems nearer to the uncontrolled case, however the PIV uncertainty does not allow to conclude.

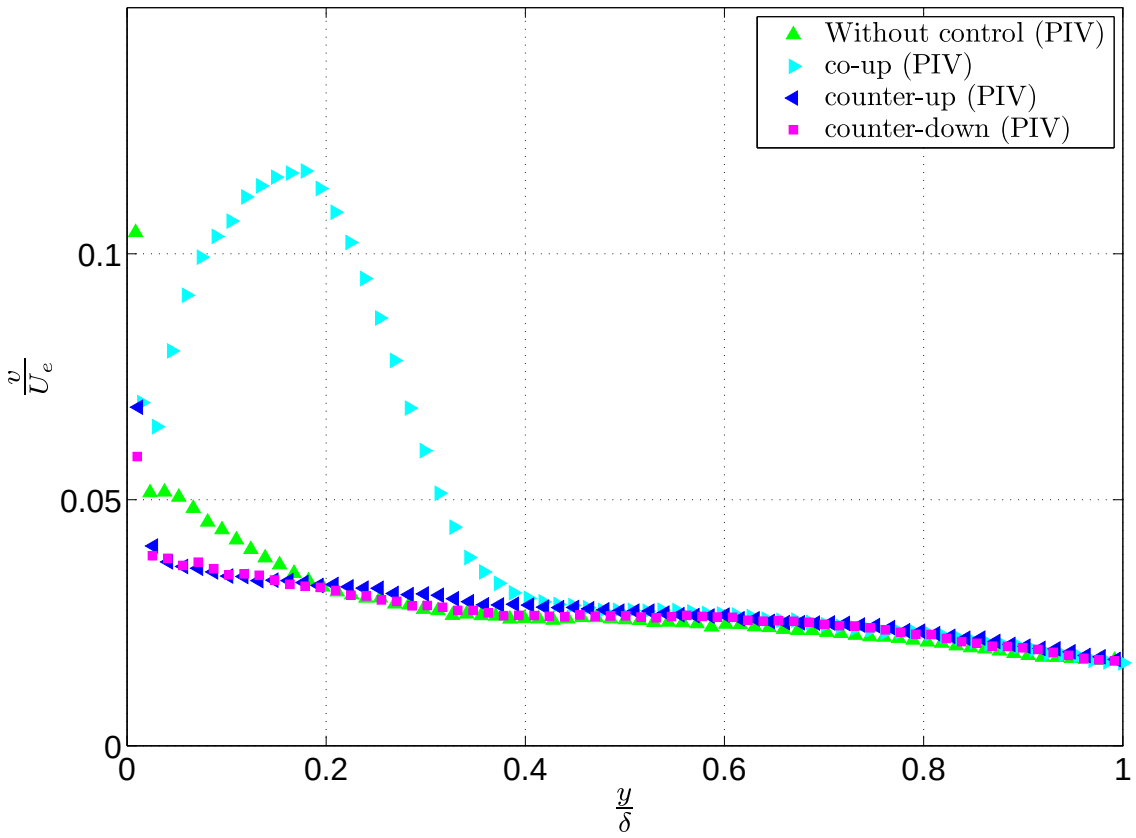

Figure 6.8: Wall normal turbulence intensity profiles in external units at hot-wire station 5, for the three control cases, compared to PIV profile without control.

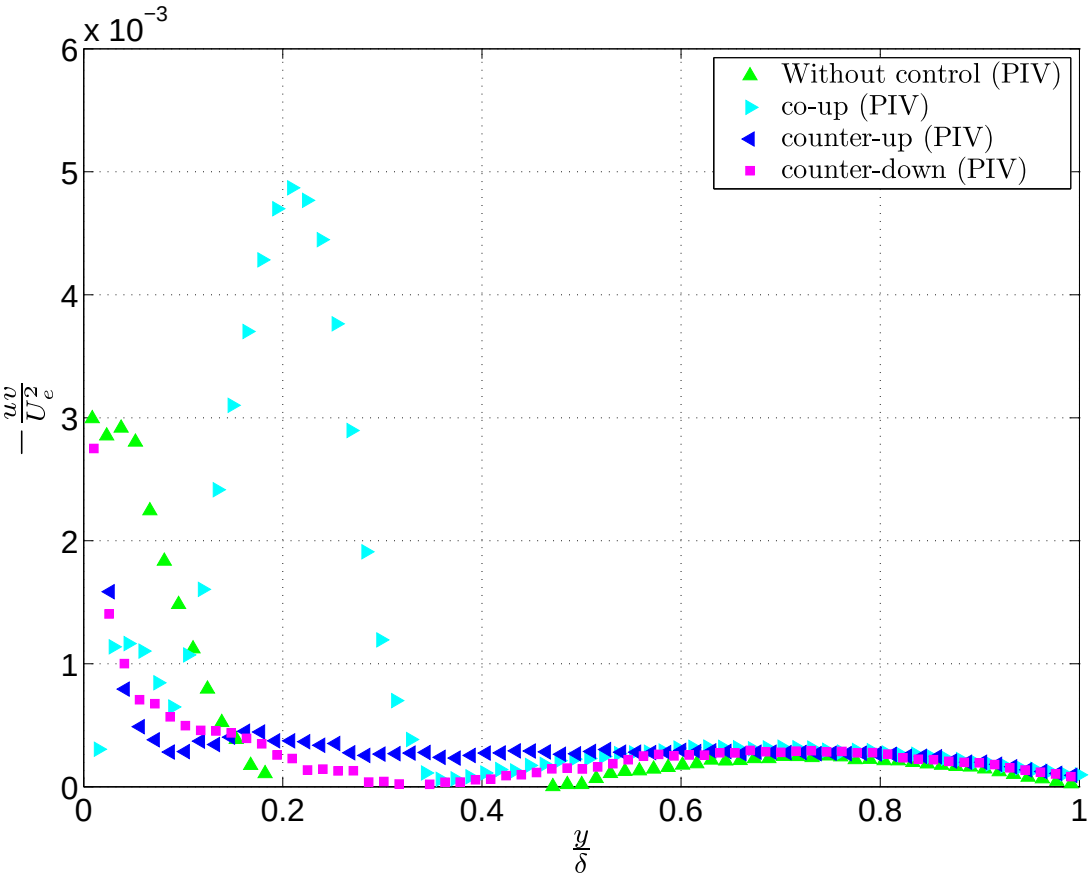

Figure 6.9: Reynolds shear stress profiles in external units at hot-wire station 5, for the three control cases, compared to PIV profile without control.

3.4 Mean velocity

3.4.1 Mean velocity fields

In this chapter, velocities are given in the local (x, y, z) reference frame to concentrate on the near wall region. Figure 6.10 shows, for the three control tests and the uncontrolled one, the mean streamwise velocity U distribution normalised by $U_\infty = 10\ m/s$. The same color scale is used for the different tests.

For the co-up case (Figure 6.10 b)), lower velocities are observed near the wall in the whole region upstream the articulation (at $X = 3.47$ m). At the corner, a small acceleration spot is observed, coherent with the suction peak in Figure 6.3. After the articulation, the flow is attached in the first part of the flap, with a shear layer much closer to the wall. Then the shear layer moves away and a small separated region (detected by the criteria $\chi = 50\%$) appears near $X = 3.8$ m. The length is 3 cm and the height is 0.5 mm. This separation was not evidenced by the wool tufts as it is too small, but agrees with the skewness given by friction probe P3 located 85 mm upstream this separated region (see Figure 5.5).

The streamwise velocity distributions for the two counter-rotating configurations (Figures 6.10 c) and d)) are quite similar. Before the articulation, due to the downwash, higher velocities are observed near the wall. The acceleration at the corner is more extended and connected to the outer flow although the suction peak was comparable with the co-up case in Figure 6.3. Over the flap, the flow is now apparantly fully reattached. The shear layer is closer to the wall and the region of velocity deficit is significantly reduced at the outlet compared to the two other cases. For the counter-up case, this agrees with the skewness given by friction probe P3 (see Figure 5.25). For the counter-down case, the skewness of probe P3 suggests a very small separation (see Figure 5.28).

To have a better assessment of possible separation, Figure 6.11 shows the backflow coefficient distribution for the different test cases. All the control tests show a backflow region close to the wall and centred around $X = 3.8$ m with a maximum χ coefficient about 0.3. Consequently, the counter-rotating cases could be slightly separated near $X = 3.8$ m. But the bubble is probably too small to be detected. The backflow region for the counter-up case (Figure 6.11 c)) is the smallest one and starts downstream $X = 3.74$ m, so downstream probe P3. For the two other control cases (Figures 6.11 b) and d)), the backflow starts upstream $X = 3.7$ m so that probe P3 is inside it. This can explain why this probe detects a separation for the co-up and counter-down cases.

From the present results, the counter-rotating configurations seem to give the best results and especially the counter-up one. However, the measurement plane does not correspond to the same flow control region. For the co-up case, it corresponds to an upwash, so a critical region and for the counter-up and counter-down cases, it corresponds to an downwash region, so a favourable one. With a spanwise information missing, concluding about the best configuration is risky.

Figure 6.12 shows the mean wall-normal velocity V distribution normalised by $U_\infty = 10\ m/s$. Again, the same color scale is used for the different tests. For the co-up case (Figure 6.12 b)), upstream the corner, positive wall-normal velocities are observed near the wall due to the upwash.

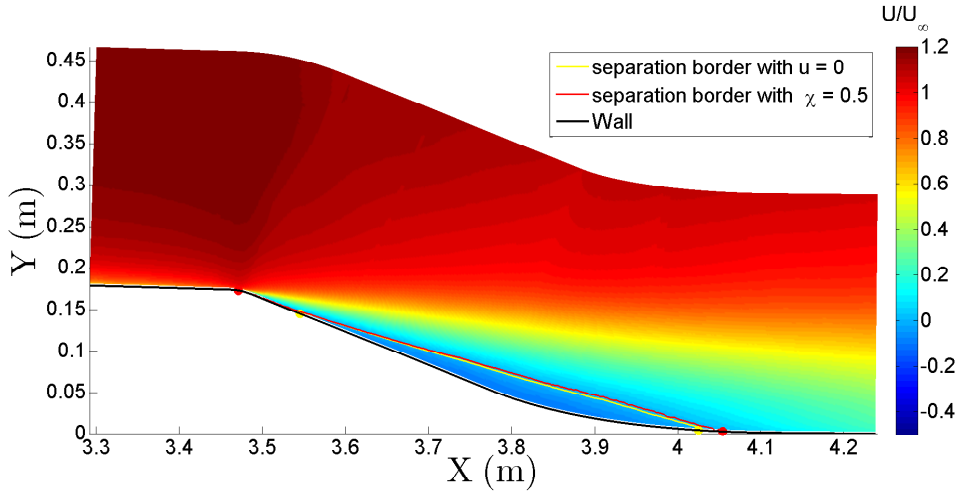
U/U∞
separation border with u = 0
separation border with χ = 0.5
Wall
Y (m)
X (m)

a)

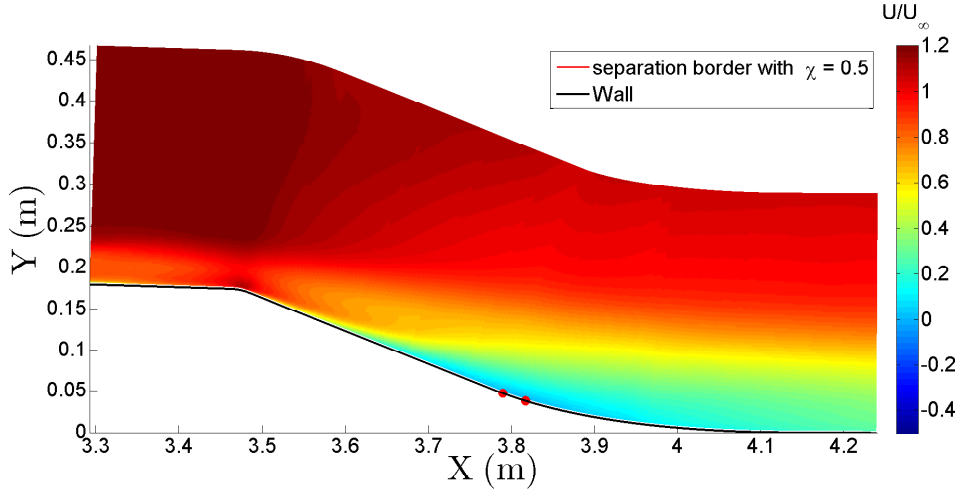
U/U∞
separation border with χ = 0.5
Wall
Y (m)
X (m)

b)

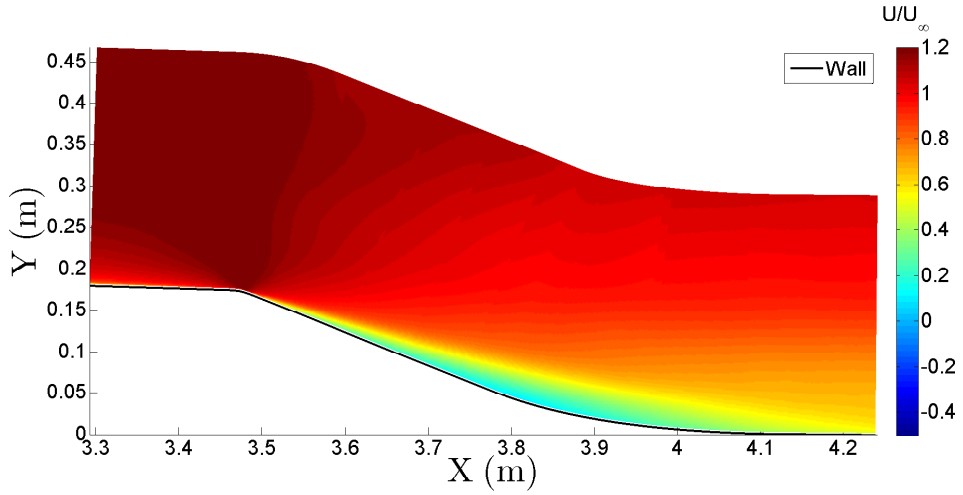
U/U∞
Wall
Y (m)
X (m)

c)

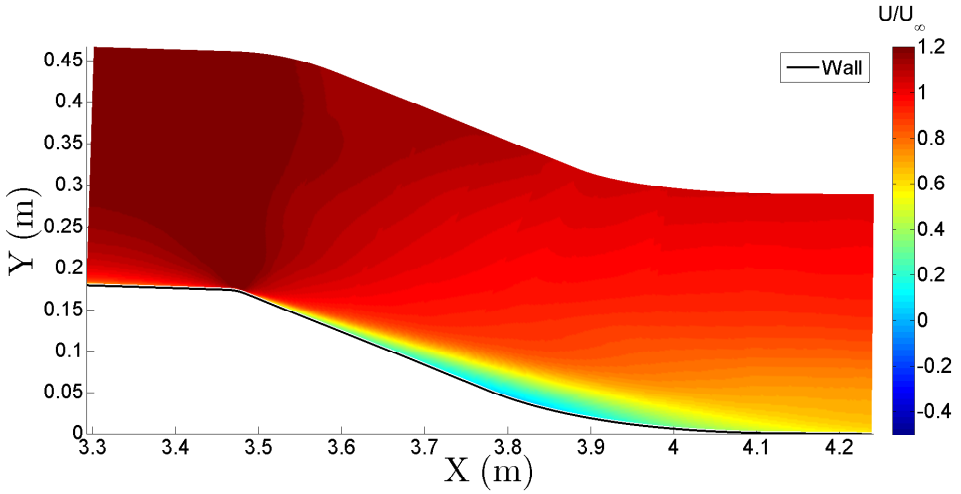

d)

Figure 6.10: Mean streamwise velocity U on the flap at mid-span of the ramp for a) the uncontrolled flow, b) the co-up case, c) the counter-up case and d) the counter-down case.

Just upstream the articulation, in the outer region, higher negative velocities are observed for the three control tests (Figures 6.12 b), c) and d)) probably linked to the acceleration observed near the corner on the streamwise component in Figure 6.10 and on the pressure distributions by a more intense suction peak.

After the corner, as in the uncontrolled case, a region of high positive values develops in the outer part for the three control tests. As was mentioned in Chapter 3, in the chosen reference frame, this indicates that the outer flow is not strictly parallel to the wall. Here, the size of this region is about similar to the uncontrolled flow but, the values are less intense which indicates a flow more parallel to the flap surface.

Downstream $X = 3.9$ m, for the co-up case (Figure 6.12 b)), low negative velocities are observed, indicating that the flow is already nearly parallel to the downstream wall. This shows that the control intensity is well adapted in the plane of observation. On the contrary, for the counter-rotating cases, a strong negative velocities region is evidenced. For the counter-up case, this region is slightly more intense and wider in the wall-normal direction than for the counter-down one. This indicates that the counter-rotating vortices are still present in this region and induce a downwash region toward the wall. The difference in size and intensity of this region between upstream and downstream blowing can be explained by the difference in VR between these two counter-rotating cases.

On the flap, close to the wall, as for the uncontrolled flow, the wall-normal velocity is nearly zero which indicates a flow parallel to the wall. This is also true for the co-up flow in the rear part of the field. However it is not the case for the counter-rotating tests which present negative values very close to the wall, probably due to the downwash generated by the counter-rotating vortices even beyond the field of view.

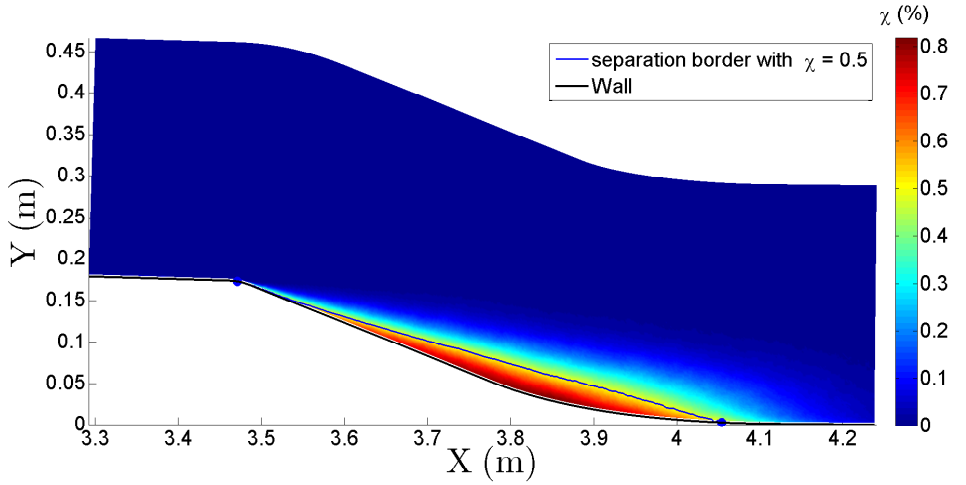
χ (%)
separation border with χ = 0.5
Wall
Y (m)
X (m)
0.45
0.4
0.35
0.3
0.25
0.2
0.15
0.1
0.05
0
3.3
3.4
3.5
3.6
3.7
3.8
3.9
4
4.1
4.2
0.8
0.7
0.6
0.5
0.4
0.3
0.2
0.1
0

a)

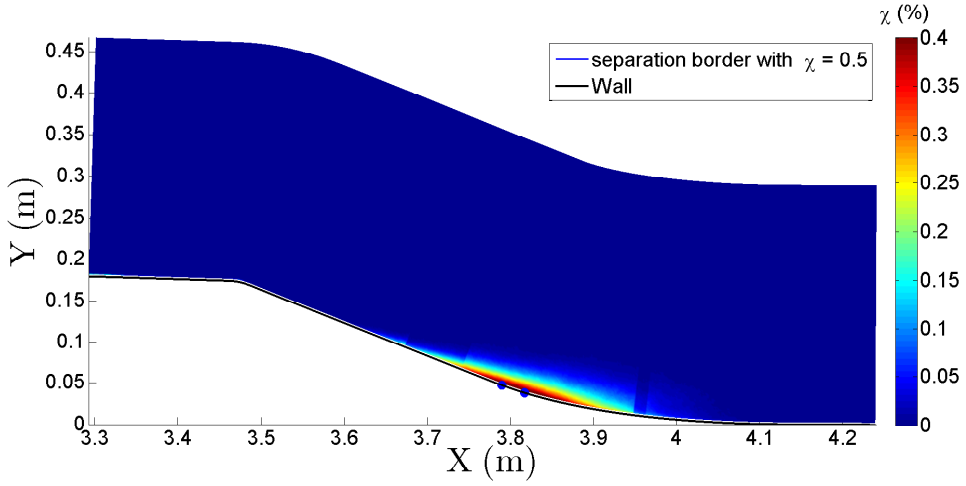
χ (%)
separation border with χ = 0.5
Wall
Y (m)
X (m)
0.45
0.4
0.35
0.3
0.25
0.2
0.15
0.1
0.05
0
3.3
3.4
3.5
3.6
3.7
3.8
3.9
4
4.1
4.2
0.4
0.35
0.3
0.25
0.2
0.15
0.1
0.05
0

b)

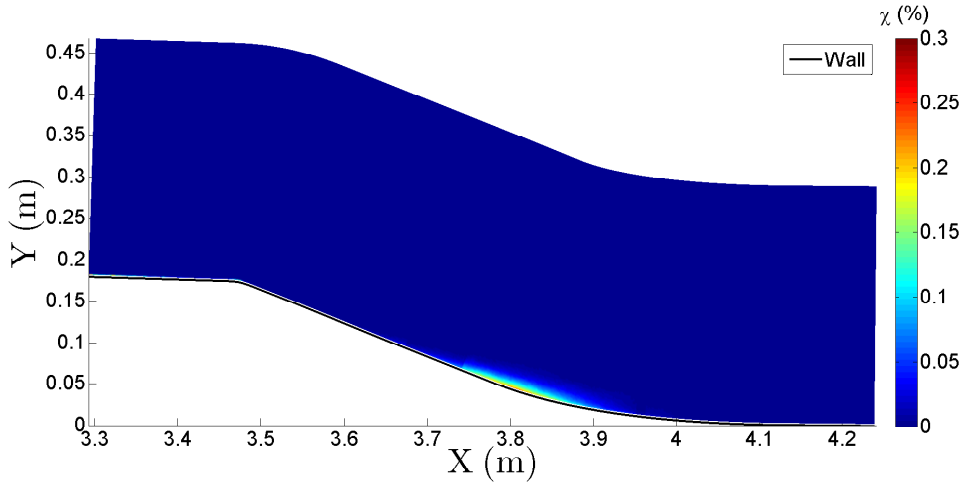
χ (%)
Wall
Y (m)
X (m)
0.45
0.4
0.35
0.3
0.25
0.2
0.15
0.1
0.05
0
3.3
3.4
3.5
3.6
3.7
3.8
3.9
4
4.1
4.2
0.3
0.25
0.2
0.15
0.1
0.05
0

c)

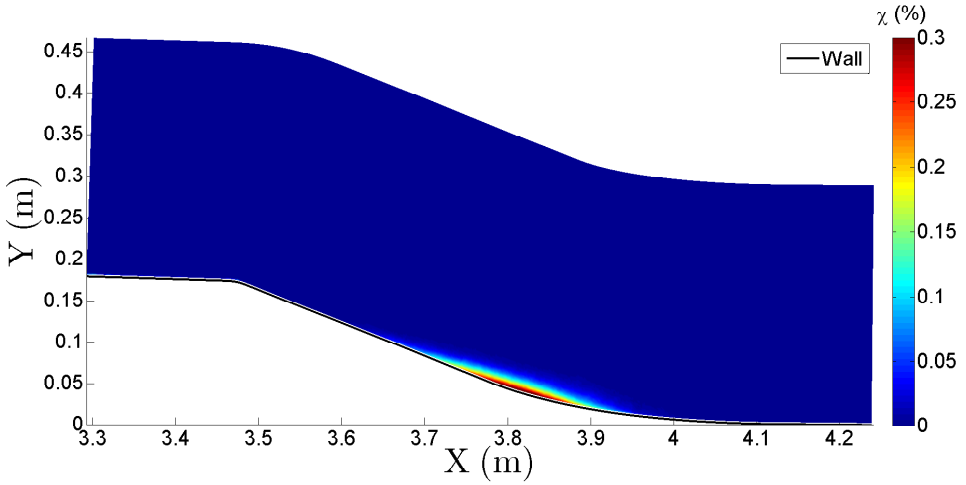

d)

Figure 6.11: Backflow coefficient on the flap at mid-span of the ramp for a) the uncontrolled flow, b) the co-up case, c) the counter-up case and d) the counter-down case.

3.4.2 Mean Velocity profiles

In order to look in more details at the flow over the flap, Figure 6.13 shows for the different cases, mean streamwise velocity profiles at the same positions as in Section 6.3.4 of Chapter 3. The same length ($H_{step} = 17.5$ m) and velocity ($U_\infty = 10$ m/s) scales are used to normalise the profiles. For the co-up case (Figure 6.13 b)), at $s = 3502$ mm and $s = 3625$ mm, as at hot-wire station 5 (Figure 6.4), the profile is S-shaped near the wall with a peak close to the wall and a large deep further away (up to $\frac{y}{H_{step}} \simeq 0.3$ at $s = 3502$ mm). An inflection point is also observed near $\frac{y}{H_{step}} \simeq 0.27$ at $s = 3502$ mm and $\frac{y}{H_{step}} \simeq 0.35$ at $s = 3625$ mm. Compared to the uncontrolled case (Figure 6.13 a)), velocities are higher near the wall and smaller near $\frac{y}{H_{step}} \simeq 0.2$. These profiles indicate that from the flap articulation down to about $X = 3.7$ m, the control takes momentum in the outer flow to redistribute it in the very near wall region. This leads apparently to the suppression of the recirculation as shown by the profiles at the intermediate stations. In the downstream part, only a slight excess of momentum is observed near the wall. At $s = 3793$ mm and 3949 mm the wall derivative is relatively small, which is coherent with the small separation observed in this case near $X = 3.8$ m. At the last two stations, the profiles are very close. This confirms that the control is not strong enough to suppress completely the separation and that its effects nearly disappear downstream of $s = 4113$ mm. Downstream $s = 3948$ mm, above $\frac{y}{H_{step}} = 0.6$, a good collapse is observed, coherent with the small V observed in this region in Figure 6.12 b).

For the two counter-rotating cases, as shown by Figures 6.13 c) and d), the control mechanism is clearly different. At the first station, the profile is nearly uniform, indicating that the momentum brought to the near wall region is coming from outside the plane of observation. This leads to a quasi-suppression of the boundary layer

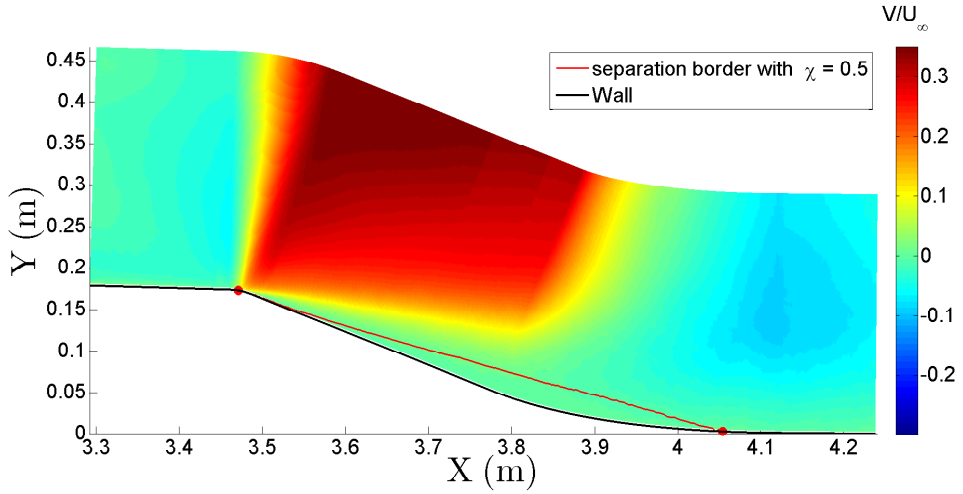
V/U∞
separation border with χ = 0.5
Wall
Y (m)
X (m)
0.45
0.4
0.35
0.3
0.25
0.2
0.15
0.1
0.05
0
3.3
3.4
3.5
3.6
3.7
3.8
3.9
4
4.1
4.2
0.3
0.2
0.1
0
-0.1
-0.2

a)

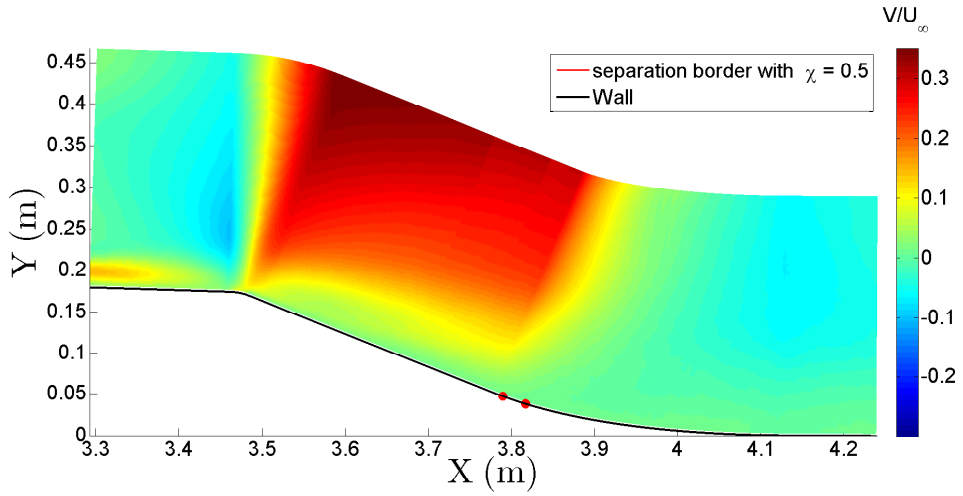
V/U∞
separation border with χ = 0.5
Wall
Y (m)
X (m)
0.45
0.4
0.35
0.3
0.25
0.2
0.15
0.1
0.05
0
3.3
3.4
3.5
3.6
3.7
3.8
3.9
4
4.1
4.2
0.3
0.2
0.1
0
-0.1
-0.2

b)

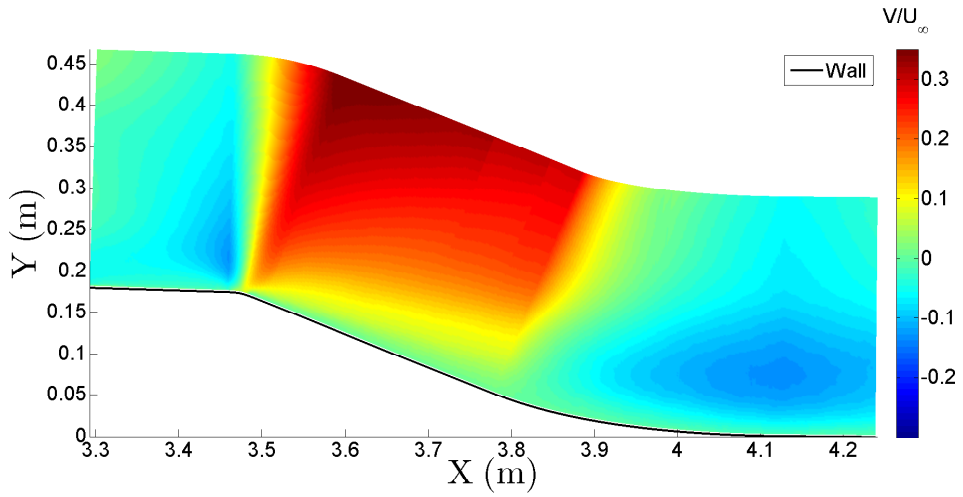
V/U∞
Wall
Y (m)
X (m)
0.45
0.4
0.35
0.3
0.25
0.2
0.15
0.1
0.05
0
3.3
3.4
3.5
3.6
3.7
3.8
3.9
4
4.1
4.2
0.3
0.2
0.1
0
-0.1
-0.2

c)

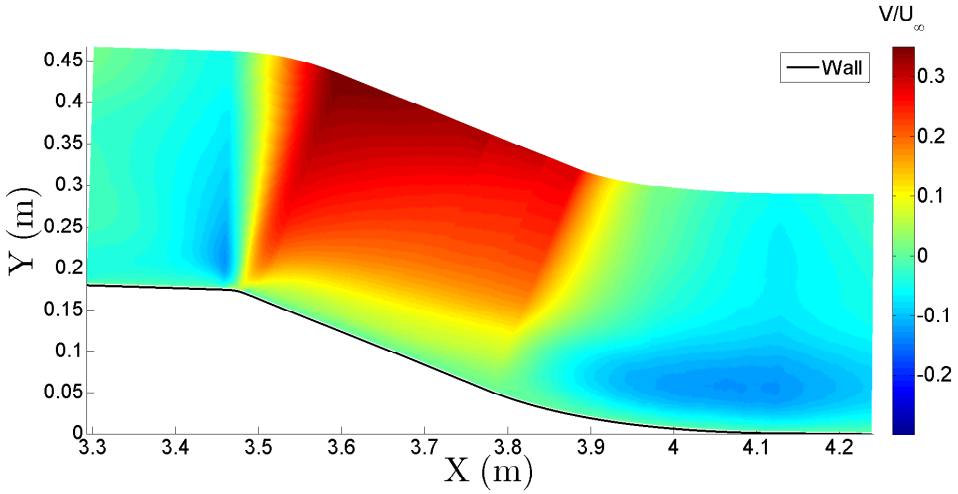

d)

Figure 6.12: Mean wall-normal velocity V on the flap at mid-span of the ramp for a) the uncontrolled flow, b) the co-up case, c) the counter-up case and d) the counter-down case.

at this station. Consequently, the recirculation is also suppressed and the profiles are more energetic at all intermediate stations compared to both uncontrolled and co-up cases. Near the wall, a higher momentum is observed compared to the co-up case and very comparable between the two counter-rotating cases. This is coherent with the backflow distribution in Figure 6.11, but in contradiction with the results of probe P3 for the counter-down case (which may be due to the spatial resolution of the PIV data near the wall). The last two profiles (i.e. at $s = 4113$ mm and at $s = 4297$ mm) show a good collapse in the external region above $\frac{y}{H_{step}} = 0.3$.

As was explained in Chapter 3, thanks to the small wall-normal extend of the separation, it is still possible in the present case to estimate boundary layer parameters. Table 6.3 contains, for the different test cases, the boundary layer characteristics obtained by PIV at the six stations of the profiles shown in Figure 6.13. The friction velocity was not estimated as no log-law was evidenced for some profiles. For the two counter-rotating configurations, at $s = 3502$ mm, as two peaks are present in the profiles (see Figures 6.13 c) and d)), δ was defined without taking the first peak near the wall into account. For all profiles downstream $s = 3624$ mm, δ was not defined as the PIV field of view was not large enough. The integral thicknesses were obtained by integrating the profiles through the entire field (or until δ when it was accessible) and are not biased too much as the velocity is just slightly increasing at the top of the field (Figure 6.13).

For all cases, the momentum thickness θ is in the same order. Except for the last station of the two counter-rotating cases, it increases with s due to the section enlargement that increases the shear layer so the velocity deficit near the wall. For the displacement thickness δ^*, for all cases, it significantly increases with s until $s = 3949$ mm and then decreases slightly. All control cases decrease however the displacement thickness compared to the uncontrolled test (i.e. they tend to

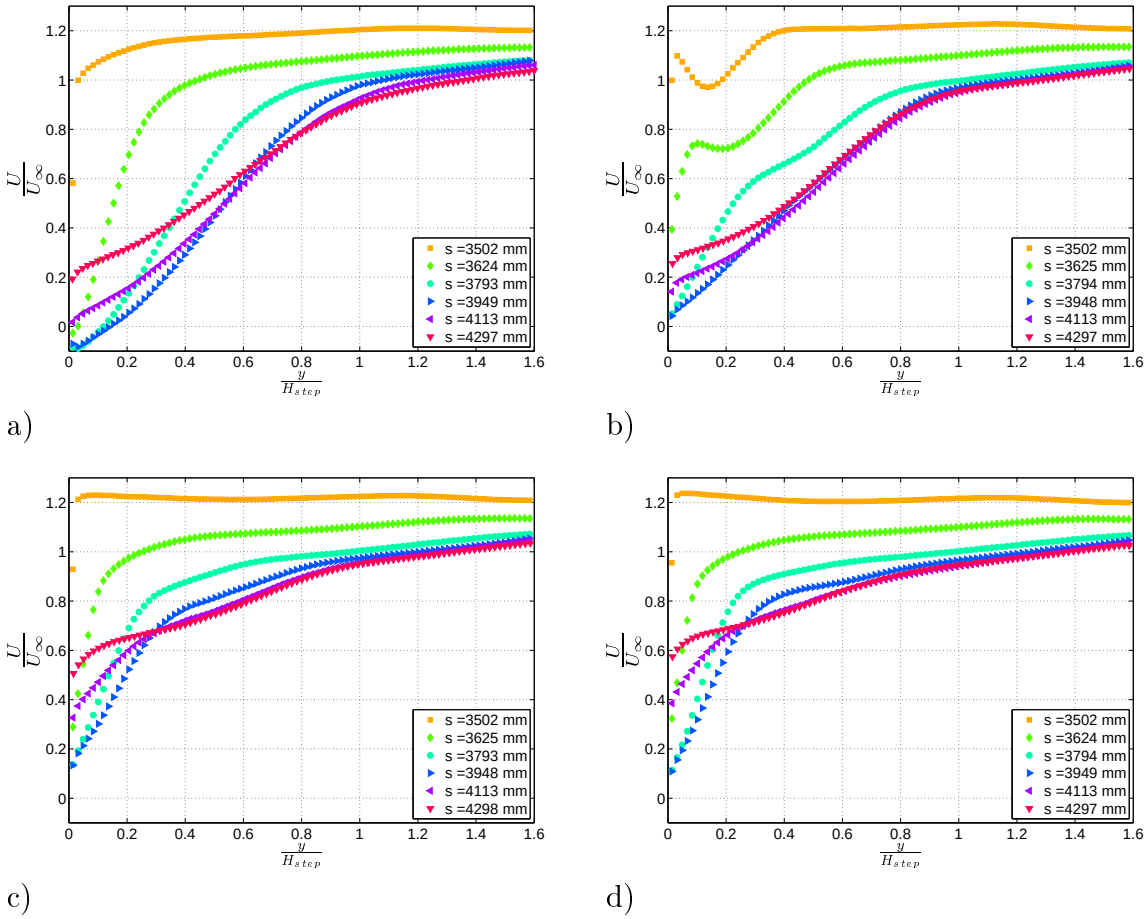

Figure 6.13: Mean streamwise velocity profiles at six stations on the flap for a) the uncontrolled flow, b) the co-up case, c) the counter-up case and d) the counter-down case.

put the fictive wall of the equivalent ideal flow nearer to the flap wall). For both counter-rotating configurations, the values are quite close and are below the co-up and uncontrolled ones. For each case, the momentum deficit due to the section enlargement is then conserved and the control tests only reorganise the momentum distribution.

Due to a momentum thickness similar between the different tests, the shape factor H follows the same trend as the displacement thickness. For the uncontrolled flow it is high, which is in agreement with the separation. At the reattachment point (i.e. at $s = 4113$ mm), it is near the value given by Dengel and Fernholz (1990) for a separation point (2.85). When it is possible to define a shape factor (i.e. for a small bubble height compared to the upstream boundary layer thickness), a strong similarity could exist between the separation and reattachment point. For the co-up case, the shape factor is also high and reaches values near the characteristic value of separation. The shape factor is then in agreement with the small separation remaining for this control case which starts at $s = 3845$ mm. At this separation point, the shape factor is 2.34, which is in agreement with the value given by Mellor and Gibson (1966) and lower the Dengel and Fernholz (1990) one. For the two

Table 6.3: Table of the boundary layer characteristics obtained by PIV at six stations on the flap for the different test cases.

Set-up	s (mm)	δ (cm)	δ^* (mm)	θ (mm)	H
without control	3502	15.7	9.7	7.3	1.32
	3625	22.5	42.3	18.6	2.28
	3793	-	84.6	24.5	3.46
	3949	-	108.8	28.7	3.79
	4113	-	104.9	35.6	2.95
	4297	-	90	42	2.2
co-up	3502	14.4	11.2	8.4	1.33
	3625	21.8	33.9	22.6	1.50
	3793	-	67.8	32.7	2.07
	3949	-	90.7	36.2	2.51
	4113	-	89.6	38.2	2.35
	4297	-	80	39	2.1
counter-up	3502	12.9*	3.7	2.5	1.48
	3625	21.7	22.3	15.5	1.45
	3793	-	46.5	26.9	1.73
	3949	-	61.2	34.1	1.80
	4113	-	58.7	37.3	1.57
	4297	-	53	36	1.46
counter-down	3502	13.6*	6.0	4.6	1.30
	3625	21.7	21.4	15.3	1.41
	3793	-	42.3	24.6	1.71
	3949	-	55.5	31.7	1.75
	4113	-	52.0	35.5	1.47
	4297	-	45	33	1.38

counter-rotating configurations, the shape factor remains below 1.8 on the flap, which agree with no separation detected on the flap.

3.5 Turbulence intensity

3.5.1 Turbulence intensity fields

As in Chapter 3, the turbulent quantities will be given in the local reference frame to get a better assessment of the near wall behaviour. Nevertheless, a global reference frame representation which can be useful for RANS computation comparisons is given Appendix E.

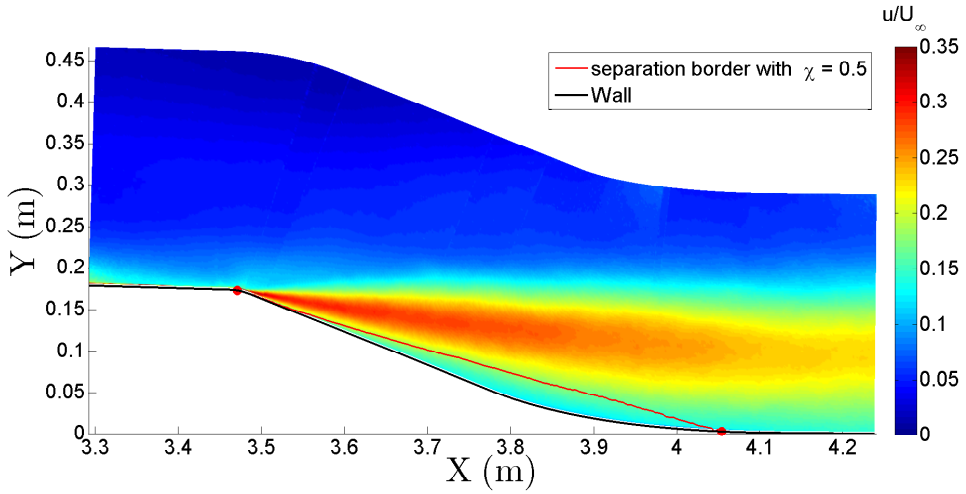
u/U∞
separation border with χ = 0.5
Wall
Y (m)
X (m)
0.45
0.4
0.35
0.3
0.25
0.2
0.15
0.1
0.05
0
3.3
3.4
3.5
3.6
3.7
3.8
3.9
4
4.1
4.2
0.35
0.3
0.25
0.2
0.15
0.1
0.05
0

a)

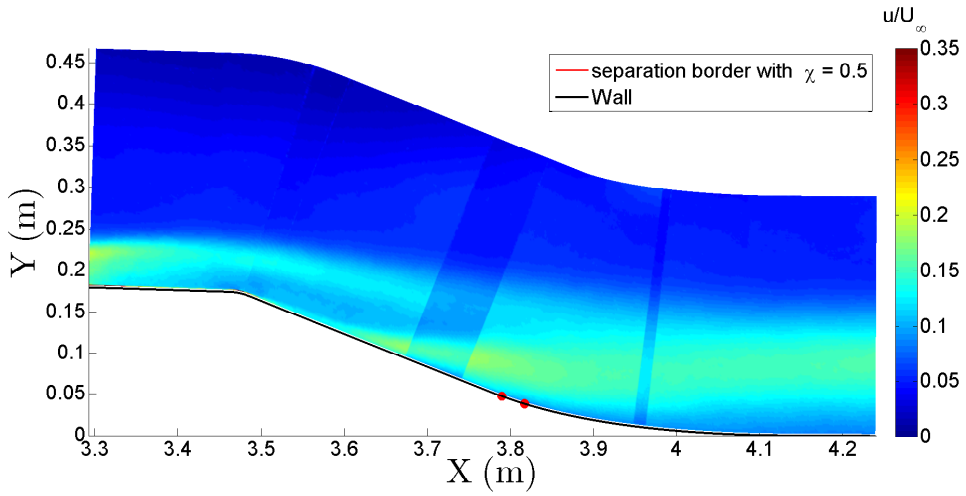
u/U∞
separation border with χ = 0.5
Wall
Y (m)
X (m)
0.45
0.4
0.35
0.3
0.25
0.2
0.15
0.1
0.05
0
3.3
3.4
3.5
3.6
3.7
3.8
3.9
4
4.1
4.2
0.35
0.3
0.25
0.2
0.15
0.1
0.05
0

b)

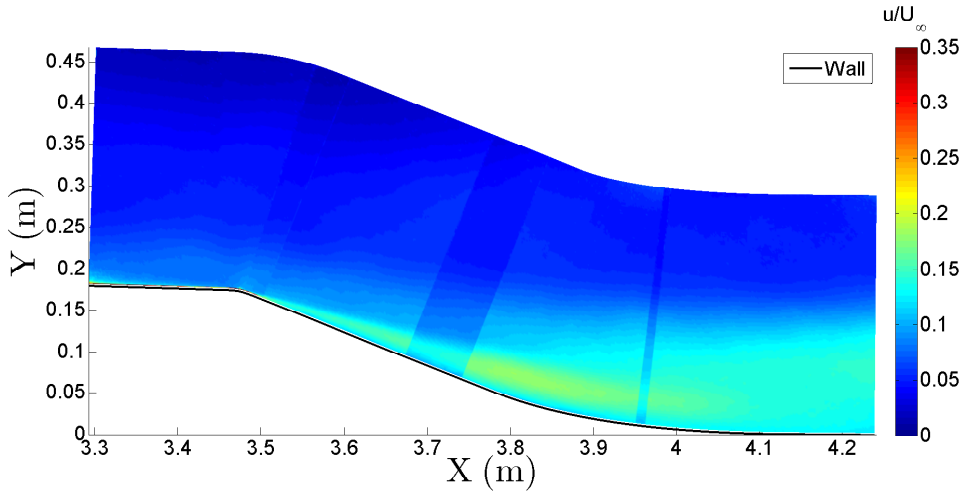
u/U∞
Wall
Y (m)
X (m)
0.45
0.4
0.35
0.3
0.25
0.2
0.15
0.1
0.05
0
3.3
3.4
3.5
3.6
3.7
3.8
3.9
4
4.1
4.2
0.35
0.3
0.25
0.2
0.15
0.1
0.05
0

c)

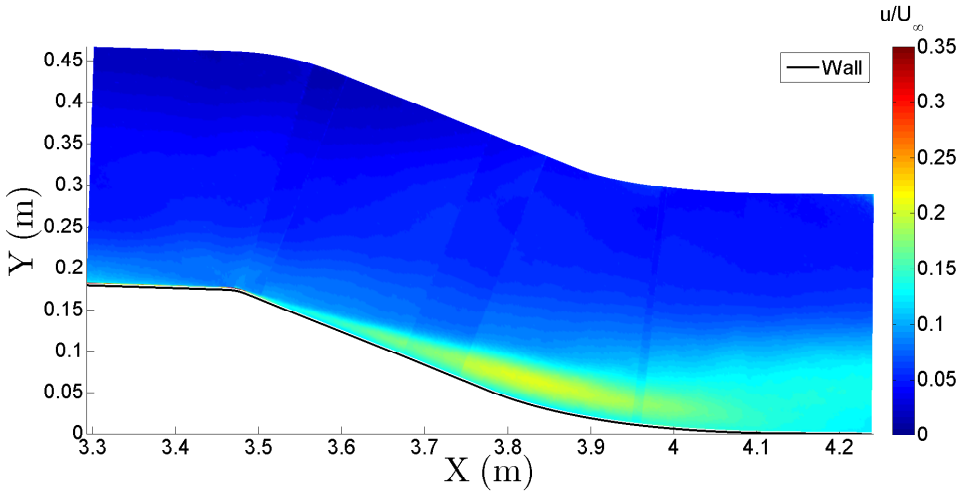

d)

Figure 6.14: Turbulent intensity field ($u = \sqrt{\overline{u'^2}}$) on the flap at mid-span of the ramp for a) the uncontrolled flow, b) the co-up case, c) the counter-up case and d) the counter-down case.

3.5.1.1 Streamwise turbulence intensity

Figure 6.14 shows the streamwise turbulent intensity distribution ($u = \sqrt{\overline{u'^2}}$) normalized by $U_\infty = 10\ m/s$, for the uncontrolled flow and the three control cases. The same color scale is used for all the cases. For the three control cases (Figures 6.14 b), c) and d)), the merging regions appear as discontinuities in the figures because larger errors are observed compared to the uncontrolled case (see Chapter 2). This is mostly due to the stronger out of plane component in the controlled cases which induces more out of plane loss of pairs in the PIV and more bias on the border of the field. It will be the case for all the following figures in this chapter which present turbulent quantity fields of the controlled configurations.

For the co-up case (Figure 6.14 b)), upstream the flap, near the wall, higher streamwise turbulent intensity is observed compared to the uncontrolled case (Figure 6.14 a)). This is attributed to the flow perturbation introduces by the control jets. The two counter-rotating configurations (Figures 6.14 c) and d)) have quite similar streamwise turbulence intensity distribution. Upstream the flap, in the near wall region, lower values are observed compared to the uncontrolled case. This agrees with the downwash region which attenuates turbulence near the wall as seen in Section 3.3.

For the three control tests, after the flap corner, a significant change is observed. Much lower values appear near the wall compared to the uncontrolled flow, even if a region of high values is also observed much nearer to the wall in the downstream part. The turbulence level in this region is however two times lower than for the uncontrolled flow. For the two counter-rotating cases, this region seems to develop closer to the wall, especially for the counter-down case (Figure 6.14 d)). However, for this counter-rotating case, the turbulence level is slightly higher than for the two

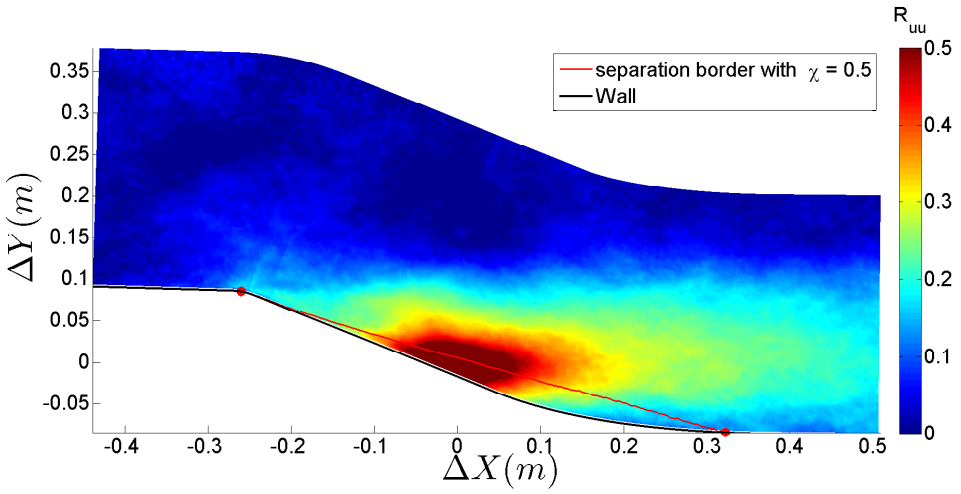
R uu
separation border with χ = 0.5
Wall
ΔY (m)
ΔX (m)

a)

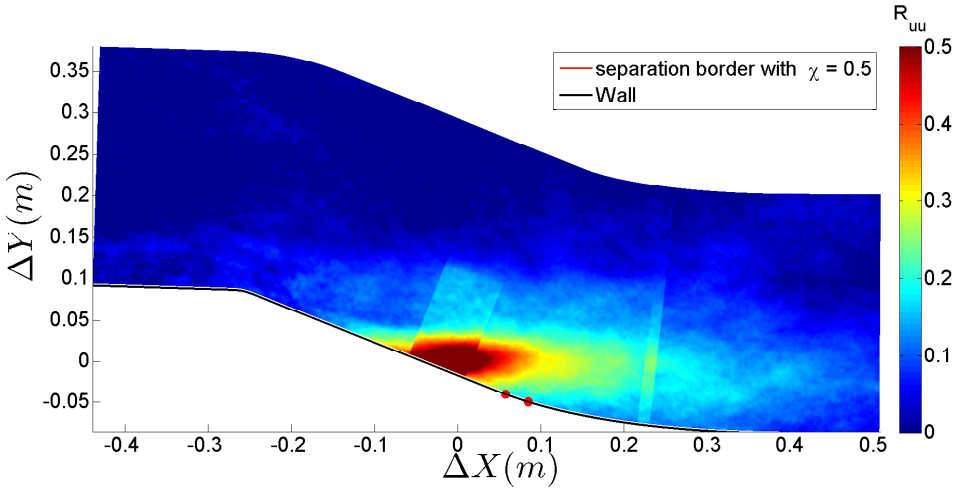
R uu
separation border with χ = 0.5
Wall
ΔY (m)
ΔX (m)

b)

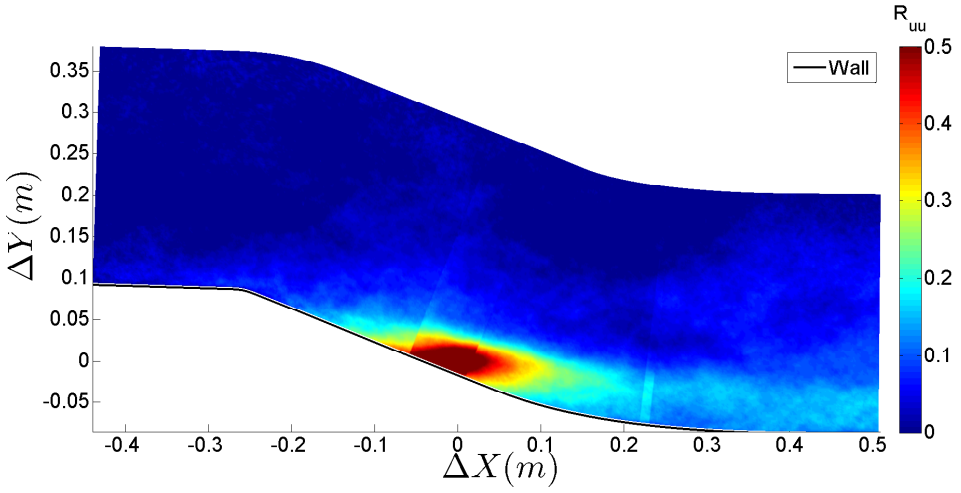
R uu
Wall
ΔY (m)
ΔX (m)

c)

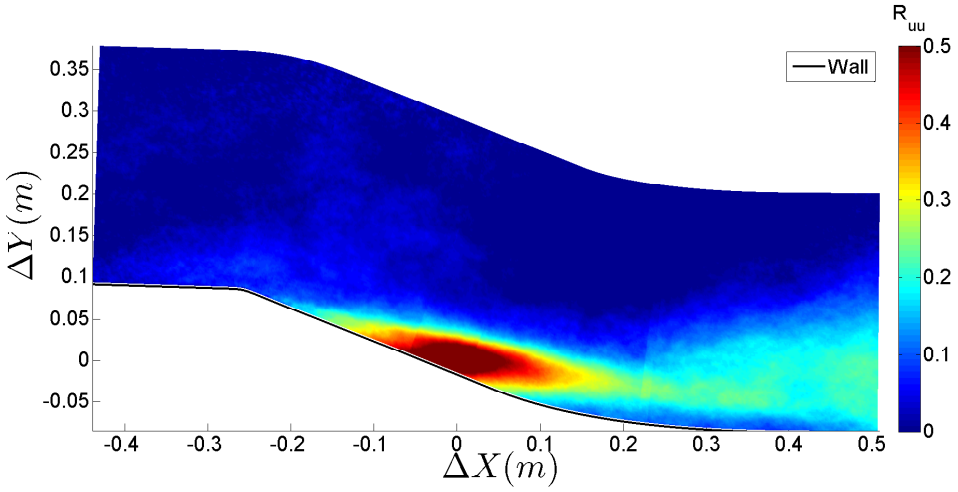

d)

Figure 6.15: Correlation coefficient R_{uu} on the flap at mid-span of the ramp for a) the uncontrolled flow, b) the co-up case, c) the counter-up case and d) the counter-down case.

other control cases.

The lower streamwise turbulence intensity value on the flap can be explained by the disappearance of the large scale structures characterized by high u' fluctuations seen in Chapter 3. Figure 6.15 shows the correlation coefficient R_{uu} for the three control cases and for the uncontrolled flow. The fixed point is the same as in Chapter 3. For the three control tests (Figures 6.15 b), c) and d)), the region of R_{uu} values greater than 0.2 is significantly reduced both in wall-normal and streamwise directions and is nearer to the wall compared to the uncontrolled flow (Figure 6.15 a)). This confirms the size reduction of these kinds of structures by the control. However, for the counter-down case (Figure 6.15 d)), the region $R_{uu} > 0.2$ remains quite long in the streamwise direction compared to the two other control tests and expands away from the wall in the downstream part of the field of view. This can explain why the peak of streamwise turbulence intensity on the flap is more intense for the counter-down case than for the other control tests. This indicates that this counter configuration is very close to separation, which confirms the optimum VR range obtained in Chapter 5 for downstream blowing (i.e. between 1.5 and 2.5).

3.5.1.2 Wall-normal turbulence intensity

Figure 6.16 shows the wall-normal turbulent intensity distribution ($v = \sqrt{\overline{v'^2}}$) normalized by $U_\infty = 10\ m/s$, for the uncontrolled flow and the three control cases. The same color scale is also used. For the co-up case (Figure 6.16 b)), upstream the flap, as for the streamwsise component (Figure 6.14 b)), significantly higher values are observed compared to the uncontrolled case (Figure 6.16 a)). This extends quite far downstream the corner. It may be due to a fluctuation of the wall-normal position of the actuating jets. On the flap, the high level region observed for the

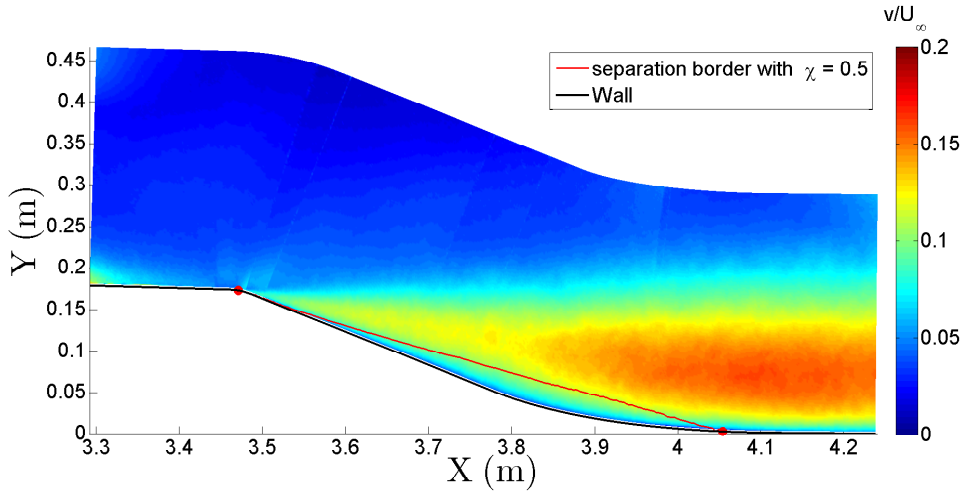
v/U∞
separation border with χ = 0.5
Wall
Y (m)
X (m)
0.45
0.4
0.35
0.3
0.25
0.2
0.15
0.1
0.05
0
3.3
3.4
3.5
3.6
3.7
3.8
3.9
4
4.1
4.2
0.2
0.15
0.1
0.05
0

a)

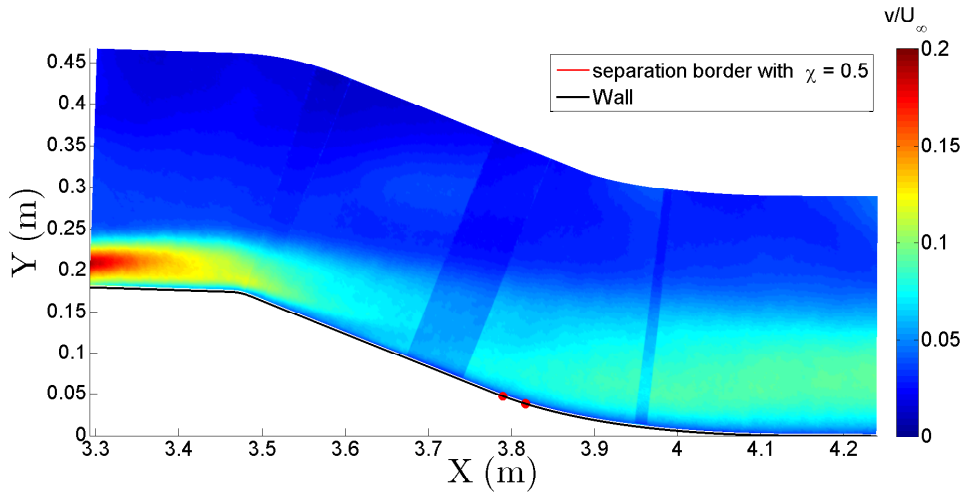
v/U∞
separation border with χ = 0.5
Wall
Y (m)
X (m)
0.45
0.4
0.35
0.3
0.25
0.2
0.15
0.1
0.05
0
3.3
3.4
3.5
3.6
3.7
3.8
3.9
4
4.1
4.2
0.2
0.15
0.1
0.05
0

b)

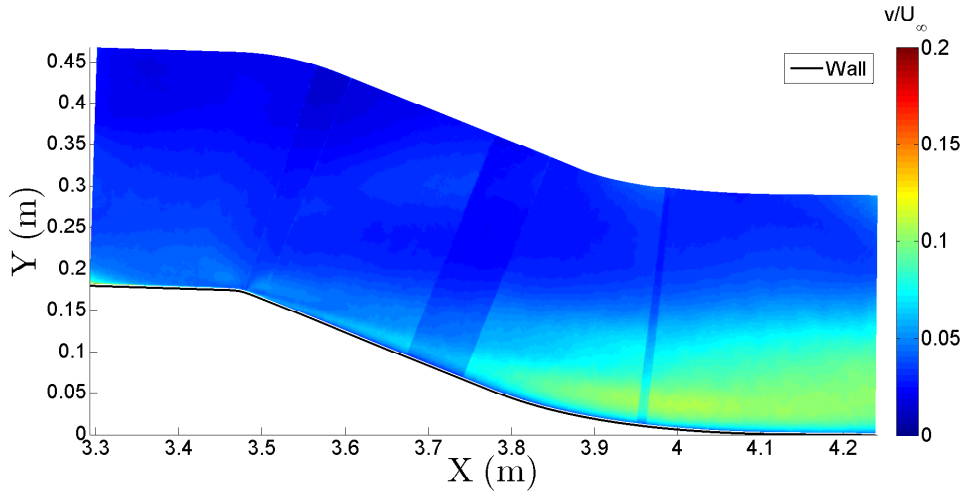
v/U∞
Wall
Y (m)
X (m)
0.45
0.4
0.35
0.3
0.25
0.2
0.15
0.1
0.05
0
3.3
3.4
3.5
3.6
3.7
3.8
3.9
4
4.1
4.2
0.2
0.15
0.1
0.05
0

c)

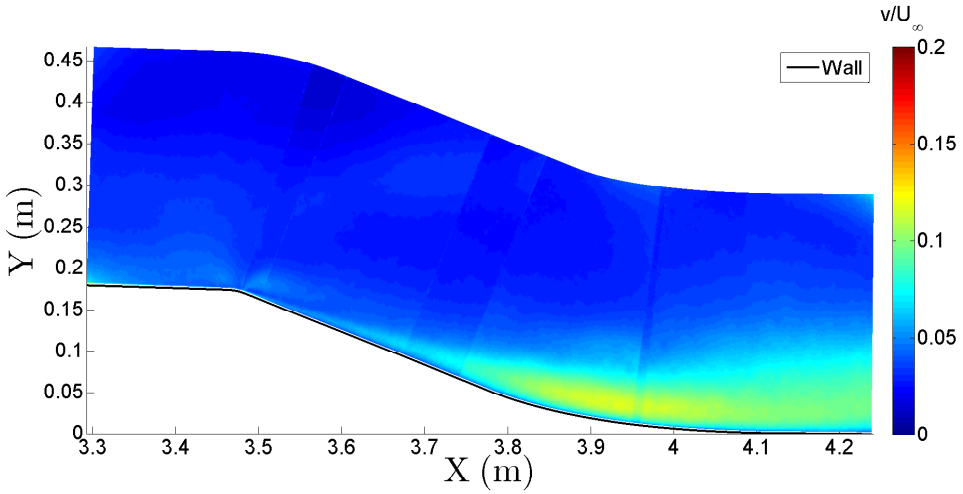

d)

Figure 6.16: Turbulent intensity field ($v = \sqrt{\overline{v'^2}}$) on the flap at mid-span of the ramp for a) the uncontrolled flow, b) the co-up case, c) the counter-up case and d) the counter-down case.

uncontrolled flow nearly disappears in the first half of the flap while it is still present with a similar size in the downstream part. However the intensity is reduced by a factor of two as for the streamwise component, which is coherent with the reduction of the separation bubble size. The similarity between the high v level region size of the co-up and uncontrolled cases in the downstream part of the flap is of interest in terms of its physical origin as the separation bubble size is very different in both cases, but difficult to explain with the information in hand.

The distributions for the two counter-rotating configurations (Figures 6.16 c) and d)) are quite similar but differ from the co-up case. The high level region of the uncontrolled flow over the first half of the flap is highly reduced in intensity (by also a factor about 2) and in size. It is even more confined in the near wall region. In the rear part, again the high level region is very similar in shape (but not in intensity) to the uncontrolled and co-up cases. This enhances the question of the physical origin of this region which seems to exist whatever the control is (or is not).

3.5.1.3 Reynolds shear stress

Figure 6.17 shows the Reynolds shear stress distribution ($-uv = -\overline{u'v'}$) for the uncontrolled flow and the three control tests normalized by U_∞^2. Again, the same color scale is used. As for the wall-normal component, for the co-up case (Figure 6.17 b)), upstream the flap, higher values near the wall are observed compared to the uncontrolled flow (Figure 6.17 a)). They are also attributed to the jets. At the beginning of the flap, 5 to 6 cm from the wall, a trace of the jets wake can be observed. Below this region, near the wall, a high value region is observed, however it is closer to the wall and less intense than for the uncontrolled flow. Similarly as

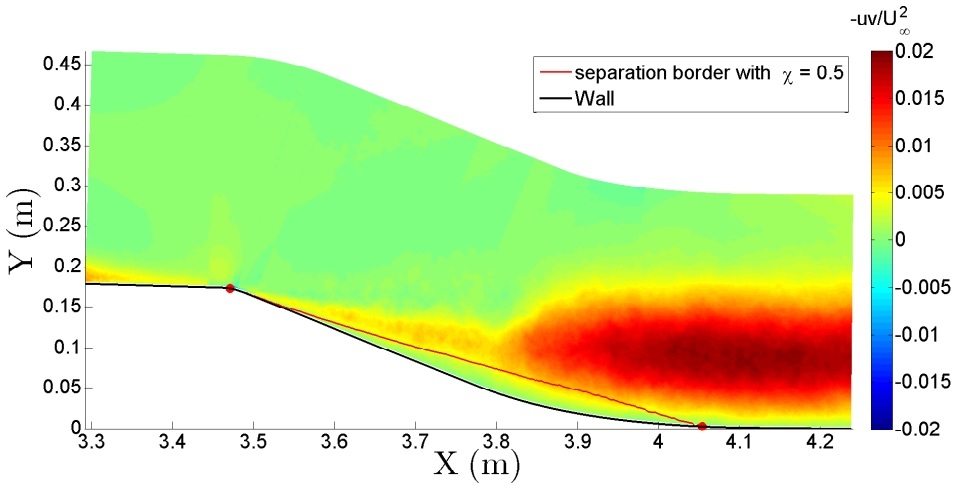
-uv/U$_\infty^2$
separation border with χ = 0.5
Wall
Y (m)
X (m)
0.45
0.4
0.35
0.3
0.25
0.2
0.15
0.1
0.05
0
3.3
3.4
3.5
3.6
3.7
3.8
3.9
4
4.1
4.2
0.02
0.015
0.01
0.005
0
-0.005
-0.01
-0.015
-0.02

a)

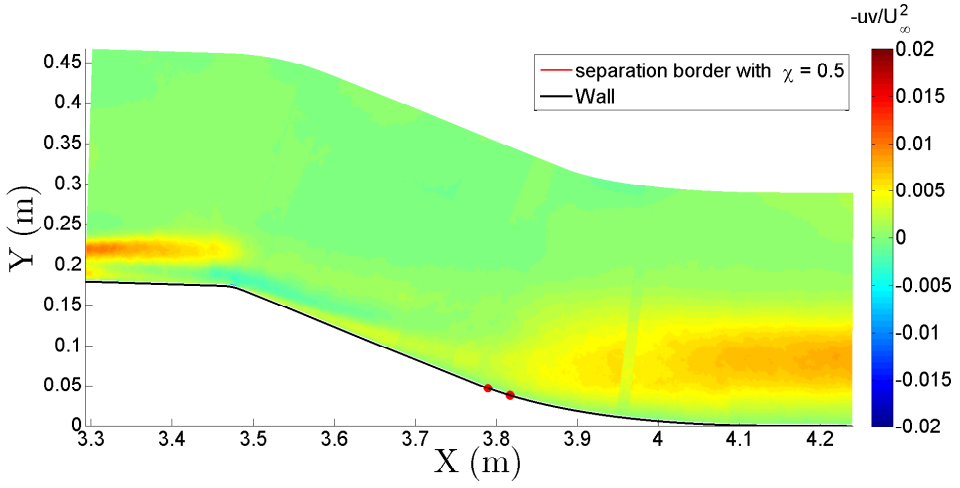
-uv/U$_\infty^2$
separation border with χ = 0.5
Wall
Y (m)
X (m)
0.45
0.4
0.35
0.3
0.25
0.2
0.15
0.1
0.05
0
3.3
3.4
3.5
3.6
3.7
3.8
3.9
4
4.1
4.2
0.02
0.015
0.01
0.005
0
-0.005
-0.01
-0.015
-0.02

b)

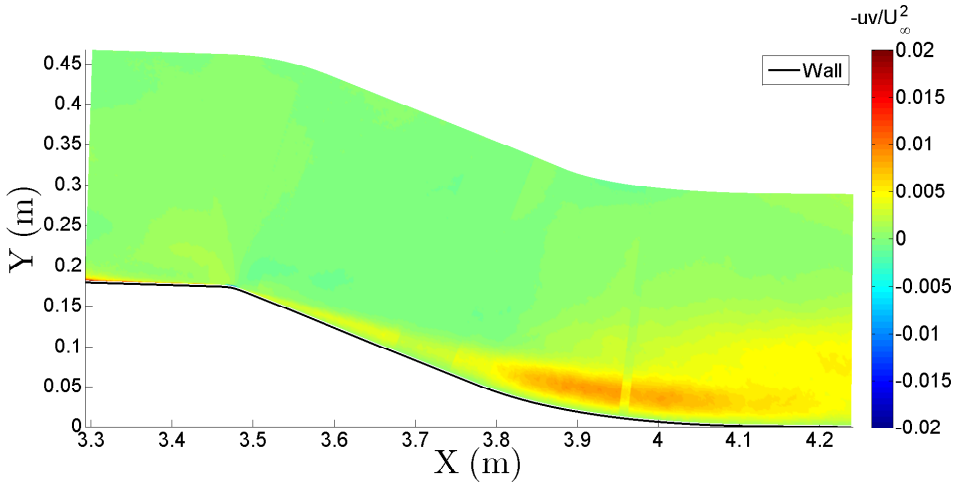
-uv/U$_\infty^2$
Wall
Y (m)
X (m)
0.45
0.4
0.35
0.3
0.25
0.2
0.15
0.1
0.05
0
3.3
3.4
3.5
3.6
3.7
3.8
3.9
4
4.1
4.2
0.02
0.015
0.01
0.005
0
-0.005
-0.01
-0.015
-0.02

c)

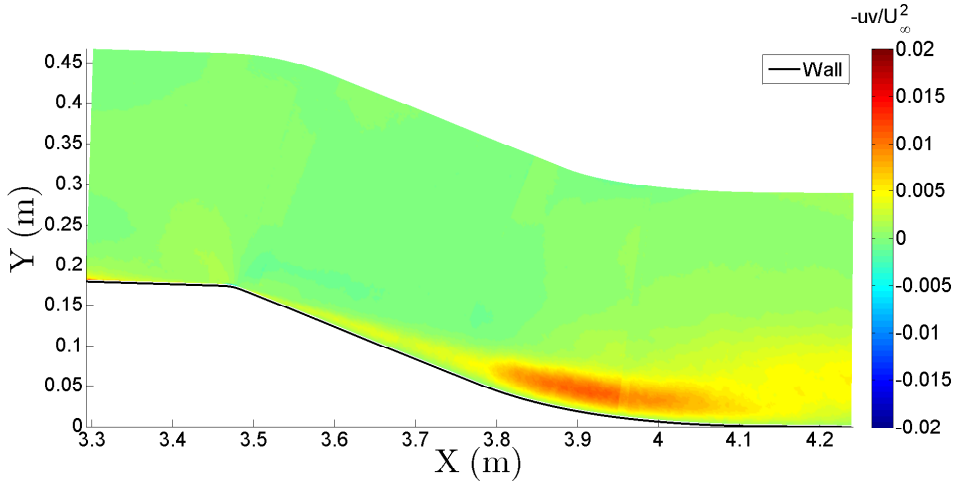

d)

Figure 6.17: Reynolds shear stress field ($uv = \overline{u'v'}$) on the flap at mid-span of the ramp for a) the uncontrolled flow, b) the co-up case, c) the counter-up case and d) the counter-down case.

for the wall-normal component, on the downstream part of the flap, a large high value region develops, in close relation to $\overline{v'^2}$. This region is similar to the one of the uncontrolled flow but about four times less intense and its wall-normal extent is slightly lower.

The distribution of the counter-up case and the counter-down cases (Figures 6.17 c) and d) respectively) are very close. The behaviour largely differs from the co-up case on the flap downstream $X = 3.8$ m. The high values region develops closer to the wall and its extent in the wall-normal direction is about two times lower. However, for each control test, it should be noted the high similarity between the wall normal turbulence intensity and the Reynolds shear stress as was also pointed out for the uncontrolled flow in Chapter 3.

3.5.1.4 Turbulence production

Figure 6.18 shows the distribution of the production term $-\overline{u'v'}\frac{\partial U}{\partial y}$ of the turbulent kinetic energy for the uncontrolled flow and the three control tests normalized by U_∞^3/H_{step}. For all cases, there is a strong similarity between the Reynolds shear stress (Figure 6.17) and the production. Upstream the flap, for the co-up case, due to the jets, there is a region of high turbulence production at about 5 cm from the wall. For the three control tests, the high production region near the wall upstream the corner is reduced compared to the base flow. For the counter-rotating tests, this is coherent with the downwash region which attenuates turbulence. For the co-up case, it is also in agreement with an upwash region which moves away from the wall the turbulence production region.

On the flap, this quantity gives a better insight of the physics involved. In fact, the different controls applied do not suppress completely the shear layer which has

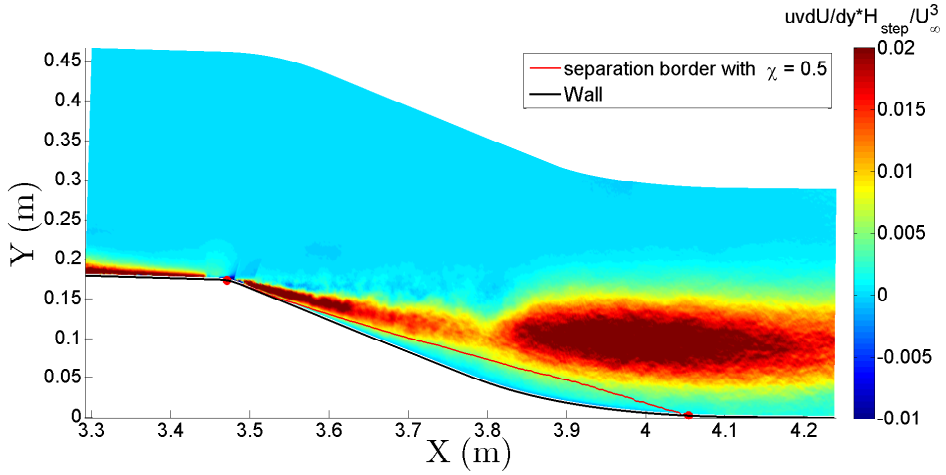
uvdU/dy*H step /U3 ∞
separation border with χ = 0.5
Wall
Y (m)
X (m)
0.45
0.4
0.35
0.3
0.25
0.2
0.15
0.1
0.05
0
3.3
3.4
3.5
3.6
3.7
3.8
3.9
4
4.1
4.2
0.02
0.015
0.01
0.005
0
-0.005
-0.01

a)

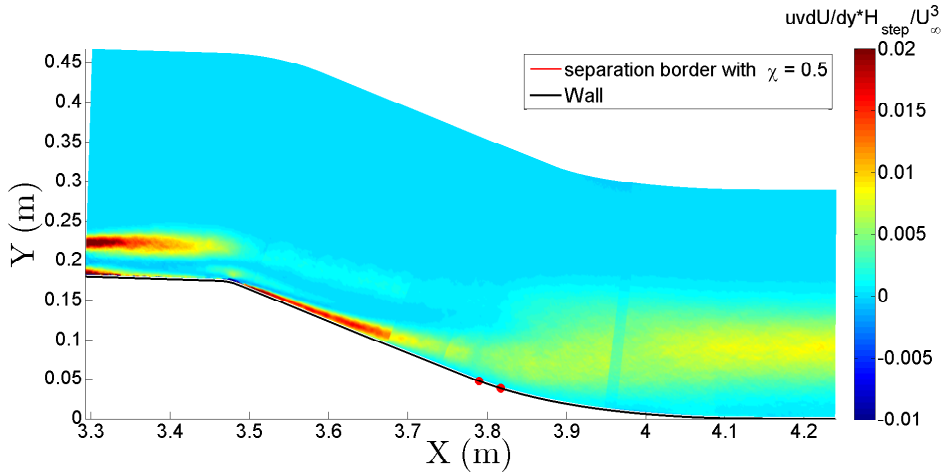
uvdU/dy*H step /U3 ∞
separation border with χ = 0.5
Wall
Y (m)
X (m)
0.45
0.4
0.35
0.3
0.25
0.2
0.15
0.1
0.05
0
3.3
3.4
3.5
3.6
3.7
3.8
3.9
4
4.1
4.2
0.02
0.015
0.01
0.005
0
-0.005
-0.01

b)

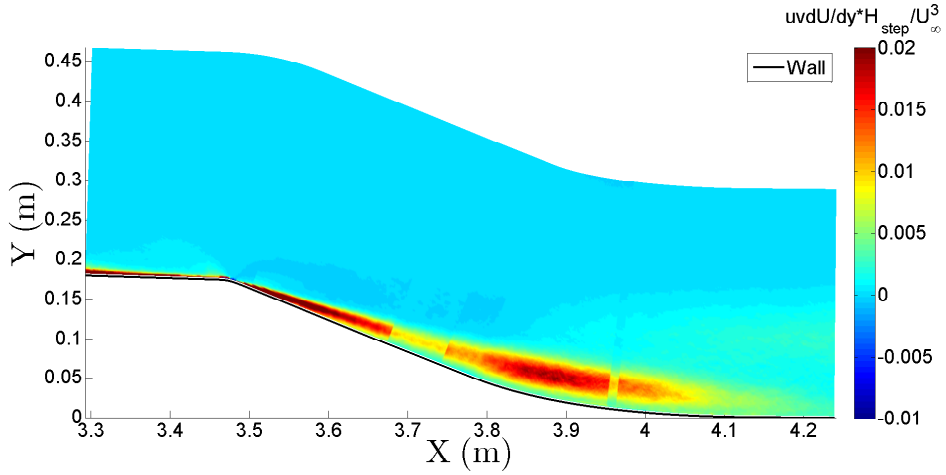
uvdU/dy*H step /U3 ∞
Wall
Y (m)
X (m)
0.45
0.4
0.35
0.3
0.25
0.2
0.15
0.1
0.05
0
3.3
3.4
3.5
3.6
3.7
3.8
3.9
4
4.1
4.2
0.02
0.015
0.01
0.005
0
-0.005
-0.01

c)

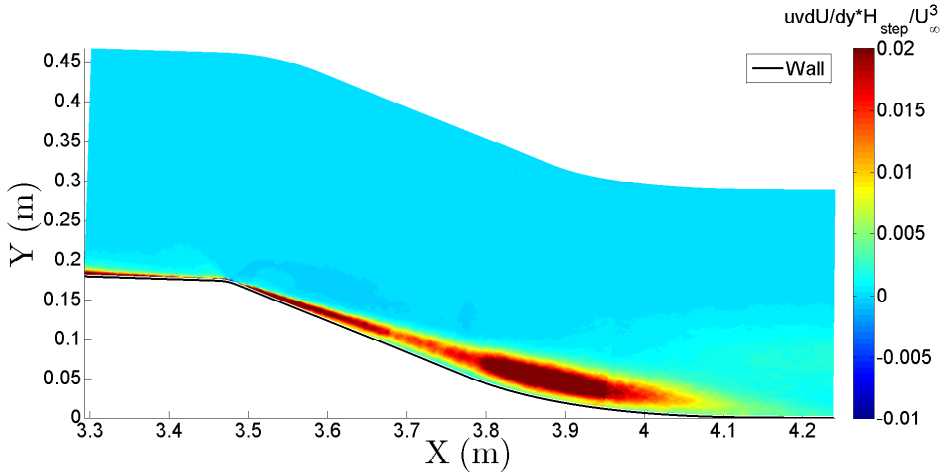

d)

Figure 6.18: Production term $-\overline{u'v'}\frac{\partial U}{\partial y}$ of the turbulent kinetic energy on the flap at mid-span of the ramp for a) the uncontrolled flow, b) the co-up case, c) the counter-up case and d) the counter-down case.

its origin at the corner and which is clearly visible on the base flow. They just squeeze it against the wall, reducing it in intensity. When reaching the middle of the flap where a concave curvature appears, around $X = 3.7 - 3.8$ m, this shear layer suddenly expands with a second production peak closely linked to the v' fluctuations. This phenomenon is not suppressed by the control, it is just attenuated and squeezed more or less on the the wall depending of the type of control applied.

Figure 6.19 gives the distribution of the production term $-\overline{u'^2}\frac{\partial U}{\partial x}$ of the turbulent kinetic energy for the different test cases. The previous analysis also applied for this quantity. The high positive values region downstream the corner is also not suppressed by the actuators. For the three control tests, its intensity is highly reduced and it is squeezed against the wall. However its streamwise extend is almost conserved. For the two other accessible production terms of the turbulent kinetic energy, the term $-\overline{u'v'}\frac{\partial V}{\partial x}$ is found negligible as for the uncontrolled flow, and the term $-\overline{v'^2}\frac{\partial V}{\partial y}$ (given in Appendix F Figure F.1) is found largely reduced in intensity and the high levels region squeezed against the wall as for the other production terms.

Concerning the production of Reynolds shear stress, for the three control tests as for the uncontrolled flow, it is dominated by the term $-\overline{v'^2}\frac{\partial U}{\partial y}$ (given in Appendix F Figure F.2), which explains the similarity observed between the Reynolds shear stress and the wall-normal turbulence intensity distributions for the different test cases. As for the production terms discussed previously, the high level region is also squeezed against the wall.

The conclusion is that the control strategies used do not modify the separation physics (at least in the plane of observation). They only changes its size, intensity and location with respect to the wall. This may be due to the fact that the separation is taking place at a singular point on the wall and that the flow control is based on

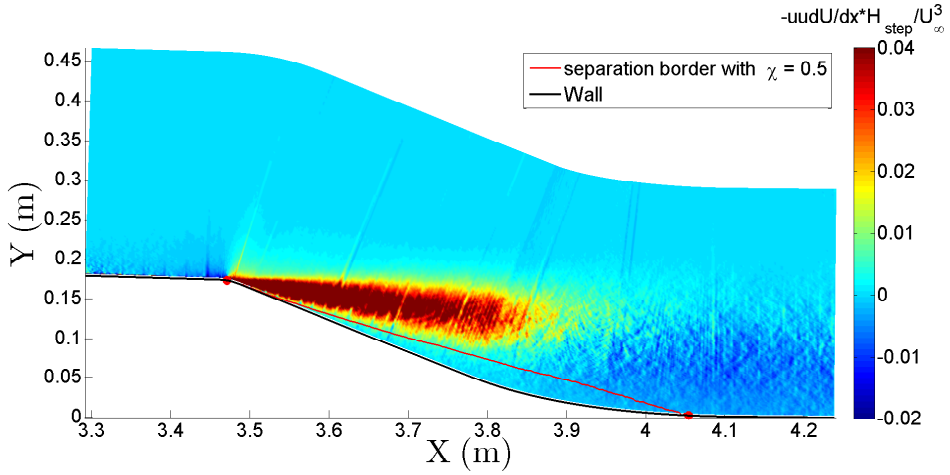
-uudU/dx*H step /U3 ∞
separation border with χ = 0.5
Wall
Y (m)
X (m)
0.45
0.4
0.35
0.3
0.25
0.2
0.15
0.1
0.05
0
3.3
3.4
3.5
3.6
3.7
3.8
3.9
4
4.1
4.2
0.04
0.03
0.02
0.01
0
-0.01
-0.02

a)

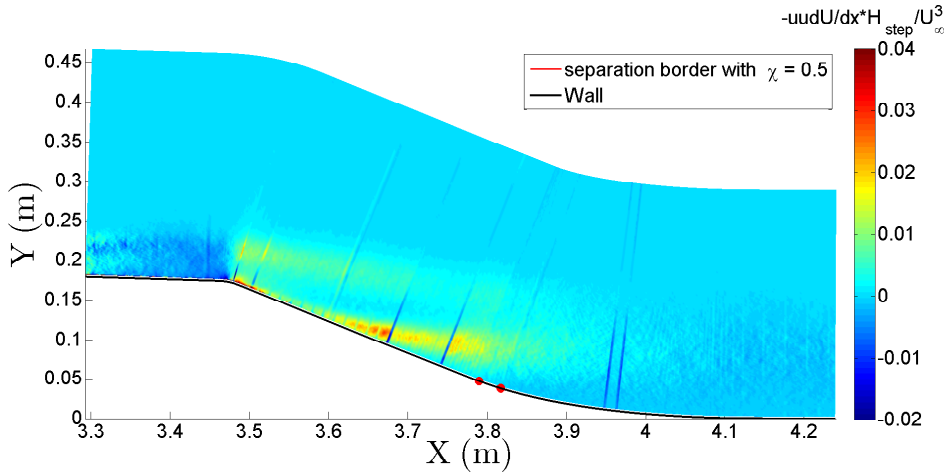
-uudU/dx*H step /U3 ∞
separation border with χ = 0.5
Wall
Y (m)
X (m)
0.45
0.4
0.35
0.3
0.25
0.2
0.15
0.1
0.05
0
3.3
3.4
3.5
3.6
3.7
3.8
3.9
4
4.1
4.2
0.04
0.03
0.02
0.01
0
-0.01
-0.02

b)

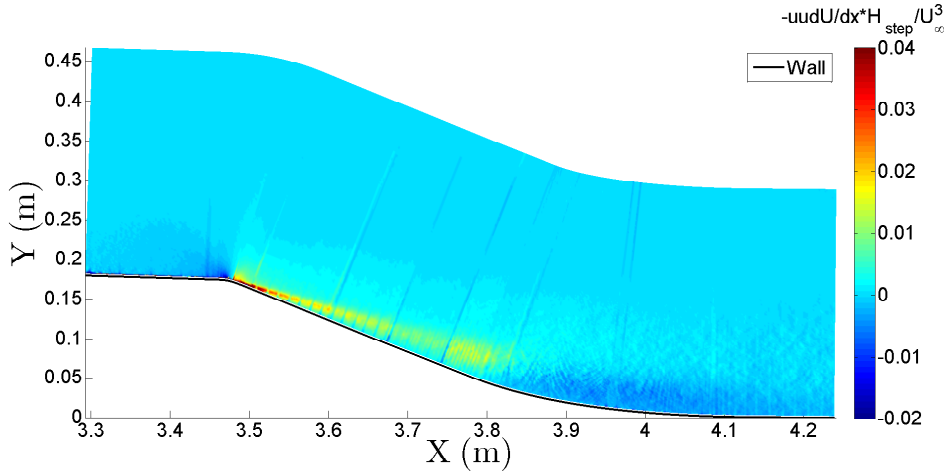
-uudU/dx*H step /U3 ∞
Wall
Y (m)
X (m)
0.45
0.4
0.35
0.3
0.25
0.2
0.15
0.1
0.05
0
3.3
3.4
3.5
3.6
3.7
3.8
3.9
4
4.1
4.2
0.04
0.03
0.02
0.01
0
-0.01
-0.02

c)

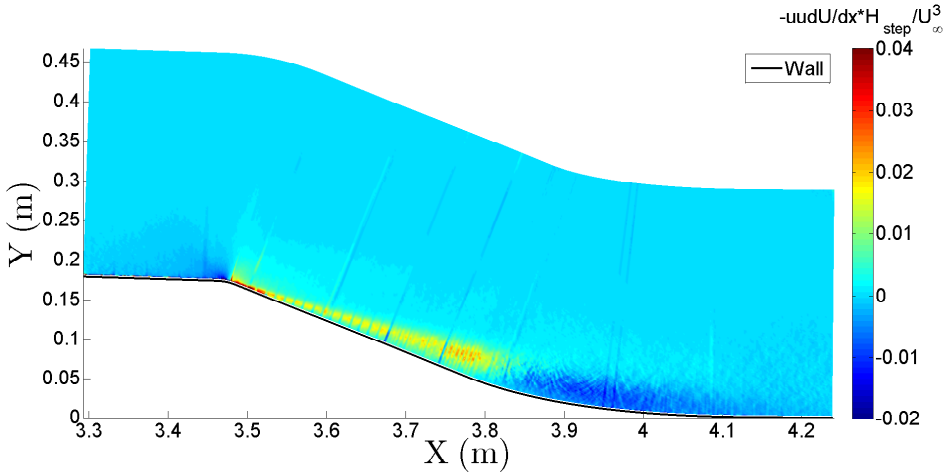

d)

Figure 6.19: Production term $-\overline{u'^2}\frac{\partial U}{\partial x}$ of the turbulent kinetic energy on the flap at mid-span of the ramp for a) the uncontrolled flow, b) the co-up case, c) the counter-up case and d) the counter-down case.

streamwise and not spanwise structures. It may also be due to the fact that the attached boundary layer on the flap is immediately submitted to an adverse pressure gradient.

3.5.2 Turbulence intensity profiles

3.5.2.1 Streamwise turbulence intensity

Figure 6.20 shows six streamwise turbulent intensity profiles for the uncontrolled flow and the three control cases at the same stations as in Figure 6.13. The same length (H_{step}) and velocity (U_∞) scales are used to normalize the profiles. For the co-up case (Figure 6.20 b)), at $s = 3502$ mm, the profile presents a peak near $\frac{y}{H_{step}} \simeq 0.23$ created by the jets wake. This peak moves away from the wall on the flap with s and decreases. At $s = 3624$ mm , it is at $\frac{y}{H_{step}} \simeq 0.35$ and at $s = 3793$ mm, it is a plateau around $\frac{y}{H_{step}} \simeq 0.5$. Downstream $s = 3793$ mm, this peak has totally disappeared. At $s = 3624$ mm, a second peak appears near the wall which moves away from the wall with s. This peak amplifies with s until $s = 3793$ mm. From $s = 3949$ mm, it remains constant but spreads significantly and absorb totally the other peak. This peak level is about 35% below the level of the uncontrolled flow but with a very similar behaviour with streamwise position.

For the counter-rotating cases (Figures 6.20 c) and d)), the profiles downstream $s = 3502$ mm show only one peak which remains also below the level of the uncontrolled flow (about -40%). The peak behaviour is almost similar for these two cases. It is closer to the wall than for the co-up and uncontrolled cases, however, it moves also away from the wall with s and spreads. Contrary to the uncontrolled case, the peak increases with s in the first part of the flap. Downstream $s = 3948$ mm, it decreases and spreads out. Upstream $s = 3948$ mm, the peak position is

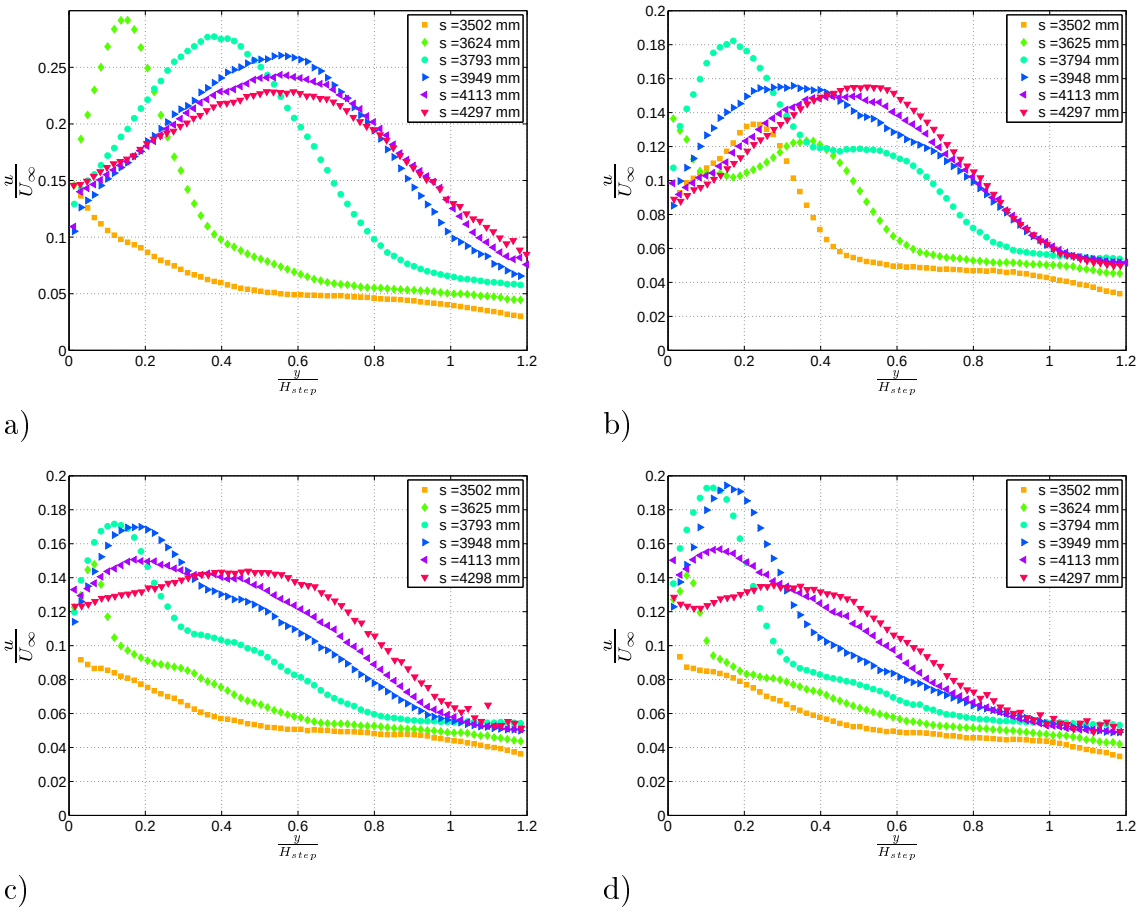

Figure 6.20: Streamwise turbulent intensity profiles at six stations on the flap for a) the uncontrolled flow, b) the co-up case, c) the counter-up case and d) the counter-down case.

about the same for the two counter-rotating tests. Downstream $s = 4113$ mm, the peak for the counter-up case is much wider and away from the wall than the one of the counter-down test.

3.5.2.2 Wall-normal turbulence intensity

Figure 6.21 shows the wall normal turbulent intensity profiles at the same stations as previously. As for the streamwise component, the co-up case has a distinct behaviour at the beginning of the flap ($3502 \leq s \leq 3794$ mm) then it looks quite similar to the uncontrolled case but with a lower level. As seen in the previous whole field figures, the two counter-rotating cases show a thin near wall peak just after the corner, which grows and spreads out first slowly and then more rapidly outward after it reaches its maximum. Again the global level is much lower than for the uncontrolled case. For both counter-rotating tests, the peaks are closer to the wall than for the co-up and uncontrolled cases and the ones of the counter-down case are slightly closer to the wall than the ones of the counter-up test. Finally, it should be remarked that, for all the configurations in Figure 6.21, the peak on the wall-normal component develops slightly closer to the wall than the peak on the streamwise one (Figure 6.20).

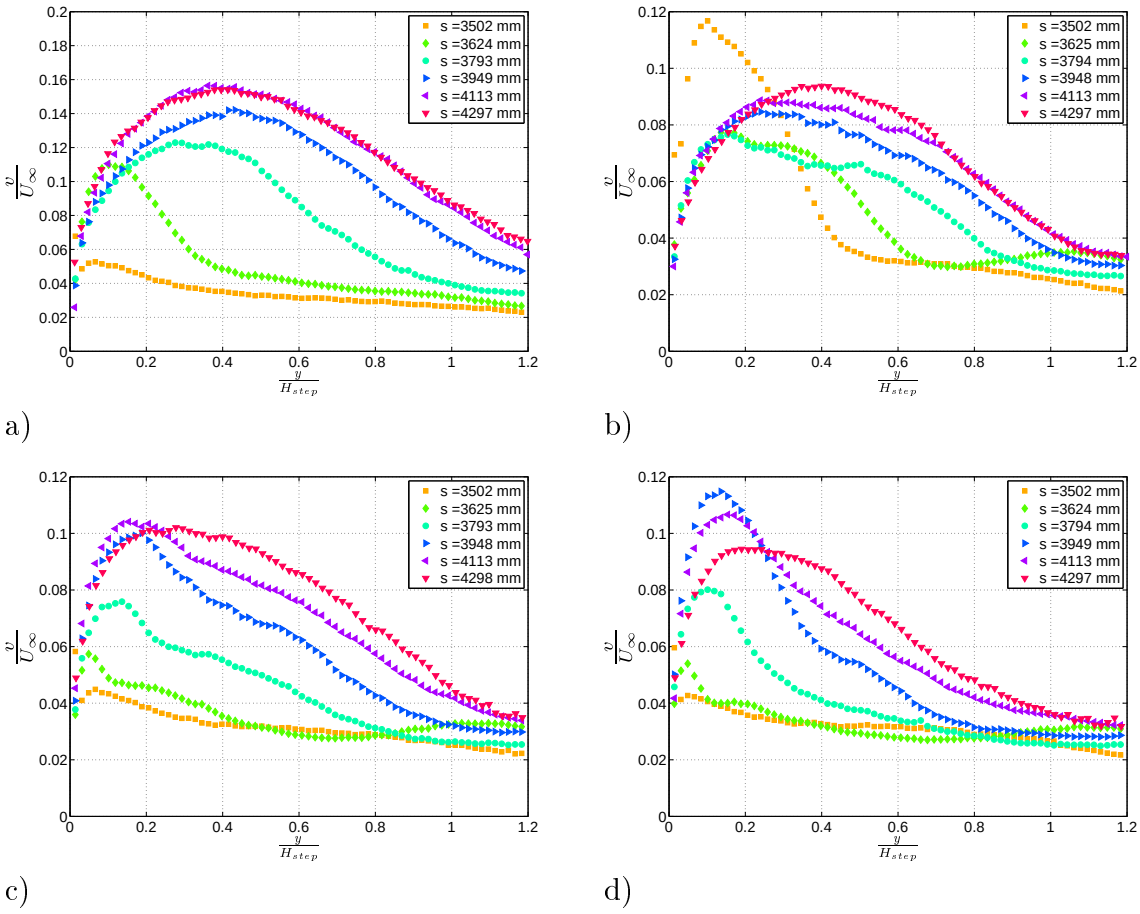

Figure 6.21: Wall-normal turbulent intensity profiles at six stations on the flap for a) the uncontrolled flow, b) the co-up case, c) the counter-up case and d) the counter-down case.

3.5.2.3 Reynolds shear stress

Figure 6.22 shows the Reynolds shear stress profiles for the uncontrolled flow and the three control cases at the same stations. Here again, the two counter rotating configurations behave in a very similar way with essentially a difference in the wall normal spreading at the last station which was not so evident in Figure 6.21. A region of negative shear stress slightly more pronounced than in the uncontrolled case is visible at stations $s = 3624$ mm and $s = 3793$ mm. The co-up case shows a strong positive peak of $-\overline{u'v'}$ close to the wall at the first two stations downstream the articulation, which is probably due to the actuating jets themselves and linked to the specific behaviour observed also on the other components. At $s = 3502$ mm, there is also a positive peak at $\frac{y}{H_{step}} \simeq 0.27$, which is at the same position as the inflection point in the mean streamwise velocity profile seen in Section 3.4.2. The jets/incoming cross-flow interaction is then able to generate a significant amount of $\overline{u'v'}$ which acts directly on the mean flow.

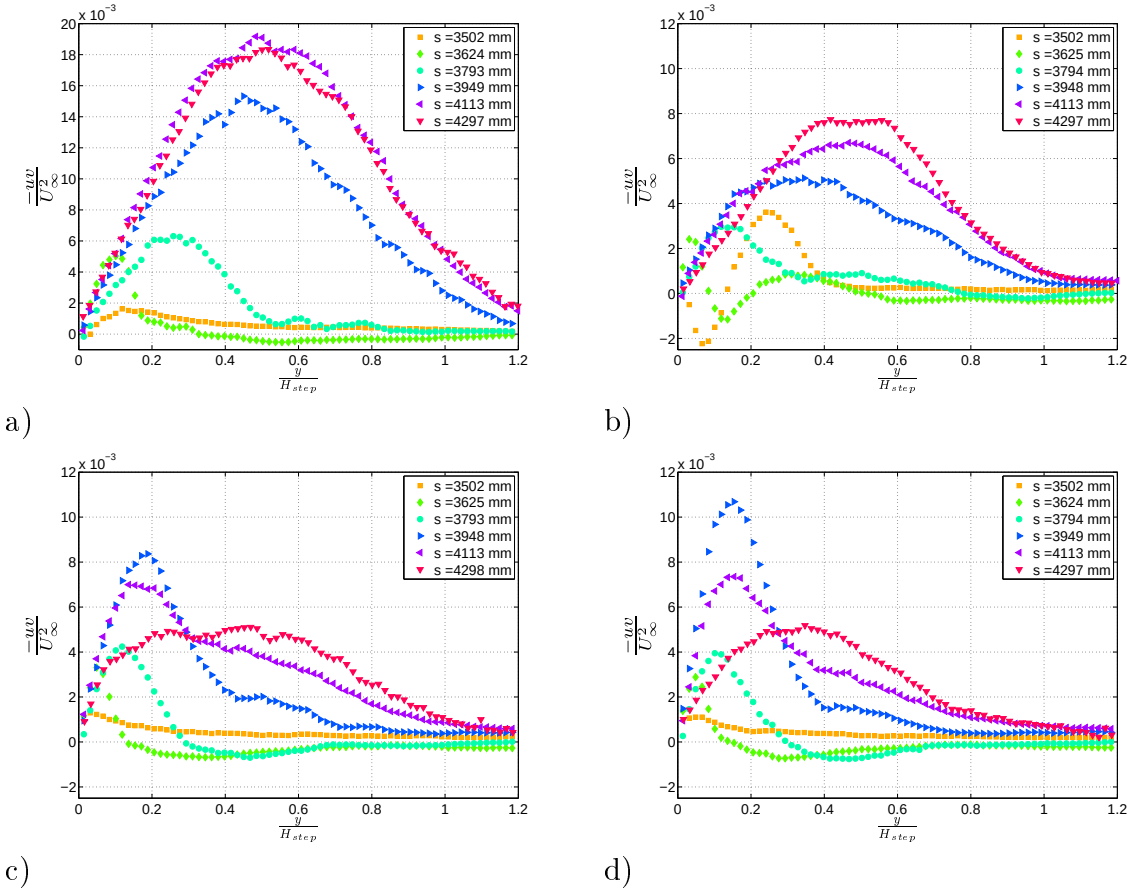

Figure 6.22: Reynolds shear stress profiles at six stations on the flap for a) the uncontrolled flow, b) the co-up case, c) the counter-up case and d) the counter-down case.

It is of interest to note that for all control cases, apart for the co-up at the first three stations, the behaviour of the Reynolds shear stress is similar to the uncontrolled case but with lower intensity level and a turbulence peak closer to

the wall, especially for the counter-rotating actuators. It seems that the control is not suppressing the shear layer due to the singular separation point but redirecting it toward the wall and attenuating it. This is a fairly different mechanism from spanwise type of actuation which directly interacts with the shear layer vorticity generation mechanisms.

3.5.2.4 Turbulence production

This analysis is confirmed by the turbulence production profiles of $-\overline{u'v'}\frac{\partial U}{\partial y}$ given in Figure 6.23 (the profiles for other production terms are given in Appendix G but will not be discussed here as they exhibit similar trends). In the case of the counter-rotating devices, the peak is localized much closer to the wall. What is remarkable is the difference in the rear part of the flap. In the uncontrolled case, production starts to decrease at the last station ($s = 4297$ mm) while for the two counter cases, this decrease is already significant at $s = 4113$ mm and production is very weak at the last station. It is also noticeable that the maximum peak level reached in these three cases is comparable, although the Reynolds shear stress levels are significantly smaller in the controlled cases.

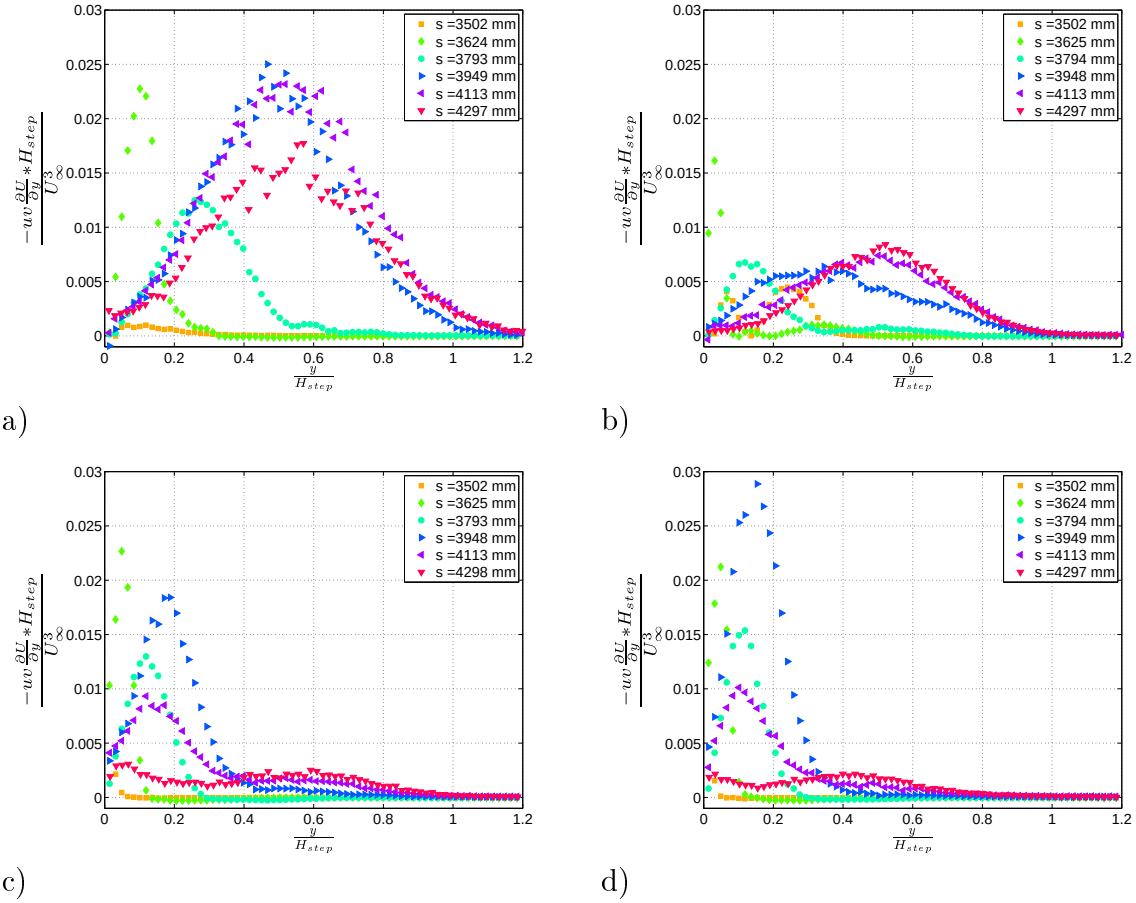

Figure 6.23: Six profiles of the production term $-\overline{u'v'}\frac{\partial U}{\partial y}$ of the turbulent kinetic energy on the flap for a) the uncontrolled flow, b) the co-up case, c) the counter-up case and d) the counter-down case.

For the co-up case, the production level is globally much lower but it appears to increase slightly and to spread out until the last station. This indicates a fairly different mechanism of the control jets interaction with the turbulence. This is not surprising as the control flow generated in the co-rotating configuration is known to be quite different from the counter-rotating one.

3.6 Flow recovery in the downstream part of the flap

Figure 6.24 shows mean streamwise velocity profiles in wall units after the reattachment point for the uncontrolled flow and the three control cases. The log-law and the FP case at 5 m/s are added for comparison. For the three control cases (Figures 6.24 b), c) and d)), a log-law region is still visible, but with a slope significantly different from the standard one. The slope of the co-up (Figure 6.24 b)) and counter-up (Figure 6.24 c)) cases seems nearer to the standard one compared to the slope of the counter-down case (Figure 6.24 d)). Maybe the generated vortex by the control are still present at the end of the PIV field which can explain a boundary layer recovery different from the uncontrolled case (Figure 6.24 a)) where a standard log-law is observed. For all the control tests however, the wake is reduced, especially for the two counter-rotating configurations.

Table 6.4 contains the boundary layer characteristics at the end of the PIV field for the different test cases. The uncertainty on the friction velocity is very high (estimated at $\pm 15\%$) dues to the standard log-law constants used for the profile fit. The friction velocity obtained for the co-up case is near the one of the uncontrolled flow which is coherent with its small separation upstream this station. The obtained u_τ for the two counter-rotating cases are in the same order and nearly two times higher than for the uncontrolled flow. This agrees with the more full profiles observed on the flap for these cases compared to the co-up ones (see Figures 6.13 c) and d)).

The integral thicknesses are reduced by each control case compared to the uncontrolled flow. However, the decrease is more marked for the two counter-rotating cases. This agrees with a control not strong enough for the co-up case, in the investigated region by PIV, to suppress totally the separation. The shape factor of the co-up configuration is then high and near the value of the uncontrolled flow and even not too far from the characteristic value of flow separation (2.85 according to Dengel and Fernholz (1990)). The shape factor for the counter-rotating configurations is not too far from the equilibrium boundary layer in zero pressure gradient, however a recovery of the standard log-law is not observed.

4 Conclusion

Flow characteristics of some active control tests of Chapter 5 were accessed quantitatively by streamwise pressure distributions and by a streamwise 2D2C PIV measurement on the flap. The configurations that were selected were the ones with the 6 mm jets at control station 2 ($s = 3219$ mm). Both co and counter-rotating configurations and both upstream and downstream blowing were investigated.

For the pressure distributions, the value of VR was set at the optimum found in Chapter 5. However, some values outside the optimum range were tested to confirm

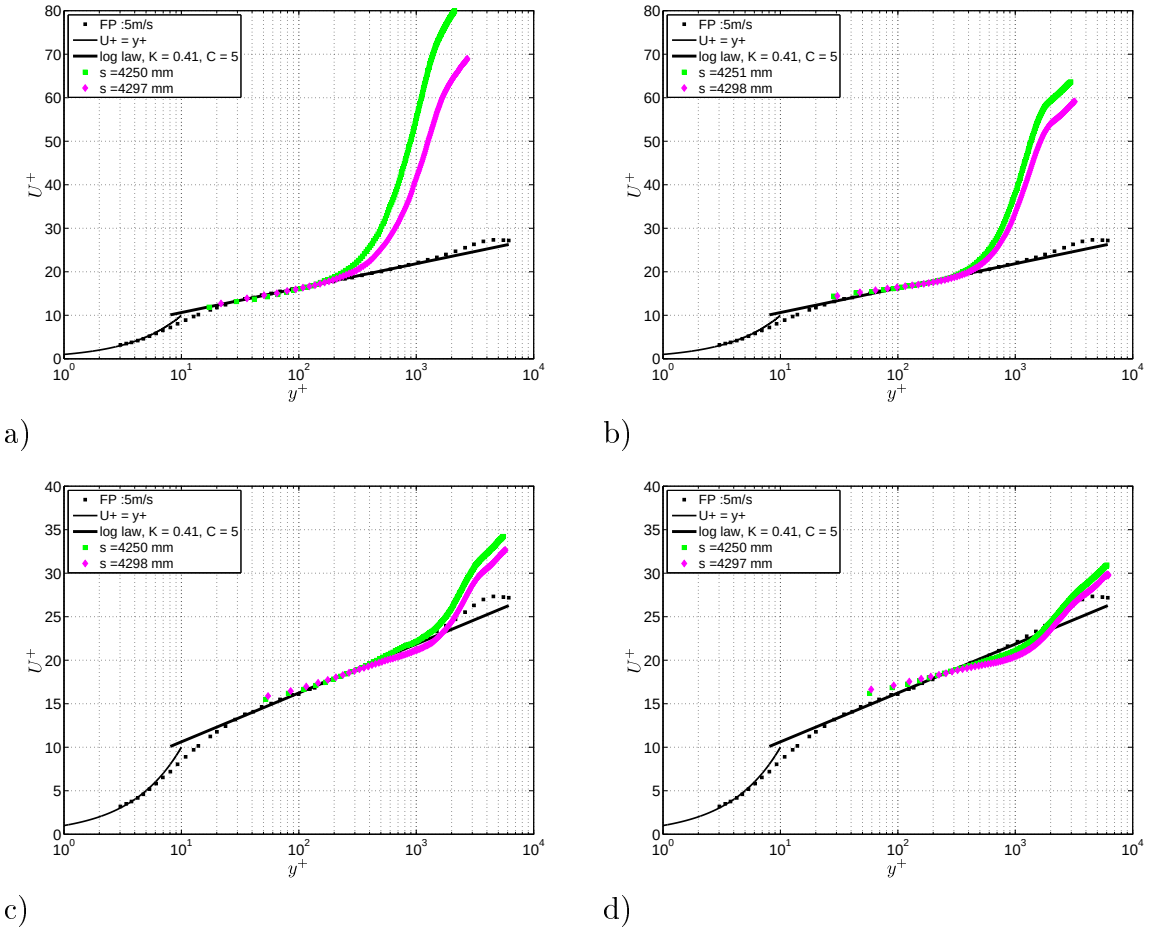

a) b)

c) d)

Figure 6.24: Mean streamwise velocity after the reattachment point in wall-units for a) the uncontrolled flow, b) the co-up case, c) the counter-up case and d) the counter-down case, and compared to the log-law and FP case at 5 m/s.

Table 6.4: Table of the boundary layer characteristics at the end of the PIV field for the different test cases.

Set-up	u_τ (m/s)	δ^* (cm)	θ (cm)	Re_θ	H
without control	0.15	9	4.2	26000	2.2
co-up	0.18	8	3.9	24000	2.1
counter-up	0.32	5.3	3.6	22000	1.46
counter-down	0.35	4.5	3.3	20500	1.38

the optimum VR value. The minimum VR value to detect control efficiency is found between 1.5 and 2 which agrees with Chapter 5. The downstream blowing configuration tested at $VR = 3.5$ gives about the same result on the pressure distribution as the ones presenting a complete suppression of the separation. This seems then to contradict the optimum VR range found for downstream blowing (between 1.5 and 2.5). However, this disagreement is attributed to a missing information about the spanwise pressure distribution.

It is also found that, for upstream blowing, the pressure distribution is nearly identical for the co and counter-rotating optimum configurations. The same observation is obtained for downstream blowing. This contradicts the conclusion of Chapter 5 where it was found that the counter-rotating configurations give best result than the co ones. However, here also, it is attributed to the missing information about the transverse control homogeneity. Finally, it is concluded that the upstream blowing configurations present best result as they give a larger suction peak.

For 3 configurations among the ones tested with the pressure distribution, a streamwise 2D2C PIV measurement was realized on the middle of the flap. Two counter-rotating configurations were retained (one in upstream blowing and one in downstream blowing), and one co-rotating (upstream blowing). The VR of upstream blowing configurations was set at 3.5 (i.e. the optimum one), and for the downstream blowing configuration, it was set at 2.5 (i.e. corresponding to the optimum VR limit).

The measurement plane for the co-rotating configuration was midway between two jets. It is found to correspond to an upwash flow region. The mean streamwise velocity profile at hot-wire station 5 presents then a S-shape in agreement with the previous studies of McManus et al. (1994), Godard and Stanislas (2006b) and Kostas et al. (2007). This S-shape introduces an inflection point in the profile at $\frac{y}{\delta} = 0.23$ which corresponds to the peak position on the Reynolds shear stress. The jet penetration is estimated about 0.3δ. This control case is found to increase the turbulence level upstream the flap articulation near $\frac{y}{\delta} = 0.2$, which reorganizes the mean flow to achieve the control efficiency. This configuration however presents a small separation near $X = 3.8$ m, with a length of about 3 cm.

The measurement plane for the counter-rotating configurations was at the middle of a counter-rotating jets pair. It is found to correspond for both configurations to a downwash flow region. In agreement with the study of Godard and Stanislas (2006b), no S-shape is observed in the mean streamwise velocity profile. The jet penetration is estimated at 0.2δ which is slightly lower than the co-rotating configuration. These two counter-rotating control cases are found to have similar flow organisation. For both configurations, upstream the flap, the turbulence level in the region near $\frac{y}{\delta} = 0.2$ is reduced. These control cases bring then external flow with low turbulence level to the wall to achieve control efficiency. No separation on the flap is detected for these configurations and higher velocities near the wall are observed compared to the co-rotating and uncontrolled configurations.

For these three control configurations, the streamwise turbulent intensity is found largely reduced on the flap, dues to a size reduction, compared to the uncontrolled case, of the very large scale structures characterized by large u'-fluctuations ($3\delta_0$ in length and $0.5\delta_0$ in width for the uncontrolled flow, with δ_0 the boundary layer

thickness at hot-wire station 5). The optimum VR for downstream blowing is also confirmed at 2.5, as these large structures, responsible of the separation, begin to reappear above this VR for the counter-down case.

The wall-normal turbulence intensity and the Reynolds shear stress on the flap are also found significantly reduced for the three control tests investigated. Moreover, on the flap, for these three control tests, as for the uncontrolled flow, a strong similarity is observed between the wall-normal turbulence intensity and the Reynolds shear stress due to the fact that the production of the last one is dominated by $\overline{v'^2}\frac{\partial U}{\partial y}$.

Finally, excepts near and upstream the flap corner for the co-up case, all the measured Reynolds stresses of each control test behave similarly as the ones of the uncontrolled flow, but with a peak region more or less squeezed against the wall and reduced in intensity. Each control strategy used has then not changed the flow physic as the shear layer is not totally suppressed. They just reduce its intensity and squeeze it more or less against the wall. This is confirmed by the turbulence production which behave similarly as the Reynolds stresses for the three control tests.

At the end of the PIV fields obtained for these three control cases, the profiles are not presenting a standard log-law region but a log region with a significantly lower slope. This is probably due to the persistence of the generated vortices at the end of the PIV field, which is especially marked for the counter-rotating cases with a strong downwash. The control applied here could then be to strong.

The co-rotating configuration is the only one selected to present a detectable small separation region of 3 cm in length. This tends to confirm that the counter-rotating configurations give best results than the co-rotating ones. This agree then with the conclusions obtained with friction probes and wool-tufts visualisations in Chapter 5. However, this conclusion has to be confirmed as only one streamwise plan was realized so, as for the pressure distribution, no transverse control information is available.

Finally, it is found that the two selected counter-rotating configurations behave similarly and give quite similar results. The downstream blowing one seems the best as less flow rate is needed to suppress the separation. However, the total suppression of the separation need the maximum available efficiency, whereas it is not the case for the upstream blowing configuration. For a stronger separation, the upstream blowing configuration can then be the best one, which confirms that upstream blowing is more robust as it was found in Chapter 5.

However, these conclusions could be contradicted by the spanwise flow organisation which is not accessible with only one streamwise measurement plane. To remove the ambiguity, a spanwise 2D3C PIV measurement at $s = 3860$ mm, corresponding to the middle of the separation bubble detected for the co-rotating configuration selected, could be performed.

General conclusion and perspectives

The aim of this work was to characterize in detail active flow control strategies over a separated turbulent boundary layers with adverse pressure gradient. It follows and complement the work done previously in the laboratory by Godard and Stanislas (2006b). A new 2D ramp model was designed for the study. It allows the boundary layer equilibrium to be manipulated and a flow separation on the flap can be imposed. This model was described in Chapter 2. The study was divided in four major parts to achieve its goal.

First, the flow over the ramp model was characterized to find a configuration which mimics the suction-side of a wing (i.e. adverse pressure gradient and flow separation). The results of this first part are given in Chapter 3. All the study was conducted at the maximum velocity of the LML wind-tunnel ($U_\infty = 10\,m/s$) to reach a momentum Reynolds number as high as possible. With streamwise wall pressure distribution measurements, it was found that for $\alpha > -0.7°$, the boundary layer on the 2 m flat plate of the ramp is encountering a favourable pressure gradient. For $\alpha < -0.7°$, it is adverse and for $\alpha = -0.7°$ it is nearly zero. The angle retained for the study was then $\alpha = -2°$, which is found to correspond to a mild adverse pressure gradient in the stabilized region ($0.2 \leq \beta_{Clauser} \leq 0.4$). Then, based on wool-tufts visualisations, the angle of the flap which leads to flow separation is found to be $\beta = -19°$. For angles below this value, the separation strength increases. The flap was set at $\beta = -22°$ to obtain a strong separation which can be clearly evidenced by wool-tufts visualisations. The retained configuration corresponds then to an adverse pressure gradient on the flat plate and a flow separation on the flap.

This configuration was characterized in more detail by oil film visualisation, hot-wire anemometry and 2D2C PIV measurements. The aim was to obtain detailed flow characteristics before applying control. The oil visualisation locates the separation line at the flap articulation. End effects are found up to about 30 cm from each wall. The separation under study is then more or less 2D on 70% of the flap span.

Single hot-wire profiles were measured on the flat plate to obtain the boundary layer characteristics. Five streamwise stations were selected. Attention was paid to the accuracy of these experiments. A high enough number of samples was acquired to assure an uncertainty of less than 1% on the mean value, less than 2.8% on turbulent intensity, less than 7.2% on the third order moment and less than 5.2% on the fourth order moment. However, it was evidenced that the room temperature, which was impossible to keep constant during an acquisition, was influencing the accuracy of the experiment. To obtain better hot-wire measurements, the room temperature should be regulated. However, it would be an investment to cool the 270 m^3 of the room which is not insulated. The length of the hot-wire used was also

too long (15 wall-units) compared to the value recommended by Klewicki and Falco (1990). Using a smaller hot-wire was impossible as it would has required a special order and an adapted hot-wire anemometer. The length of the hot-wire used was then reducing the level of the turbulent intensity peak near the wall. Finally, the acquisition chain used was limiting the acquisition frequency at 11 kHz, which was slightly insufficient to capture all the turbulent scales.

The flow along the ramp has a boundary layer thickness of the order of 20 cm and a momentum Reynolds number about 11500. The shape factor is about 1.21. The uncertainty on the boundary layer characteristics is of the order of $\pm 5\%$ except for the boundary layer thickness where it is $\pm 10\%$. These uncertainties could be reduced by improving the uncertainty on the hot-wire measurements and by taking more points in the external region. The friction velocity was determined by a Clauser's chart method. However, a modified log-law, which takes into account the pressure gradient, was introduced to improve the fit. Despite this modified log-law, the estimation of the uncertainty on the friction velocity remains quite high at about $\pm 5\%$. In the stabilized pressure gradient region, the parameter $(\frac{\partial P}{\partial s})^+$ is about 0.0005, which corresponds to a mild to small adverse pressure gradient. The boundary layer under study is found in equilibrium state as defined by Castillo and George (2001) but not in the Clauser's definition. The value of Λ is found near 0.2.

A second peak in the turbulent intensity profiles together with a knee point are exhibited. As the knee point is staying at the same position (near $y^+ \simeq 2000$), it was attributed to the external turbulence intensity of the incoming boundary layer that has been seriously attenuated by the favourable pressure gradient encountered in the converging part. The second peak in the turbulence intensity profiles was then interpreted as an instability triggered by the change of sign of the pressure gradient near pressure tap 6 (i.e. at the end of the converging part). However, the interpretation of these knee point and second peak as a new internal layer by Baskaran et al. (1987), Webster et al. (1996), Wu and Squires (1998), etc. could also applied. In the third, fourth, skewness and flatness profiles, the trace of this instability near pressure tap 6 are also evidenced by a second local minimum or maximum.

Due to technical constrains, crossed hot-wires measurements at the same stations were not carried out. This type of measurement could bring information about the flow organisation, especially with uv-probes. Also, it could be interesting to study the influence of the adverse pressure gradient strength on the mean velocity and on Reynolds stresses. For that, the adverse pressure gradient along the ramp could be increased by decreasing α from $-2°$ to $-4°$ for example (i.e. the minimum value). With this stronger APG, the second peak observed in the streamwise turbulence intensity profiles should develop and be more intense and could even absorb the near wall peak as it is the case in Webster et al. (1996)'s study. However, the minimum flap angle β would be $-17°$, and it is not sure that this angle will lead to detectable separation. Finally, to confirm the benefit of the modified log-law and to study the scaling of the profiles, the friction velocity should be measured with an independent method, for example the oil-film interferometric method.

To complete the flow characterisation of the selected ramp configuration, a streamwise 2D2C PIV measurement on all the flap was performed. Four 2k by

2k cameras were used for that. Between two cameras there was a common region (called "merging region") so that a continuous field from the four cameras was obtained. The merging regions were also used to assess the PIV accuracy. The size of the obtained field along the wall is about 94 cm and normal to it, about 28.7 cm. The number of vectors was 642 by 188 which conducts to a resolution of about 45 wall-units, with u_τ taken upstream the flap articulation at hot-wire station 5. A total of 5000 fields were acquired, and the obtained uncertainty on the mean field is below $\pm 1\%$ of U_∞ ($= 10\ m/s$) and on the turbulent intensities below $\pm 0.8\%$ of U_∞. Near the wall, due to stronger mean velocity gradient, these uncertainties are higher of about respectively 4 and 3 % of U_∞. The uncertainty estimation on the mean velocity was validated by a good superposition of the PIV profile with the hot-wire one.

The separation border was detected by two criterion defined by Simpson (1989), the first one being $U = 0$, with U the mean streamwise velocity, and the second one being $\chi = 0.5$, with χ the backflow coefficient. According to the studies of Dengel and Fernholz (1990) and Lögdberg et al. (2010), the second criteria was completed by a linear extrapolation of the backflow coefficient at the wall where, at minimum, the first two points from the wall in the wall-normal direction were presenting a χ coefficient greater than 0.3. The criteria $\chi = 0.5$ gives the best estimation of the separation characteristics. It gives a separation point near the flap articulation coherent with the oil-film visualisation, a separation length of 61 cm ($\frac{L_{sep}}{H_{step}} = 3.5$, with $H_{step} = 17.5$ cm, the ramp step height defined in Figure 2.2) and a maximum separation height of 3 cm ($\frac{H_{sep}}{H_{step}} = 0.17$). The separation length obtained is largely bigger than the one of Lin (1999) and Selby et al. (1992) ($\frac{L_{sep}}{H_{step}} \simeq 1.3$) for a similar configuration at about the same momentum Reynolds number. This difference was explained by a larger momentum thickness here compared to the one of Lin (1999) and Selby et al. (1992) ($\theta = 3.3$ mm) which was noticed by Simpson (1989) to increase $\frac{L_{sep}}{H_{step}}$ for a backward facing step.

The flow is found unable to follow the sudden change in wall direction imposed at the flap articulation. This is exhibited by strong wall-normal velocities near the corner and by the creation of a shear layer above the flap. This shear layer generates an important turbulent intensity region (streamwise, wall-normal and Reynolds shear stress) above the bubble border which was studied in detail. This region is found to grow in wall-normal direction with X the streamwise coordinate, but remains in the interval $0.1 \leq \frac{y}{H_{step}} \leq 0.6$, where y is the distance from the wall in wall-normal direction. At each streamwise position, the peak of wall-normal Reynolds stress is found however closer to the wall that the one of $\overline{u'^2}$. The high streamwise turbulence intensity region on the flap is found related to very large scale structures (more than $3\delta_0$ in length and $0.5\delta_0$ in width, with δ_0 the upstream boundary layer thickness at hot wire station 5) characterized by high u' fluctuations.

The production of streamwise Reynolds stress in the separated region is the main source of turbulent kinetic energy. This production on the flap is found strong but dispatched into two parts, one near the beginning of the separation and an other which starts at the middle of the bubble (i.e. at $X = 3.8$ m) where there is a change in wall direction. The first region is due to the deceleration and is dominated by the

term $-\overline{u'^2}\frac{\partial U}{\partial x}$. The second region, in the downstream part of the flap, is dominated by $-\overline{u'v'}\frac{\partial U}{\partial y}$ as for a 2D ZPG boundary layer. This region is probably due to the wall-normal flapping motion of the large scale structures characterized by high u' fluctuations, which induces high levels of v' so high levels of $-\overline{u'v'}$. The production of $\overline{v'^2}$ is found negative in the first half of the separation region and negligible in the rest of the field. As $\overline{v'^2}$ increases with X, a redistribution from $\overline{u'^2}$ to $\overline{v'^2}$ is supposed to explain the observations. Concerning the Reynolds shear stress, its production is found governed by $\overline{v'^2}\frac{\partial U}{\partial y}$, and this explains the strong similarity observed between the wall-normal turbulence intensity and the Reynolds shear stress distributions. Finally, on the rear part of the flap, the turbulence production organisation is found similar to that of a 2D ZPG boundary layer, but more away from the wall.

The boundary layer recovery downstream the separation is found very fast for the mean velocity profile and slower concerning the Reynolds stresses ones. At the end of the PIV field, a log-law region is observed, however the boundary layer remains quite destabilised with a shape factor of 2.2.

The 2D nature of the flow separation over the flap in the middle of the model was confirmed by oil film visualisation, but this is not quantitative. It would be interesting to perform a spanwise 2D3C PIV measurement near the end of the flap glass window insert to quantify the 2D nature of the separation. It would be then possible to access all the Reynolds stresses and some missing production terms to confirm or to complete the conclusions drawn (i.e. there could be also a redistribution from $\overline{u'^2}$ to $\overline{w'^2}$ or from $\overline{w'^2}$ to $\overline{v'^2}$, etc.). With a large spanwise PIV field (which can be obtained with two stereo PIV set-ups with the cameras on the top-wall of the wind tunnel and on each side of the laser sheet), the spanwise vortices generated at the separation point could be evidenced and quantified. However this plane would be very difficult to realise as the flow will pass through it in one direction on the top, and in the other direction near the bottom.

On this ramp/flap set-up characterized in detail, passive control strategies were applied, first to build control effect quantification tools, then to find optimum configurations. The generators used were thin triangular plates as the ones used by Godard and Stanislas (2006a). The control effects quantification was done with wool-tufts visualisations on all the flap and with four friction probes. The gain in friction given by the probes was found not sufficient to characterize the flow reattachment on the flap as they are not sensitive to the flow direction. The skewness of the output voltage of a probe is however adapted to quantify the control result. A skewness around -0.7 is found characteristic of a separated flow and a skewness above -0.4, characteristic of an attached one. The wool-tufts visualisations and the gain in friction and skewness given by the probes were then the tools used to find the optimum passive configurations.

Co and counter-rotating arrangement were tested. The starting parameters were the ones found by Godard and Stanislas (2006a). It appears that the counter-rotating configurations give best control effects and are the only ones which can totally suppress the separation, which is in agreement with previous studies (Betterton et al. (2000), Godard and Stanislas (2006a), etc.). The co-rotating configurations are found only able to delay and reduce the separation bubble. The optimum parameters found are summarized in Table 7.1, where the bold parameters correspond to

the best of the best. These optimum parameters almost agree with previous studies (Lin (1999), Godard and Stanislas (2006a), etc.). The best parameters for passive devices are then not too much sensitive to the flow in which they are embedded. Maybe it is then not useful to test these optimum parameters in a stronger adverse pressure gradient flow (which can be obtained by decreasing α) and on a stronger separation (which can be obtained by decreasing β).

Table 7.1: Optimum parameters for co and counter-rotating passive configurations tested.

	β	$\frac{h}{\delta}$	$\frac{l}{h}$	$\frac{L}{h}$	$\frac{\lambda}{h}$	$\frac{\Delta X_{vg}}{h}$
co-rotating	18°	0.08 - **0.15**	2	-	6	8
counter-rotating	±18°	**0.08** - 0.15	2	2.5	6	8

After the passive tests, active continuous jets have been investigated and optimised. Here also, the starting parameters were the optimum ones found by Godard and Stanislas (2006b) and both co and counter-rotating arrangements were tested. Before beginning the tests, a flow rate quantification circuit supplying the jets was realised. It allows to tune and measure the mass flow rate at ±2% in the large range $2.4 - 4800\ kg/h$.

Two jet diameter were selected ($\Phi = 6$ and 12 mm) and both upstream and downstream blowing were investigated. Some of the tested configurations suppress totally the separation. The minimum VR to detect control effect is 1.5. In agreement with previous studies (Godard and Stanislas (2006b), Betterton et al. (2000), Tilmann et al. (2000), McManus et al. (1994), Selby et al. (1992), etc.), for both co and counter-rotating configurations, for upstream blowing, the control efficiency increases continuously with VR. For downstream blowing it is not the case and there is an optimum between 1.5 and 2.5, which was not really observed in the literature. Downstream blowing optimum configurations reattach then the flow at a lower VR than upstream blowing ones, however the maximum control efficiency was needed. For a stronger separation, upstream blowing could then be more adapted as higher control power is available. This could be confirmed by decreasing the flap angle β to its minimum (i.e. $\beta = -24°$ for $\alpha = -2°$).

The smallest diameter tested is found the best one, which is a good thing for real applications as the mass flow rate is a critical parameter. However, the holes should have a not too small diameter so that they are realisable and the needed pressure supply to reach large VR is not too big. To confirm this result, it would be interesting to test smaller diameters of jets.

Finally, two actuators positions were tested at different distances from the separation line ($\frac{\Delta X_{vg}}{\delta} = 0.6$ and 1.4). However, both were to close to the corner of the flap to observe effects of this parameter. By inverting the four plates which compose the ramp flat plate, higher values of this parameter could be tested (i.e. up to $\frac{\Delta X_{vg}}{\delta} = 10$). This test would also be interesting as counter-rotating vortices are known to be more persistent in the boundary layer, so the control effect of co-rotating configurations should decrease more rapidly with $\frac{\Delta X_{vg}}{\delta}$.

The optimum parameters found are summarized in Table 7.2, where, as for the passive actuators, the bold parameters correspond to the best of the best.

Table 7.2: Optimum parameters for co and counter-rotating active configurations tested.

	$\frac{\Phi}{\delta}$	β	α	$\frac{\lambda}{\Phi}$	$\frac{L}{\Phi}$	VR
co	0.03	35	55	13.6	-	2
	0.03	35	**125**	13.6	-	3.5
counter	0.03	35	55	27.3	15	2
	0.03	35	**125**	27.3	15	3.5

This optimization leads, at constant diameter, to the same number of jets for co and counter-rotating set-up. The optimum co-rotating configuration for $\Phi = 12$ mm gives better results than the optimum counter-rotating one with the same jet diameter. However, the optimum counter-rotating configuration with $\Phi = 6$ mm gives better results than the optimum co-rotating one with the same jet diameter. As the best parameter of $\frac{\Phi}{\delta}$ is 0.03, the best configuration found in this study is the counter-rotating, $\Phi = 6$ mm, $\frac{\lambda}{\Phi} = 27.3$, $\frac{L}{\Phi} = 15$ and $\alpha = 125°$ (upstream blowing), with a VR larger than 3.

Finally, passive and active actuators were compared. It results that, in agreement with Godard and Stanislas (2006b), the co-rotating passive configurations seem to be clearly different from the active ones. Indeed, the best passive co-rotating configuration is obtained for $\frac{\lambda}{\delta} = 0.9$ and the best active co-rotating configuration is obtained for $\frac{\lambda}{\delta} = 0.4$. The active configuration has then 2 times more actuators than the passive one, but it is the only one which can suppress the separation. The difference between the two could be explained by a difference in the physic of the vortex generation.

Also in agreement with Godard and Stanislas (2006b), the counter-rotating passive configurations seem to behave similarly to the active ones. The best passive counter-rotating configuration is obtained for $\frac{\lambda}{\delta}$ between 0.5 to 0.9, and for $\frac{L}{\delta}$ between 0.20 to 0.38. The best active counter-rotating configuration is obtained for $\frac{\lambda}{\delta} = 0.8$ and for $\frac{L}{\delta}$ between 0.36 to 0.48. The parameters $\frac{\lambda}{\delta}$ and $\frac{L}{\delta}$ are thus very close for the best passive and the best active counter-rotating configurations. This can explain why they give almost the same results. As expected, this study shows that active VGs (both co and counter-rotating with a preference for the last one) can successfully replace passive ones in real applications.

Finally, to get a better understanding of the flow physic of some active VGs, a more detailed flow characterisation was realised on some selected optimum active configurations. The configurations that were retained were the optimum ones with the 6 mm jets at control station 2 ($s = 3219$ mm). Both co and counter-rotating configurations and both upstream and downstream blowing were investigated. The advance flow characterisation was done through streamwise pressure distributions and 2D2C PIV measurements on the flap with the same set-up than the one used

to characterize the separation.

For the pressure distributions, the VR tested was near the optimum one plus some values outside the optimum range, whereas for the PIV measurements, it was only set at the optimum value (i.e. 3.5 for upstream blowing and 2.5 for downstream blowing configurations).

The minimum VR value to detect control efficiency is confirmed by the streamwise pressure distributions (i.e. between 1.5 and 2). However, for downstream blowing, the VR limit (i.e. 2.5) is not confirmed. This was attributed to a missing information about the spanwise pressure distribution. This would be difficult to resolve as inserting new pressure taps could deteriorate the ramp.

With the pressure distributions, it is also found that, for upstream blowing, the pressure distribution is nearly identical for the co and counter-rotating optimum configurations. The same is true for downstream blowing. This contradicts the previous conclusion (i.e. the counter-rotating configurations give better result than the co ones). Here also, it is attributed to the missing information about the transverse control homogeneity. Finally, it is concluded that the upstream blowing configurations present better result as they give a larger suction peak.

Concerning the PIV tests on the active VGs, the co-rotating downstream blowing configuration was not tested to reduce the amount of data to process. The measurement plane for the co-rotating configuration (i.e. upstream blowing one) was midway between two jets. It is found to correspond to an upwash flow region. The mean streamwise velocity profile at hot-wire station 5 presents then a S-shape in agreement with the previous studies of McManus et al. (1994), Godard and Stanislas (2006b) and Kostas et al. (2007). This S-shape introduces an inflection point in the profile at $\frac{y}{\delta} = 0.23$ which corresponds to the peak position on the Reynolds shear stress. The jet penetration is estimated about 0.3δ. This control case is found to increase the turbulence level upstream the flap articulation near $\frac{y}{\delta} = 0.2$, which reorganizes the mean flow to achieve the control efficiency. This configuration however evidences a small separation near $X = 3.8$ m (detected by the criterion $\chi = 50\%$), with a length of about 3 cm.

The measurement plane for the counter-rotating configurations was at the middle of a counter-rotating jets pair. It is found to correspond for both configurations to a downwash flow region. In agreement with the study of Godard and Stanislas (2006b), no S-shape is observed on the mean streamwise velocity profile. The jet penetration is estimated at 0.2δ which is slightly lower than the co-rotating configuration. These two counter-rotating control cases are found to have similar flow organisation. For both configurations, upstream the flap, the turbulence level in the region near $\frac{y}{\delta} = 0.2$ is reduced. These control cases bring then external flow with low turbulence level to the wall to achieve control efficiency. No separation on the flap is detected for these configurations and higher velocities near the wall are observed compared to the co-rotating and uncontrolled configurations.

For these three control configurations retained, the streamwise turbulent intensity is found largely reduced on the flap, due to a reduction in size of the very large scale structures characterized by large u'-fluctuations ($3\delta_0$ in length and $0.5\delta_0$ in width for the uncontrolled flow, with δ_0 the boundary layer thickness at hot-wire station 5) compared to the uncontrolled case. The optimum VR for downstream

blowing is also confirmed at 2.5, as these large structures, responsible of the separation, begin to reappear above this VR for the counter-rotating downstream blowing case. A characterisation of these structures appears then quite interesting. This could be achieve based on the tools developed by Lin (2006) for detecting streaks. The field of view here on the flap should be long enough to obtain not too biased mean length of these structures. They could correspond to the Low Momentum Regions observed by Lee and Sung (2009) in the external region which are reinforced by the pressure gradient.

The wall-normal turbulence intensity and the Reynolds shear stress on the flap are also found significantly reduced for the three control tests investigated. Moreover, on the flap, for these control tests, as for the uncontrolled flow, a strong similarity is observed between the wall-normal turbulence intensity and the Reynolds shear stress due to the fact that the production of the last one is dominated by $\overline{v'^2}\frac{\partial U}{\partial y}$.

Finally, excepts near and upstream the flap corner for the co-up case, all the measured Reynolds stresses of each control test behave similarly as the ones of the uncontrolled flow, but with a peak region more or less squeezed against the wall and reduced in intensity. Each control strategy used has then not changed the flow physic as the shear layer is not totally suppressed. They just reduce its intensity and squeeze it more or less against the wall. This is confirmed by the turbulence production terms which behave similarly as the Reynolds stresses for the three control tests.

At the end of the PIV fields obtained for these three control cases, the profiles are not presenting a standard log-law region but a log region with a significantly lower slope. This is probably due to the persistence of the generated vortices at the end of the PIV field, which is especially marked for the counter-rotating cases with a strong downwash. The control applied here could then be too strong.

As the co-rotating configuration is the only one selected to present a detectable small separation region of 3 cm in length, it tends to confirm that the counter-rotating configurations give better results than the co-rotating ones. However, the measurement plane does not correspond to the same flow region (upwash for co and downwash for counter-rotating). To conclude quantitatively about the optimum configuration with PIV, an other streamwise plane, with the same PIV set-up, could be realised easily at mid-way between two pairs of counter-rotating VGs, which corresponds to an upwash region.

Finally, to obtain the spanwise control organisation of each case selected, it would be interesting to perform a spanwise 2D3C PIV plane as for the uncontrolled flow. This plane could be placed at $s = 3860$ mm, which corresponds to the middle of the separation bubble detected for the co-rotating configuration retained. For the counter-rotating cases, the induced vortices should be clearly evidenced as a downwash region is observed at the end of the fields of view, whereas they should be more difficult to detect for the co test. The spanwise structures generated by the separation could also be studied to see if the streamwise vortices generated by the control succeed to brake some of them.

As general conclusion, this study has brought some new insight about the flow reorganisation by active control with continuous jet actuators. This was obtained

with a careful characterisation of the flow under study with and without control. An optimisation of the VGs was also performed in the perspective of implementing jet actuators on real applications. However, it is found that the selected control strategies which induce streamwise vortices do not suppress totally the mechanisms generated by the separation and the shear layer. They just squeeze them more or less against the wall and reduce their intensity, depending on the control strength of the actuators arrangement selected (co or counter-rotating). The flow instabilities still persist and to prevent them to develop, a very strong control has to be applied (VR as large as 3.5), which could be problematic for real applications. More studies are then needed to improve the active configurations selected, and probably this could be achieve by reducing the holes diameters and by pulsing the jets. Actuators based on spanwise vortices such as a slot for example, could also be considered as they act directly on the spanwise vorticity production mechanism. However it is not sure that they will give better results as Lin (2002) found that, for passive VGs, the streamwise vortex generators are much more efficient than spanwise ones.

Bibliography

Adrian, R. J. (1991). Particle-imaging techniques for experimental fluid mechanics. *Annu. Rev. Fluid Mech.*, 23:261–304.

Adrian, R. J., Meinhart, C. D., and Tomkins, C. D. (2000). Vortex organization in the outer region of the turbulent boundary layer. *Journal of Fluid Mechanics*, 422:1–54.

Afzal, N. (1996). Wake layer in a turbulent boundary layer with pressure gradient: a new approach. In *IUTAM Symposium on Asymptotic Methods for Turbulent Shear flows at High Reynolds Numbers (ed. K. Gersten)*, pages 95–118. Kluwer Academic Publishers.

Angele, K. P. (2003). *Experimental studies of turbulent boundary layer separation and control*. PhD thesis, Dept. Mechanics, Royal Institute of Technology, Stockholm.

Angele, K. P. and Grewe, F. (2007). Instantaneous behavior of streamwise vortices for turbulent boundary layer separation control. *Journal of Fluids Engineering*, 129:226–235.

Angele, K. P. and Muhammad-Klingmann, B. (2005). The effect of streamwise vortices on the turbulence structure of a separating boundary layer. *European Journal of Mechanics B/Fluids*, 24:539–554.

Angele, K. P. and Muhammad-Klingmann, B. (2006). Piv measurements in a weakly separating and reattaching turbulent boundary layer. *European Journal of Mechanics B/Fluids*, 25:204–222.

Atkinson, C. (2011). *Une Technique Expérimentale pour L'étude de L'organisation Tridimensionnelle de la Turbulence de Paroi*. PhD thesis, Ecole Centrale de Lille.

Aubertine, C. D. and Eaton, J. K. (2005). Turbulence development in a non-equilibrium turbulent boundary layer with mild adverse pressure gradient. *Journal of Fluid Mechanics*, 532:345–364.

Baskaran, V., Smits, A. J., and Joubert, P. N. (1987). A turbulent flow over a curved hill part 1. growth of an internal boundary layer. *Journal of Fluid Mechanics*, 182:47–83.

Becker, R., King, R., Petz, R., and Nitsche, W. (2007). Adaptive closed-loop separation control on a high-lift configuration using extremum seeking. *AIAA journal*, 45(6):1382–1392.

Bernard, A., Foucaut, J. M., Dupont, P., and Stanislas, M. (2003). Decelerating boundary layer: A new scaling and mixing length model. *AIAA Journal*, 41(2):248–255.

Betterton, J. G., Hackett, K. C., Ashill, P. R., Wilson, M. J., Woodcock, I. J., Tilmann, C. P., and Langan, K. J. (2000). Laser doppler anemometry investigation on subboundary layer vortex generators for flow control, in: 10th intl. symp. on appl. of laser tech. to fluid mech. Lisbon.

Blackwelder, R. F. and Kovasznay, L. S. G. (1972). Times scales and correlations in a turbulent boundary layer. *Phys. Of Fluids*, 15:1545–1554.

Blasius, H. (1908). Grenzschichten in flüssigkeiten mit kleiner reibung. *Z. Math. Phys.*, 56:1–37.

Bradshaw, P. (1967). The response of a constant-pressure turbulent boundary layer to the sudden application of an adverse pressure gradient. Technical report, Royal Society, R. and M. No. 3575.

Bradshaw, P. (1973). Advances in turbulent shear flow. In *Notes for Von Kármán Institute for fluid dynamics short course, March 19-23.*

Brown, G. L. and Thomas, A. S. W. (1977). Large structure in turbulent boundary layer. *Phys. Of Fluids*, 20(10):243–252.

Buschmann, M. H. and Gad-El-Hak, M. (2003). Debate concerning the mean-velocity profile of a turbulent boundary layer. *AIAA Journal*, 41(4):565–572.

Carlier, J. (2001). *Etude des structures cohérentes de la turbulence de paroi à grand nombre de Reynolds par vélocimétrie par images de particules.* PhD thesis, Université des sciences et technologies de Lille.

Carlier, J. and Stanislas, M. (2005). Experimental study of eddy structures in a turbulent boundary layer using particule image velocimetry. *Journal of Fluid Mechanics*, 535(36):143–188.

Castillo, L. and George, W. K. (2001). Similarity analysis for boundary layer with pressure gradient : outer flow. *AIAA journal*, 39(1):41–47.

Castillo, L. and Walker, D. J. (2002). Effect of upstream conditions on the outer flow of turbulent boundary layers. *AIAA Journal*, 40(7):1292–1299.

Chehroudi, B. and Simpson, R. L. (1985). Space-time results for a separating turbulent boundary layer using a rapidly scanning laser anemometer. *Journal of Fluid Mechanics*, 160:77–92.

Clauser, F. H. (1954). The turbulent boundary layer in adverse pressure gradient. *Journal of the aeronautical sciences*, 21:91–108.

Clauser, F. H. (1956). The turbulent boundary layer. *Adv Appl Mech*, 4:1–51.

Coles, D. (1956). The law of the wake in the turbulent boundary layer. *Journal of Fluid Mechanics*, 1:191–226.

Compton, D. and Johnston, J. (1992). Streamwise vortex production by pitched and skewed jets in a turbulent boundary layer. *AIAA paper*, 30:640–647.

Cuvier, C., Braud, C., Foucaut, J., and Stanislas, M. (2010). Flow characterisation and parametric study of passive and active vortex generators on the lml-avert ramp. Technical report, AVERT.

Cuvier, C., Braud, C., Foucaut, J.-M., and Stanislas, M. (2011a). Characterization of a separated turbulent boundary layer for flow control purpose. In *Seventh International Symposium on Turbulence and Shear Flow Phenomena, July 28 - 31, Ottawa, Canada.*

Cuvier, C., Braud, C., Foucaut, J.-M., and Stanislas, M. (2011b). Flow control over a ramp using active vortex generators. In *Seventh International Symposium on Turbulence and Shear Flow Phenomena, July 28 - 31, Ottawa, Canada.*

Dandois, J., Verbeke, C., Monnier, J. C., De-Coninck, J. L., Brunet, V., Braud, C., Stanislas, M., and Liddle, S. (2009). Onera l1 wind tunnel test result (ec project: Avert). Technical report, ONERA-LML.

DeGraaff, D. B. (1999). *Reynolds number scaling of the turbulent boundary layer on a flat plate and on swept and unswept bumps.* PhD thesis, Stanford university.

DeGraaff, D. B. and Eaton, J. K. (2000). Reynolds-number scaling of the flat-plate turbulent boundary layer. *Journal of Fluid Mechanics*, 422:319–346.

Dengel, P. and Fernholz, H. (1990). An experimental investigation of an incompressible turbulent boundary layer in the vicinity of separation. *Journal of Fluid Mechanics*, 212:615–636.

Dixit, S. A. and Ramesh, O. N. (2008). Pressure-gradient-dependent logarithmic laws in sink flow turbulent boundary layers. *Journal of Fluid Mechanics*, 615:445–475.

Dixit, S. A. and Ramesh, O. N. (2009). Determination of skin friction in strong pressure-gradient equilibrium and near-equilibrium turbulent boundary layers. *Experiment in Fluids*, 47:1045–1058.

Dixon, W. J. and Massey, F. J. (1957). *Introduction to statistical analysis.* MacGraw Hill.

Elsinga, G. E., Scarano, F., Wieneke, B., and Van-Oudheusden, B. W. (2006). Tomographic particle image velocimetry. *Exp. in Fluids*, 41:933–947.

Fernholz, H. H. and Finley, P. J. (1996). The incompressible zero-pressure-gradient turbulent boundary layer: An assessment of the data. *Prog. Aerospace Sci.*, 32:245–311.

Fernholz, H. H. and Warnack, D. (1998). The effects of a favourable pressure gradient and of the reynolds number on an incompressible axisymmetric turbulent boundary layer. part 1. the turbulent boundary layer. *Journal of Fluid Mechanics*, 359:329–356.

Foucaut, J., Milliat, B., Perenne, N., and Stanislas, M. (2003). Characterisation of different piv algorithm using the europiv synthetic image generator and real images from a turbulent boundary layer. In Springer, editor, *EUROPIV2 workshop, Zaragoza, Spain.*

Gad-El-Hak, M. (2000). *Flow Control : passive, active and reactive flow management.* Cambridge.

Gad-El-Hak, M. and Bandyopadhyay, P. R. (1994). Reynolds number effects in wall-bounded flows. *Appl. Mach. Rev.*, 47(8):307–365.

Gardarin (2009). *Contrôle par générateur de vortex d'un écoulement turbulent décollé.* PhD thesis, Ecole Polytechnique.

George, W. K. (2006). Recent advancements toward the understanding of turbulent boundary layers. *AIAA*, 44:2435–2449.

George, W. K. (2007). Is there a universal log law for turbulent wall-bounded flows? *Philosophical Transactions of the Royal Society London, Series A (Mathematical, Physical and Engineering Sciences)*, 365:789–806.

George, W. K. (2010). Lectures in turbulence for the 21st century. Department of Applied Mechanics, Chalmers University of Technology, Gothenburg, Sweden.

George, W. K. and Castillo, L. (1997). Zero-pressure-gradient turbulent boundary layer. *Appl. Mech. Rev.*, 50:689–729.

Godard, G., Foucaut, J., and Stanislas, M. (2006). Control of a decelerating boundary layer. part 2: Optimization of slotted jets vortex generators. *Aerospace Science and Technology*, 10(5):394–400.

Godard, G. and Stanislas, M. (2006a). Control of a decelerating boundary layer. part 1: Optimization of passive vortex generators. *Aerospace Science and Technology*, 10(3):181–191.

Godard, G. and Stanislas, M. (2006b). Control of a decelerating boundary layer. part 3: Optimization of round jets vortex generators. *Aerospace Science and Technology*, 10(6):455–464.

Goodman, J. W. (1968). *Introduction to Fourier optics*. Mc GrawHill.

Gopalan, S., Abraham, B. M., and Katz, J. (2004). The structure of a jet in cross flow at low velocity ratios. *Phys. Fluids*, 16(6):2067–2087.

Herpin, S., Wong, C. Y., Stanislas, M., and Soria, J. (2008). Stereoscopic piv measurements of a turbulent boundary layer with a large spatial dynamic range. *Exp Fluids*, 45:745–763.

Indinger, T., Buschmann, M. H., and Gad-El-Hak, M. (2006). Mean-velocity profile of a turbulent boundary layer approaching separation. *AIAA Journal*, 44(11):2465–2474.

Keane, R. D. and Adrian, R. J. (1992). Theory of cross-correlation analysis of piv images. *Applied Scientific Research*, 49:191–215.

Khan, Z. U. (1999). *On the dominant vortex created by a pitched and skewed jet in a cross-flow*. PhD thesis, Stanford university.

Khan, Z. U. and Johnston, J. P. (2000). On vortex generating jets. *International Journal of Heat and Fluid Flow*, 21:506–511.

Kim, H. T., Kline, S. J., and Reynolds, W. C. (1971). The production of turbulence near a smooth wall in a turbulent boundary layer. *Journal of Fluid Mechanics*, 50:133–160.

King, L. V. (1904). On the convection of heat from small cylinders in a stream of fluid: Determination of the convection constants of small platinum wires with applications to hot-wire anemometry. *Philosophical Transactions of the Royal Society of London. Series A*, 214:373–432.

Klewicki, J. C. and Falco, R. E. (1990). On accurately measuring statistics associated with small-scales structure in turbulent boundary layers using hot-wire probes. *Journal of Fluid Mechanics*, 219:119–142.

Kline, S. J., Reynolds, W. C., Schraub, F. A., and Runstadler, P. W. (1967). The structure of turbulent boundary layers. *Journal of Fluid Mechanics*, 30:741–773.

Kostas, J., Foucaut, J.-M., and Stanislas, M. (2005). Application of double spiv on the near wall turbulence structure of an adverse pressure gradient turbulent boundary layer. In *6th International Symposium on PIV, Pasadena, CA*.

Kostas, J., Foucaut, J.-M., and Stanislas, M. (2007). The flow structure produced by pulsed-jet vortex generators in a turbulent boundary layer in an adverse pressure gradient. *Flow Turbulence Combust*, 78:331–363.

Kostas, J., Foucaut, J.-M., and Stanislas, M. (2009). The effects of pulse frequency and duty cycle on the skin friction downstream of pulsed-jet vortex generators in an adverse pressure gradient turbulent boundary layer. *Aerospace Science and Technology*, 13:36–48.

Krogstad, P.-A. and Kaspersen, J. H. (2002). Structure inclination angle in a turbulent adverse pressure gradient boundary layer. *Journal of Fluids Engineering*, 124:1025–1033.

Krogstad, P.-A. and Skåre, P. E. (1995). Influence of a strong adverse pressure gradient on the turbulent structure in a boundary layer. *Phys. Of Fluids*, 7(8):2014–2024.

Lagraa, B., Labraga, L., and Mazouz, A. (2004). Characterization of low-speed streaks in the near-wall region of a turbulent boundary layer. *European Journal of Mechanics B/Fluids*, 23:587–599.

Lee, J. H. and Sung, H. J. (2009). Structures in turbulent boundary layers subjected to adverse pressure gradients. *Journal of Fluid Mechanics*, 639:101–131.

Lin, J. (2006). *Detailed study of the coherent structures of the buffer layer of wall turbulence using stereo particle image velocimetry.* PhD thesis, École Centrale de Lille.

Lin, J. C. (1999). Control of turbulent boundary layer separation using micro-vortex generators. *AIAA Paper*, (99-3404).

Lin, J. C. (2002). Review of research on low-profil vortex generators to control boundary layer separation. *Progress in Aerospace Sciences*, 38:389–420.

Lin, J. C., Howard, F. G., and Bushnell, D. M. (1990). Investigation of several passive and active methods for turbulent flow separation control, in: 21st fluid dynamics, plasma dynamics and lasers conference. *AIAA*, (paper 90-1598).

Lin, J. C., Selby, G. V., and Howard, F. G. (1991). Exploratory study of vortex-generating devices for turbulent flow separation control, in: 29th aerospace sciences meeting, january 7−10, reno, nevada. *AIAA*, (paper 91-0042).

Lögdberg, O. (2008). *Turbulent boundary layer separation and control.* PhD thesis, Royal Institute of Technology KTH Mechanics, Stockholm, Sweden.

Lögdberg, O., Angele, K., and Alfredsson, H. (2010). On the robustness of separation control by streamwise vortices. *European Journal of Mechanics B/Fluids*, 29:9–17.

Ludwieg, H. and Tillmann, W. (1949). Investigation of the wall shearing stress in turbulent boundary layer. Technical Report 1285, NACA.

Maciel, Y., Rossignol, K. S., and Lemay, J. (2006). Self-similarity in the outer region of adverse pressure gradient boundary layers. *AIAA paper*, 44:2450–2464.

Magill, J., Bachmann, M., Rixon, G., and McManus, K. (2001). Dynamic stall control using a model-based observer. *39th AIAA Aerospace Sciences Meeting and Exhibit, 8-11 January, Reno, Nevada*, (0251).

Marquillie, M., Laval, J.-P., and Dolganov, R. (2008). Direct numerical simulation of a separated channel flow with a smooth profile. *Journal of Turbulence*, 9.

McManus, K. R., Joshi, P. B., Legner, H. H., and Davis, S. J. (1994). Active control of aerodynamic stall using pulsed jet actuators. *AIAA paper*, 94:2218.

Mellor, G. L. and Gibson, D. M. (1966). Equilibrium turbulent boundary layers. *Journal of Fluid Mechanics*, 24:225–253.

Meroney, R. N. and Bradshaw, P. (1975). Turbulent boundary-layer growth over a longitudinally curved surface. *AIAA Journal*, 13(11):1448–1453.

Milanovic, I. V. and Zaman, K. B. M. Q. (2004). Fluid dynamics of highly pitched and yawed jets in cross-flow. *AIAA Journal*, 42(5):874–882.

Milanovic, I. V. and Zaman, K. B. M. Q. (2005). Synthetic jets in crossflow. *AIAA Journal*, 43(5):929–940.

Millikan, C. B. (1938). A critical discussion of turbulent flows in channels and circular tubes. In *In Proc. 5th Intl Congress for App. Mech.*, pages 386–392.

Nagabushana, K. A., Agarwal, N. K., and Simpson, R. L. (1988). Features of separating turbulent boundary layers. In *AIAA, Aerospace Sciences Meeting, 26th, Reno, NV, Jan. 11-14.*

Nagano, Y., Tsuji, T., and Houra, T. (1998). Structure of turbulent boundary layer subjected to adverse pressure gradient. *International Journal of Heat and Fluid Flow*, 19:563–572.

Neuilly, M. and Cetama (1998). *Modélisation et estimation des erreurs de mesure.* 2 edition.

Nickels, T. B. (2004). Inner scaling for wall-bounded flows subject to large pressure gradients. *Journal of Fluid Mechanics*, 521:217–239.

Pailhas, G., Barricau, P., Touvet, Y., and Perret, L. (2009). Friction measurement in zero and adverse pressure gradient boundary layer using oil droplet interferometric method. *Experiment in Fluids*, 47:195–207.

Patel, V. C. (1969). The effects of curvature on the turbulent boundary layer. Technical Report R&M 3599, Aeronautical Research Council London.

Patel, V. C. and Sotiropoulos, F. (1997). Longitudinal curvature effects in turbulent boundary layers. *Prog. In Aerospace Sci.*, 33:1–71.

Perry, A. E. and Schofield, W. H. (1973). Mean velocity and shear stress distributions in turbulent boundary layers. *Physics of Fluids*, 16:2068–2074.

Prandtl, L. (1904). Über flüssigkeitsbewegung bei sehr kleiner reibung. In *Third Intern. Math Congress, Heidelberg*, pages 484–491.

Prandtl, L. (1926). Über die ausgebildete turbulenz. In *Second International Congress of Applied Mechanics, Zürich, 12-17 September*, pages 62–75.

Prandtl, L. (1932). Zur turbulenten strömung in rohren und längs platten. In *Ergeb. Aerod. Versuch Göttingen, IV Lieferung, 4.*

Raffel, M., Willert, C., and Kompenhans, J. (1998). *Particle Image Velocimetry, A practical guide.* Springer Verlag.

Robinson, S. K. (1991). Coherent motions in the turbulent boundary layer. *Annu. Rev. Fluid Mech.*, 23:601–639.

Schoppa, W. and Hussain, F. (2000). Coherent structure dynamics in near-wall turbulence. *Fluid Dynamics Research*, 26:119–139.

Selby, G. V., Lin, J. C., and Howard, F. G. (1992). Control of low-speed turbulent separated flow using jet vortex generators. *Experiments in Fluids*, 12:394–400.

Shaqarin, T. (2011). *Closed-loop active control to reattach a thick turbulent boundary layer.* PhD thesis, University of Lille 1.

Shaqarin, T., Braud, C., Coudert, S., and Stanislas, M. (2011). Open and closed-loop experiments to reattach a thick turbulent boundary layer. In *Seven international symposium on turbulence and shear flow phenomena, July 28-31, Ottawa Canada.*

Simpson, R. L. (1983). A model for the backflow mean velocity profile. *AIAA Journal*, 21:142–143.

Simpson, R. L. (1989). Turbulent boundary layer separation. *Ann. Rev. Fluid Mech.*, 21:205–234.

Simpson, R. L. (1996). Aspects of turbulent boundary layer separation. *Prog. Aerospace Sci.*, 32:457–521.

Simpson, R. L. and Shivaprasad, B. G. (1983). The structure of a separating turbulent boundary layer. part 5. frequency effects on periodic unsteady free-stream flows. *Journal of Fluid Mechanics*, 131:319–339.

Skote, M. (2001). *Studies of turbulent boundary layer flow through direct numerical simulation.* PhD thesis, Royal Institute of Technology, Stockholm, Sweden.

Skote, M. and Henningson, D. S. (2002). Direct numerical simulation of separating turbulent boundary layers. *Journal of Fluid Mechanics*, 471:107–136.

Smith, F. T. (1994). Theoretical prediction and design for vortex generators in turbulent boundary layers. *Journal of Fluid Mechanics*, 270:91–131.

Song, S. and Eaton, J. K. (2004). Flow structures of a separating, reattaching, and recovering boundary layer for a large range of reynolds number. *Experiments in Fluids*, 36:642–653.

Spalart, P. R. (1986). Numerical study of sink flow boundary layers. *Journal of Fluid Mechanics*, 172:307–328.

Standborn, V. A. and Kline, S. J. (1961). Flow models in boundary-layer stall inception. *J. Basic Eng.*, 83:317–327.

Stanislas, M., Perret, L., and Foucaut, J.-M. (2008). Vortical structures in the turbulent boundary layer: a possible route to a universal representation. *Journal of Fluid Mechanics*, 602:327–382.

Österlund, J. M. (2000). *Experimental studies of zero-pressure gradient turbulent boundary-layer flow*. PhD thesis, KTH, Stockholm, Sweden.

Tani, I. (1962). Production of longitudinal vortices in the boundary layer along a concave wall. *J. Geophys Res.*, 67:3075–3080.

Taylor, H. D. (1947). The elimination of diffuser separation by vortex generators. Technical Report No. R-4012-3, United Aircraft Corporation.

Tilmann, C. P., Langan, K. L., Betterton, J. G., and Wilson, M. J. (2000). Characterization of pulsed vortex generator jets for active flow control. In *RTO AVT Symposium on "Active Control Technology" for Enhanced Performance Operational Capabilities of Military Aircraft, Land Vehicles and Sea Vehicles*, Germany.

Tilmann, K. P. (2001). Enhancement of transonic airfoil performance using pulsed jets for separation control. In *Aerospace Sciences Meeting and Exhibit, 39th, Reno, NV, Jan. 8-11.*

Townsend, A. A. (1956). The properties of equilibrium boundary layers. *Journal of Fluid Mechanics*, 1:561–573.

Townsend, A. A. (1961). Equilibrium layers and wall turbulence. *Journal of Fluid Mechanics*, 12:97–120.

Townsend, A. A. (1976). The structure of turbulent shear flow. *Cambridge Univ. Press.*

Tulapurkara, E. G., Khoshnevis, A. B., and Narasimhan, J. L. (2001). Wake-boundary layer interaction subjected to convex and concave curvatures and adverse pressure gradient. *Experiments in Fluids*, 31:697–707.

Van-Driest, E. R. (1956). On turbulent flow near a wall. *J. Aerosp. Sci*, 23:1007–1012.

Von-Kármán, T. (1930). Mechanische Ähnlichkeit und turbulenz. In *Nachr. Ges. Wiss. Math-Phys Klasse Göttingen 5*, pages 58–76.

Wallace, J. M., Eckelmann, H., and Brodkey, R. S. (1972). The wall region in turbulent shear flow. *Journal of Fluid Mechanics*, 54:39–48.

Webster, D. R., DeGraaff, D. B., and Eaton, J. K. (1996). Turbulence characteristics of a boundary layer on a two-dimensional bump. *Journal of Fluid Mechanics*, 320:53–69.

Wu, X. and Squires, K. D. (1998). Numerical investigation of the turbulent boundary layer over a bump. *Journal of Fluid Mechanics*, 362:229–271.

Zagorala, M. V. and Smits, A. (1998a). Mean flow scaling of turbulent pipe flow. *Journal of Fluid Mechanics*, 373:33–79.

Zagorala, M. V. and Smits, A. J. (1998b). A new mean velocity scaling for turbulent boundary layers. *ASME Fluids Engineering Division Summer Meeting June 21-25, Washington DC*, FEDSM98-4950.

Zaman, K. B. M. Q. and Foss, J. K. (1997). The effect of vortex generators on a jet in a cross-flow. *Phys. Fluids*, 9(1):106–114.

Zhou, H. and Lu, L. (1997). Effect of pressure gradient on coherent structures in a turbulent boundary layer. *Science in China*, 40(4):441–448.

Zhou, J., Adrian, R. J., and Balachandar, S. (1996). Autogeneration of near-wall vortical structures in channel flow. *Phys. Fluids*, 8:288–290.

Appendices

Appendix A

Uncertainty estimation due to King's law calibration fit

The least square fit calibration uncertainty on the King's law is estimated by the method developed by Neuilly and Cetama (1998). For that, the King's law is written as : $E^2 = E_0^2 + bU^n = f(U, E_0, b, n) = f(U, a_1, a_2, a_3)$. Each point used for the calibration is noted : (E_i^2,U_i) and their standard deviation : ($\sigma_{E_i^2}$,σ_{U_i}). To determine the optimum parameters E_0, b and n, the least square fit method used was the Deming's method. To begin the Deming's method, the initial parameters were chosen to $E_{0_0} = a_{1_0} = 1.6$, $b_0 = a_{2_0} = 1.3$ and $n_0 = a_{3_0} = 0.5$. After that, the weight for each point was computed as : $\frac{K}{g_i} = \frac{\sigma_{E_i^2}^2}{n_i} + [\frac{\partial f}{\partial U}(U_i, E_{0_0}, b_0, n_0).\sigma_{U_i}]^2$, with n_i the number of values obtained for E_i^2, and K an arbitrary constant to obtain a weight of order 1, so that all the numbers in the iterative procedure are not too big or too small (in this case, K was chosen at 10). The advantage of considering a weight that is not 1 for all the points, is that it takes into account the uncertainty on E^2 in the residue. Then the matrix W and the vector V were computed as followed : W = $(W_{jj'})$=$(\sum_i g_i.\frac{\partial f}{\partial a_j}(U_i, E_{0_0}, b_0, n_0).\frac{\partial f}{\partial a_{j'}}(U_i, E_{0_0}, b_0, n_0))$ and V = (V_j) = $(\sum_i g_i.(E_i^2 - f(U_i, E_{0_0}, b_0, n_0)).\frac{\partial f}{\partial a_j}(U_i, E_{0_0}, b_0, n_0))$. The new parameters E_{0_1}, b_1 and n_1 were obtained by solving : $W.(A_1 - A_0) = V$, with $A_1 = (A_{1_j}) = (a_{j_1})$ and $A_0 = (A_{0_j}) = (a_{j_0})$. Then the residue $Q = \sum_i g_i.[E_i^2 - f(U_i, a_{1_0}, a_{2_0}, a_{3_0})]^2$ was computed. To obtain the final optimum parameters of the King's law, this procedure was repeated with $A_0 = A_1$ as initial parameter until the convergence on Q and A_1 was reached.

When the convergence is reached, the fit uncertainty on U can be estimated. Indeed, the variance $s_{E_i^2}^2$ corresponding to the uncertainty of calibration on E_i^2 is calculated as : $s_{E_i^2}^2 = \frac{Q}{(N-3).Det(W)}.\sum_j \sum_{j'} B_{jj'} \frac{\partial f}{\partial a_j}(U_i, E_0, b, n).\frac{\partial f}{\partial a_{j'}}(U_i, E_0, b, n)$, with N the number of point used for the calibration ($N - 3$ correspond to the number of degree of freedom), and $B_{jj'}$ the cofactors of W. The corresponding variance $s_{U_i}^2$ corresponding to the uncertainty of calibration on U_i is calculated as : $s_{U_i}^2 = \frac{s_{E_i}^2}{\frac{\partial f}{\partial U}(U_i, E_0, b, n)}$. Finally, the calibration fit uncertainty on U is $\pm 2.s_{U_i}$.

Appendix B

PIV accuracy results

1 Introduction

Based on the method presented in Section 5.2.4.1 of Chapter 2, the different PIV uncertainties have been computed for the uncontrolled and the three control cases selected in each merging region. In the following figures the uncertainties are plotted in percentage of the reference velocity $U_\infty = 10\ m/s$. The flow separation border (if it exists) is also represented in these figures.

2 PIV accuracy for the uncontrolled flow

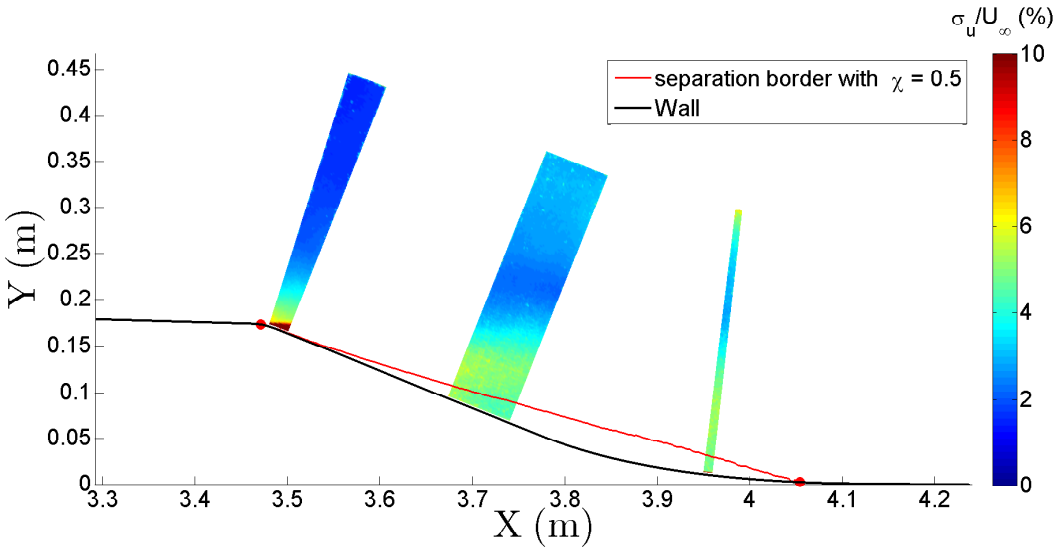

Figure B.1: Random PIV uncertainty on the streamwise velocity without control.

Figure B.1 shows the random part of the uncertainty on the streamwise velocity component scaled with U_∞. In the external region, this uncertainty is ±2% (±0.11 px) near $X = 3.5$ m and increases with X to reach ±4% (±0.23 px) near

$X = 3.95$ m. This uncertainty is higher than the 0.06 px obtained by Foucaut et al. (2003). This was predictable as the particle image diameter is below the optimum one, the mean velocity gradient is not negligible and the out of plane motion also. However it remains acceptable. Due to stronger turbulence intensities which induce stronger out of plane motion and to stronger mean velocity gradient, near the wall and near the separation border, the uncertainty increases but remains under $\pm 5\%$ (or $\pm 0.28\, px$) (excepts very near the flap articulation where it can reach $\pm 10\%$, probably due to a combination of the laser reflection and strong mean velocity gradient which increases the errors).

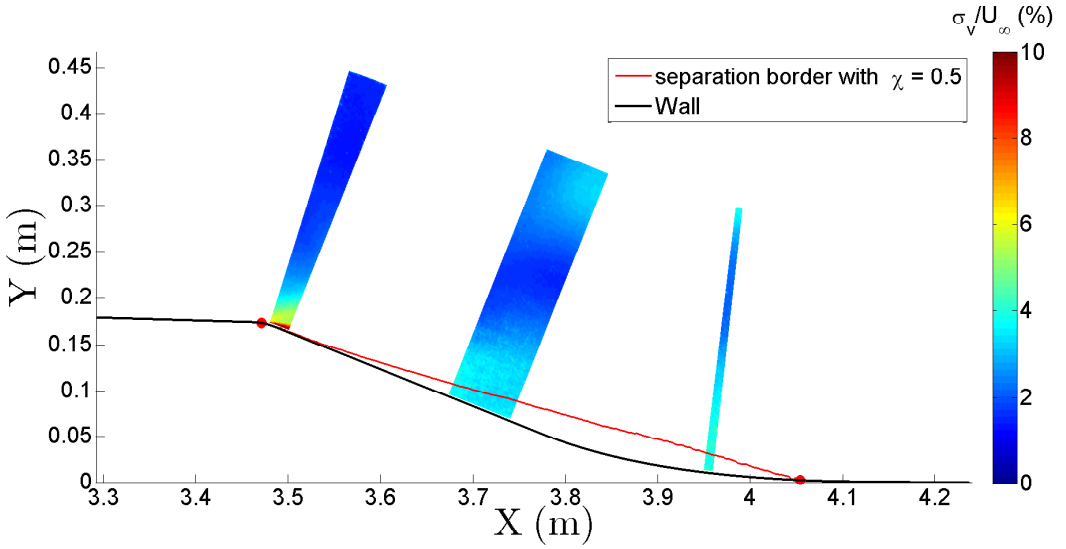

Figure B.2: Random PIV uncertainty on the wall-normal velocity without control.

Figure B.2 shows the random part of the uncertainty on the wall-normal velocity component scaled by U_∞. It is quite similar to the one on the streamwise component. This is not surprising as the two directions of the cameras used are identical.

The uncertainty on the mean streamwise velocity U, relative to U_∞ (Figure B.3) is around $\pm 1\%$ in most part of the field. In the near wall region, it is about $\pm 4\%$, due to the mean velocity gradient which decreases the PIV accuracy. Near $X = 3.5$ m, in the top field, the uncertainty is about $\pm 2\%$, probably due to possible worse laser sheets superposition in this region or to optical distortions that where not corrected (in the image mapping process, the projection errors near the image borders can reach 3 px, which was supposed small enough to be neglected for a 2D2C PIV analysis).

The uncertainty on the mean wall-normal velocity V, relative to U_∞ (Figure B.4) is very similar to the one on U. However, the region of higher uncertainty at the top of the field is larger than for U. Maybe this velocity component is more affected by the optical distortions or by the possible worse laser sheets superposition.

Figure B.5 gives the uncertainty on the turbulence intensity $\sqrt{\overline{u'^2}}$ relative to U_∞. Very similar results are obtained for $\sqrt{\overline{v'^2}}$. The uncertainty remains under 0.8%,

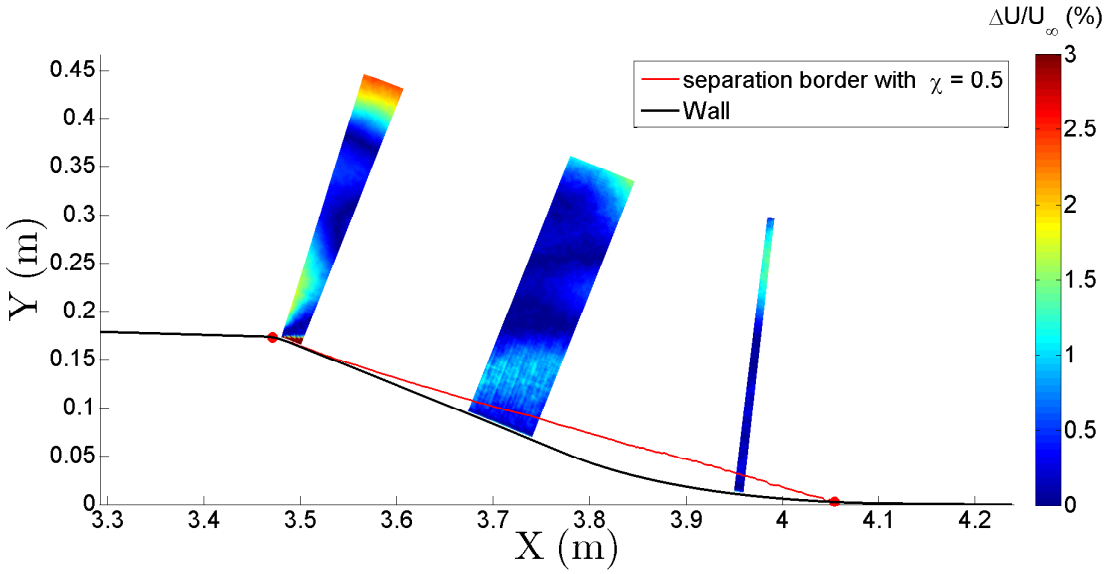

Figure B.3: PIV uncertainty on the mean streamwise velocity component (U) without control.

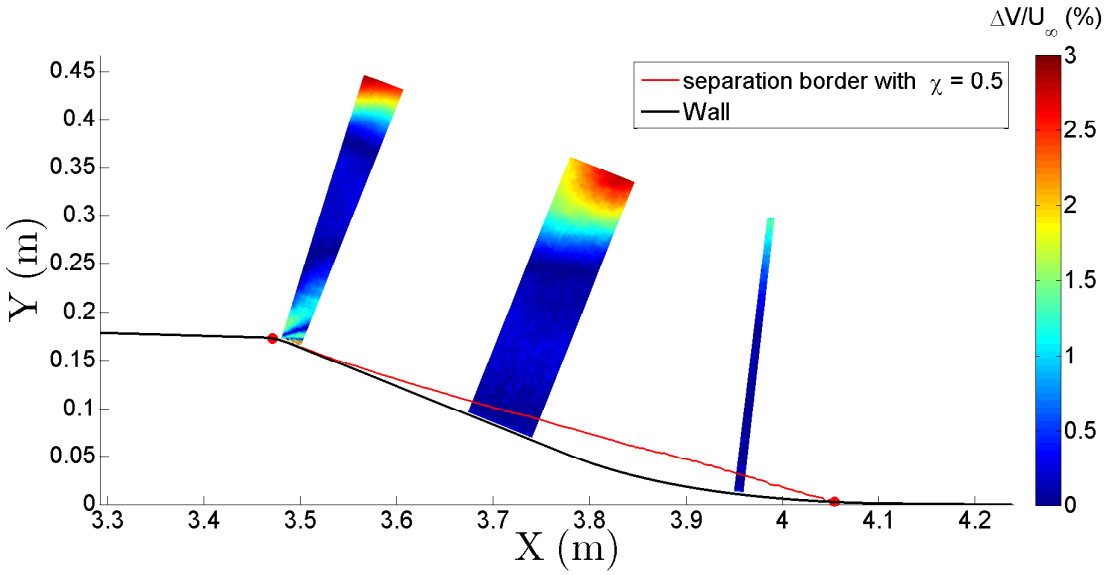

Figure B.4: PIV uncertainty on the mean wall-normal velocity component (V) without control.

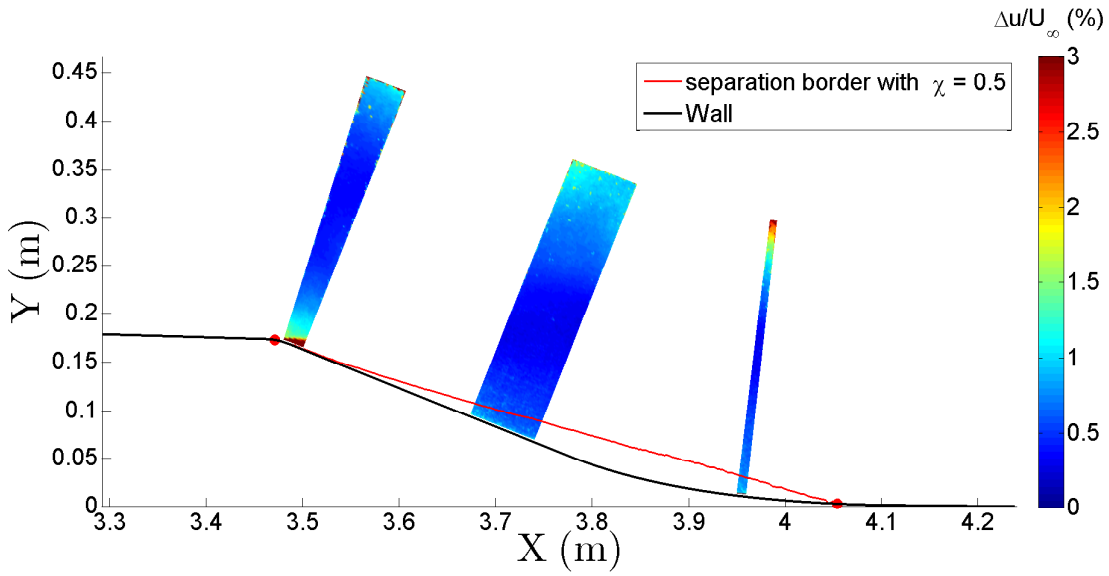

Figure B.5: PIV uncertainty on the turbulence intensity ($u = \sqrt{\overline{u'^2}}$) without control.

excepts near the wall and the top field where it can reach ±3%, probably due to the higher uncertainty on the mean velocity in these regions.

3 PIV accuracy for the controlled flow

The same PIV set-up was used on active control experiments, two configurations with counter-rotating VGs (one in upstream blowing and one in downstream blowing configuration) and one with co-rotating VGs (upstream blowing configuration). Figure B.6 shows the random part of the uncertainty on the streamwise velocity component with upstream blowing counter-rotating jets. Similar result are obtained for the wall-normal component. However, as for the uncontrolled case, the uncertainty on v is slightly better than on u. For u, it is ±2.5% (±0.13 px) near $X = 3.5$ m, and increases with X to reach ±9% (±0.51 px) near $X = 3.95$ m. In the wall region, the uncertainty is higher of about ±15% (±0.85 px) due to the strong mean velocity gradient and maybe also to a strong out of plane motion introduced by the control. The random PIV uncertainty is then higher than for the uncontrolled case. This seems principally due to the out of plane motion introduced by the control, and especially on the flap.

Figure B.7 shows the same results as in Figure B.6 for upstream blowing counter-rotating jets. The two results are almost identical, excepts for $X \geq 3.7$ m where it is 1% lower in Figure B.7. The uncertainty is also deteriorated by this control case but less than for the co-rotating case. This may be due to a weaker out of plane motion for the counter-rotating case.

Figures B.8 shows the results for the downstream blowing counter-rotating jets. Near $X = 3.5$ m, the uncertainty is comparable to the two other configurations. After the articulation, the uncertainty is about two times lower than for the two

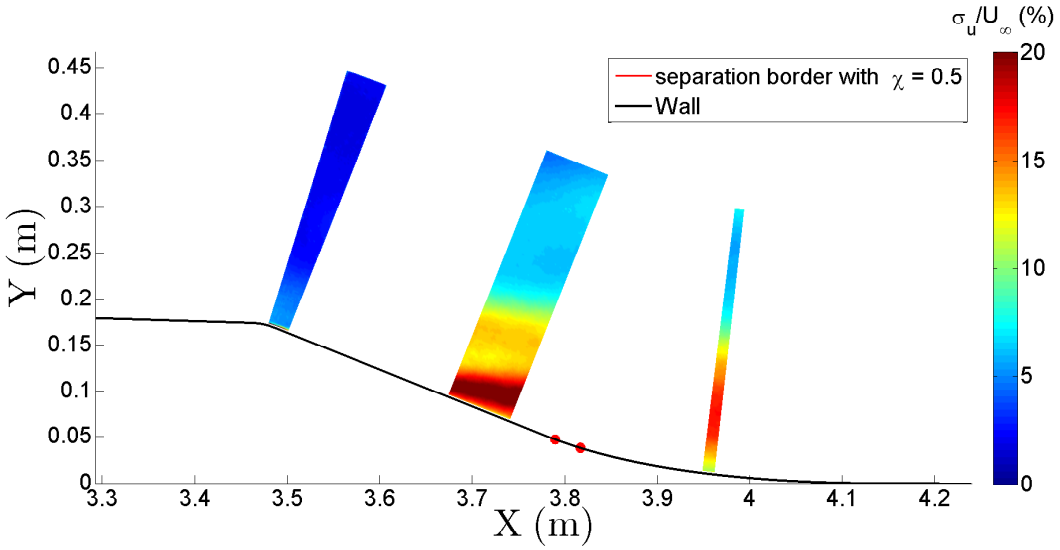

Figure B.6: Random PIV uncertainty on the streamwise velocity with upstream blowing co-rotating jets.

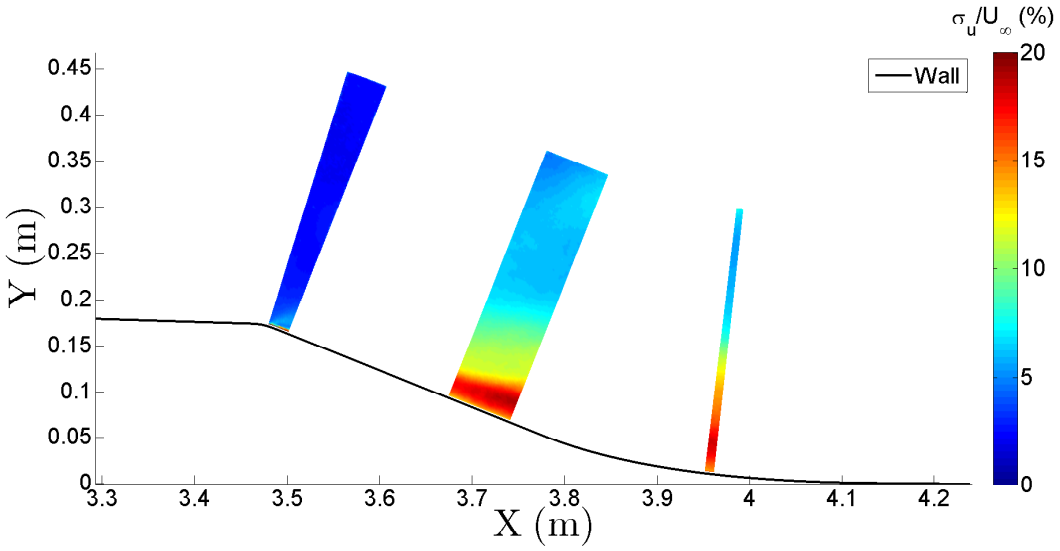

Figure B.7: Random PIV uncertainty on the streamwise velocity with upstream blowing counter-rotating jets.

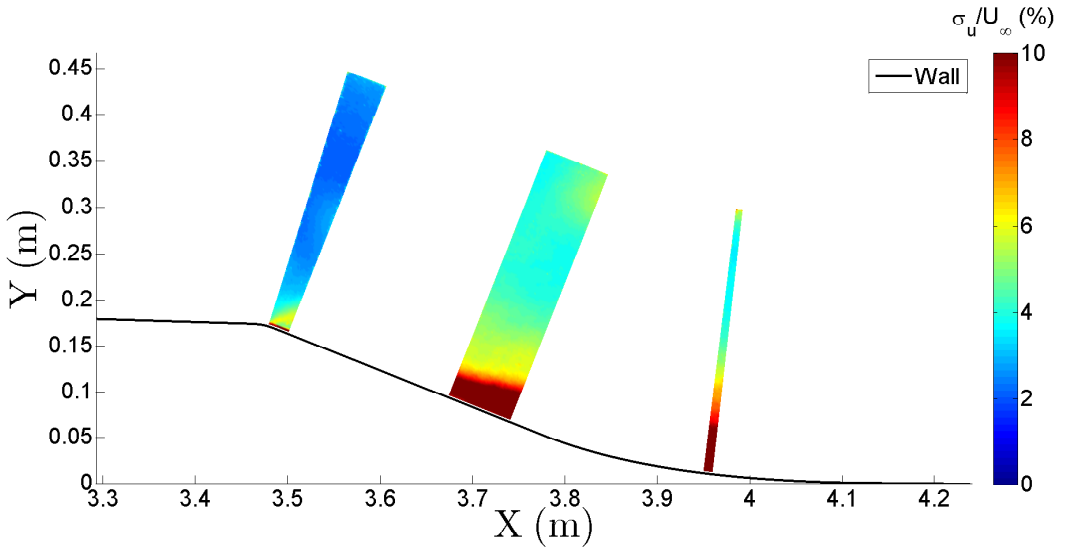

Figure B.8: Random PIV uncertainty on the streamwise velocity with downstream blowing counter-rotating jets.

other control cases. It is about 4.5% for $X \geq 3.7$ m (or 0.25 px) in the external region. This is just slightly above the value obtained for the uncontrolled case. This control case probably a negligible out of plane motion compared to the two other control cases. This is coherent with the lower vortex strength in this experiment as the VR is 2.5 and for the two other control cases it is 3.5 (see Chapter 5 and 6 for the choice of VR).

The uncertainty on the mean wall-normal velocity relative to U_∞ for these three control cases was found very similar to the one for the uncontrolled case. Figure B.9 shows the uncertainty on the mean streamwise velocity relative to U_∞ with upstream blowing co-rotating jets. This uncertainty is about $\pm 1.5\%$, except near the wall (where it is of the order of $\pm 4\%$ due to the mean velocity gradient) and in the external region (where it is below $\pm 2\%$ due to the out of plane motion).

Figure B.10 shows the uncertainty on the mean streamwise velocity relative to U_∞ for upstream blowing counter-rotating jets. Compared to the co-rotating configuration (Figure B.9), lower uncertainty is obtained near the wall. However, slightly higher uncertainty is found in the external region.

Figure B.11 shows the uncertainty on the mean streamwise velocity relative to U_∞ for downstream blowing counter-rotating jets. The result is very close as for the upstream blowing counter-rotating configuration (Figure B.10).

Figure B.12 shows the uncertainty on the turbulence intensity relative to U_∞ for the downstream blowing counter-rotating configuration. The uncertainty obtained on the wall-normal turbulence intensity was similar but slightly lower. For the three control cases studied, the uncertainty on this two quantities was found also very close. Near the wall and near the top field, the uncertainty is below $\pm 4\%$. Between these two regions, it is lower of about $\pm 2\%$ (and below $\pm 1\%$ near $X = 3.5$ m).

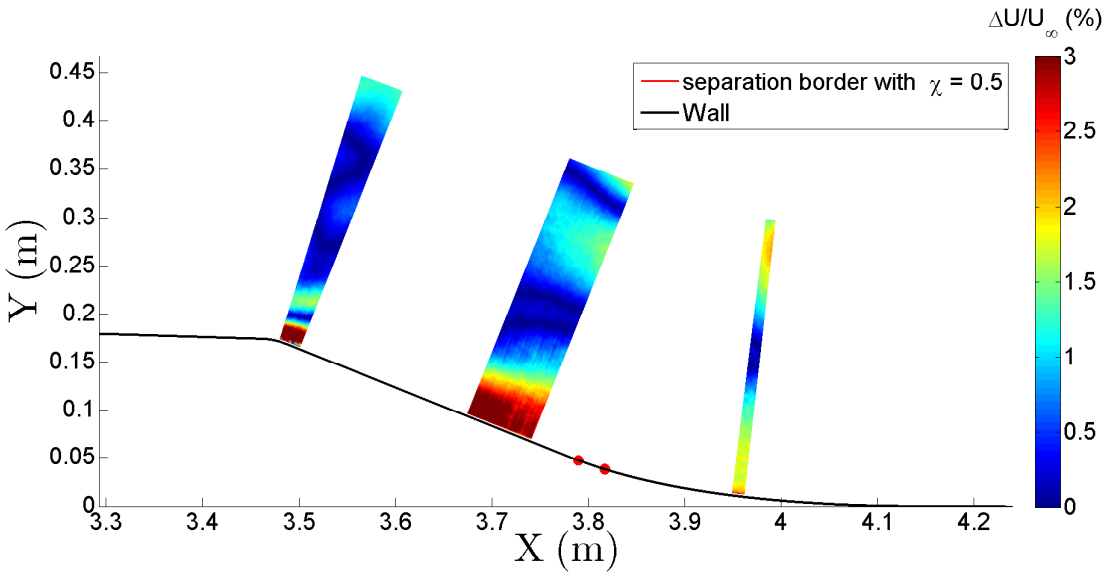

Figure B.9: PIV uncertainty on the mean streamwise velocity with upstream blowing co-rotating jets.

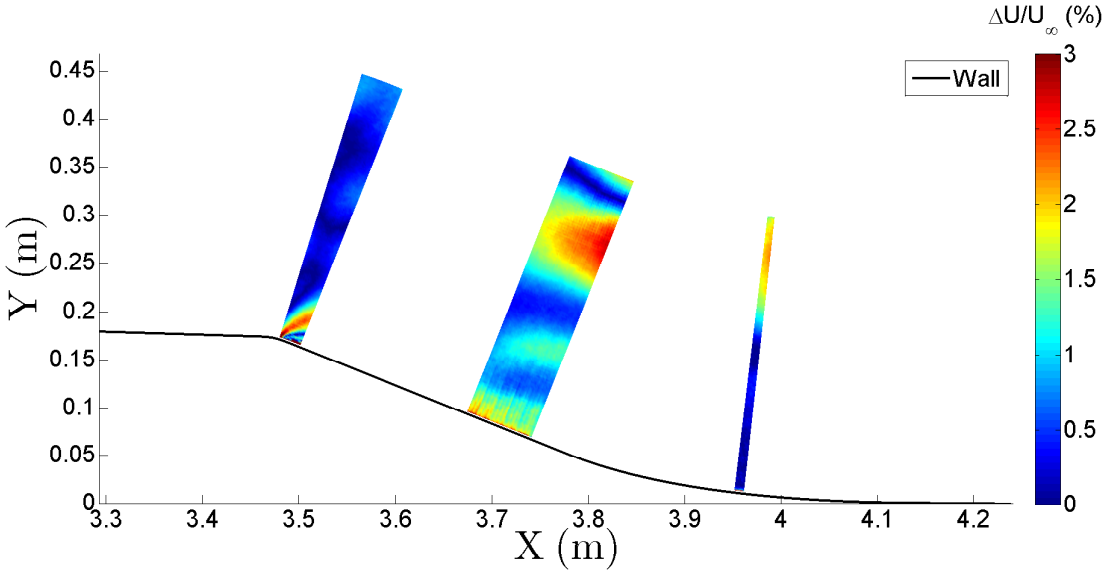

Figure B.10: PIV uncertainty on the mean streamwise velocity with upstream blowing counter-rotating jets.

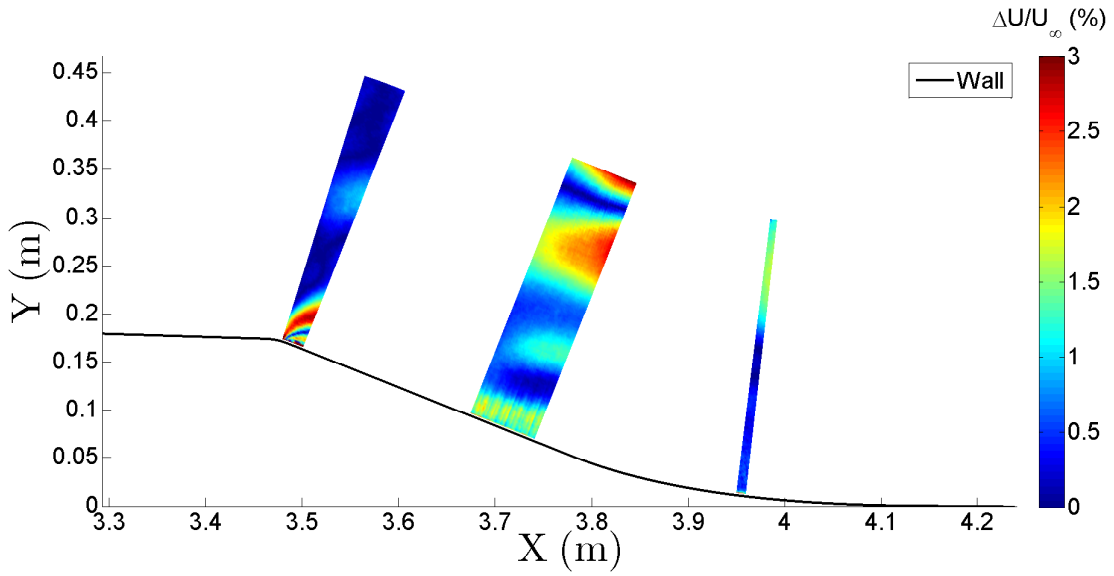

Figure B.11: PIV uncertainty on the mean streamwise velocity with downstream blowing counter-rotating jets.

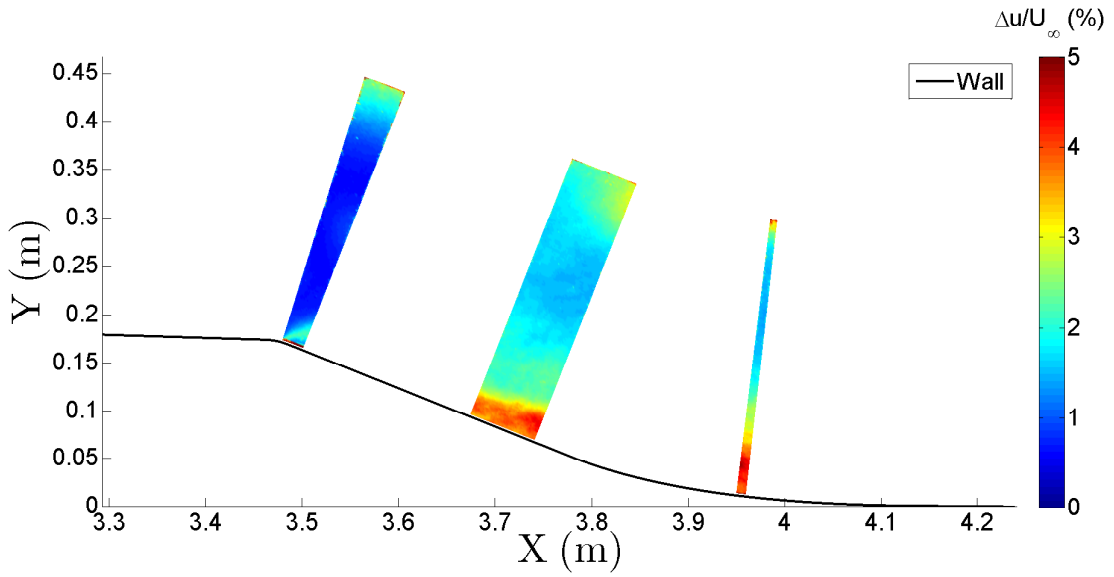

Figure B.12: PIV uncertainty on the turbulence intensity ($u = \sqrt{\overline{u'^2}}$) with downstream blowing counter-rotating jets.

Appendix C

Transport equations for the Reynolds stresses and the turbulent kinetic energy

The transport equation for the Reynolds stress $\overline{u_i' u_j'}$ is given in equation (C.1) (with $\tau_{ij}' = \mu \left(\frac{\partial u_i'}{\partial x_j} + \frac{\partial u_j'}{\partial x_i} \right)$) :

$$\begin{aligned} \underbrace{\rho \frac{\partial \overline{u_i' u_j'}}{\partial t}}_{1} + \underbrace{\rho U_k \frac{\partial \overline{u_i' u_j'}}{\partial x_k}}_{2} = & \underbrace{- \rho \overline{u_i' u_k'} \frac{\partial U_j}{\partial x_k} - \rho \overline{u_j' u_k'} \frac{\partial U_i}{\partial x_k}}_{3} + \underbrace{\frac{\partial (\overline{u_i' \tau_{jk}'} + \overline{u_j' \tau_{ik}'})}{\partial x_k}}_{4} \\ & \underbrace{- \frac{\partial (\overline{u_i' p'} \delta_{jk} + \overline{u_j' p'} \delta_{ik})}{\partial x_k}}_{5} - \underbrace{\rho \frac{\partial \overline{u_i' u_j' u_k'}}{\partial x_k}}_{6} \\ & \underbrace{+ \overline{p' \frac{\partial u_i'}{\partial x_j}} + \overline{p' \frac{\partial u_j'}{\partial x_i}}}_{7} \underbrace{- \overline{\tau_{ik}' \frac{\partial u_j'}{\partial x_k}} - \overline{\tau_{jk}' \frac{\partial u_i'}{\partial x_k}}}_{8} \end{aligned} \tag{C.1}$$

The term number 1 corresponds to the unsteady one, 2 to the convection by the mean flow, 3 to the production, 4 to the viscous diffusion, 5 to the diffusion by pressure fluctuations, 6 to the diffusion by velocity fluctuations, 7 to the redistribution (i.e. for returning to isotropy) and 8 to the viscous dissipation. When contracting this equation (i.e. by taking j = i), the transport equation for the turbulent kinetic energy ($k = \frac{1}{2} \overline{u_i' u_i'}$) is obtained (the terms signification is the same as in equation (C.1)) :

$$\underbrace{\rho \frac{\partial \overline{k}}{\partial t}}_{1} + \underbrace{\rho U_k \frac{\partial \overline{k}}{\partial x_k}}_{2} = \underbrace{- \rho \overline{u_i' u_k'} \frac{\partial U_i}{\partial x_k}}_{3} + \underbrace{\frac{\partial \overline{u_i' \tau_{ik}'}}{\partial x_k}}_{4} \underbrace{- \frac{\partial \overline{u_k' p'}}{\partial x_k}}_{5} \underbrace{- \frac{1}{2} \rho \frac{\partial \overline{u_i' u_i' u_k'}}{\partial x_k}}_{6} \underbrace{- \overline{\tau_{ik}' \frac{\partial u_i'}{\partial x_k}}}_{8} \tag{C.2}$$

For a stationary 2D flow in the plane (x_1, x_2), the term 1 in these equations is

zero, the mean velocity along x_3 (U_3) is zero and the derivatives along x_3 are also null. The production terms for the Reynolds stress $\overline{u_i' u_j'}$ are then :

$$- \overline{u_i' u_1'} \frac{\partial U_j}{\partial x_1} - \overline{u_i' u_2'} \frac{\partial U_j}{\partial x_2} - \overline{u_j' u_1'} \frac{\partial U_i}{\partial x_1} - \overline{u_j' u_2'} \frac{\partial U_i}{\partial x_2} \tag{C.3}$$

and for the turbulent kinetic energy :

$$- \overline{u_1' u_1'} \frac{\partial U_1}{\partial x_1} - \overline{u_1' u_2'} \frac{\partial U_1}{\partial x_2} - \overline{u_1' u_2'} \frac{\partial U_2}{\partial x_1} - \overline{u_2' u_2'} \frac{\partial U_2}{\partial x_2} \tag{C.4}$$

Appendix D

Turbulent quantity distributions of the separated flow in the global wind-tunnel reference frame

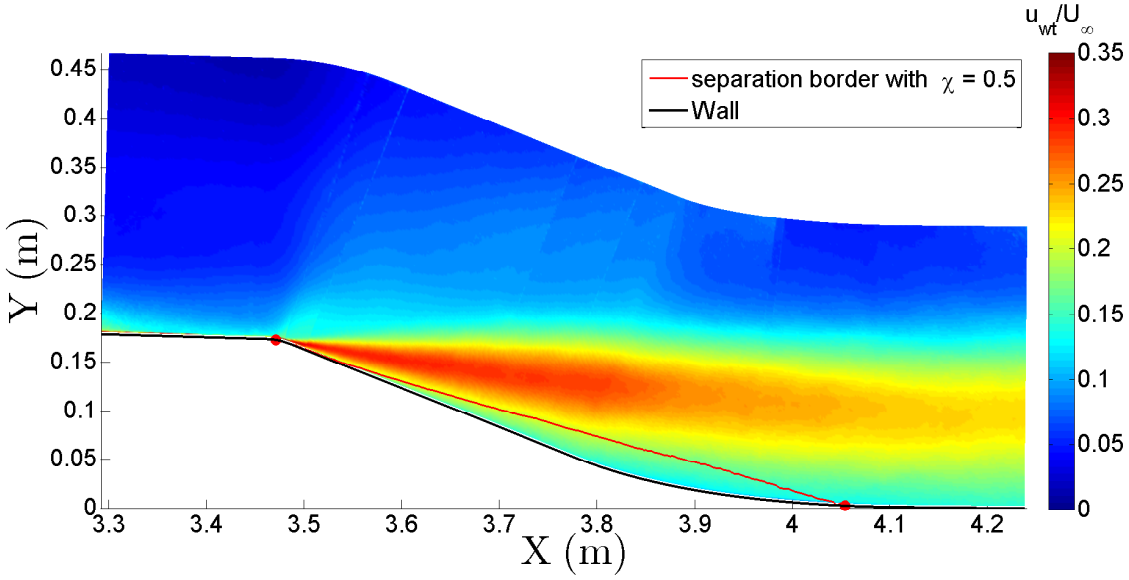

Figure D.1: Streamwise turbulence intensity field ($u_{wt} = \sqrt{\overline{u'^2_{wt}}}$) on the flap at mid-span of the ramp.

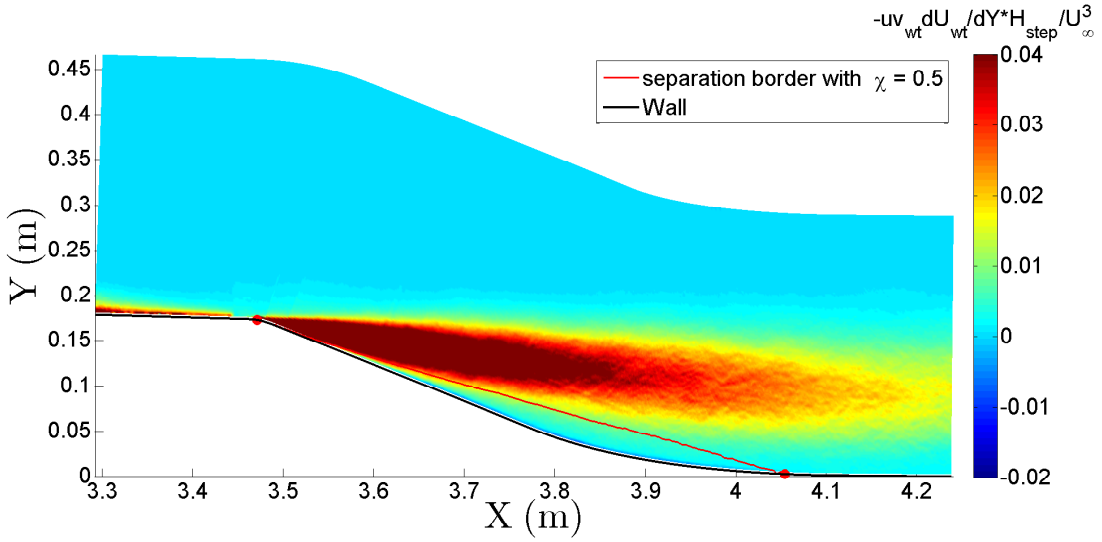

Figure D.2: Production term $-\overline{u'_{wt}v'_{wt}}\frac{\partial U_{wt}}{\partial Y}$ of $\frac{1}{2}\overline{u'^2_{wt}}$ on the flap at mid-span of the ramp.

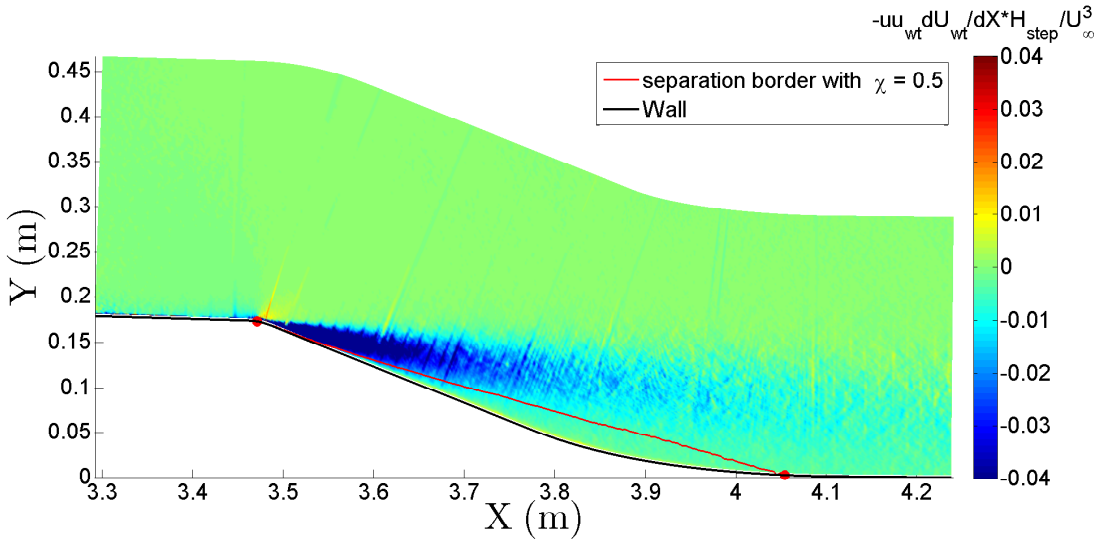

Figure D.3: Production term $-\overline{u'^2_{wt}}\frac{\partial U_{wt}}{\partial X}$ of $\frac{1}{2}\overline{u'^2_{wt}}$ on the flap at mid-span of the ramp.

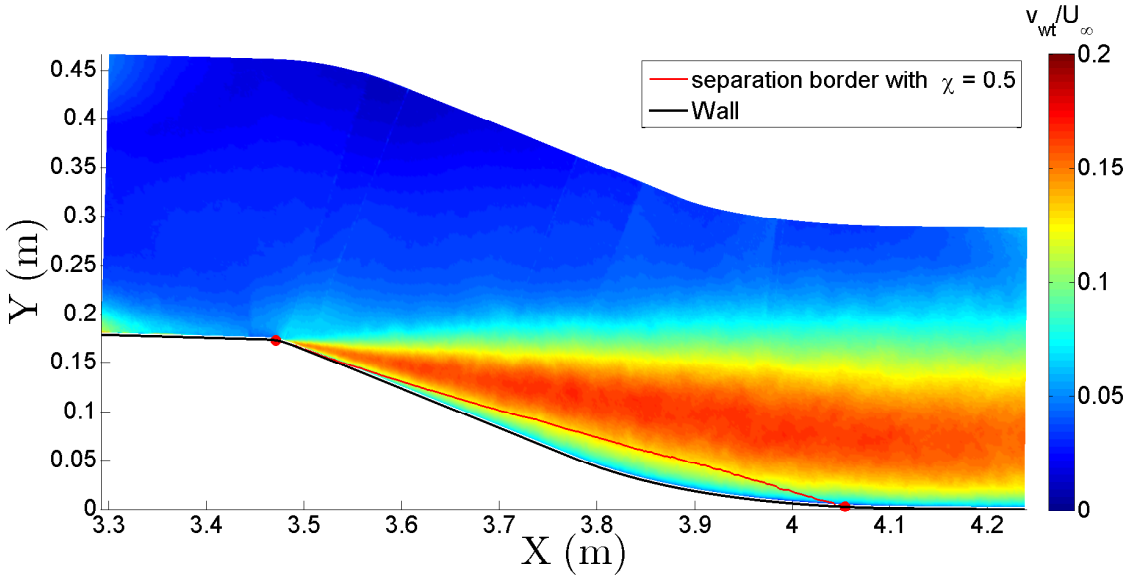

Figure D.4: Wall-normal turbulence intensity field ($v_{wt} = \sqrt{\overline{v_{wt}'^2}}$) on the flap at mid-span of the ramp.

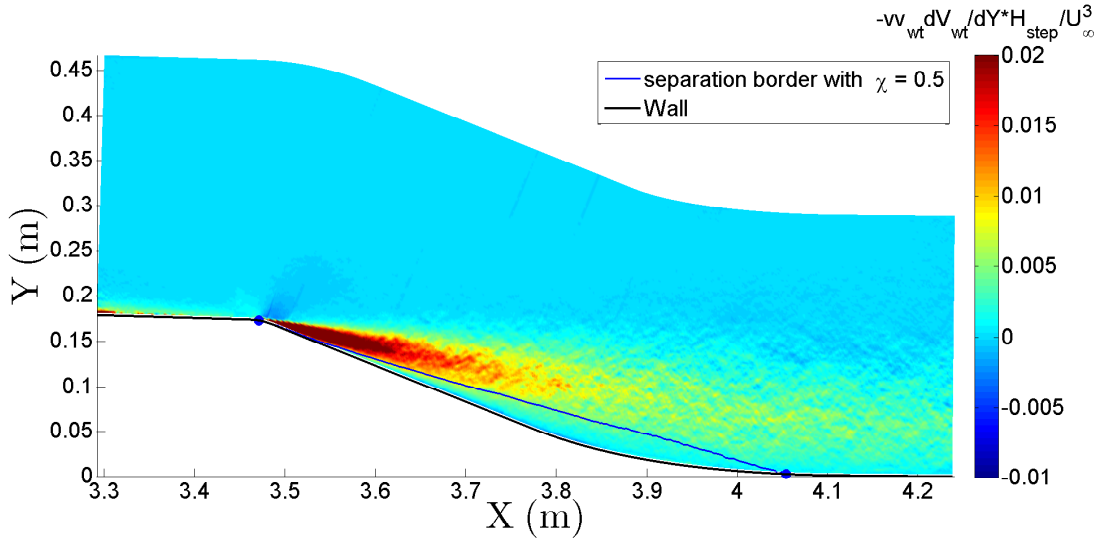

Figure D.5: Production term $-\overline{v_{wt}'^2}\frac{\partial V_{wt}}{\partial Y}$ of $\frac{1}{2}\overline{v_{wt}'^2}$ on the flap at mid-span of the ramp.

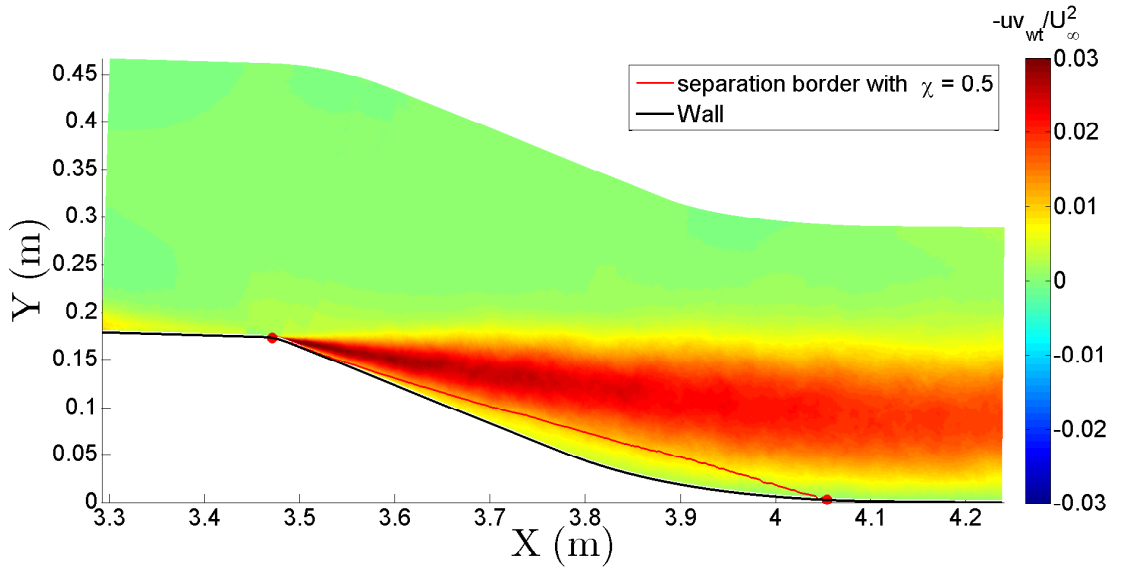

Figure D.6: Reynolds shear stress field ($uv_{wt} = \overline{u'_{wt}v'_{wt}}$) on the flap at mid-span of the ramp.

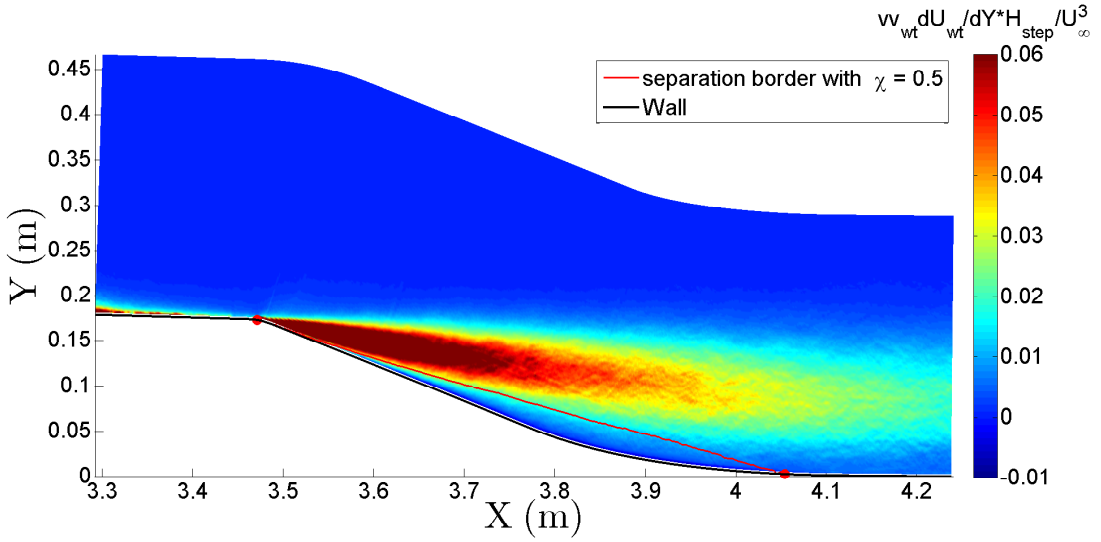

Figure D.7: Production term $\overline{v'^2_{wt}}\frac{\partial U_{wt}}{\partial Y}$ of $-\overline{u'_{wt}v'_{wt}}$ on the flap at mid-span of the ramp.

Appendix E

Turbulent quantity distributions of active control tests in the global wind-tunnel reference frame

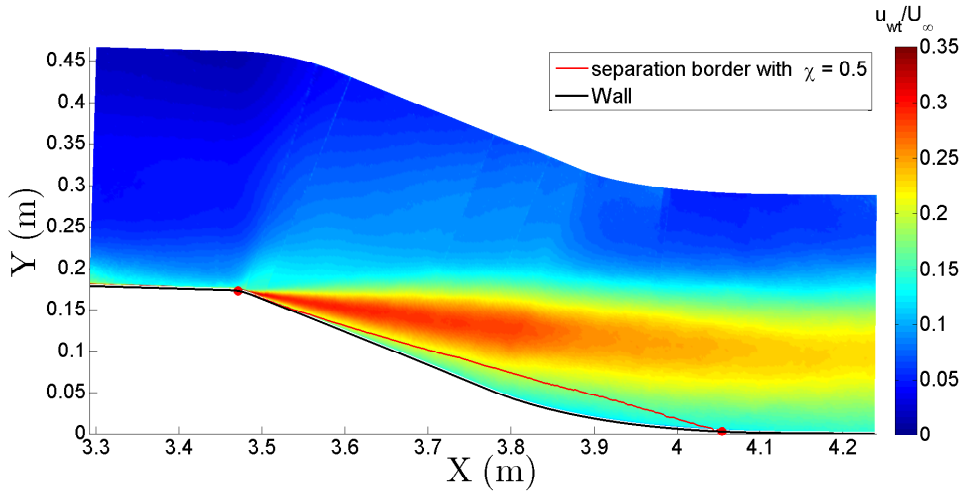
u_wt/U_∞
separation border with χ = 0.5
Wall
Y (m)
X (m)
0.45
0.4
0.35
0.3
0.25
0.2
0.15
0.1
0.05
0
3.3
3.4
3.5
3.6
3.7
3.8
3.9
4
4.1
4.2
0.35
0.3
0.25
0.2
0.15
0.1
0.05
0

a)

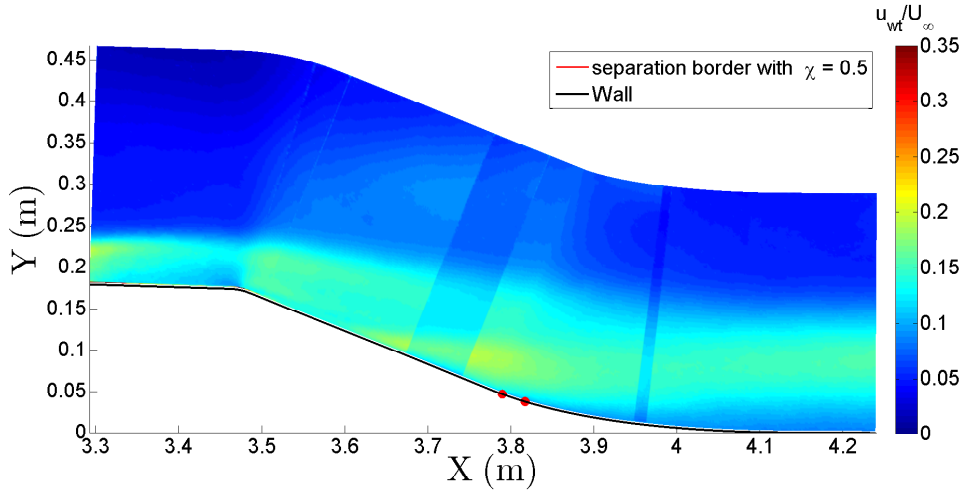
u_wt/U_∞
separation border with χ = 0.5
Wall
Y (m)
X (m)
0.45
0.4
0.35
0.3
0.25
0.2
0.15
0.1
0.05
0
3.3
3.4
3.5
3.6
3.7
3.8
3.9
4
4.1
4.2
0.35
0.3
0.25
0.2
0.15
0.1
0.05
0

b)

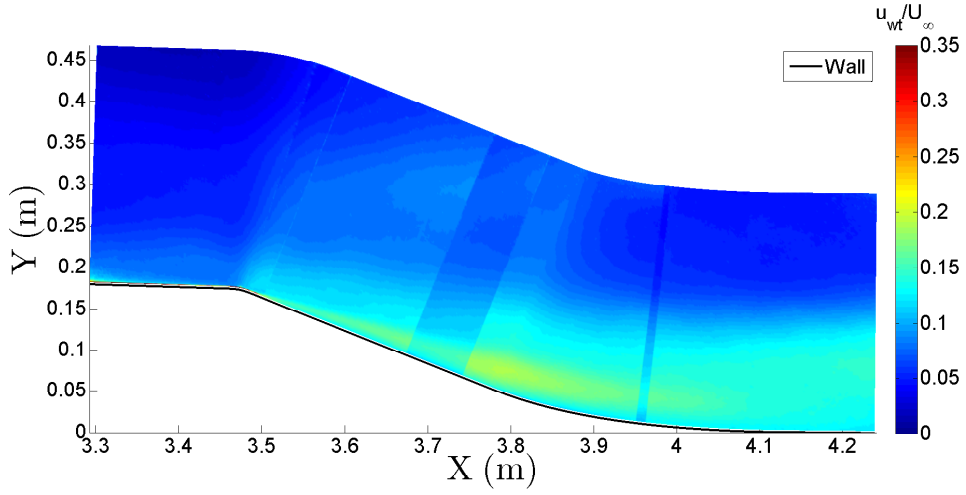
u_wt/U_∞
Wall
Y (m)
X (m)
0.45
0.4
0.35
0.3
0.25
0.2
0.15
0.1
0.05
0
3.3
3.4
3.5
3.6
3.7
3.8
3.9
4
4.1
4.2
0.35
0.3
0.25
0.2
0.15
0.1
0.05
0

c)

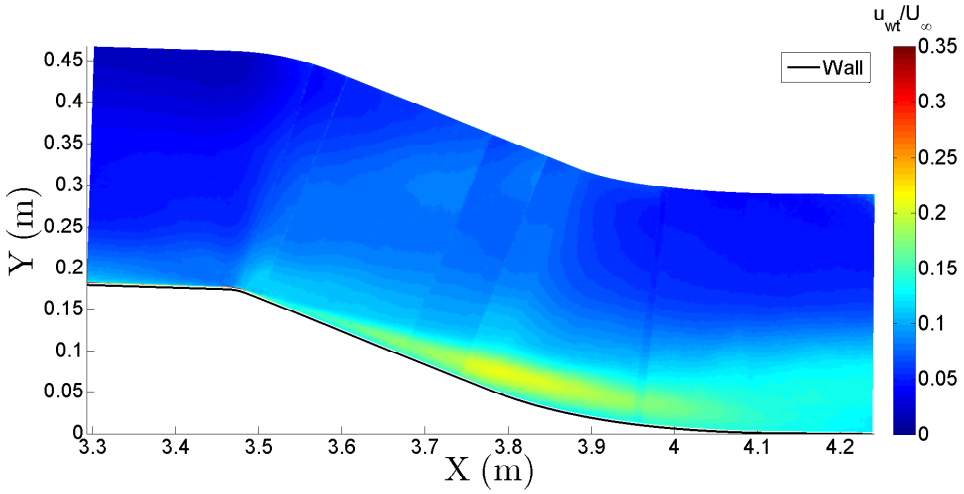

d)

Figure E.1: Turbulent intensity field ($u_{wt} = \sqrt{\overline{u'^2_{wt}}}$) on the flap at mid-span of the ramp for a) the uncontrolled flow, b) the co-up case, c) the counter-up case and d) the counter-down case.

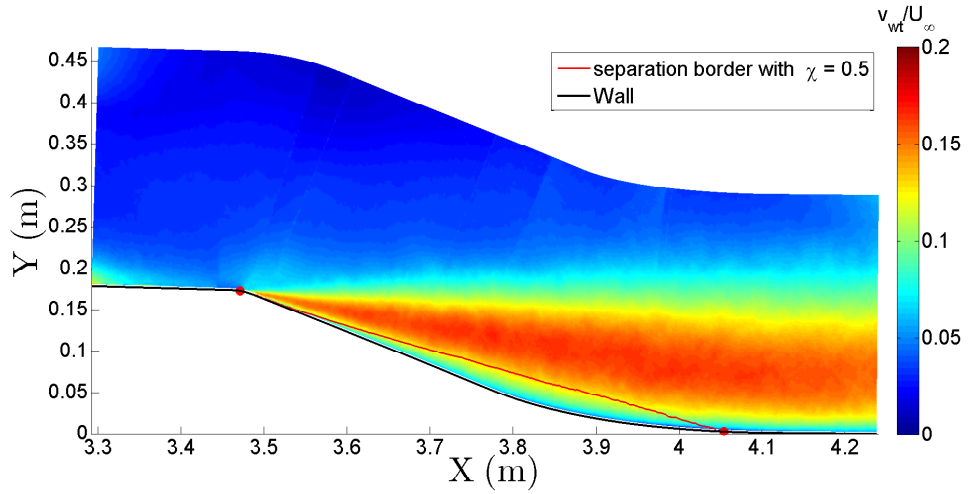
v_wt/U_∞
separation border with χ = 0.5
Wall
Y (m)
X (m)
0.45
0.4
0.35
0.3
0.25
0.2
0.15
0.1
0.05
0
3.3
3.4
3.5
3.6
3.7
3.8
3.9
4
4.1
4.2
0.2
0.15
0.1
0.05
0

a)

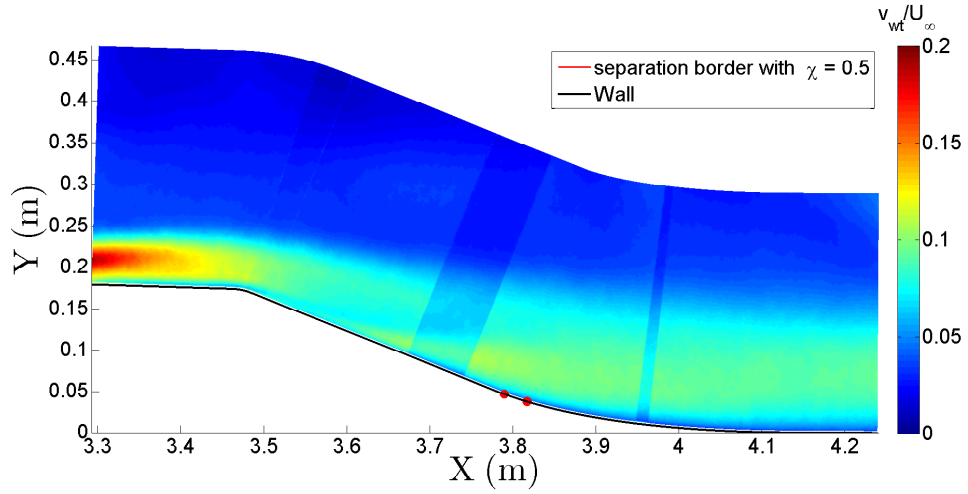
v_wt/U_∞
separation border with χ = 0.5
Wall
Y (m)
X (m)
0.45
0.4
0.35
0.3
0.25
0.2
0.15
0.1
0.05
0
3.3
3.4
3.5
3.6
3.7
3.8
3.9
4
4.1
4.2
0.2
0.15
0.1
0.05
0

b)

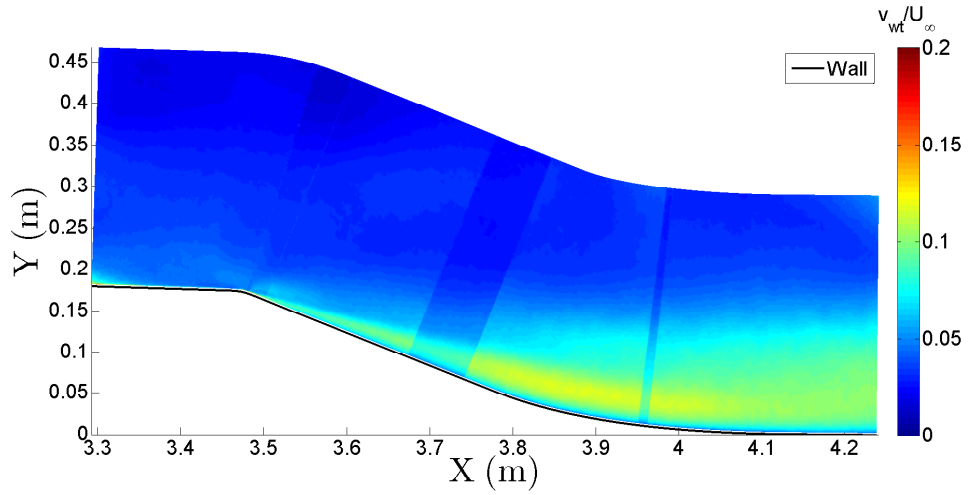
v_wt/U_∞
Wall
Y (m)
X (m)
0.45
0.4
0.35
0.3
0.25
0.2
0.15
0.1
0.05
0
3.3
3.4
3.5
3.6
3.7
3.8
3.9
4
4.1
4.2
0.2
0.15
0.1
0.05
0

c)

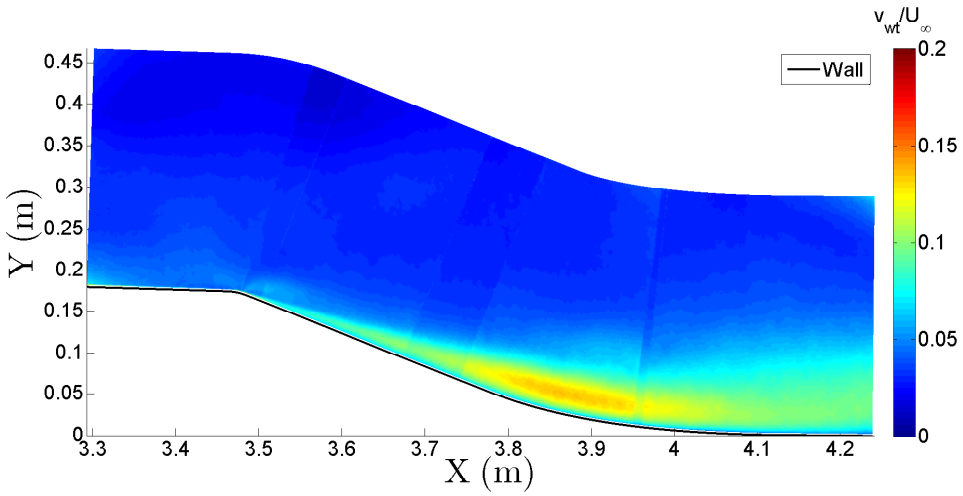

d)

Figure E.2: Turbulent intensity field ($v_{wt} = \sqrt{\overline{v_{wt}'^2}}$) on the flap at mid-span of the ramp for a) the uncontrolled flow, b) the co-up case, c) the counter-up case and d) the counter-down case.

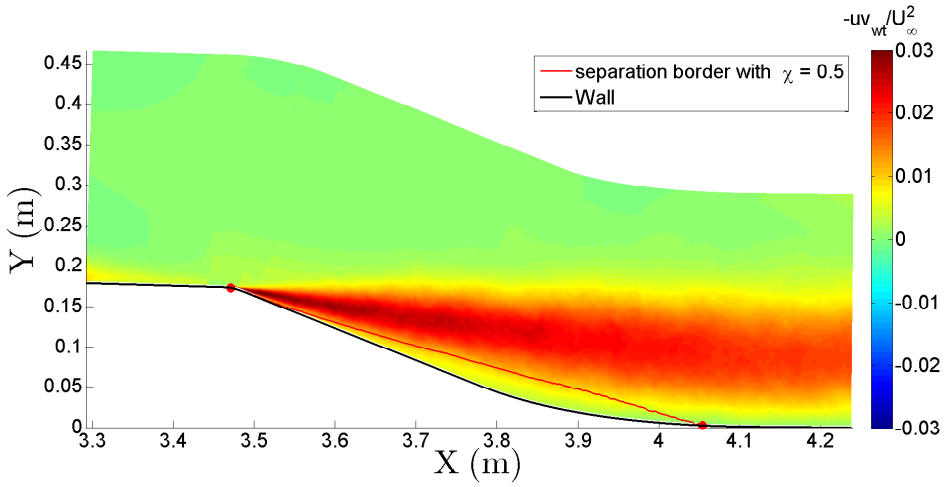
-uv_wt/U²_∞
separation border with χ = 0.5
Wall
Y (m)
X (m)
0.45
0.4
0.35
0.3
0.25
0.2
0.15
0.1
0.05
0
3.3
3.4
3.5
3.6
3.7
3.8
3.9
4
4.1
4.2
0.03
0.02
0.01
0
-0.01
-0.02
-0.03

a)

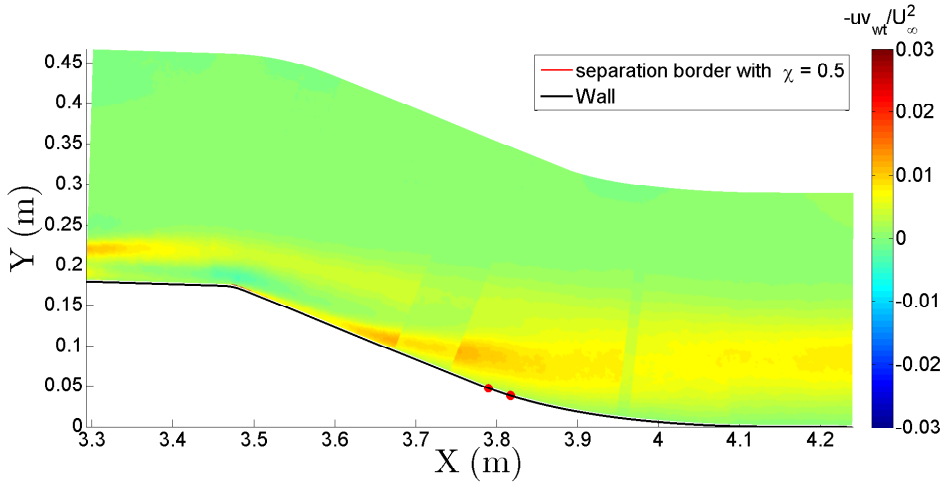
-uv_wt/U²_∞
separation border with χ = 0.5
Wall
Y (m)
X (m)
0.45
0.4
0.35
0.3
0.25
0.2
0.15
0.1
0.05
0
3.3
3.4
3.5
3.6
3.7
3.8
3.9
4
4.1
4.2
0.03
0.02
0.01
0
-0.01
-0.02
-0.03

b)

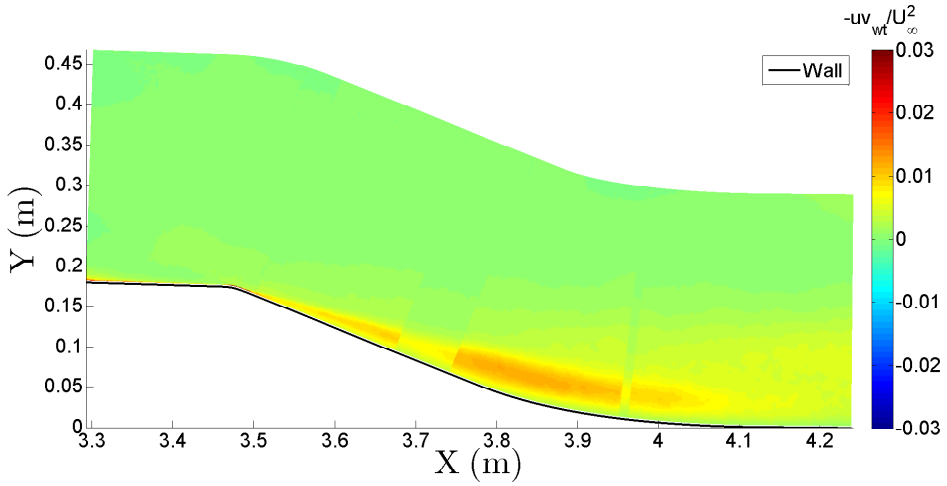
-uv_wt/U²_∞
Wall
Y (m)
X (m)
0.45
0.4
0.35
0.3
0.25
0.2
0.15
0.1
0.05
0
3.3
3.4
3.5
3.6
3.7
3.8
3.9
4
4.1
4.2
0.03
0.02
0.01
0
-0.01
-0.02
-0.03

c)

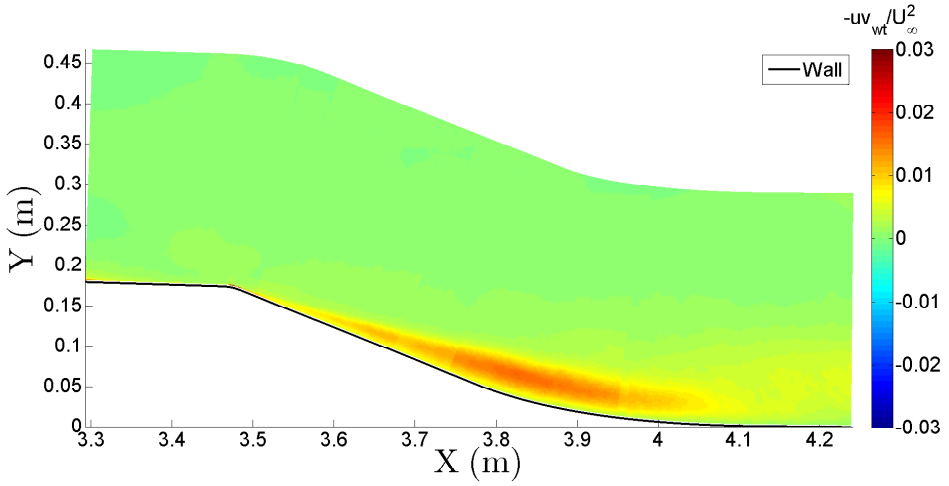

d)

Figure E.3: Reynolds shear stress field ($uv_{wt} = \overline{u'_{wt}v'_{wt}}$) on the flap at mid-span of the ramp for a) the uncontrolled flow, b) the co-up case, c) the counter-up case and d) the counter-down case.

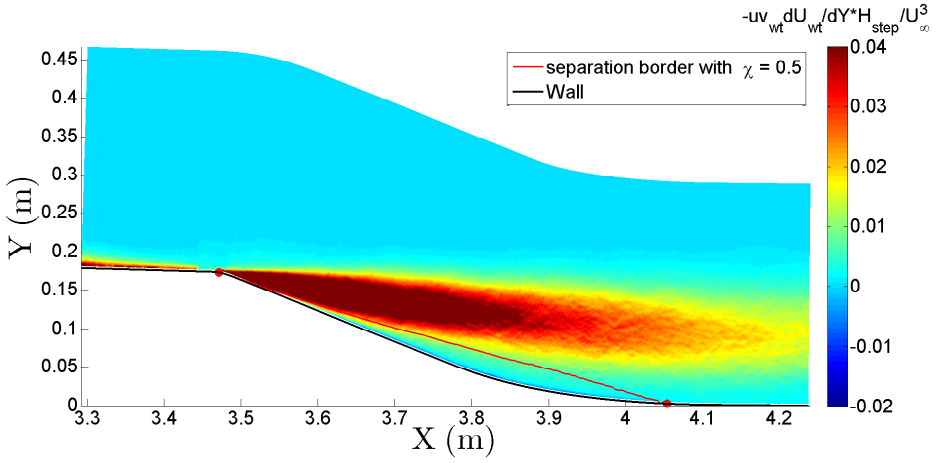
-uv_wt dU_wt/dY*H_step/U_∞^3
separation border with χ = 0.5
Wall
Y (m)
X (m)
0.45
0.4
0.35
0.3
0.25
0.2
0.15
0.1
0.05
0
3.3
3.4
3.5
3.6
3.7
3.8
3.9
4
4.1
4.2
0.04
0.03
0.02
0.01
0
-0.01
-0.02

a)

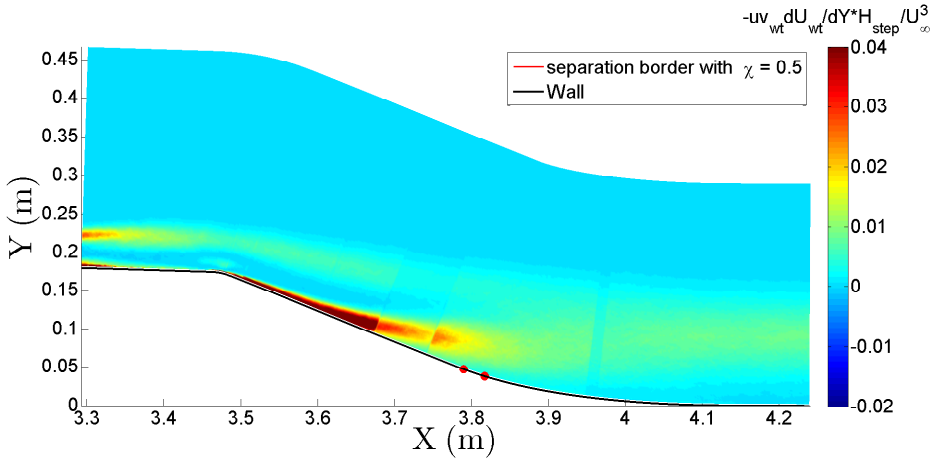
-uv_wt dU_wt/dY*H_step/U_∞^3
separation border with χ = 0.5
Wall
Y (m)
X (m)
0.45
0.4
0.35
0.3
0.25
0.2
0.15
0.1
0.05
0
3.3
3.4
3.5
3.6
3.7
3.8
3.9
4
4.1
4.2
0.04
0.03
0.02
0.01
0
-0.01
-0.02

b)

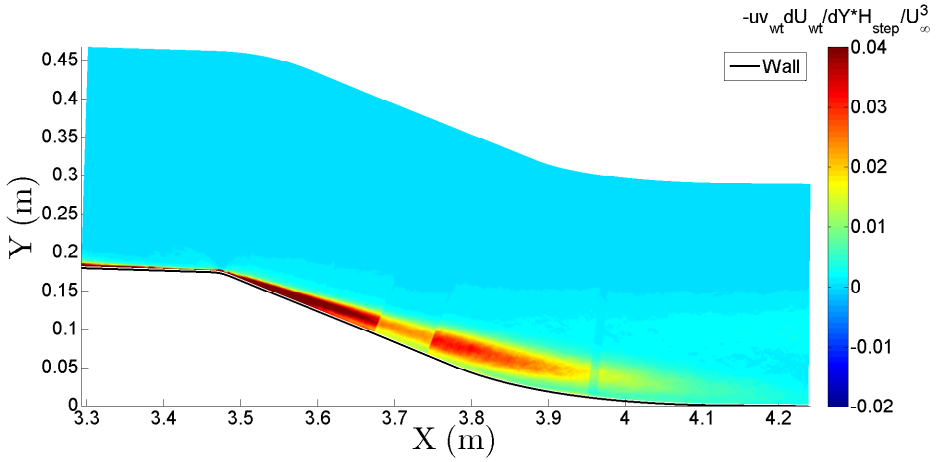
-uv_wt dU_wt/dY*H_step/U_∞^3
Wall
Y (m)
X (m)
0.45
0.4
0.35
0.3
0.25
0.2
0.15
0.1
0.05
0
3.3
3.4
3.5
3.6
3.7
3.8
3.9
4
4.1
4.2
0.04
0.03
0.02
0.01
0
-0.01
-0.02

c)

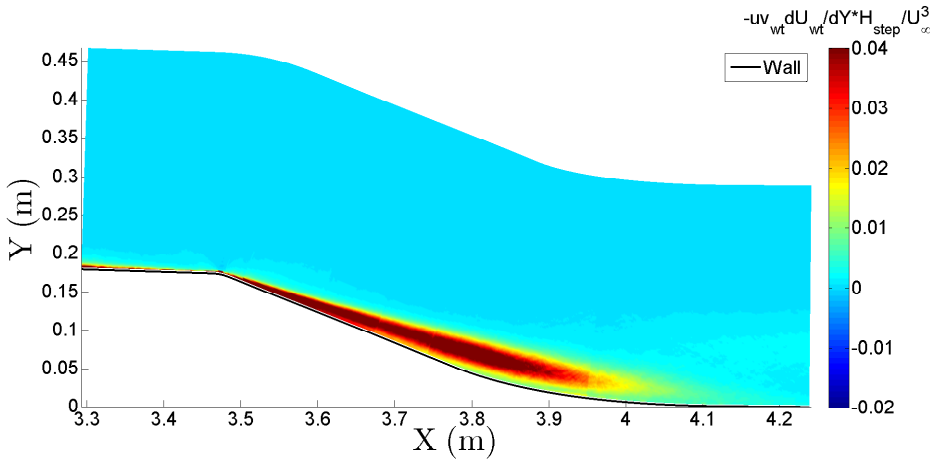

d)

Figure E.4: Production term $-\overline{u'_{wt}v'_{wt}}\frac{\partial U_{wt}}{\partial Y}$ of the turbulent kinetic energy on the flap at mid-span of the ramp for a) the uncontrolled flow, b) the co-up case, c) the counter-up case and d) the counter-down case.

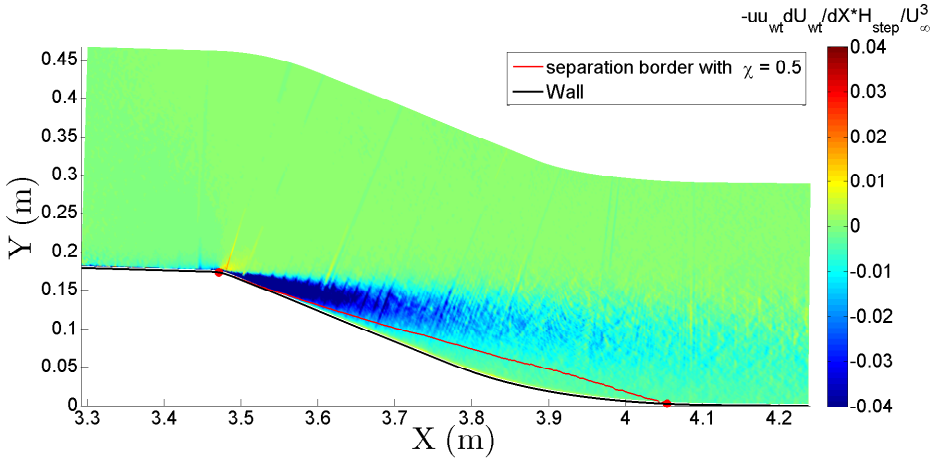
-uu_wt dU_wt/dX*H_step/U_∞^3
separation border with χ = 0.5
Wall
Y (m)
X (m)
0.45
0.4
0.35
0.3
0.25
0.2
0.15
0.1
0.05
0
3.3
3.4
3.5
3.6
3.7
3.8
3.9
4
4.1
4.2
0.04
0.03
0.02
0.01
0
-0.01
-0.02
-0.03
-0.04

a)

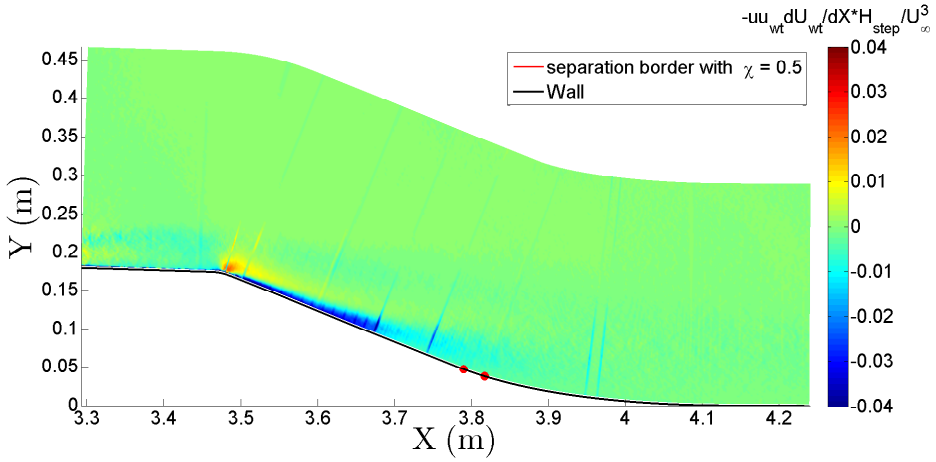
-uu_wt dU_wt/dX*H_step/U_∞^3
separation border with χ = 0.5
Wall
Y (m)
X (m)
0.45
0.4
0.35
0.3
0.25
0.2
0.15
0.1
0.05
0
3.3
3.4
3.5
3.6
3.7
3.8
3.9
4
4.1
4.2
0.04
0.03
0.02
0.01
0
-0.01
-0.02
-0.03
-0.04

b)

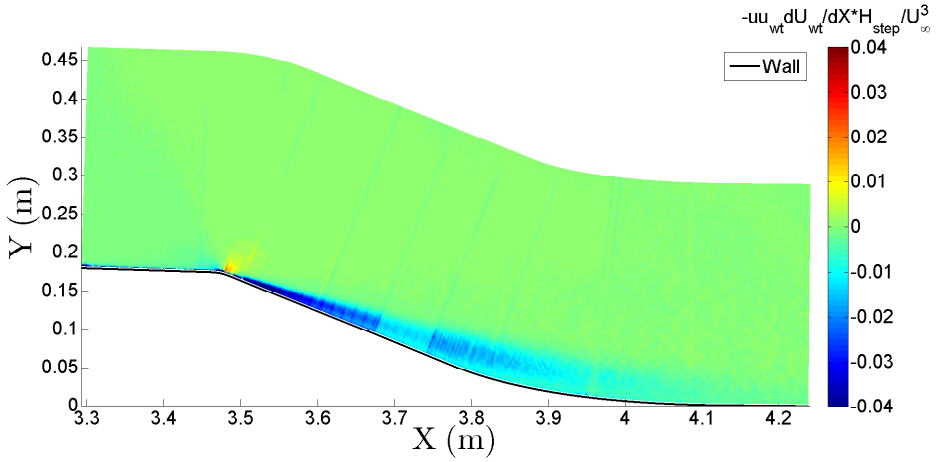
-uu_wt dU_wt/dX*H_step/U_∞^3
Wall
Y (m)
X (m)
0.45
0.4
0.35
0.3
0.25
0.2
0.15
0.1
0.05
0
3.3
3.4
3.5
3.6
3.7
3.8
3.9
4
4.1
4.2
0.04
0.03
0.02
0.01
0
-0.01
-0.02
-0.03
-0.04

c)

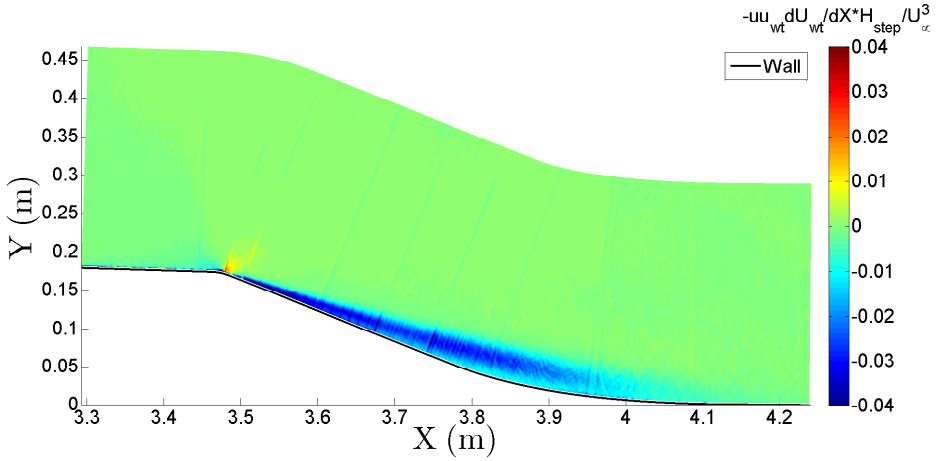

d)

Figure E.5: Production term $-\overline{u'^2_{wt}}\frac{\partial U_{wt}}{\partial X}$ of the turbulent kinetic energy on the flap at mid-span of the ramp for a) the uncontrolled flow, b) the co-up case, c) the counter-up case and d) the counter-down case.

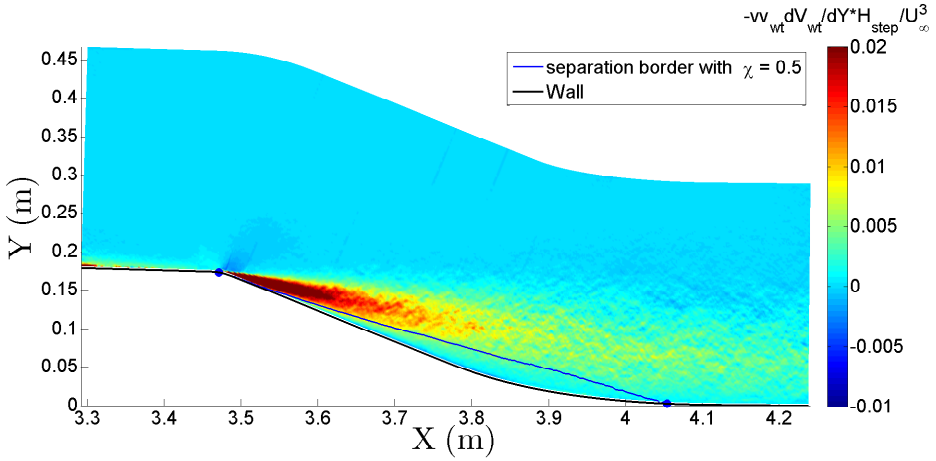
-vv_wt dV_wt/dY*H_step/U∞³
separation border with χ = 0.5
Wall
Y (m)
X (m)
0.45
0.4
0.35
0.3
0.25
0.2
0.15
0.1
0.05
0
3.3
3.4
3.5
3.6
3.7
3.8
3.9
4
4.1
4.2
0.02
0.015
0.01
0.005
0
-0.005
-0.01

a)

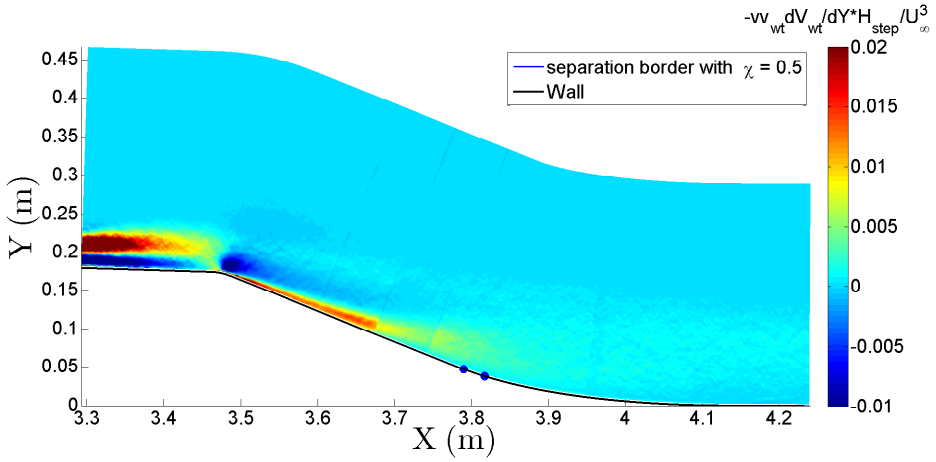
-vv_wt dV_wt/dY*H_step/U∞³
separation border with χ = 0.5
Wall
Y (m)
X (m)
0.45
0.4
0.35
0.3
0.25
0.2
0.15
0.1
0.05
0
3.3
3.4
3.5
3.6
3.7
3.8
3.9
4
4.1
4.2
0.02
0.015
0.01
0.005
0
-0.005
-0.01

b)

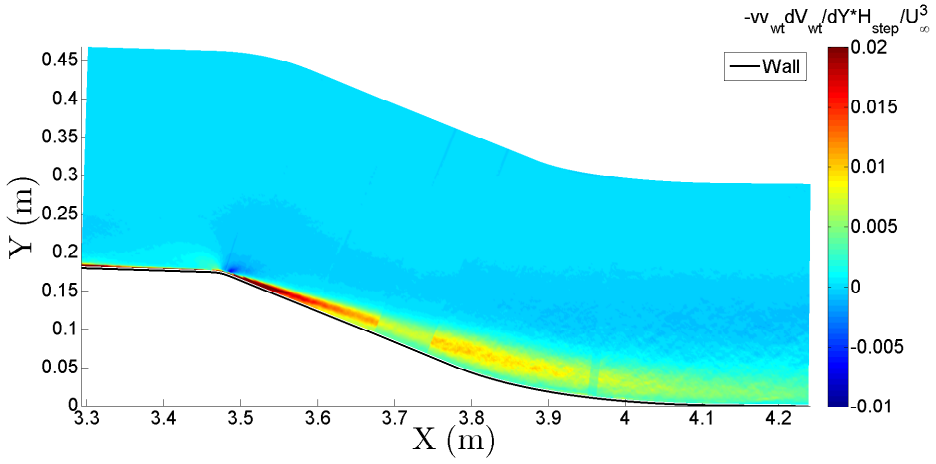
-vv_wt dV_wt/dY*H_step/U∞³
Wall
Y (m)
X (m)
0.45
0.4
0.35
0.3
0.25
0.2
0.15
0.1
0.05
0
3.3
3.4
3.5
3.6
3.7
3.8
3.9
4
4.1
4.2
0.02
0.015
0.01
0.005
0
-0.005
-0.01

c)

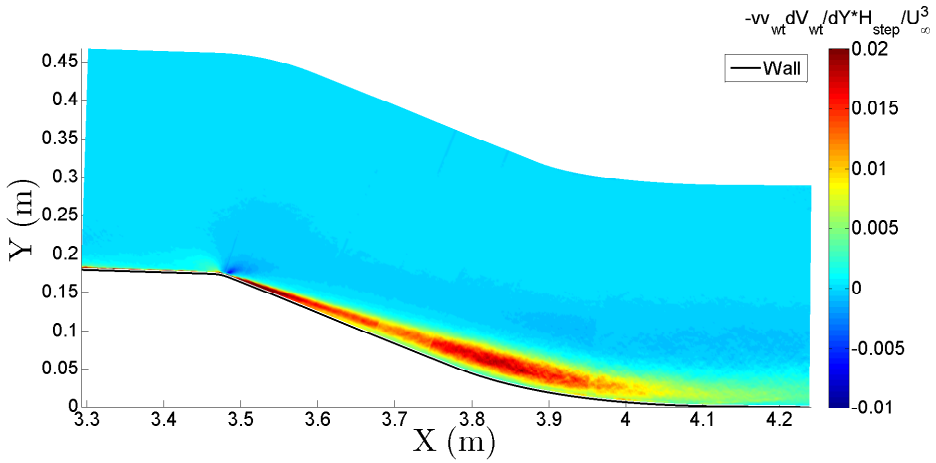

d)

Figure E.6: Production term $-\overline{v'^2_{wt}}\frac{\partial V_{wt}}{\partial Y}$ of the turbulent kinetic energy on the flap at mid-span of the ramp for a) the uncontrolled flow, b) the co-up case, c) the counter-up case and d) the counter-down case.

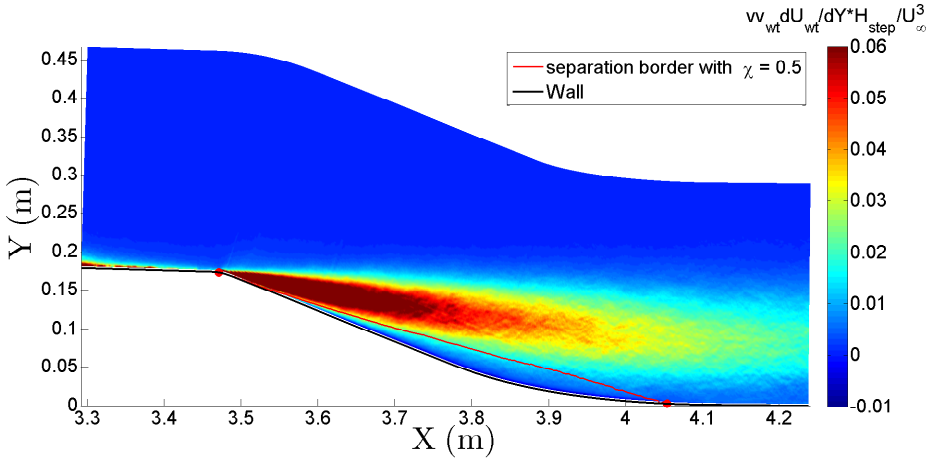
vv_wt dU_wt/dY*H_step/U³∞
separation border with χ = 0.5
Wall
Y (m)
X (m)
0.45
0.4
0.35
0.3
0.25
0.2
0.15
0.1
0.05
0
3.3
3.4
3.5
3.6
3.7
3.8
3.9
4
4.1
4.2
0.06
0.05
0.04
0.03
0.02
0.01
0
-0.01

a)

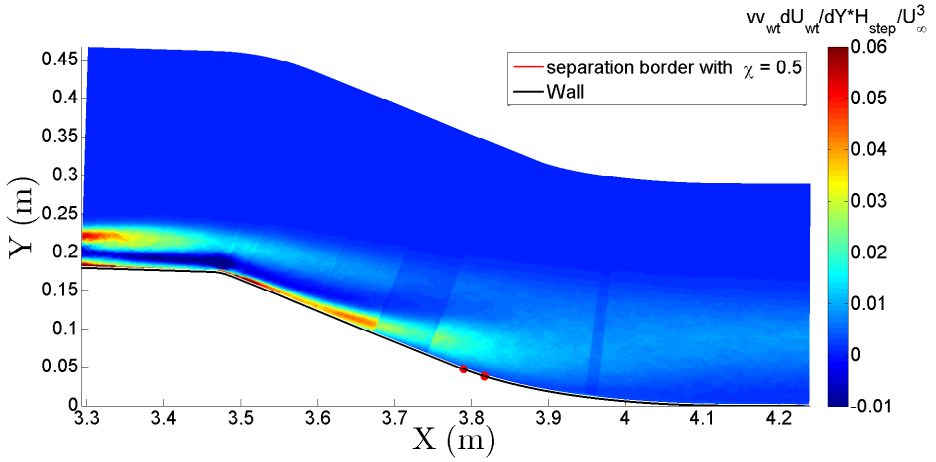
vv_wt dU_wt/dY*H_step/U³∞
separation border with χ = 0.5
Wall
Y (m)
X (m)
0.45
0.4
0.35
0.3
0.25
0.2
0.15
0.1
0.05
0
3.3
3.4
3.5
3.6
3.7
3.8
3.9
4
4.1
4.2
0.06
0.05
0.04
0.03
0.02
0.01
0
-0.01

b)

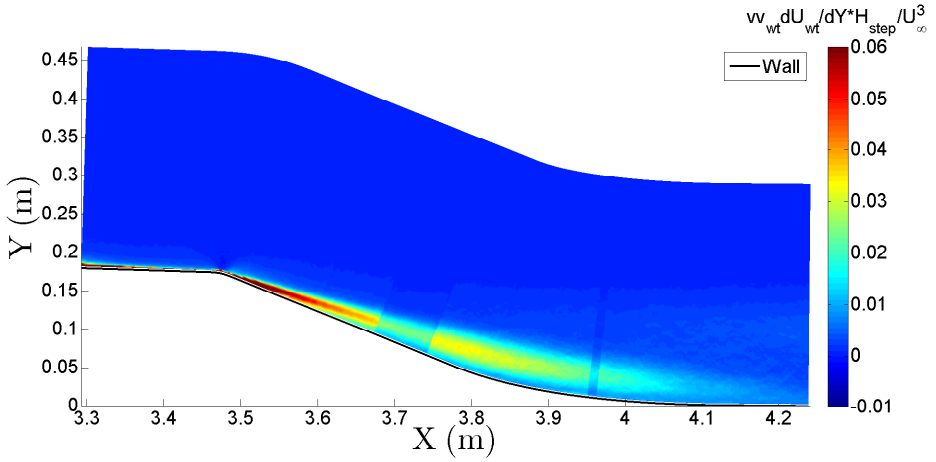
vv_wt dU_wt/dY*H_step/U³∞
Wall
Y (m)
X (m)
0.45
0.4
0.35
0.3
0.25
0.2
0.15
0.1
0.05
0
3.3
3.4
3.5
3.6
3.7
3.8
3.9
4
4.1
4.2
0.06
0.05
0.04
0.03
0.02
0.01
0
-0.01

c)

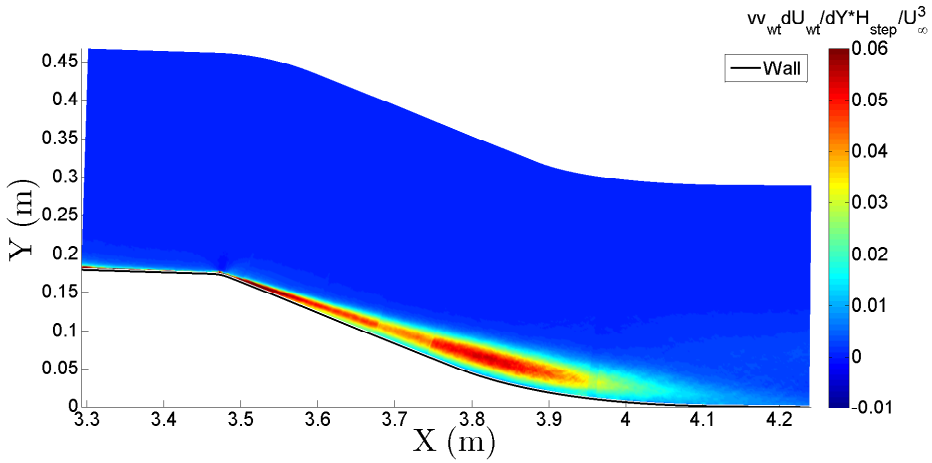

d)

Figure E.7: Main production term $\overline{v'^2_{wt}}\frac{\partial U_{wt}}{\partial Y}$ of the Reynolds shear stress on the flap at mid-span of the ramp for a) the uncontrolled flow, b) the co-up case, c) the counter-up case and d) the counter-down case.

Appendix F

Distribution of some turbulent production terms of active control tests in the local reference frame

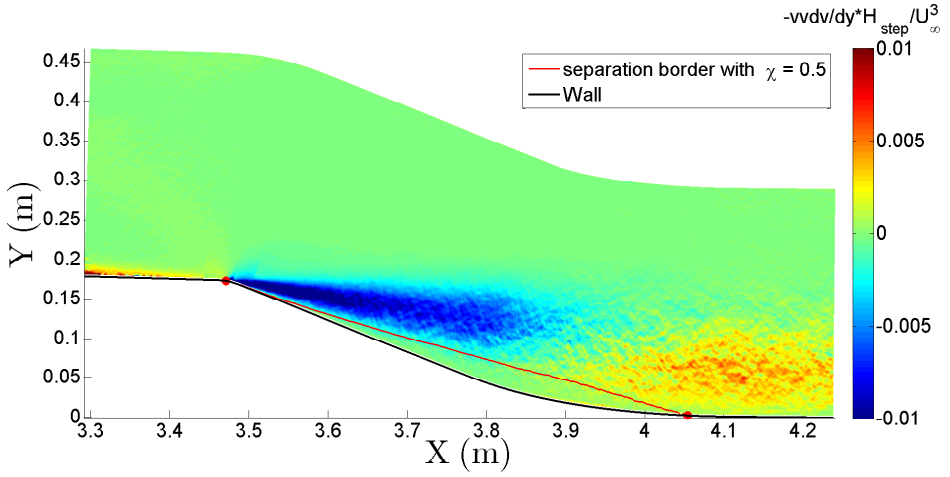
-vvdv/dy*H step /U3 ∞
separation border with χ = 0.5
Wall
0.01
0.005
0
-0.005
-0.01
Y (m)
X (m)
0.45
0.4
0.35
0.3
0.25
0.2
0.15
0.1
0.05
0
3.3
3.4
3.5
3.6
3.7
3.8
3.9
4
4.1
4.2

a)

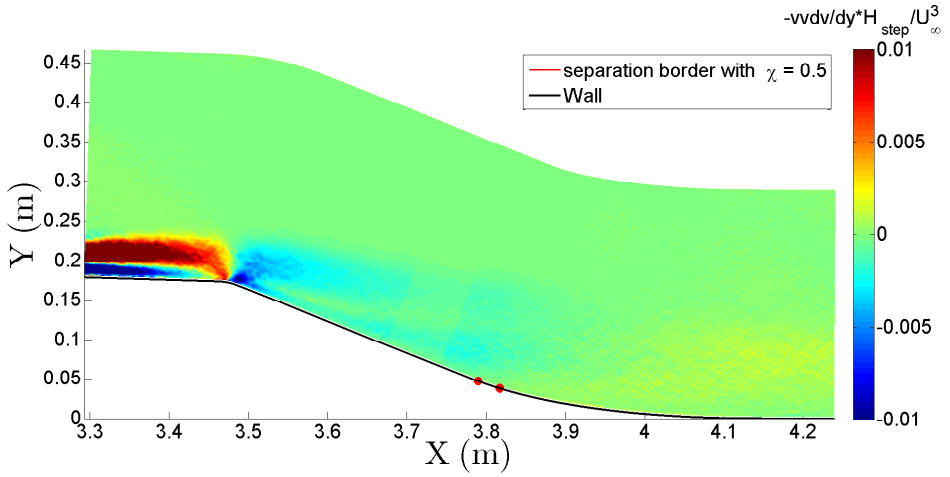
-vvdv/dy*H step /U3 ∞
separation border with χ = 0.5
Wall
0.01
0.005
0
-0.005
-0.01
Y (m)
X (m)
0.45
0.4
0.35
0.3
0.25
0.2
0.15
0.1
0.05
0
3.3
3.4
3.5
3.6
3.7
3.8
3.9
4
4.1
4.2

b)

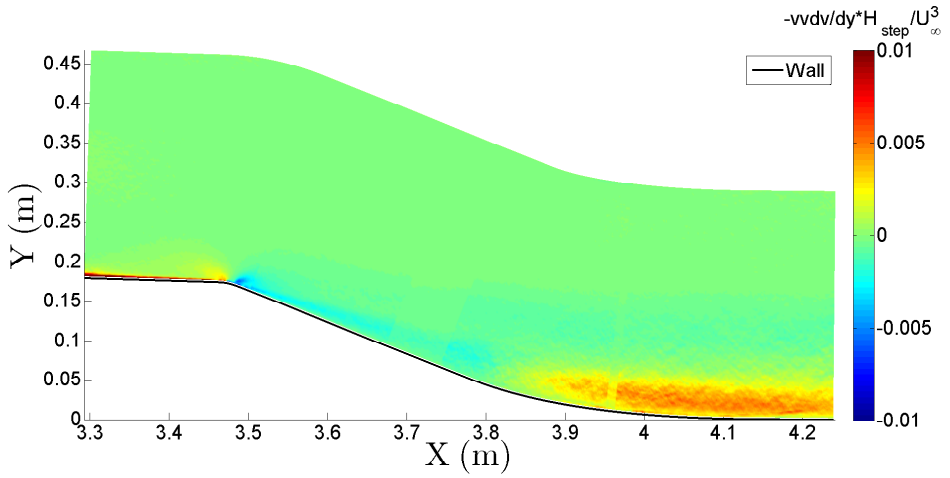
-vvdv/dy*H step /U3 ∞
Wall
0.01
0.005
0
-0.005
-0.01
Y (m)
X (m)
0.45
0.4
0.35
0.3
0.25
0.2
0.15
0.1
0.05
0
3.3
3.4
3.5
3.6
3.7
3.8
3.9
4
4.1
4.2

c)

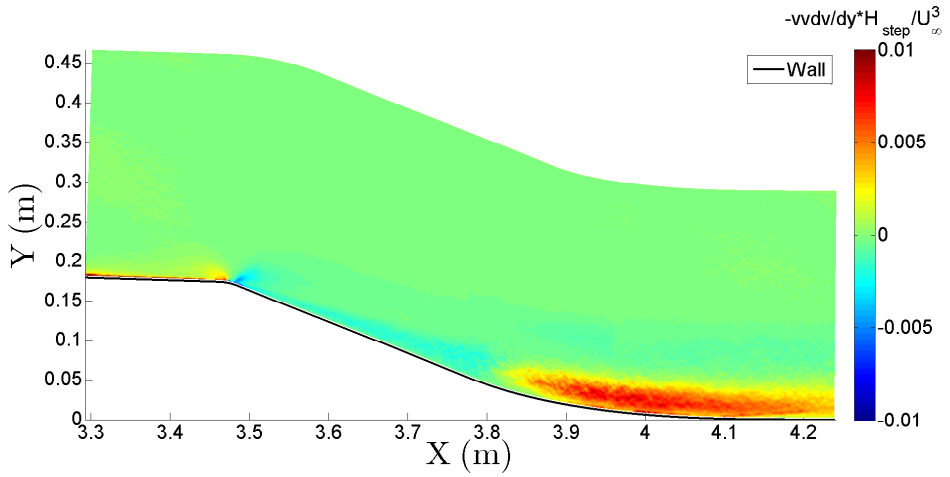

d)

Figure F.1: Production term $-\overline{v'^2}\frac{\partial V}{\partial y}$ of the turbulent kinetic energy on the flap at mid-span of the ramp for a) the uncontrolled flow, b) the co-up case, c) the counter-up case and d) the counter-down case.

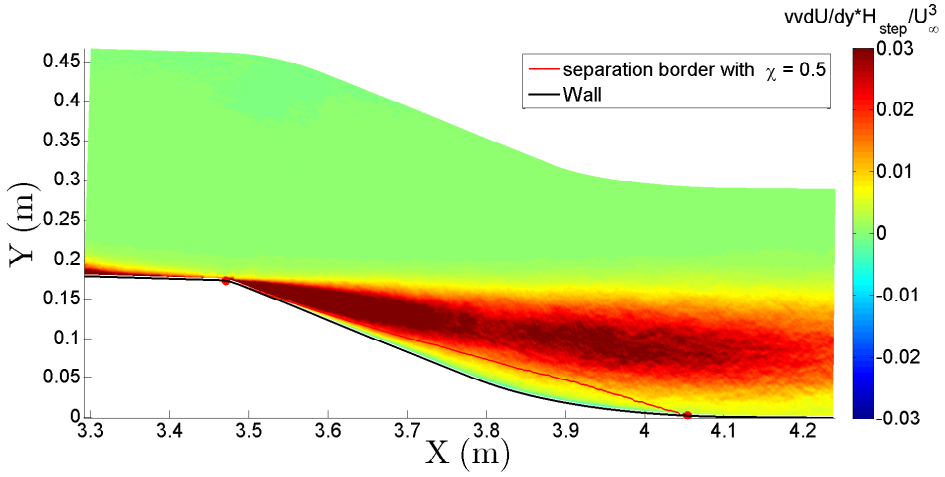
vvdU/dy*H step /U3 ∞
separation border with χ = 0.5
Wall
Y (m)
X (m)
0.45
0.4
0.35
0.3
0.25
0.2
0.15
0.1
0.05
0
3.3
3.4
3.5
3.6
3.7
3.8
3.9
4
4.1
4.2
0.03
0.02
0.01
0
-0.01
-0.02
-0.03

a)

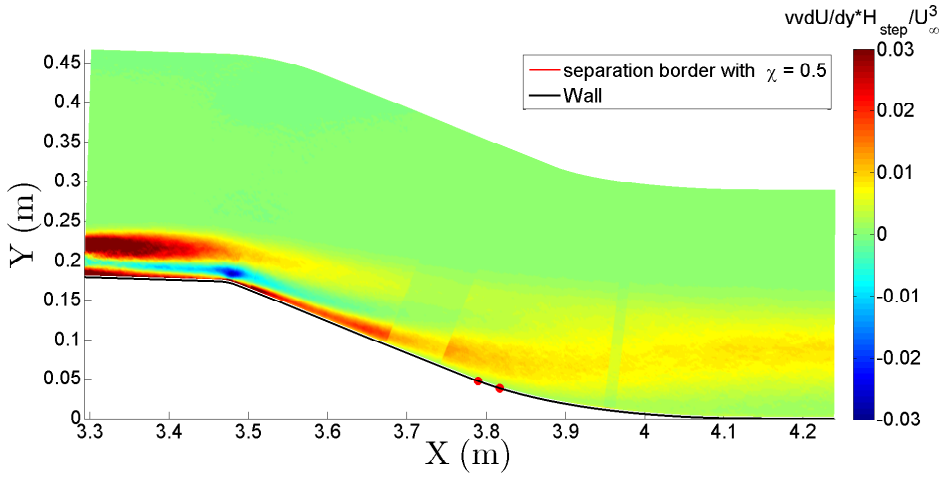
vvdU/dy*H step /U3 ∞
separation border with χ = 0.5
Wall
Y (m)
X (m)
0.45
0.4
0.35
0.3
0.25
0.2
0.15
0.1
0.05
0
3.3
3.4
3.5
3.6
3.7
3.8
3.9
4
4.1
4.2
0.03
0.02
0.01
0
-0.01
-0.02
-0.03

b)

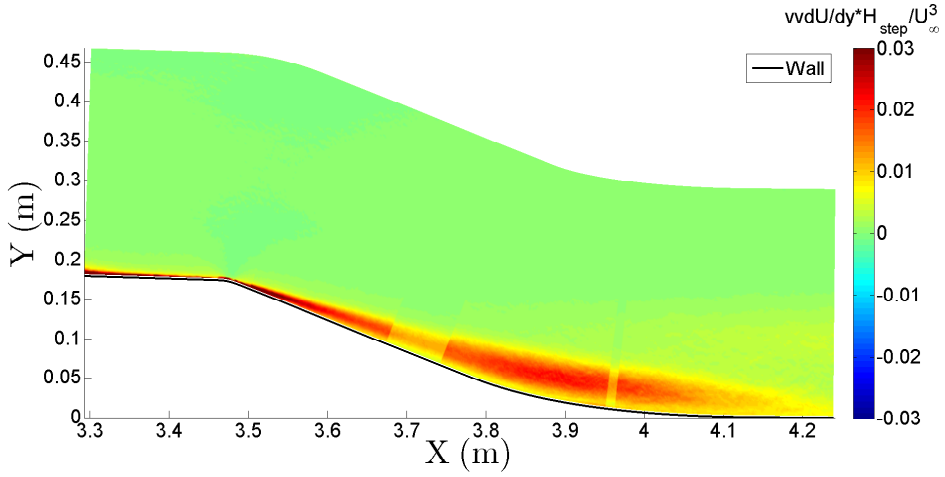
vvdU/dy*H step /U3 ∞
Wall
Y (m)
X (m)
0.45
0.4
0.35
0.3
0.25
0.2
0.15
0.1
0.05
0
3.3
3.4
3.5
3.6
3.7
3.8
3.9
4
4.1
4.2
0.03
0.02
0.01
0
-0.01
-0.02
-0.03

c)

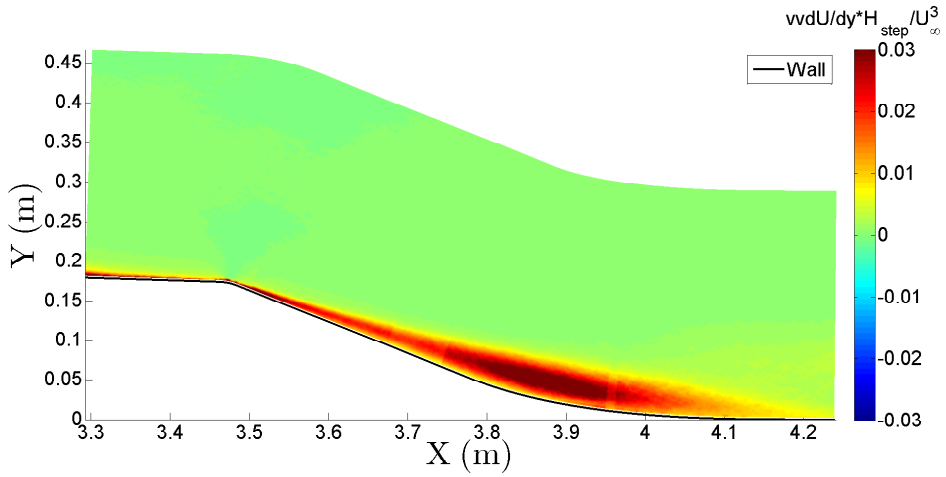

d)

Figure F.2: Main production term $\overline{v'^2}\frac{\partial U}{\partial y}$ of the Reynolds shear stress on the flap at mid-span of the ramp for a) the uncontrolled flow, b) the co-up case, c) the counter-up case and d) the counter-down case.

Appendix G

Profiles on the flap of some turbulent production terms of active control tests

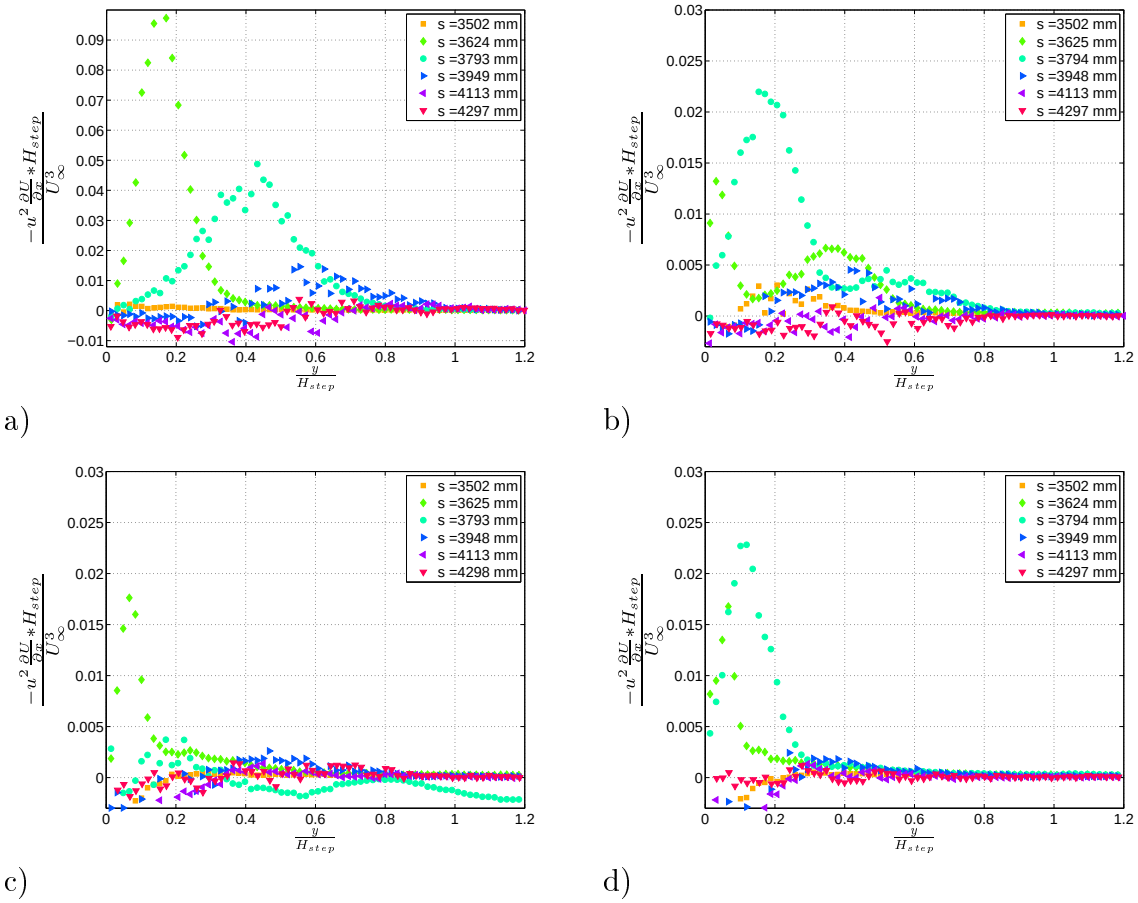

Figure G.1: Six profiles of the production term $-\overline{u'^2}\frac{\partial U}{\partial x}$ of the turbulent kinetic energy on the flap for a) the uncontrolled flow, b) the co-up case, c) the counter-up case and d) the counter-down case.

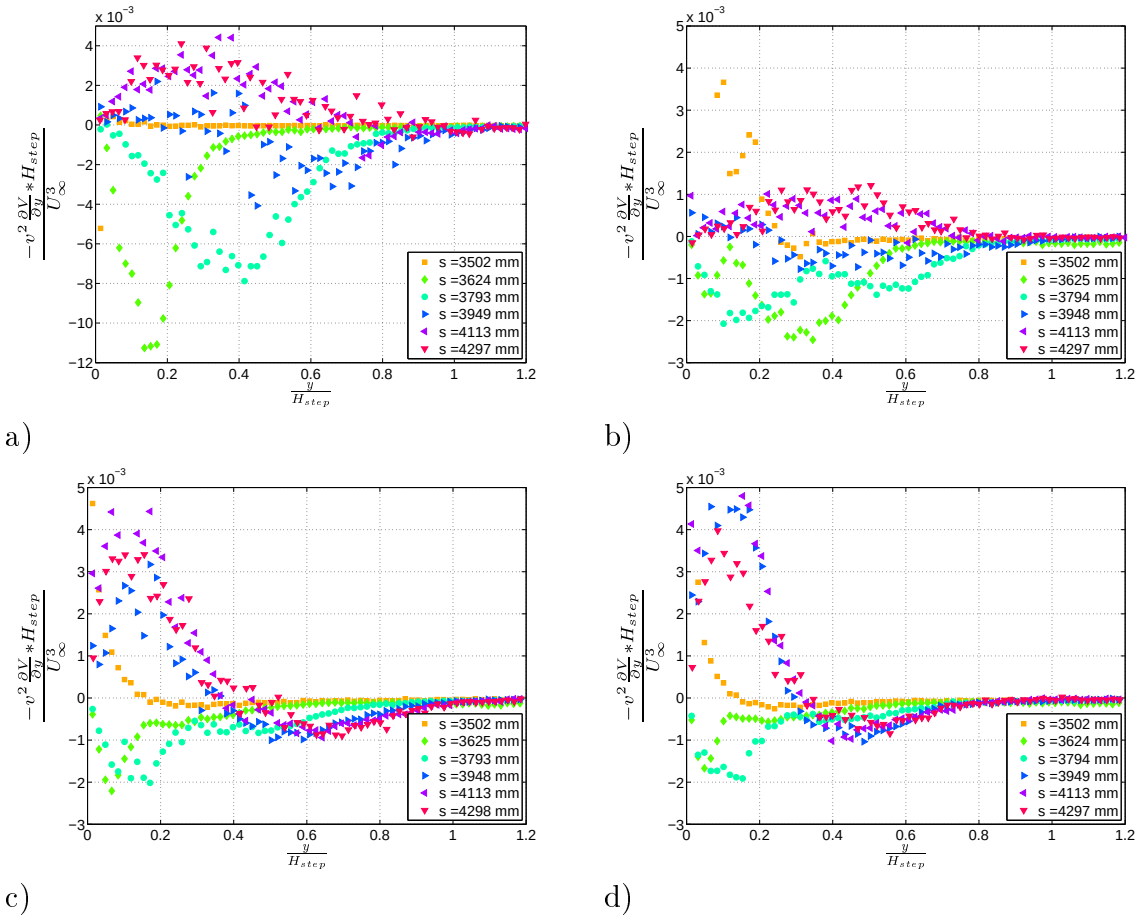

Figure G.2: Six profiles of the production term $-\overline{v'^2}\frac{\partial V}{\partial y}$ of the turbulent kinetic energy on the flap for a) the uncontrolled flow, b) the co-up case, c) the counter-up case and d) the counter-down case.

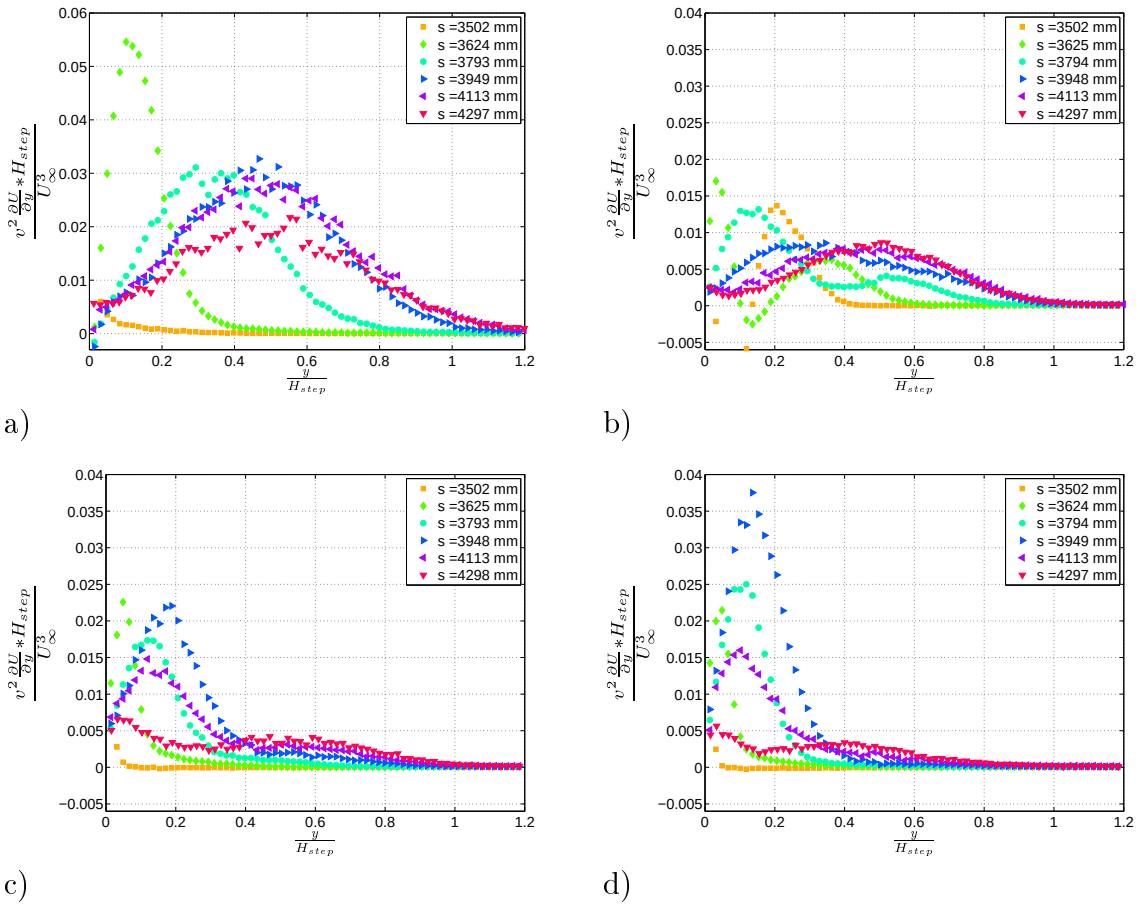

Figure G.3: Six profiles of the main production term $\overline{v'^2}\frac{\partial U}{\partial y}$ of the Reynolds shear stress on the flap for a) the uncontrolled flow, b) the co-up case, c) the counter-up case and d) the counter-down case.

Appendix H

Articles presented in TSFP7 conference

CHARACTERIZATION OF A SEPARATED TURBULENT BOUNDARY LAYER FOR FLOW CONTROL PURPOSE.

C. Cuvier[1,2], **C. Braud**[1,3], **J.M. Foucaut**[1,2], **M. Stanislas**[1,2]
Univ Lille Nord de France[1] F-59000 Lille, EC Lille[2], CNRS[3],
Laboratoire de Mécanique de Lille (UMR 8107)
Boulevard Paul Langevin,
59655 Villeneuve d'Ascq Cédex, France.
christophe.cuvier@gmail.com
caroline.braud@univ-lille1.fr
jean-marc.foucaut@ec-lille.fr
michel.stanislas@ec-lille.fr

ABSTRACT

The flow over a two dimensional ramp has been characterized. First, some configurations of the ramp were characterized rapidly with only wall pressure measurements and wool tufts visualisations. The aim of this first work was to check the spanwise homogeneity and to find the angle α and β of the ramp that give a ramp configuration with an adverse pressure gradient on the 2 m flat plate and a separation on the flap. It was found that for $\alpha = -2^\circ$, the separation occur on the flap for β under -19°. The configuration with $\alpha = -2^\circ$ and $\beta = -22^\circ$ was then selected and characterized more carefully with hot-wire profiles. On this configuration, the boundary layer over the ramp is around 20 cm and the Reynolds number based on the momentum thickness (Re_θ) is around 11 000. The boundary layer under study develops with a mild adverse pressure gradient with a Clauser pressure parameter between 0.2 and 1.4. At the end of the 2 m flat plate of the ramp, there is a separation on the flap which is more or less two dimensional on 70 % of the span. This flow mimics the suction side of a wing and is then adapted to do parametric studies of flow control.

Key words : Turbulent boundary layers, adverse pressure gradient, hot-wire, flow separation.

INTRODUCTION

Turbulent Boundary Layer (TBL) that encountered adverse pressure gradient (APG) seems to be inevitable in turbomachinery and aircraft applications. Sometimes, the APG encountered is strong enough to lead to a flow separation. The flow detachment has drastic consequences on the efficiency of turbo-machineries and can lead to a loss of control of an aircraft. The studies of a boundary layer in adverse pressure gradient with separation is thus interesting for industrial applications. It is not surprising that recently many experimental (Webster et al., 1996; Bernard et al., 2003; Aubertine and Eaton, 2005; Elsberry et al., 2000; Angele and Muhammad-Klingmann, 2006; etc.) and numerical (Wu and Squires, 1998; etc.) studies have appeared on APG boundary layers.

From the experimental point of view, there are three major ways to generate and study the boundary layers in adverse pressure gradient. The first one is a wind tunnel with a flexible wall that allows the diverging cross section to be tuned in order to fix the pressure gradient (like in Elsberry et al., 2000; Angele and Muhammad-Klingmann, 2006). The second one is a bump shaped model sets in the test section of a wind tunnel (like in Webster et al., 1996; Bernard et al., 2003). The last one is very closed to a bump. it corresponds to a ramp (like in Aubertine and Eaton, 2005). Bump and ramp have to be distinguished because the boundary layer over a bump is influenced by both adverse pressure gradient and surface curvature effects. In some flow, it was shown that surface curvature can have more effects on the turbulent quantities than the adverse pressure gradient (Talapurkara et al., 2001). The three major ways of generating adverse pressure gradient give a huge numbers of different experiments, which differ also from one another by the strength of the adverse pressure gradient that can lead or not to a flow separation.

The scaling of the mean velocity profile and the turbulent shear stress seems to be not yet fixed. For the inner region near to the wall, it seems to be accepted that the velocity scale is the friction velocity ($u_\tau = \sqrt{\frac{\tau_w}{\rho}}$, where τ_w is the friction at the wall) and the length scale is $\frac{\nu}{u_\tau}$ (George, 2005). For the outer part it is more controversial. The first theory for the scaling of the outer part was the Clauser one (Clauser, 1954). It this theory, the proposed velocity scale of the outer part was u_τ and the proposed length scale was δ, the boundary layer thickness. In that theory, the profiles have to collapse by plotting $\frac{U_e - U}{u_\tau} = f(\frac{y}{\delta})$, with U_e the free-stream velocity. By merging the outer law and the inner law, the log-law is obtained. As the Clauser's theory was not fully satisfactory, new theories, based on similarity analysis, have appeared for boundary layers in APG. Castillo and George (2001), for infinite Reynolds number boundary layers, proposed U_e for the velocity scale

in the outer part. If their theory is right, the profiles would collapse by plotting $\frac{U_e-U}{U_e} = f(\frac{y}{\delta})$. However, it seems to be not really the case. Zagarola and Smits (1998) have propose $U_e \frac{\delta^*}{\delta}$ as outer velocity scales. This representation seems to work quite well in many experiments. Maciel et al. (2006) explain that the Zagarola outer velocity scale gives a Reynolds number correction to the similarity analysis of Castillo and George (2001). It seems to appear that the inner velocity scale is different from the outer velocity scale. According to George (2005), the different velocity scales for the inner and the outer layer lead to the impossibility of a log layer. This discredit the estimation done by many authors of the friction velocity u_τ by fitting a log-law on the mean velocity profile as suggested by Clauser (1956).

The experiment presented here is a two dimensional ramp-type, designed for the AVERT (Aerodynamic Validation of Emission Reducing Technologies) FP6 EC project, with a mild adverse pressure gradient on a 2 m flat plate. At the end of the flat plate, there is an imposed separation on a flap. This flow is well adapted to a detail study of flow separation control as it mimics the flow on the suction side of a wing.

THE EXPERIMENT

The wind tunnel facility and the ramp

The experiment was conducted in the LML boundary layer wind tunnel at $U_\infty = 10$ m/s. A boundary layer develops on the 20 m long lower wall to reach around 30 cm at the end. This thick boundary layer allows good spatial resolution of the measurements. The test section is 2 m span and 1 m height and the free-stream velocity is ranging from 1 to 10 m/s ($\pm 0.5\%$). In this experiment, the wind tunnel was used in close-loop configuration with temperature regulation ($\pm 0.2°C$). For details characteristics of the wind tunnel, see Carlier and Stanislas (2005).

The ramp model was mounted on the wind tunnel floor such as the beginning of the ramp was 14.4 m downstream of the entrance of the test section. Figure 1 gives a schematic view of the ramp. It is composed of four parts. The first one is a smooth converging part with a contraction ratio of 0.75 to allow to generate a pressure gradient flow after it. At the beginning of the converging part, suction (not used in the present experiment) can be applied to tune the incoming boundary layer. The second part is an articulated flat plate of more than 2 m. The angle between this plate and the wind tunnel floor is called α and is counted positive if it corresponds to a positive rotation around the z axis (Figure 1). The angle α tunes the pressure gradient of the boundary layer that develops on the 2.1 m flat plate. α is ranging from $2°$ to $-4°$. The third part of the ramp is an other articulated flat plate (called flap). The angle between this plate and the wind tunnel floor is called β and its sign used the same convention as α. β is ranging from $-5°$ to $-40°$. The aim of the flap is to allow to create and fix a flow separation. The angle β tunes the strength and the extend of the flow separation. The last part is a flexible plate to allow smooth connection between the end of the flap and the floor of the wind tunnel.

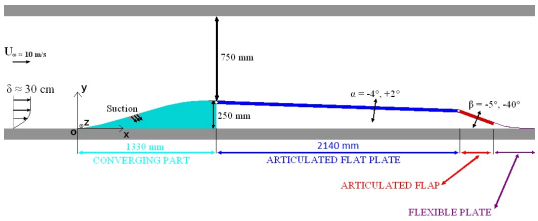

Figure 1. Schematic view of the ramp.

Experimental techniques

Different measurement techniques were used to characterize the flow over the ramp.

Wool tufts and oil film visualisations Wool tufts visualisations was performed on the flat plate and on the flap to characterize the two dimensional behaviour of the flow over the ramp. They were also used to evidence flow separation. Several lines of wool tufts of 4 cm long were placed on the flat plate on all the span. On the flap, a larger density of wool tufts was applied because flow separation was expected on it. In the case with an adverse pressure gradient on the flat plate and a separation on the flap ($\alpha = -2°$ and $\beta = -22°$), oil film visualisation was applied on the flap to characterized the two dimensional behaviour of the separation. The mixture used was composed of paraffin oil (82%), oleic acid (9%) and titanium dioxide (9%).

Pressure measurements Wall pressure measurements were used to characterize the pressure distribution on the ramp for different angles α and β ($-2° \leq \alpha \leq 0°$ and $-22° \leq \beta \leq -6°$). The pressure taps are 0.5 mm in diameter. They were connected with a manual scanivalve and read with a Furness micro-manometer differential sensor (reference FC014, range: 0 to 10 mmH_2O, accuracy : $\pm 0.5\%$ of the measured value in the range 0.01 to 10 mmH_2O). The pressure coefficient C_p ($C_p = \frac{P-P_6}{\frac{1}{2}\rho U_\infty^2}$) was calculated with pressure tap number 6 as reference (i.e. the last in the converging part). The uncertainty is estimated to be $\pm 1.3\%$ for C_p and $\pm 6\%$ for $\frac{dC_p}{ds}$. More details about these uncertainty estimations can be found in Cuvier et al. (2010).

Single hot-wire measurements Single hot-wire measurements were performed on the configuration with $\alpha = -2°$ and $\beta = -22°$ to assess the boundary layer characteristics. The anemometer used was a constant temperature AN 1003 manufactured by AAlabSystems with a boundary layer type hot-wire with a diameter of 2.5 μm and a length of 0.5 mm. The length of the wire used is about 15 wall units, that is slightly too large for highly accurate measurements of turbulent intensity compared to the value recommended by Klewicki and Falco (1990). The calibration of the wire was done in situ at mid height of the wind-tunnel. A pitot tube was set at the same place, separated by 20 cm in span to measure the speed. A King's law was used for the calibration. Each profile is composed of 49 points distributed logarithmically along the wall normal. The first point is about 0.2 mm

from the wall and was measured with a cathetometer at ± 0.05 mm. Based on the study of Carlier and Stanislas (2005), the acquisition frequency was 11 kHz and the cut off frequency was 5 kHz. 1.1 million samples were taken for the first 30 points, 2.2 million for the 14 following, and 4.4 million for the last points. The estimated uncertainty on the mean velocity is about $\pm 1\%$, on the turbulent intensity $\pm 2.8\%$, on the third order moment $\pm 7.2\%$ and on the four order moment $\pm 5.2\%$. More details about these uncertainty estimations can be found in Cuvier et al. (2010).

RESULTS AND DISCUSSION

The wool tufts visualisations, for all the angles α and β tested, have shown that there is no separation on the flat plate. End effects appear near the side walls and grow near the flap to reach 10 cm at the flap articulation when $\alpha = -2^\circ$ and $\beta = -22^\circ$. By combining the results of wool tufts visualisations and spanwise pressure distribution at two stations on the flat plate, it appears that the flow remains two dimensional in the mean over more than 90% of the span. Separation occurs on the flap for β under -19° and $\alpha = -2^\circ$. The end effects are larger on the flap (about 30 cm) due to a stronger pressure gradient. The spanwise homogeneity of the separation was checked by oil film visualisation ($\alpha = -2^\circ$ and $\beta = -22^\circ$). It results that the separation on the flap remains more or less 2D on 70% (i.e. 1400 mm) of the span of the flap and it is fixed at the flap articulation.

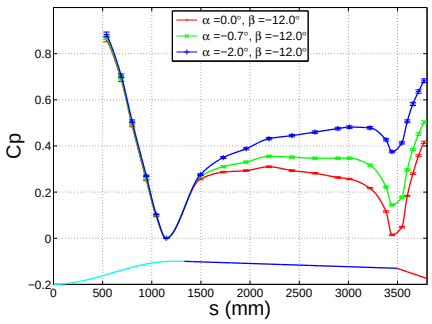

Figure 2. Streamwise pressure coefficient distribution, for different α, $\beta = -12^\circ$ and $U_\infty = 10$ m/s.

Figures 2 and 3 give the pressure coefficient distribution and the pressure gradient distribution for different angles α and $\beta = -12^\circ$. The flow accelerates in the converging part $0 \leq s \leq 1360$ mm (s is the curvilinear coordinate along the ramp) which induces a decrease of the pressure coefficient until the suction peak at $s = 1146$ mm (pressure tap number 6). Then a pressure recovery occurs on the flat plate which is modified by α. At the flap articulation, a new suction peak occurs which can be seen at $s = 3443$ mm corresponding to pressure tap 17. Then a pressure recovery is observed on the flap which can be tuned by β. In the middle of the flat plate, the pressure gradient is almost constant (Figure 3), and a zero pressure gradient is obtained in this 60 cm long area

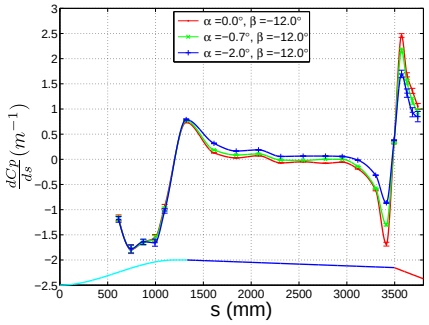

Figure 3. Streamwise pressure gradient distribution, for different α, $\beta = -12^\circ$ and $U_\infty = 10$ m/s.

for $\alpha = -0.7^\circ$, a favourable for $\alpha > -0.7^\circ$ and an adverse for $\alpha < -0.7^\circ$. It was checked that there is no influence of the parameter β on the pressure gradient on the flat plate until $s = 3010$ mm or pressure tap number 14. Figure 4 gives the pressure gradient distribution for $\alpha = -2^\circ$ and $\beta = -22^\circ$, which corresponds to the ramp configuration where the hot-wire profiles were obtained.

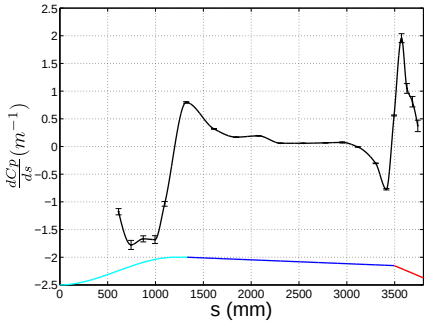

Figure 4. Streamwise pressure gradient distribution, for $\alpha = -2^\circ$, $\beta = -22^\circ$ and $U_\infty = 10$ m/s.

Figure 5 gives the positions on the ramp of the five hot-wire profiles that were carried out on the configuration with $\alpha = -2^\circ$, $\beta = -22^\circ$ and $U_\infty = 10$ m/s. Each profile was repeated several times in order to obtained three coherent profiles that superimposed better than 2%. The boundary layer parameters are given in Table 1. The Reynolds number based on the momentum thickness is of the order of 11 000, that is about the Reynolds number of the LML wind tunnel in flat plate (FP) configuration at 5 m/s. The near wall region of all the profiles obtained can thus be compared to this FP configuration.

The boundary layer thickness δ begins at 17.4 cm at station 1 and grows with s and with the adverse pressure gradient to reach 21.2 cm at station 4. Between stations 4 and 5, the boundary layer thickness decreases as the suction peak in this area introduces favourable pressure gradient. The shape factor H follows the same behaviour as δ. It begins at 1.18 at

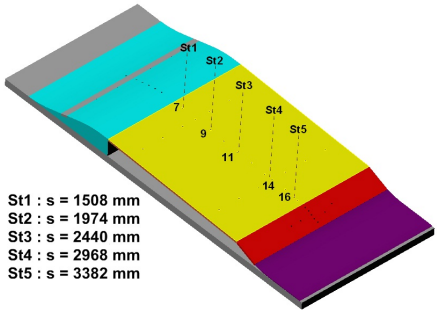

Figure 5. Location of the hot-wire profiles.

Table 1. Boundary layer characteristics at $U_\infty = 10$ m/s, $\alpha = -2°$, $\beta = -22°$.

St	s (mm)	δ (cm)	δ^* (mm)	θ (mm)	Re_θ
St1	1508	17.4	14.4	12.2	10100
St2	1974	19.6	16.5	13.7	10600
St3	2440	20.3	17.9	14.7	11700
St4	2968	21.2	20.3	16.5	12600
St5	3382	19.0	16.4	13.5	10100

St	H	U_e (m/s)	u_τ (m/s)	$(\frac{\partial P}{\partial s})^+$ $(\times 10^3)$	$\beta_{Clauser}$
St1	1.18	12.9	0.482	3.28	1.44
St2	1.21	12.6	0.459	1.47	0.70
St3	1.22	12.5	0.462	0.46	0.24
St4	1.23	12.4	0.435	0.67	0.38
St5	1.21	12.3	0.465	-5.54	-2.56

station 1. This value is coherent with the shape factor of the incoming boundary layer (1.3) on the ramp as it is decreased in the converging part where favourable pressure gradient is encountered.

The friction velocity was determined by fitting equation (1) on the mean velocity profile (Bernard et al., 2003) in adverse pressure gradient (stations 1 to 4) and a log-law in favourable pressure gradient (station 5). Equation (1) is obtained by integrating the inner boundary layer equation and by supposing that the mixing length theory remains valid for adverse pressure gradient boundary layer. The constant of integration C2 is obtained by identifying equation (1) with the standard log-law as the term $(\frac{\partial P}{\partial x})^+ y^+$ becomes small compare to 1. C2 is given by equation (2). κ was taken as 0.41 and C as 5.0. The advantage of this equation compare to the log-law is that it presents a curvature that follows better the mean velocity profile. To optimize the fit, the value y_0 of the first point was adjusted in its uncertainty interval.

$$U^+ = \frac{1}{\kappa}(2\sqrt{1+(\frac{\partial P}{\partial x})^+ y^+} + \ln|\sqrt{1+(\frac{\partial P}{\partial x})^+ y^+} - 1| - \ln(\sqrt{1+(\frac{\partial P}{\partial x})^+ y^+} + 1)) + C2 \quad (1)$$

$$C2 = -\frac{1}{\kappa}(2 - \ln(2) + \ln\frac{1}{2}|(\frac{\partial P}{\partial x})^+|) + C \quad (2)$$

The uncertainty on δ is about $\pm 10\%$, and on δ^*, θ and u_τ about $\pm 5\%$. The uncertainty on U_e is $\pm 0.6\%$. The uncertainties on the pressure parameters are then higher of about $\pm 20\%$ due mostly to the uncertainty on the pressure gradient and on u_τ.

As was introduce by Castillo and George (2001), the boundary layer is in equilibrium state if the free-stream velocity is proportional to the boundary layer thickness at power $-\Lambda$ with $\Lambda = \frac{\delta}{\rho U_e^2 \frac{d\delta}{dx}} \frac{dP}{dx}$. This was checked for the first four stations that are in adverse pressure gradient. $\ln(U_e)$ versus $\ln(\delta)$ is almost linear with $\Lambda = 0.2$, close to the value of 0.22 observed by these authors for adverse pressure gradient. The boundary layer seems then to be in an equilibrium state as defined by Castillo and George (2001), for the first four stations.

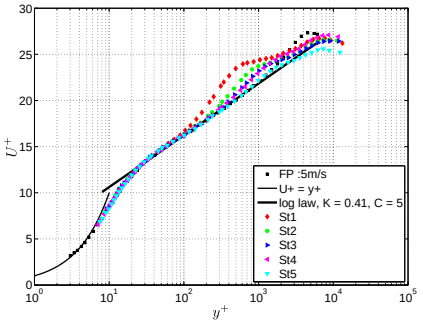

Figure 6. Mean velocity profiles, $\alpha = -2°$, $\beta = -22°$ and $U_\infty = 10$ m/s.

Figure 6 shows the five mean velocity profiles obtained along the ramp in wall units and compared to the FP at 5 m/s. The profiles begin at $y^+ = 9$ for stations 1 to 3, and at $y^+ = 7.5$ for stations 4 and 5 (corresponding to $y \simeq 0.2$ mm). For the three first stations, the probe was not approached nearer to the wall as vibrations were observed and measured by an acceleration sensor stuck on the wall. The displacement was obtained by integrating twice the output of the acceleration sensor. Samples of 10 s were acquired for each station at 11 kHz with a cut-off frequency at 5 kHz to allow to compute spectrum and statistics. The amplitude (estimated by 2σ, with σ the standard deviation) of these vibrations is about 0.5 wall units for stations 1 and 5, and 2 wall units for stations 2 to 4. As these vibrations have an amplitude less than two wall units and their frequencies are small (under 20 Hz), the flow is not affected.

All the profiles collapse for $8 \leq y^+ \leq 100$. This is coherent with the theory as the Reynolds number is almost the same and the pressure gradient is negligible in this region (In equation (1), the term $(\frac{\partial P}{\partial x})^+ y^+$ is smaller than 0.1 for the five stations so negligible compared to 1). The log region extension increases by the decrease of the strength of the adverse pressure gradient from stations 1 to 4. This is not surprising as the shrink of the log region with the strength of the adverse pressure gradient has also been observed by other authors (Aubertine and Eaton, 2005; Bernard et al., 2003;...). After $y^+ > 2000$, the profiles of stations 1 to 4 seem to collapse. This lets supposing that u_τ can be the appropriate external velocity scale. This contradicts the theory of Castillo

and George (2001).

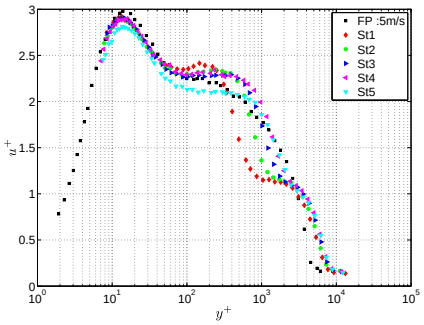

Figure 7. Turbulent intensity profiles, $\alpha = -2°$, $\beta = -22°$ and $U_\infty = 10$ m/s.

Figure 7 shows the evolution of the turbulence intensity profile along the ramp in wall units. The y^+ axis is logarithmic to show in the same plot the near wall region and the region away from the wall. Except for station 5 and FP, all the profiles collapse for $8 \leq y^+ \leq 40$. A first peak of turbulence is observed for all the profiles at $y^+ \simeq 14$ which is characteristic of near wall turbulence. This peak has a value of 2.9 which is slightly smaller than the FP case. This can be attributed to the averaging over the length of the hot-wire (Klewicki and Falco, 1990). The value is smaller at station 5 because the pressure gradient is favourable at this station and tends to attenuate turbulence.

A second peak is observed at the first four stations, around $y^+ \simeq 150$ at station 1, and moving away from the wall with s, to reach $y^+ \simeq 350$ at station 4. This peak is replaced by a plateau at station 5 and for the FP case. This second peak is accompanied with a knee point at $y^+ \simeq 2000$ for the first four stations. The second peak and the knee point were also observed by Webster et al. (1996), Wu and Squires (1998), Baskaran et al. (1987), etc.. The knee point is attributed by Webster et al. (1996) to a proof that a new internal layer near the wall has been triggered in the converging part by the change in curvature. The second peak on the profiles is then attributed to a remnant of the upstream internal layer.

Here, this interpretation is questionable as the knee point seems to stay at the same position. This knee point seems more related to the external turbulence intensity of the incoming boundary layer that has been seriously attenuated by the favourable pressure gradient encounter in the converging part. The second peak in the turbulence intensity profiles is then interpreted as an instability triggered by the change of sign of the pressure gradient near pressure tap 6. This is more coherent because the pressure gradient effects becomes non-negligible in the equations after $y^+ \simeq 100$ in the present study, that is near the position of the second turbulence peak at station 1. The first turbulence peak is not attenuated in the converging part as the pressure gradient effects is small in the near wall region. This first peak is then only governed by the shear due to the wall. This explain why it scale in wall units. In Webster et al. (1996) study, the same explanations on the turbulence intensity profiles seems to apply as it seems that the first turbulence peak that they found scales with wall units. However, contrary to the present study, they found that the first peak position moves away from the wall with the streamwise position. This differences in conclusion can be explain by the difference in the strength of their pressure gradient (compared to the present study, their pressure gradient $\frac{\partial P}{\partial x}^+$ is ten time larger).

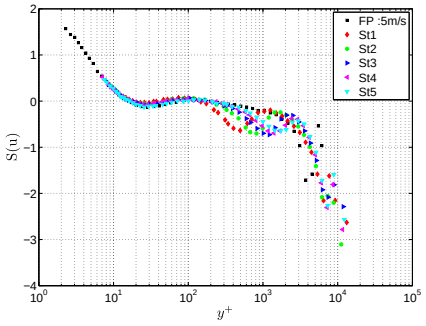

Figure 8. Skewness profiles, $\alpha = -2°$, $\beta = -22°$ and $U_\infty = 10$ m/s.

Figure 8 shows the skewness profiles for the five stations in wall units compared to the FP case. All profiles superimpose with the FP case below $y^+ \simeq 200$. The skewness decreases with y^+ to reach zero at $y^+ \simeq 14$. After it stays constant near zero in the logarithmic region and decreases in the wake region. Contrary to the FP case, it shows a minimum at $y^+ \simeq 500$ for station 1, which moves away from the wall to $y^+ \simeq 1700$ at station 5. After this minimum, all the profiles superimpose with the FP case. The positive values of the skewness under $y^+ \simeq 14$ are the result of wall intermittency (low and high speed streaks, ejections and sweeps). The negative values of the skewness in the wake region are the result of external intermittency. The minimum of skewness near $y^+ \simeq 500$ to 1700 is clearly related again to the instability triggered near pressure tap 6.

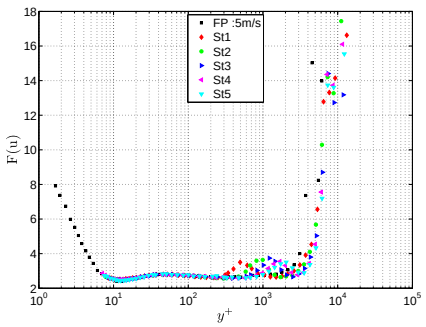

Figure 9. Flatness profiles, $\alpha = -2°$, $\beta = -22°$ and $U_\infty = 10$ m/s.

Figure 9 shows the flatness profiles for the five stations in wall units compared to the FP case. All the profiles superimpose for $y^+ \leq 300$. The flatness decreases from the wall with y^+, to reach a minimum at $y^+ \simeq 14$. Then it slightly increases to reach a value around 2.6 - 2.7 in the logarithmic region. After, the flatness profiles for the five stations differ from the FP case. Indeed, a peak appears around $y^+ \simeq 500$ for station 1, which moves away from the wall with s to reach $y^+ \simeq 2000$ at station 5. This peak is clearly related again to the instability triggered near pressure tap 6. After this second peak, the flatness increases strongly at all five stations, due to intermittency, and superimpose with the FP case.

CONCLUSIONS

The flow characterisation of a two dimensional ramp is presented. Zero, favourable and adverse pressure gradients can be obtained on the flat plate at respectively $\alpha = -0.7°$, $\alpha > -0.7°$ and $\alpha < -0.7°$. A separation occurs on the flap for $\beta = -19°$ and $\alpha = -2°$. The flap adverse pressure gradient tuned by β has no significant effects on the flat plate pressure distribution fixed by α, except on the suction peak just before the flap articulation. The amplitude of this suction peak is characteristic of the separation.

A configuration of the ramp with a mild adverse pressure gradient on the flat plate and a flow separation on the flap is obtained for $\alpha = -2°$, $\beta = -22°$ and $U_\infty = 10$ m/s. This configuration has been characterized more precisely with single hot-wire anemometry. It appears that the boundary layer thickness is around 20 cm, the shape factor is around 1.2 and the Reynolds number based on θ is about 11 000 and is of the same order as for the FP case at $U_\infty = 5$ m/s. The mean velocity profiles exhibit a log region that shrinks with the adverse pressure gradient strength. The existence of a log region was used to estimate the value of the friction velocity with a modified log-law (equation (1)).

The turbulent intensity profiles obtained present two peaks, one near $y^+ = 14$ and one near $y^+ = 150$ at station 1. This second peak moves away from the wall with s. The first peak is attributed to standard near wall turbulence as its scales in wall units. The second one is attributed to an instability triggered by the change of sign of the pressure gradient in the converging part near pressure tap 6. The knee-point in all the turbulence profiles at $y^+ \simeq 2000$ is attributed to a remnant of the external turbulence intensity of the incoming boundary layer that has been seriously attenuated by the favourable pressure gradient encountered in the converging part.

On the skewness and flatness profiles, a local extremum is observed near $y^+ = 500$ at station 1 that moved away from the wall with s. This local extremum is also attributed to the instability triggered by the change of sign of the pressure gradient in the converging part near pressure tap 6.

ACKNOWLEDGEMENTS

The authors would like to thank the European Communauty for their financial support under the contract AVERT/RTD REG/H.3(2006)A/142121. The International Campus on Safety and Intermodality in Transportation (CISIT) is also acknowledge for their financial support.

REFERENCES

Angele, K. P. and Muhammad-Klingmann, B. (2006). Piv measurements in a weakly separating and reattaching turbulent boundary layer. *European Journal of Mechanics B/Fluids*, 25:204–222.

Aubertine, C. D. and Eaton, J. K. (2005). Turbulence development in a non-equilibrium turbulent boundary layer with mild adverse pressure gradient. *Journal of Fluid Mechanics*, 532:345–364.

Baskaran, V., Smits, A. J., and Joubert (1987). A turbulent flow over a curved hill. part 1. growth of an internal boundary layer. *Journal of Fluid Mechanics*, 182:47–83.

Bernard, A., Foucaut, J. M., Dupont, P., and Stanislas, M. (2003). Decelerating boundary layer: A new scaling and mixing length model. *AIAA Journal*, 41(2):248–255.

Carlier, J. and Stanislas, M. (2005). Experimental study of eddy structures in a turbulent boundary layer using particule image velocimetry. *Journal of Fluid Mechanics*, 535(36):143–188.

Castillo, L. and George, W. K. (2001). Similarity analysis for boundary layer with pressure gradient : outer flow. *AIAA journal*, 39(1):41–47.

Clauser, F. H. (1954). The turbulent boundary layer in adverse pressure gradient. *Journal of the aeronautical sciences*, 21:91–108.

Clauser, F. H. (1956). The turbulent boundary layer. *Adv Appl Mech*, 4:1–51.

Cuvier, C., Braud, C., Foucaut, J., and Stanislas, M. (2010). Flow characterisation and parametric study of passive and active vortex generators on the lml-avert ramp. Technical report, AVERT.

Elsberry, K., Loeffler, J., Zhou, M. D., and Wygnanski, I. (2000). An experimental study of a boundary layer that is maintained on the verge of separation. *Journal of Fluid Mechanics*, 423:227–261.

George, W. K. (2005). Recent advancements toward the understanding of turbulent boundary layers. *4th AIAA Theoretical Fluid Mechanics Meeting, 6 - 9 June, Toronto, Canada*, (4669).

Klewicki, J. C. and Falco, R. E. (1990). On accurately measuring statistics associated with small-scales structure in turbulent boundary layers using hot-wire probes. *Journal of Fluid Mechanics*, 219:119–142.

Maciel, Y., Rossignol, K. S., and Lemay, J. (2006). Self-similarity in the outer region of adverse pressure gradient boundary layers. *AIAA paper*, 44:2450–2464.

Talapurkara, E. G., Khosnevis, A. B., and Narasimhan, J. L. (2001). Wake-boundary layer interaction subject to convex and concave curvatures and adverse pressure gradient. *Experiments in Fluids*, 31:697–707.

Webster, D. R., DeGraaff, D. B., and Eaton, J. K. (1996). Turbulence characteristics of a boundary layer on a two-dimensional bump. *Journal of Fluid Mechanics*, 320:53–69.

Wu, X. and Squires, K. D. (1998). Numerical investigation of the turbulent boundary layer over a bump. *Journal of Fluid Mechanics*, 362:229–271.

Zagarola, M. V. and Smits, A. J. (1998). A new mean velocity scaling for turbulent boundary layers. *ASME Fluids Engineering Division Summer Meeting June 21-25, Washington DC*, FEDSM98-4950.

FLOW CONTROL OVER A RAMP USING ACTIVE VORTEX GENERATORS.

C. Cuvier[1,2], **C. Braud**[1,3], **J.M. Foucaut**[1,2], **M. Stanislas**[1,2]
Univ Lille Nord de France[1] F-59000 Lille, EC Lille[2], CNRS[3],
Laboratoire de Mécanique de Lille (UMR 8107)
Boulevard Paul Langevin,
59655 Villeneuve d'Ascq Cédex, France.
christophe.cuvier@gmail.com
caroline.braud@univ-lille1.fr
jean-marc.foucaut@ec-lille.fr
michel.stanislas@ec-lille.fr

ABSTRACT

A parametric study of separation control using continuous jets vortex generators was conducted on a two-dimensional ramp with a mild adverse pressure gradient on a 2 m flat plate and a flow separation on a flap. Two jets diameters were investigated : 6 and 12 mm. For both diameters, co and counter-rotating arrangements were analysed. The control efficiency was quantified by wool-tufts visualisations and by four friction probes placed on the flap. It was found that a skewness of the output voltage of a friction probe greater than -0.4 is characteristic of flow reattachment. Different spacing between jets, different pitch angles, different distances of the jets to the separation line and different VR were tested. The best configuration obtained is a counter-rotating one, with $\frac{\Phi}{\delta} = 0.03$, $\frac{\lambda}{\Phi} = 27.3$, $\frac{L}{\Phi} = 15$ and $\alpha = 135°$.

Key words : Turbulent boundary layers, adverse pressure gradient, flow separation, control, continuous jets.

INTRODUCTION

Turbulent Boundary Layer (TBL) separation induces by strong adverse pressure gradient (APG) or by sudden discontinuity of curvature can lead to a drop in efficiency of a turbomachinery or to a loss of aircraft control. In a way of improving continuously the performances and the safeness of all the machineries that interact with fluids (aircraft, turbomachineries, cars, etc.), preventing and/or controlling turbulent boundary layer flow separation seems to be a crucial point that has to be solved.

Since the beginning of the 1990s, many studies were performed on flow separation control (see Lin et al., 1990; Lin et al., 1991; Lin, 1999; Selby et al., 1992; McManus et al., 1994; Godard and Stanislas, 2006a; Godard and Stanislas, 2006b; etc.). Flow separation control experiments can be classified in two types. The first one corresponds to passive control strategies (Lin et al., 1990; Lin et al., 1991; Lin, 1999; Godard and Stanislas, 2006a; etc.). The second one concerns active control (Selby et al., 1992; McManus et al., 1994; Godard and Stanislas, 2006b; etc.). The active control strategies can be divided also in two families. The first one concerns steady continuous jets vortex generators (VGs) (Selby et al., 1992; Godard and Stanislas, 2006b; etc.), and the second one concerns unsteady VGs (like pulsed-jets in McManus et al., 1994; etc.). Good reviews of control strategies can be found in GadelHak (2000) and Lin (2002).

For real flow control applications, it seems that the active strategies are the most appropriate as on an aircraft, the actuators can be turned off when they are not necessary, to avoid any additional drag and reactive control (closed-loop) can be achieved. Round jets are popular active VGs (Godard and Stanislas, 2006b; Selby et al., 1992; McManus et al., 1994; etc.). Their control efficiency depends on many parameters such as the diameter, the orientation, the exit velocity, the arrangement (co or counter-rotating), etc. (see Compton and Johnston, 1991 or Godard and Stanislas, 2006b). Moreover, the flow where the actuators is embedded has significant influence on the control results as the adverse pressure gradient tends to increase interactions between vortices and thus decrease the control efficiency (Lin, 2002). This explains the existing disagreement between investigators on the optimal active control parameters.

The experiment presented here was performed on a two dimensional ramp, designed for the AVERT (Aerodynamic Validation of Emission Reducing Technologies) FP6 EC project. The ramp was tuned such as a boundary layer with mild adverse pressure gradient develops on the 2 m flat plate. At the end of this flat plate, there is an imposed separation with a flap which is used to quantified the control efficiency.

THE EXPERIMENT

The wind tunnel facility and the ramp

This parametric active control experiment has been conducted in the LML boundary layer wind tunnel at $U_\infty = 10$ m/s. A boundary layer develops on the 20 m long lower wall

to reach around 30 cm at the end. This thick boundary layer allows good spatial resolution. The test section is 2 m span and 1 m height and the free-stream velocity is ranging from 1 to 10 m/s ($\pm 0.5\%$). In this experiment, the wind tunnel was used in close-loop configuration to allow temperature regulation ($\pm 0.2^{\circ}C$). For detailed characteristics of the wind tunnel, see Carlier and Stanislas (2005).

The ramp model was mounted on the wind tunnel floor such as the beginning of the ramp was 14.4 m downstream of the entrance of the test section. Figure 1 gives a schematic view of the ramp. It is composed of four parts. The first one is a smooth converging part with a contraction ratio of 0.75. The second part is an articulated flat plate of more than 2 m. The angle between this plate and the wind tunnel floor is called α and is counted positive if it corresponds to a positive rotation around the z axis (Figure 1). The angle α tunes the pressure gradient of the boundary layer that develops on the 2.1 m flat plate. α is ranging from 2° to -4°. The third part of the ramp is an other articulated flat plate (called flap). The angle between this plate and the wind tunnel floor is called β and its sign used the same convention as α. β is ranging from -5° to -40°. The aim of the flap is to allow to create and fix a flow separation. The angle β tunes the strength and the extend of the flow separation. The last part is a flexible plate to allow smooth connection between the end of the flap and the floor of the wind tunnel.

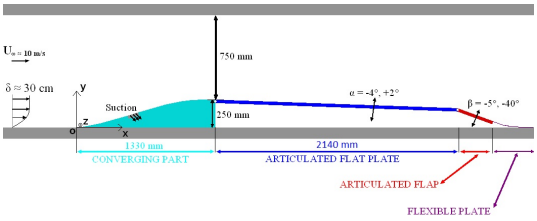

Figure 1. Schematic view of the ramp.

In the present study, the angles α and β were fixed at respectively -2° and -22°. This configuration corresponds to an adverse pressure gradient on the flat plate and a separation on the flap. It was characterized carefully with wall pressure measurements and by 5 hot-wire profiles on the flat plate. Details about the flow characterization of the ramp can be found in Cuvier et al. (2010) and in Cuvier et al. (2011). Figure 2 gives the pressure gradient distribution along the ramp and Table 1 gives the main boundary layer parameters. The separation begin at the flap articulation at $s = 3500$ mm (With s the curvilinear coordinate of the ramp with O as origin (Figure 1)).

Experimental techniques

Different measurement techniques were used to quantified the control efficiency on flow separation.

Wool tufts visualisations Wool tufts visualisations were used on the flap to check visually the separation and its extend. Several lines of wool tufts of 4 cm long were

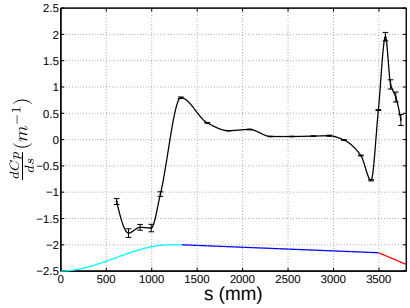

Figure 2. Streamwise pressure gradient distribution, for $\alpha = -2^{\circ}$, $\beta = -22^{\circ}$ and $U_\infty = 10$ m/s.

Table 1. Boundary layer characteristics at $U_\infty = 10$ m/s, $\alpha = -2^{\circ}$, $\beta = -22^{\circ}$.

St	s (mm)	δ (cm)	δ^* (mm)	θ (mm)	Re_θ
St1	1508	17.4	14.4	12.2	10100
St2	1974	19.6	16.5	13.7	10600
St3	2440	20.3	17.9	14.7	11700
St4	2968	21.2	20.3	16.5	12600
St5	3382	19.0	16.4	13.5	10100

St	H	U_e (m/s)	u_τ (m/s)	$(\frac{\partial P}{\partial s})^+$ $(\times 10^3)$	$\beta_{Clauser}$
St1	1.18	12.9	0.482	3.28	1.44
St2	1.21	12.6	0.459	1.47	0.70
St3	1.22	12.5	0.462	0.46	0.24
St4	1.23	12.4	0.435	0.67	0.38
St5	1.21	12.3	0.465	-5.54	-2.56

placed on all the span of the flap and on the flexible plate. The length of the separation is about 80 cm (Figure 3). An example of wool tufts visualisation with a complete suppression of separation by control is shown in Figure 4.

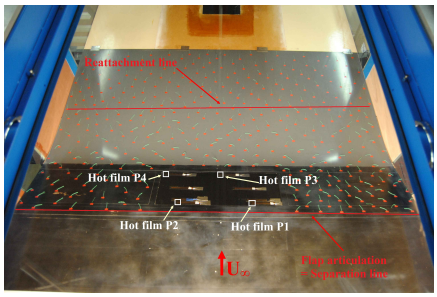

Figure 3. Wool tufts visualisation of the separation, $\alpha = -2^{\circ}$, $\beta = -22^{\circ}$ and $U_\infty = 10$ m/s.

Hot-film friction probes The control effects are assessed quantitatively using four friction probes placed on the flap. The coordinates of these probes are given in Table 2

Figure 4. Example of wool tufts visualisation with control and no separation, $\alpha = -2°$, $\beta = -22°$ and $U_\infty = 10$ m/s.

and are shown in Figure 3. The friction probes that were used are Senflex SF9902 hot film probe. They are 1.5 mm long and they are deposited on a polyamyde substrate with a thickness less than 0.2 mm. They can be glued directly on the surface with 60 μm double-sided tape. As was introduced by Godard and Stanislas (2006a), a hole of 2 mm in diameter and 1 mm in depth was drilled under the sensor to minimize heat losses to the substrate. The probes were connected to a 4 channels AN 1003 anemometer manufactured by AAlabSystems. The acquisition frequency was 11 kHz and the cut-off frequency 5 kHz. Fifteen packets of 10 s were acquired for each measurement to achieve good convergence of the mean value, standard deviation, PDF and spectrum.

An in-situ calibration of the hot film friction probes was not possible. A pseudo calibration based on the calibrations done by Godard and Stanislas (2006b) for the same type of probes was developed. The King's law is for these probes : $E^2 = E_0^2 + b.\tau^n$, where E is the output voltage of the bridge, and τ the wall friction. The parameters to be estimated are E_0, b and n. The pseudo calibration consists in estimating the coefficient of the King's law with $E_{0_{wts}}$, that corresponds to the output voltage of the bridge when the wind tunnel is stopped and at the temperature of calibration ($T_{calibration}$). For all calibrations done by Godard, the value $\left(\frac{E_0}{E_{0_{wts}}}\right)^2$ and $\frac{b}{E_{0_{wts}}^2}$ were computed. It appears that these two values remain almost constants and equal respectively to 0.91 and 0.52. So by measuring only $E_{0_{wts}}$, an estimated value of E_0 and b can be obtained. The parameter n was taken as $\frac{1}{3}$ as Godard found it constant and equal to this value.

A lot of configurations were acquired without control at different temperatures and on different days, to check the repeatability of the method. It can reached around $\pm 10\%$ on different days and $\pm 5\%$ on the same day.

Table 2. Coordinates of the friction probes.

probe	P1	P2	P3	P4
s (mm)	3555	3555	3759	3759
z (mm)	164	-205	0	-286

Hot film friction probes are not sensitive to the flow direction, so they give the absolute value of the wall friction $|\tau|$. The criterion to detect the separation is not as easy as $\tau < 0$ corresponds to separated flow and $\tau > 0$ to attached flow. The criterion that was used to detect separation was build with the variation of $|\tau|$ and the variation of the skewness of the output voltage of the bridge. For flow without control, the PDF of the output voltage of the bridge is not Gaussian and this signal has a skewness between -0.8 and -0.7. When the flow is completely attached (that was verified with wool tufts visualisations), the PDF of the output voltage of the bridge tends to be Gaussian. The skewness is between -0.4 and 0. A skewness greater than -0.4 was then considered as an attached flow.

Flow rate regulation and quantification circuit The jets were supplied with filtered and dried compressed air through a regulation and quantification circuit and a 90 liters tank. The compressed air circuit is provided with a pressure regulator and a progressive valve to allow to tune the flow rate. The flow rate is measured by an adequate vortex meter. Finally, the pressure and the temperature of the compressed air are measured to access the density. The regulation and quantification circuit allows to measure the mass flow rate of the jets at less than $\pm 2\%$ for $2 \leq Q_v \leq 560\ m^3/h$.

Tests description

Figures 5 and 6 illustrate the definition of the different parameters of the jets. The jets parameters tested were chosen based on the study of Godard and Stanislas (2006b). Two diameters of jets were tested : 6 and 12 mm, corresponding respectively to $\frac{\Phi}{\delta} = 0.03$ and 0.06. Both co-rotating and counter-rotating arrangements were used. The skew angle β (see Figures 5 and 6) was fixed at 45°, and two values of the pitch angle α (see Figures 5 and 6) were tested : $\alpha = 45°$ (downstream blowing) and $\alpha = 135°$ (upstream blowing). Tests were performed at two distances from the separation line : $s = 3383$ mm (station 1) and $s = 3219$ mm (station 2). These stations correspond to $\frac{\Delta X_{vg}}{\delta} = 0.6$ and 1.4, with ΔX_{vg} the distance between the jets position and the separation line ($s = 3500$ mm). At station 1, $\delta = 19$ cm and at station 2, δ was estimated at 20.2 cm.

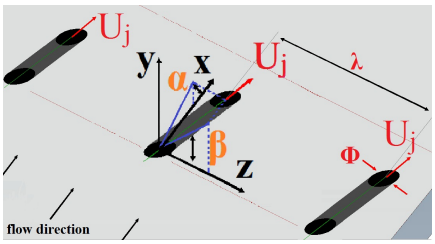

Figure 5. Co-rotating jet parameters.

For the co-rotating configurations, for each jet diameter, two values of $\frac{\lambda}{\Phi}$ were tested : 6.8 and 13.6 for $\Phi = 12$ mm, and 13.6 and 27.2 for $\Phi = 6$ mm. For $\Phi = 12$ mm, and upstream blowing, $\frac{\lambda}{\Phi} = 20.4$ and 27.2 were also tested. For the counter-rotating configurations, two values of $\frac{\lambda}{\Phi}$ were tested : 27.3 and 54.6. The $\frac{L}{\Phi}$ parameter was chosen as 15. For $\Phi = 12$ mm,

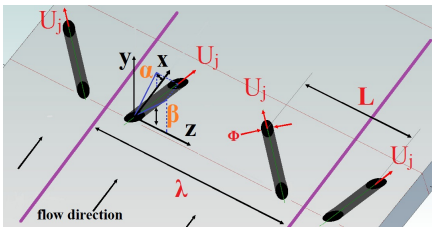

Figure 6. Counter-rotating jet parameters.

$\frac{L}{\Phi} = 12.3$ was also tested.

The velocity ratio VR tested for each configuration varies between 0.5 and 3.5 by steps of 0.5. VR is defined by $VR = \frac{U_{mean}}{U_e}$, where U_{mean} is the mean jets exit velocity and U_e the local free-stream velocity. For $\Phi = 12$ mm, it was found that $U_j = 1.2U_{mean}$ and for $\Phi = 6$ mm, it was found that $U_j = 1.236U_{mean}$, with U_j the maximum exit velocity of the jets. The differences between jets were checked. For VR between 0.5 to 5, it was found less than $\pm 10\%$ differences on the maximum jet exit velocity for $\Phi = 12$ mm and $\pm 2\%$ for $\Phi = 6$ mm. The actuators were placed on the full 2 m span of the ramp. Tables 3 and 4 give a summary of all the tests that were carried out. Each configuration tested (i.e. one Φ, one α, one $\frac{\Delta X_{vg}}{\Phi}$ one $\frac{\lambda}{\Phi}$ and one $\frac{L}{\Phi}$) has been numbered case 1 to 44. More details can be found in Cuvier et al. (2010).

Table 3. List of the co-rotating control cases tested.

Φ	β	α	$\frac{\Delta X_{vg}}{\Phi}$	$\frac{\lambda}{\Phi}$	VR
6	45	45, 135	19.5, 46.8	13.6, 27.2	0.5-3.5
12	45	45, 135	9.8, 23.4	6.8, 13.6[1]	0.5-3.5

Table 4. List of the counter-rotating control cases tested.

Φ	β	α	$\frac{\Delta X_{vg}}{\Phi}$	$\frac{\lambda}{\Phi}$	$\frac{L}{\Phi}$	VR
6	45	45, 135	19.5, 46.8	27.3, 54.6	15	0.5-3.5
12	45	45, 135	9.8, 23.4	27.3, 54.6	12.3, 15	0.5-3.5

RESULTS AND DISCUSSION

For all the tests carried out, for the same vortex generators (VGs) configuration at $\frac{\Delta X_{vg}}{\delta} = 0.6$ and 1.4, no difference was observed. Maybe the investigated values of $\frac{\Delta X_{vg}}{\delta}$ were to small to make a difference as Godard and Stanislas (2006b) found that active jets VGs are efficient for $\frac{\Delta X_{vg}}{\delta} = 7.2$ and Lin et al. (1990) for $\frac{\Delta X_{vg}}{\delta} = 40$, so much further away. It can also be concluded that there is no effect of $\frac{\Delta X_{vg}}{\Phi}$ in the investigated interval (i.e. between 9.8 to 46.8).

Figures 7 and 8 give respectively the gain in friction and the skewness with VR, versus the spanwise position z,

[1]For $\alpha = 135°$, $\frac{\lambda}{\Phi} = 20.4$ and 27.2 were also tested.

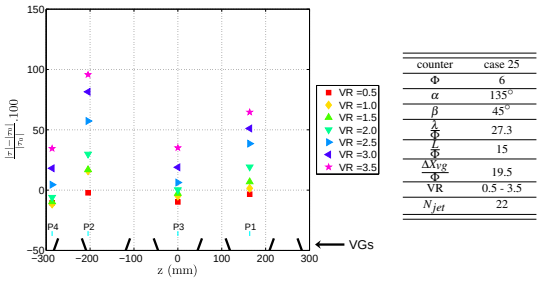

counter	case 25
Φ	6
α	135°
β	45°
$\frac{\lambda}{\Phi}$	27.3
$\frac{L}{\Phi}$	15
$\frac{\Delta X_{vg}}{\Phi}$	19.5
VR	0.5 - 3.5
N_{jet}	22

Figure 7. Gain in friction for case 25 and different VR.

for case 25, corresponding to a counter-rotating configuration with $\Phi = 6$ mm, $\alpha = 135°$, $\frac{\lambda}{\Phi} = 27.3$, $\frac{L}{\Phi} = 15$ and $\frac{\Delta X_{vg}}{\delta} = 0.6$. The position of the friction probes used (Table 2) are represented. A schematic view of the jets axis position projected in (oyz) plane is represented at the bottom of the figures. The beginning of the lines corresponds to the spanwise jets position. In all the following figures, the same scale is used to allow comparisons between the different cases. For case 25, the skewness (so the efficiency of control) continuously increases with VR for probes P1 and P2. For probes P3 and P4, it increases after $VR = 2.5$. This means that the separation is first delayed and then suppressed. The same behaviour is observed on the gain in friction (Figure 7). At $VR = 3.5$, the separation is totally suppressed and, for all the friction probes, the skewness is constant around -0.2, but the gain in friction is not constant. This explains the choice of the skewness as a criterion rather than the gain in friction.

Using only wool tufts visualisations, an optimum of VR higher than 3.5 was looked for in case 25. At VR around 10 the separation was also totally suppressed. For all the test cases with upstream blowing ($\alpha = 135°$), the same behaviour as case 25 was observed. For upstream blowing, the efficiency of control continuously increases with VR, however, to obtain visible effects on the wool tufts, a value of VR greater than 1.5 is needed. This is in agreement with previous study of Godard and Stanislas (2006b), Betterton et al. (2000), McManus et al. (1994) and Selby et al. (1992).

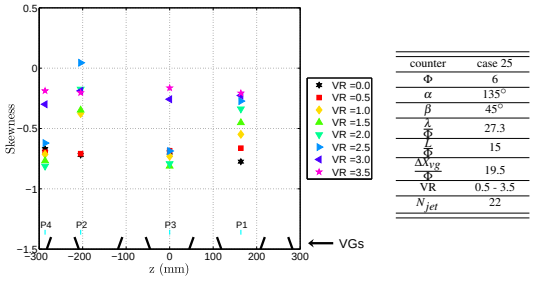

counter	case 25
Φ	6
α	135°
β	45°
$\frac{\lambda}{\Phi}$	27.3
$\frac{L}{\Phi}$	15
$\frac{\Delta X_{vg}}{\Phi}$	19.5
VR	0.5 - 3.5
N_{jet}	22

Figure 8. Skewness for case 25 and different VR.

Figure 9 gives the skewness for different VR, versus the

spanwise position z, for case 27. This case differs from case 25 only by α ($\alpha = 45°$, i.e. downstream blowing). In this case, to obtain visible effects on the wool tufts, a value of VR greater than 1.5 is also needed. The skewness increases with VR (probe P1 and P2) until $VR = 1.5 - 2.5$, then it decreases. It seems then that there is an optimum VR between 1.5 and 2.5 for downstream blowing. This is surprising as it seems to has never been observed. Upstream blowing appears then to be more robust than downstream blowing as VR can be continuously increased to increase the control efficiency.

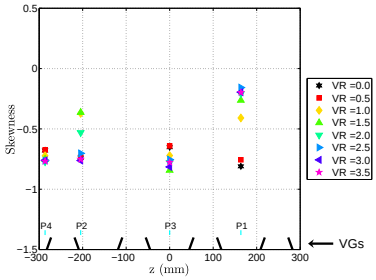

counter	case 27
Φ	6
α	45°
β	45°
$\frac{\lambda}{\Phi}$	27.3
$\frac{L}{\Phi}$	15
$\frac{\Delta X_{vg}}{\Phi}$	19.5
VR	0.5 - 3.5
N_{jet}	22

Figure 9. Skewness for case 27 and different VR.

For the co-rotating cases with $\frac{\lambda}{\Phi} = 6.8$, the control results were contentious as the wool tufts took the jets direction. An other flow is then created that does not correspond to a good control result. The parameter $\frac{\lambda}{\Phi}$ for co-rotating VGs has to be greater than 6.8. Figure 10 gives the skewness for case 7 with $VR = 2.5$ and for case 8 with $VR = 3.5$. The scheme of the jets corresponds to case 8. These cases correspond to co-rotating upstream blowing configurations with $\Phi = 6$. The result are almost the same. For case 7 and $VR = 2.5$, $Q_{v_7} = 69m^3/h$ and $C_{\mu_7} = 0.023$, and for case 8 and $VR = 3.5$, $Q_{v_8} = 48m^3/h$ and $C_{\mu_3} = 0.024$, with Q_v the volumetric flow rate and C_μ the momentum coefficient ($C_\mu = \frac{\rho_{jet} \cdot N_{jet} \cdot S_{jet} \cdot U^2_{mean}}{\frac{1}{2} \cdot \rho_e \cdot \Delta z \cdot \delta \cdot U^2_e}$, with ρ_{jet} the density of the jet, ρ_e the density in the wind tunnel, N_{jet} the number of jets, S_{jet} the cross section of a jet, Δz the span of control and δ the boundary layer thickness). Case 8 with $\frac{\lambda}{\Phi} = 27.2$ seems to give better result at constant Q_v or C_μ, however, to obtain a complete suppression of the separation for case 8, a velocity ratio of 5.5 is needed, which is unrealistic for aircraft or car applications. For the other tests of $\frac{\lambda}{\Phi}$ for the co-rotating arrangement, almost the same results were obtained. It was concluded that the optimum value of $\frac{\lambda}{\Phi}$ is about 13.6 for co-rotating VGs that is two times greater than Godard and Stanislas (2006b) one.

For the counter-rotating VGs, the cases with $\frac{\lambda}{\Phi} = 54.6$ need a VR greater than 6 in upstream blowing configuration to suppress totally the separation, which is unrealistic. For the corresponding cases with downstream blowing, no total suppression of the separation was achieved. It was concluded that $\frac{\lambda}{\Phi} = 27.3$ is the best value for counter-rotating jets.

Figure 11 gives the skewness for case 21 and 37 with $VR = 3.5$. The difference between these two cases is the parameter $\frac{L}{\Phi}$. The scheme of the jets corresponds to case 37. Case 37 gives better result. The parameter $\frac{L}{\Phi} = 12.3$ is then

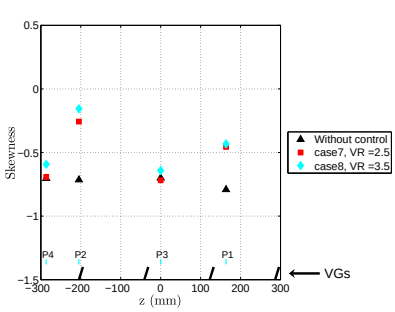

co	case 7
Φ	6
α	135°
β	45°
$\frac{\lambda}{\Phi}$	13.6
$\frac{\Delta X_{vg}}{\Phi}$	19.5
VR	2.5
N_{jet}	22

co	case 8
Φ	6
α	135°
β	45°
$\frac{\lambda}{\Phi}$	27.2
$\frac{\Delta X_{vg}}{\Phi}$	19.5
VR	3.5
N_{jet}	11

Figure 10. Skewness for case 7 and $VR = 2.5$, and for case 8 and $VR = 3.5$.

better than 15. However, no result is observed on probe P3. The spacing between two pairs of VGs are too large. The value of $\frac{\lambda}{\Phi}$ has then to be reduced. This suggests that the optimum value of $\frac{\lambda}{\Phi}$ has to be smaller than $2\frac{L}{\Phi}$. The parameter $\frac{L}{\Phi} = 12.3$ seems to be better than 15, but as $\frac{\lambda}{\Phi}$ has to be decreased to obtain a spanwise uniform control, more jets are needed, so more flow rate. The configuration $\frac{\lambda}{\Phi} = 27.3$ and $\frac{L}{\Phi} = 15$ is then an efficient compromise and can be considered near optimum. The optimum interval between 12.5 and 16 for $\frac{L}{\Phi}$ found by Godard and Stanislas (2006b) is then confirmed by the present study.

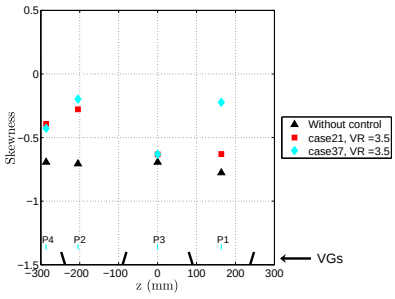

counter	case 21
Φ	12
α	135°
β	45°
$\frac{\lambda}{\Phi}$	27.3
$\frac{L}{\Phi}$	15
$\frac{\Delta X_{vg}}{\Phi}$	9.8
VR	3.5
N_{jet}	10

counter	case 37
Φ	12
α	135°
β	45°
$\frac{\lambda}{\Phi}$	27.3
$\frac{L}{\Phi}$	12.3
$\frac{\Delta X_{vg}}{\Phi}$	9.8
VR	3.5
N_{jet}	12

Figure 11. Skewness for case 21 and 37, $VR = 3.5$.

The effects of the parameter $\frac{\Phi}{\delta}$ was also investigated. At constant VR, except for the co-rotating configurations with $\Phi = 12$ mm and upstream blowing, for all the configurations investigated, the configurations with $\frac{\Phi}{\delta} = 0.03$ give better or comparable results. Looking at the flow rate or C_μ, as between $\frac{\Phi}{\delta} = 0.06$ and $\frac{\Phi}{\delta} = 0.03$ configurations, the total cross section is divided by 2, for all the configurations tested, the parameter $\frac{\Phi}{\delta} = 0.03$ is the best one.

Figure 12 compares the results of the optimum counter-rotating and the optimum co-rotating configuration found. The counter-rotating gives better results. Finally, for the same jets diameter, the optimum co and counter-rotating configurations have the same number of jets for 2 m span.

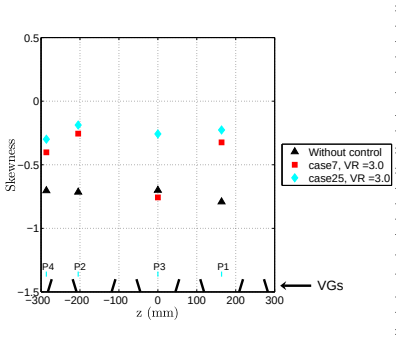

co	case 7
Φ	6
α	135°
β	45°
$\frac{\lambda}{\Phi}$	13.6
$\frac{\Delta X_{vg}}{\Phi}$	19.5
VR	3
N_{jet}	22

counter	case 25
Φ	6
α	135°
β	45°
$\frac{\lambda}{\Phi}$	27.3
$\frac{L}{\Phi}$	15
$\frac{\Delta X_{vg}}{\Phi}$	19.5
VR	3
N_{jet}	22

Figure 12. Skewness for case 7 and 25, $VR = 3$.

CONCLUSIONS

A parametric study of active jets VGs base on the study of Godard and Stanislas (2006b) has been conducted on a ramp with a mild adverse pressure gradient and a flow separation on a flap. Both counter and co-rotating arrangements were tested. Two diameters of jets were analysed : $\Phi = 6$ and 12 mm. The control efficiency is characterized by wool tufts visualisations and four friction probes on the flap. The adapted reattachment criterion for friction probes is a skewness of the output voltage greater than -0.4.

It results that there is no effect of $\frac{\Delta X_{vg}}{\delta}$ in the investigated interval between 0.6 and 1.4. The minimum of VR to obtain visible effects on wool tufts is 1.5. For upstream blowing, it was found that the efficiency of control continuously increased with VR, whereas for downstream blowing an optimum exist between 1.5 and 2.5. Upstream blowing is then more robust as the maximum available control efficiency is higher.

For co-rotating configurations, it was found that the optimum of $\frac{\lambda}{\Phi}$ is 13.6, and for counter-rotating configurations, it was found that $\frac{\lambda}{\Phi}$ has to be smaller than $2\frac{L}{\Phi}$. It was also confirmed that the optimum value for $\frac{L}{\Phi}$ is between 12.3 and 16 and the configuration with $\frac{L}{\Phi} = 15$ and $\frac{\lambda}{\Phi} = 27.3$ is then a good compromise.

Finally the best $\frac{\Phi}{\delta}$ found is 0.03, as at constant VR, the configurations with the smaller diameter ($\frac{\Phi}{\delta} = 0.03$) tested give results comparable to the corresponding one with $\frac{\Phi}{\delta} = 0.06$ but with less flow rate.

Table 5 gives a summary of the optimum parameters for co and counter-rotating configurations found. The best of all configurations investigated is the counter-rotating one, $\frac{\Phi}{\delta} = 0.03$, $\frac{\lambda}{\Phi} = 27.3$, $\frac{L}{\Phi} = 15$ and $\alpha = 135°$ (in bold in Table 5).

Table 5. Optimum parameters for co and counter-rotating configuration tested.

	$\frac{\Phi}{\delta}$	β	α	$\frac{\lambda}{\Phi}$	$\frac{L}{\Phi}$	VR
co	0.03	45	45	13.6	-	2
	0.03	45	135	13.6	-	3.5
counter	0.03	45	45	27.3	15	2
	0.03	**45**	**135**	**27.3**	**15**	**3.5**

ACKNOWLEDGEMENTS

The authors would like to thank the European Communauty for their financial support under the contract AVERT/RTD REG/H.3(2006)A/142121. The International Campus on Safety and Intermodality in Transportation (CISIT) is also acknowledge for their financial support.

REFERENCES

Betterton, J. G., Hackett, K. C., Ashill, P. R., J.Wilson, M., Woodcock, I. J., Tilmann, C. P., and Langan, K. J. (2000). Laser doppler anemometry investigation on sub-boundary layer vortex generators for flow control, in: 10th intl. symp. on appl. of laser tech. to fluid mech. Lisbon.

Carlier, J. and Stanislas, M. (2005). Experimental study of eddy structures in a turbulent boundary layer using particule image velocimetry. *Journal of Fluid Mechanics*, 535(36):143–188.

Compton, D. and Johnston, J. (1991). Streamwise vortex production by pitched and skewed jets in a turbulent boundary layer. *AIAA paper*, 91-0038.

Cuvier, C., Braud, C., Foucaut, J., and Stanislas, M. (2010). Flow characterisation and parametric study of passive and active vortex generators on the lml-avert ramp. Technical report, AVERT.

Cuvier, C., Braud, C., Foucaut, J., and Stanislas, M. (2011). Characterization of a separated turbulent boundary layer for flow control purpose. *Seventh International Symposium on Turbulence and Shear Flow Phenomena, July 28 - 31, Ottawa*.

GadelHak, M. (2000). *Flow Control : passive, active and reactive flow management*. Cambridge.

Godard, G. and Stanislas, M. (2006a). Control of a decelerating boundary layer. part 1: Optimization of passive vortex generators. *Aerospace Science and Technology*, 10(3):181–191.

Godard, G. and Stanislas, M. (2006b). Control of a decelerating boundary layer. part 3: Optimization of round jets vortex generators. *Aerospace Science and Technology*, 10(6):455–464.

Lin, J. C. (1999). Control of turbulent boundary layer separation using microvortex generators. *AIAA Paper*, (99-3404).

Lin, J. C. (2002). Review of research on low-profil vortex generators to control boundary layer separation. *Progress in Aerospace Sciences*, 38:389–420.

Lin, J. C., Howard, F. G., and Bushnell, D. M. (1990). Investigation of several passive and active methods for turbulent flow separation control, in: 21st fluid dynamics, plasma dynamics and lasers conference. *AIAA*, (paper 90-1598).

Lin, J. C., Selby, G. V., and Howard, F. G. (1991). Exploratory study of vortex-generating devices for turbulent flow separation control, in: 29th aerospace sciences meeting, january 7−10, reno, nevada. *AIAA*, (paper 91-0042).

McManus, K. R., Joshi, P. B., Legner, H. H., and Davis, S. J. (1994). Active control of aerodynamic stall using pulsed jet actuators. *AIAA paper*, 94:2218.

Selby, G. V., Lin, J. C., and Howard, F. G. (1992). Control of low-speed turbulent separated flow using jet vortex generators. *Experiments in Fluids*, 12:394–400.

Résumé étendu

Le contrôle d'écoulement permet d'éliminer le phénomène de décollement de couches limites, très néfaste pour les performances des machines interagissant avec un fluide (avions, voitures, turbomachines ...). Dans ces travaux, nous nous intéressons plus particulièrement au contrôle actif d'écoulement au moyen de jets continus. Une maquette permettant de manipuler l'équilibre de la couche limite a été conçue et installée dans la soufflerie du Laboratoire de Mécanique de Lille. Celle-ci permet de créer, sur une plaque plane articulée de 2m de long, un écoulement avec un gradient de pression adverse, nul ou favorable, éventuellement suivi d'un décollement sur le volet. Un schéma de la maquette est donné en Figure 1.

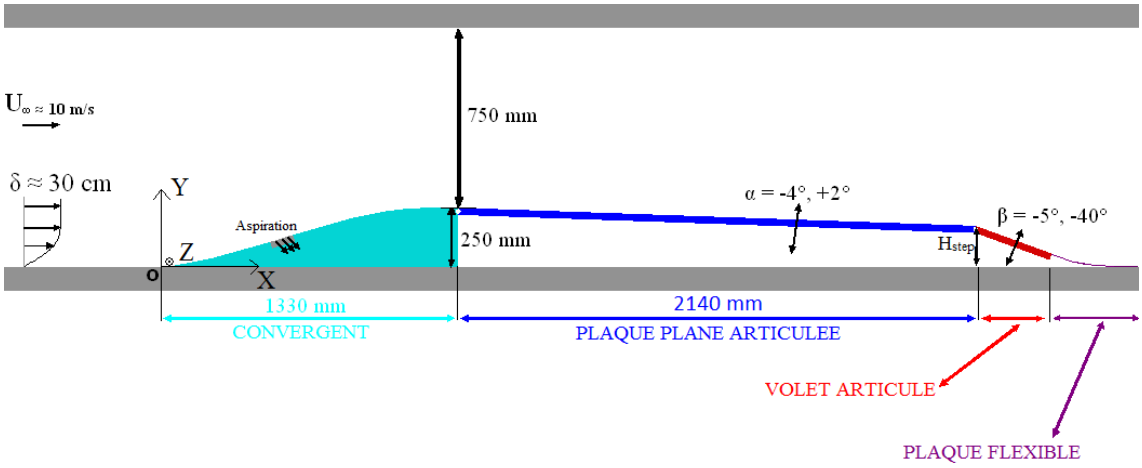

FIGURE 1 – Schéma de la maquette.

La première partie du travail a consisté à caractériser rapidement l'écoulement autour du modèle à l'aide de visualisations par fils de laine et de mesures de répartitions de pression, afin de définir la configuration de la maquette la plus appropriée pour les études de contrôle. Il ressort de ces premiers tests, que le gradient de pression qui s'établit sur la plaque plane est favorable pour $\alpha > -0.7°$, nul pour $\alpha = -0.7°$ et adverse pour $\alpha < -0.7°$. Finalement, pour α fixé à $-2°$, un décollement apparaît sur le volet pour β inférieur à $-19°$. La configuration retenue pour les tests de contrôle est $\alpha = -2°$ et $\beta = -22°$. Elle correspond à un écoulement en léger gradient de pression adverse sur la plaque plane suivi d'une séparation sur le volet, assez intense pour être correctement détectable grâce à une visualisation par fils de laine. Cette configuration produit un écoulement assez similaire à celui sur l'extrados d'une aile d'avion. Une caractérisation plus poussée de cette configuration a ensuite été effec-

tuée à l'aide d'une visualisation par enduit gras et de mesures par anémométrie à fil chaud et par PIV. L'objectif étant d'avoir une connaissance détaillée de l'écoulement étudié avant d'appliquer le contrôle.

La visualisation de la séparation par enduit gras confirme la localisation de la ligne de séparation au niveau de l'articulation du volet. De plus, la zone de recirculation est plus ou moins 2D sur 70% de l'envergure de la maquette (les effets de bord atteignent environ 30 centimètres sur chaque paroi latérale de la soufflerie).

Ensuite, cinq profils de vitesse longitudinale ont été réalisés par anémométrie à fils chaud afin de connaître précisément les caractéristiques de la couche limite sur la plaque plane. Une attention particulière a été portée à la précision des mesures afin d'obtenir une base de données de bonne qualité. L'incertitude sur la vitesse moyenne est inférieure à $\pm 1\%$ de la valeur locale et inférieure à $\pm 2.8\%$, $\pm 7.2\%$ et $\pm 5.2\%$ sur l'intensité turbulente, le moment d'ordre 3 et le moment d'ordre 4 respectivement. Néanmoins, la longueur du fil chaud utilisé (15 unités de paroi) était légèrement trop importante par rapport à la valeur conseillée par Klewicki and Falco (1990), ce qui conduit à sous estimer le pic de turbulente de proche paroi.

La couche limite étudiée à une épaisseur de l'ordre de 20 cm et un nombre de Reynolds basé sur l'épaisseur de quantité de mouvement d'environ 11 500. Le facteur de forme, quant à lui, est de l'ordre de 1.21. La vitesse de frottement pariétal a été déterminée par la méthode développée par Clauser (1956). Afin d'améliorer l'ajustement de la loi logatithmique sur le profil de vitesse dans les zones de gradient de pression adverse, une loi logarithmique modifiée a été introduite. Néanmoins, cette nouvelle fonction n'améliore que très légèrement les résultats. Le gradient de pression dans la zone stabilisée est légèrement adverse ($\left(\frac{\partial P}{\partial s}\right)^+ = 0.0005$ ou $\beta_{Clauser} = 0.3$). Finalement, cette couche limite est en équilibre au sens défini par Castillo and George (2001) mais pas au sens défini par Clauser (1954).

En plus du pic habituel proche paroi, les profils d'intensité turbulente comportent un pic secondaire accompagné par un point d'inflexion. Ce point d'inflexion restant à la même position par rapport à la paroi ($y^+ = 2000$), il a été attribué à l'intensité turbulente externe de la couche limite amont, qui a été fortement atténuée dans la partie convergente de la maquette par le gradient de pression favorable rencontré. Le pic secondaire est quant à lui attribué à une instabilité générée par le changement de signe du gradient de pression vers la fin de la partie convergente. Cependant, l'interprétation de Baskaran et al. (1987), Webster et al. (1996), Wu and Squires (1998), etc. de ce pic secondaire et de ce point d'inflexion comme une nouvelle couche interne déclenchée par le changement de courbure est tout aussi pertinente. Cette instabilité se retrouve dans les profils des moments d'ordre 3 et 4 et dans les profils des coefficients de dissymétrie et d'aplatissement par un minimum ou maximum local.

Pour compléter la caractérisation de l'écoulement, des mesures par PIV 2D2C selon un plan longitudinal à l'écoulement et englobant toute la zone de séparation ont été réalisées avec 4 caméras $2048 * 2048\ px^2$. Une zone commune entre 2 caméras a permis d'obtenir un champ continu de ces 4 dispositifs de PIV. Ces zones communes ont aussi été utilisées pour évaluer la précision de la mesure. Le champ de vitesse obtenu a une taille d'environ 94 cm le long de la paroi et 28.7 cm dans la direction normale à celle-ci. Le nombre de vecteurs est de 642 par 188, ce qui

conduit à une résolution de 45 unités de paroi (avec u_τ pris à la station numéro 5 des profils de vitesse à fil chaud). Au total, 5 000 champs ont été enregistrés pour obtenir une incertitude sur la vitesse moyenne de moins de $\pm 1\%$ de U_∞ ($= 10\ m/s$), et sur l'intensité turbulente de moins de $\pm 0.8\%$ de cette même vitesse de référence. L'incertitude sur ces grandeurs est plus importante à proximité de la paroi, à cause d'un gradient de vitesse moyen plus important. Elle vaut $\pm 4\%$ et $\pm 3\%$ de U_∞ respectivement. Ces incertitudes ont été validées par une bonne superposition des profils de vitesse moyenne obtenus par anémométrie à fil chaud et par PIV.

La frontière de la bulle de recirculation a été détectée par les deux critères défini par Simpson (1989), le premier étant $U = 0$, avec U la vitesse moyenne locale, le second étant $\chi = 0.5$, avec χ le rapport entre le temps où l'écoulement est dans le sens inverse et le temps total. Les études de Dengel and Fernholz (1990) et de Lögdberg et al. (2010) nous ont permis de compléter le second critère par une extrapolation linéaire du coefficient χ à la paroi où, au minimum, les deux points les plus proches de la paroi dans la direction normale à celle-ci présentaient un coefficient χ supérieur à 0.3. Ce second critère a été jugé plus pertinent pour obtenir les caractéristiques de la séparation. Il donne une ligne de séparation proche de l'articulation du volet en très bon accord avec la visualisation par enduit gras, une longueur de séparation de 61 cm (soit $\frac{L_{sep}}{H_{step}} = 3.5$, avec $H_{step} = 17.5$ cm, la hauteur de la " marche " descendante de la maquette définie sur la Figure 1), et une hauteur maximum de la bulle de recirculation de 3 cm (soit $\frac{H_{sep}}{H_{step}} = 0.17$). Cette longueur de séparation est plus importante que celle obtenue par Lin (1999) et Selby et al. (1992) ($\frac{L_{sep}}{H_{step}} \simeq 1.3$) pour une configuration assez similaire et pour un nombre de Reynolds basé sur l'épaisseur de quantité de mouvement assez proche. Cette différence s'explique par le fait que l'épaisseur de quantité de mouvement θ est ici beaucoup plus importante que dans les études de Lin (1999) et Selby et al. (1992) (Simpson (1989) a noté que la longueur de séparation augmente avec θ pour une marche descendante).

L'incapacité de l'écoulement à suivre le changement brutal de pente de la paroi imposé à l'articulation du volet a été constaté. Ceci se traduit par des vitesses normales à la paroi positives dans la région proche du point de séparation et par la création d'une couche de cisaillement au dessus du volet. Cette dernière génère une zone d'intensité turbulente (longitudinale, normale et croisée) très importante au dessus de la bulle de recirculation. Cette région s'accroît dans la direction normale à la paroi avec X, la position longitudinale. Cependant, le pic de chacune des composantes du tenseur de Reynolds mesurée reste dans l'intervalle $0.1 \leq \frac{y}{H_{step}} \leq 0.6$, avec y la distance à la paroi dans la direction normale à celle-ci. A chaque position longitudinale, le pic de la composante longitudinale $\overline{u'^2}$ est plus éloigné de la paroi que celui de la composante normale $\overline{v'^2}$. La région de forte intensité turbulente longitudinale est en relation étroite avec des structures de très grandes échelles, caractérisées par de fortes fluctuations longitudinales (u').

La production de la contrainte de Reynolds longitudinale sur le volet est la principale source d'énergie cinétique turbulente. Cette production est très intense au dessus de la bulle de recirculation mais elle se décompose en deux régions distinctes : une au début du volet et une autre qui commence vers le milieu de la zone de séparation (i.e. vers $X = 3.8$ m) et qui s'étend au-delà du champ de mesure. La première

région dû à la forte décélération de l'écoulement est dominée par le terme $-\overline{u'^2}\frac{\partial U}{\partial x}$. La seconde est dominée par le terme $-\overline{u'v'}\frac{\partial U}{\partial y}$ comme pour une couche limite 2D en gradient de pression nul. Cette région est probablement générée par le mouvement de battement dans la direction normale à la paroi des structures à grandes échelles (caractérisées par de fortes valeurs de u') qui induit de fortes valeurs de v' et donc de $\overline{u'v'}$. La production de $\overline{v'^2}$ est négative sur la première partie du volet et négligeable dans le reste du plan de mesure. Comme $\overline{v'^2}$ augmente avec X, une redistribution de $\overline{u'^2}$ vers $\overline{v'^2}$ est supposée pour expliquer cette augmentation. Concernant $-\overline{u'v'}$, sa production est dominée par $-\overline{v'^2}\frac{\partial U}{\partial y}$, ce qui explique la forte similitude observée entre la distribution de cette contrainte de Reynolds et $\overline{v'^2}$. Finalement, dans la partie aval du volet, l'organisation de la production de turbulence est très similaire à celle d'une couche limite 2D en gradient de pression nul, néanmoins elle est plus éloignée de la paroi.

La récupération de la couche limite en aval de la séparation s'est avérée être très rapide pour le profil de vitesse moyenne mais beaucoup plus lente pour les profils des contraintes de Reynolds. A l'extrémité aval du champ de mesure, une zone logarithmique est observée, mais la couche limite reste très déstabilisée avec un facteur de forme de 2.2.

Une fois l'écoulement caractérisé en détail, des stratégies de contrôle passif ont été testées, premièrement pour construire des outils de quantification des effets du contrôle, et deuxièmement pour déterminer les configurations optimales. Les générateurs de vortex utilisés étaient des plaques fines triangulaires similaire à celle utilisées par Godard and Stanislas (2006a). La quantification des effets de contrôle a été effectuée à l'aide de visualisations aux fils de laine sur tout le volet et de quatre sondes de frottement. Le gain en frottement donné par les sondes a été jugé insuffisant pour caractériser le recollement, car elles sont insensibles au sens de l'écoulement. Le facteur de dissymétrie S de la sortie en volt donnée par les sondes est, quant à lui, adapté pour quantifier les résultats de contrôle. Pour $S < -0.7$, l'écoulement est détaché, pour $S > -0.4$, il est complètement rattaché. Les visualisations aux fils de laine ainsi que les gains en frottement et en facteur de dissymétrie fournis par les sondes ont donc été utilisés pour quantifier les résultats de contrôle.

Deux configurations : co- et contrarotative ont été testées. Les paramètres utilisés pour débuter l'optimisation étaient ceux trouvés par Godard and Stanislas (2006a). En accord avec les études précédentes de Betterton et al. (2000) et de Godard and Stanislas (2006a), les configurations contrarotatives ont permis d'aboutir à de meilleurs résultats et sont les seules capables de supprimer totalement la séparation. Les configurations co-rotatives ont seulement réduit et repoussé la bulle de séparation. Les meilleurs paramètres déterminés sont regroupés dans la Table 1. Les paramètres les plus optimaux y figurent en gras.

Après les tests des actionneurs passifs, des actionneurs à jet continu ont été testés et optimisés. Là encore, les paramètres utilisés pour débuter l'optimisation étaient ceux trouvés par Godard and Stanislas (2006b) et les configurations co- et contrarotatives ont été étudiées. Avant de commencer les tests, un circuit d'air comprimé alimentant les jets a été réalisé. Il permet de régler et de mesurer le débit massique à moins de $\pm 2\%$ sur une gamme variant de 2 kg/h à 4800 kg/h.

Deux diamètres de jet ont été retenus : $\Phi = 6$ et 12 mm, et les deux sens de

TABLE 1 – Paramètres optimaux pour les configurations passives co et contrarotatives testées.

	β	$\frac{h}{\delta}$	$\frac{l}{h}$	$\frac{L}{h}$	$\frac{\lambda}{h}$	$\frac{\Delta X_{vg}}{h}$
co-rotative	18°	0.08 - **0.15**	2	-	6	8
contrarotative	±18°	**0.08** - 0.15	2	2.5	6	8

soufflage (vers l'amont et vers l'aval) ont été testés. Certaine des configurations sélectionnées ont supprimé complètement la séparation. Le VR minimum pour détecter des effets du contrôle est de 1.5. En accord avec les études précédentes de Godard and Stanislas (2006b), Betterton et al. (2000), Tilmann et al. (2000), McManus et al. (1994), Selby et al. (1992), etc., pour les configurations co- et contrarotatives en soufflage vers l'amont, l'efficacité du contrôle augmente continûment avec VR. En soufflage vers l'aval, ce n'est pas le cas. Il y a un optimum pour VR entre 1.5 et 2.5, ce qui n'a pas vraiment été observé dans la littérature. Les configurations optimales en soufflage aval réussissent donc à rattacher l'écoulement à un VR plus faible que celles à soufflage amont.

Le plus petit diamètre testé a donné de meilleurs résultats, ce qui est une bonne chose pour des applications réelles où le débit massique est l'un des paramètres critiques. Finalement, les deux distances testées entre les générateurs de vortex et la ligne de séparation (ΔX_{vg}) n'ont pas permis de mettre en évidence un effet de ce paramètre, certainement parce qu'elles sont toutes deux trop proches de la ligne de séparation.

Les meilleurs paramètres obtenus sont regroupés dans la Table 2. Les paramètres les plus optimaux y figurent en gras.

TABLE 2 – Paramètres optimaux pour les configurations actives co et contrarotatives testées.

	$\frac{\Phi}{\delta}$	β	α	$\frac{\lambda}{\Phi}$	$\frac{L}{\Phi}$	VR
co-rotative	0.03	35	55	13.6	-	2
	0.03	35	**125**	13.6	-	3.5
contrarotative	0.03	35	55	27.3	15	2
	0.03	35	**125**	27.3	15	3.5

À diamètre de jet constant, les configurations optimales co- et contrarotatives ont le même nombre de jets. La configuration co-rotative optimale pour $\Phi = 12$ mm donne un meilleur résultat que la contrarotative correspondante. Le contraire est obtenu pour les configurations avec $\Phi = 6$ mm. Comme le plus petit diamètre testé donne de meilleurs résultats, la meilleure configuration trouvée est la contrarotative avec $\frac{\Phi}{\delta} = 0.03$, $\frac{\lambda}{\Phi} = 27.3$, $\frac{L}{\Phi} = 15$ et $\alpha = 125°$ (i.e. soufflage amont).

Finalement, les actionneurs actifs et passifs ont été comparés. En accord avec Godard and Stanislas (2006b), les configurations passives co-rotatives se comportent

très différemment des actives co-rotatives : seules certaines des configurations actives optimales ont réussit à supprimer la séparation et, pour les passives, le paramètre optimal pour $\frac{\lambda}{\delta}$ est 0.9 tandis qu'il est environ deux fois plus petit pour les configurations actives. Cette différence peut certainement s'expliquer par une différence dans la physique de la génération des vortex.

En ce qui concerne les contrarotatives, là aussi, en accord avec Godard and Stanislas (2006b), les configurations actives et passives semblent se comporter d'une manière assez similaire. En effet, pour les actives, la valeur optimale pour $\frac{\lambda}{\delta}$ est entre 0.5 et 0.9 et pour $\frac{L}{\delta}$ entre 0.2 et 0.38. Pour les passives, la valeur optimale pour $\frac{\lambda}{\delta}$ est de 0.8 et pour $\frac{L}{\delta}$ entre 0.36 et 0.48. La proximité des valeurs optimales de ces paramètres pour ces deux stratégies de contrôle peut expliquer pourquoi elles donnent des résultats similaires. Comme espéré, cette étude a montré que les configurations actives à jet continu peuvent bien remplacer les passives sur des applications réelles. Elle a aussi montré que les configurations contrarotatives sont légèrement meilleures que les co-rotatives.

Finalement, pour obtenir une meilleure compréhension de la physique de certaines configurations actives optimales, une caractérisation plus poussée de l'écoulement a été réalisée avec des mesures de répartition longitudinale de pression et par PIV sur tout le volet (i.e. avec le même système PIV qui a été utilisé pour caractériser la séparation). Les configurations qui ont été sélectionnées sont les optimales avec $\Phi = 6$ mm à la position $s = 3219$ mm. Les deux sens de soufflage ainsi que les deux types d'organisation des actionneurs ont été testés.

Pour les mesures de distributions de pression, les VR testés correspondent à une valeur proche de l'optimum et à certaines valeurs en dehors de la gamme optimale. Pour les mesures par PIV, seul la valeur optimale a été testée (i.e. 3.5 pour le soufflage amont et 2.5 pour le soufflage aval).

La valeur minimale de VR pour détecter des effets de contrôle est confirmée par les distributions de pression (i.e. entre 1.5 et 2). Cependant, la valeur optimale de VR (2.5) pour les configurations en soufflage vers l'aval, n'est pas confirmée. Ceci est certainement dû à un manque d'information sur la répartition de pression transverse. Les configurations co- et contrarotatives en soufflage amont ont une répartition longitudinale de pression très similaire. La même conclusion est aussi vraie pour les configurations en soufflage aval. Ceci semble contredire les conclusions évoquées plus haut (i.e. les configurations contrarotatives sont meilleures que les co). Là encore, ceci peut provenir du manque d'information sur la répartition de pression transverse. Finalement, le pic d'aspiration des configurations à soufflage amont est légèrement plus large, ce qui indique qu'elles donnent un meilleur résultat.

En ce qui concerne les mesures par PIV, la configuration co-rotative en soufflage aval n'a pas été testée pour réduire la quantité de données à traiter. Pour la configuration co-rotative étudiée (soufflage amont), le plan de mesure était au milieu de deux jets. Il correspond à une zone de soulèvement de l'écoulement par les vortex. Le profil de vitesse moyenne longitudinale à la station 5 du fil chaud est en forme de " S " proche de la paroi, ce qui est en accord avec les résultats obtenus par McManus et al. (1994), Godard and Stanislas (2006b) et Kostas et al. (2007). Ce " S " introduit un point d'inflexion dans le profil à $\frac{y}{\delta} = 0.23$, qui correspond à la position du pic dans le profil de la contrainte de Reynolds $-\overline{u'v'}$. La pénétration

des jets dans la couche limite est estimée à $\frac{y}{\delta} = 0.3$. Cette configuration de contrôle augmente l'intensité turbulente en amont de l'articulation du volet pour réorganiser l'écoulement moyen afin d'atteindre son objectif. Cependant cette configuration présente une petite zone de séparation aux alentours de $X = 3.8$ m, détectée par $\chi = 0.5$.

Le plan de mesure pour les configurations contrarotatives testées était au milieu de deux paires de jets. Il correspond à une zone de rabattement de l'écoulement vers la paroi. En accord avec l'étude de Godard and Stanislas (2006b), aucune forme en " S " dans les profils de vitesse moyenne longitudinale à la station 5 du fil chaud n'est observée. La pénétration des jets dans la couche limite est estimée à $\frac{y}{\delta} = 0.2$, ce qui est légèrement plus faible que dans le cas co-rotatif. Pour les deux configurations contrarotatives retenues, l'intensité turbulente est réduite en amont du volet en raison du rabattement de l'écoulement vers la paroi. Ces cas de contrôle ramènent donc l'écoulement externe avec un taux de turbulence faible vers la paroi, ce qui donne l'efficacité du contrôle. Aucune séparation n'est détectée pour ces deux configurations et des vitesses plus importantes à proximité de la paroi sont observées par rapport aux configurations co-rotative et non contrôlée.

Pour les trois configurations de contrôle actif retenues, l'intensité turbulente longitudinale est largement réduite sur le volet par rapport au cas sans contrôle. Cette diminution est causée par une réduction de la taille des structures de grandes échelles caractérisées par de fortes valeurs de u'. Le VR optimum trouvé pour les configurations à soufflage vers l'aval (i.e. 2.5) a aussi été confirmé par ces mesures car pour la configuration contrarotative à soufflage aval testée, ces structures réapparaissent pour des VR à partir de 2.5.

L'intensité turbulente normale à la paroi ainsi que la contrainte de Reynolds $-\overline{u'v'}$ sont aussi fortement réduites sur le volet. Comme pour le cas sans contrôle, une forte similitude entre les distributions de ces deux quantités est observée pour ces trois cas de contrôle. Ceci s'explique aussi par le fait que dans chacun des cas, la production du second est dominée par le terme $\overline{v'^2}\frac{\partial U}{\partial y}$.

Finalement, excepté proche et en amont de l'articulation du volet pour le cas co-rotatif, pour chaque cas de contrôle retenu, chacune des composantes mesurées du tenseur de Reynolds se comporte similairement à celle de l'écoulement sans contrôle. Cependant la région de haute valeur est plus ou moins plaquée contre la paroi et réduite en intensité. Chaque configuration testée n'a donc pas modifié la physique de l'écoulement car la couche de cisaillement n'est pas totalement supprimée. Elle réduit seulement son intensité et la comprime plus ou moins contre la paroi. Ceci est également confirmé par les termes de production turbulente qui se comportent comme les composantes du tenseur des Reynolds pour les trois cas de contrôle sélectionnés.

A la fin du champ de vitesse obtenu par PIV, pour les trois configurations de contrôle retenues, les profils de vitesse moyenne longitudinale ne présentent pas une loi logarithmique standard mais une loi logarithmique avec une pente fortement diminuée. Ceci est certainement dû à une persistance, à la fin du champ de mesure, des vortex générés par le contrôle. Cette persistance est fortement marquée pour les deux cas contrarotatifs qui présentent un fort rabattement de l'écoulement vers la paroi à l'extrémité du champ. Le contrôle appliqué pourrait donc être trop intense.

En conclusion générale, cette étude apporte un éclairage nouveau sur la réorganisation de l'écoulement consécutive au contrôle actif au moyen de jet continu. En particulier, elle comporte une caractérisation détaillée de l'écoulement avec et sans contrôle. Une optimisation des actionneurs a été effectuée dans le but de les mettre en oeuvre sur des applications réelles. Les stratégies de contrôle retenues qui induisent des vortex longitudinaux, ne suppriment pas les mécanismes de la séparation. Selon la configuration de jets choisie et l'intensité du contrôle, elles les plaquent plus ou moins contre la paroi et réduisent leur intensité. Les instabilités de l'écoulement peuvent alors persister, et un contrôle très fort doit être appliqué (VR de l'ordre de 3) pour empêcher leur développement. Ceci pourrait être problématique pour des applications réelles (des avions par exemple). D'autres études apparaissent alors nécessaires pour améliorer les actionneurs. Une piste pourrait être de réduire le diamètre des jets et de les pulser. Des actionneurs basés sur des vortex transverses pourraient aussi être envisagés car ils agissent directement sur les mécanismes de production de la vorticité transverse. Cependant il n'est pas certain qu'ils donnent de meilleurs résultats car Lin (2002) a prouvé que ce type d'actionneur, mais passif, donne de moins bon résultats que ceux basés sur la génération de vortex longitudinaux.

Contrôle actif du décollement d'une couche limite turbulente en gradient de pression adverse

Le contrôle d'écoulement permet d'éliminer le phénomène de décollement de couches limites, très néfaste pour les performances des machines interagissant avec un fluide (avions, voitures, turbomachines ...). Ces travaux s'intéressent plus particulièrement au contrôle actif d'écoulement au moyen de jets continus. Une maquette permettant de manipuler l'équilibre de la couche limite a été conçue et installée dans la soufflerie du Laboratoire de Mécanique de Lille. La première partie du travail a consisté en la caractérisation de l'écoulement autour du modèle à l'aide de visualisations par fils de laine et par enduit gras, de mesures de répartition de pression, de mesures par anémométrie à fils chauds et par PIV. Ceci a permis de définir la configuration du modèle la plus appropriée pour les études de contrôle mais aussi de connaître précisément les caractéristiques de l'écoulement sélectionné. La configuration retenue correspond à un écoulement en gradient de pression adverse suivi d'une séparation sur le volet, un peu comme sur l'extrados d'une aile d'avion. L'utilisation de sondes de frottement associées à des visualisations aux fils de laine ont permis d'étudier et d'optimiser des actionneurs passifs, puis des actionneurs à jets continus. Certaines des configurations actives optimales ont ensuite été caractérisées plus en détail par une mesure par PIV englobant toute la zone de séparation. Il apparaît que les jets continus ne suppriment pas complètement les mécanismes de la séparation mais réduisent leur intensité et les concentrent plus ou moins près de la paroi.

Mots-clés : couche limite, turbulence, gradient de pression adverse, PIV, contrôle d'écoulements, décollement, générateurs de vortex

Active control of a separated turbulent boundary layer in adverse pressure gradient

Flow control allows to suppress boundary layers separation, which largely deteriorates the performances of machineries which interact with fluid (aircraft, cars, turbomachineries, etc.). This study concentrates more particularly on active flow control with continuous jets. A ramp model which allows to manipulate the boundary layer equilibrium was realized and set in Laboratoire de Mécanique de Lille wind tunnel. The first part of the work was to characterize the flow over the model with wool-tufts and oil-film visualisations, pressure distribution, hot-wire anemometry and PIV measurements. The aim was to define a ramp configuration for the flow control study and to know precisely the characteristics of the retained flow. The selected configuration corresponds to an adverse pressure gradient flow followed by a separation on the flap, which mimics the flow on the suction side of a wing. With friction probes coupled with wool-tufts visualisations, passive actuators and active continuous jets were studied and optimised. Finally, some of the optimum active configurations found were characterized in more details with PIV measurements over the entire separated region. It appears that continuous jets do not suppress the separation mechanisms, but only reduce their intensity and squeeze them more or less against the wall.

Keywords : Boundary layer, turbulence, adverse pressure gradient, PIV, flow control, flow separation, vortex generators